PET/MRI in Oncology

Current Clinical Applications

Andrei Iagaru
Thomas Hope
Patrick Veit-Haibach

Editors

🐎 Springer

PET/MRI in Oncology

Andrei Iagaru • Thomas Hope
Patrick Veit-Haibach

Editors

PET/MRI in Oncology

Current Clinical Applications

Springer

Editors
Andrei Iagaru
Division of Nuclear Medicine and
Molecular Imaging
Stanford University
Stanford, California, USA

Thomas Hope
Radiology and Biomedical Imaging
University of California, San Francisco
San Francisco, California, USA

Patrick Veit-Haibach
Dept. of Nuclear Medicine
University of Zurich
Zurich, Switzerland

Foreword

Biomedical imaging has continued to rapidly evolve over the last few decades. One of the most important technologies that we now have in our toolbox is positron emission tomography combined with magnetic resonance imaging (PET-MRI). This book is a timely and important resource for those wanting to understand the fundamental building blocks of PET-MRI technology and exciting emerging clinical applications. I want to commend the editors for their hard efforts in putting together a truly important, well-written, and timely resource. Leaders from around the world have come together to help any imaging scientist or physician understand many key aspects of PET-MRI. Each chapter has been well written to provide succinct informative details. Highly useful figures along with the latest references for each chapter should make this a very useful book for readers with diverse backgrounds. Comparisons to PET combined with computed tomography (PET-CT) are made throughout and are important to understand. Issues related to quantitation are also covered and will be important if PET-MRI is to be truly standardized and results made comparable in the same patient over time and across patients. I think you will enjoy reading it as well as having it around as a useful resource for future reference. Although the killer applications of PET-MRI continue to be actively explored and are yet to emerge, I am confident that PET-MRI will be around to stay for many decades to come. Progress often appears slow in the early years of any technology, but then rapidly accelerates as a solid foundation is built and more investigators have the technology available to them. I am optimistic that we will see acceleration of the use of PET-MRI in multiple clinical applications in the years to come. We should insist on rigorous studies to prove the utility and cost-effectiveness of PET-MRI and not let the field stagnate by poorly designed single-institution studies. Furthermore, we should not be impatient as killer applications will take some time to emerge and validated. This book should be a terrific new resource for the biomedical imaging community and should help educate an entire new generation of trainees for whom PET-MRI should play an increasing role in the daily management of patients.

Stanford, CA, USA   Sanjiv Sam Gambhir, MD, PhD

Contents

About the Editor

Andrei Iagaru is an Associate Professor of Radiology—Nuclear Medicine and the Chief of the Division of Nuclear Medicine and Molecular Imaging at Stanford University Medical Center. He completed medical school at Carol Davila University of Medicine, Bucharest, Romania, and an internship at Drexel University College of Medicine, Graduate Hospital, in the Department of Medicine in Philadelphia. He began his residency at the University of Southern California (USC) Keck School of Medicine, Los Angeles, in the Division of Nuclear Medicine, where he was the chief resident. Dr. Iagaru finished his residency and completed a PET/CT fellowship at Stanford University's School of Medicine in the Division of Nuclear Medicine. His research interests include PET/MRI and PET/CT for early cancer detection, clinical translation of novel PET radiopharmaceuticals, peptide-based diagnostic imaging and therapy, and targeted radionuclide therapy.Over the past ten years since joining the faculty at Stanford, Dr. Iagaru has received several awards including the Society of Nuclear Medicine (SNM) 2009 Image of the Year Award; American College of Nuclear Medicine (ACNM) Mid-Winter Conference 2010 Best Essay Award; 2009, 2014, and 2015 Western Regional SNM Scientist Award; 2011 SNM Nuclear Oncology Council Young Investigator Award; and a Stanford Cancer Center 2009 Developmental Cancer Research Award in Translational Science. Dr. Iagaru presented more than 150 abstracts at national and international meetings and published more than 110 papers in peer-reviewed journals, as well as seven book chapters.

PET System Technology Designs for Achieving Simultaneous PET/MRI

Brian J. Lee, Chen-Ming Chang, and Craig S. Levin

Contents

B.J. Lee • C.-M. Chang
Department of Radiology, Stanford University, Stanford, CA, USA
e-mail: dl-wns87@stanford.edu; ming1116@stanford.edu

C.S. Levin (✉)
Departments of Radiology, Physics, Electrical Engineering and Bioengineering,
Stanford University, Stanford, CA, USA
e-mail: cslevin@stanford.edu

1.1   Introduction to MRI-Compatible PET System Technology

Most of the technical developments of combining emission and x-ray tomography began in the 1990s; the first multimodality scanner combining positron emission tomography (PET) and computed tomography (CT) sequentially was introduced to the medical imaging community in 1991 [1, 2].

Despite the software co-registration issues, limited soft tissue contrast, higher radiation dose (over 10 mSv), and significantly higher cost of the integrated PET/CT system, the stand-alone PET system disappeared in about a 4-year period after the first PET/CT system was introduced [3]. Even though integrating PET and magnetic resonance imaging (MRI) was suggested earlier in the early mid-1990s [4], it was the successes as well as limitations of PET/CT that further motivated the integration of PET with MRI. It took about 15 years of research and development to arrive at the first commercially available whole-body simultaneous PET/MRI system [5–8]. The main reason for this slow development progress is due to a very complicated, and hence costly, integration process.

There have been several attempts to combine MRI and PET for preclinical and clinical applications from research groups and industry [5–25]. The combination of MRI and PET has proven to be very challenging due to the mutual interference between the two subsystems affecting each other's performance [26–28]. The extremely complicated and high-power electromagnetic fields emitted from the MR scanner exclude the use of standard photomultiplier tubes (PMT), add noise in the readout electronics, and induce eddy currents on conductive metal surfaces and traces employed to shield and read out the detector, and the presence of conductors and electrical signals from the PET system can distort and attenuate the B_0 and B_1 and gradient fields of the MR system. Even though the challenges of integrating PET and MRI are significant, there are some advantages of PET/MRI over PET/CT [29–31]. MRI is more versatile in some aspects than CT due to its wide range of contrast mechanisms available through a variety of imaging pulse sequences [32]. MRI also boasts superior contrast in soft tissue regions of the body [33]. The spatially and temporally co-registered MRI data can be used to improve the quality and accuracy of the PET data [29–31]. Also, the total delivered ionizing radiation dose can be reduced significantly for PET/MRI compared to PET/CT, as no dose is generated by MRI.

There are different options for a PET/MRI system configuration [34–36]. The least complicated approach to integrate PET and MRI is to place them in-line, allowing for sequential acquisition in a similar manner as for PET/CT; since this approach does not allow simultaneous acquisition, it leads to potential image co-registration issues, as well as lengthy acquisition times. However, "full" integration, possible only through placing the PET inside the MRI system, is an attractive alternative configuration as it enables simultaneous PET and MRI acquisition, resulting in shorter acquisition times comparable to MRI acquisition and better spatial and temporal co-registration compared to the sequential acquisition.

More detail on promising clinical applications of integrated PET/MR are introduced in other chapters. Besides the clinical potentials, there is also a large research potential for PET/MRI [31]. There is potential for a new generation of unique functional studies

as MRI is not limited to anatomical imaging [37, 38]. Dynamic processes in the body can be investigated and quantified [38], and new PET/MRI multimodality tracers can be explored as well to provide multiparameter characterization of disease [31].

In this chapter, we describe some important issues and choices involved in PET/ MRI system design and technology. We discuss the advantages and limitations of the available configurations, giving the reader an overview of the different setups investigated by the various groups working on PET/MRI system prototypes.

1.2 Electromagnetic Interference

Even though the combination of MRI and PET provides complementary anatomical, functional, and molecular information, by nature, they are physically incompatible. Thus, there are technical challenges due to the potential mutual interference with each other's performance [26–28]. As discussed in the last section, the intense static magnetic field, rapidly oscillating gradient fields, and high-power RF pulses from the MRI scanner may interact with the PET component and the conductive materials and signals created in the PET system may interfere with the MRI component of a simultaneous PET/MRI system.

Given the many potential sources of mutual interference inherent to the fully integrated approach, great attention is paid to all aspects of MRI compatibility of PET detector components, including the selection and production of non-ferromagnetic components, Faraday shielding considerations, differential signal processing for analog detector signals, readout circuit layout to avoid eddy currents and heating, and minimizing RF emissions from power supplies. This section is intended to provide an overview of technical features and challenges associated with combining PET and MRI.

1.2.1 Magnetic Susceptibility

MRI consists of a powerful static magnetic field (B_0) to align the magnetic moments of atomic nuclei. Magnetic susceptibility artifacts refer to a variety of MRI artifacts that share distortions or local signal change due to local magnetic field inhomogeneities from a variety of materials that may be present inside the MR system bore. Since MR image quality is strongly dependent on the uniformity of the static magnetic field [39], materials with high susceptibility should be either avoided or placed as far from the field of view (FOV) as possible.

As the PET is placed inside the MRI bore, concerns rise regarding the PET components affecting the magnetic field uniformity and MR image quality. When the PET and MR systems are apart from each other, as they are in sequential PET/MRI systems, the magnetic susceptibility is a minor issue. However, for fully integrated PET/MRI or a PET insert configuration, where the PET detectors are located inside the MRI bore, there is a higher risk of distorting the magnetic field or gradients.

Materials with high magnetic susceptibility need to be avoided in the PET detectors and electronics designs, especially when placed closer to the center of the MRI bore. Even with careful design, some degree of field distortion is inevitable, but

minor distortions could be corrected effectively by shimming, which is an MR system calibration process to make the main magnetic field more homogeneous. In passive shimming, small pieces of sheet metal or ferromagnetic pellets are placed to correct for the distorted field, and in active shimming, currents are controlled in a specialized coil for further improvement in the field homogeneity.

Although the static magnetic field mostly constrains the PET component selection, there is a benefit of high static field for the PET resolution performance. Due to the Lorentz force, the positron range or the maximum distance that the positively charged positron travels before the annihilation inside a strong magnetic field is reduced in the direction orthogonal to MRI system axis [30]. The reduced positron range thus improves the PET spatial resolution in that transaxial direction.

1.2.2   Shielding Effectiveness

Any electronics within the magnet bore may be susceptible to MRI RF interference. The electronic cross talks between the modalities are potential sources of image artifacts and general performance degradation to both systems [27, 40].

In the MRI system, the gradient fields are in the order of 10^2–10^3 Hz, and the RF pulses are at the Larmor frequency (42.58 MHz/Tesla for protons) and subsequent harmonics, which are the integer multiples of the fundamental frequency. These intense RF excitation pulses and switching gradient fields can add unwanted signals in the PET front-end electronics. Furthermore, high frequency signals from the PET electronics, such as clock signals or other sources of high frequency noise, can be emitted and picked up by the sensitive MR acquisition system. Therefore, great care must be taken with electronic circuit layouts, component choices, and RF shielding designs in order to mitigate the interferences between PET and MRI.

Besides appropriate RF shielding to prevent the intense time-varying fields of the MRI system from interfering with the PET detector and vice versa, filter designs can be employed to avoid such interference; however, this could degrade the PET performance [41–43].

A design criterion of a shielding enclosure is the shielding effectiveness, which indicates the losses undergone by a signal going through it. The shielding effectiveness is primarily due to reflection and absorption properties of the shield, and copper and aluminum with high conductivities are great reflection shield materials, whereas mu-metal (a nickel-iron soft magnetic alloy) with very high magnetic permeability is excellent for absorption [44]. In addition, the skin depth, which is the depth at which the incident field magnitude drops to e^{-1}, needs to be considered [45]. The skin depth is inversely proportional to the square root of the electrical conductivity, the magnetic permeability, and the signal frequency.

Despite of the reflective and absorptive properties of the shielding designs, there are several constraints, such as the PET annihilation photon attenuation and the eddy current induction, that need to be considered. More discussions on these will be discussed in the following sections.

1.2.3   Eddy Current

Besides the static magnetic field and the RF field, the gradient system also is another main source of interference that needs to be considered when PET is within the MR system. A gradient system in MRI systems is usually built with high spatial linearity and fidelity as well as fast switching time. Gradient fields are switched rapidly at frequencies of the order 10^2–10^3 Hz. These rapidly switching magnetic fields at that frequency can induce eddy current loops in any conductive components introduced into the MRI bore, including the PET circuitry or the shielding structure. These undesirable eddy currents in the front-end circuit and conductive shielding structures add noise to the PET signals and, furthermore, can also lead to heating, mechanical vibrations, and secondary fields that can further affect PET performance [46].

Any non-ideal conductor (e.g., a metal) with electrical current flowing through it will be heated by Joule heating. This heating effect can cause discomfort or burn patients when they are in contact with conductive objects. In addition, the heating can degrade performance of temperature-sensitive electronic components. In the case of silicon photomultipliers (SiPMs) [70], a silicon-based photodetector, temperature variations shift the breakdown voltage, leading to a gain alteration, which then leads to variations in photon detection efficiency and dark counts. These consequences degrade the energy and coincidence time resolution of the PET detectors and result in reconstruction artifacts and quantification errors [47]. Several cooling approaches to stabilize the thermal variation of the detector system have been introduced as well [48–50].

In addition, the time-varying eddy currents induced in conductors that are placed within the static magnetic field cause mechanical vibrations due to the Lorentz force. The vibration amplifies with the magnetic flux density and the induced current magnitude. The dimensions and the properties of the coil will determine the frequency of the vibration modes [51, 52]. The significant mechanical vibration of the large metallic structures, such as the RF shielding of the PET detector, can lead to further instability of the PET performance.

Furthermore, secondary magnetic field is produced by an induced eddy current. This secondary magnetic field degrades the spatial and temporal performance of the primary field generated by the gradient coils. During specific RF sequences with intense gradient fields, the reconstructed images are distorted, and artifacts, such as the Nyquist ghosting artifact, are introduced to the reconstructed image [53, 54].

There are some methods to modify the shielding design to reduce these problematic eddy currents. The use of segmented or mesh structure, limiting the conductive loops along the shield surface, can alleviate this problem [55]. In addition, double-sided shielding designs with offset breaks could be used as well [56]. Furthermore, carbon fiber composite is an alternative shielding material with high conductivity at high frequencies (MHz range) to reflect the RF fields and high resistivity at low frequencies (kHz range) to impede the gradient-induced eddy currents [40, 57].

1.2.4   Annihilation Photon Attenuation

When the annihilation photons interact with different materials in the PET FOV, some photons are taken away from their original trajectory due to the Compton scatter interaction in those materials. This leads to significant loss in the number of detected photons in any given line of response (LOR) formed by two opposing detector elements in the PET detector ring, which exponentially decreases with the thickness and attenuation coefficients of the materials in which it traverses [58, 59]. This effect is referred to as "photon attenuation." Furthermore, another common problem in PET acquisition is when those Compton scattered photons that left their original LOR were detected by another detector pair, leading to an erroneous count placed in another LOR. This effect is known as "scatter background". These undesirable effects degrade the PET image signal-to-noise ratio (SNR) and accuracy.

Addressing these effects requires special correction algorithms to be applied during the image reconstruction. Different algorithms for PET photon attenuation correction and their implications will be discussed in Chap. 6. Methods for scatter correction may be found in references [92–101].

1.3   Signal Generation and Processing in PET

A typical signal generation and processing chain in a PET system is shown in Fig. 1.1. Five major components that constitute a typical PET system hardware are scintillators, photodetectors, front-end readout electronics, back-end data acquisition system, and a computer workstation to control the acquisition and image reconstruction. Since most photodetectors are transparent to the highly energetic (511 keV) annihilation photons emitted from the subject, scintillators are used to convert the high-energy annihilation photons to lower-energy photons in the ultraviolet and visible light range, which can then be detected by photodetectors. Photodetectors further convert these lower-energy photons into an electric current, which is relayed to the front-end readout electronics and data acquisition system, which amplify the signal and extract the energy, time (for coincidence detection), and position information from the signal. The energy, time, and position information are then sent to a workstation for image reconstruction to generate the PET images. In the following sections, further details on scintillators, photodetectors, and readout electronics will be given, with special attention paid to their applications in PET/MRI.
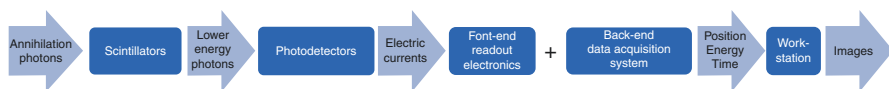
Fig. 1.1 Signal generation and processing in a typical PET system

Table 1.1 Properties of common inorganic scintillators used in PET

Properties	BGO[a]	LSO(Ce)[b]	GSO(Ce)[c]	LGSO(Ce)[d]	LaBr3 (Ce)[e]
Effective atomic number (Z)	73	66	59	59	47
Density (g/cm³)	7.1	7.4	6.7	7.2	5.3
Decay time (ns)	60/300 (fast/slow)	40	60/600 (fast/slow)	30–65	16–18
Photon yield (per keV)	8	20–30	12–15	25–35	61
Peak emission (nm)	480	420	430	420	360
Hygroscopic?	No	No	No	No	Yes
Magnetic susceptibility?	No	No	Yes	Yes	No

[a]Bismuth germanate ($Bi_4 Ge_3 O_{12}$)
[b]Cerium-doped lutetium oxyorthosilicate ($Lu_2 SiO_5$:Ce)
[c]Cerium-doped gadolinium orthosilicate ($Gd_2 SiO_5$:Ce)
[d]Cerium-doped lutetium-gadolinium orthosilicate ($Lu_x Gd_{2-x} SiO_5$:Ce)
[e]Cerium-doped lanthanum bromide ($LaBr_3$:Ce)

1.3.1 Scintillators

Scintillators are used to convert annihilation photons to lower-energy (visible light) photons, which can be detected by photodetectors. Characteristics of an ideal scintillator for PET applications include high effective atomic number (Z) and density (for higher probability to interact with annihilation photons), high light yield and short decay time (for good energy resolution and precise timing of the detection of annihilation photons), a light emission spectrum matching the absorption spectrum of the photodetectors, and non-hygroscopicity to simplify construction. Due to these desired characteristics, the most widely used scintillators in PET systems are inorganic scintillators [65]. Some important properties of common inorganic scintillators used in PET systems are summarized in Table 1.1.

Applications in PET/MRI In order to be compatible to MR systems, scintillators with magnetic materials should be avoided when possible. For example, GSO(Ce) and LGSO(Ce) contain gadolinium, which is commonly used in MRI contrast agents, and can distort the magnetic field, causing artifacts in MR images [66].

1.3.2 Photodetectors

Photodetectors are used to convert the scintillation light pulse into a detectable electrical signal. Two major groups of devices to detect scintillation light signals in PET are *PMTs* and solid-state photodetectors, which include *avalanche photodiodes (APDs)* and *SiPM*.

1.3.2.1 Photomultiplier Tubes
A PMT consists of a light entrance window, a photocathode coated at the inner side of the entrance window, a series of electrodes (dynodes), and an anode, which is

connected to readout electronics that integrate the resulting current [65]. All PMT components are housed in a vacuum-sealed glass enclosure. A positive voltage is applied to the anode relative to the photocathode, and each dynode is maintained at a higher potential than the previous one. When the scintillation photons strike the photocathode, electrons are liberated from the surface of the photocathode. These primary photoelectrons are focused and accelerated toward the first dynode due to the electric field established between the photocathode and the first dynode. These accelerated photoelectrons then strike the first dynode, which liberates more secondary electrons from it, which are accelerated toward the second dynode. The same process repeats through several dynode stages, creating an avalanche of electrons, which are collected at the anode and processed by the readout electronics. The electron multiplication process through several dynode stages leads to a high internal gain (10^6–10^7).

Applications in PET/MRI Since the electron multiplication process in a PMT depends on electron trajectories between electrodes, PMTs are highly sensitive to magnetic field due to the Lorentz force, which bends the path of the electrons. Therefore, PMTs cannot operate near a strong magnetic field and are generally considered not MRI compatible. However, some of the earliest PET systems for PET/MRI are constructed with PMTs [67, 68]. This requires using optical fibers to channel the light generated in the scintillators to PMTs placed away from the MRI system. More discussions on these systems will be given in Sect. 4.

1.3.2.2 Avalanche Photodiodes

An APD is a semiconductor photodetector device that consists of a reverse-biased n-p junction with depleted drift region and a high gain avalanche region. The avalanche region contains high doping concentrations, such that a large internal electric field is created within this region when the reverse bias is applied. Incident scintillation photons create electron-hole pairs at the surface of the device. The bias voltage applied to the device separates these charge carriers before they can recombine with each other, and the electrons drift into the high gain region of the device. As the electrons enter the avalanche region, the strong electric field accelerates the electrons to energies large enough to ionize Si atoms via impact ionization, creating secondary electrons that can further ionize more Si atoms, resulting in an avalanche of moving charge, which induces a large current on the electrodes. The reverse bias voltage is set below the breakdown voltage of the device such that the charge signal obtained is proportional to the original number of electron-hole pairs produced [28]. This avalanche process provides the internal gains of APDs, which are in the order of 10–1000. The gains of APDs are much lower than the gains of PMTs (10^6–10^7).

Therefore, the charge signal produced by APDs is more susceptible to the internal noise of the device and the amplification process, as well as external noise from the readout electronics and the ambient environment.

Applications in PET/MRI Unlike PMTs, APDs can be made very compact (few millimeters) compared to PMTs (few centimeters). Compactness is important in the

integration of PET with MRI, as PET system has to fit into a limited MRI bore size. In addition, in contrast to a PMT, in an APD device, the generation, multiplication, and collection of electrons occur within at most a few hundred μm as opposed to centimeters, making the signal generation in APDs much less sensitive to effects of the Lorentz force induced by a strong magnetic field. It has been shown that the performance of APDs is not affected by magnetic fields up to 9.4 T [23]. This allows the placement of APDs inside a MR system and therefore direct coupling between the scintillators and the APDs in order to achieve high scintillation light detection efficiency, preserving high detector signal SNR. An overview of some PET system designs for PET/MRI based on APDs will be given in Sect. 4.

1.3.2.3 Silicon Photomultiplier

SiPMs are semiconductor photon-counting devices consisting of many densely packed, electrically decoupled APD microcells (typical size 20–30 μm) placed on a common silicon substrate [70]. These APD microcells are biased at above their breakdown voltage so that they operate in Geiger mode (a scintillation photon that hits any microcell produces a Geiger discharge signal). Each microcell operates digitally as a binary device that generates a constant charge pulse when it is triggered, regardless of the number of triggering photons. Therefore, the energy information is lost in a single microcell but instead is determined by the number of microcells that are triggered by the flash of scintillation photons.

   Digital SiPMs (dSiPMs) are an evolution of the SiPM technology [71]. Instead of outputting an analog signal that represents the scintillation pulse, dSiPMs have digital electronics integrated with the SiPMs in the same chip that converts and outputs the position, energy, and time stamp information in the digital format.

Applications in PET/MRI SiPMs combine many advantages of APDs and PMTs. Like APDs, SiPMs are insensitive to strong magnetic field and compact in size, which allows SiPMs to be operated inside the MR bore and be directly coupled to scintillators for high detector SNR. Unlike APDs, SiPMs operate in Geiger mode and have high intrinsic gains (10^6–10^7) that are comparable to PMTs so the output signal is less susceptible to the intrinsic noise of the device and the noise from the readout electronics. The high SNR of the SiPM output allows precise timing of the scintillation pulse with extraordinary timing resolution [72], which enables advanced time-of-flight (ToF)-PET performance. As described in Sect. 3.3, ToF measurement can be used to enhance the image quality and accuracy in PET. Due to these favorable characteristics of SiPMs, most recent PET systems developed for PET/MRI are constructed with SiPMs [24, 73–78]. An overview of some of these systems will be given in Sect. 4.

1.3.3   Readout Electronics

Readout electronics is developed to amplify and process the electrical signal produced by the photodetectors and facilitate the recording of the energy, time, and position information of the scintillation event.

Energy The energy information of the scintillation pulse is used to select the events that fall into the 511 keV photopeak for further processing and reduce the number of photons that scatter in tissue before entering the detector. Commonly used methods to obtain energy of scintillation pulses include integrating the electrical current and detecting the pulse amplitude of scintillation pulses. More information on how to acquire energy information of a scintillation pulse can be found in [79].

Time The timing information of the scintillation pulse is used to collect pairs of coincident annihilation photons that originated from the same positron decay event and reduce the number of random (i.e., accidental) two-photon coincidences resulting from distinct positron decay events. A system capable of detecting coincident events with excellent coincidence time resolution (e.g., <400 ps FWHM, full width at half maximum) will have advance ToF-PET performance. ToF measurement can be used during image reconstruction to localize the placement of counts along any given LOR connecting a pair of opposing detector elements that detect an annihilation photon pair. This constraining of the annihilation event placement along an LOR increases the reconstructed image SNR and hence the effective system sensitivity. It also improves noise performance and accuracy of PET image reconstruction [80].

Position In a PET system design with one-to-one coupling between the scintillators, photodetectors, and readout channels, each readout channel corresponds to a unique scintillator. In some applications to achieve high spatial resolution (e.g., small animal systems) or to reduce the number of readout channels, multiplexing with light sharing in the scintillation crystal array or charge sharing in the photodetector readout is used. Common multiplexing schemes to map the position of the scintillators to the readout channels include Anger logic [81] and cross-strip [82]. Recently, a multiplexing scheme based on compressed sensing has been used in a PET detector system [83], promising better compromise between multiplexing ratio and detector SNR compared to other multiplexing schemes [84].

Applications in PET/MRI Readout electronics has to be carefully designed in order to maximize PET performance and minimize interference with the MR systems. At the system level, there is a trade-off regarding how much readout electronics to be placed within the MR system bore. Placing readout electronics as close to the photodetectors as possible to amplify or even digitize the signals immediately from the photodetectors preserves the detector SNR and hence the PET performance. However, placing more readout electronics within the MRI system increases the chance to interfere with the MRI system. Moreover, the size of the MRI bore often limits the amount of electronic components that can be placed close to the photodetectors.

Electronic components that go into the printed circuit boards (PCB) of the front-end detector modules within the MRI bore should avoid using magnetic materials whenever possible. Good PCB layout practices such as minimizing the current loops should be closely followed, as unwanted magnetic fields can be generated

from these current loops and picked up by the MRI system. To minimize the eddy currents due to the alternating gradient fields from the MR system, large conductive area in the front-end detector modules should be minimized. For the same reason, the traces in the PCB should be carefully routed to avoid large conductive loops, which can generate currents due to switching magnetic flux and degrade the PET signal. Since the performance of APDs and SiPMs are highly dependent on temperature, thermal regulation needs to be implemented when designing the front-end readout electronics, especially if more power-consuming electronic components are used.

Cables are often used to supply the power to the PET detector, send out the PET data to the back-end data acquisition system, and interface the communication between the front end and back end. However, electrical cables connecting to and from the front-end detectors can act as antenna and couple the electromagnetic fields from the MR system into the PET detectors and vice versa, degrading the performance of both PET and MR systems.

1.4 Overview of PET System Designs for PET/MRI

Many PET systems for PET/MRI have been designed in research groups and industry. As mentioned in this chapter, a lot of design aspects should be considered when combining PET and MRI. In most cases, the PET systems have incorporated unique features and technologies to allow combined PET and MR imaging. In this section, we present some details of each system that enabled the PET system to be MR compatible for integration and simultaneous operation of the two modalities.

1.4.1 Preclinical PET/MRI

PMT-Based PET/MRI The first approach to combine PET and MRI for preclinical imaging was in 1997 from UCLA [68]. To acquire simultaneous PET and MR images, a 0.2 T open magnet MRI system and a PMT-based PET system were used. LSO scintillation crystals were placed inside the MR scanner, and 4-m-long optical fibers were used to connect the scintillation signals to PMTs and readout electronics, which resided a safe distance outside the fringe magnetic field (<0.01 T) to effectively eliminate electromagnetic interferences between PET electronics and MRI. The MR body coil and a RF receiver coil (outside the PET ring) were used for MR image acquisition.

A few other research groups also studied PMT-based PET/MRI system designs. A team from West Virginia [22] built a preclinical PET system for insertion into a 3T MRI scanner. The PET system was based on two LSO block detectors coupled to fiber-optic light guides formed by bundling 2 mm diameter single-clad acrylic fiber-optic cables, which coupled the scintillation crystals sitting inside the magnet bore to the "flat panel" position-sensitive (PS)-PMTs residing outside in a magnetically shielded cage. The flat panel PS-PMTs were designed with very compact

dynode chains so that the signal was less sensitive to the Lorentz force from the MR fringe fields. For MR imaging, a saddle receiver coil was built to fit inside the limited-angle PET scanner with only two PET detectors, then the body coil was used to transmit RF.

Similarly, Kobe City College's team [19] developed a MRI-compatible PET system for a 0.3 T permanent magnet open MRI system. The PET system consisted of a full ring of dual-layer LGSO crystals with the scintillation light transferred to PS-PMTs by slanted light guides and optical fiber bundles. The PS-PMTs were placed in a magnetically shielded cage at the back of the MRI system where the magnetic field was sufficiently low. For MR imaging, a solenoidal receiver coil was placed inside the PET ring. The dual layer of LGSO crystals provided photon depth of interaction (DOI) information and yielded slightly higher transaxial spatial resolution at the edge of the FOV compared to the non-DOI configuration.

Although PMTs have low noise and good efficiency, limitations of the PMT-based PET/MRI system design were inherent. For example, coupling the scintillation crystals to optical fiber/light guides significantly degraded the PET performance due to a significant (50–75%) scintillation light attenuation and temporal dispersion, degrading the crystal identification, energy resolution, and timing resolution. The bore size for preclinical imaging was limited as well; since the optical fibers and/or light guides occupy too much space, the scalability was restricted.

To mitigate some of these PMT limitations, some novel approaches were pursued. The PET/MRI system from University of Cambridge [60] had the PET detectors reside in the gap between a split magnet, allowing a relatively large scintillation crystal volume inside the gap within the MRI system, and relatively shorter (120 cm) optical fibers (compared to the previous PMT-based optical fiber systems) transmitted scintillation light signal radially out from the magnet bore. Similarly, the University of Western Ontario [61] designed a field-cycled MRI with a conventional PMT-based PET system which read out the PET signals only when the magnetic field was shut off. Although both of these ideas were unique and showed a significantly better PET performance than the conventional PMT-based PET systems, these systems had drawbacks as well. They only operated at low magnetic fields restricting the flexibility of the imaging applications, had to modify the MRI system substantially, and/or suffer from a significant dead time for the PET acquisition during the MRI system operation.

APD-Based PET/MRI In 2006, APDs, which are magnetic field insensitive and solid-state photon detectors, emerged in PET system designs as replacements for PMTs which were suffering from the known SNR and mechanical limitations [16, 18, 62, 63, 69].

UC Davis's preclinical PET insert system [69] consisted of LSO scintillation crystals at the axial center of the FOV and PS-APDs along with charge-sensitive preamplifier relayed axially out through relatively short optical fibers (10 cm). The PS-APDs and the preamplifiers were enclosed in metal housing for shielding electromagnetic interference (EMI) between the PET and MRI systems. As APDs were

less sensitive to the magnetic field than the PMTs, the APDs could be placed much closer to the scintillation crystals and within the MR bore. The PET insert was placed inside a 7T MRI scanner, and a transmit/receive (TX/RX) RF coil was used for MR image acquisition.

Similarly, the preclinical PET insert system from Tubingen University [63] employed a full ring of LSO-APD with charge-sensitive preamplifier, and the signals were read out by 6 m fully shielded nonmagnetic coaxial cables routed to the control room. This system did not use optical fibers to relay the scintillation light to the APDs, instead directly coupled LSO to an APD array with a light diffuser in between. The detector modules were enclosed inside a doubled-sided PCB coated with copper and positioned inside a 7T MRI. The combined TX/RX RF coil was placed inside the PET detector ring for MR acquisition.

Stony Brook University built a PET system [18] that can be inserted into a 9.4T micro-MRI system. LSO crystals were one-to-one coupled to APDs employing a nonmagnetic socket mounted on a flexible PCB, which rolled up and was secured in a plastic housing. A custom-built TX/RX RF coil fitting inside the PET ring was used for MR imaging. The PET system did not have any shielding, and EMI from the MRI system was observed in the PET data.

In general, APD-based PET systems required charge-sensitive preamplifiers to be placed as close as possible to the detectors inside the MR bore to minimize the capacitance, ensuring lower noise and better signal quality. The detector modules were enclosed in shielding cages to mitigate the EMI between the PET's front-end readout system and MRI's RF and gradient system.

Analog SiPM-Based PET/MRI Despite a mature technology of the APD detector, there were limitations including the lower gain of signals and inferior coincidence time resolution compared with PMTs. The SiPM gained attention as a promising photodetector for PET/MRI systems because it is insensitive to magnetic fields and has high amplification gain and superior timing resolution, comparable to those of the PMT [70]. Therefore, several research groups [10, 13, 64, 74] have worked on the development of SiPM-based PET/MR systems.

Sogang University's PET system [10] consisted of LYSO scintillation crystals and SiPM arrays enclosed in detector modules; then the output charge signal was transmitted to a preamplifier located remotely through 300 cm length shielded flexible flat cables. This analog charge signal transmission approach decreased the space requirements inside the MR bore and minimized the mutual interference between PET and MRI eliminating the need for RF shielding. Therefore, no RF shielding was applied to the detector modules. A TX/RX RF coil was used for MR imaging.

RWTH Aachen University [64] developed a SiPM-based preclinical PET insert for a human 3T MRI system. LYSO scintillation crystals were coupled to SiPM arrays, which were directly digitized by a custom integrated circuit (IC)-based readout board. The detector module was integrated with fluid cooling and enclosed inside RF shielding. Then, a TX/RX birdcage RF coil fitting inside a PET ring was used for MR image acquisition.

Seoul National University [74] built a PET system based on LGSO and SiPM detector modules enclosed in a dual-layer copper shielding cage. Nonmagnetic foil-screened twisted-pair cables were used to transfer the data from the detector module inside the MRI bore to the data acquisition system in the control room. The PET ring was inserted into a 3T whole-body MRI; An MRI body coil was used for RF transmission, and a loop receiver coil was located inside the PET system for MR acquisition. Despite the fact that the gadolinium in the LGSO is magnetically susceptible (see Sect. 3.1), MRI susceptibility artifacts were not observed in a 3T environment [19].

Eulji University [13] developed a SiPM-based PET with the LYSO scintillation crystals, short optical fiber bundles, and SiPMs residing outside the shielding cage, and only the front-end electronics with a resistive charge division network and a differential amplifier were enclosed in a copper shielding cage. The PET ring was inserted into a 3T MRI bore, and MRI body coil and a surface receiver coil were used for MR image acquisition.

Digital SiPM-based PET/MRI dSiPMs emerged as the latest evolutionary step in silicon-based photodetectors. As mentioned earlier, dSiPMs actively quench and digitize the breakdown of individual single photon avalanche diodes (SPADs), and the digitized breakdowns are summed up for signal processing.

As of date, only Aachen University has built a dSiPM-based PET/MRI system [9, 14, 50, 85]. Each detector module was assembled with LYSO scintillation crystals and dSiPMs, which are liquid cooled via rectangular brass pipes, and enclosed inside a carbon fiber composite shielding cage. Data transfer from and to the PET detector modules were done by optical transceivers. The PET ring was inserted into a 3T whole-body MRI, and a combined TX/RX RF coil was used for MR image acquisition.

Commercial Preclinical PET/MRI Recently a number of commercially available combined PET/MRI systems for preclinical imaging (Mediso [16, 89], MR Solutions [91], Bruker [90]) have emerged. Mediso has developed a NanoScan small animal PET insert for sequential in-line PET/MRI [16, 89], for which the PET system consists of LYSO crystals connected to a light guide and magnetically shielded PS-PMTs. For MR imaging, a 1T permanent magnet or a 3T cryogen-free magnet, featured with built-in gradient coils and a TX/RX RF coil, is used. The detector modules are RF and magnetically shielded. MR Solutions and Bruker built PET inserts that enable both sequential and simultaneous PET/MRI studies [90, 91], allowing scientists to choose any mode for their preferences. The PET insert of MR Solutions consists of dual-layer LYSO, for DOI detection capability, coupled to SiPMs, which is inserted within the cryogen-free 3T, 4.7T, or 7T MRI magnet. Bruker built a sequential in-line PET/MRI (3T) system and a simultaneous PET insert system (for 4.7T, 7T, and 9T MRI). Both systems consisted of continuous LYSO crystals with DOI detection capability and SiPMs.

1.4.2   Commercial Clinical Integrated PET/MRI Systems

Currently there are two commercial clinical PET/MRI systems that allow simultaneous clinical PET and MR acquisition: Siemens Biograph mMR and GE SIGNA PET/MR. Both are permanently integrated systems: the PET and MRI systems are permanently locked together, which means typically the customer procures both systems plus covers the cost of a new installation.

1.4.2.1 Siemens BrainPET and Biograph mMR

A PET system dedicated for PET/MRI brain scanning was developed by Siemens (BrainPET) [12]. A RF head coil was included inside the PET system to transmit and receive the RF fields for MRI brain imaging. The detector module comprised a 12×12 array of $2.5 \times 2.5 \times 20$ mm^3 LSO crystals coupled to a 3×3 array of APDs. The smaller scintillator crystals used in this system allows a reconstructed spatial resolution of <3 mm FWHM, compared to 4.3 mm reported for the Biograph mMR as described in the following section, which uses $4.0 \times 4.0 \times 20$ mm^3 LSO crystals. More details on the performance of this system can be found in [12].

In 2011, Siemens introduced the first commercial whole-body integrated PET/MRI system (Biograph mMR), which was based on a similar detector technology used in the brain PET system. Figure 1.2 shows drawings of this system design. Components that constitute the system from the inside to the outside are the MRI RF body coil, PET detector rings, gradient coil assembly, primary magnet coil (with 3 T magnetic field strength), and magnet shielding coil. Since the PET detectors are integrated between the RF body coil and gradient coil, careful design of the body coil is required to reduce its attenuation to the 511-keV photons to preserve the PET image quality. PET detectors also have to be nonmagnetic and "transparent" to the
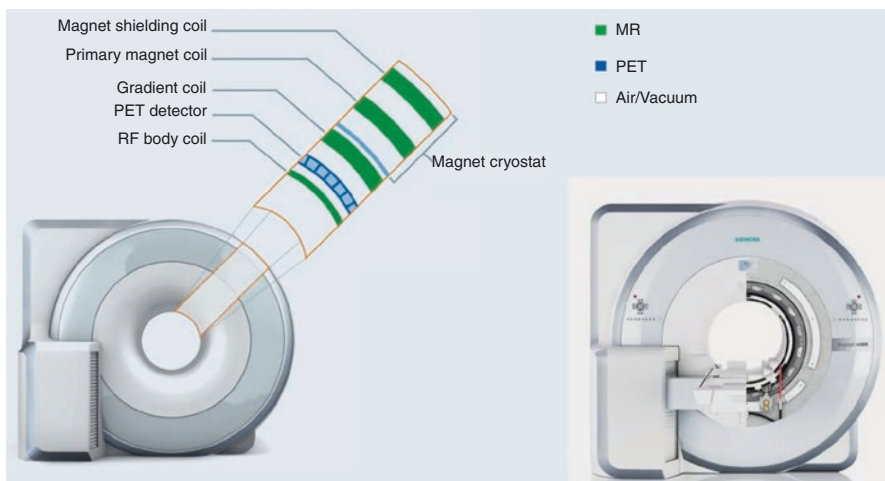
Fig. 1.2 Schematic drawing and photograph of Siemens Biograph mMR (reprinted from [88], courtesy of Siemens Healthineers)
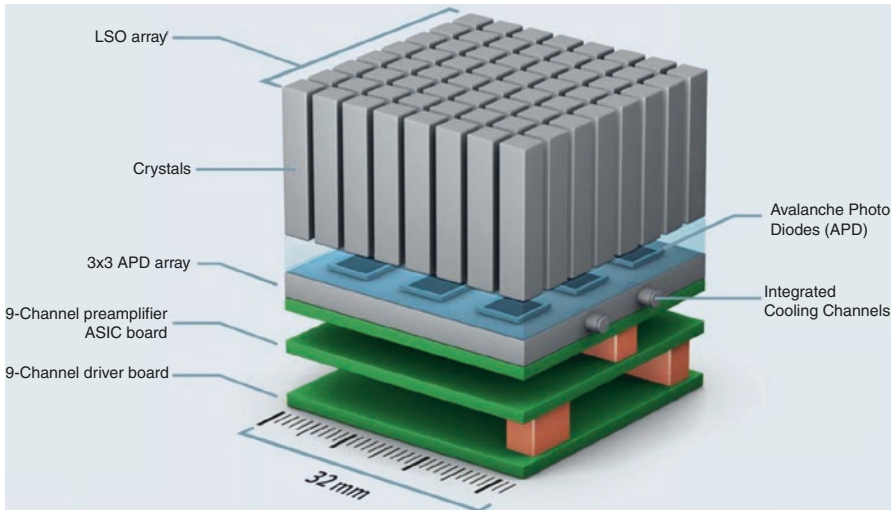
Fig. 1.3 PET detector assembly for Siemens mMR (reprinted from [88], courtesy of Siemens Healthineers)

gradient fields generated by the gradient coils in order to not distort the linearity of the fast switching gradient fields used for encoding spatial information to form the MRI images. A wide-bore (70 cm diameter) MRI magnet technology is used, and after the integration of the PET detectors, the available bore size of the integrated system is 60 cm.

Figure 1.3 shows one PET detector assembly for the Biograph mMR. It consists of 64 LSO crystals arranged in an 8 × 8 array coupled to a 3 × 3 array of APDs. A 9-channel preamplifier ASIC (application-specific integrated circuit) and driver boards as well as water cooling channels are integrated behind the APDs, which complete each detector block. The detector block is designed free of magnetic components. Fifty-six of such blocks form one PET detector ring, and eight detector rings form the PET subsystem in the Biograph mMR that spans an axial FOV of 25.8 cm. The specs and performance of the Biograph mMR are summarized in Table 1.2.

1.4.2.2 GE SIGNA PET/MR

In 2016, General Electric (GE) introduced the first whole-body ToF-PET/MRI integrated system. Figure 1.4a shows the schematic drawings of the integrated system. The system is designed based on the 3T MR750w MRI scanner (GE Healthcare), a whole-body MRI system with a 70 cm diameter patient bore. The RF body coil and its shield were redesigned in order to accommodate the PET detectors: an inward dip in the RF shield (Fig. 1.4a) allows space to place the PET detector ring with minimal photon attenuation. Like the Siemens mMR system, the body coil resides just inside the PET ring. The PET detector ring is 25 cm axially, and after the integration of the PET detectors, the bore diameter of the integrated system is 60 cm. To

Table 1.2 Summary of PET subsystems of commercial integrated PET/MR systems

Performance metrics	Siemens Biograph mMR [8]	GE SIGNA PET/MR [7]
Scintillator	LSO[a]	LBS[b]
Photodetector	APDs	SiPMs
Transaxial FOV[c] (cm)	59.4	60
Axial FOV (cm)	25.8	25
Energy resolution (%)	14.5	10.5
Time resolution (ps)	2930	390
Spatial resolution[d] (mm)	4.3	4.4
Sensitivity[d] (cps[e]/kBq)	15	23
Peak NECR[f] (kcps)	184 (at 23.1 kBq/ml)	218 (at 17.8 kBq/ml)

[a]Lutetium oxyorthosilicate
[b]Lutetium-based scintillator
[c]Field of view
[d]Measured at the center of the system
[e]Count per second
[f]Noise-equivalent count rate
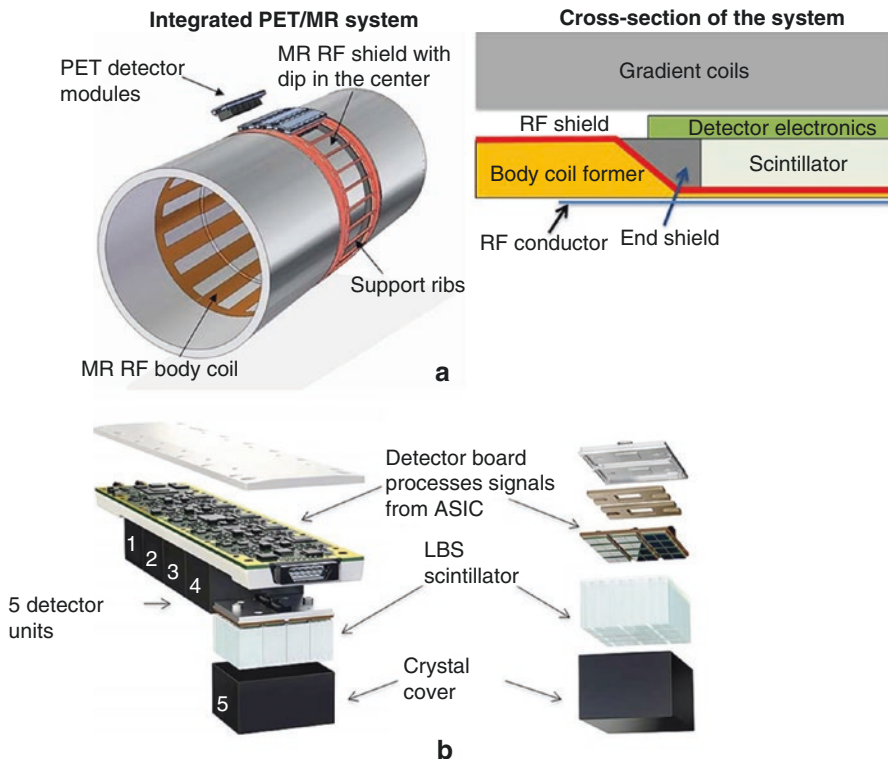
Fig. 1.4 (**a**) Schematic drawing of GE SIGNA integrated PET/MRI system, showing the cross section of a detector integrated with the RF body coil. (**b**) Schematic of a detector module and unit (reprinted from [6] with permission from Dr. Craig S. Levin at Department of Radiology, Stanford University)

minimize interference between the PET and MRI subsystems, all communication between the front-end readout electronics and back-end data acquisition system is over optical fibers, and the only electrical connection to the front-end detector module is through a double-shielded (braid plus foil) cable that carries power and timing clock over twisted pair wiring.

The PET detector ring comprises 28 identical detector modules (Fig. 1.4b). Each detector module comprises 720 $3.95 \times 5.3 \times 25$ mm^3 lutetium-based scintillator (LBS) crystals read by arrays of SiPMs. Signals from the SiPM arrays are amplified and processed by ASICs mounted on the same board to acquire position, energy, and timing signals. The high gain of the SiPMs, in conjunction with the readout electronics placed close to the SiPMs to amplify and digitize the signal, preserves the detector SNR and allows advanced ToF-PET performance for this system (Sects. 3.2.3 and 3.3). Active thermal regulation is employed in this system: each detector module is water cooled. In addition, 280 thermistors are implemented to measure the temperature throughout the PET ring. The temperature map is used to control the bias voltage applied to each individual SiPMs to correct any gain shift of the SiPMs, which is temperature dependent. The specifications and performance of this system is summarized in Table 1.2.

1.4.3   Clinical PET Insert Systems for PET/MRI

A PET insert is a separate system that can be installed into (and removed from) a MRI system for simultaneous PET and MRI acquisition. A PET insert allows a MRI site to achieve PET/MRI by only acquiring the PET insert, which is expected to reduce the cost compared to acquiring an integrated PET/MRI system, as it avoids the cost to purchase both PET and MRI systems and does not require costly room renovations. This section gives an overview of PET insert systems developed for clinical use.

Sogang Neuro-PET   A neuro-PET insert has been developed at Sogang University in Seoul, South Korea. Figure 1.5 shows photos of this PET insert system placed inside a 3T MRI system.

This neuro-PET insert system uses $3 \times 3 \times 20$ mm^3 LYSO crystals that are one-to-one coupled to 3×3 mm^2 SiPMs. As shown in Fig. 1.5 (right), the signals generated by the SiPMs are relayed to the readout electronics placed in a shielded box outside the MRI bore using 300 cm flexible flat cables (FFC), which was also used in the small animal PET insert system [10] developed by the same group. To minimize electromagnetic interference, the PET gantry hosting the LYSO crystals and SiPMs is shielded with gold-plated conductive fabric tape of 0.1 mm thickness, and the 300-cm-long FFCs are shielded with a mesh-type aluminum sheet of 0.24 mm thickness. All PET acquisition electronics are located outside the MR bore and enclosed in an aluminum box with a thickness of 10 mm. The transaxial FOV and axial FOV of the scanner as reported in [77] are 250 mm and 12.9 mm, respectively. A recent paper from the same group showed that the axial FOV has been extended to 60 mm [87].
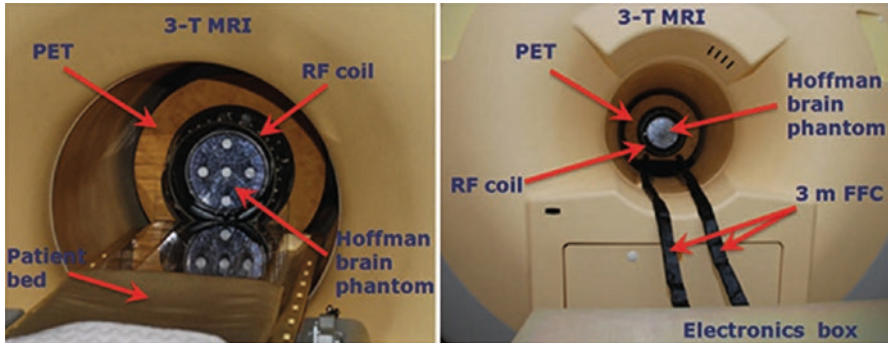
Fig. 1.5 Frontal (*left*) and rear (*right*) view of the Sogang neuro-PET insert with the RF coil placed inside a 3T MRI system (Reprinted from [77], with permission from Dr. Yong Choi, Department of Electrical Engineering, Sogang University)
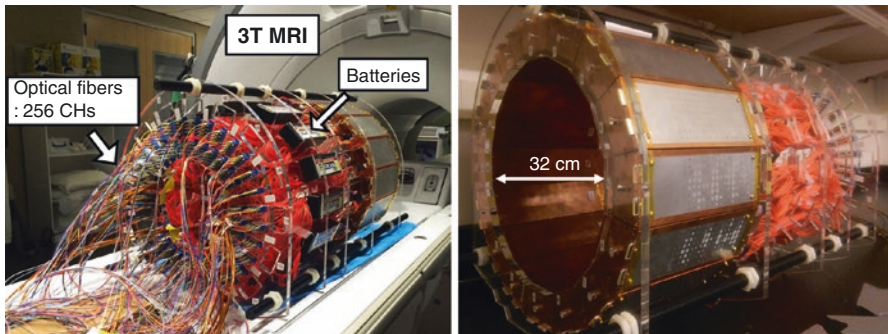
Fig. 1.6 (*Left*) Rear view of the Stanford RF-penetrable BrainPET insert for a 3T MRI system. (*Right*) Frontal view of the system

Stanford "RF-Penetrable" BrainPET Insert for Simultaneous PET/ MRI Another brain PET insert system for PET/MRI has been developed at Stanford University (Fig. 1.6) [24, 83, 86]. The ring is formed by 16 shielded modules, each comprising arrays of $3 \times 3 \times 20$ mm^3 LYSO scintillation crystals coupled one-to-one to 3×3 mm^2 pixels of SiPM arrays. The PET insert has an inner diameter of 32 cm and an axial FOV of 2.8 cm. Unlike all other PET inserts for MRI, this ring is "RF penetrable" [102, 103], that is, the RF field from the built-in body coil of the MRI system can transmit through small (1 mm) inter-module gaps in the PET ring to excite the spins within the subject to be imaged, with relatively low field attenuation (and the RF fields generated from the relaxation processes of these spins can also penetrate the PET ring and be detected by the RF body coil). The key to this unusual feature is that the PET ring is electrically floating with respect to the MRI system. There are two basic technologies facilitating this isolation: (1) this system utilizes electro-optical signal transmission [104], instead of electrical cables, where the analog signals from the SiPMs drive small telecommunication lasers that convert the electrical current to coherent near-infrared light,

which is transferred out of the MRI bore through 20 m length optical fibers to an optical data acquisition system residing in the adjacent control room. (2) Electrically isolated batteries placed close to the PET detector modules are used to power the PET detectors with short electrical cables. In addition to enabling RF penetrability, this configuration reduces other potential sources of electromagnetic interference between the PET and MRI systems. Therefore, simultaneous PET and MRI images can be acquired with this PET insert system by using only the built-in body coil of the MR system [86], and there is no need to implement a combined RF TX/RX coil within the PET insert, which was required for all other PET insert systems.

This alternative RF-penetrable PET insert approach can also be scaled to a large diameter, potentially reducing the development complexity of a whole-body PET/MRI system, since the body coil does not have to be reengineered to reside inside the PET ring as it is for the GE and Siemens PET/MRI system designs (see Figs. 1.2 and 1.4), which have to bring the RF transmitter coil inside the PET ring since the latter is not RF penetrable. Typically, better MR image quality may be achieved with this RF-penetrable PET insert by using the body coil as the RF transmitter but a high-sensitivity receive-only coil placed within the PET insert as the RF receiver. Using the built-in body coil for RF transmission would also maximize the useful patient bore diameter, as no RF TX coil is needed inside the PET ring. Eliminating coil materials placed within the PET insert would also reduce 511 keV photon scatter and attenuation, potentially improving PET image quality and accuracy. More details on the RF-penetrable PET detector design and performance evaluation of the prototype system shown in Fig. 1.6 can be found in [24, 83, 86].

Several Other Research Groups Are also Working on Brain-Dedicated PET Insert Systems for PET/MRI. A research group at the National Institute of Radiological Sciences in Chiba, Japan, has developed a prototype detector using four layers of LGSO scintillators with depth-of-interaction (DOI) capability [105], which can improve the spatial resolution uniformity across the system FOV. However, they reported influence on the MRI measurement due to the magnetic susceptibility of the LGSO crystals used in the prototype detector [105].

A research group at the Institute for Instrumentation in Molecular Imaging (I3M) in Valencia, Spain, is developing a PET insert system with sufficient resolution and sensitivity to visualize neurotransmitter pathways and their disruptions in mental disorders using simultaneous PET/MRI measurements for diagnosis and follow-up treatment (the Multimodal Imaging of Neurological Disorders (MINDView) project) [106]. Feasibility studies on prototype detectors based on two crystal designs, namely, a three-layer staggered array of 1.5 mm LYSO crystals and a black-painted monolithic LYSO block, were reported in [106].

Another research group at the University of Pisa in Italy is developing a tri-modal (PET/MRI/EEG) scanner (the TRIMAGE project). Initial results on the prototype detector of this system based on $3.3 \times 3.3 \times 8$ mm dual-layer staggered LYSO crystals combined with readout electronics based on TRIROC ASIC were reported in [107].

1.5   Summary and Conclusion

Significant efforts to achieve simultaneous PET/MRI have been made during the past several years. In conjunction with key technical advancements in the detector technology (e.g., the SiPM), a number of unique and creative designs were introduced to mitigate the mutual interferences between PET and MRI. The consistent efforts from research groups and industry have led to high-performance commercial simultaneous PET/MRI systems for whole-body clinical imaging. Broader dissemination of clinical simultaneous PET/MR systems is necessary to enable a large number of researchers and clinicians to investigate the clinical impact of the technology. Owing to the large costs of integrated PET/MRI systems, MRI-compatible PET insert systems may be a promising direction to achieve broader dissemination and use of PET/MRI.

References

1. Townsend DW. Combined PET/CT: the historical perspective. Semin Ultrasound CT MR. 2008;29(4):232–5.
2. Beyer T, Townsend DW, Brun T, Kinahan PE, Charron M, Roddy R, Jerin J, Young J, Byars L, Nutt R. A Combined PET/CT Scanner for Clinical Oncology. J Nucl Med. 2000;41:1369–79.
3. Townsend DW. Positron emission tomography/computed tomography. Semin Nucl Med. 2008;38:152–66.
4. Hammer BE, Christensen NL, Heil BG. Use of a magnetic field to increase the spatial resolution of positron emission tomography. Med Phys. 1994;21:1917–20.
5. Zaidi H, Ojha N, Morich M, Griesmer J, Hu Z, Maniawski P, Ratib O, Izquierdo-Garcia D, Fayad ZA, Shao L. Design and performance evaluation of a whole-body Ingenuity TF PET-MRI system. Phys Med Biol. 2011;56:3091–106.
6. Levin CS, Maramraju SH, Khalighi MM, Deller TW, Delso G, Jansen F. Design features and mutual compatibility studies of the time-of-flight PET capable GE SIGNA PET/MR system. IEEE Trans Med Imaging. 2016;35:1907–14.
7. Grant AM, Deller TW, Khalighi MM, Maramraju SH, Delso G, Levin CS. NEMA NU 2-2012 performance studies for the SiPM-based ToF-PET component of the GE SIGNA PET/MR system. Med Phys. 2016;43:2334–43.
8. Delso G, Furst S, Jakoby B, Ladebeck R, Ganter C, Nekolla SG, Schwaiger M, Ziegler SI. Performance measurements of the Siemens mMR integrated whole-body PET/MR scanner. J Nucl Med. 2011;52:1914–22.
9. Schug D, Wehner J, Dueppenbecker PM, Weissler B, Gebhardt P, Goldschmidt B, Salomon A, Kiessling F, Schulz V. PET performance and MRI compatibility evaluation of a digital, ToF-capable PET/MRI insert equipped with clinical scintillators. Phys Med Biol. 2015;60:7045.
10. Jihoon K, Choi Y, Hong KJ, Hu W, Jung JH, Huh Y, Kim B-T. A small animal PET based on GAPDs and charge signal transmission approach for hybrid PET-MR imaging. J Instrum. 2011;6:P08012.
11. Mollet P, Keereman V, Clementel E, Vandenberghe S. Simultaneous MR-compatible emission and transmission imaging for PET using time-of-flight information. IEEE Trans Med Imaging. 2012;31:1734–42.
12. Kolb A, Wehrl HF, Hofmann M, Judenhofer MS, Eriksson L, Ladebeck R, Lichy MP, Byars L, Michel C, Schlemmer H-P, Schmand M, Claussen CD, Sossi V, Pichler BJ. Technical performance evaluation of a human brain PET/MRI system. Eur Radiol. 2012;22:1776–88.

13. Hong SJ, Kang HG, Ko GB, Song IC, Rhee JT, Lee JS. SiPM-PET with a short optical fiber bundle for simultaneous PET-MR imaging. Phys Med Biol. 2012;57:3869–83.

14. Wehner J, Weissler B, Dueppenbecker P, Gebhardt P, Schug D, Ruetten W, Kiessling F, Schulz V. PET/MRI insert using digital SiPMs: investigation of MR-compatibility. Nucl Instrum Methods Phys Res A. 2014;734(Part B):116–21.

15. Weissler B, Gebhardt P, Lerche CW, Wehner J, Solf T, Goldschmidt B, Mackewn JE, Marsden PK, Kiessling F, Perkuhn M, Heberling D, Schulz V. MR compatibility aspects of a silicon photomultiplier-based PET/RF insert with integrated digitisation. Phys Med Biol. 2014;59:5119.

16. Nagy K, Tóth M, Major P, Patay G, Egri G, Hggkvist J, Varrone A, Farde L, Halldin C, Gulys B. Performance evaluation of the small-animal nanoScan PET/MRI system. J Nucl Med. 2013;54:1825–32.

17. Wehrl HF, Judenhofer MS, Thielscher A, Martirosian P, Schick F, Pichler BJ. Assessment of MR compatibility of a PET insert developed for simultaneous multi-parametric PET/MR imaging on an animal system operating at 7 T. Magn Reson Med. 2011;65:269–79.

18. Maramraju SH, Smith SD, Junnarkar SS, Schulz D, Stoll S, Ravindranath B, Purschke ML, Rescia S, Southekal S, Pratte JF, Vaska P, Woody CL, Schlyer DJ. Small animal simultaneous PET/MRI: initial experiences in a 9.4 T microMRI. Phys Med Biol. 2011;56:2459–80.

19. Yamamoto S, Imaizumi M, Kanai Y, Tatsumi M, Aoki M, Sugiyama E, Kawakami M, Shimosegawa E, Hatazawa J. Design and performance from an integrated PET/MRI system for small animals. Ann Nucl Med. 2010;24:89–98.

20. Mackewn JE, Halsted P, Charles-Edwards G, Page R, Totman JJ, Sunassee K, Strul D, Hallett WA, Jauregui-Osoro M, Liepins P, Williams SCR, Schaeffter T, Keevil SF, Marsden PK. Performance evaluation of an MRI-compatible pre-clinical PET system using long optical fibers. IEEE Trans Nucl Sci. 2010;57:1052.

21. Judenhofer MS, Catana C, Swann BK, Siegel SB, Jung WI, Nutt RE, Cherry SR, Claussen CD, Pichler BJ. PET/MR images acquired with a compact MR-compatible PET detector in a 7-T magnet. Radiology. 2007;244:807–14.

22. Raylman RR, Majewski S, Lemieux SK, Velan SS, Kross B, Popov V, Smith MF, Weisenberger AG, Zorn C, Marano GD. Simultaneous MRI and PET imaging of a rat brain. Phys Med Biol. 2006;51:6371–9.

23. Pichler BJ, Lorentz E, Mirzoyan R, Pimpl W, Roder F, Schwaiger M, Ziegler SI. Performance test of a LSO-APD PET module in a 9.4 Tesla magnet. IEEE Nucl Sci Symp. 1997;2:1237–9.

24. Olcott PD, Kim E, Hong KJ, Lee BJ, Grant AM, Chang C-M, Glover G, Levin CS. Prototype positron emission tomography insert with electro-optical signal transmission for simultaneous operation with MRI. Phys Med Biol. 2015;60:3459.

25. Chang C-M, Grant A, Lee B, Levin C. Preliminary PET performance evaluation of an RF field-penetrable brain-sized PET insert for simultaneous PET/MR imaging. J Nucl Med. 2015;56:99.

26. Yamamoto S, Watabe H, Kanai Y, Aoki M, Sugiyama E, Watabe T, Imaizumi M, Shimosegawa E, Hatazawa J. Interference between PET and MRI sub-systems in a silicon-photomultiplier-based PET/MRI system. Phys Med Biol. 2011;56:4147.

27. Peng BJ, Walton JH, Cherry SR, Willig-Onwuachi J. Studies of the interactions of an MRI system with the shielding in a combined PET/MRI scanner. Phys Med Biol. 2010;55:265–80.

28. Vandenberghe S, Marsden PK. PET-MRI: a review of challenges and solutions in the development of integrated multimodality imaging. Phys Med Biol. 2015;60:R115–54.

29. Wehrl HF, Sauter AW, Divine MR, Pichler BJ. Combined PET/MR: a technology becomes mature. J Nucl Med. 2015;56:165–8.

30. Kolb A, Sauter AW, Eriksson LA, Vandenbrouke A, Liu C-C, Levin CS, Pichler BJ, Rafecas M. Shine-through in PET/MRI: effects of the magnetic field on positron range and subsequent image artifacts. J Nucl Med. 2015;56:951.

31. Bailey DL, Pichler BJ, Gckel B, Barthel H, Beer AJ, Bremerich J, Czernin J, Drzezga A, Franzius C, Goh V, Hartenbach M, Iida H, Kjaer A, la Fougre C, Ladefoged CN, Law I,

Nikolaou K, Quick HH, Sabri O, Schfer J, Schfers M, Wehrl HF, Beyer T. Combined PET/MRI: multi-modality multi-parametric imaging is here. Mol Imaging Biol. 2015;17:595–608.

32. Chang AE, Matory YL, Dwyer AJ, Hill SC, Girton ME, Steinberg SM, Knop RH, Frank JA, Hyams D, Doppman JL. Magnetic resonance imaging versus computed tomography in the evaluation of soft tissue tumors of the extremities. Ann Surg. 1987;205(4):340–8.

33. Aisen AM, Martel W, Braunstein EM, McMillin KI, Phillips WA, Kling T. MRI and CT evaluation of primary bone and soft-tissue tumors. Am J Roentgenol. 1986;146(4):749–56.

34. Daftary A. PET-MRI: challenges and new directions. Ind J Nucl Med. 2010;25:3–5.

35. de Rosales RTM. Potential clinical applications of bimodal PET-MRI or SPECT-MRI agents. J Label Compd Radiopharm. 2014;57:298–303.

36. Torigian DA, Zaidi H, Kwee TC, Saboury B, Udupa JK, Cho Z-H, Alavi A. PET/MR Imaging: Technical Aspects and Potential Clinical Applications. Radiology. 2013;267:26–44.

37. Logothetis NK. What we can do and what we cannot do with fMRI. Nature. 2008;453(7197):869–78.

38. Wehrl HF, Hossain M, Lankes K, Liu C-C, Bezrukov I, Martirosian P, Schick F, Reischl G, Pichler BJ. Simultaneous PET-MRI reveals brain function in activated and resting state on metabolic, hemodynamic and multiple temporal scales. Nat Med. 2013;19(9):1184–9.

39. Schenck JF. The role of magnetic susceptibility in magnetic resonance imaging: MRI magnetic compatibility of the first and second kinds. Med Phys. 1996;23:815–50.

40. Peng BJ, Wu Y, Cherry SR, Walton JH. New shielding configurations for a simultaneous PET/MRI scanner at 7T. J Magn Reson. 2014;239:50–6.

41. Eclov N, Kim H, Chen HT, Chin-Tu C, Ronzhin A, Ramberg E, Los S, Murat P, Wyrwicz AM, Limin L, et al. Notch filtering of RF interference in PET data for simultaneous PET-MR acquisition. In: 2014 IEEE nuclear science symposium and medical imaging conference (NSS/MIC), 8–15 Nov 2014. IEEE; 2014. p. 1–3.

42. Stevenson RA. Electromagnetic interference (emi) filter and process for providing electromagnetic compatibility of an electronic device while in the presence of an electromagnetic emitter operating at the same frequency. Google Patents. 2002.

43. Huh YS, Choi Y, Hong KJ, Jung JH, Hu W, Kang JH, Min BJ, Shin SH, Lim HK, Song MS, et al. Development of filtering methods for PET signals contaminated by RF pulses for combined PET-MRI. In: 2009 IEEE nuclear science symposium conference record (NSS/MIC). IEEE; 2009. p. 3812–5.

44. Chung DDL. Materials for electromagnetic interference shielding. J Mater Eng Perform. 2000;9:350–4.

45. Preault V, Corcolle R, Daniel L, Pichon L. Influence of skin effect on the effective shielding effectiveness of composite materials. J Appl Phys. 2014;115:154904.

46. Camacho CR, Plewes DB, Henkelman RM. Nonsusceptibility artifacts due to metallic objects in MR imaging. J Magn Reson Imaging. 1995;5:75–88.

47. Ramilli M. Characterization of SiPM: temperature dependencies. In: nuclear science symposium conference record, 2008. NSS '08. IEEE; 2008. p. 2467–70.

48. Raylman RR, Stolin A, Majewski S, Proffitt J. A large area, silicon photomultiplier-based PET detector module. Nucl Instrum Methods Phys Res A. 2014;735:602.

49. Morich MA, DeMeester GD, Griesmer JJ, Solf TJ, Schulz V, Weissler B. Thermally stabilized pet detector for hybrid PET-MR system. Google Patents. 2013.

50. Schug D, Lerche C, Dueppenbecker P, Gebhardt P, Goldschmidt B, Salomon A, Wehner J, Weissler B, Kiessling F, Schulz V. PET performance evaluation of a preclinical digital PET/MRI insert. EJNMMI Phys. 2014;1(1):1–2.

51. Hayes CE, Edelstein WA, Schenck JF, Mueller OM, Eash M. An efficient, highly homogeneous radiofrequency coil for whole-body NMR imaging at 1.5 T. J Magn Reson. 1969;63(3):622–8.

52. Roemer PB, Edelstein WA, Hayes CE, Souza SP, Mueller OM. The NMR phased array. Magn Reson Med. 1990;16(2):192–225.

53. van der Zwaag W, Marques JP, Lei H, Just N, Kober T, Gruetter R. Minimization of Nyquist ghosting for echo-planar imaging at ultra-high fields based on a negative readout gradient strategy. J Magn Reson Imaging. 2009;30:1171–8.

54. Jezzard P, Barnett AS, Pierpaoli C. Characterization of and correction for eddy current artifacts in echo planar diffusion imaging. Magn Reson Med. 1998;39:801–12.

55. Dharma Raj C, Ramyasree MVSL, Sravan Kumar V. Analysis of wire mesh screen for shielding effectiveness in different frequency ranges. In: 2011 international conference on computer, communication and electrical technology (ICCCET). IEEE; 2011. p. 198–203.

56. Frederick PS, Zimmermann WA, Roemer PB. Double-sided RF shield for RF coil contained within gradient coils used in high speed NMR imaging. General Electric Company. 5,680,046. 1994.

57. Chung DDL. Electromagnetic interference shielding effectiveness of carbon materials. Carbon. 2001;39:279–85.

58. Kinahan PE, Townsend DW, Beyer T, Sashin D. Attenuation correction for a combined 3D PET/CT scanner. Med Phys. 1998;25:2046–53.

59. Turkington TG. Attenuation correction in hybrid positron emission tomography. Semin Nucl Med. 2000;30:255–67.

60. Lucas AJ, Hawkes RJ, Ansorge RE, Williams GB, Nutt RE, Clark JC, Fryer TD, Carpenter TA. Development of a combined microPET-MR system. Technol Cancer Res Treat. 2006;5(4):337–41.

61. Gilbert KM, Handler WB, Scholl TJ, Odegaard JW, Chronik BA. Design of field-cycled magnetic resonance systems for small animal imaging. Phys Med Biol. 2006;51(11):2825.

62. Grazioso R, Zhang N, Corbeil J, Schmand M, Ladebeck R, Vester M, Schnur G, Renz W, Fischer H. APD-based PET detector for simultaneous PET/MR imaging. Nucl Instrum Methods Phys Res Sect A. 2006;569(2):310–05.

63. Pichler BJ, Judenhofer MS, Catana C, Walton JH, Kneilling M, Nutt RE, Siegel SB, Claussen CD, Cherry SR. Performance test of an LSO-APD detector in a 7-T MRI scanner for simultaneous PET/MRI. J Nucl Med. 2006;47(4):639–47.

64. Schulz V, Weissler B, Gebhardt P, Solf T, Lerche CW, Fischer P, Ritzert M, Mlotok V, Piemonte C, Goldschmidt B, Vandenberghe S, Salomon A, Schaeffter T, Marsden PK. SiPM based preclinical PET/MR insert for a human 3T MR: first imaging experiments. In: IEEE nuclear science symposium conference record, Valencia. IEEE; 2011. p. 4467–9.

65. Cherry SR, Sorenson JA, Phelps ME. Physics in nuclear medicine. Philadelphia: Elsevier; 2012.

66. Yamamoto S, Kuroda K, Senda M. Scintillator selection for MR-compatible gamma detectors. IEEE Trans Nucl Sci. 2003;50:1683–5.

67. Slates RB, Cherry SR, Boutefnouchet A, Shao YP, Dahlbom M, Farahani K. Design of a small animal MR compatible PET scanner. IEEE Trans Nucl Sci. 1999;46:565–70.

68. Shao YP, Cherry SR, Farahani K, Meadors K, Siegel S, Silverman RW, Marsden PK. Simultaneous PET and MR imaging. Phys Med Biol. 1997;42:1965–70.

69. Catana C, Wu Y, Judenhofer MS, Jinyi Q, Pichler BJ, Cherry SR. Simultaneous acquisition of multislice PET and MR images: initial results with a MR-compatible PET scanner. J Nucl Med. 2006;47:1968–76.

70. Buzhan P, Dolgoshein B, Filatov L, Ilyin A, Kantzerov V, Kaplin V, Karakash A, Kayumov F, Klemin S, Popova E, Smirnov S. Silicon photomultiplier and its possible applications. Nucl Instrum Methods Phys Res Sect A. 2003;504:48–52.

71. Frach T, Preshcer G, Degenhardt C, de Gruyter R, Schmit A, Ballizany R. The digital silicon photomultiplier - principle of operation and intrinsic detector performance. In: IEEE nuclear science symposium conference record. IEEE; 2009. p. 1959–65.

72. Cates JW, Levin CS. Advances in coincidence time resolution for PET. Phys Med Biol. 2016;61:2255–64.

73. Goertzen AL, Stortz G, Jonathan JD, Bishop D, Khan MS, Kozlowski P, Retiere F, Schellenberg G, Shams E, Sossi V, Thompson CJ. First results from a high-resolution small animal SiPM PET insert for PET/MR imaging at 7T. IEEE Trans Nucl Sci. 2016;63:2424–33.

74. Yoon HS, Ko GB, Kwon SI, Lee CM, Ito M, Song IC, Lee DS, Hong SJ, Lee JS. Initial results of simultaneous PET/MRI experiments with an MRI-compatible silicon photomultiplier PET scanner. J Nucl Med. 2012;53:608–14.

75. Schulz V, Solf T, Weissler B, Gebhardt P, Fischer P, Ritzert M, Mlotok V Piemonte C, Zorzi N, Melchiorri M, Vandenberghe S, Keereman V, Schaeffter T, Marsden PK. A preclinical PET/MR insert for a human 3T MR scanner. In: 2009 IEEE nuclear science symposium conference record (NSS/MIC). IEEE; 2009. p. 2577–9.

76. Yamamoto S, Watabe T, Watabe H, Aoki M, Sugiyama E, Imaizumi M, Kanai Y, Shimosegawa E, Hatazawa J. Simultaneous imaging using Si-PM-based PET and MRI for development of an integrated PET/MRI system. Phys Med Biol. 2012;57:N1–N13.

77. Hong K, Choi Y, Jung JH, Kang J, Hu W, Lim HK, Huh Y, Kim S, Jung JW, Kim KB, Song MS, Park HW. A prototype MR insertable brain PET using tileable GAPD arrays. Med Phys. 2013;40:042503-1–12.

78. Yamaya T, Obata T, Shimizu K, Suga M, Inadama N, Tachibana A, Yoshida E, Ito H, Yamaya T. Feasibility of a brain-dedicated PET-MRI system using four-layer DOI detectors integrated with an RF head coil. Nucl Instrum Methods Phys Res Sect A. 2014;756:6–13.

79. Knoll GF. Radiation detection and measurement. Hoboken: Wiley; 2010.

80. Karp JS, Surti S, Daube-Witherspoon ME, Muehllehner G. Benefit of time-of-flight in PET: experimental and clinical results. J Nucl Med. 2008;49:462–70.

81. Anger HO. Scintillation camera with multichannel collimators. J Nucl Med. 1964;5:515–31.

82. Siegmund OHW, Zaninovich J, Tremsin AS, Hull JS. Cross strip anodes for MCP imaging detectors. Proc SPIE. 2009;3445:397–406.

83. Chang CM, Grant AM, Lee BJ, Kim E, Hong K, Levin CS. Performance characterization of compressed sensing positron emission tomography detectors and data acquisition system. Phys Med Biol. 2015;60:6407–21.

84. Chinn G, Olcott PD, Levin CS. Sparse signal recovery methods for multiplexing PET detector readout. IEEE Trans Med Imaging. 2013;32:932–42.

85. Weissler B, Gebhardt P, Duppenbecker PM, Wehner J, Schug D, Lerche CW, Gold-schmidt B, Salomon A, Verel I, Heijman E, Perkuhn M, Heberling D, Botnar RM, Kiessling F, Schulz V. A digital preclinical PET/MRI insert and initial results. IEEE Trans Med Imaging. 2015;34:2258–70.

86. Grant AM, Lee BJ, Chang C-M, Levin CS. Simultaneous PET/MR imaging with a radio frequency-penetrable PET insert. Med Phys. 2017;44(1):11220.

87. Jung JH, Choi Y, Jung J, Kim S, Lim HK, Im KC, Oh CH, Park HW, Kim KM, Kim JG, et al. Med Phys. 2015;42(5):2354–63.

88. Quick HH, Ladebeck R, Georgi J-C. Whole-body MR/PET hybrid imaging: technical considerations, clinical workflow, and initial results. MAGNETOM Flash, vol. 1. p. 88–100. 2011.

89. Mediso. nanoScan PET, retrieved from http://www.mediso.com/uploaded/ NPMPCB_0816_web.pdf.

90. Bruker. PET Insert brochure, retrieved from https://www.bruker.com/ fileadmin/user_upload/8- PDF- Docs/PreclinicalImaging/ Brochures/PET_Insert_T161857.pdf.

91. MR Solutions. Simultaneous and sequential acquisition of PET & MR-MRS-PET, retrieved from http://www.mrsolutions.com/products/imaging-systems/petmr/.

92. Bailey DL, Meikle SR. A convolution-subtractions scatter correction method for 3DPET. Phys Med Biol. 1994;39:411–24.

93. Bentourkia M, Msaki P, Cadorette J, Lecomte R. Assessment of scatter components in high-resolution PET: correction by nonstationary convolution subtraction. J Nucl Med. 1995;36:121–30.

94. Levin CS, Dahlbomand M, Hoffman EJ. A Monte-Carlo correction for the effect of Compton scattering in 3-D PET brain imaging. IEEE Trans Nucl Sci. 1995;42(4):1181–5.

95. Cherry SR, Meikleand SR, Hoffman EJ. Correction and Characterisation of Scattered Events in three-dimensional PET using scanners with retractable septa. J Nucl Med. 1993;34:671–8.

96. Shao L, Freifelder R, Karp JS. Triple energy window scatter correction technique in PET. IEEE Trans Med Imaging. 1994;13(4):641–8.

97. Grootoonk S, Spinks TJ, Sashin D, Spryou NM, Jones T. Correction for scatter in 3D brain PET using a dual energy window method. Phys Med Biol. 1996;41:2757–74.

98. Stearns CW. Scatter correction method for 3D PET using 2D fitted Gaussian functions. J Nucl Med. 1995;36:105P.

99. Cherry SR, Huang S-C. Effects of scatter on model parameter estimates in 3D PET studies of the human brain. IEEE Trans Nucl Sci. 1995;42(4):1174–9.

100. Ollinger JM. Model-based scatter correction for fully 3D PET. Phys Med Biol. 1996;4:1153–76.

101. Watson CC, Newport D, Casey ME. A single-scatter simulation technique for scatter correction in 3D PET. In Grangeat P, Amans JL, editors. Three-dimensional image reconstruction in radiology and nuclear medicine. Dordrecht: Kluwer Academic; 1996. ISBN:0-7923-4129-5.

102. Lee BJ, Grant AM, Chang CM, Glover GH, Levin CS. RF-transmissive PET detector insert for simultaneous PET/MRI. In: 2014 IEEE nuclear science symposium and medical imaging conference (NSS/MIC). IEEE; 2014. p. 1–3.

103. Lee BJ, Olcott PD, Hong KJ, Grant AM, Chang C-M, Levin CS. Studies of electromagnetic interference of PET detector insert for simultaneous PET/MRI. In: nuclear science symposium and medical imaging conference (NSS/MIC), 2013. IEEE; 2013. p. 1–3.

104. Olcott PD, Peng H, Levin CS. Novel electro-optical coupling technique for magnetic resonance–compatible positron emission tomography detectors. Mol Imaging. 2009;8(2):74–86.

105. Nishikido F, et al. Feasibility of a brain-dedicated PET-MRI system using four-layer DOI detectors integrated with an RF head coil. Nucl Instrum Methods Phys Res Sect A. 2014;756:6–13.

106. Gonzlez AJ, et al. The MINDView brain PET detector, feasibility study based on SiPM arrays. Nucl Instrum Methods Phys Res Sect A. 2016;818:82–90.

107. Sportellietal G. The TRIMAGE PET data acquisition system: initial results. IEEE Trans Radiat Plasma Med Sci. 2017;1(2):168–77.

MR Pulse Sequences for PET/MRI

2

Peder E.Z. Larson and Valentina Taviani

Contents

2.1 Introduction

PET/MRI systems have incredible potential because they combine the broad range of soft tissue contrasts available with MRI with the functional and metabolic information from PET in a single scan. MRI acquisitions, using specific MR pulse sequences,

P.E.Z. Larson (✉)

Department of Radiology and Biomedical Imaging, University of California, San Francisco, San Francisco, CA, USA

UC Berkeley-UCSF Graduate Program in Bioengineering, University of California, Berkeley, Berkeley, CA, USA
e-mail: peder.larson@ucsf.edu

V. Taviani
Global MR Applications & Workflow, GE Healthcare, Menlo Park, CA, USA

27

have some unique requirements in PET/MRI given the workflow, PET reconstruction, and clinical applications of these systems. PET/MRI workflow typically requires whole-body imaging and benefits substantially from accelerated MRI strategies. PET reconstruction requires accurate attenuation correction, which is challenging because MRI measures the proton density but not the electron density that determines attenuation. PET reconstruction also benefits from MRI-based motion management. Clinical PET/MRI applications are mostly focused on oncology, often requiring monitoring of pulmonary nodules and the use of diffusion-weighted MRI. This chapter describes current MRI acquisition strategies available or being developed that address the specific requirements imposed by PET/MRI systems.

2.2   Standard MR Pulse Sequences

MRI generates multiple soft tissue contrasts through the use of different pulse sequences [1]. These pulse sequences define how the MRI scanner excites hydrogen atoms in water molecules to create signals and how spatial information is encoded using magnetic field gradients. Excitation of hydrogen atoms, also commonly referred to as "spins," is performed with radio-frequency (RF) fields, which are created by RF transmit antennas, commonly referred to as "coils." RF receive antennas/coils are used to receive the signal coming from spins after excitation. Magnetic field gradients, referred to as "gradients," change the magnetic field at different spatial positions, which allow for encoding of spatial information. Gradients can be applied in the X, Y, and Z directions (G_X, G_Y, G_z), which allow for creation of images in arbitrary scan planes (axial, coronal, sagittal, and any oblique orientation). Gradients are also used for encoding motion information such as flow and diffusion.

Most MR pulse sequences fall into two classes: gradient-echo and spin-echo pulse sequences (Fig. 2.1). These can be used to generate multiple types of contrast

gradient echo   spin echo

| out of phase GRE | pre-contrast T1 | portal venous phase T1 | single shot fast spin echo | DWI (b=50) |
| in phase GRE | arterial phase T1 | hepatobiliary phase T1 | Fast spin echo (FSE) | DWI (b=600) |

Generally used for T1 weighted imaging and pre/post contrast imaging. Fast and usually done as volumetric acquisitions

Generally used for T2 weighted imaging and diffusion weighed imaging.
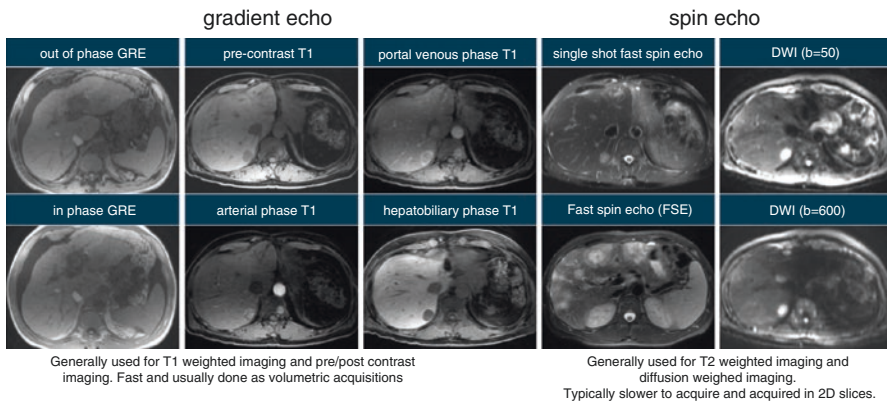Typically slower to acquire and acquired in 2D slices.

Fig. 2.1 Sample MR images using gradient-echo and spin-echo pulse sequences in the abdomen. Gradient-echo (GRE) images shown include examples of T1 weighting and fat/water separation. Gradient echo is often used for post-contrast imaging. Spin-echo images include T2-weighted anatomical imaging with fast spin-echo and diffusion-weighted imaging (DWI)

including T1 weighting, T2 weighting, and diffusion weighting. The contrast is primarily defined by the echo time (TE), which is the time between RF excitation and data acquisition, the repetition time (TR), which is the time between successive RF excitations, and the amount of RF excitation, which is defined by the flip angle. During the time between consecutive RF excitations, the spins evolve according to two characteristic relaxation times, called T1 and T2, where T2 determines the rate of signal decay following an RF excitation, and T1 determines the rate of magnetization recovery between successive RF excitations. As an example, in a spin-echo pulse sequence, T2 weighting is created with a long TR, by increasing the TE, whereas T1 weighting is created with a short TE, by decreasing TR.

Gradient-echo (GE or GRE) pulse sequences consist of an RF excitation followed by imaging gradients. They typically use short echo times (TEs) and short repetition times (TRs), so are mostly used for T1-weighted imaging. Post-contrast imaging is performed with T1-weighted GRE sequences. The short TR also allows for efficient volumetric acquisitions. Fat/water imaging, as discussed later in this chapter, typically uses GRE sequences.

Spin-echo (SE, FSE, TSE) pulse sequences use one or more additional RF pulses to "refocus" sources of imperfection in the magnetic field that would otherwise lead to signal loss. This refocusing implies longer TEs with respect to gradient echo; thus, spin-echo pulse sequences are generally used for T2-weighted imaging. Diffusion-weighted imaging is also based on spin echo. Typically, multiple spin echoes are used for anatomical imaging in the so-called fast or turbo spin-echo (FSE, TSE) sequences for faster scanning.

2.3 General Considerations

2.3.1 System Limitations

Simultaneous PET/MRI systems include both PET and MRI hardware. The major modification of the MRI hardware is that a wide-bore magnet design is used to accommodate the PET hardware, slightly compromising the performance of the magnetic field gradients and the RF transmit ("body") coil. However, these gradients and body coil are equivalent to current wide-bore MRI-only systems, which can easily meet the requirements of clinical imaging pulse sequences. PET/MRI systems can also use the same receive coil arrays as on MRI-only systems, although some consideration should be given to making these coils PET invisible (i.e., limiting their attenuation).

2.3.2 Whole-Body Imaging

The workflow for many PET/MRI studies includes a whole-body acquisition; so simultaneous whole-body MRI protocols need to maximize overall scan efficiency (see Chap. 10). Many MRI whole-body techniques have been developed and can be

applied to PET/MRI. Whole-body diffusion-weighted imaging is particularly challenging and is discussed in more detail later in this chapter.

Whole-body workflows often aim for 3–5 min per bed position to keep a reasonable overall scan time [2]. Pulse sequences that are inherently fast by design are typically used in PET/MRI protocols. These include single-shot fast spin echo (SSFSE, HASTE) for T2-weighted imaging [3] and two-point Dixon [4] for T1-weighted imaging. Single-shot fast spin-echo pulse sequences acquire a complete 2D image following a single RF excitation. The main limitations of this technique are blurring due to T2 decay during the long train of refocusing RF pulses and high levels of energy deposition to the patient that are counterbalanced by relatively low resolution and long repetition times, respectively. Technical developments now adopted by all major vendors have greatly improved speed and resolution [5], so that single-shot fast spin echo can now achieve adequate resolution and repetition times of less than a second per slice, which allows full coverage of motion-prone regions (chest, abdomen) in a single breath-hold. While the clinical acceptance of single-shot fast spin echo is increasing, conventional fast spin echo (FSE, TSE, RARE) is still often preferred for the generally superior image quality, despite the considerably longer acquisition times and associated motion sensitivity.

In particular, STIR (short-tau inversion recovery) [6] and radial fast spin-echo imaging (PROPELLER, BLADE) [7, 8] are commonly used. STIR is a fat-suppression preparation, whereby all spins are inverted before the RF excitation is played out and the start of the host pulse sequence is timed to coincide with the time when the longitudinal magnetization of fat is zero. While this ensures uniform fat suppression even in the presence of large field inhomogeneities, which are often present given the large coverage required for whole-body imaging, SNR is significantly degraded as all the other tissues are also recovering according to T1 at the time of excitation; therefore, longer scan times are generally necessary to achieve adequate signal levels.

Radial fast spin echo is a fast spin-echo-based technique where the central part of k-space (the spatial frequency space where raw MR signals are stored before image reconstruction) is repeatedly sampled during the acquisition [7]. A dedicated image reconstruction exploits this data redundancy to create motion-free images during free breathing [8]. While image quality can be superior to single-shot fast spin echo (higher resolution, reduced blurring), motion insensitivity comes with longer acquisitions that can be problematic, especially in the context of whole-body imaging.

T1-weighted imaging is often performed using high-resolution 3D gradient-echo pulse sequences [9]. Water/fat resolved imaging, discussed in more detail later in this chapter, is often used for the excellent image quality, speed, and the characteristic of providing several image contrasts in a single acquisition, namely, a "water-only" image (similar to a fat-suppressed image), an "in-phase" image (effectively a nonfat-suppressed image), an "out-of-phase" image characterized by a dark rim between water and fatty tissues, and a "fat-only" image that depicts only fat-containing tissues (Fig. 2.2). While water-/fat-separated imaging can often achieve relatively high-image resolution, depending on the specific implementation, there can be a limit on the maximum matrix size that the user can prescribe. In these cases, other fat-suppression methods (SPECIAL, SPAIR) can be used in conjunction with conventional fast 3D gradient-echo pulse sequences for high-resolution, fat-suppressed T1-weighted imaging.
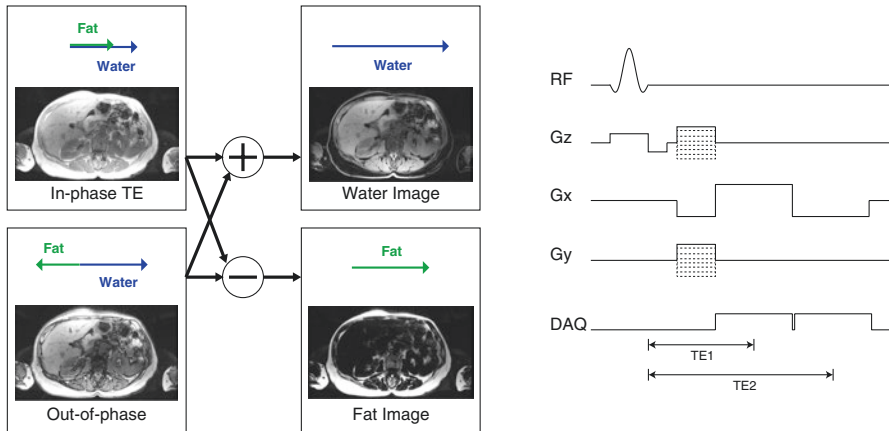
Fig. 2.2 Fat/water imaging using a two-echo Dixon acquisition is performed by acquiring data at multiple TEs with different relative phases between fat and water and then combining them to produce water-only and fat-only images, illustrated for the ideal scenario above

A recently proposed alternative for T1-weighted imaging, with excellent motion properties, is 3D radial gradient-echo imaging [10]. The MR signals are encoded according to a stack-of-stars pattern, whereby several "stars" are consecutively acquired to cover the desired 3D volume. Because the center of k-space is repeatedly sampled for each "star," motion artifacts can be greatly mitigated by advanced image reconstruction algorithms.

In general, considerations on speed, as well as robustness to motion and system imperfections (B0 and B1 inhomogeneities), often dictate which pulse sequence should be used for a specific protocol. Accelerated imaging strategies such as parallel imaging and compressed sensing can be used to speed up the acquisition, at the cost of reduced signal-to-noise ratio and with performance dependent on the specific array coil used for signal reception. Parallel imaging methods are standard on clinical PET/MRI systems, under the names ASSET and ARC (GE) and mSENSE and GRAPPA (Siemens). These methods use receive coil arrays, undersample data in k-space, and use specialized image reconstructions [11, 12]. Compressed sensing utilizes the inherent sparsity of MR images to accelerate acquisitions [13], which is now implemented for some pulse sequences in current commercial scanners. The use of compressed sensing will likely increase in the future.

2.3.3   MR Attenuation Correction

Accurate PET reconstruction requires an estimate of the photon attenuation prior to detection. In the body, there is a range of attenuation in soft tissues, and bone attenuation is higher than soft tissues. In PET/CT systems, the attenuation is derived from CT, which is a direct measurement of the electron density that determines the attenuation. However, MRI measures signals from protons, and does not provide any direct measurements of electron density. This has proven to be a challenge for PET/MRI,

and current promising strategies are based on imaging atlases as well as specialized pulse sequences for soft tissue and bone imaging. In this chapter, we will describe the principles of the specialized pulse sequences used for MR-based attenuation correction (MRAC). Chapter 6 ("PET/MRI: attenuation correction") describes how the resulting images are used for attenuation correction and PET reconstruction.

2.3.4 Fat/Water Imaging

Many MRAC strategies use fat-water separation imaging methods, also known as "Dixon" or "IDEAL" methods [4, 14, 15]. These methods acquire data at multiple echo times (TEs). Since fat and water have different resonance frequencies due to their chemical shift, they will appear with different phases as a function of TE. With the known frequency shift between fat and water, images of the fat fractional signal and water fractional signal are generated with these methods. These can then be used to account for the differences in attenuation between fatty tissues and water soft tissues, as described in Chap. 6.

The principle of fat/water imaging methods is illustrated in Fig. 2.2. In an ideal situation, images are acquired at two different TEs, chosen such that fat and water are "in phase" for one TE and "out of phase" for the other. These images then can be used to generate fat and water images. In reality, the phase also evolves as a function of TE due to resonance frequency shifts due to magnetic field inhomogeneities. This can be accounted for by either acquiring a third TE image to explicitly measure these field variations ("three-point Dixon" [16]) or by using only two TE images with some assumption of spatial smoothness of the field variations ("two-point Dixon" [14]).

For MRAC, typically two-point Dixon approaches are used, as they are faster and the smooth field variation assumption has been shown to be robust for clinical imaging. The RF body coil is typically used for transmit and receive, as local receive RF coil arrays can introduce undesirable variations across the images. To provide the volumetric coverage required, 3D gradient-recalled echo (GRE) sequences with two TEs are used as shown in Fig. 2.2. The two TE images are then combined to generate fat-fraction and water-fraction images from which soft tissue attenuation coefficients can be assigned [17].

2.3.5 Bone Imaging

Conventional MR imaging pulse sequences do not detect any signal from the bone due to its rapid MR signal decay rate (T2* ≈ 0.4 ms [18–20]). This has been a major challenge in PET/MRI because the bone has the largest photon attenuation among all tissue types but is difficult to image with MRI. Neglecting the bone leads to large errors in PET uptake in and around the bone, measured to be between 10% and 15% [21–23]. Specialized MRI pulse sequences, so-called ultrashort echo-time (UTE) and zero echo-time (ZTE) pulse sequences, offer the potential to capture the rapidly decaying signal from the bone and thus are being actively developed and applied to improve MRAC.

Conventional MRI pulse sequences, such as the gradient-echo sequence illustrated in Fig. 2.2, have minimum TEs of approximately 1 ms. This is due to the time required to play out a slice-selective RF pulse as well as the frequency and phase-encoding gradients. UTE and ZTE can achieve TEs below 100 μs on clinical MRI scanners by using specialized RF pulse and image-encoding strategies, examples of which are shown in the pulse sequences in Fig. 2.3. For RF excitation, the TE can be minimized by using volumetric excitation with no slice-selection, minimum-phase slab excitation (UTE only), or half-pulse slice-selective excitation [24] (UTE only). For image encoding, radial k-space sampling is most commonly used (as shown in Fig. 2.3), but spiral or cones k-space trajectories are also possible [25, 26] (UTE only). These encoding strategies require using a nonuniform Fourier transform reconstruction. ZTE also has the unique property of near-silent scanning but requires advanced reconstructions or additional acquisitions to fill in missing data at the center of k-space. A more detailed comparison of UTE and ZTE can be found [27].

Due to its low proton density and rapid decay rate, bone has a relatively low signal even with UTE and ZTE MRI. This signal difference has been used to estimate bone density for attenuation correction from ZTE MRI [28, 29]. MRAC including the bone has also been accomplished by separating the bone based on its relaxation rate, T2* [30–35]. Fat/water separation can be included in UTE MRI by adding additional TEs and using the processing methods described in the previous section. Sample
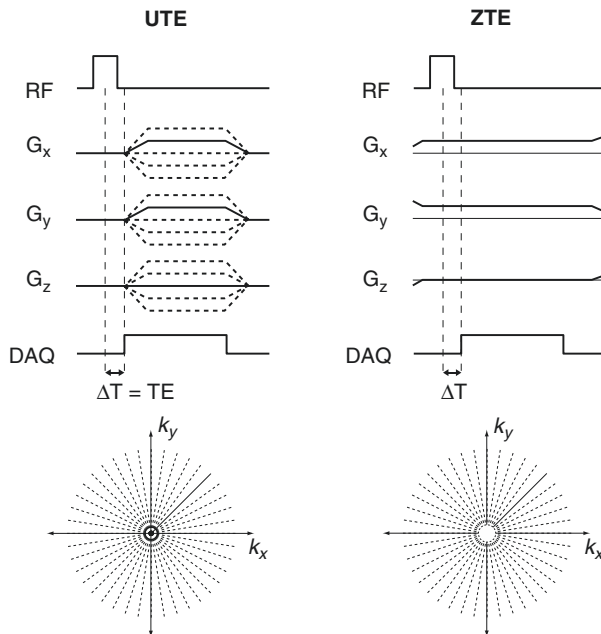

Fig. 2.3 UTE and ZTE MRI pulse sequences that can image the bone for estimation of tissue attenuation coefficients. (**a**) 3D imaging sequences, most commonly used for MRAC, are shown with (**b**) two dimensions of the k-space sampling
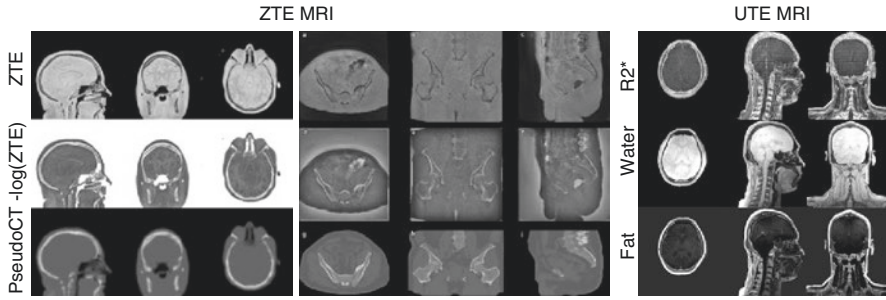
Fig. 2.4 Bone imaging examples using ZTE and UTE pulse sequences. ZTE Images acquired with proton-density weighting (*top row*) can be converted to the pseudoCTs (*bottom row*) for MRAC as described in [27, 28] with processing that includes inverse logarithm scaling of the ZTE images (*middle row*) to more clearly show bone signal. UTE images with multiple echo times can be used for relaxation time ($R^{2*} = 1/T2^*$), water, and fat measurements, where the relaxation time images result in CT-like contrast with high intensity for the bone and can be converted into pseudoCTs [32]

images in the brain and pelvis from UTE and ZTE acquisitions are shown in Fig. 2.4. MRAC generation methods are described in greater detail in Chap. 6.

2.3.6 Diffusion-Weighted Imaging

Water molecules diffuse in biological tissues under the effect of Brownian thermal motions. Because the diffusion of water molecules is restricted by the presence of obstacles, such as macromolecules, membranes, etc., measuring the diffusivity of these molecules in different tissues provides information on the underlying microstructure [36]. The more cellular the tissue, the more restricted the diffusion.

Diffusion-weighted imaging (DWI) is often achieved by playing out two identical gradient lobes on either sides of the refocusing RF pulse of a spin-echo pulse sequence. Immediately after the RF excitation pulse, all spins are aligned along the same direction in the transverse plane. While the first gradient lobe is played out, static spins dephase at a rate that depends on the local magnetic field imposed by the gradient itself. The refocusing RF pulse flips them over, while the direction of dephasing remains unchanged. Because these spins are static, they experience exactly the same local magnetic field while the second gradient lobe is applied, so that at the time of the spin echo, they end up back in phase as if no gradients were played out.

Diffusing spins, unlike static spins, experience slightly different local magnetic fields before and after the refocusing RF pulse, as their spatial location in the direction of the applied gradients has slightly changed due to random motion at molecular level. As a result, at the time of the spin echo, not all spins end up back in phase, and the measured signal is reduced by a factor that depends on the mean diffusivity of water molecules in that specific tissue.

Similar to T2-weighted imaging, where longer TEs are used to increase the amount of T2 weighting, larger diffusion-sensitizing gradients can be used to increase the amount of diffusion weighting. In practice, the amount of diffusion weighting is

expressed by a quantity called b value. The higher the b value, the higher the amount of diffusion weighting. A standard T2-weighted image is also a b=0 image (i.e., no diffusion-sensitizing gradients applied). A heavily diffusion-weighted image will be characterized by low signal intensities in regions of unrestricted diffusion (fluids) and high signal intensities in areas of restricted diffusion (e.g., tumors). In truth, high signal intensity in a diffusion-weighted image can be due to either restricted diffusion or long T2. Apparent diffusion coefficients (ADC) can be computed from two diffusion-weighted images with different b values to provide a measure of diffusivity independent of T2.

From an acquisition point of view, diffusion-weighted imaging typically relies on echo-planar imaging (EPI), because of its speed, signal-to-noise efficiency, and robustness to motion [37]. However, EPI is also extremely sensitive to off-resonance, leading to significant distortion and image artifacts, especially for whole-body imaging [38].

2.3.7   Whole-Body Diffusion-Weighted Imaging

Distortion is proportional to the local off-resonance field and the duration of the EPI readout. Whole-body imaging requires large anatomical coverage, which means relatively long readouts even for a modest image resolution. At the same time, field inhomogeneities due to eddy currents, susceptibility variations, chemical shift, and other system imperfections are more difficult to control over large imaging volumes.

Parallel imaging techniques are routinely used to reduce distortion, although their effectiveness is limited by the performance of the specific coil array used for signal reception. Higher-order eddy current compensation strategies, either prospective or retrospective, are often implemented to reduce distortion induced by eddy currents [39]. STIR is the preferred fat-suppression method for whole-body imaging due to its robustness to B0 and B1 inhomogeneities, despite the lower intrinsic SNR. Chemically selective fat-suppression methods (fat presaturation, spectral-spatial RF pulses, and gradient reversal), even when used in combination, can result in fat-suppression failures that translate in chemical shifts of several pixels across the imaged FOV. Signal averaging during free breathing is routinely used to compensate for the otherwise low SNR due to STIR, and usually no more than two *b* values are acquired to avoid lengthy acquisitions. Free-breathing diffusion-weighted imaging using STIR and signal averaging is referred to as DWIBS (diffusion-weighted imaging with background suppression) [40].

Whole-body diffusion imaging is typically performed axially, with coronal/sagittal reformats generated for the purpose of visualization. A common artifact observed in sagittal reformats is the typical stair-step appearance of the spine, due to center frequency mismatch between different beds. Recently developed prospective and retrospective corrections aimed at minimizing this artifact have greatly improved the appearance of sagittal and coronal reformats of whole-body imaging datasets [41–43] (Fig. 2.5).

2.3.8   Lung Imaging

A significant limitation to widespread clinical implementation of PET/MRI is poor evaluation of the lung parenchyma. Pulmonary imaging is challenging for MRI due
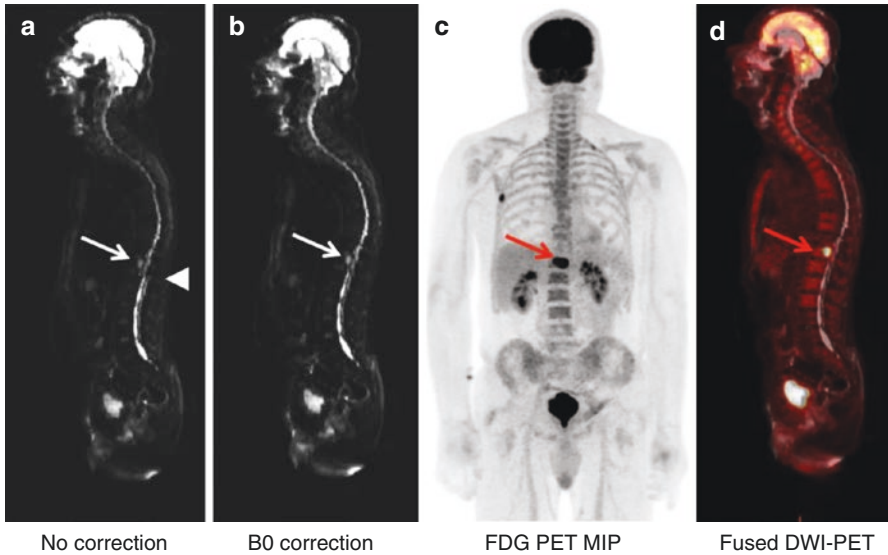
Fig. 2.5 B0 field inhomogeneities result in artifacts in whole-body diffusion-weighted imaging including signal loss and anatomic misregistration (**a**, *white arrow head*). Real-time center frequency adjustment can significantly reduce these artifacts (**b**). Advanced prospective and retrospective corrections also improve anatomical co-registration of MR and PET data. A whole-body FDG PET imaging with a metastatic lesion in the spine (**c**, *red arrow*), which co-registers with the acquired whole-body DWI acquisition (**d**, *red arrow*) when using advanced correction techniques

to low tissue density, motion, and rapid signal decay rates with T2* ≈ 0.5–3 ms [43–47]. With these limitations, MRI detection rates of large pulmonary nodules (>1 cm) are high; however, the detection rate of subcentimeter nodules remains inadequate for routine clinical evaluation. See Chap. 15 ("Lung nodules and lung cancer") for a more detailed description of pulmonary PET/MRI.

The ultrashort echo-time (UTE) and zero echo-time (ZTE) MRI pulse sequences, described previously for bone imaging to improve MRAC (Figs. 2.3 and 2.4), are also a promising approach for lung imaging. They can capture the rapidly decaying signals in the lung and additionally are much more robust to motion than conventional pulse sequences. 3D imaging is typically used (similar pulse sequences to Fig. 2.3), though often with slab-selective excitation to minimize aliasing artifacts [48]. Pulmonary nodule imaging results with UTE MRI are shown in Fig. 2.6, with detection of nodules down to 3–5 mm in size [49]. To compensate for motion and improve image quality, randomized ordering strategies and self-gating from the repeated central k-space sampling can be applied. Compressed sensing and parallel imaging strategies can also be incorporated to improve image quality.
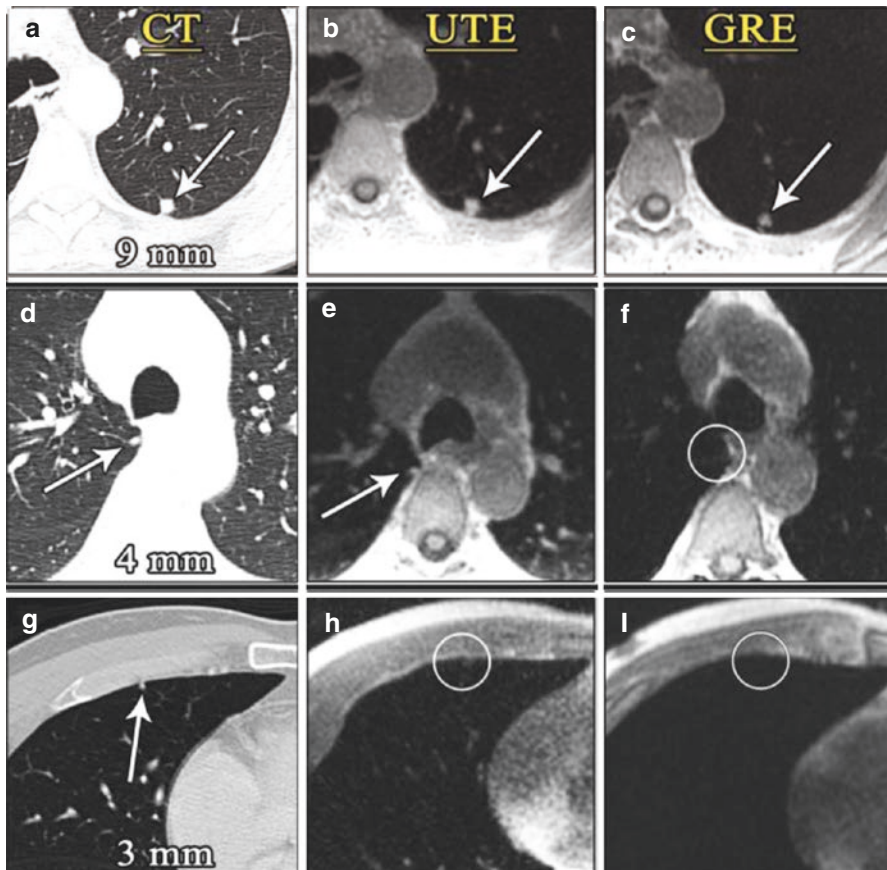
Fig. 2.6 Patient examples of nodule detection by CT (**a**, **d**, **g**), UTE (**b**, **e**, **h**), and dual-echo GRE (**c**, **f**, **i**) techniques (acquired on a PET/MRI) [48]. UTE shows relatively high-image quality for pulmonary MRI, identifying nodules down to 3–5 mm in size. UTE images show small pulmonary nodules (*middle column*, **e** and **h**) that cannot be visualized using conventional gradient-echo techniques (*right column*, **f** and **i**)

References

1. Plewes DB, Kucharczyk W. Physics of MRI: a primer. J Magn Reson Imaging. 2012;35(5):1038–54.
2. Martinez-Möller A, Eiber M, Nekolla SG, et al. Workflow and scan protocol considerations for integrated whole-body PET/MRI in oncology. J Nucl Med. 2012;53:1415–26.
3. Semelka RC, Kelekis NL, Thomasson D, Brown MA, Laub GA. HASTE MR imaging: description of technique and preliminary results in the abdomen. J Magn Reson Imaging. 1996;6:698–9.
4. Dixon WT. Simple proton spectroscopic imaging. Radiology. 1984;153:189–94.
5. Loening AM, Litwiller DV, Saranathan M, Vasanawala SS. Increased speed and image quality for pelvic single-shot fast spin-echo imaging with variable refocusing flip angles and full-fourier acquisition. Radiology. 2016;282:561–8.

6. Bydder GM, Young IR. MR imaging: clinical use of the inversion recovery sequence. J Comput Assist Tomogr. 1985;9:659–75.

7. Pipe JG. Motion correction with PROPELLER MRI: application to head motion and free-breathing cardiac imaging. Magn Reson Med. 1999;42:963–9.

8. Pipe JG, Zwart N. Turboprop: Improved PROPELLER imaging. Magn Reson Med. 2006;55:380–5.

9. Hargreaves BA. Rapid gradient-echo imaging. J Magn Reson Imaging. 2012;36:1300–13.

10. Feng L, Axel L, Chandarana H, Block KT, Sodickson DK, Otazo R. XD-GRASP: golden-angle radial MRI with reconstruction of extra motionstate dimensions using compressed sensing. Magn Reson Med. 2015. https://doi.org/10.1002/mrm.25665.

11. Griswold MA, Jakob PM, Heidemann RM, et al. Generalized autocalibrating partially parallel acquisitions (GRAPPA). Magn Reson Med. 2002;47:1202–10.

12. Pruessmann KP, Weiger M, Scheidegger MB, Boesiger P. SENSE: sensitivity encoding for fast MRI. Magn Reson Med. 1999;42:952–62.

13. Lustig M, Donoho D, Pauly JM. Sparse MRI: the application of compressed sensing for rapid MR imaging. Magn Reson Med. 2007;58:1182–95.

14. Ma J. Dixon techniques for water and fat imaging. J Magn Reson Imaging. 2008;28:543–58.

15. Reeder SB, Brittain JH, Grist TM, Yen Y-F. Least-squares chemical shift separation for (13)C metabolic imaging. J Magn Reson Imaging. 2007;26:1145–52.

16. Glover GH. Multipoint dixon technique for water and fat proton and susceptibility imaging. J Magn Reson Imaging. 1991;1:521–30.

17. Wollenweber SD, Ambwani S, Lonn AHR, et al. Comparison of 4-class and continuous fat/water methods for whole-body, mr-based PET attenuation correction. IEEE Trans Nucl Sci. 2013;60:3391–8.

18. Du J, Carl M, Bydder M, Takahashi A, Chung CB, Bydder GM. Qualitative and quantitative ultrashort echo time (UTE) imaging of cortical bone. J Magn Reson. 2010;207:304–11.

19. Horch RA, Nyman JS, Gochberg DF, Dortch RD, Does MD. Characterization of 1H NMR signal in human cortical bone for magnetic resonance imaging. Magn Reson Med. 2010;64:680–7.

20. Krug R, Larson PEZ, Wang C, et al. Ultrashort echo time MRI of cortical bone at 7 tesla field strength: a feasibility study. J Magn Reson Imaging. 2011;34:691–5.

21. Mehranian A, Zaidi H. Impact of time-of-flight PET on quantification errors in MR imaging-based attenuation correction. J Nucl Med. 2015;56:635–41.

22. Ouyang J, Chun SY, Petibon Y, Bonab AA, Alpert N, Fakhri GE. Bias atlases for segmentation-based PET attenuation correction using PET-CT and MR. IEEE Trans Nucl Sci. 2013;60:3373–82.

23. Samarin A, Burger C, Wollenweber SD, et al. PET/MR imaging of bone lesions–implications for PET quantification from imperfect attenuation correction. Eur J Nucl Med Mol Imaging. 2012;39:1154–60.

24. Pauly JM, Conolly SM, Nishimura DG, Macovski A. Slice-selective excitation for very short T2 species. Proceedings of the SMRM, 8th Annual Meeting; 1989. p. 28.

25. Du J, Bydder M, Takahashi AM, Chung CB. Two-dimensional ultrashort echo time imaging using a spiral trajectory. Magn Reson Imaging. 2008;26:304–12.

26. Gurney PT, Hargreaves BA, Nishimura DG. Design and analysis of a practical 3D cones trajectory. Magn Reson Med. 2006;55:575–82.

27. Larson PEZ, Han M, Krug R, et al. Ultrashort echo time and zero echo time MRI at 7T. MAGMA. 2015. https://doi.org/10.1007/s10334-015-0509-0.

28. Leynes AP, Yang J, Shanbhag DD, et al. Hybrid ZTE/Dixon MR-based attenuation correction for quantitative uptake estimation of pelvic lesions in PET/MRI. Med Phys. 2017. https://doi.org/10.1002/mp.12122.

29. Wiesinger F, Sacolick LI, Menini A, et al. Zero TE MR bone imaging in the head. Magn Reson Med. 2015. https://doi.org/10.1002/mrm.25545.

30. Berker Y, Franke J, Salomon A, et al. MRI-based attenuation correction for hybrid PET/MRI systems: a 4-class tissue segmentation technique using a combined ultrashort-echo-time/Dixon MRI sequence. J Nucl Med. 2012;53:796–804.

31. Cabello J, Lukas M, Förster S, Pyka T, Nekolla SG, Ziegler SI. MR-based attenuation correction using ultrashort-echo-time pulse sequences in dementia patients. J Nucl Med. 2015;56:423–9.
32. Delso G, Carl M, Wiesinger F, et al. Anatomic evaluation of 3-dimensional ultrashort-echo-time bone maps for PET/MR attenuation correction. J Nucl Med. 2014;55:780–5.
33. Juttukonda MR, Mersereau BG, Chen Y, et al. MR-based attenuation correction for PET/MRI neurological studies with continuous-valued attenuation coefficients for bone through a conversion from R2* to CT-Hounsfield units. NeuroImage. 2015;112:160–8.
34. Keereman V, Fierens Y, Broux T, De Deene Y, Lonneux M, Vandenberghe S. MRI-based attenuation correction for PET/MRI using ultrashort echo time sequences. J Nucl Med. 2010;51:812–8.
35. Navalpakkam BK, Braun H, Kuwert T, Quick HH. Magnetic resonance-based attenuation correction for PET/MR hybrid imaging using continuous valued attenuation maps. Investig Radiol. 2013;48:323–32.
36. Le Bihan D. Looking into the functional architecture of the brain with diffusion MRI. Nat Rev Neurosci. 2003;4:469–80.
37. Mansfield P. Multiplanar image formation using NMR spin-echoes. J Phys Chem Solid State Phys. 1977;10:L55.
38. Le Bihan D, Poupon C, Amadon A, Lethimonnier F. Artifacts and pitfalls in diffusion MRI. J Magn Reson Imaging: JMRI. 2006;24:478–88.
39. Xu D, Maier JK, King KF, et al. Prospective and retrospective high order eddy current mitigation for diffusion weighted echo planar imaging. Magn Reson Med. 2013;70:1293–305.
40. Takahara T, Imai Y, Yamashita T, Yasuda S, Nasu S, Van Cauteren M. Diffusion weighted whole body imaging with background body signal suppression (DWIBS): technical improvement using free breathing, STIR and high resolution 3D display. Radiat Med. 2004;22:275–82.
41. Fung M, Gaohong, Wu, Xu, Dan, Hinks, Scott, Bayram, Ersin. Realtime B0 Inhomogeneity Correction in Multi-Station Diffusion Imaging. Proceedings of the 23rd Annual Meeting of the ISMRM; 2015. p. 1606.
42. Lee S-K, Hancu I. Patient-to-patient variation of susceptibility-induced B0 field in bilateral breast MRI. J Magn Reson Imaging: JMRI. 2012;36:873–80.
43. Mori S, Muro I, Moriguchi H, et al. Distortion correction of body diffusion weighted images using three point-dixon method. Proceedings of the 18th Annual Meeting of the ISMRM; 2010. p. 4718.
44. Ohno Y, Koyama H, Yoshikawa T, et al. T2* measurements of 3-T MRI with ultrashort TEs: capabilities of pulmonary function assessment and clinical stage classification in smokers. AJR Am J Roentgenol. 2011;197:W279–85.
45. Stock KW, Chen Q, Hatabu H, Edelman RR. Magnetic resonance T2* measurements of the normal human lung in vivo with ultra-short echo times. Magn Reson Imaging. 1999;17:997–1000.
46. Theilmann RJ, Arai TJ, Samiee A, et al. Quantitative MRI measurement of lung density must account for the change in T(2) (*) with lung inflation. J Magn Reson Imaging. 2009;30:527–34.
47. Yu J, Xue Y, Song HK. Comparison of lung T2* during free-breathing at 1.5 T and 3.0 T with ultrashort echo time imaging. Magn Reson Med. 2011;66:248–54.
48. Johnson KM, Fain SB, Schiebler ML, Nagle S. Optimized 3D ultrashort echo time pulmonary MRI. Magn Reson Med. 2013;70:1241–50.
49. Burris NS, Johnson KM, Larson PEZ, et al. Detection of small pulmonary nodules with ultrashort echo time sequences in oncology patients by using a PET/MR system. Radiology. 2015:150489. https://doi.org/10.1148/radiol.2015150489.

MRI Contrast Agents

3

Thomas A. Hope

Contents

The goal of most MRI contrast agents is to shorten the T1 of water in an imaged voxel. By shortening the T1, the signal intensity of the voxel increases on T1-weighted images, thereby making signal brighter. This is applied for both vascular enhancement as well as increasing the conspicuity of tumors. Unlike CT contrast agents, we do not image the contrast agents in MRI directly, but rather the contrast agents affect the adjacent water molecules in a way that shorten their T1.

T.A. Hope
Department of Radiology and Biomedical Imaging, University of California, San Francisco, San Francisco, CA, USA

Department of Radiology, San Francisco VA Medical Center, San Francisco, CA, USA
e-mail: thomas.hope@ucsf.edu

3.1   Gadolinium-Based Contrast Agents (GBCAs)

Gadolinium is a paramagnetic metal with seven unpaired electrons. These electrons precess in the magnetic field similar to protons but at a different frequency. The energy stored in the precessing electrons acts as a reservoir of magnetization that can be transferred to adjacent water protons helping them reaccumulate longitudinal magnetization more quickly after an excitation pulse. This pool of magnetization acts to shorten the T1 of adjacent protons, thereby increasing their signal intensity on T1-weighted images. Remember that T1 contrast is a steady-state effect during sequences with short repetition times (TRs). The faster the reaccumulation of longitudinal magnetization (i.e. the shorter the T1), the higher the steady-state longitudinal magnetization of the voxel and therefore the brighter the signal intensity is on T1-weighted images (Fig. 3.1).

Gadolinium-based contrast agents (GBCAs) are broken down by two categories (Fig. 3.2, Table 3.1). The first category is ionic and nonionic, and the second is linear and macrocyclic [1]. These four categories created have different characteristics that have important clinical implications. The most important implication is the relative stabilities of the agents. Macrocyclic compounds have a higher stability compared to linear compounds, and ionic compounds have a higher stability compared to nonionic compounds. Therefore the most thermodynamically stable agent available is gadoterate meglumine, although there is no discernable difference in clinically relevant stability between the three available macrocyclic agents.

3.1.1   Extracellular Contrast Agents

The majority of GBCAs are termed extracellular contrast agents. This means that the agents initially distribute in the blood pool and within minutes distribute into the extravascular space. This biodistribution is nearly identical to that of iodinated
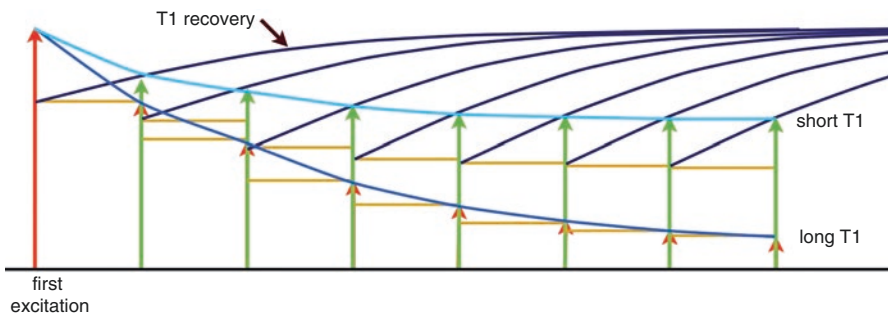
Fig. 3.1 Source of T1 contrast by effecting T1 recovery. Tissues with long T1s do not reaccumulate their longitudinal magnetization between excitations (*dark blue*), and therefore the steady-state longitudinal magnetization is very low resulting in low signal. A tissue with a shorter T1, meaning that there is more T1 recovery between excitations, has a higher steady-state magnetization (*light blue*). The higher the steady-state magnetization, the more signal in the resultant T1-weighted images
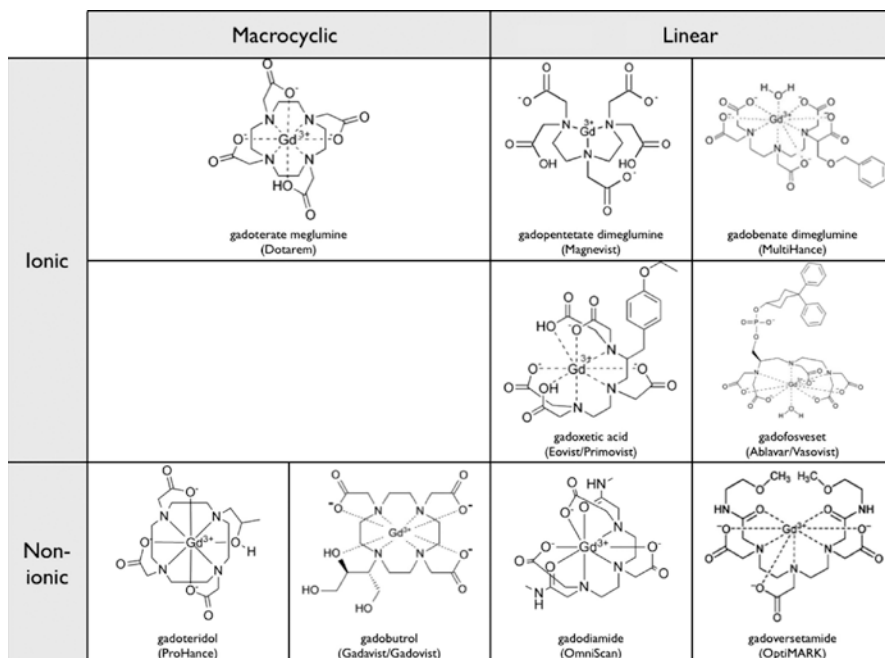
Fig. 3.2 Available gadolinium based contrast agents used clinically. Agents are broken into two major categories (linear and macrocyclic agents)

Table 3.1 Gadolinium-based contrast agents structure, stability, concentration, dose and relaxivity

Generic name	Brand name	Structure	Stability (K_{therm}) [5]	Concentration (mmol/mL)	Dose (mL/kg)	$R1$ at 3T [2]
Gadodiamide	Omniscan	Linear, nonionic	16.9	0.5	0.2	4.5
Gadopentetate dimeglumine	Magnevist	Linear, ionic	22.1	0.5	0.2	3.7
Gadobenate dimeglumine	MultiHance	Linear, ionic	22.6	0.5	0.2	5.5
Gadoversetamide	OptiMARK	Linear, nonionic	16.6	0.5	0.2	N/A
Gadoterate meglumine	Dotarem	Macrocyclic, ionic	25.8	0.5	0.2	3.5
Gadoteridol	ProHance	Macrocyclic, nonionic	23.8	0.5	0.2	3.7
Gadobutrol	Gadavist	Macrocyclic, nonionic	21.8	1.0	0.1	5.0
Gadoxetate disodium	Eovist	Linear, ionic	23.5	0.25	0.1	6.2
Gadofosveset trisodium	Ablavar	Linear, ionic	N/A	0.25	0.12	9.9

contrast agents. Therefore there are two components to the enhancement of a tissue of the administration of an extracellular agent: the intravascular volume and the interstitial space. The vast majority of extracellular contrast agents are cleared by the kidneys relatively quickly in patients with normal renal function.

There are four approved linear extracellular contrast agents: gadodiamide, gadoversetamide, gadopentetate dimeglumine, and gadobenate dimeglumine. There are three approved macrocyclic extracellular contrast agents: gadoterate meglumine, gadoteridol, and gadobutrol. Each of these agents has slightly different properties that are important in their clinical use. First are differences in relaxivities of each agent. The effect of each agent on the T1 of adjacent water molecules is not equivalent, and the agents with higher relaxivities will result in higher contrast given the same administered dose of gadolinium. The extracellular agents with the two highest relaxivities are gadobenate dimeglumine and gadobutrol [2]. This can have an important impact on clinical use, as agents with higher relaxivity result in better lesion contrast and higher detection rates [3, 4]. The second difference is the stability of each compound, with compounds with higher stabilities considered less likely to be associated with NSF. In general macrocyclic contrast agents are more stable than linear agents [5], and their popularity has increased dramatically since the discovery of NSF (discussed below).

3.1.2   Hepatobiliary Contrast Agents

Hepatobiliary contrast agents are defined by hepatic clearance of the agent. There are two hepatobiliary contrast agents on the market: gadoxetate disodium and gadobenate dimeglumine. Roughly 50% of gadoxetate is renally cleared and 50% is hepatobiliary cleared, while with gadobenate only 5% of the contrast agent is cleared by the liver. Due to the accumulation of contrast in the liver, the hepatic parenchyma will become brighter over time on T1-weighted images (Fig. 3.3). This is termed the hepatobiliary phase and is defined as a time point after injection of a hepatobiliary contrast agent where the hepatic parenchyma is hyperintense relative to the vasculature [6]. Due to the decreased hepatobiliary excretion seen with gadobenate, the hepatobiliary phase occurs much later than with gadoxetate (60–120 min with gadobenate versus 10–20 min with gadoxetate). Hepatobiliary contrast agents are helpful for detecting hepatic metastases and will be discussed in the chapter focused on liver imaging.

3.1.3   Blood Pool Contrast Agents

Blood pool contrast agents are those that remain intravascular for a prolonged period of time after their administration allowing for improved vascular imaging. Gadofosveset is the only FDA-approved blood pool contrast agent, and it stays within the blood pool by binding to albumin. It was used for vascular imaging, in particular for characterizing vascular lesions in the lower extremities. Unfortunately this agent has been removed from the market in both Europe and the United States.
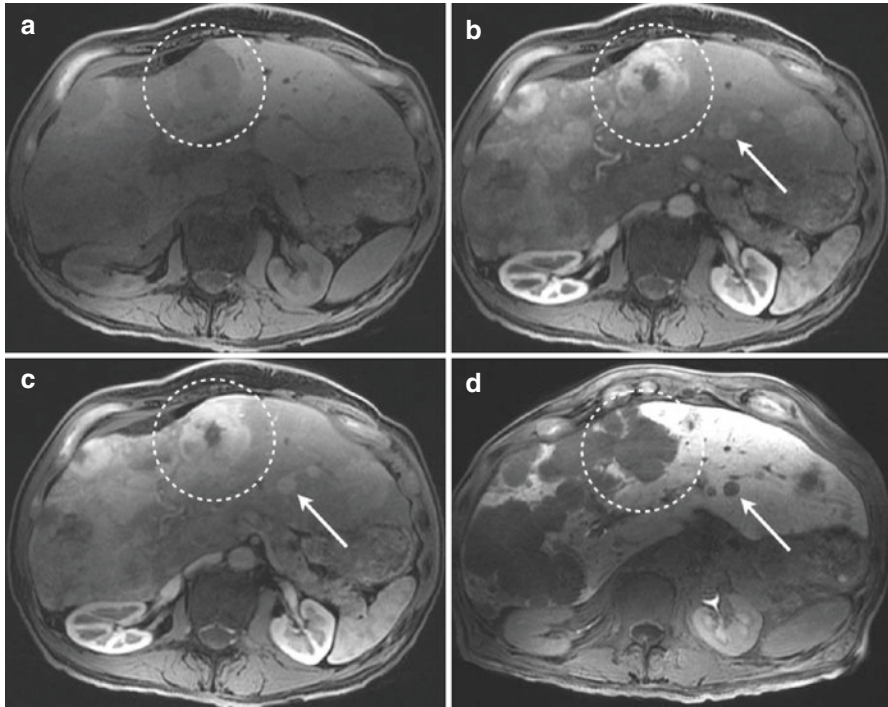
Fig. 3.3 Contrast-enhanced liver MRI in a patient with metastatic carcinoid. Gadoxetate diso-dium, a hepatobiliary agent, was administered. Pre-contrast T1 (**a**), arterial phase T1 (**b**), portal venous phase T1 (**c**), and hepatobiliary phase (HBP) T1 (**d**) are shown. Lesion enhancement improves the contrast of metastatic lesions compared to the adjacent liver parenchyma in the arterial and portal venous phase (**a**–**c**, *dotted circles*). During the HBP, the liver parenchyma becomes hyperintense, while metastatic lesions to the liver become hypointense. This improves the lesion contrast during the hepatobiliary phase and allows for the detection of smaller lesions than is possible with extracellular contrast agents (**b**–**d**, *white arrow*)

3.1.4   Safety Concerns

Gadolinium is a toxic ion that has an LD50 of 0.2 mmol/kg in mice, which is the concentration that is administered in the clinical setting. In order to prevent human toxicity, the gadolinium ion is bound by a chelator. As long as gadolinium is attached to the chelator, it is believed that GBCAs remain safe. Unlike iodinated contrast, there is minimal nephrotoxicity associated with administration, likely due to the lower concentration of administration with GBCAs. GBCAs have roughly 2–3 times higher osmolarity than iodinated contrast but are administered in 1/10 of the volume. Although the osmolarity of GBCAs is higher than that of iodinated contrast, it is much less viscous (threefold lower). It is also administered at a much lower rate (1–2 mL/s versus up to 5 mL/s with iodinated contrast). The lower rate, lower volume, and lower viscosity result in less renal toxicity and less risk of significant infiltration.

3.1.5   Safety Concerns: Nephrogenic Systemic Fibrosis

Nephrogenic systemic fibrosis (NSF) was originally described in 2000 in a series of dialysis patients and was originally termed nephrogenic fibrosing dermopathy [7, 8]. It was not until 2004, when systemic manifestations were demonstrated at autopsy, that the name was changed to NSF [9]. Two years later, the first reports connecting NSF to GBCA administration were reported [10, 11]. Subsequently both the Food and Drug Administration (FDA) and the European Medicines Agency (EMA) released warnings on the administration of GBCAs. In short, they recommended not using GBCAs in patients with glomerular filtration rates (GFR) less than 30 mL/min or in patients with acute renal failure. Since 2009, there have been no additional cases of NSF reported, indicating that these restrictions prevented the development of disease. Prior to NSF, GBCAs were frequently used in patients with kidney disease due to the absence of significant renal toxicity, but with the risk of NSF being present only in patients with a low GFR, GBCAs are no longer used in renal failure patients.

3.1.6   Safety Concerns: Brain Deposition of Gadolinium

In 2014, the first imaging studies demonstrated that gadolinium deposition could be visualized in the dentate nucleus and the basal ganglia after multiple administrations of GBCAs [12]. Subsequent autopsy studies have shown that the increased signal intensity was in fact associated with gadolinium deposition [13]. Studies have suggested that gadolinium deposition can only be seen with linear contrast agents, but not with macrocyclic agents [14–16]. Although clearly gadolinium is deposited in regions in the brain after administration of multiple doses of gadolinium in patients with normal renal function, there is no known associated disorder that is caused by this deposition. Based on issues related to brain deposition and NSF, the European Medicines Agency suspended approval of four linear agents (gadobenic acid, gadodiamide, gadopentetic acid, and gadoversetamide) [17]. In the United States, the Food and Drug Administration decided not to suspend approval given the absence of data suggesting a harmful effect of GBCAs [18].

3.1.7   Safety Concerns: Allergic Reactions

Before the association of NSF to GBCAs, the main concern with GBCAs was the development of anaphylactic reactions. The rate of severe reactions is around 1 in 10,000 to 1 in 50,000, with the majority being anaphylactic reactions [19, 20]. Interestingly it appears that the agent that has the best safety profile for allergic reactions is gadodiamide, which has one of the worst safety profiles in terms of NSF [20]. At the same time, the agent with the highest rate of allergic reactions is gadobenate dimeglumine, which has a rate of death associated with anaphylaxis that is 18 times higher than that of gadodiamide [20].

3.1.8   Safety Concerns: Overview

As with all drugs, the utilization of GBCAs should be considered carefully as a balance between the risks associated with the agent and the benefits of improved diagnostic performance. Given the various safety concerns and agent characteristics, there is no single extracellular contrast agent that is considered the correct agent to use. In general, both in the United States and Europe, macrocyclic agents are becoming more commonly used compared to linear agents due to the associated higher stability and theoretical lower rate of NSF. Overall there is a discussion in the community about whether or not the reaction to NSF has been so large that it has prevented patients from receiving imaging studies that are clinically important and that we might consider administering gadolinium to patients with lower GFRs especially now that macrocyclic agents are replacing linear agents in clinical use [21].

3.2   Superparamagnetic Iron Oxides

3.2.1   Ferumoxytol

Ferumoxytol (Feraheme, AMAG Pharmaceuticals, Cambridge, MA) is an ultrasmall superparamagnetic iron oxide (USPIO) particle that was originally evaluated as an MRI contrast agent [22] but eventually approved as an intravenous iron replacement therapy for patients with iron deficiency anemia [23, 24]. Due to its large size, ferumoxytol remains within the blood pool for a prolonged time allowing for high-resolution vascular imaging superior to that obtained using GBCAs [25]. Although clearly useful for vascular imaging, ferumoxytol also has a role in oncologic imaging. Unlike GBCAs, which are cleared by the kidneys, ferumoxytol is cleared through the reticuloendothelial system (RES). As ferumoxytol accumulates within the RES, the tissues become progressively darker on T2-weighted imaging to the shortening of T2* associated with the high concentrations of iron. This feature of USPIOs was originally leveraged with Combidex to characterize lymph node metastases; malignant nodes would retain their T2 signal while benign lymph nodes become dark after ferumoxytol administration [26]. Similar work has been performed using ferumoxytol suggesting that it can help distinguish between benign and malignant nodes (Fig. 3.4) [27]. Although this approach has yet to be leverage in simultaneous PET/MRI, it has promise in characterizing small nodal disease that may be below the resolution of PET.

3.2.2   Safety Concerns: Anaphylaxis

One benefit of ferumoxytol is that there is no associated renal toxicity and therefore can be used in patients with renal failure. This makes it an important alternative to GBCAs for evaluation vasculature in patients with chronic kidney disease. Unfortunately ferumoxytol has a higher risk of anaphylaxis than GBCAs, with
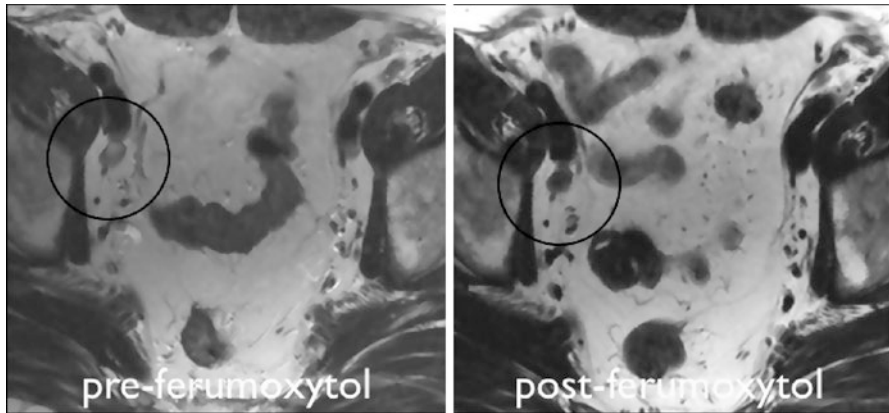
Fig. 3.4 An example of malignant lymph node in patients with prostate cancer demonstrating decreased signal 48 h after administration of ferumoxytol. On preadministration of T2-weighted images (*left*, *black circle*), the lymph node measures 1.0 cm and is intermediate to relatively hyperintense and suspicious for nodal metastases. After the administration of ferumoxytol, the node retains the compound and becomes darker on T2-weighted imaging consistent with a benign lymph node (*right*, *black circle*)

roughly 1:10K patients developing a severe allergic reaction and 1:50K dying of anaphylaxis based on reported data [28]. Due to the increased risk of anaphylaxis, it is recommended to administer the ferumoxytol as a slow infusion over 15 min in a hospital setting.

3.3 MR Contrast Agents in Development

There are a number of MRI contrast agents, the majority of which incorporate gadolinium, that are in development for imaging tumors. These include agents that are bound to targeting motifs that localize the agent in the tumor or vasculature, liposomes that are targeted using antibodies, and many other techniques [29]. Below we will focus on hyperpolarized MRI contrast agents.

3.3.1 Hyperpolarized MRI

Hyperpolarized imaging is early in development but has the potential to allow for the interrogation of cellular pathways and underlying of physiology that is not possible with GBCAs [30]. The technique works by taking molecules (typically 13-carbon-labeled compounds) and hyperpolarizing them using dynamic nuclear polarization [31]. Remember that only seven of every million protons are aligned with the magnetic field in conventional MRI, which limits the signal that you can acquire. By hyperpolarizing a molecular, one can increase the percent of atoms aligned with the magnetic field 10,000 fold. This results in significant increase in

signal that can be acquired. The main limitation of this technique is the short time frame that the agents remain polarized: first the agents have to be made in the vicinity of the imaging and administered immediately after synthesis, second imaging has to be performed within 1–2 min of administration before the signal decays, and third the limited time frame limits the imaging window that can be performed preventing whole body acquisitions.

What is unique about hyperpolarized MRI is that you can image the spectroscopic signature of the labeled carbon as the injected molecule is metabolized within cells. The most commonly used agent in hyperpolarized MRI is pyruvate. Pyruvate is taken into cancer cells where it is converted to lactate, and this conversion can be directly measured allowing for the noninvasive evaluation of metabolic pathways within cancer cells. To date, this has been performed in patients with prostate cancer with the hope that aggressive cancer can be distinguished from low-grade prostate cancer prior to definitive therapy [32, 33]. Beyond pyruvate, there are a number of other compounds that can be polarized that allow one to interrogate perfusion, oxidation, pH, necrosis, and glutaminolysis. To date, the combination of hyperpolarized MRI with PET imaging has yet to be performed, but there is potential for synergistic information when combining the two modalities.

Conclusion

MRI contrast agents have various properties that provide specific benefits over iodinated contrast used in CT. Increased lesion contrast and detection sensitivity is critical in intracranial diseases and hepatic lesions. In particular, hepatobiliary contrast agents offer improved detection for liver metastases over both iodinated and extracellular contrast agents. A number of novel contrast agents are in development that have the potential to add significant value in the setting of PET/MRI, including hyperpolarized MR contrast agents.

References

1. Idée J-M, Port M, Raynal I, Schaefer M, Le Greneur S, Corot C. Clinical and biological consequences of transmetallation induced by contrast agents for magnetic resonance imaging: a review. Fundam Clin Pharmacol. 2006;20:563–76.
2. Rohrer M, Bauer H, Mintorovitch J, Requardt M, Weinmann H-J. Comparison of magnetic properties of MRI contrast media solutions at different magnetic field strengths. Investig Radiol. 2005;40:715–24.
3. Rumboldt Z, Rowley HA, Steinberg F, et al. Multicenter, double-blind, randomized, intra-individual crossover comparison of gadobenate dimeglumine and gadopentetate dimeglumine in MRI of brain tumors at 3 tesla. J Magn Reson Imaging. 2009;29:760–7.
4. Knopp MV, Runge VM, Essig M, et al. Primary and secondary brain tumors at MR imaging: bicentric intraindividual crossover comparison of gadobenate dimeglumine and gadopentetate dimeglumine. Radiology. 2004;230:55–64.
5. Bongartz G. Imaging in the time of NFD/NSF: do we have to change our routines concerning renal insufficiency? MAGMA (New York, NY). 2007;20:57–62.
6. Hope TA, Fowler KJ, Sirlin CB, et al. Hepatobiliary agents and their role in LI-RADS. Abdom Imaging. 2015;40:613–25.

7. Cowper SE, Robin HS, Steinberg SM, Su LD, Gupta S, LeBoit PE. Scleromyxoedema-like cutaneous diseases in renal-dialysis patients. Lancet. 2000;356:1000–1.

8. Cowper SE, Su LD, Bhawan J, Robin HS, LeBoit PE. Nephrogenic fibrosing dermopathy. Am J Dermatopathol. 2001;23:383–93.

9. Ting WW, Stone MS, Madison KC, Kurtz K. Nephrogenic fibrosing dermopathy with systemic involvement. Arch Dermatol. 2003;139:903–6.

10. Grobner T. Gadolinium – a specific trigger for the development of nephrogenic fibrosing dermopathy and nephrogenic systemic fibrosis? Nephrol Dial Transplant. 2006;21:1104–8.

11. Marckmann P, Skov L, Rossen K, et al. Nephrogenic systemic fibrosis: suspected causative role of gadodiamide used for contrast-enhanced magnetic resonance imaging. J Am Soc Nephrol. 2006;17:2359–62.

12. Kanda T, Ishii K, Kawaguchi H, Kitajima K, Takenaka D. High signal intensity in the dentate nucleus and globus pallidus on unenhanced T1-weighted MR images: relationship with increasing cumulative dose of a gadolinium-based contrast material. Radiology. 2014;270:834–41.

13. Kanda T, Fukusato T, Matsuda M, et al. Gadolinium-based contrast agent accumulates in the brain even in subjects without severe renal dysfunction: evaluation of autopsy brain specimens with inductively coupled plasma mass spectroscopy. Radiology. 2015;276:228–32.

14. Stojanov DA, Aracki-Trenkic A, Vojinovic S, Benedeto-Stojanov D, Ljubisavljevic S. Increasing signal intensity within the dentate nucleus and globus pallidus on unenhanced T1W magnetic resonance images in patients with relapsing-remitting multiple sclerosis: correlation with cumulative dose of a macrocyclic gadolinium-based contrast agent, gadobutrol. Eur Radiol. 2016;26:807–15.

15. Radbruch A, Weberling LD, Kieslich PJ, et al. Gadolinium retention in the dentate nucleus and globus pallidus is dependent on the class of contrast agent. Radiology. 2015;275:783–91.

16. Kanda T, Osawa M, Oba H, et al. High signal intensity in dentate nucleus on unenhanced T1-weighted MR images: association with linear versus macrocyclic gadolinium chelate administration. Radiology. 2015;275:803–9.

17. PRAC concludes assessment of gadolinium agents used in body scans and recommends regulatory actions, including suspension for some marketing authorisations. ema.europa.eu. http://www.ema.europa.eu/ema/index.jsp?curl=pages/medicines/human/referrals/Gadolinium-containing_contrast_agents/human_referral_prac_000056.jsp&mid=WC0b01ac05805c516f. Accessed 20.06.2017.

18. FDA identifies no harmful effects to date with brain retention of gadolinium-based contrast agents for MRIs; review to continue. U.S. Food and Drug Administration. Center for Drug Evaluation and Research. https://www.fda.gov/Drugs/DrugSafety/ucm559007.htm. Accessed 20.06.2017.

19. Jung J-W, Kang H-R, Kim M-H, et al. Immediate hypersensitivity reaction to gadolinium-based MR contrast media. Radiology. 2012;264:414–22.

20. Prince MR, Zhang H, Zou Z, Staron RB, Brill PW. Incidence of immediate gadolinium contrast media reactions. Am J Roentgenol. 2011;196:W138–43.

21. Penfield JG, Reilly RF. Gadolinium and nephrogenic systemic fibrosis: have we overreacted? Semin Dial. 2011;24:480–6.

22. Prince MR, Zhang HL, Chabra SG, Jacobs P, Wang Y. A pilot investigation of new superparamagnetic iron oxide (ferumoxytol) as a contrast agent for cardiovascular MRI. J Xray Sci Technol. 2003;11:231–40.

23. Spinowitz BS, Schwenk MH, Jacobs PM, et al. The safety and efficacy of ferumoxytol therapy in anemic chronic kidney disease patients. Kidney Int. 2005;68:1801–7.

24. Provenzano R, Schiller B, Rao M, Coyne D, Brenner L, Pereira BJG. Ferumoxytol as an intravenous iron replacement therapy in hemodialysis patients. Clin J Am Soc Nephrol. 2009;4:386–93.

25. Hope MD, Hope TA, Zhu C, et al. Vascular imaging with ferumoxytol as a contrast agent. Am J Roentgenol. 2015;205:W366–73.

26. Harisinghani MG, Barentsz J, Hahn PF, et al. Noninvasive detection of clinically occult lymph-node metastases in prostate cancer. N Engl J Med. 2003;348:2491–9.

27. Turkbey B, Agarwal HK, Shih J, et al. A phase I dosing study of ferumoxytol for MR lymphography at 3 T in patients with prostate cancer. Am J Roentgenol. 2015;205:64–9.
28. Vasanawala SS, Nguyen K-L, Hope MD, et al. Safety and technique of ferumoxytol administration for MRI. Magn Reson Med. 2016;75:2107–11.
29. Zhou Z, Lu ZR. Gadolinium-based contrast agents for magnetic resonance cancer imaging. Wiley Interdiscip Rev Nanomed. 2013;5:1–8.
30. Kurhanewicz J, Bok R, Nelson SJ, Vigneron DB. Current and potential applications of clinical 13C MR spectroscopy. J Nucl Med. 2008;49:341–4.
31. Keshari KR, Wilson DM. Chemistry and biochemistry of 13 C hyperpolarized magnetic resonance using dynamic nuclear polarization. Chem Soc Rev. 2014;43:1627–59.
32. Wilson DM, Kurhanewicz J. Hyperpolarized 13C MR for molecular imaging of prostate cancer. J Nucl Med. 2014;55:1567–72.
33. Nelson SJ, Kurhanewicz J, Vigneron DB, et al. Metabolic Imaging of patients with prostate cancer using hyperpolarized [1-^{13}C]pyruvate. Sci Transl Med. 2013;5:198ra108.

PET/MRI: Attenuation Correction

4

Gaspar Delso and Johan Nuyts

Contents

4.1   Introduction

Despite the early introduction in 2006 of a brain PET insert capable of operating within a 3T MRI system [1], it wasn't until 2011 that clinical PET/MRI scanners became commercially available. Since then, this modality has been steadily gaining relevance both for research and clinical practice. The latest estimates

G. Delso (✉)
GE Healthcare, Waukesha, WI, USA
e-mail: gaspar.delso@ge.com

J. Nuyts
Nuclear Medicine and Medical Imaging Research Center, K. U. Leuven, Leuven, Belgium

53

indicate that more than one hundred hybrid PET/MRI systems are currently in operation worldwide.

Four commercial PET/MRI systems are currently cleared for clinical use: two sequential designs, the Ingenuity TF (Koninklijke Philips N.V., Amsterdam, NL) [2] and the Tri-Modality (General Electric, Waukesha, WI) [3], and two fully integrated designs, the Biograph mMR (Siemens AG, Berlin, DE) [4] and the SIGNA PET/MR (General Electric, Waukesha, WI) [5].

In all cases, a 3T MRI system has been combined with a whole-body PET detector ring, with varying degrees of integration: the Tri-Modality consists essentially of two standard systems in adjacent rooms, communicated with a mutually compatible patient bed; in the case of the Ingenuity TF, a magnetically shielded PET system is placed within the MRI radiofrequency cage, sharing a rotating patient bed with the MRI system; in the case of the Biograph mMR and the SIGNA PET/MR, the PET system has been entirely redesigned to fit within the MRI bore, between the radio-frequency and gradient coils.

Except for the Tri-Modality, these designs share a very significant trait: the CT detector, common to all modern PET systems, had to be sacrificed in order to oper-ate within the magnetic field. In consequence, no transmission measurements can be performed, and alternative methods must be used to estimate the attenuation of all elements within the field of view.

4.2   Attenuation Correction

In a typical PET scan, most of the positron-annihilation photons emitted by the radiotracer will undergo one or more Compton interactions with elements along their path. As a reference, the half-value layer of water at 511 keV is barely 7.24 cm. The fact that PET relies on coincidence detection of pairs of photons further increases the impact of Compton interactions. When the affected photon pair still reaches the detector ring, we speak of scattered coincidences. If, on the other hand, the trajectory of either photon is deflected in such a way that it no longer intersects the detector ring, that count is irrecoverably lost and we speak of attenuation.

Scattered coincidences cause increased noise levels in the images, as well as add-ing a slowly changing background distribution—like a blurred version of the true image—which leads to uptake overestimation. Attenuation also leads to noisy images and, when left uncorrected, also to severe alterations in uptake distribution, such as reduced activity in core structures, increased activity on the body surface and low attenuation regions (e.g., lungs), and apparent tracer uptake in background regions surrounded by activity (e.g., between the body and the arms) [6]. It follows that accurate attenuation and scatter correction are critical to obtain quantitatively and qualitatively correct PET images.

The one thing that most modern attenuation and scatter correction approaches have in common is the need for an estimate of the distribution of attenuating ele-ments in the field of view, also called "attenuation map." The accuracy of this atten-uation map will, to a great extent, define the accuracy of the final reconstructed emission image [7].

The most straightforward method to obtain such an estimate of annihilation-photon attenuation is by transmission measurement, using an external radiation source [8]. This method has the advantage of constituting a direct measurement of the magnitude of interest, as the energy of the transmitted photons is equivalent to that of the annihilation photons emitted by the radiotracer. However, both the emission and the detection of high-energy photons are inefficient processes. This leads to very long acquisitions (taking almost half of the examination time) and poor attenuation maps, of limited contrast and resolution.

With the advent of integrated positron emission tomography and computed tomography (PET/CT) scanners, the quality of attenuation maps made a leap forward. Indeed, CT technology offers high-resolution, high-contrast transmission measurements with practically negligible acquisition times. Admittedly, these are indirect measurements, and the attenuation data obtained at X-ray energies must be rescaled to estimate the corresponding attenuation at annihilation-photon energies (~511 keV) [9, 10]. Nevertheless, CT-based attenuation correction compared well to existing techniques [11, 12] and the advantages in terms of clinical workflow and diagnostic value were enough to ensure rapid commercial success.

4.3   Attenuation Correction in PET/MRI

As an unfortunate consequence of the considerable redesign effort required to make PET compatible with the strong magnetic field generated by the MRI system, none of the currently available PET/MRI systems are equipped with a CT detector. This has forced manufacturers to find alternative means of creating an attenuation map, based on the available PET and MR data.

However, the image contrast in magnetic resonance imaging is based on the relaxation patterns of hydrogen nuclei, related to proton density and the chemical properties of tissue. These reflect entirely different physical principles than those involved in photon scattering/attenuation, which are related to interactions with the electron shell of tissue elements. In consequence, it is not possible to obtain a simple, continuous mapping of MRI measurements to attenuation values, like was the case in PET/CT [13]. Instead, MRI-based attenuation correction (MRAC) requires more advanced approaches, often relying on a priori knowledge of the object being imaged.

The field of PET/MRI attenuation correction has been the object of very active research for the past 10 years. The present chapter will focus exclusively on those methods currently implemented in commercial PET/MRI systems, as well as those likely to be made available with the next software upgrades. Excellent reviews of broader scope are available in the literature [14–17].

4.4   Segmentation-Based MRAC

All three manufacturers of clinical PET/MRI systems have chosen a segmentation-based approach for their basic attenuation correction method [18]. The idea behind segmentation-based MRAC is to acquire a predefined MRI sequence and then apply

a series of post-processing steps to partition the image into a given set of tissue classes. Then each image voxel is assigned an a priori attenuation coefficient according to the tissue class it belongs to (e.g., air, lung, fat, and soft tissue). An example is given in Fig. 4.1.

Perhaps the most critical parameter of these methods is the number of tissue classes considered. For whole-body imaging, the Ingenuity TF uses a three-class model (air, lung, and soft tissue) [19], whereas the Biograph mMR and SIGNA PET/MR use a four-class model (air, lung, fat, and soft tissue) [20, 21], in the latter case allowing voxels to have intermediate values between the fat and soft tissue classes.

There have been several published studies discussing the impact of the number of MRAC tissue classes on PET quantitative accuracy [7, 22, 23]. Keereman et al. concluded that at least five classes should be considered (air, lung, soft tissue, spongious bone, and cortical bone), with the addition of a sixth (adipose tissue) for increased accuracy. With this setup, they report PET errors below 5%. Ouyang et al. report errors of 4%, 7%, 13%, and 15% (respectively, for fat, soft tissue, bone, and lung) when using a four-class model. They also conclude that a three-class model is sufficient to obtain errors below 5% when imaging the heart, liver, or kidneys.

Almost as important as the number of tissue classes considered are the actual values assigned to these classes. The Ingenuity TF uses 0.0219 cm^{-1} for the lung and 0.0950 cm^{-1} for soft tissue; the Biograph mMR assigns 0.0240 cm^{-1} to the lung, 0.0854 cm^{-1} to fat, and 0.0100 cm^{-1} to soft tissue; the SIGNA 0.0180 cm^{-1} to the lung and between 0.0860 and 0.0100 cm^{-1} to fat and soft tissue. Notice the considerable discrepancy in the attenuation coefficient assigned to lung tissue. As a matter of fact, a point of agreement between the two studies cited above is the desirability of considering the inter-patient variability of lung tissue, something not yet implemented in any of the commercial systems.
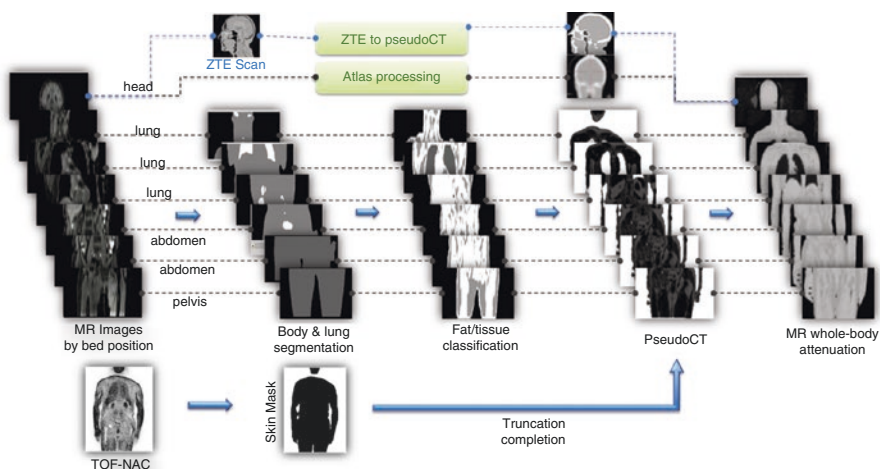
Fig. 4.1 Example of MRI-based attenuation correction, as implemented in the SIGNA PET/MR

The preferred MRI sequences for tissue segmentation purposes are typically fast T1-weighted acquisitions, short enough to be acquired in a single breath-hold (~20 s per bed position). In the case of the Ingenuity TF, a simple gradient-echo sequence with body coil receive suffices. The Biograph mMR and SIGNA PET/MR, on the other hand, require double-echo sequences capable of fat/water differentiation [24, 25]: a coronal Dixon-VIBE with local coil receive for the Biograph and an axial LAVA-FLEX with body coil receive for the SIGNA.

It is worth pointing out that the dual-echo processing used by these sequences is susceptible to a certain type of artifact called "fat/water swap." These are generally limited to the periphery of the field of view, where the reduced magnetic field homogeneity causes small regions to be misclassified. However, in some exceptional cases (e.g., patients with large fluid accumulations), this has been known to cause the misclassification of large portions of the attenuation map.

Another relevant factor is the receive coil used to acquire the MRI signal. Surface coils placed directly on (or beneath) the patient offer the best image quality in terms of signal-to-noise ratio, as well as enabling acceleration via parallel imaging. The built-in body coil, on the other hand, yields more uniform intensity homogeneity, leading to a more robust post-processing of the images. This entails a trade-off between the possibility of obtaining MRAC images of diagnostic quality (saving the time of a second T1-weighted acquisition) and giving users more freedom in their patient setup.

4.5   Bone Attenuation

None of the currently available clinical PET/MRI systems include the bone in their default segmentation-based attenuation correction. The reason for this is the difficulty of imaging bone with standard MRI sequences. Indeed, bone tissue is characterized by a low proton density (it contains only a 20% of water) and a heterogeneous structure causing fast dephasing of MRI signals (T2 ~ 390 μs at 3T) [26].

On the other hand, the importance of accounting for bone attenuation has been reported repeatedly [7, 27–33]. Ignoring bone attenuation is known to cause both quantitative and qualitative bias in the brain (in the (−20%, −10%) range [34]), as well as in the proximity of large bone structures in the body.

For this reason, some manufacturers are including alternative attenuation correction methods for regions such as the head and hips. Two main approaches exist for this purpose: the registration of anatomical atlas information to the default MRAC images and the acquisition of short echo time sequences capable of capturing the fast-decaying signal from the bone [35, 36].

The SIGNA PET/MR includes an atlas-based method for the head station [37–39]. It relies on the nonrigid registration of a prerecorded head atlas, based on CT data, to the same LAVA-FLEX acquisition used by the default MRAC. Aside from the incorporation of bone information, this approach has the advantage of not needing additional acquisition time and being very robust to image artifacts (e.g., caused by metallic implants). On the minus side, it can only account for isomorphic

variations in patient anatomy. In other words, the registration can't create holes: a patient with a craniotomy will result in an attenuation map with a complete skull; a toothless patient will result in an attenuation map with teeth. Similarly, the method doesn't account for inter-patient density variability, the attenuation coefficients being defined by the model (e.g., a separate atlas must be provided for pediatric patients, due to their significantly different bone tissue density). Various improvements to work around these inherent limitations of atlas MRAC have been proposed in the literature, such as the combination with machine learning or the use of multi-atlas, patch-based approaches [40–43]. However, none of these improvements have yet made it into clinical practice.

The Biograph mMR includes a bone MRAC method based on the ultrashort echo time (UTE) sequence [35, 44]. UTE is a radial acquisition with a modified, fast excitation pulse, enabling sub-millisecond echo times, capable of capturing some of the short-lived signal from bone tissue. By performing a dual-echo acquisition, $T2^*$ values can be estimated and used to identify the bone. In other words, comparing the images from the first and second echoes, voxels with particularly rapid signal decay can be identified and classified as bone.

A similar method has been recently released for the SIGNA, in this case using a zero echo time (ZTE) sequence [36, 45]. ZTE is also a radial center-out acquisition, with the particularity that the gradient fields are not ramped down between excitations. This imposes some limitations on the sequence (e.g., nonselective excitation) but enables even shorter echo times, increasing the signal obtained from the bone. This can be exploited to perform single-echo acquisitions for bone segmentation, with the corresponding savings in scan time. An example is shown in Fig. 4.2.

Several potential improvements for these methods have been reported in the literature. They include modifications to the sequences to increase acquisition speed, in combination with Dixon methods for fat/water separation and more elaborate post-processing to reduce the number of unwanted structures being classified as the bone [46–53].

Unfortunately, adapting these methods to other anatomical regions than the head is challenging (e.g., larger FOV, cardiorespiratory and peristaltic motion, variable coil setup, etc.). A promising new atlas-based approach has been recently presented

Fig. 4.2 Example of MRI-based bone segmentation based on a zero echo time acquisition

for the hip and thigh area, relying on individual registration of a set of bone components (femur, pelvic parts, spine) [54]. This is currently a very active field of research, driven both by PET/MRI and radiotherapy, and several new methods are likely to appear in the near future.

4.6   Truncation Correction

A common problem to CT-based and MRI-based attenuation correction arises when the field of view of these modalities is smaller than the scanner bore [55, 56]. When this happens, some elements (typically the patient's arms and shoulders) may fall outside the field of view, resulting in an incomplete attenuation map. If left uncorrected, this leads to artifacts in the reconstructed PET images, proportional to the amount of unaccounted attenuation. Typically, the artifacts will be maximal on the truncated regions and rapidly decrease away from them, with a pattern that depends on the reconstruction algorithm.

Despite the apparent similarities, the problem of attenuation map truncation is more challenging in PET/MRI than it is in PET/CT. To begin with, the typical MRI field of view is significantly smaller than that of CT (between 40 and 45 cm, compared to the 50 cm of CT). Also, the transaxial size of the FOV is not constant like in CT but wider at the axial center of each station and narrower at the edges. More importantly, CT data do still contain data about the truncated regions, due to the projective nature of the acquisition. This can be exploited to create truncation-corrected reconstructions [57]. In contrast, truncated regions cannot be recovered from MRI data, and the missing attenuation information must be obtained from alternative sources.

Siemens has reported a method to enable MRI acquisition beyond the usual field of view, by applying a readout gradient optimized to compensate the static field inhomogeneity and gradient field nonlinearities that limit the range of regular sequences [58, 59]. The main drawbacks of this approach are the relatively long acquisition time and the need for different readout gradients—and hence separate acquisitions—on each side of the patient.

Another readily available source of information about the truncated regions is provided by the PET measurements themselves. As a matter of fact, the default truncation correction approaches implemented in clinical PET/MRI systems rely either on the segmentation of non-attenuation-corrected PET reconstructions [60, 61] or on the estimation of attenuation information from the raw emission data [62].

4.6.1   PET Segmentation

The idea behind the segmentation approach is simple: identify the patient body in the reconstructed emission images, and use that information to fill in the truncated regions of the attenuation map (the field of view of PET usually encompasses the entire scanner bore).

There are some caveats to this relatively simple idea:

Firstly, it assumes that the radiopharmaceutical causes sufficient unspecific uptake to be able to differentiate the patient body from the background. While generally true for most of the clinical indications of PET, this may become a serious limitation for more advanced tracers.

Secondly, while emission images can provide the patient outline, they contain little information about the different tissue classes involved. Therefore, segmentation-based truncation correction approaches usually assign a constant attenuation value to the recovered regions.

Finally, note that truncation correction is a required step in attenuation correction, which in turn is a required step in PET reconstruction. It follows that the emission images used for truncation correction must be non-attenuation-corrected (NAC) ones. Unfortunately, the contour of the patient is severely distorted in regular NAC images (e.g., concavities are lost) [56]. However, in the case of systems with time-of-flight (TOF) capability, NAC images display the correct contour of the patient due to the increased robustness of TOF reconstruction to inconsistent data [63, 64].

4.6.2 Joint Estimation of Emission and Transmission

Many researchers have attempted to jointly estimate the activity image and the attenuation from the emission data, to eliminate the need for an additional transmission measurement. For SPECT and non-TOF PET, these attempts have not been very successful [65, 66], although Mihlin and Levin recently reported promising results for non-TOF PET at very high iteration numbers [67]. This approach was never introduced in clinical practice, except for cases where the problem could be stabilized because much prior knowledge was available [65, 68]. However, the introduction of time of flight clearly makes the PET data much richer, resulting in reconstructions with increased signal-to-noise ratio [69] and improved robustness against data inconsistencies [63]. Salomon et al. constrained the joint estimation algorithm of [65] with contours obtained from the MRI image and obtained excellent results for the Philips TOF-PET/MRI system [70]. Soon after, it was shown that TOF-PET data are indeed rich enough to enable stable joint reconstruction of the attenuation factors and the activity image up to a single scale factor, provided that the activity is distributed over an object which is large compared to the TOF resolution [71, 72]. It has been shown that for ^{18}F-FDG, which has a significant uptake almost everywhere in the body, the accurate activity and attenuation images can be reconstructed with a joint estimation approach [70, 72–74]. There are several ways in which TOF can be used to estimate attenuation [75]. The straightforward way is to estimate the attenuation image. This approach is illustrated in Fig. 4.3, where the attenuation estimate from the TOF-PET data is compared to the MRI-based attenuation map. Alternatively, the TOF information can be used to estimate the attenuation sinogram (i.e., the sinogram with the attenuation factor for every line of response (LOR)), without explicitly requiring that this sinogram should correspond
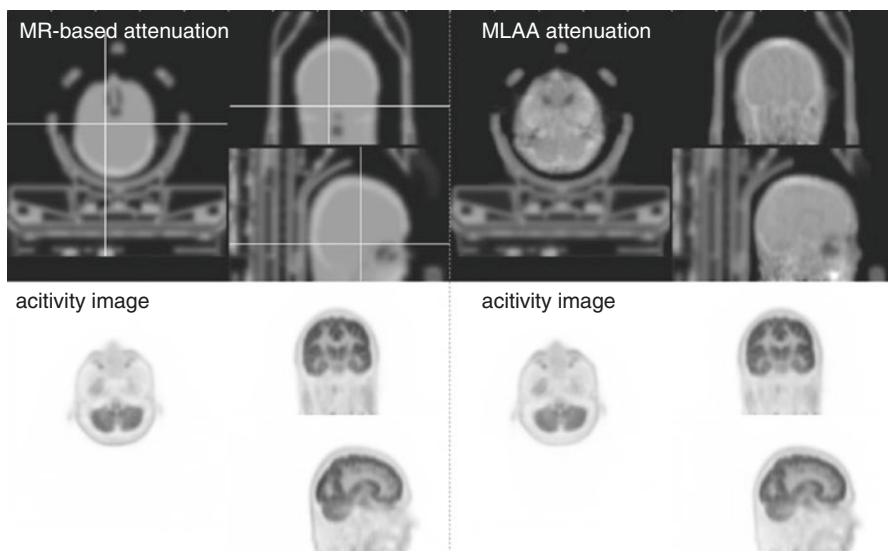
Fig. 4.3 *Left*: the estimated attenuation for a brain scan on the GE SIGNA PET/MR system. The attenuation of the hardware is obtained from a template; the attenuation of the patient head is estimated with an atlas-based approach. *Right*: the attenuation of the patient head was estimated with the MLAA algorithm [72] in combination with the same hardware template. The corresponding attenuation-corrected activity images are shown as well

to the forward projection of an attenuation image [76, 77]. If a possibly mismatched attenuation image is available (as would typically be the case in PET/CT), one can make use of the TOF information to estimate a (nonrigid) deformation that optimally aligns this attenuation image to the emission data [78, 79]. Since the number of hybrid PET/MRI systems with TOF capability is increasing, joint estimation is an interesting approach to improve attenuation correction in MRI [75] (Fig. 4.4).

This joint estimation of attenuation and activity is not free of problems. One is that some prior knowledge is required to estimate the scale factor: multiplying the activity image with a constant and dividing the attenuation sinogram with the same constant result in the same attenuated sinogram. Note that a scaled attenuation sinogram does not correspond to a scaled attenuation image; the scale factor manifests itself in the attenuation image as a position-dependent intensity change. If the attenuation is estimated as an image of attenuation coefficients, one can (partially) segment this image to identify a soft tissue region and adjust the scale factor such that this region is reconstructed with the known attenuation coefficient at 511 keV (0.00875/mm for fat and around 0.0099/mm for other tissues). If the attenuation is estimated by deforming an available attenuation map, the scale factor is automatically determined by that attenuation map. If the attenuation is estimated as a sinogram of attenuation factors, then, unfortunately, determining the scale factor is not straightforward.

Another problem is that some LORs provide very limited attenuation information, particularly those along which the activity is concentrated in a small region
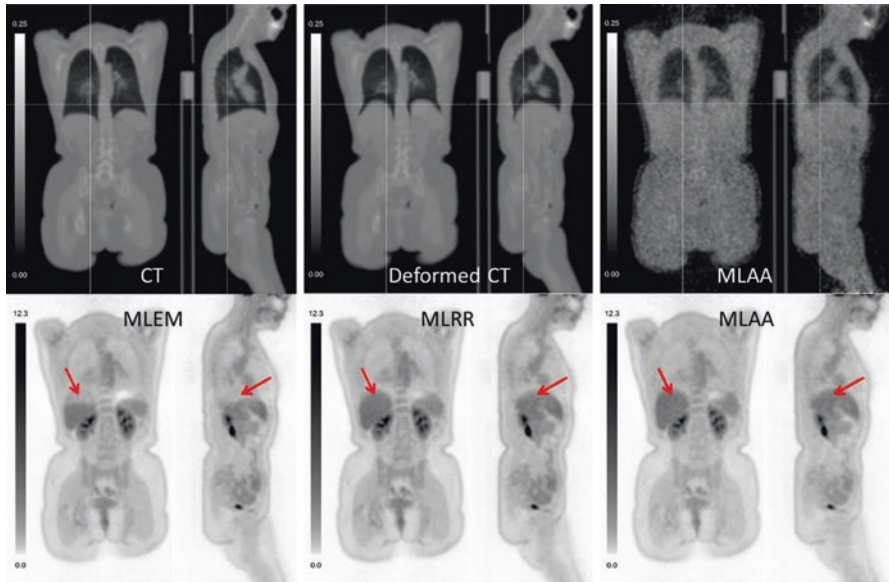
Fig. 4.4 The CT-based attenuation and attenuation-corrected activity for a whole-body scan on the Siemens mCT. Part of the liver is under-corrected for attenuation because the CT was taken during inhalation (*left*). The MLRR algorithm [78] deforms the CT to maximize the likelihood of the TOF-PET data, correcting for the mismatch (*center*). The MLAA result is shown in the *third column*

(relative to the TOF resolution) and those for which only few photon pairs are measured. This is typically the case for LORs close to the edge of the object. As a result, the joint estimation performs poorly near the boundary of the patient body. For tracers that have a more targeted accumulation than ^{18}F-FDG, this problem will be more pronounced. The use of anatomical information provided by MRI or CT is very helpful here.

Validation of the joint estimation algorithms is less straightforward than one might think. An obvious approach would be to use the MLEM reconstruction using a CT-based attenuation map as the gold standard (after verifying that there is no mismatch due to patient motion). However, if there is some inconsistency in the data, MLEM and the joint estimation methods converge to different results. This is because MLEM can only use the activity values to "explain" the data inconsistencies, whereas the joint estimation method can also manipulate the attenuation values. Such inconsistencies can be caused by any imperfection in the acquisition model. Scatter correction is very challenging, and although the current scatter estimation algorithms are powerful, the scatter estimate is still approximate and can sometimes differ significantly from the true scatter contribution [80].

Despite these problems, joint estimation is a promising approach for improving attenuation correction in PET/MRI. The simultaneously acquired MRI image provides an abundant amount of anatomical information which can be exploited to overcome the limitations of the joint estimation, while the joint estimation will

provide the attenuation coefficients which cannot be deduced from the MR image [64, 70, 81]. The manufacturers continue to improve the TOF resolution of their systems, and the performance of joint estimation will improve accordingly. Existing methods could be combined to produce a method that applies strong constraining based on the MR image [70] while correcting for a possible misalignment of that image [78, 79], which determines the scale factor by imposing the known attenuation to some structures identified in the MR image and estimates the attenuation of the other structures.

4.7   Hardware Correction

An often-overlooked factor in the attenuation correction of PET/MRI data is the attenuation caused by hardware structures [82]. Indeed, any components within the PET detector ring will introduce a certain degree of photon attenuation and therefore need to be accounted for during the reconstruction, to obtain accurate emission measurements. While the effect of non-moving parts (e.g., the body coil) is included in the normalization factors computed during the daily calibration of the system, moving parts must be included in each patient's attenuation map.

The most commonly found hardware structures in a PET/MRI scan are the patient bed and local radiofrequency coils. However, any device in the field of view can potentially affect the emission image: positioning aids, medical probes, fMRI goggles, dielectric pads, etc. In most cases, the effect on the PET images is qualitatively negligible. Still, each new device should be carefully considered to determine whether the quantitative impact is acceptable for the intended purpose of the examination [83–89].

Contrary to patient-related attenuation, hardware structures cannot be detected by conventional MRI sequences. As a matter of fact, coil designers usually select materials that minimize the MRI visibility of their hardware, to prevent it from causing artifacts in the patient images (e.g., signal from coil components phase wrapping onto the body). In consequence, PET/MRI manufacturers have chosen to provide a correction only for rigid structures with known positions (e.g., patient bed and head/neck coils) by means of prerecorded attenuation templates [90] that are overlaid on each patient's attenuation map.

There have been a few methods proposed in the literature to account for the attenuation of non-fixed and nonrigid coils. These approaches rely either on the incorporation of MRI-visible landmarks on the coil [91, 92] or the use of short echo time sequences capable of capturing short-lived signals from the hardware [93]. However, both approaches suffer from practical drawbacks and have not yet been adopted by clinical systems: in the former case, there is the need for coil redesign, as well as the risk of landmark signal contaminating diagnostic MRI series. In the latter case, there is the need for the additional, comparatively long MRI sequence, as well as the subsequent nontrivial registration of a coil attenuation model.

This last point deserves some attention: indeed, the benefit of incorporating hardware models into the attenuation map is heavily dependent on the accuracy with

which they can be positioned. Thus, an incorrectly placed model will not only fail to perform the correction but also introduce an overcorrection, achieving practically the opposite of the desired effect. As a rule of thumb, attenuation models must be positioned with an accuracy equivalent to the size/resolution of the structures included in them. For this reason, hardware models found in clinical systems are usually coarse low-resolution versions stripped of all moving parts (e.g., head coil mirrors and cables).

Another important point to consider is that even perfect attenuation correction won't bring back those lost counts. As a reference, some coils can cause the loss of 5–10% of the events that would otherwise be detected. For this reason, the presence of hardware structures should be minimized in all cases. Also, manufacturers are progressively introducing redesigned coils, where the amount of casing material has been minimized and high-attenuation electronic components have been moved away from the center of the field of view.

4.8 Unsolved Issues

There are several remaining open topics in MRI-based attenuation correction. In some cases, like patient motion, solutions are slowly being incorporated into commercial systems, while for other cases, like MRI metal artifacts, a practical solution remains unavailable. We present here a summary of these topics and their latest reported progress.

4.8.1 Metal Artifacts

The fact that metallic implants interfere with attenuation correction is already known from PET/CT [94]. However, the physical principles involved are completely different in PET/MRI: metal artifacts in CT are caused by lost transmission information in line of response intersecting a high-attenuation object. This results in bright starlike structures in the images, from which long streaks radiate (sometimes across the entire image). In contrast, metal artifacts in MRI are caused by the alterations in the static and gradient fields caused by the magnetization of the metallic object. This results in large (~1–5 cm) approximately spherical regions devoid of signal.

Arguably, many metallic implants are counter-indicated for MRI imaging, like pacemakers and neurostimulators. Nevertheless, there are many implants commonly allowed in clinical PET/MRI for which a solution would be desirable. This is particularly relevant for indications such as oncology, dealing mostly with elderly patients and where hip, shoulder, and dental prostheses are frequently encountered [95].

If left uncorrected, signal-void regions caused by metal implants in the sequences used for MRAC will cause those regions to be classified as air in the attenuation map. This will lead to bias in the reconstructed PET images, centered on the position of the implant but also spreading to the surrounding area, with a pattern dependent on the reconstruction algorithm [96].

Some correction approaches have been proposed in the literature, either by identifying gaps within the patient and filling them with tissue attenuation or by image inpainting [97, 98] or by using multispectral MRI sequences, capable of recovering the signal around metal [99]. Unfortunately, there are practical drawbacks to all these methods. For example, assuming that large cavities are caused by artifacts and should be filled with tissue is a valid assumption (and one used by some systems) for certain regions, like the pelvis and legs. But implementing this same assumption in the abdomen requires careful consideration to prevent bowel air misclassification. Also, the signal-void regions are often quite large and can connect to the background, complicating their detection and correction.

Interestingly, recent results indicate that time-of-flight reconstruction has a mitigating effect on metal artifacts [96, 100]. This is due to the increased robustness of TOF reconstruction to data inconsistencies. However, it is important to notice that TOF is not making those errors disappear, just distributing them differently (perhaps more conveniently) over the field of view (Fig. 4.5).

4.8.2   Motion Artifacts

Patient motion is a common source of artifacts in almost any imaging modality. For PET imaging, particularly when considering attenuation correction, patient motion leads to mismatch between the attenuation map and the corresponding emission data. This results in uptake bias around the moving areas, such as the well-known "banana artifacts" found around the diaphragm in PET/CT images.

The issue of patient motion comprises several distinct scenarios, such as periodic motion (e.g., cardiorespiratory), irregular motion (e.g., tremors), and bulk motion (e.g., repositioning). Despite the common underlying principles in terms of artifact
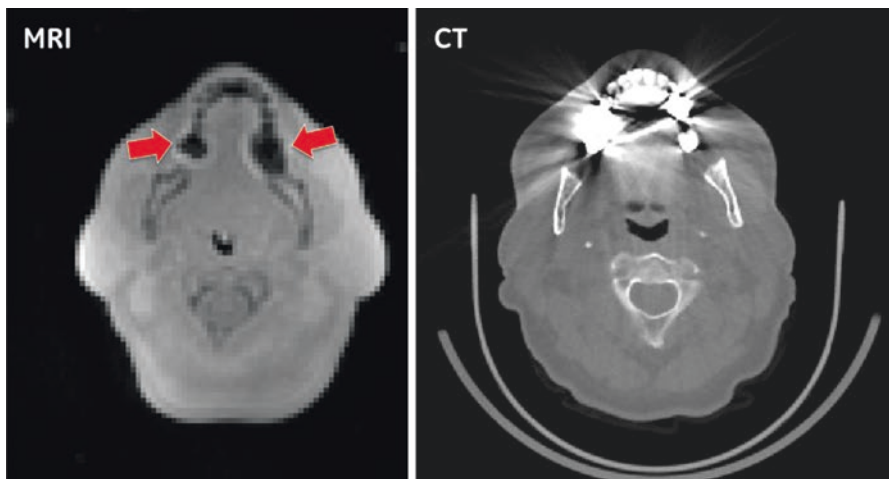
Fig. 4.5 Axial views showing artifacts caused by metallic dental implants in MRI and CT

formation, addressing these issues requires quite specific solutions, and they are best considered as entirely independent problems.

The case of cardiorespiratory motion is perhaps the best known and most extensively studied. Several potential solutions can be found in the PET/CT literature, usually relying on some sort of dynamic CT acquisition [101–103]. As a matter of fact, the ability of PET/MRI to provide radiation-free dynamic imaging is considered by some as one of the main—unexploited—strengths of this modality. An increasing number of publications can be found concerning the correction of respiratory motion in PET/MRI. However, the issue of attenuation correction is often lost within the larger problem of compensating patient motion during the acquisition of emission data. Discussing these methods would therefore overflow the scope of the present chapter. Readers are instead referred to the literature for more information on this topic [104, 105].

A key fact to remember is that, while full-fledged motion correction is technically complex and not always straightforward to integrate into clinical routine, motion-corrected attenuation correction is relatively simple to implement and apply. Indeed, the MR sequences used for attenuation correction can be readily modified to yield four-dimensional datasets representing the respiratory cycle. With these in hand, regular PET gating techniques can be used to match emission and attenuation datasets. As a side note, time-of-flight reconstruction has also been reported to mitigate respiratory mismatch artifacts [100].

Head motion has also been the object of study in PET/MRI, given the obvious interest of this modality for brain research and the importance of accurate quantitation in this field [106]. In contrast to respiratory motion, head motion is better suited for motion correction implementation (several manufacturers have introduced it in their products), and there is no benefit to addressing motion on the attenuation map only. On the other hand, with head attenuation correction approaches now incorporating longer MRI sequences capable of bone imaging, motion during the acquisition can noticeably affect the attenuation map [107]. Head motion can be accurately tracked with marker-based or markerless optical motion tracking systems. Some of those are MRI compatible [108]: their use would avoid the loss of MR scanning time for motion tracking and provide motion data with high temporal resolution, enabling motion correction for both devices.

4.8.3 Contrast

There has been relatively little work on the impact of MRI contrast agents on MRI-based attenuation correction. Contrast agents don't affect the actual attenuation of the sample but rather the MRI acquisitions used to estimate the attenuation map.

Of the existing publications [109, 110], one concludes that gadolinium-based T1 contrasts are not expected to bias attenuation maps, whereas a more recent study reveals these agents to potentially influence fat/water separation. Generally, contrast-enhanced sequences should be acquired after all attenuation correction acquisitions have been performed.

Iron oxide-based T2* contrast, on the other hand, has been reported to potentially cause susceptibility artifacts and bias attenuation maps. In this case, there is the additional drawback of the long persistence time of some T2* shortening preparations (weeks to months in uncommon cases).

4.8.4   Other Radiopharmaceuticals

As in the case of contrast agents, the literature on PET/MRI for radiotracers other than fluorine-18 (or fluorodeoxyglucose) is limited, at least in terms of their technical performance. A notable exception is the work of Soderlund et al. [111]. Within the scope of the present chapter, little trouble is expected from such tracers in terms of attenuation correction for the MRI-driven methods. In contrast, the performance of PET-driven methods may deteriorate for very specific tracers. PET segmentation methods for solving MR truncation problems will only work if there is significant tracer uptake in the missing body parts. Also, the joint estimation methods are sensitive to the tracer distribution. An extreme case would be the almost exclusive uptake of a very specific tracer in a small lesion. If that lesion would be small compared to the TOF resolution, the joint estimation methods would fail. A more realistic scenario would be the accumulation of the tracer in some parts of the body but not in others. The joint estimation method only enables estimation of the attenuation along LORs intersecting the active region. For methods that estimate only the attenuation sinogram, this is not a major problem, since the attenuation along LORs without activity is irrelevant. Methods estimating the attenuation image will produce attenuation maps with artifacts, because of the missing data. However, the resulting attenuation may still be accurate; this remains to be investigated. Similarly, methods estimating the required deformation of an available attenuation may not produce the exact deformation, but that does not imply that the associated attenuation correction must be inaccurate. Very focal activity uptake in only a few regions can also complicate the estimation of the unknown scale factor. As shown in [63], there is a single scale factor for all active regions that are intersected by common LORs. Consequently, in a typical 18F-FDG image, there is a single scale factor for the entire volume. However, regions of clustered activity which do not share LORs do not share the same scale factor, implying that determining the correct scale will be more complicated.

Certain tracers (e.g., gallium-68), delivered in high activities for dynamic imaging, have been reported to cause scatter correction issues. Scatter tail fitting is, in general, a delicate issue in narrow-bore PET/MRI scanners and closely linked with the quality of truncation correction.

4.8.5   Phantoms

Finally, the issue of nonhuman attenuation correction needs to be discussed. As stated previously in this chapter, PET/MRI systems do not have at their disposal any

means of direct transmission measurement, like an X-ray or annihilation photon source. In consequence, the MRI-based attenuation correction must rely heavily on a priori knowledge about the object being imaged (i.e., a human patient). This is true both for the MRI sequences used to acquire the data and for the algorithm that transforms the acquired MRI data into an attenuation map.

The unfortunate consequence of this fact is that the default MRAC methods used by clinical PET/MRI systems are not suitable for anything other than human imaging [112]. The further the subject being imaged is from the patient model assumed by the system (an incorrectly positioned patient, a patient with large anatomical deviations, an animal, a phantom), the poorer results will be obtained.

The case of PET phantoms is particularly severe. Indeed, PET phantoms are generally large water containers where trace amounts of radioactive material is dissolved or solid constructs where a long-lived radioactive element is embedded in an epoxy-like matrix. And, by principle, MR imaging performs poorly on large bodies of water and on dry solids. Furthermore, the issue here is not whether a carefully chosen and parameterized MR sequence could yield good images of a given phantom. The question is whether such a sequence (let alone the default MRAC sequence for human imaging) could perform equally well on any arbitrary phantom setup.

Some alternative phantom-filling fluids have been suggested to mitigate this problem [113], but they all have significant drawbacks in terms of cost, ease of preparation, cleanup, and disposal. While these are useful tricks to be used for specific research studies, they do not provide a general solution to this issue.

Manufacturers are of course aware of this limitation and provide template-based solutions for the most commonly used phantoms (e.g., germanium sources and NEMA IQ) [114]. While this is a practical approach that covers the needs of most sites, an important fact must be acknowledged: at the present time, the only way of testing a PET/MRI system as a whole or its MRAC is by scanning an actual human subject, with all the limitations that entails.

References

1. Schmand M, Burbar Z, Corbeil J, Zhang N, Michael C, Byars L, et al. BrainPET: First human tomograph for simultaneous (functional) PET and MR imaging. J Nucl Med Meeting Abstracts. 2007;48(MeetingAbstracts_2):45P.
2. Zaidi H, Ojha N, Morich M, Griesmer J, Hu Z, Maniawski P, et al. Design and performance evaluation of a whole-body ingenuity TF PET-MRI system. Phys Med Biol. 2011;56(10):3091–3106. Epub 2011/04/22. https://doi.org/10.1088/0031-9155/56/10/013.
3. Veit-Haibach P, Kuhn FP, Wiesinger F, Delso G, von Schulthess G. PET-MR imaging using a tri-modality PET/CT-MR system with a dedicated shuttle in clinical routine. Magn Reson Mater Phys. 2013;26(1):25–35. Epub 2012/10/12. https://doi.org/10.1007/s10334-012-0344-5.
4. Delso G, Furst S, Jakoby B, Ladebeck R, Ganter C, Nekolla SG, et al. Performance measurements of the Siemens mMR integrated whole-body PET/MR scanner. J Nucl Med. 2011;52(12):1914–1922. Epub 2011/11/15. https://doi.org/10.2967/jnumed.111.092726.
5. Levin CS, Jansen F, Deller T, Maramraju SH, Grant A, Iagaru A. Performance of a high sensitivity time-of-flight PET ring operating simultaneously within a 3T MR system. EJNMMI Phys. 2014;1(Suppl 1):A72. Epub 2014/07/01. https://doi.org/10.1186/2197-7364-1-s1-a72.

6. Nuyts J, Stroobants S, Dupont P, Vleugels S, Flamen P, Mortelmans L. Reducing loss of image quality because of the attenuation artifact in uncorrected PET whole-body images. J Nucl Med. 2002;43(8):1054–62. Epub 2002/08/07.

7. Keereman V, Holen RV, Mollet P, Vandenberghe S. The effect of errors in segmented attenuation maps on PET quantification. Med Phys. 2011;38(11):6010–6019. Epub 2011/11/04. https://doi.org/10.1118/1.3651640.

8. Meikle SR, Dahlbom M, Cherry SR. Attenuation correction using count-limited transmission data in positron emission tomography. J Nucl Med. 1993;34(1):143–50. Epub 1993/01/01.

9. Kinahan PE, Townsend DW, Beyer T, Sashin D. Attenuation correction for a combined 3D PET/CT scanner. Med Phys. 1998;25(10):2046–53. Epub 1998/11/04.

10. Burger C, Goerres G, Schoenes S, Buck A, Lonn AH, Von Schulthess GK. PET attenuation coefficients from CT images: experimental evaluation of the transformation of CT into PET 511-keV attenuation coefficients. Eur J Nucl Med Mol Imaging. 2002;29(7):922–927. Epub 2002/07/12. https://doi.org/10.1007/s00259-002-0796-3.

11. Kamel E, Hany TF, Burger C, Treyer V, Lonn AH, von Schulthess GK, et al. CT vs 68Ge attenuation correction in a combined PET/CT system: evaluation of the effect of lowering the CT tube current. Eur J Nucl Med Mol Imaging. 2002;29(3):346–50. Epub 2002/05/11.

12. Visvikis D, Costa DC, Croasdale I, Lonn AH, Bomanji J, Gacinovic S, et al. CT-based attenuation correction in the calculation of semi-quantitative indices of [18F]FDG uptake in PET. Eur J Nucl Med Mol Imaging. 2003;30(3):344–353. Epub 2003/03/14. https://doi.org/10.1007/s00259-002-1070-4.

13. Vandenberghe S, Marsden PK. PET-MRI: a review of challenges and solutions in the development of integrated multimodality imaging. Phys Med Biol. 2015;60(4):R115.

14. Hofmann M, Pichler B, Scholkopf B, Beyer T. Towards quantitative PET/MRI: a review of MR-based attenuation correction techniques. Eur J Nucl Med Mol Imaging. 2009;36(Suppl 1):S93–104. Epub 2008/12/24. https://doi.org/10.1007/s00259-008-1007-7.

15. Wagenknecht G, Kaiser HJ, Mottaghy FM, Herzog H. MRI for attenuation correction in PET: methods and challenges. Magn Reson Mater Phys. 2013;26(1):99–113. Epub 2012/11/28. https://doi.org/10.1007/s10334-012-0353-4.

16. Bezrukov I, Mantlik F, Schmidt H, Scholkopf B, Pichler BJ. MR-based PET attenuation correction for PET/MR imaging. Semin Nucl Med. 2013;43(1):45–59. Epub 2012/11/28. https://doi.org/10.1053/j.semnuclmed.2012.08.002.

17. Visvikis D, Monnier F, Bert J, Hatt M, Fayad H. PET/MR attenuation correction: where have we come from and where are we going? Eur J Nucl Med. 2014;41(6):1172–5. https://doi.org/10.1007/s00259-014-2748-0.

18. Beyer T, Lassen ML, Boellaard R, Delso G, Yaqub M, Sattler B, et al. Investigating the state-of-the-art in whole-body MR-based attenuation correction: an intra-individual, inter-system, inventory study on three clinical PET/MR systems. MAGMA. 2016;29(1):75–87. Epub 2016/01/08. https://doi.org/10.1007/s10334-015-0505-4.

19. Schulz V, Torres-Espallardo I, Renisch S, Hu Z, Ojha N, Bornert P, et al. Automatic, three-segment, MR-based attenuation correction for whole-body PET/MR data. Eur J Nucl Med Mol Imaging. 2011;38(1):138–152. Epub 2010/10/06. https://doi.org/10.1007/s00259-010-1603-1.

20. Martinez-Moller A, Souvatzoglou M, Delso G, Bundschuh RA, Chefd'hotel C, Ziegler SI, et al. Tissue classification as a potential approach for attenuation correction in whole-body PET/MRI: evaluation with PET/CT data. J Nucl Med. 2009;50(4):520–526. Epub 2009/03/18. https://doi.org/10.2967/jnumed.108.054726.

21. Wollenweber SD, Ambwani S, Lonn AHR, Shanbhag DD, Thiruvenkadam S, Kaushik S, et al. Comparison of 4-class and continuous fat/water methods for whole-body, MR-based PET attenuation correction. IEEE Trans Nucl Sci. 2013;60(5):3391–8. https://doi.org/10.1109/tns.2013.2278759.

22. Navalpakkam BK, Braun H, Kuwert T, Quick HH. Magnetic resonance-based attenuation correction for PET/MR hybrid imaging using continuous valued attenuation maps. Investig Radiol. 2013;48(5):323–332. Epub 2013/02/28. https://doi.org/10.1097/RLI.0b013e318283292f.

23. Ouyang Y, Judenhofer MS, Walton JH, Marik J, Williams SP, Cherry SR. Simultaneous PET/MRI imaging during mouse cerebral hypoxia-ischemia. J Vis Exp: JoVE. 2015;103:e52728. Epub 2015/10/06. https://doi.org/10.3791/52728.

24. Dixon WT. Simple proton spectroscopic imaging. Radiology. 1984;153(1):189–194. Epub 1984/10/01. https://doi.org/10.1148/radiology.153.1.6089263.

25. Ma J. Dixon techniques for water and fat imaging. J Magn Reson Imaging: JMRI. 2008;28(3):543–558. Epub 2008/09/09. https://doi.org/10.1002/jmri.21492.

26. Du J, Carl M, Bydder M, Takahashi A, Chung CB, Bydder GM. Qualitative and quantitative ultrashort echo time (UTE) imaging of cortical bone. J Magn Reson. 2010;207(2):304–311. Epub 2010/10/29. https://doi.org/10.1016/j.jmr.2010.09.013.

27. Samarin A, Burger C, Wollenweber SD, Crook DW, Burger IA, Schmid DT, et al. PET/MR imaging of bone lesions – implications for PET quantification from imperfect attenuation correction. Eur J Nucl Med Mol Imaging. 2012;39(7):1154–1160. Epub 2012/04/25. https://doi.org/10.1007/s00259-012-2113-0.

28. Teuho J, Johansson J, Linden J, Saunavaara V, Tolvanen T, Teras M, editors. Quantitative bias in PET/MR from attenuation correction and reconstruction: a comparison with PET and PET/CT with an anatomical brain phantom and Hoffman brain phantom. In: Nuclear Science Symposium and Medical Imaging Conference (NSS/MIC). IEEE, October 27 2013–November 2 2013.

29. Keller SH, Holm S, Hansen AE, Sattler B, Andersen F, Klausen TL, et al. Image artifacts from MR-based attenuation correction in clinical, whole-body PET/MRI. Magn Reson Mater Phys. 2013;26(1):173–181. Epub 2012/09/22. https://doi.org/10.1007/s10334-012-0345-4.

30. Aznar MC, Sersar R, Saabye J, Ladefoged CN, Andersen FL, Rasmussen JH, et al. Whole-body PET/MRI: the effect of bone attenuation during MR-based attenuation correction in oncology imaging. Eur J Radiol. 2014;83(7):1177–1183. Epub 2014/05/02. https://doi.org/10.1016/j.ejrad.2014.03.022.

31. Izquierdo-Garcia D, Sawiak S, Knesaurek K, Narula J, Fuster V, Machac J, et al. Comparison of MR-based attenuation correction and CT-based attenuation correction of whole-body PET/MR imaging. Eur J Nucl Med. 2014;41(8):1574–84. https://doi.org/10.1007/s00259-014-2751-5.

32. Bezrukov I, Schmidt H, Gatidis S, Mantlik F, Schäfer JF, Schwenzer N, et al. Quantitative evaluation of segmentation- and atlas-based attenuation correction for PET/MR on pediatric patients. J Nucl Med. 2015;56(7):1067–74. https://doi.org/10.2967/jnumed.114.149476.

33. Andersen FL, Ladefoged CN, Beyer T, Keller SH, Hansen AE, Hojgaard L, et al. Combined PET/MR imaging in neurology: MR-based attenuation correction implies a strong spatial bias when ignoring bone. NeuroImage. 2014;84:206–216. Epub 2013/09/03. https://doi.org/10.1016/j.neuroimage.2013.08.042.

34. Cabello J, Lukas M, Rota Kops E, Ribeiro A, Shah NJ, Yakushev I, et al. Comparison between MRI-based attenuation correction methods for brain PET in dementia patients. Eur J Nucl Med Mol Imaging. 2016;43:2190–2200. Epub 2016/04/21. https://doi.org/10.1007/s00259-016-3394-5.

35. Catana C, Van der Kouwe A, Benner T, Hamm C, Michel CJ, Fenchel M, et al. MR-based PET attenuation correction for neurological studies using dual-echo UTE sequences. In: Joint annual meeting of the International Society of Magnetic Resonance in Medicine and the European Society for Magnetic Resonance in Medicine and Biology, May, Stockholm; 2010. p. 3953.

36. Wiesinger F, Sacolick LI, Menini A, Kaushik SS, Ahn S, Veit-Haibach P, et al. Zero TE MR bone imaging in the head. Magn Reson Med. 2016;75(1):107–14.

37. Qian H, Shanbhag D, Kaushik S, Thiruvenkadam S, Novak G, Lonn A, et al. Whole-body PET/MR attenuation correction on a sequential, tri-modality PET/CT and MR imaging setup combing image segmentation, truncation completion and atlas-based skull segmentation. In: Proceedings new paradigms in molecular imaging conference, Elba, Italy, Tuesday, 29th May 2012.

38. Wollenweber SD, Ambwani S, Lonn AHR, Mullick R, Wiesinger F, Piti Z, et al., editors. Evaluation of an atlas-based PET head attenuation correction using PET/CT & MR patient data. In: Nuclear Science Symposium and Medical Imaging Conference (NSS/MIC). IEEE; October 27 2012–November 3 2012.

39. Sekine T, Buck A, Delso G, Ter Voert EE, Huellner M, Veit-Haibach P, et al. Evaluation of atlas-based attenuation correction for integrated PET/MR in human brain: application of a head atlas and comparison to true CT-based attenuation correction. J Nucl Med. 2016;57(2):215–220. Epub 2015/10/24. https://doi.org/10.2967/jnumed.115.159228.

40. Hofmann M, Steinke F, Scheel V, Charpiat G, Farquhar J, Aschoff P, et al. MRI-based attenuation correction for PET/MRI: a novel approach combining pattern recognition and atlas registration. J Nucl Med. 2008;49(11):1875–1883. Epub 2008/10/18. https://doi.org/10.2967/jnumed.107.049353.

41. Burgos N, Cardoso MJ, Thielemans K, Modat M, Pedemonte S, Dickson J, et al. Attenuation correction synthesis for hybrid PET-MR scanners: application to brain studies. IEEE Trans Med Imaging. 2014;33(12):2332–2341. Epub 2014/07/24. https://doi.org/10.1109/TMI.2014.2340135.

42. Chen Y, Juttukonda M, Su Y, Benzinger T, Rubin BG, Lee YZ, et al. Probabilistic air segmentation and sparse regression estimated pseudo CT for PET/MR attenuation correction. Radiology. 2015;275(2):562–569. Epub 2014/12/19. https://doi.org/10.1148/radiol.14140810.

43. Torrado-Carvajal A, Herraiz JL, Alcain E, Montemayor AS, Garcia-Canamaque L, Hernandez-Tamames JA, et al. Fast patch-based pseudo-CT synthesis from T1-weighted MR images for PET/MR attenuation correction in brain studies. J Nucl Med. 2016;57(1):136–143 . Epub 2015/10/24. https://doi.org/10.2967/jnumed.115.156299.

44. Keereman V, Fierens Y, Broux T, De Deene Y, Lonneux M, Vandenberghe S. MRI-based attenuation correction for PET/MRI using ultrashort echo time sequences. J Nucl Med. 2010;51(5):812–818. Epub 2010/05/05. https://doi.org/10.2967/jnumed.109.065425.

45. Delso G, Wiesinger F, Sacolick LI, Kaushik SS, Shanbhag DD, Hullner M, et al. Clinical evaluation of zero-echo-time MR imaging for the segmentation of the skull. J Nucl Med. 2015;56(3):417–422. Epub 2015/02/14. https://doi.org/10.2967/jnumed.114.149997.

46. Hu L, Su K-H, Pereira GC, Grover A, Traughber B, Traughber M, et al. k-space sampling optimization for ultrashort TE imaging of cortical bone: applications in radiation therapy planning and MR-based PET attenuation correction. Med Phys. 2014;41(10):102301. https://doi.org/10.1118/1.4894709.

47. Cabello J, Lukas M, Förster S, Pyka T, Nekolla SG, Ziegler SI. MR-based attenuation correction using UTE pulse sequences in dementia patients. J Nucl Med. 2015;56:423–9. https://doi.org/10.2967/jnumed.114.146308.

48. Khateri P, Saligheh Rad H, Jafari AH, Fathi Kazerooni A, Akbarzadeh A, Shojae Moghadam M, et al. Generation of a four-class attenuation map for MRI-based attenuation correction of PET data in the head area using a novel combination of STE/Dixon-MRI and FCM clustering. Mol Imaging Biol. 2015;17(6):884–892. Epub 2015/04/29. https://doi.org/10.1007/s11307-015-0849-1.

49. Berker Y, Franke J, Salomon A, Palmowski M, Donker HC, Temur Y, et al. MRI-based attenuation correction for hybrid PET/MRI systems: a 4-class tissue segmentation technique using a combined ultrashort-echo-time/Dixon MRI sequence. J Nucl Med. 2012;53(5):796–804. Epub 2012/04/17. https://doi.org/10.2967/jnumed.111.092577.

50. Dickson JC, O'Meara C, Barnes A. A comparison of CT- and MR-based attenuation correction in neurological PET. Eur J Nucl Med Mol Imaging. 2014;41(6):1176–1189. Epub 2014/01/16. https://doi.org/10.1007/s00259-013-2652-z.

51. Roy S, Wang WT, Carass A, Prince JL, Butman JA, Pham DL. PET attenuation correction using synthetic CT from ultrashort echo-time MR imaging. J Nucl Med. 2014;55(12):2071–2077. Epub 2014/11/22. https://doi.org/10.2967/jnumed.114.143958.

52. Johansson A, Karlsson M, Nyholm T. CT substitute derived from MRI sequences with ultrashort echo time. Med Phys. 2011;38(5):2708–14.

53. Delso G, Zeimpekis K, Carl M, Wiesinger F, Hullner M, Veit-Haibach P. Cluster-based segmentation of dual-echo ultra-short echo time images for PET/MR bone localization. EJNMMI Phys. 2014;1(1):7. Epub 2015/10/27. https://doi.org/10.1186/2197-7364-1-7.
54. Paulus DH, Quick HH, Geppert C, Fenchel M, Zhan Y, Hermosillo G, et al. Whole-body PET/MR imaging: quantitative evaluation of a novel model-based MR attenuation correction method including bone. J Nucl Med. 2015;56(7):1061–6. https://doi.org/10.2967/jnumed.115.156000.
55. Beyer T, Bockisch A, Kühl H, Martinez M-J. Whole-body 18F-FDG PET/CT in the presence of truncation artifacts. J Nucl Med. 2006;47(1):91–9.
56. Delso G, Martinez-Moller A, Bundschuh RA, Nekolla SG, Ziegler SI. The effect of limited MR field of view in MR/PET attenuation correction. Med Phys. 2010;37(6):2804–12. Epub 2010/07/17.
57. Mawlawi O, Erasmus JJ, Pan T, Cody DD, Campbell R, Lonn AH, et al. Truncation artifact on PET/CT: impact on measurements of activity concentration and assessment of a correction algorithm. AJR Am J Roentgenol. 2006;186(5):1458–1467. Epub 2006/04/25. https://doi.org/10.2214/AJR.05.0255.
58. Blumhagen JO, Braun H, Ladebeck R, Fenchel M, Faul D, Scheffler K, et al. Field of view extension and truncation correction for MR-based human attenuation correction in simultaneous MR/PET imaging. Med Phys. 2014;41(2):022303. Epub 2014/02/11. https://doi.org/10.1118/1.4861097.
59. Blumhagen JO, Ladebeck R, Fenchel M, Scheffler K. MR-based field-of-view extension in MR/PET: B0 homogenization using gradient enhancement (HUGE). Magn Reson Med. 2012. https://doi.org/10.1002/mrm.24555.
60. Schramm G, Langner J, Hofheinz F, Petr J, Lougovski A, Beuthien-Baumann B, et al. Influence and compensation of truncation artifacts in MR-based attenuation correction in PET/MR. IEEE Trans Med Imaging. 2013;32(11):2056–63. https://doi.org/10.1109/tmi.2013.2272660.
61. Qian H, Shanbhag D, Kaushik S, Thiruvenkadam S, Novak G, Lonn A, et al. Whole-body PET/MR attenuation correction combining image segmentation, truncation completion and atlas-based skull segmentation PET/MR and SPECT/MR. In: New paradigms for combined modalities in molecular imaging conference; Elba2012.
62. Nuyts J, Bal G, Kehren F, Fenchel M, Michel C, Watson C. Completion of a truncated attenuation image from the attenuated PET emission data. IEEE Trans Med Imaging. 2013;32(2):237–246. Epub 2012/09/28. https://doi.org/10.1109/TMI.2012.2220376.
63. Conti M. Why is TOF PET reconstruction a more robust method in the presence of inconsistent data? Phys Med Biol. 2011;56(1):155–168. Epub 2010/12/02. https://doi.org/10.1088/0031-9155/56/1/010.
64. Mehranian A, Zaidi H. Emission-based estimation of lung attenuation coefficients for attenuation correction in time-of-flight PET/MR. Phys Med Biol. 2015;60(12):4813–4833. Epub 2015/06/06. https://doi.org/10.1088/0031-9155/60/12/4813.
65. Nuyts J, Dupont P, Stroobants S, Benninck R, Mortelmans L, Suetens P. Simultaneous maximum a posteriori reconstruction of attenuation and activity distributions from emission sinograms. IEEE Trans Med Imaging. 1999;18(5):393–403. Epub 1999/07/23. https://doi.org/10.1109/42.774167.
66. Krol A, Bowsher JE, Manglos SH, Feiglin DH, Tornai MP, Thomas FD. An EM algorithm for estimating SPECT emission and transmission parameters from emission data only. IEEE Trans Med Imaging. 2001;20(3):218–32. https://doi.org/10.1109/42.918472.
67. Mihlin A, Levin CS, editors. An MLEM method for joint tissue activity distribution and photon attenuation map reconstruction in PET. In: 2013 IEEE nuclear science symposium and medical imaging conference (2013 NSS/MIC), October 27 2013–November 2 2013.
68. Bousse A, Bertolli O, Atkinson D, Arridge S, Ourselin S, Hutton BF, et al. Maximum-likelihood joint image reconstruction/motion estimation in attenuation-corrected respiratory gated PET/CT using a single attenuation map. IEEE Trans Med Imaging. 2016;35(1):217–228. Epub 2015/08/11. https://doi.org/10.1109/tmi.2015.2464156.

69. Tomitani T. Image reconstruction and noise evaluation in photon time-of-flight assisted positron emission tomography. IEEE Trans Nucl Sci. 1981;28(6):4581–9. https://doi.org/10.1109/tns.1981.4335769.

70. Salomon A, Goedicke A, Schweizer B, Aach T, Schulz V. Simultaneous reconstruction of activity and attenuation for PET/MR. IEEE Trans Med Imaging. 2011;30(3):804–813. Epub 2010/12/02. https://doi.org/10.1109/TMI.2010.2095464.

71. Defrise M, Rezaei A, Nuyts J. Time-of-flight PET data determine the attenuation sinogram up to a constant. Phys Med Biol. 2012;57(4):885.

72. Rezaei A, Defrise M, Bal G, Michel C, Conti M, Watson C, et al. Simultaneous reconstruction of activity and attenuation in time-of-flight PET. IEEE Trans Med Imaging. 2012;31(12):2224–2233. Epub 2012/08/18. https://doi.org/10.1109/TMI.2012.2212719.

73. Boellaard R, Hofman MB, Hoekstra OS, Lammertsma AA. Accurate PET/MR quantification using time of flight MLAA image reconstruction. Mol Imaging Biol. 2014;16(4):469–477. Epub 2014/01/17. https://doi.org/10.1007/s11307-013-0716-x.

74. Mehranian A, Zaidi H. Joint estimation of activity and attenuation in whole-body TOF PET/MRI using constrained Gaussian mixture models. IEEE Trans Med Imaging 2015. Epub 2015/03/15. doi: https://doi.org/10.1109/TMI.2015.2409157.

75. Berker Y, Li Y. Attenuation correction in emission tomography using the emission data – a review. Med Phys. 2016;43(2):807–32. https://doi.org/10.1118/1.4938264.

76. Defrise M, Rezaei A, Nuyts J. Transmission-less attenuation correction in time-of-flight PET: analysis of a discrete iterative algorithm. Phys Med Biol. 2014;59(4):1073–1095. Epub 2014/02/08. https://doi.org/10.1088/0031-9155/59/4/1073.

77. Rezaei A, Defrise M, Nuyts J. ML-reconstruction for TOF-PET with simultaneous estimation of the attenuation factors. IEEE Trans Med Imaging. 2014;33(7):1563–1572. Epub 2014/04/25. https://doi.org/10.1109/TMI.2014.2318175.

78. Rezaei A, Michel C, Casey ME, Nuyts J. Simultaneous reconstruction of the activity image and registration of the CT image in TOF-PET. Phys Med Biol. 2016;61(4):1852–1874. Epub 2016/02/09. https://doi.org/10.1088/0031-9155/61/4/1852.

79. Bousse A, Bertolli O, Atkinson D, Arridge S, Ourselin S, Hutton BF, et al. Maximum-likelihood joint image reconstruction and motion estimation with misaligned attenuation in TOF-PET/CT. Phys Med Biol. 2016;61(3):L11–L19. Epub 2016/01/21. https://doi.org/10.1088/0031-9155/61/3/l11.

80. Defrise M, Salvo K, Rezaei A, Nuyts J, Panin V, Casey M, editors. ML estimation of the scatter scaling in TOF PET. In: 2014 IEEE nuclear science symposium and medical imaging conference (NSS/MIC), 8–15 November 2014.

81. Ahn S, Shanbhag D, Qian H, Kaushik S, Thiruvenkadam S, Manjeshwar R. Improved attenuation correction in PET/MRI by combining MR image segmentation and joint estimation approaches. J Nucl Med. 2013;54(Supplement 2):150.

82. Eldib M, Bini J, Faul DD, Oesingmann N, Tsoumpas C, Fayad ZA. Attenuation correction for magnetic resonance coils in combined PET/MR imaging: a review. PET Clin. 2016;11(2):151–160. Epub 2016/03/10. https://doi.org/10.1016/j.cpet.2015.10.004.

83. Wollenweber SD, Delso G, Deller T, Goldhaber D, Hullner M, Veit-Haibach P. Characterization of the impact to PET quantification and image quality of an anterior array surface coil for PET/MR imaging. MAGMA. 2014;27(2):149–159. Epub 2013/06/27. https://doi.org/10.1007/s10334-013-0388-1.

84. Delso G, Martinez-Moller A, Bundschuh RA, Ladebeck R, Candidus Y, Faul D, et al. Evaluation of the attenuation properties of MR equipment for its use in a whole-body PET/MR scanner. Phys Med Biol. 2010;55(15):4361–4374. Epub 2010/07/22. https://doi.org/10.1088/0031-9155/55/15/011.

85. MacDonald LR, Kohlmyer S, Liu C, Lewellen TK, Kinahan PE. Effects of MR surface coils on PET quantification. Med Phys. 2011;38(6):2948–56. Epub 2011/08/06.

86. Ferguson A, McConathy J, Su Y, Hewing D, Laforest R. Attenuation effects of MR headphones during brain PET/MR studies. J Nucl Med Technol. 2014;42(2):93–100. Epub 2014/02/22. https://doi.org/10.2967/jnmt.113.131995.

87. Zhang B, Pal D, Hu Z, Ojha N, Guo T, Muswick G, et al., editors. Attenuation correction for MR table and coils for a sequential PET/MR system. In: Nuclear science symposium conference record (NSS/MIC). IEEE, October 24 2009–November 1 2009.

88. Mantlik F, Hofmann M, Werner MK, Sauter A, Kupferschlager J, Scholkopf B, et al. The effect of patient positioning aids on PET quantification in PET/MR imaging. Eur J Nucl Med Mol Imaging. 2011;38(5):920–929. Epub 2011/02/11. https://doi.org/10.1007/s00259-010-1721-9.

89. Aklan B, Paulus DH, Wenkel E, Braun H, Navalpakkam BK, Ziegler S, et al. Toward simultaneous PET/MR breast imaging: evaluation and integration of a radiofrequency breast coil. Med Phys. 2013;40(2):024301. https://doi.org/10.1118/1.4788642.

90. Eldib M, Faul D, Ladebeck R, Pawlak J, Doshi N. A method for estimating the attenuation correction for the MR hardware of an MR/PET scanner. J Nucl Med. 2012;53(supplement 1):371.

91. Paulus DH, Braun H, Aklan B, Quick HH. Simultaneous PET/MR imaging: MR-based attenuation correction of local radiofrequency surface coils. Med Phys. 2012;39(7):4306–4315. Epub 2012/07/27. https://doi.org/10.1118/1.4729716.

92. Kartmann R, Paulus DH, Braun H, Aklan B, Ziegler S, Navalpakkam BK, et al. Integrated PET/MR imaging: automatic attenuation correction of flexible RF coils. Med Phys. 2013;40(8):082301. Epub 2013/08/10. https://doi.org/10.1118/1.4812685.

93. Eldib M, Bini J, Robson PM, Calcagno C, Faul DD, Tsoumpas C, et al. Markerless attenuation correction for carotid MRI surface receiver coils in combined PET/MR imaging. Phys Med Biol 2015;60(12):4705-4717. Epub 2015/05/29. doi: https://doi.org/10.1088/0031-9155/60/12/4705.

94. Kamel EM, Burger C, Buck A, von Schulthess GK, Goerres GW. Impact of metallic dental implants on CT-based attenuation correction in a combined PET/CT scanner. Eur Radiol. 2003;13(4):724–728. Epub 2003/03/29. https://doi.org/10.1007/s00330-002-1564-2.

95. Brendle C, Schmidt H, Oergel A, Bezrukov I, Mueller M, Schraml C, et al. Segmentation-based attenuation correction in positron emission tomography/magnetic resonance: erroneous tissue identification and its impact on positron emission tomography interpretation. Investig Radiol. 2015;50(5):339–346. Epub 2015/01/15. https://doi.org/10.1097/RLI.0000000000000131.

96. Davison H, Voert ET, Barbosa FDG, Veit-Haibach P, Delso G. Incorporation of TOF information reduces metal artifacts in simultaneous PET/MR: a simulation study. Investig Radiol 2015;50(7):423–9.

97. Schramm G, Maus J, Hofheinz F, Petr J, Lougovski A, Beuthien-Baumann B, et al. Evaluation and automatic correction of metal-implant-induced artifacts in MR-based attenuation correction in whole-body PET/MR imaging. Phys Med Biol. 2014;59(11):2713–2726. Epub 2014/05/08. https://doi.org/10.1088/0031-9155/59/11/2713.

98. Ladefoged C, Andersen F, Keller S, Löfgren J, Hansen A, Holm S, et al. PET/MR imaging of the pelvis in the presence of endoprostheses: reducing image artifacts and increasing accuracy through inpainting. Eur J Nucl Med. 2013:1–8. https://doi.org/10.1007/s00259-012-2316-4.

99. Burger IA, Wurnig MC, Becker AS, Kenkel D, Delso G, Veit-Haibach P, et al. Hybrid PET/MR imaging: an algorithm to reduce metal artifacts from dental implants in Dixon-based attenuation map generation using a multiacquisition variable-resonance image combination sequence. J Nucl Med. 2015;56(1):93–7. https://doi.org/10.2967/jnumed.114.145862.

100. Mehranian A, Zaidi H. Impact of time-of-flight PET on quantification errors in MR imaging-based attenuation correction. J Nucl Med. 2015;56(4):635–641. Epub 2015/03/07. https://doi.org/10.2967/jnumed.114.148817.

101. Pan T, Mawlawi O, Nehmeh SA, Erdi YE, Luo D, Liu HH, et al. Attenuation correction of PET images with respiration-averaged CT images in PET/CT. J Nucl Med. 2005;46(9):1481–7. Epub 2005/09/15.

102. Alessio AM, Kohlmyer S, Branch K, Chen G, Caldwell J, Kinahan P. Cine CT for attenuation correction in cardiac PET/CT. J Nucl Med. 2007;48(5):794–801. https://doi.org/10.2967/jnumed.106.035717.

103. Ho CY, Wu TH, Mok GS. Interpolated average CT for PET attenuation correction in different lesion characteristics. Nuclear Med Commun. 2015. Epub 2015/11/10. https://doi.org/10.1097/mnm.0000000000000435.
104. Catana C. Motion correction options in PET/MRI. Semin Nucl Med. 2015;45(3):212–223. Epub 2015/04/07. https://doi.org/10.1053/j.semnuclmed.2015.01.001.
105. Bal G, Fenchel M, Panin V, Koesters T, Fei G, Howe C, et al., editors. Multi-bed elastic motion correction for whole body MR-PET. In: 2014 IEEE nuclear science symposium and medical imaging conference (NSS/MIC); 2014. 8–15 November 2014.
106. Catana C, Benner T, van der Kouwe A, Byars L, Hamm M, Chonde DB, et al. MRI-assisted PET motion correction for neurologic studies in an integrated MR-PET scanner. J Nucl Med. 2011;52(1):154–161. Epub 2010/12/30. https://doi.org/10.2967/jnumed.110.079343.
107. Delso G, Zeimpekis K, Wiesinger F, Khalighi M, Carl M, Veit-Haibach P. Impact of patient motion on bone attenuation maps. J Nucl Med. 2014;55(supplement 1):2104.
108. Jensen RR, Olesen OV, Benjaminsen C, Højgaard L, Larsen R. Markerless PET motion correction: tracking in narrow gantries through optical fibers. IEEE nuclear science symposium and medical imaging conference (NSS/MIC); 2014.
109. Lois C, Bezrukov I, Schmidt H, Schwenzer N, Werner M, Kupferschläger J, et al. Effect of MR contrast agents on quantitative accuracy of PET in combined whole-body PET/MR imaging. Eur J Nucl Med. 2012;39(11):1756–66. https://doi.org/10.1007/s00259-012-2190-0.
110. Ruhlmann V, Heusch P, Kuhl H, Beiderwellen K, Antoch G, Forsting M, et al. Potential influence of Gadolinium contrast on image segmentation in MR-based attenuation correction with Dixon sequences in whole-body 18F-FDG PET/MR. MAGMA. 2015. Epub 2015/12/17. https://doi.org/10.1007/s10334-015-0516-1.
111. Soderlund AT, Chaal J, Tjio G, Totman JJ, Conti M, Townsend DW. Beyond 18F-FDG: characterization of PET/CT and PET/MR scanners for a comprehensive set of positron emitters of growing application – 18F, 11C, 89Zr, 124I, 68Ga, and 90Y. J Nucl Med. 2015;56(8):1285–91. https://doi.org/10.2967/jnumed.115.156711.
112. Boellaard R, Rausch I, Beyer T, Delso G, Yaqub M, Quick HH, et al. Quality control for quantitative multicenter whole-body PET/MR studies: a NEMA image quality phantom study with three current PET/MR systems. Med Phys. 2015;42(10):5961. Epub 2015/10/03. https://doi.org/10.1118/1.4930962.
113. Ziegler S, Braun H, Ritt P, Hocke C, Kuwert T, Quick HH. Systematic evaluation of phantom fluids for simultaneous PET/MR hybrid imaging. J Nucl Med. 2013;54(8):1464–1471. Epub 2013/06/25. https://doi.org/10.2967/jnumed.112.116376.
114. Ziegler S, Jakoby BW, Braun H, Paulus DH, Quick HH. NEMA image quality phantom measurements and attenuation correction in integrated PET/MR hybrid imaging. EJNMMI Phys. 2015;2(1):18. Epub 2015/10/27. https://doi.org/10.1186/s40658-015-0122-3.

PET/MRI: Motion Correction

5

Ciprian Catana

Contents

5.1 Introduction

The theoretical spatial resolution of current-generation PET scanners can rarely be achieved in practice because of subject motion. Motion negatively impacts virtually all types of PET studies and can be broadly classified into rigid-body motion in which the whole organ of interest moves as a whole (e.g., brain) and nonrigid-body motion (e.g., cardiac, respiratory, bulk) in which deformations of the internal organs occur. The former is relevant in neurological studies, while the latter negatively

C. Catana
Athinoula A. Martinos Center for Biomedical Imaging, Department of Radiology,
Massachusetts General Hospital and Harvard Medical School, Charlestown, MA, USA
e-mail: ccatana@nmr.mgh.harvard.edu

degrades the quality of whole-body studies in oncology and cardiology. In addition to the "image blurring" effect that makes the characterization of small features of interest (e.g., cortical gray matter regions in neurology, primary or metastatic lesions in oncology, myocardial perfusion defects in cardiology) even more difficult, motion leads to bias in quantification and artifacts due to mismatches between the emission and attenuation data.

Recently, integrated PET/MRI scanners capable of simultaneous data acquisition have been introduced [1, 2] and used in numerous proof-of-principle studies in various patient populations, as discussed in the other chapters. Most of the methods previously proposed for motion control (i.e., gating or binning the acquisition into shorter frames that are minimally affected by motion) for both MR and PET are also available in these integrated devices. Although these techniques are not specifically reviewed in this chapter, we note that gating of the emission data is a required step for virtually all the MR-based motion correction approaches discussed. However, the obvious disadvantage of gating is that the signal-to-noise ratio (SNR) in the images obtained from short frames is significantly reduced as a large proportion of the recorded events are discarded. PET data-driven motion estimation has also been a highly researched topic with several promising methods having been developed over the last decades [3]. Although they could be used in integrated PET/MR scanners as we previously described [4], these approaches will not be covered in this chapter, and instead we will focus on the methods that have been specifically suggested in the context of PET/MRI. This novel technology allows the use of motion estimates derived from one modality to perform motion compensation of the data acquired with the other technique. The obvious example and the most widely explored direction to date is the use of MR-derived motion estimates for PET motion correction. However, a cross-modality validation of the motion estimates could be performed in an integrated device, and it is not unconceivable that PET-based estimates could eventually also be used to minimize the effects of motion on the MR images in certain scenarios.

	Displacement (mm)		
	Cranio-caudal	Anterior-posterior	Lateral
Lung lesions	10	9	8
Heart	3.8–23.5	−1.3 to 11.5	−1.8 to 6.1
Liver			
Normal inspiration	10 to 26	10	10
Deep inspiration	75		
Spleen	20	10	5
Pancreas tumor	13–42	3–13	
Kidney	2.5–20.5	0.6–8	0.4–5.9
Prostate	0.5–10.6	0.3–10	

There are several types of motion that negatively impact research and clinical PET/MRI studies [4]. Head motion is random and often occurs very rapidly but can be characterized by simple rigid-body rotations and translations. Respiratory motion

on the other hand can be assumed to be periodic, but it leads to nonrigid displacements of the internal organs in the thorax and abdomen. Furthermore, the amplitude of the motion depends on the type of respiration, with larger displacements being observed after a deep inspiration often used before breath-hold techniques. Even the path along which the various organs travel during inspiration is different than the one followed in expiration, a phenomenon termed hysteresis. The magnitudes of the respiratory-induced displacements for several internal organs (e.g., lung tumor [5], heart [6], liver [7–10], spleen [11], pancreas tumor [12, 13], kidney [14], prostate [15]) are summarized in the adjacent table (see [4] for a more detailed discussion). The motion of the heart throughout the cardiac cycle can also be assumed to be periodic but is very complex, involving longitudinal and radial contractions, as well as rotations of the apex and base in opposing directions [16]. Finally, bulk motion often occurs when patients adjust their position in the scanner. This "nonphysiological" motion is nonperiodic and leads to unpredictable displacements and deformations of the internal organs.

All these types of motion can be characterized using MR although the challenges and solutions are different in each case. For example, for head motion estimation, high temporal resolution methods are required to characterize the motion throughout the whole acquisition as no periodicity can be assumed, but the displacement of the head instead of each of the individual voxels is needed as the brain moves as a whole. On the other hand, periodic respiratory or cardiac motion can be modeled, but the motion vector fields that describe the displacements of all the voxels in the volume of interest have to be derived.

In the next sections, we will discuss several of the MR-based motion estimation and PET data correction strategies that have recently been proposed in the context of PET/MRI. It was not our intention to provide an exhaustive review of the literature and instead decided to focus on those methods that have the highest clinical potential, meaning they could be used routinely without minimal modification of the clinical protocols. First, the MR-based techniques for head, respiratory, cardiac, and bulk motion characterization will be introduced. Next, the algorithms for performing the actual PET data motion correction using these estimates will be briefly covered. Finally, the various methods proposed for the qualitative and quantitative assessment of the impact of motion correction on the PET data will be discussed.

5.2   MR-Based Motion Characterization

5.2.1   Head Motion

Numerous methods for estimating head motion from the MR have been developed but only a handful of them have been used in the context of PET/MR imaging. Head motion estimates can be derived from structural images acquired repeatedly (and ideally frequently) or from embedded navigators. The first human study that demonstrated that MR-based motion estimates can be used for PET motion correction was performed using the BrainPET prototype (Fig. 5.1) [17]. The echo planar
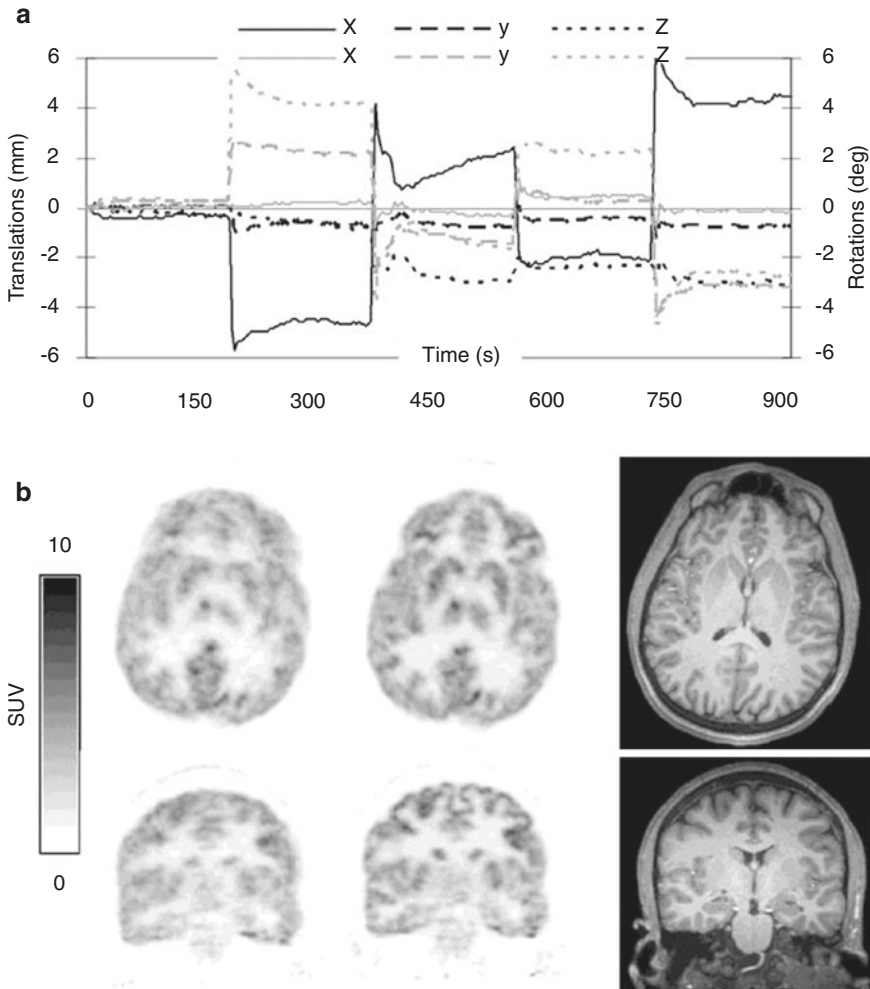
Fig. 5.1 MR-based motion correction in a healthy volunteer: (**a**) EPI-derived motion estimates obtained over a 15 min acquisition; (**b**) FDG PET images reconstructed before (left) and after motion correction (middle) and the corresponding MR images (right). Note the substantial improvement in PET image quality after motion correction. Figures originally published in The Journal of Nuclear Medicine [17]

imaging (EPI)-based estimates were obtained every time a complete volume was acquired (i.e., every 2–3 s). This concept is similar to the prospective acquisition correction (PACE) techniques [18] frequently used in functional MRI studies, except that the individual EPI volumes are coregistered offline using more accurate algorithms. Additionally, estimates were also obtained during high-resolution anatomic imaging using cloverleaf navigators [19]. Briefly, a k-space map was acquired at the beginning of the scan in 12 s. A short-duration (i.e., 20 ms) navigator inserted

every repetition time of a 3D-encoded fast low-angle shot (FLASH) sequence was used to estimate the transformation between the current head position relative to the initial map. These motion estimates were used for both prospective MR and retrospective PET data motion correction.

EPI-derived motion estimates were also used for PET motion correction by some of the other BrainPET early adopters [20–22]. Subsequently, the use of short 3D EPI volumetric navigators (vNavs) embedded in 3D multiecho magnetization-prepared rapid gradient-echo (MPRAGE), 3D T2-weighted sampling perfection with application optimized contrast using different flip angle evolution (SPACE), and 3D T2SPACE fluid-attenuated inversion recovery (FLAIR) sequences (routinely used to acquire high-resolution morphological brain data) was demonstrated to reduce the motion sensitivity of these sequences without degrading their performance [23]. The motion estimates derived from vNavs can be used for PET motion correction in the case of simultaneous PET/MR data acquisition.

Siemens introduced a head motion estimation and correction algorithm, called BrainCOMPASS, for the Biograph mMR scanner. It uses a PACE-based navigator [18] to obtain the head motion estimates simultaneously with the PET data acquisition in list-mode format. If the motion amplitude exceeds a certain threshold, the movement time and the corresponding translations and rotations are saved and later written into the DICOM header of the list-mode data.

A different approach for tracking the head motion involved wireless MR active markers [24] and dedicated MR sequences [25]. The wireless maker consists of a small NMR microsample bulb filled with doped water placed inside a matching size solenoid wireless MR coil. Using three such markers attached to the head of the subject is sufficient for characterizing the motion of the whole volume. A dedicated MR sequence is required to obtain the locations of the wireless markers by measuring their X, Y, and Z projections using separate gradient readouts along each of the directions.

5.2.2 Respiratory Motion

Respiratory motion characterization is a twofold problem. On one hand, a respiratory signal is required to bin the data into gates corresponding to the different phases of the respiratory cycle. On the other hand, a motion model [26] that characterizes the motion of the internal organs between these respiratory phases has to be generated. In the model generation phase, both the respiratory signal and the MR data required for calculating the model are acquired in the same time. Subsequently, only the respiratory signal is used to inform the application of the model, while other MR sequences are run.

The respiratory surrogate signal can be obtained using an external device such as a pressure sensor mounted in a chest belt that monitors the changes related to the displacement of the thoracic cage. Alternatively, navigator pulses derived directly from the MRI data could track the cranio-caudal motion of the right hemidiaphragm [27]. A more advanced method that can be used in the case of motion-insensitive

k-space sampling (e.g., radial or spiral trajectories) consists of deriving a self-gating signal from the k-space [28]. For example, in the case of a stack-of-stars trajectory in which radial sampling is performed in the k_{xy} plane at golden-angle increments and Cartesian sampling is performed in the k_z direction, the self-gating signal can be obtained from the central k-space partition. Additionally, the golden-angle acquisition allows the retrospective binning of the MR data into any desired number of gates. Good correlation between the respiratory signals generated from MR (and PET) data and those obtained from external devices has been reported [29].

To derive a respiratory model, a series of 2D images repeatedly acquired over several respiratory cycles can be used to generate the 3D volumes corresponding to the different respiratory phases [30–32]. Alternatively, these volumes can be obtained from the data collected with 3D radial stack-of-stars spoiled gradient-echo sequences and binned based on respiratory signal derived either from the k-space [28] or using a slice-projection navigator [33].

Once these 4D data (i.e., 3D volumes at multiple time points during the respiratory cycle) are available, various nonrigid registration algorithms (e.g., dense displacement sampling [34], demons [35], vector spline regularization [36], etc.) can be used to compute the motion vector fields between each of the respiratory gates and the reference gate.

Other MR motion estimation techniques such as tagged MRI, phase contrast MRI, and pulsed field gradient methods [37] have been proposed for estimating respiratory motion in the abdomen and thorax in early proof-of-principle PET/MRI studies. In fact, tagged MRI was first suggested in this context for tracking the respiratory motion in the abdomen, and proof-of-principle studies were performed in phantoms and animals [38, 39]. CSPAMM was used for tagging, while the motion fields were estimated using regularized HARP [38]. These methods will not be further discussed here because they have limited clinical potential, as they require long acquisition times and involve nondiagnostic MR sequences.

5.2.3 Cardiac Motion

Characterizing cardiac motion also requires a signal to divide the cardiac cycle into short frames (e.g., 50–100 ms). Although numerous techniques have been proposed for deriving a surrogate signal in MRI [40], the electrocardiogram (ECG)-based gating is the most widely used approach, being applied either prospectively or retrospectively. The latter method, in which data acquired continuously are time-stamped so that they can be retrospectively binned [41], is the one most relevant for motion estimation. Similar to the detection of the respiratory signal, cardiac self-gating can be used to obtain a cardiac signal directly from the k-space data [42, 43].

Once a cardiac signal is available and the data can be binned in different gates, a motion model to describe the transformations between the different cardiac phases needs to be generated.

MRI tagging is a technique that has been widely used in cardiac MRI, in which a virtual pattern (e.g., grid) is superimposed on the tissue of interest using a

selective radio-frequency pulse [44], through the spatial modulation of the magnetization (SPAMM) [45] or a train of RF pulses as in the delay alternating with nutation for tailored excitation (DANTE) sequence [46]. Contrast is thus introduced between the tagged and untagged voxels. The deformation of the tagging pattern is dependent on the motion of the underlying tissue, and various methods (e.g., active contour detection, optical flow, or template matching approaches) can be used to extract motion vector fields from these data. The feasibility of performing cardiac tagging on an integrated PET/MR scanner was first demonstrated using a cardiac beating phantom [47]. A SPAMM sequence was used for tagging the myocardium and nonrigid B-spline registration algorithm [48] for estimating the motion fields in all three directions from the tagged MRI volumes.

As already mentioned, one big disadvantage of the standard tagged MRI approach is that it requires long acquisition times. To address this limitation, accelerated tagged MRI using either parallel imaging (GRAPPA algorithm with up to four times acceleration) or compressed sensing (kt-FOCUSS algorithm) techniques has been suggested [49]. Furthermore, tagging is not useful for tracking the motion of structures on which the tags cannot be superimposed or fade very rapidly. This is the case when imaging the coronary arteries, which is of interest in patients with suspected coronary atherosclerotic disease. Obtaining the motion vector fields from the fat tissue that surrounds the whole heart has been suggested as an alternative [50].

A different framework for simultaneous respiratory motion-corrected cardiac MR angiography and PET imaging was recently developed [51]. The cardiac MR angiography data are acquired during free breathing but with ECG-triggering using a 3D T1-weighted spoiled gradient-echo sequence with a golden-step Cartesian spiral profile sampling trajectory. One spiral interleaf is acquired every cardiac cycle. The data acquired using a 2D image navigator repeated every cycle is used to estimate the translational motion in the foot-head and right-left direction. The respiratory signal obtained from the foot-head motion is used to bin the data into different respiratory phases, and the corresponding MR images are reconstructed using an iterative SENSE approach [52]. Finally, respiratory motion fields are obtained by nonrigidly registering the MR bins and applied to both the MR and PET data.

5.2.4   Dual Respiratory and Cardiac Motion

Although the initial efforts in the PET/MRI field have focused on developing methods for compensating for respiratory and cardiac motion separately, both sources have to be addressed in the same time for in vivo cardiac studies. Dual gating can be performed using external devices to generate the bins required to capture the heart in the various phases along the respiratory and cardiac cycles. Simulation studies been performed to demonstrate the feasibility of dual motion estimation [50, 53].

An elegant approach recently proposed and assessed in vivo uses a 3D golden-radial phase encoding scheme [54]. The data are acquired over 5 min during free breathing and without ECG-triggering to cover several respiratory and cardiac cycles. The respiratory and cardiac signals are obtained from the k-space data using

the self-gating approach previously described and from an external ECG, respectively. The data are split into 8 respiratory and 12 cardiac motion states. Each acquired k-space spoke is assigned to a certain respiratory and cardiac motion state. The data are first reordered based on the respiratory motion states; the volumes corresponding to each respiratory state are reconstructed and registered to determine the respiration-induced heart motion. Next, respiratory motion is compensated for in the k-space, and the data are reordered based on the cardiac motion states. Finally, the motion-free volumes reconstructed from these data are nonrigidly coregistered to obtain the motion vector fields characterizing the motion of the heart during the cardiac cycle. This approach is summarized in Fig. 5.2.

In a different approach, respiratory and motion estimation is performed in two stages [53]. First, the respiratory-gated PET images are used to estimate the respiratory motion vector fields using a B-spline nonrigid registration algorithm and mean square difference as the cost function. These fields are then used to respiratory-motion correct the respiratory gates corresponding to each of the cardiac gates and generate respiratory motion-suppressed images in the reference phase. The cardiac-gated MR data are used to estimate the gate-to-gate cardiac motion vector fields that are finally used to cardiac-motion correct each of the respiratory motion-corrected cardiac gates.
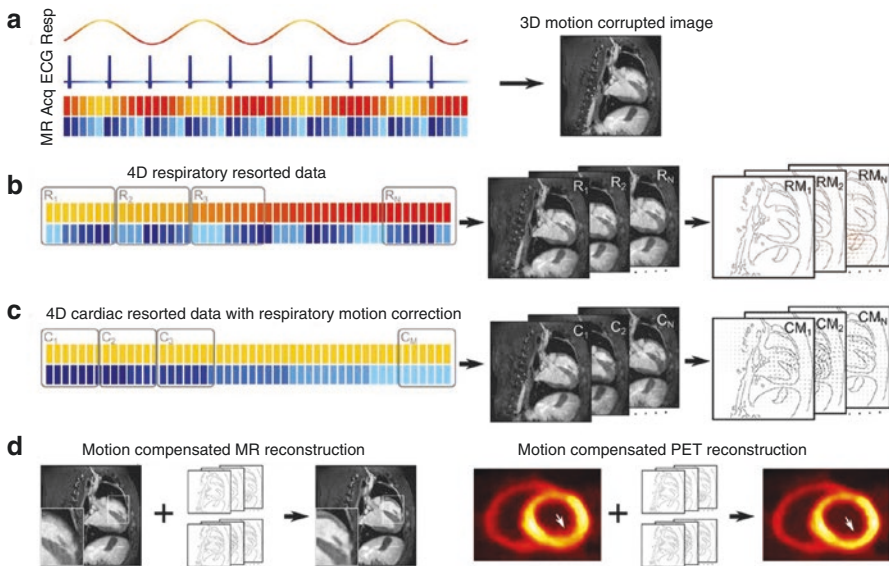
Fig. 5.2 Respiratory and cardiac motion estimation and correction algorithm: (**a**) the MR data are labeled according to the respiratory (yellow-red) and cardiac (blue-cyan) motion states; (**b**) the 4D data are first sorted based on the respiratory labels and used to generate the 3D images corresponding to the *N* respiratory phases from which the respiratory motion fields (RM) are obtained; (**c**) in the next step, respiratory motion correction is performed, the k-space data are resorted based on the cardiac signal, and the M cardiac states obtained are used to calculate the cardiac motion fields (CM); (**d**) finally, dual motion compensation of the MR and PET data is performed. Figures originally published in *The Journal of Nuclear Medicine* [54]

5.2.5   Bulk Motion

MRI can also be used for detecting nonperiodic bulk motion such as that caused by the repositioning of the subject on the scanner table. In the only approach proposed to date, a 3D high-resolution radial phase encoding scheme was used to reconstruct MR images with three different temporal resolutions from the same data. The high temporal resolution images are used to detect the times when bulk motion occurs. Second, the "static" images between the detected time points are generated and used to estimate nonrigid-body motion vector fields between the different states. Finally, motion-compensated PET (and MR) images are reconstructed using the motion vector fields [55].

5.3   PET Data Motion Compensation Algorithms

5.3.1   Before Image Reconstruction

This class of methods was mainly used for rigid-body motion correction of the brain [17, 20–22]. In the motion compensation approach proposed in [17], the list-mode emission data acquired simultaneously with the MR data are first divided into frames of progressively longer duration according to the desired dynamic protocol. Each of these frames is subsequently divided into subframes based on the available MR-based motion estimates. The prompt and random events corresponding to each of the subframes are obtained in the line-of-response space by histogramming the list-mode data. Next, a reference position is selected (e.g., first subframe), and rigid-body transformation matrices for all the subsequent subframes are derived from the MR data. For each event detected in a particular line-of-response, the motion is accounted for by applying the transformer to the corresponding line and identifying the line-of-response in which the event should have been detected in the absence of motion using nearest neighbor interpolation. Alternatively, this can be viewed as "moving" the coordinates of all the crystals based on the transformer or that an event detected in a pair of crystals is assigned to a different pair of crystals based on the transformation matrix derived from the three rotations and three translations that define the rigid-body motion. Motion-compensated prompt and random event sinograms for each subframe are generated from these data. The emission data from all the subframes are added to obtain the motion-compensated prompt and random coincidence sinogram for each frame. The attenuation (and scatter) of the MR radio-frequency coil is accounted for separately since it is stationary with respect to the scanner. The motion-compensated sensitivity data are used to generate the normalization sinogram. Head attenuation and scatter correction sinogram are estimated only in the reference position. The motion-corrected PET volumes are reconstructed from these motion-compensated sinograms using the standard reconstruction algorithm.

A generic reconstruction library called PRESTO (PET reconstruction software toolkit) was proposed to transfer the data into a generic project space previous to

image reconstruction [22]. This approach avoids the degradation of motion-compensated projection data by the axial and transaxial compression that are typically performed for sinogram-based reconstruction. In an effort to reduce the computation time, a patient-specific algorithm to generate subframes only when the measured head displacement between two consecutive time points exceeds a certain threshold was subsequently suggested [21].

Although pre-reconstruction motion compensation algorithms are particularly useful for brain applications, it is worth noting that a similar approach could be used to perform respiratory motion compensation for cardiac studies as previously suggested [56] under the assumption that the heart moves rigidly with respiration.

5.3.2   During Image Reconstruction

The approach most often used for incorporating the MR-derived motion estimates is called motion-compensated image reconstruction (MCIR). Similar to the pre-reconstruction techniques, MCIR has the advantage that all the recorded events contribute to the final image, which leads to significantly improved counting statistics compared to the standard gating techniques in which the majority of the events are discarded. Furthermore, the Poisson nature of the data is maintained as opposed to the post-reconstruction techniques described in the next section.

To perform MCIR for whole-body applications, the PET data are first binned into to the desired number of respiratory or cardiac phases as described above. One of the gates is set as the reference position, and all the motion vector fields that transform the other gates into the reference position are obtained. The PET system matrix (that represents the probability of detecting in a specific line-of-response an event originating from a particular voxel) is modified to account for the nonrigid change in the activity distribution by applying a motion-warping operator [57]. Gate-specific attenuation maps are also generated from the MR-based attenuation map by applying the inverse transformations.

Several of the standard image reconstruction algorithms have been extended to incorporate motion vector fields into the system matrix in the context of PET/MRI such as the one-pass list-mode expectation maximization [31], maximum a posteriori (MAP) [33], maximum likelihood expectation maximization (MLEM) [38], and ordered-subsets expectation maximization (OSEM) [32, 58, 59]. An example of using MCIR for lung motion correction is shown in Fig. 5.3 [33].

Although most popular for whole-body applications, MCIR was also applied to head motion correction using vNav-derived motion estimates [60]. To optimize the computing resources, the list-mode data was adaptively binned into 4D sinograms based on the extent of motion. The mean voxel displacement in the imaging volume was calculated after each vNav acquisition and a new sinogram was generated whenever a threshold was exceeded. In order to account for motion, the authors used a 4D image reconstruction algorithm and a data augmentation method based on the alternating direction method of multipliers [61] that enabled to inclusion of a sparsity constraint to improve image quality.
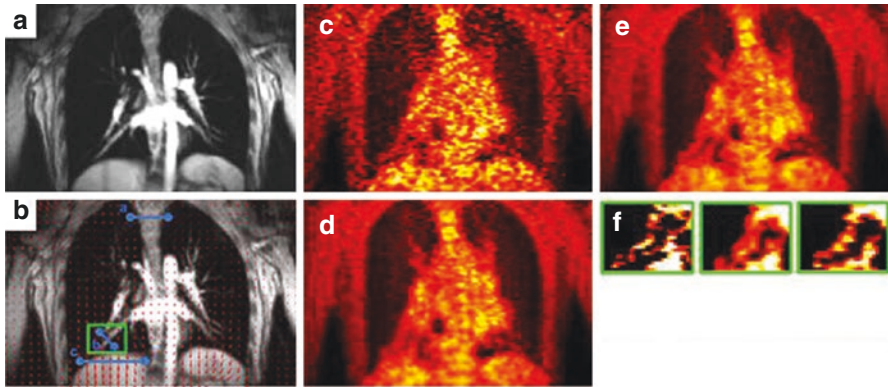
Fig. 5.3 Respiratory motion correction for lung imaging: (**a**) coronal MR image in the reference position and (**b**) overlaid deformation fields; (**c**) one-gated, (**d**) ungated, and (**e**) motion-corrected PET images; (**f**) magnified views of a blood vessel located near the diaphragm demonstrating significantly reduced blurring after motion correction. Figures originally published in *Medical Physics* [33]

5.3.3   After Image Reconstruction

Head motion correction post image reconstruction is used in the BrainCOMPASS approach proposed by Siemens. At the end of the acquisition, the PET data are binned into the motion states defined by the patient's movement exceeding the thresholds. The overall motion is limited to 20 mm (translation) and 8° (rotation). Up to 100 motion frames can be reconstructed. The original attenuation map is transformed to the position of each of the motion frames so that the attenuation correction is correctly performed. After all PET motion frames are reconstructed, the PET image volumes are transformed back to the position of a reference PET frame and summed together.

When using this approach for whole-body applications, the PET images corresponding to each of the gates are first reconstructed using the standard algorithms, and the MR-derived motion vector fields are applied to warp these images into the reference gate.

In one of the first proof-of-principle human studies that used an after image reconstruction approach, the PET gates were first reconstructed using the OSEM algorithm. The Dixon-based attenuation map acquired at end-expiration was warped using the MR-derived motion vector fields to obtain gate-specific attenuation maps. To generate the final image, the gated PET images were coregistered using the motion vector fields, scaled based on the total number of counts in each gate and summed on a voxel-by-voxel basis [30]. A similar approach was used in [28] except that the images corresponding to the individual gates were combined using weights proportional to the intra-bin amplitude range of the self-gating signal.

More recently, a post-reconstruction approach was used for free-breathing respiratory motion-corrected simultaneous cardiac MR angiography and PET

imaging [51]. The authors reconstructed each respiratory bin using the OSEM algorithm and gate-specific attenuation maps.

5.4   Performance Evaluation of MR-Based PET Motion Correction

5.4.1   Methods

There is currently no technique to serve as the gold standard for validating MR-based motion estimation approaches and no accepted metric for quantifying the impact of motion correction on the PET data. Several of the qualitative and quantitative approaches that have been proposed for this purpose in the proof-of-principle PET/MRI studies are summarized in this section.

5.4.1.1 Head Motion

Substantial improvement in the FDG image quality was observed after MR-assisted motion correction in the first proof-of-principle study performed in a healthy volunteer [17]. A better delineation of brain structures and an apparent increase in gray matter uptake were observed after motion correction. Although the authors mainly focused on the static images generated from the data, images from 3 min subframes were also reconstructed and used to generate time activity curves for several gray matter structures. The shapes of these time activity curves were more similar to each other and consistent with the expected FDG kinetics only after motion correction.

Similar improvement in image quality and reduction of artifacts were observed in the brain phantom and patient studies subsequently performed on another BrainPET prototype [20, 21].

5.4.1.2 Respiratory Motion

Fayad et al. [31] compared the images obtained using the MCIR method to those produced using a post-reconstruction approach and the uncorrected ones. Data from 11 patients with metastatic lesions were included in the analysis. The qualitative analysis of the profiles drawn across the lesions showed good correlation between the motion-corrected images and differences compared to the uncorrected ones. The following figures of merit were selected for the quantitative analysis: differences in SNR (the signal and background noise were defined as the mean and standard deviation measured from ten 3 cm diameter regions of interest (ROIs) positioned across the liver), improvement in lesion-to-background contrast (mean lesion signal measured on the slice with the maximum count density and the background as the mean activity in a 3 cm diameter ROI placed in the background organ for each lesion), and full width at half maximum (FWHM) changes in lesion position and size. The improvements reported for the MCIR and post-reconstruction techniques were 28% and 24.2% mean SNR increases, 60.4% and 47.9% lesion size reduction, 70.1% and 57.2% lesion contrast increase, and 60.9% and 46.7% lesion position change, respectively.

Manber et al. [59] first validated the PET-derived respiratory signal against that obtained from the MR pencil-beam navigator on nine subjects who were imaged with either ^{18}F-FDG or ^{68}Ga-DOTATATE. The motion-corrected and uncorrected images were compared in four additional patients who underwent clinical PET/MRI scans. Increased sharpness for several of the lesions was observed by qualitatively examining the line profiles. The changes in standardized uptake values (SUVs) from a ROI defined in an area with high tracer uptake were chosen as the figure of merit for quantitative analysis. Mean increases in peak and maximum SUV of 23.1% and 34.5%, respectively, were observed in a patient with four pancreatic lesions.

Dutta et al. [33] performed simulation studies using the 4D XCAT phantom with 12 added spherical pulmonary lesions of 10 and 14 mm diameters. Three additional patients underwent PET/MRI scans to validate their motion correction framework. Bias and variance for the simulated lesions were evaluated for regularization parameters tuning. Additionally, the contrast-to-noise ratio (CNR, defined as the ratio of the sum of the means over the square root of the sum of the squared standard deviations (SDs) of the intensities in the ROI and background muscle tissue) was computed for high-intensity lung lesions. The authors also computed the mutual information between the features of interest in the PET images before and after motion correction and the corresponding features in the MR image. The bias was comparable for the one gate and motion-corrected images, while the standard deviation was higher for the former. The CNR was substantially improved for the latter.

Rank et al. [58] also performed simulations in addition to evaluating their algorithm in six patients with bronchial carcinoma. ROIs for every lesion were defined using a region-growing algorithm starting from the voxels with the maximum intensity. The SUV_{mean}, SUV_{max}, contrast (defined as the difference in the means in the lesion and background over the mean in the background), and SNR (defined as the difference in the means in the lesion and background over the standard deviation in the background) were calculated in these ROIs. Additionally, the lesion FWHM was calculated for the simulated data. Increases in SUV_{mean}, SUV_{max}, and contrast and a decrease of FWHM/lesion volume were reported for the motion compensation strategies. The SNR of the motion-corrected images was larger than that for the uncorrected case.

Manber et al. [32] evaluated the joint motion model generation method using data from 45 patients. The quantitative figures of merit were mutual information and sum of squared differences, Euclidean distance between deformation fields, and performance index that reflects percentage improvement. The motion compensation methodology was tested in five additional oncology patients who underwent PET-MRI studies. The PET image reconstruction improvements and artifact reduction were assessed visually, and increased sharpness was noted. The SUV_{max} and SUV_{peak} in avid lesion significantly increased after motion correction.

Munoz et al. [51] evaluated the motion-compensated cardiac MR angiography approach in ten subjects. Coronary vessel sharpness and length were used as metrics of MR image quality. The improvements reported were 37.9% and 49.1% for sharpness and 48.0% and 36.7% for length in the left and right coronary arteries, respectively. The PET motion correction strategy was evaluated in five oncology

patients. The PET images were analyzed by drawing profiles across the ventricle and by comparing the mean and coefficient of variation of the SUV in a myocardium ROI. The authors reported that the sharpness of the myocardium was improved after motion correction, while the noise was reduced compared to the gated images. Representative images from this study are shown in Fig. 5.4. The mean increased for three of the patients but remained almost constant for the other two after motion correction.

5.4.1.3 Cardiac Motion

In an effort to remove the influence of respiratory motion on cardiac studies, phantom and simulation studies were initially performed to study the effect of cardiac motion on the detection of cardiac lesions. For example, a beating nonrigid cardiac
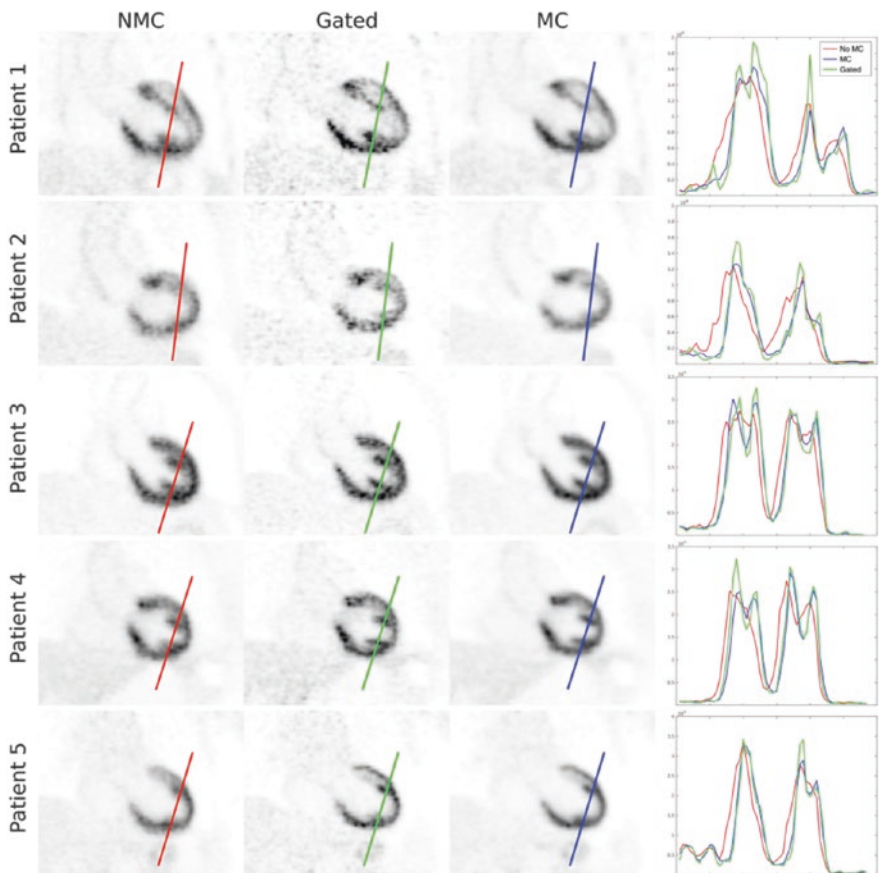

Fig. 5.4 Motion-corrected cardiac images. Coronal PET slices and profiles across the myocardium for five patients showing non-motion-corrected (NMC), gated, and motion-corrected (MC) images. MC improves myocardium sharpness compared to NMC and reduces noise compared to the gated reconstruction. Figures originally published in *Magnetic Resonance in Medicine* [51]

phantom filled with hot ^{18}F gel that also included cold gel inserts of different sizes to mimic transmural and non-transmural myocardial defects was used by Petibon et al. [47]. The defect/myocardium contrast recovery and image background statistical noise levels were compared between the different reconstructions. The authors also used a channelized Hotelling observer to perform a defect detectability study. Reduced spillover from the myocardium to background and defects was reported, leading to improved defect/myocardium contrast recovery (i.e., up to 206%). The improvement in lesion detectability ranged from 62% to 235% being dependent on the defect location (e.g., defects located in the lateral wall underwent the largest motion and demonstrated the largest improvement after motion compensation). These results were further improved after the incorporation of the scanner point spread function in the reconstruction [47].

The same group recently reported the results of a follow-up study in which they assessed the impact of motion and partial volume effects corrections on PET myocardial perfusion imaging in healthy pigs that underwent simultaneous dynamic ^{18}F-Flurpiridaz PET/MRI examinations. As respiratory-induced heart motion is minimal in this particular model, respiratory motion was not performed. Segment- and voxel-wise myocardial blood flow maps were obtained from the dynamic data using a two-tissue compartment model. The 17 American Heart Association (AHA) segments were analyzed. Myocardium-to-blood concentration ratios and wall thickness along profiles in the inferior-superior direction at various positions were estimated. When compared to the uncorrected data, the mean myocardium-to-blood ratio was increased by 20.3% and 13.6% for the motion-corrected and gated data, respectively. The mean apparent myocardial wall thickness was significantly lower after motion correction and gating. Similarly, the myocardial blood flow values were higher in these cases, although the variability was also increased for the gated images. As in the phantom study above, location-dependent differences in mean myocardial blood flow values were reported between the methods [62].

5.4.1.4 Dual Cardiac and Respiratory Motion

Simulation studies have shown that dual motion correction could improve the detection of atherosclerotic plaques [50] and myocardial perfusion defects [53]. Plaque- and defect-to-background contrast were used as the contrast metrics, and receiver operating characteristic analyses using channelized Hotelling observers were performed to study the effect of motion correction on the plaque/defect detectability.

Kolbitsch et al. [54] assessed the improvement in image quality and diagnostic accuracy using five dogs (myocardial infarction model) and one human subject. A qualitative assessment of myocardial uptake was performed using the AHA 17-segment bull's-eye plot. Quantitatively, the FWHM and CNR (defined as the difference between peak myocardial signal and mean blood pool signal over the SD of the latter) of the tracer uptake in the myocardium were estimated at locations that exhibited high cardiac motion in all the animals. When comparing the motion-corrected and uncorrected images of the canine myocardium, the FWHM and CNR improvement was 13% ± 5% and 90% ± 57%, respectively. Similar values (i.e., 18% and 103%, respectively) were reported for the human subject. Additionally, the

sharpness of the right coronary artery was measured from the MR images. An 85% ± 72% increase was reported after motion correction.

5.5   Beyond Proof-of-Principle Studies

Not surprisingly, most of the early research efforts in this field were aimed at demonstrating the feasibility of performing motion correction for various applications and assessing its potential impact on PET data qualitative and quantitative analyses. The focus has been slowly shifting to implementing practical methods that could be used for routine research studies and the hope is that such techniques will eventually be clinically useful. The first requirement for this to happen is to develop techniques in which the data needed for motion characterization are acquired efficiently or in the background of the sequences used for clinical purposes. While some of the early methods required long acquisition time that prevented the acquisition of clinical MR sequences [38, 39], the more recent ones allow the generation of the motion model from the data acquired in only 1 min [58, 59], or clinically relevant MR images can be obtained from the same data [51, 54]. Second, the quantitative accuracy of the PET data should be preserved, which seems to be the case as the consensus in the field is that quantification is actually improved after motion correction. Third, the data processing and image reconstruction time should be comparable to that of the current algorithms when using similar hardware, which is still challenging because the computational requirements for motion estimation/correction are extremely high. Fourth, studies with larger number of patients and in different clinical scenarios need to be performed to validate the various motion estimation/correction techniques. Fifth, additional MR sequences that allow the simultaneous acquisition of the information needed for characterizing the motion and that required for clinical purposes have to be implemented and validated. Finally, the major equipment manufacturers need to make these advanced algorithms available on their scanners and streamline them so that even non-experts can use them. Encouragingly, the head motion correction algorithm BrainCOMPASS is already commercially available on the Siemens Biograph mMR scanner, and recently, an extension of this technique, called BodyCOMPASS, has been introduced to enable motion-free imaging in other body regions such as the abdomen (similar to [28]).

For the BrainPET prototype, we have developed a package for automatic data processing and image reconstruction, called Masamune [63], that, among other capabilities, allows non-expert users to estimate the head motion from the MR data and generate MR-based motion-corrected dynamic frames. This allows head motion correction to be routinely used for research studies performed at the Martinos Center. Most recently, we performed MR-based head motion correction for studying the interaction between dopamine signaling and neural networks changes during working memory [64] and investigating the involvement of the dopaminergic system in the mechanisms of maternal bonding [65]. In a different study focusing on Alzheimer' disease patients, preliminary results showed the variability in the PET estimation of the cerebral metabolic rate of glucose is reduced after motion

correction [66], suggesting that PET data optimization may enable more careful assessment of subtle changes in brain metabolism and allow for reduced sample sizes in future research studies and clinical trials.

In conclusion, the feasibility of performing MR-based PET motion correction for brain and whole-body applications has been demonstrated. Several "practical" MR-based methods to estimate the motion that could be used routinely in research and clinical studies have already been proposed. Virtually all the proof-of-principle studies performed to date have shown that the quality of the PET (and in many cases of the MR) images substantially improves after motion correction, suggesting that MR-based motion correction could be a game changer in the PET/MR field much the same way CT-based attenuation correction has proven in the PET/CT field [67, 68].

References

1. Drzezga A, Souvatzoglou M, Eiber M, et al. First clinical experience with integrated whole-body PET/MR: comparison to PET/CT in patients with oncologic diagnoses. J Nucl Med. 2012;53:845–55.
2. Levin C, Glover G, Deller T, et al. Prototype time-of-flight PET ring integrated with a 3 T MRI system for simultaneous whole-body PET/MR imaging. J Nucl Med. 2013;54:148.
3. Kesner AL, Schleyer PJ, Büther F, et al. On transcending the impasse of respiratory motion correction applications in routine clinical imaging – a consideration of a fully automated data driven motion control framework. EJNMMI Phys. 2014;1:8.
4. Catana C. Motion correction options in PET/MRI. Semin Nucl Med. 2015;45:212–23.
5. Allen AM, Siracuse KM, Hayman JA, et al. Evaluation of the influence of breathing on the movement and modeling of lung tumors. Int J Radiat Oncol Biol Phys. 2004;58:1251–7.
6. McLeish K, Hill DL, Atkinson D, et al. A study of the motion and deformation of the heart due to respiration. IEEE Trans Med Imaging. 2002;21:1142–50.
7. Suramo I, Paivansalo M, Myllyla V. Cranio-caudal movements of the liver, pancreas and kidneys in respiration. Acta Radiol Diagn. 1984;25:129–31.
8. Korin HW, Ehman RL, Riederer SJ, et al. Respiratory kinematics of the upper abdominal organs - a quantitative study. Magn Reson Med. 1992;23:172–8.
9. Clifford MA, Banovac F, Levy E, et al. Assessment of hepatic motion secondary to respiration for computer assisted interventions. Comput Aided Surg. 2002;7:291–9.
10. Shimizu S, Shirato H, Aoyama H, et al. High-speed magnetic resonance imaging for four-dimensional treatment planning of conformal radiotherapy of moving body tumors. Int J Radiat Oncol Biol Phys. 2000;48:471–4.
11. Brandner ED, Wu A, Chen H, et al. Abdominal organ motion measured using 4D CT. Int J Radiat Oncol Biol Phys. 2006;65:554–60.
12. Feng M, Balter JM, Normolle D, et al. Characterization of pancreatic tumor motion using cine MRI: surrogates for tumor position should be used with caution. Int J Radiat Oncol Biol Phys. 2009;74:884–91.
13. Mori S, Hara R, Yanagi T, et al. Four-dimensional measurement of intrafractional respiratory motion of pancreatic tumors using a 256 multi-slice CT scanner. Radiother Oncol. 2009;92:231–7.
14. Yamashita H, Yamashita M, Futaguchi M, et al. Individually wide range of renal motion evaluated by four-dimensional computed tomography. SpringerPlus. 2014;3:131.
15. Dinkel J, Thieke C, Plathow C, et al. Respiratory-induced prostate motion: characterization and quantification in dynamic MRI. Strahlenther Onkol. 2011;187:426–32.
16. Sengupta PP, Korinek J, Belohlavek M, et al. Left ventricular structure and function: basic science for cardiac imaging. J Am Coll Cardiol. 2006;48:1988–2001.

17. Catana C, Benner T, van der Kouwe A, et al. MRI-assisted PET motion correction for neuro-logic studies in an integrated MR-PET scanner. J Nucl Med. 2011;52:154–61.

18. Thesen S, Heid O, Mueller E, et al. Prospective acquisition correction for head motion with image-based tracking for real-time fMRI. Magn Reson Med. 2000;44:457–63.

19. van der Kouwe AJW, Benner T, Dale AM. Real-time rigid body motion correction and shim-ming using cloverleaf navigators. Magn Reson Med. 2006;56:1019–32.

20. Scheins J, Ullisch M, Tellmann L, et al. MR-guided PET motion correction in LOR space using generic projection data for image reconstruction with PRESTO. Nucl Instrum Methods Phys Res Sect A. 2013;702:64–6.

21. Ullisch MG, Scheins J, Weirich C, et al. MR-guided data framing for PET motion correction in simultaneous MR-PET: a preliminary evaluation. Nucl Instrum Methods Phys Res Sect A. 2013;702:67–9.

22. Ullisch MG, Scheins JJ, Weirich C, et al. MR-based PET motion correction procedure for simultaneous MR-PET neuroimaging of human brain. PLoS One. 2012;7:e48149.

23. Tisdall MD, Hess AT, Reuter M, et al. Volumetric navigators for prospective motion correction and selective reacquisition in neuroanatomical MRI. Magn Reson Med. 2012;68:389–99.

24. Ackerman JL, Offutt MC, Buxton RB, et al. Rapid 3D tracking of small RF coils. Paper pre-sented at: Proceedings of the 5th annual meeting of SMRM, Montreal, Canada. 1986.

25. Huang C, Ackerman JL, Petibon Y, et al. Motion compensation for brain PET imaging using wireless MR active markers in simultaneous PET-MR: phantom and non-human primate stud-ies. NeuroImage. 2014;91:129–37.

26. McClelland JR, Hawkes DJ, Schaeffter T, et al. Respiratory motion models: a review. Med Image Anal. 2013;17:19–42.

27. Ehman RL, Felmlee JP. Adaptive technique for high-definition MR imaging of moving struc-tures. Radiology. 1989;173:255–63.

28. Grimm R, Furst S, Dregely I, et al. Self-gated radial MRI for respiratory motion compensation on hybrid PET/MR systems. Med Image Comput Comput Assist Interv. 2013;16:17–24.

29. Furst S, Grimm R, Hong I, et al. Motion correction strategies for integrated PET/MR. J Nucl Med. 2015;56:261–9.

30. Wurslin C, Schmidt H, Martirosian P, et al. Respiratory motion correction in oncologic PET using T1-weighted MR imaging on a simultaneous whole-body PET/MR system. J Nucl Med. 2013;54:464–71.

31. Fayad H, Schmidt H, Wuerslin C, et al. Reconstruction-incorporated respiratory motion cor-rection in clinical simultaneous PET/MR imaging for oncology applications. J Nucl Med. 2015;56:884–9.

32. Manber R, Thielemans K, Hutton BF, et al. Joint PET-MR respiratory motion models for clini-cal PET motion correction. Phys Med Biol. 2016;61:6515–30.

33. Dutta J, Huang C, Li Q, et al. Pulmonary imaging using respiratory motion compensated simultaneous PET/MR. Med Phys. 2015;42:4227–40.

34. Heinrich MP, Jenkinson M, Brady SM, et al. Globally optimal deformable registration on a minimum spanning tree using dense displacement sampling. In: Ayache N, Delingette H, Golland P, Mori K, editors. Medical image computing and computer-assisted intervention – MICCAI 2012: 15th international conference, Nice, France, October 1–5, 2012, proceedings, part III. Berlin, Heidelberg: Springer; 2012. p. 115–22.

35. Kroon DJ, Slump CH. MRI modality transformation in demon registration. Paper presented at: 2009 IEEE International Symposium on Biomedical Imaging: From Nano to Macro; June 28–July 1 2009. 2009.

36. Sorzano COS, Thévenaz P, Unser M. Elastic registration of biological images using vector-spline regularization. IEEE Trans Biomed Eng. 2005;52:652–63.

37. Ozturk C, Derbyshire JA, McVeigh ER. Estimating motion from MRI data. Proc IEEE. 2003;91:1627–48.

38. Guerin B, Cho S, Chun SY, et al. Nonrigid PET motion compensation in the lower abdomen using simultaneous tagged-MRI and PET imaging. Med Phys. 2011;38:3025–38.

39. Chun SY, Reese TG, Ouyang JS, et al. MRI-Based nonrigid motion correction in simultaneous PET/MRI. J Nucl Med. 2012;53:1284–91.
40. Scott AD, Keegan J, Firmin DN. Motion in cardiovascular MR imaging. Radiology. 2009;250:331–51.
41. Lenz GW, Haacke EM, White RD. Retrospective cardiac gating: a review of technical aspects and future directions. Magn Reson Imaging. 1989;7:445–55.
42. Larson AC, White RD, Laub G, et al. Self-gated cardiac cine MRI. Magn Reson Med. 2004;51:93–102.
43. Crowe ME, Larson AC, Zhang Q, et al. Automated rectilinear self-gated cardiac cine imaging. Magn Reson Med. 2004;52:782–8.
44. Zerhouni EA, Parish DM, Rogers WJ, et al. Human-heart-tagging with MR imaging - a method for noninvasive assessment of myocardial motion. Radiology. 1988;169:59–63.
45. Axel L, Dougherty L. MR imaging of motion with spatial modulation of magnetization. Radiology. 1989;171:841–5.
46. Mosher TJ, Smith MB. A DANTE tagging sequence for the evaluation of translational sample motion. Magn Reson Med. 1990;15:334–9.
47. Petibon Y, Ouyang J, Zhu X, et al. Cardiac motion compensation and resolution modeling in simultaneous PET-MR: a cardiac lesion detection study. Phys Med Biol. 2013;58:2085.
48. Ledesma-Carbayo MJ, Derbyshire JA, Sampath S, et al. Unsupervised estimation of myocardial displacement from tagged MR sequences using nonrigid registration. Magn Reson Med. 2008;59:181–9.
49. Huang C, Petibon Y, Ouyang J, et al. Accelerated acquisition of tagged MRI for cardiac motion correction in simultaneous PET-MR: phantom and patient studies. Med Phys. 2015;42:1087–97.
50. Petibon Y, El Fakhri G, Nezafat R, et al. Towards coronary plaque imaging using simultaneous PET-MR: a simulation study. Phys Med Biol. 2014;59:1203–22.
51. Munoz C, Neji R, Cruz G, et al. Motion-corrected simultaneous cardiac positron emission tomography and coronary MR angiography with high acquisition efficiency. Magn Reson Med. 2017. doi:10.1002/mrm.26690.
52. Pruessmann KP, Weiger M, Scheidegger MB, et al. SENSE: Sensitivity encoding for fast MRI. Magn Reson Med. 1999;42:952–62.
53. Wang X, Rahmim A, Tang J. MRI assisted dual motion correction for myocardial perfusion defect detection in PET imaging. Med Phys. 2017;44(9):4536–47. doi: 10.1002/mp.12429.
54. Kolbitsch C, Ahlman MA, Davies-Venn C, et al. Cardiac and respiratory motion correction for simultaneous cardiac PET/MR. J Nucl Med. 2017;58:846–52.
55. Kolbitsch C, Prieto C, Tsoumpas C, et al. A 3D MR-acquisition scheme for nonrigid bulk motion correction in simultaneous PET-MR. Med Phys. 2014;41:082304.
56. Livieratos L, Stegger L, Bloomfield PM, et al. Rigid-body transformation of list-mode projection data for respiratory motion correction in cardiac PET. Phys Med Biol. 2005;50:3313–22.
57. Lamare F, Ledesma Carbayo MJ, Cresson T, et al. List-mode-based reconstruction for respiratory motion correction in PET using non-rigid body transformations. Phys Med Biol. 2007;52:5187–204.
58. Rank CM, Heusser T, Wetscherek A, et al. Respiratory motion compensation for simultaneous PET/MR based on highly undersampled MR data. Med Phys. 2016;43:6234.
59. Manber R, Thielemans K, Hutton BF, et al. Practical PET respiratory motion correction in clinical PET/MR. J Nucl Med. 2015;56:890–6.
60. Pedemonte S, Catana C, Van Leemput K. 4-D PET-MR with volumetric navigators and compressed sensing. In: Gao F, Shi K, Li S, editors. Computational methods for molecular imaging. Cham: Springer; 2015. p. 93–101.
61. Boyd S, Parikh N, Chu E, et al. Distributed optimization and statistical learning via the alternating direction method of multipliers. Found Trends® Mach Learn. 2011;3:1–122.

62. Petibon Y, Guehl NJ, Reese TG, et al. Impact of motion and partial volume effects correction on PET myocardial perfusion imaging using simultaneous PET-MR. Phys Med Biol. 2017;62:326–43.

63. Chonde DB, Izquierdo-Garcia D, Chen K, et al. Masamune: a tool for automatic dynamic PET data processing, image reconstruction and integrated PET/MRI data analysis. EJNMMI Phys. 2014;1:A57.

64. Roffman JL, Tanner AS, Eryilmaz H, et al. Dopamine D-1 signaling organizes network dynamics underlying working memory. Sci Adv. 2016;2:10.

65. Atzil S, Touroutoglou A, Rudy T, et al. Dopamine in the medial amygdala network mediates human bonding. Proc Natl Acad Sci U S A. 2017;114:2361–6.

66. Chen KT, Hutchcroft W, Salcedo S, et al. Improved quantification of dementia PET data using temporally and spatially correlated MR data. In: World molecular imaging conference. New York, NY. 2016.

67. Townsend DW, Carney JP, Yap JT, et al. PET/CT today and tomorrow. J Nucl Med. 2004;45(Suppl 1):4S–14S.

68. Kinahan PE, Townsend DW, Beyer T, et al. Attenuation correction for a combined 3D PET/CT scanner. Med Phys. 1998;25:2046–53.

PET/MRI: Reliability/Reproducibility of SUV Measurements

6

Habib Zaidi and Irene A. Burger

Contents

6.1 The Standardized Uptake Value (SUV) Metric

Qualitative visual interpretation of PET images is commonly performed to report abnormal tracer uptake in suspected regions. This is usually achieved by comparing observed patterns to expected normal biodistribution. However, the human visual system bears a number of limitations, and as such, this approach intrinsically suffers from intra- and interobserver variability owing to the subjective nature of visual interpretation [1]. Subsequently, guidelines on interpretation of PET images in clinical oncology advocated the adoption of simplified versions of PET metrics including semiquantitative indices, such as the standardized uptake value (SUV) [2].

H. Zaidi (✉)
Division of Nuclear Medicine and Molecular Imaging, Geneva University Hospital, Geneva, Switzerland
e-mail: Habib.Zaidi@hcuge.ch

I.A. Burger
Department of Nuclear Medicine, University Hospital Zurich, Zurich, Switzerland
e-mail: Irene.Burger@usz.ch

Several methods for measuring PET tracer accumulation were proposed in the literature. The base is to measure the in vivo radioactivity concentration in the suspected malignant lesion (kBq/mL), which is directly linked to the tracer concentration. The two most significant sources of variation of tracer accumulation are the injected dose and the body weight representing whole-body distribution volume [1]. In practice, the SUV is calculated by dividing the decay-corrected activity concentration in the volume of interest (VOI) drawn around the lesion (MBq/mL) by the injected dose (MBq) divided by the body weight (g) [3]:

$$SUV = \frac{Mean\ ROI\ concentration\ (MBq/mL)}{Injected\ dose\ (MBq) \Big/ Body\ weight\ (g)} \times \frac{1}{decay\ factor} \tag{6.1}$$

The SUV metric is widely used in the clinic because of its simplicity, ease of use, reproducibility, and compatibility with conventional whole-body PET/CT acquisition protocols, requiring only a static scan as opposed to full kinetic modeling approaches, which require complex dynamic studies and arterial blood sampling. Virtually all commercial and open-source medical image display software platforms offer the option to measure SUVs. However, considerable inconsistencies have been reported among the different software packages used in clinical and research settings as demonstrated in a recent study conducted by the PET technical committee of the Quantitative Imaging Biomarker Alliance initiative [4]. It should also be noted that most packages normalize SUV to patient's body weight (Eq. (6.1)). However, since adipose tissue is not as metabolically active as other tissues, other variants were suggested, including normalization to lean body mass (SUV$_{LBM}$ or SUL) [5] or body surface area (SUV$_{BSA}$) [6].

The maximum SUV (SUV$_{max}$), representing the highest voxel SUV value, and mean SUV (SUV$_{mean}$), representing the average SUV across all voxels in a defined VOI, are undoubtedly the most widely used semiquantitative metrics (Fig. 6.1). Conversely, SUV$_{peak}$ (Fig. 6.1), defined in PERCIST criteria as representing the SUV$_{mean}$ in a

$$SUV_{max} = \frac{C_{max}\ (Bq/cc)}{A_{inj}\ (Bq)\ /\ W\ (g)}$$

$$SUV_{peak} = \frac{C_{1cm^3 ROI}\ (Bq/cc)}{A_{inj}\ (Bq)\ /\ W\ (g)}$$

$$SUV_{mean} = \frac{C_{ROI}\ (Bq/cc)}{A_{inj}\ (Bq)\ /\ W\ (g)}$$

SUV$_{max}$
SUV$_{peak}$
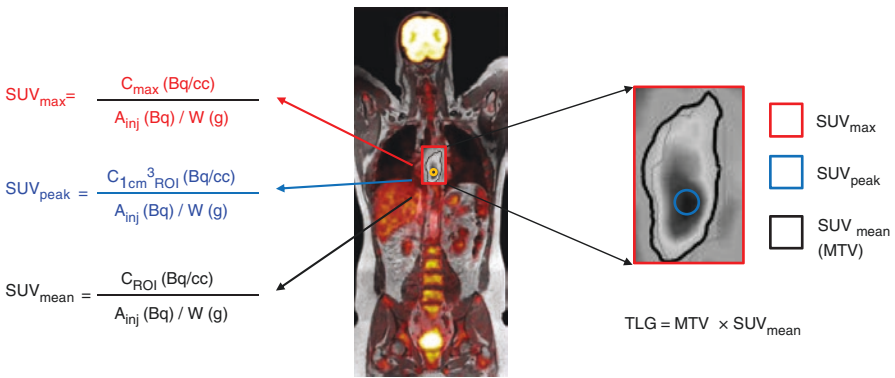SUV$_{mean}$ (MTV)

$$TLG = MTV \times SUV_{mean}$$

Fig. 6.1 Illustration of the basic foundations of PET quantification and the factors involved in the calculation of first- and second-order image-derived PET metrics used in clinical oncology

spherical VOI (1.2 cm diameter or 1 mL volume) placed over the most active part of a malignant lesion, was advocated as a more robust semiquantitative metric less vulnerable to artifacts [7]. Depending on the defined VOI, a variety of definitions of SUV_{peak} can be envisaged, obviously significantly affecting the resulting values [8].

6.2   Limitations of the SUV Metric

Despite its popularity and wide adoption in clinical and research settings, the SUV metric intrinsically bears a number of shortcomings which has limited its adoption in large clinical multicenter trials. The SUV also depends on the time course of the activity concentration in the blood plasma and the time point of acquisition and therefore imposes strict standardization of the uptake time, usually to 60 min with an acceptable range of 55–75 min according to the EANM guidelines 2015 [2]. Also the dependency of SUV on acquisition frame times, reconstruction parameters, physical and physiological factors, and scanner calibrations limits its potential in providing an objective assessment of whole-body PET images across baseline and follow-up studies for robust disease monitoring. Therefore, large multicenter clinical trials require standardization of data acquisition and processing protocols on different scanners for harmonization of PET quantification to enable pooling of data collected at different centers [9, 10].

To overcome the limitations of the SUV metric, alternative measures have been proposed including an uptake time-corrected version of the SUV including an uptake time quotient to normalize to 75 min [11] or simplified population-based blood pool activity-corrected estimations of FDG uptake, both trying to overcome the strong variability of SUV from uptake time and blood pool activity as approximations for more robust PET quantification [12]. The underlying principle for calculation of the glucose influx into the cell (MRGlu) was suggested about 25 years ago [13], but the fact that dynamic acquisition is needed did not render it feasible for whole-body imaging [14] until the advent of whole-body parametric imaging [15], which is now receiving considerable attention by the molecular imaging community. It can be anticipated that the additional information provided by parametric imaging through exploitation of the 4D spatiotemporal nature of the complete list-mode PET data, beyond the currently established semiquantitative SUV metric, might be valuable in whole-body PET imaging for multiparametric assessment of metastatic tumors across multiple beds and for improved reproducibility and evaluation of response to treatment over long periods [15].

Furthermore, volume-based PET metrics such as the total lesion glycolysis (TLG), calculated by multiplying SUV_{mean} by the metabolic tumor volume (MTV) [16], radiomic and texture analysis [17, 18], and parametric imaging have been suggested [14, 15]. The TLG, used to assess global metabolic response of the whole lesion thus providing complementary information to SUV and it variants, was shown to be highly correlated with other PET response parameters and is reproducible [19]. Recent advances in PET image segmentation and delineation of lesion contours [20] combined with progress in partial volume correction techniques have enabled to automate the calculation procedure. More recently, radiomics and texture

analysis emerged as new promising approaches enabling to circumvent the limitations of the above described oversimplified approaches by providing additional features including intratumoral heterogeneity through advanced image processing techniques and knowledge in systems biology [17, 18]. An increasing number of pioneering studies support the underlying assumptions of these hypotheses; however, further research and development efforts using large clinical databases are still required before these approaches can translate to valuable and reliable tools that can be adopted in the clinic.

6.3   Repeatability of SUV Measurements

A number of studies investigated the reproducibility of multiple PET metrics including SUV_{max}, SUV_{mean}, TLG, and MTV. All publications conclude that PET metrics are reproducible [21], with an almost perfect interobserver agreement for SUV_{max} [22, 23]. Furthermore, numerous studies showed that SUV_{max} has a prognostic value and correlates with progression-free and overall survival [24, 25]. This led to the widespread use of SUV_{max} as predictive and prognostic value for oncology PET assessments supported by the recommendations of the European Association of Nuclear Medicine guidelines 1.0 for PET/CT [26]. Six years later, the updated version 2.0 still recommends reporting SUV_{max} with the addition of SUV_{peak} to quantify tumor activity. SUV_{peak} is using a 3D 1.2 cm diameter (and 1.0 mL volume) spherical VOI positioned such that the average value across all positions within the lesion is maximized [7]. This alternative measure of the highest activity within a tumor was introduced due to the major limitation of SUV_{max}, that is, the high variability introduced by the statistical noise associated with a single voxel analysis. As has been shown in phantom and dynamic patient studies, this statistical noise substantially impairs the repeatability of SUV_{max} [27–29]. Averaging the values of a number of voxels within a given VOI, as proposed by SUV_{peak} [30, 31], can reduce this noise and therefore increases the repeatability without significant reduction of reproducibility. Using SUV_{peak} rather than an averaged number of the hottest voxels in a VOI has the advantage of a standardized volume irrespective of reconstruction methods and voxel sizes. However, the absolute activity drops compared to an averaged number of the hottest voxels in a VOI since not all voxels within SUV_{peak} have a high activity, which might impair the discrimination between high-activity lesions [32].

6.4   Clinical Relevance of the SUV

The use of FDG PET for therapy response assessment and evaluation of tumor aggressiveness is increasing. Most publications using PERCIST 1.0 as the base for PET-based therapy response assessment for solid and nonsolid tumors are based on SUV_{max} or SUV_{peak} [7, 33, 34]. PERCIST 1.0 suggested a cutoff at 30% increase for progressive disease and 30% decrease for partial remission, which is a slight increase in difference compared to the 25% according to the 1999 EORTC recommendation. A study comparing both evaluation systems for response assessment in

metastatic colorectal cancer came to the conclusion that they were equivalent [35]; however, several studies comparing CT-based RECIST with FDG quantification found that PET was superior in predicting histopathological therapy response [36, 37], time to progression [38], or overall survival [39].

Besides the increasing use of FDG PET for therapy response assessment, baseline quantitative PET metrics are also increasingly used to predict outcome. Initially these were predominantly based on SUV_{max} [24, 25, 40]. However, more and more publications come to the conclusion that volume-based PET metrics, such as MTV or TLG, are superior prognostic markers on baseline PET scans compared to SUV_{max} [41–43].

For cardiac FDG-PET evaluation, the absolute SUV values are less important than the relative difference within the cardiac wall using polar maps normalized to the peak activity. Here a direct comparison of the relative activity in the 20 cardiac segments between PET/CT and PET/MR showed an excellent correlation between both modalities that was even slightly improved for PET/MR with time-of-flight (TOF) capability (mean -1.3%) compared to non-TOF PET/MR (mean -2.1%) [44].

Analog to cardiac PET, also quantification of neuro-PET is rather performed based on tumor-to-background (TBR) ratios than absolute SUV values. The first study comparing PET quantification between PET/CT and PET/MR was performed for ^{11}C-methionine PET for gliomas and ^{68}Ga-DOTATOC in meningiomas. The authors concluded that the computed TBR exhibited an excellent accordance between PET/MR and PET/CT systems, with a correlation coefficient of 0.98 and a mean relative error of 7.9% [45].

6.5   Clinical Studies Comparing SUV Measurements Between PET/CT and PET/MRI in Oncology

Since the introduction of fully integrated PET/MR systems, multiple studies have been published comparing quantitative and qualitative results between PET/CT and PET/MR. In most of these studies, a same-day protocol with a single injection was performed. The majority had a significant difference in uptake time between PET/CT (commonly injected 60 min after injection) and the secondary PET/MR scan (with uptake times from 135 min [46] up to 180 min [47]). Table 6.1 summarizes results of studies comparing SUVs estimated on PET/CT and PET/MR images. Despite the sometimes large differences between uptake times, most studies came to the conclusion that there was a high positive correlation for all SUV quantification metrics between both exams and that most of the differences were due to the variance in uptake time between both scans [44–48, 50, 51, 53, 54, 57, 59–61, 64]. In only two studies, some scans were performed on the PET/MR scanner first [52, 58], and in two studies, all PET/MR scans were performed before PET/CT [49, 56]. All other studies had a longer uptake time of 51–120 min (mean 81 min) for the PET/MR scans and showed a slight increase in SUV between both exams. Sher et al. performed 40 scans, 31 on the PET/MR system and 9 on the PET/CT first. They showed that SUV values were always higher on the second scan for malignant lesion further supporting that the observed difference in the other studies is rather due to the increasing uptake over time than different technology.

Table 6.1 Summary of results presented in the literature comparing SUVs estimated on PET/CT images to those measurements on PET/MR images

Authors (reference)	Year	Journal	Tracers	Patient number	PET/CT uptake	PET/MRI uptake	Indication	Scanner	Main conclusions
Boss et al. [45]	2010	JNM	^{11}C-methionine, ^{68}Ga-DOTATOC	10	60 min	90–120 min	Brain tumors	Biograph mMR	Tumor-to-reference tissue ratios with excellent correlation (0.98), with a mean relative error of 7.9%
Drzezga et al. [48]	2012	JNM	^{18}F-FDG	32	86 min	140 min	Cancer general	Biograph mMR	High correlation between mean SUVs on PET/MRI and PET/CT in lesions ($r = 0.93$) and background tissue ($r = 0.92$)
Varoquaux et al. [49]	2014	EJNMMI	^{18}F-FDG	32	146 min	85 min	Head and neck	Ingenuity TF PET/MR	Excellent correlation between SUVs on both modalities, with an underestimation on PET/MRI as compared to PET/CT
Kershah et al. [50]	2013	MIB	^{18}F-FDG	40	66 min	117 min	Cancer general	Ingenuity TF PET/MR	High correlation for SUV values obtained from PET/MRI compared to those from PET/CT, as the reference standard

Wiesmüller et al. [51]	2013	EJNMMI	18F-FDG, 18F-FEC, 68Ga-D-TATE	43	60 min	140 min	Cancer general	Biograph mMR	Differences demonstrated in quantification of tracer uptake between PET/CT and PET/MRI were minor but statistically significant
Schäfer et al. [52]	2014	Radiology	18F-FDG	20	60 min/118 min[a]	128 min/63 min[a]	Pediatrics	Biograph mMR	13.1% deviation of SUVs for bone marrow and 5% deviation for other tissues
Afshar-Oromich et al. [53]	2014	EJNMMI	68Ga-PSMA	20	60 min	180 min	Prostate cancer	Biograph mMR	Scatter correction on PET/MRI challenging and direct comparison of SUVs from PET/CT and PET/MRI needs to be conducted carefully
Al-Nabhani et al. [46]	2014	JNM	18F-FDG, 68Ga-D-TATE, 18F-FECH	50	56 min	135 min	Cancer general	Biograph mMR	PET data on both modalities were similar with significant correlation between mean SUVs

(continued)

Table 6.1 (continued)

Authors (reference)	Year	Journal	Tracers	Patient number	PET/CT uptake	PET/MRI uptake	Indication	Scanner	Main conclusions
Sachpekidis et al. [54]	2015	AJNMMI	^{18}F-FDG	30	60 min	120 min	Multiple myeloma	Biograph mMR	Significant correlation between the two techniques was demonstrated, despite the statistically significant differences in lesional SUVs between PET/CT and PET/MRI
Queiroz et al. [55]	2015	PLoS One	^{18}F-FDG	75	na	na	Cancer general	SIGNA PET/MR	TOF-PET/MRI device requires significantly less activity to generate PET images with good-to-excellent image quality
Lyons et al. [56]	2015	AJR	^{18}F-FDG	35	108 min	61 min	Pediatrics	Ingenuity TF PET/MR	Good correlation for SUV on both modalities, PET/MRI underestimated SUV compared with PET/CT

Vontobel et al. [44]	2015	EJNMMI	^{18}F-FDG	23	60 min	106 min	Cardiac	SIGNA PET/MR	PET/MRI with and without TOF showed minimal underestimation of tracer uptake (−2.08 and −1.29%, respectively), compared to PET/CT
Iagaru et al. [57]	2015	Clin Nucl Med	^{18}F-FDG	36	74 min	161 min	Cancer general	SIGNA PET/MR	The mean SUV$_{max}$ values were higher in PET/MRI than PET/CT for all lesions
Sher et al. [58]	2016	AJR	^{18}F-FDG	40	90 min/132 min[b]	71 min/124 min	Pediatric lymphoma	Ingenuity TF PET/MR	PET/MRI quantification strongly correlated with PET/CT, but the SUVs were not interchangeable
Freitag et al. [47]	2016	EJNMMI	^{68}Ga-PSMA	26	60 min	180 min	Prostate cancer	Biograph mMR	The correlation between PET/MRI and PET/CT SUVs was linear in lymph nodes and bone metastases

(continued)

Table 6.1 (continued)

Authors (reference)	Year	Journal	Tracers	Patient number	PET/CT uptake	PET/MRI uptake	Indication	Scanner	Main conclusions
Sawicki et al. [59]	2016	JNM	^{18}F-FDG	121	61 min	113 min	Pulmonary nodules	Biograph mMR	Lesion size, SUV, and characterization correlate strongly between the two modalities
Atkinson et al. [60]	2016	Abdom Radiol	^{18}F-FDG	18	60 min	na	Lymphoma	Biograph mMR	SUV values were comparable with high positive correlation. Similar lesion detection rate
Xin et al. [61]	2016	Eur J Radiol	^{18}F-FDG	45	64 min	170 min	Abdominal/pelvic	Ingenuity TF PET/MR	High correlation between the two modalities in terms of SUV_{max} and SUV_{mean} in focal lesions
Karlberg et al. [62]	2016	EJNMMI Phys	^{18}F-FDG	Phantom	na	na	na	Biograph mMR	NECRs and sensitivity are higher for PET/MRI. Differences in image quality are most evident for challenging settings. PET/CT performance better owing to TOF capability

Seith et al. [63]	2016	Invest Radiol	^{18}F-FDG, ^{68}Ga-DOTATATE, ^{11}C-choline	66	na	na	Cancer general	Biograph mMR	MRI-based AC is accurate in most tissues (SUV deviations generally <10%). Underestimations in the bone and overestimation close to the lung can be pronounced
Afaq et al. [64]	2017	Clin Nucl Med	^{18}F-FDG	68	64 min	136 min	Lymphoma	Biograph mMR	SUV_{max} correlated significantly with a correlation coefficient of 0.84
Law et al. [65]	2017	Clin Nucl Med	^{18}F-FDG	100	63 min	116 min	Cancer general	Biograph mMR	Excellent correlation between SUVs in lesions on PET/MRI and PET/CT, across all body regions and in all tumor types studied

[a]In four patients PET/MRI scans were performed before PET/CT
[b]For nine scans PET/CT before PET/MRI

To investigate the influence of MR-based attenuation correction (AC) on absolute SUV, Seith et al. used the same PET dataset from an integrated PET/MR scanner and reconstructed it either with the tissue segmentation-based MRAC μ-map or the CTAC μ-map using a nonrigid registration of the CT to the MR-based μ-map. They showed that MR-based AC is very accurate in most tissues with SUV deviations of generally <10%. A systematic underestimation of SUV was only present in the bones, while some lesions close to the lung were overestimated [63]. These results are in line with earlier published simulation data showing a significant decrease of up to 30% in sclerotic lesion, after subtraction of all voxels with bone density from the CTAC μ-map (Fig. 6.3) [38].

A quantitative phantom study comparing image quality between TOF PET/CT (Siemens Biograph mCT) and non-TOF PET/MR (Siemens Biograph mMR) showed that the spatial resolution was similar for the two systems. Average sensitivity was higher for the mMR (13.3 kcps/MBq) compared to the mCT system (10.0 kcps/MBq), and peak noise equivalent count rate (NECR) was slightly higher for the mMR (196 kcps @ 24.4 kBq/mL) compared to the mCT (186 kcps @ 30.1 kBq/mL). Highest hot contrast for the smallest sphere (10 mm) was achieved with the combination of TOF and PSF on the mCT compared to the mMR. Overall the differences between both systems were mainly due to the TOF possibility on the mCT, which resulted in an overall better image quality, especially for the more challenging settings with higher background activity and small uptake volumes [62]. For the fully integrated PET/MR scanner with TOF, only a few studies were published comparing PET quantification on PET/CT and PET/MR until today [44, 55, 57]. A prospective trial comparing TOF PET/CT (Discovery D 690 PET/CT, GE Healthcare) and TOF PET/MR (SIGNA PET/MR) in 75 patients based on phantom NECR curves investigated the potential dose reduction for PET/MR with equivalent image quality. They concluded that a reduction of FDG activity of slightly more the 50% can be achieved thanks to improvements in detector geometry and technologies [55].

6.6   Reliability of SUV Measurements in PET/MRI

The challenges faced by quantitative PET/CT imaging have been investigated since the commercial availability of this technology more than 15 years ago, and several professional societies established committees and task groups (e.g., QIBA/RSNA, CQIE/ACRIN, QIN/AAPM, etc.) to support and promote the use of quantitative imaging biomarkers in the context of cancer staging and therapy response assessment. The deployment of hybrid PET/MRI in the clinic poses new challenges and additional difficulties to enable reliable, quantitative imaging biomarkers. The primary challenge is the lack of a robust MRI-guided attenuation correction particularly in whole-body imaging. Furthermore, partial volume and motion correction need to be considered to produce artifact-free and quantitative PET images, with robust and reliable quantitative indices for routine application and advanced tools for clinical and research applications. The bulk of quantitative PET/MRI research to date focused on addressing the challenges of MRI-guided PET attenuation correction. Three categories of MRI-guided attenuation correction techniques have emerged [66]. This

includes (1) segmentation-based approaches, which segment MR images into different tissue classes and assign predefined attenuation coefficients to each class, (2) atlas-based and machine learning techniques in which co-registered MR-CT Atlas pairs are used to derive a pseudo-CT image or to learn a mapping function that predicts the pseudo-CT from actual patient's MRI, and (3) the recently revisited joint emission and attenuation reconstruction algorithms or maximum likelihood reconstruction of attenuation and activity (MLAA), in which the attenuation map is estimated from emission or transmission data. Figure 6.2 shows a representative clinical FDG brain PET study comparing various attenuation correction strategies.

Segmented MRI-guided attenuation correction widely used on commercial PET/MRI systems suffers the lack of bones in the derived attenuation map, which induces underestimation of the SUV in the corresponding regions within or close
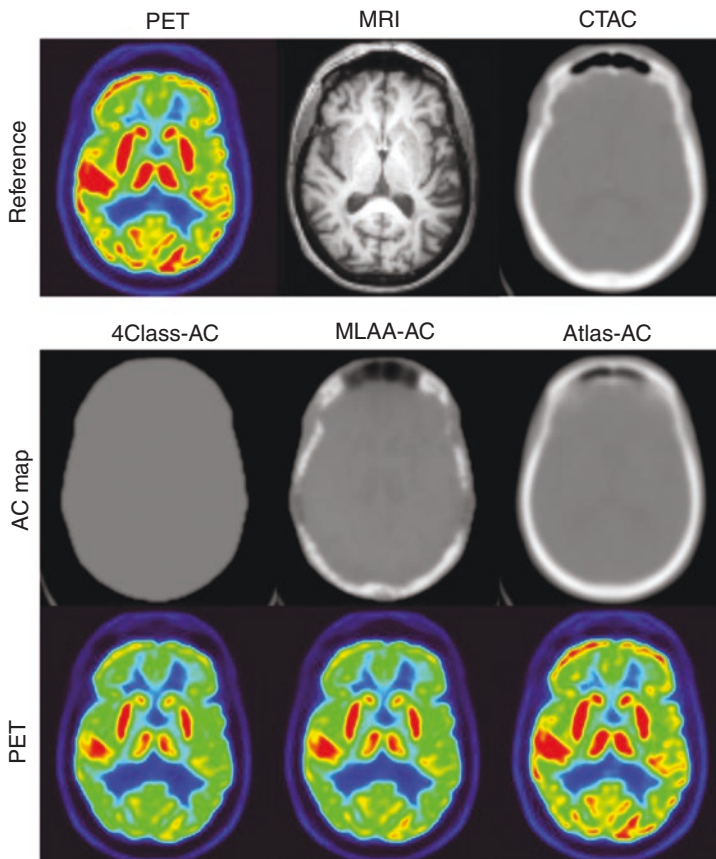
Fig. 6.2 Representative clinical FDG brain PET study showing from left to right: (top row) PET, MR, and CT images used as reference for evaluation, (middle row) attenuation maps derived using different attenuation correction approaches including segmented MRI, Atlas-guided, and maximum likelihood reconstruction of attenuation and activity (MLAA) technique, (bottom row) corresponding reconstructed PET images. Note the limitations of segmented MRI-based approach which ignores the skull and air cavities. The Atlas-based approach better matches the patient's CT image, clearly outperforming the MLAA algorithm

to the bones on PET images (Fig. 6.3) [67, 68]. Likewise, metal artifacts can lead to substantial signal voids and underestimation of SUV. This can be compensated by exploiting TOF reconstruction [69, 70], which was shown to reduce the SUV bias compared to non-TOF-PET emission data [71, 72]. Further improvement is possible with the joint emission-transmission reconstruction algorithm which showed promise in the correction of metal susceptibility artifacts by estimating the high attenuation coefficients of metallic implants [73]. Furthermore, the development of appropriate MR sequences, such as multi-acquisition variable-resonance image combination (MAVRIC) [74], can reduce metal artifacts. An additional complexity arises from the attenuation and scattering of annihilation photons by objects present in the field of view, which may also induce SUV underestimation if not accounted for. This includes patient's bed, MRI radiofrequency body or surface coils, and patient positioning aids [66]. Transmission or CT scanning-based predetermination of attenuation maps for rigid objects (bed, body coils, etc.) and nonrigid registration of templates of flexible objects (surface coils) [75] is currently used to account for the additional attenuation from these items. Joint reconstruction of emission and transmission images was purportedly promoted as potential approach enabling to estimate the attenuation maps of these objects. However, the performance of this approach for recovering objects lacking support from emission data remains to be demonstrated in clinical setting.

6.7   Summary

Objective quantification of PET tracer uptake is gaining significance with the increasing use of PET as a prognostic biomarker for therapy response assessment. Ease of use, availability, as well as excellent reproducibility and correlation with
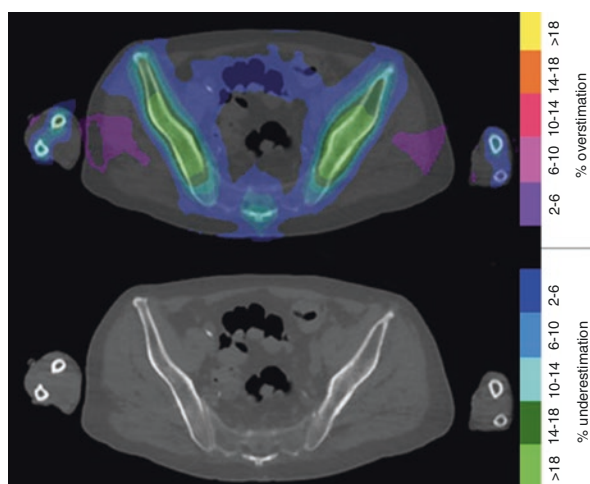

Fig. 6.3 Relative difference between PET images reconstructed with and without considering bony structures on CTAC attenuation map with the corresponding axial CT image

tumor aggressiveness lead to widespread use of SUV_{max} for tumor assessment, despite its well-known limitations, such as high variability with uptake time, blood pool activity, and limited repeatability.

With PET/MRI as a new hybrid modality being now commercially available, additional challenges are faced for reliable PET quantification. Although numerous studies showed an overall high correlation among SUV measurements between PET/CT and PET/MR, impaired attenuation correction due to the missing density of bone and metal implants can substantially affect SUV values within the bones and adjacent structures. More research and development efforts are required to improve MRI-based attenuation correction using machine learning algorithms to create a pseudo-CT or through advanced priors for joint estimation of emission, and attenuation using TOF-PET data to correct the attenuation map is currently ongoing and will further improve reliable PET quantification for PET/MRI.

References

1. Basu S, Zaidi H, Houseni M, et al. Novel quantitative techniques for assessing regional and global function and structure based on modern imaging modalities: implications for normal variation, aging and diseased states. Semin Nucl Med. 2007;37:223–39.
2. Boellaard R, Delgado-Bolton R, Oyen WJ, et al. FDG PET/CT: EANM procedure guidelines for tumour imaging: version 2.0. Eur J Nucl Med Mol Imaging. 2015;42:328–54.
3. Huang SC. Anatomy of SUV. Standardized uptake value. Nucl Med Biol. 2000;27:643–6.
4. Pierce LA II, Elston BF, Clunie DA, Nelson D, Kinahan PE. A digital reference object to analyze calculation accuracy of PET standardized uptake value. Radiology. 2015;277:538–45.
5. Zasadny KR, Wahl RL. Standardized uptake values of normal tissues at PET with 2-[fluorine-18]-fluoro-2-deoxy-D-glucose: variations with body weight and a method for correction. Radiology. 1993;189:847–50.
6. Kim CK, Gupta NC, Chandramouli B, Alavi A. Standardized uptake values of FDG: body surface area correction is preferable to body weight correction. J Nucl Med. 1994;35:164–7.
7. Wahl RL, Jacene H, Kasamon Y, Lodge MA. From RECIST to PERCIST: evolving considerations for PET response criteria in solid tumors. J Nucl Med. 2009;50:122S–150.
8. Vanderhoek M, Perlman SB, Jeraj R. Impact of the definition of peak standardized uptake value on quantification of treatment response. J Nucl Med. 2012;53:4–11.
9. Boellaard R. Optimisation and harmonisation: two sides of the same coin? Eur J Nucl Med Mol Imaging. 2013;40:982–4.
10. Sunderland JJ, Christian PE. Quantitative PET/CT scanner performance characterization based upon the society of nuclear medicine and molecular imaging clinical trials network oncology clinical simulator phantom. J Nucl Med. 2015;56:145–52.
11. Hofheinz F, Apostolova I, Oehme L, Kotzerke J, van den Hoff J. Test-retest variability of lesion SUV and lesion SUR in 18F-FDG PET: an analysis of data from two prospective multicenter trials. J Nucl Med. 2017. https://doi.org/10.2967/jnumed.117.190736.
12. Burger IA, Burger C, Berthold T, Buck A. Simplified quantification of FDG metabolism in tumors using the autoradiographic method is less dependent on the acquisition time than SUV. Nucl Med Biol. 2011;38:835–41.

13. Patlak CS, Blasberg RG, Fenstermacher JD. Graphical evaluation of blood-to-brain transfer constants from multiple-time uptake data. J Cereb Blood Flow Metab. 1983;3:1–7.

14. Dimitrakopoulou-Strauss A, Pan L, Strauss LG. Parametric imaging: a promising approach for the evaluation of dynamic PET-18F-FDG studies – the DKFZ experience. Hell J Nucl Med. 2010;13:18–22.

15. Karakatsanis NA, Casey ME, Lodge MA, Rahmim A, Zaidi H. Whole-body direct 4D parametric PET imaging employing nested generalized Patlak expectation-maximization reconstruction. Phys Med Biol. 2016;61:5456–85.

16. Larson SM, Erdi Y, Akhurst T, et al. Tumor treatment response based on visual and quantitative changes in global tumor glycolysis using PET-FDG imaging. The visual response score and the change in total lesion glycolysis. Clin Positron Imaging. 1999;2:159–71.

17. Yip SS, Aerts HJ. Applications and limitations of radiomics. Phys Med Biol. 2016;61:R150–66.

18. Hatt M, Tixier F, Pierce L, et al. Characterization of PET/CT images using texture analysis: the past, the present… any future? Eur J Nucl Med Mol Imaging. 2017;44:151–65.

19. Houshmand S, Salavati A, Hess S, et al. An update on novel quantitative techniques in the context of evolving whole-body PET imaging. PET Clin. 2015;10:45–58.

20. Hatt M, Lee J, Schmidtlein CR, et al. Classification and evaluation strategies of auto-segmentation approaches for PET: report of AAPM task group no. 211. Med Phys. 2017;44(6):e1–e42.

21. Weber WA, Ziegler SI, Thodtmann R, Hanauske AR, Schwaiger M. Reproducibility of metabolic measurements in malignant tumors using FDG PET. J Nucl Med. 1999;40:1771–7.

22. Benz MR, Evilevitch V, Allen-Auerbach MS, et al. Treatment monitoring by 18F-FDG PET/CT in patients with sarcomas: interobserver variability of quantitative parameters in treatment-induced changes in histopathologically responding and nonresponding tumors. J Nucl Med. 2008;49:1038–46.

23. Jacene HA, Leboulleux S, Baba S, et al. Assessment of interobserver reproducibility in quantitative 18F-FDG PET and CT measurements of tumor response to therapy. J Nucl Med. 2009;50:1760–9.

24. Kidd EA, Siegel BA, Dehdashti F, Grigsby PW. The standardized uptake value for F-18 fluorodeoxyglucose is a sensitive predictive biomarker for cervical cancer treatment response and survival. Cancer. 2007;110:1738–44.

25. Pandit N, Gonen M, Krug L, Larson SM. Prognostic value of [18F]FDG-PET imaging in small cell lung cancer. Eur J Nucl Med Mol Imaging. 2003;30:78–84.

26. Boellaard R, O'Doherty MJ, Weber WA, et al. FDG PET and PET/CT: EANM procedure guidelines for tumour PET imaging: version 1.0. Eur J Nucl Med Mol Imaging. 2010;37:181–200.

27. Burger IA, Huser DM, Burger C, von Schulthess GK, Buck A. Repeatability of FDG quantification in tumor imaging: averaged SUVs are superior to SUVmax. Nucl Med Biol. 2012;39:666–70.

28. de Langen AJ, Vincent A, Velasquez LM, et al. Repeatability of 18F-FDG uptake measurements in tumors: a metaanalysis. J Nucl Med. 2012;53:701–8.

29. Schwartz J, Humm JL, Gonen M, et al. Repeatability of SUV measurements in serial PET. Med Phys. 2011;38:2629–38.

30. Akamatsu G, Ikari Y, Nishida H, et al. Influence of statistical fluctuation on reproducibility and accuracy of SUVmax and SUVpeak: a phantom study. J Nucl Med Technol. 2015;43:222–6.

31. Lodge MA, Chaudhry MA, Wahl RL. Noise considerations for PET quantification using maximum and peak standardized uptake value. J Nucl Med. 2012;53:1041–7.

32. Laffon E, Lamare F, de Clermont H, Burger IA, Marthan R. Variability of average SUV from several hottest voxels is lower than that of SUVmax and SUVpeak. Eur Radiol. 2014;24:1964–70.

33. Hyun OJ, Luber BS, Leal JP, et al. Response to early treatment evaluated with F-18-FDG PET and PERCIST 1.0 predicts survival in patients with ewing sarcoma family of tumors treated with a monoclonal antibody to the insulinlike growth factor 1 receptor. J Nucl Med. 2016;57:735–40.

34. Pinker K, Riedl CC, Ong L, et al. The impact that number of analyzed metastatic breast cancer lesions has on response assessment by F-18-FDG PET/CT using PERCIST. J Nucl Med. 2016;57:1102–4.

35. Skougaard K, Nielsen D, Jensen BV, Hendel HW. Comparison of EORTC criteria and PERCIST for PET/CT response evaluation of patients with metastatic colorectal cancer treated with irinotecan and cetuximab. J Nucl Med. 2013;54:1026–31.
36. Burger IA, Casanova R, Steiger S, et al. 18F-FDG PET/CT of non-small cell lung carcinoma under neoadjuvant chemotherapy: background-based adaptive-volume metrics outperform TLG and MTV in predicting histopathologic response. J Nucl Med. 2016;57:849–54.
37. Denecke T, Rau B, Hoffmann KT, et al. Comparison of CT, MRI and FDG-PET in response prediction of patients with locally advanced rectal cancer after multimodal preoperative therapy: is there a benefit in using functional imaging? Eur Radiol. 2005;15:1658–66.
38. Kanemura S, Kuribayashi K, Funaguchi N, et al. Metabolic response assessment with 18F-FDG-PET/CT is superior to modified RECIST for the evaluation of response to platinum-based doublet chemotherapy in malignant pleural mesothelioma. Eur J Radiol. 2017;86:92–8.
39. Yoon JW, Kim S, Kim SW, et al. PET/CT response criteria (European Organization for Research and Treatment of cancer) predict survival better than response evaluation criteria in solid tumors in locally advanced cervical cancer treated with chemoradiation. Clin Nucl Med. 2016;41:677–82.
40. Borst GR, Belderbos JS, Boellaard R, et al. Standardised FDG uptake: a prognostic factor for inoperable non-small cell lung cancer. Eur J Cancer. 2005;41:1533–41.
41. Chung HW, Lee KY, Kim HJ, Kim WS, So Y. FDG PET/CT metabolic tumor volume and total lesion glycolysis predict prognosis in patients with advanced lung adenocarcinoma. J Cancer Res Clin Oncol. 2014;140:89–98.
42. Hyun SH, Ahn HK, Kim H, et al. Volume-based assessment by (18)F-FDG PET/CT predicts survival in patients with stage III non-small-cell lung cancer. Eur J Nucl Med Mol Imaging. 2014;41:50–8.
43. Lee JW, Kang CM, Choi HJ, et al. Prognostic value of metabolic tumor volume and total lesion glycolysis on preoperative (1)(8)F-FDG PET/CT in patients with pancreatic cancer. J Nucl Med. 2014;55:898–904.
44. Vontobel J, Liga R, Possner M, et al. MR-based attenuation correction for cardiac FDG PET on a hybrid PET/MRI scanner: comparison with standard CT attenuation correction. Eur J Nucl Med Mol Imaging. 2015;42:1574–80.
45. Boss A, Bisdas S, Kolb A, et al. Hybrid PET/MRI of intracranial masses: initial experiences and comparison to PET/CT. J Nucl Med. 2010;51:1198–205.
46. Al-Nabhani KZ, Syed R, Michopoulou S, et al. Qualitative and quantitative comparison of PET/CT and PET/MR imaging in clinical practice. J Nucl Med. 2014;55:88–94.
47. Freitag MT, Radtke JP, Hadaschik BA, et al. Comparison of hybrid (68)Ga-PSMA PET/MRI and (68)Ga-PSMA PET/CT in the evaluation of lymph node and bone metastases of prostate cancer. Eur J Nucl Med Mol Imaging. 2016;43:70–83.
48. Drzezga A, Souvatzoglou M, Eiber M, et al. First clinical experience with integrated whole-body PET/MR: comparison to PET/CT in patients with oncologic diagnoses. J Nucl Med. 2012;53:845–55.
49. Varoquaux A, Rager O, Poncet A, et al. Detection and quantification of focal uptake in head and neck tumours: (18)F-FDG PET/MR versus PET/CT. Eur J Nucl Med Mol Imaging. 2014;41:462–75.
50. Kershah S, Partovi S, Traughber BJ, et al. Comparison of standardized uptake values in normal structures between PET/CT and PET/MRI in an oncology patient population. Mol Imaging Biol. 2013;15:776–85.
51. Wiesmuller M, Quick HH, Navalpakkam B, et al. Comparison of lesion detection and quantitation of tracer uptake between PET from a simultaneously acquiring whole-body PET/MR hybrid scanner and PET from PET/CT. Eur J Nucl Med Mol Imaging. 2013;40:12–21.
52. Schafer JF, Gatidis S, Schmidt H, et al. Simultaneous whole-body PET/MR imaging in comparison to PET/CT in pediatric oncology: initial results. Radiology. 2014;273:220–31.
53. Afshar-Oromieh A, Haberkorn U, Schlemmer HP, et al. Comparison of PET/CT and PET/MRI hybrid systems using a 68Ga-labelled PSMA ligand for the diagnosis of recurrent prostate cancer: initial experience. Eur J Nucl Med Mol Imaging. 2014;41:887–97.
54. Sachpekidis C, Hillengass J, Goldschmidt H, et al. Comparison of (18)F-FDG PET/CT and PET/MRI in patients with multiple myeloma. Am J Nucl Med Mol Imaging. 2015;5:469–78.

55. Queiroz MA, Delso G, Wollenweber S, et al. Dose optimization in TOF-PET/MR compared to TOF-PET/CT. PLoS One. 2015;10:e0128842.
56. Lyons K, Seghers V, Sorensen JI, et al. Comparison of standardized uptake values in normal structures between PET/CT and PET/MRI in a tertiary pediatric hospital: a prospective study. AJR Am J Roentgenol. 2015;205:1094–101.
57. Iagaru A, Mittra E, Minamimoto R, et al. Simultaneous whole-body time-of-flight 18F-FDG PET/MRI: a pilot study comparing SUVmax with PET/CT and assessment of MR image quality. Clin Nucl Med. 2015;40:1–8.
58. Sher AC, Seghers V, Paldino MJ, et al. Assessment of sequential PET/MRI in comparison with PET/CT of pediatric lymphoma: a prospective study. AJR Am J Roentgenol. 2016;206:623–31.
59. Sawicki LM, Grueneisen J, Buchbender C, et al. Comparative performance of (1)(8)F-FDG PET/MRI and (1)(8)F-FDG PET/CT in detection and characterization of pulmonary lesions in 121 oncologic patients. J Nucl Med. 2016;57:582–6.
60. Atkinson W, Catana C, Abramson JS, et al. Hybrid FDG-PET/MR compared to FDG-PET/CT in adult lymphoma patients. Abdom Radiol (NY). 2016;41:1338–48.
61. Xin J, Ma Q, Guo Q, et al. PET/MRI with diagnostic MR sequences vs PET/CT in the detection of abdominal and pelvic cancer. Eur J Radiol. 2016;85:751–9.
62. Karlberg AM, Saether O, Eikenes L, Goa PE. Quantitative comparison of PET performance-siemens biograph mCT and mMR. EJNMMI Phys. 2016;3:5.
63. Seith F, Gatidis S, Schmidt H, et al. Comparison of positron emission tomography quantification using magnetic resonance- and computed tomography-based attenuation correction in physiological tissues and lesions: a whole-body positron emission tomography/magnetic resonance study in 66 patients. Investig Radiol. 2016;51:66–71.
64. Afaq A, Fraioli F, Sidhu H, et al. Comparison of PET/MRI with PET/CT in the evaluation of disease status in lymphoma. Clin Nucl Med. 2017;42:e1–7.
65. Law WP, Maggacis N, Jeavons SJ, Miles KA. Concordance of 18F-FDG PET uptake in tumor and normal tissues on PET/MRI and PET/CT. Clin Nucl Med. 2017;42:180–6.
66. Mehranian A, Arabi H, Zaidi H. Vision 20/20: magnetic resonance imaging-guided attenuation correction in PET/MRI: challenges, solutions, and opportunities. Med Phys. 2016;43:1130–55.
67. Samarin A, Burger C, Wollenweber SD, et al. PET/MR imaging of bone lesions--implications for PET quantification from imperfect attenuation correction. Eur J Nucl Med Mol Imaging. 2012;39:1154–60.
68. Arabi H, Rager O, Alem A, et al. Clinical assessment of MR-guided 3-class and 4-class attenuation correction in PET/MR. Mol Imaging Biol. 2015;17:264–76.
69. Davison H, Ter Voert EE, de Galiza Barbosa F, Veit-Haibach P, Delso G. Incorporation of time-of-flight information reduces metal artifacts in simultaneous positron emission tomography/magnetic resonance imaging: a simulation study. Investig Radiol. 2015;50:423–9.
70. Ter Voert EE, Veit-Haibach P, Ahn S, et al. Clinical evaluation of TOF versus non-TOF on PET artifacts in simultaneous PET/MR: a dual centre experience. Eur J Nucl Med Mol Imaging. 2017;44(7):1223–33.
71. Mehranian A, Zaidi H. Impact of time-of-flight PET on quantification errors in MRI-based attenuation correction. J Nucl Med. 2015;56:635–41.
72. Delso G, Khalighi M, Ter Voert E, et al. Effect of time-of-flight information on PET/MR reconstruction artifacts: comparison of free-breathing versus breath-hold MR-based attenuation correction. Radiology. 2017;282:229–35.
73. Fuin ND, Pedemonte SD, Catalano OA, et al. PET/MR imaging in the presence of metal implants: completion of the attenuation map from PET emission data. J Nucl Med. 2017;58:840–5.
74. Gunzinger J, Delso G, Boss A, et al. Metal artifact reduction in patients with dental implants using multispectral three-dimensional data acquisition for hybrid PET/MRI. EJNMMI Phys. 2014;1:102.
75. Kartmann R, Paulus DH, Braun H, et al. Integrated PET/MR imaging: automatic attenuation correction of flexible RF coils. Med Phys. 2013;40:082301–14.

PET/MRI: Safety Considerations

7

Richard K.G. Do and David W. Dick

Contents

Safety is an important consideration in PET/MRI and is complicated by the coexistence of the safety concerns of MRI and PET. These issues have significant impact on both patient workflow and the design of the PET/MRI facility. When considering patient workflow, one must consider where patients will be injected with the

R.K.G. Do (✉)
Department of Radiology, Memorial Sloan Kettering Cancer Center, New York, NY, USA
e-mail: dok@mskcc.org

D.W. Dick (✉)
Department of Radiology, University of Iowa, Iowa City, IA, USA
e-mail: david-dick@uiowa.edu

radiotracer and when screening for MRI safety occurs. Additionally, PET/MRI facilities should be designed with both MRI and radiation safeties in mind. Below we discuss the specific safety concerns associated with PET and MRI separately.

7.1 PET Safety

7.1.1 Workflow for Radioactivity

When considering safety with regard to PET imaging, the chief concern is radiation exposure. Thus, it is important to recognize the workflow for radioactivity and acknowledge the potential for radiation exposure at each step.

Typically, the first step is the preparation of the radiopharmaceutical dose. Often this is provided as a "unit dose," where the providing radiopharmacy has already dispensed the patient dose into a syringe. In this instance, the administering technologist will need only to verify the dosage in a well counter and possibly adjust the dose if there is an excess of radioactivity. There are also instances where the radiopharmaceutical is provided in a bulk vial, and it is the responsibility of the technologist or radiopharmacist to draw up the correct amount of radioactivity into a syringe and measure it in a well counter. Both procedures will expose the technologist's or radiopharmacist's hands to radiation in varying degrees, as well as whole-body radiation exposure.

The second step is to inject the patient with the radiopharmaceutical. While shielding is used during this procedure, there will be localized radiation exposure to the hands as well as some whole-body radiation exposure. Depending on the protocol, there may be an uptake period where the patient is resting in a room before the imaging study begins. It is important to note that during this time the entire patient is a diffuse source of radioactivity that will result in whole-body radiation exposure to the technologists and/or other staff that interact with the patient during this time.

The next step is the imaging study itself. As with the uptake period, the entire patient is a diffuse source of radioactivity that will result in whole-body radiation exposure to the technologists and/or other staff that interact with the patient during this time.

The final step is the discharge of the patient. Again, the patient is still a diffuse source of radioactivity. Time will have elapsed, so the patient will not be as radioactive as at the start of the scan. However, the degree to which they are still radioactive depends greatly on the radionuclide being used. A patient that was imaged using copper-64 (12.7 hour half-life) will not have much decay of the radiopharmaceutical from the beginning of the scan, whereas a patient that was imaged using oxygen-15 (122 second half-life) will only be radioactive for a few minutes following the conclusion of the PET scan.

7.1.2 Isotope Parameters

While all PET radioisotopes will ultimately produce two 511 keV gamma rays due to positron-electron annihilation, other properties of the radioisotopes will vary.

Table 7.1 Properties of common PET radionuclides

Isotope	Half-life [1]	Positron fraction [1]	Positron energy (MeV) [1]	Other gamma emissions [1]	Gamma-ray dose constant ((μSv/h)/ MBq) (((mrem/h)/ mCi)) at 1 m [2]
C-11	20.4 min	99+%	0.9608	None	0.1908 (0.7060)
N-13	9.96 min	100%	1.190	None	0.1909 (0.7063)
O-15	122.1 s	99+%	1.723	None	0.1911 (0.7071)
F-18	109.7 min	96.9%	0.635	None	0.1851 (0.6849)
Cu-64	12.7 h	17.86%	0.657	1.346 MeV	0.03514 (0.1300)
Ga-68	68.3 min	90%	1.899, 0.8	1.077 MeV	0.1763 (0.6523)
Rb-82	1.25 min	96%	3.35, 2.57	777 keV	0.2076 (0.7681)
I-124	4.15 days	25.0%	2.13, 1.53, 0.808	603, 723, 1509, 1691 keV	0.2033 (0.7522)

The pertinent properties of common PET radioisotopes are shown in Table 7.1. With regard to safety, the half-life, other gamma-ray emissions, and gamma-ray dose constant are the most important variables to consider. Longer half-lives will mean that the patient is an exposure risk for a longer time period. Gamma-ray emissions other than the 511 keV gammas from positron-electron annihilation need to be considered for potential exposure risk as well, which feeds into the gamma-ray dose constant. The higher the gamma-ray dose constant, the more exposure one will receive per unit of radioactivity (MBq/mCi).

7.1.3   Radiation Protection Goals

A large part of PET safety is ensuring that radiation protection goals are met. Thus it is important to recognize the limits set forth by the US Nuclear Regulatory Commission (NRC). The limits are divided into two categories: radiation workers and the general public.

Radiation workers have annual limits set by the NRC based on the radiation sensitivity of different parts of the body. Radiation workers are limited to receiving a 5000 mrem (50 mSv) total effective dose equivalent per year to the torso/vital organs [3]. Additionally, radiation workers are limited to 50,000 rem (500 mSv) extremity (hand) dose and 15,000 rem (150 mSv) lens of eye dose per year [3]. A female radiation worker that declares her pregnancy has a limit of 500 mrem (5 mSv) dose to the fetus [4].

The general public is allowed no more than 100 mrem/year (1 mSv/year), and the dose rate to members of the public may not exceed 2 mrem in any given hour (0.02 mSv/h) [5]. In order to meet these goals, it is important to design the facility and plan workflows with these limits in mind. Rooms that will contain radioactivity should not be adjacent to general public areas, if at all possible, in order to reduce the amount of shielding needed in the walls.

An important aspect of radiation safety is the ALARA principle. ALARA stands for As Low As Reasonably Achievable. This means we should take all steps that are

reasonable to lower radiation doses for everyone (general public, patients, and radiation workers). This can be achieved with engineering controls (permanent and mobile shielding) as well as with appropriate procedures for handling radioactive material and interaction with radioactive patients.

7.1.4 Shielding Material Properties

Lead and concrete are the two building materials most often used for shielding within a nuclear medicine facility. The amount of shielding each room will need depends on the expected workload, adjacent rooms, and amount of radiation present.

Lead is available as lead-impregnated wallboard, sheet stock, and bricks. The choice of building material depends on the thickness of lead needed. Lead provides a half value layer of 3.98 mm at 511 keV. The term half value layer describes the thickness of material required to decrease the intensity of radiation by one half.

Concrete has densities in the range of 1.84–2.35 g/cm^3, which yields half value layer of 3.4–4.3 cm at 511 keV. Thus, the concrete used in floors (and sometimes walls) of many facilities will provide some attenuation of radioactivity emitted by the patient.

The MR magnet and the magnetic/RF shielding of the imaging room will provide enough attenuation that usually one does not have to worry about adding lead to the walls of the imaging suite. Rather, the shielding will be more important for the hot lab and the patient uptake areas. This shielding could be taken care of by either localized shielding within the rooms (rolling lead shields, lead bricks, lead L-blocks, etc.) or adding lead or concrete to the floor, walls, and/or ceiling of the room. It is important to involve health physicists in the planning and implementation of a PET/MRI facility to make sure that radiation exposure calculations are performed and appropriate shielding is utilized to meet regulatory requirements for radiation exposure.

7.1.5 Shielding Calculations

While beyond the scope of this text, it is useful to look at what goes into determining the shielding for a PET/MRI facility. Knowing the variables will aid in the planning of the facility, whether it be new construction or renovation of existing space. When creating a shielding report, the health physicist will need to do the following:

- Obtain a scale drawing of the entire facility and rooms adjacent to facility.
- Determine the expected workload of the facility. This is derived from the number of patients examined per day, the radioisotope(s) being injected, the amount of radioactivity being injected into each patient, and the amount of time the patient will be spending in each of the rooms within the facility.
- Determine the location and initial activities of all non-patient sources of radioactivity (phantoms, dose drawing, etc.).

- Determine the classification of rooms (radiation worker or general public access) within the facility and adjacent to the facility and then determine the occupancy times of these rooms.
- Calculate the radiation exposure to these rooms based on all of the radioactivity sources (patients, phantoms, dose drawing, etc.).
- Determine whether the rooms are within compliance of radiation exposure limits. If not, determine the amount of shielding needing to be added to the walls to bring the room into compliance.

7.1.6   Radiation Safety Issues

Generally the most important safety issue in a PET imaging operation is the radiation exposure to the PET technologists, as they are the personnel that administer the radiopharmaceutical dose and attend to the radioactive patient throughout the imaging study. There are three tenets to radiation safety that are used to minimize the radiation exposure to the PET technologist: distance, shielding, and time.

Radioactivity is emitted equally in all directions. Thus, exposure levels decrease the further you get away from the source, as the surface area of the "sphere" of radioactive emissions increases, resulting in fewer emissions per unit area. The geometry of these emissions (as seen in Fig. 7.1) is such that the radiation exposure
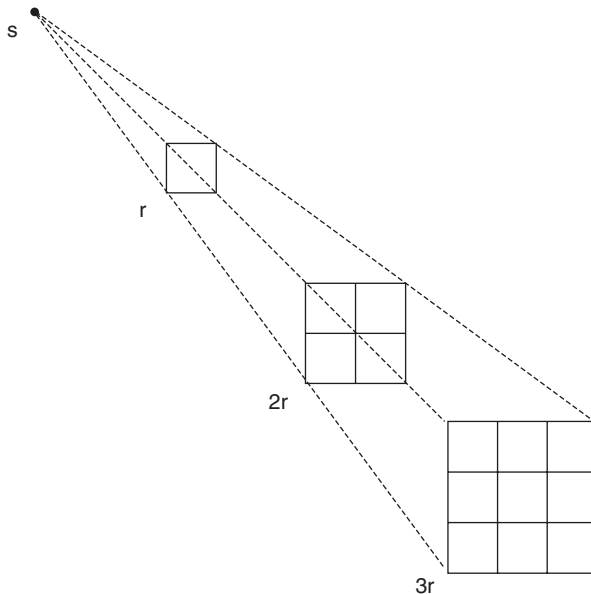

Fig. 7.1 Inverse square law depiction. A point source S will emit radiation equally in all directions. Looking at a given subtended area, the radiation fluence at a distance r will be spread over four times the area at distance $2 r$ and nine times the area at distance $3 r$

rate is inversely proportional to the square of the distance from the source, a property commonly known as the inverse square law. Thus, an important technique for the technologist is to work at a distance whenever practical. Examples of using distance include:

- Performing injections at a comfortable arm's length rather than in close to the body.
- Talking to the patient from 3 ft away rather than directly in front of them. Table 7.2 shows dose rates from patients injected with fluorine-18, highlighting the radiation exposure reduction benefit from interacting with the patient from a distance. Please note that the exposure rate does not preclude medical personnel from performing any medical actions necessary to ensure the safety of the patient should a medical emergency arise.
- Holding the syringe shield from the plunger side of the syringe rather than the needle side (the bulk of the radiation will be near the needle, rather than at the end of the syringe).

Another way to reduce radiation exposure is to stop some or all of the gamma rays before they make it to the technologist. Shielding, using high-density materials, will serve this purpose. There are various operations that lend themselves to using shielding:

- Drawing patient doses from behind a lead-shield "L-block"
- Surrounding the dose calibrator chambers with lead rings
- Using syringe shields when administering the radiopharmaceutical to the patient
- Having lead shields around the sharps container

There are also some practical suggestions that will reduce radiation exposure to the technologists, such as:

- Completing any patient instructions and surveys before injection of the radio-pharmaceutical rather than after
- Using a cart to transport the radiopharmaceutical rather than carrying it, increasing the distance from the radiopharmaceutical to the technologist

Table 7.2 Mean dose rate measurements of patients injected with F-18 FDG [16]. Measurements were taken at various distances immediately following injection of F-18 FDG. 115 patients were used for the chest measurements, 19 patients for side (mid-trunk) measurements, and 8 patients each for head and feet measurements

Distance	Chest dose rate/ MBq (μSv/h)	Side dose rate/ MBq (μSv/h)	Head dose rate/ MBq (μSv/h)	Feet dose rate/ MBq (μSv/h)
0.1 m	1.28	1.04	0.68	0.10
0.5 m	0.41	0.39	0.28	0.05
1.0 m	0.15	0.16	0.11	0.03
2.0 m	0.06	0.07	0.04	0.02

• Performing additional MR sequences after the PET acquisition, rather than before (for nonsimultaneous PET/MRI), which allows some radioactive decay before helping the patient off the imaging equipment at the end of the study

Federal regulations regarding the release of radioactive patients state that patients may be released if it is unlikely that members of the public will be exposed to more than 5 mSv (0.5 rem) as a result of the patient's release [6]. The amount of positron-emitting radionuclide needed to exceed this exposure limit is well in excess of what is administered for a PET scan, so patients are released following their image study, assuming there are no other medical conditions that would prevent their release.

7.2   MRI Safety

An MRI environment presents a number of unique challenges to ensuring the safety of both patients and staff members. Assuming that a PET/MRI is being installed in a radiology department that already has experience with at least one MRI suite, the same policies and procedures for MRI safety should be applied. A new challenge may be to educate and train radiology personnel who are more familiar with PET/CT but unfamiliar with MRI. We will review general safety guidelines for patients in the MRI environment and review policies that can be implemented for the maintenance of MRI safety for both patients and staff. There are three major sources of risk when using an MRI (Fig. 7.2). The first is the static magnetic field that results in the missile effect. The second are the varying gradients used in imaging that can result in peripheral nerve stimulation and loud noises. The third are the radio-frequency (rf) pulses that can result in heating of tissue.
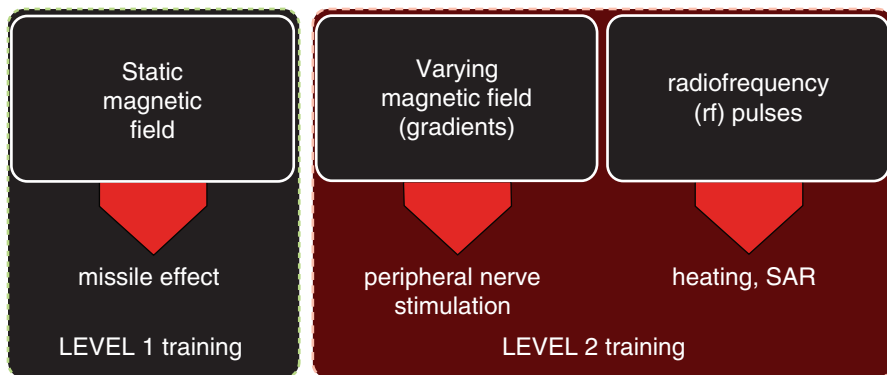
Fig. 7.2   Three sources of MRI hazards. The static magnetic field poses a danger to personnel and patients at all times and results in the missile effect. Level 1 training covers risks associated with the static magnetic field and allows personnel to enter Zone 4 when imaging is not being performed. The varying magnetic fields (gradients) and radio-frequency (rf) pulses used during imaging of a patient can also injure patients through heating and nerve stimulation. Level 2 training is required for personnel to screen and image patients

7.2.1 The Magnet Is Always On: The Static Magnetic Field

For PET/CT practitioners who are more familiar with a CT and radiation safety, an MRI scanner is different from a CT scanner because it is always on, with a strong static magnetic field usually up to 1.5 or 3.0 Tesla (T). The magnetic field rapidly drops off as one moves away from the center of the bore, reaching 5 G or 0.5 mT within a few meters. While magnetic field interactions are negligible at 5 G (for comparison, a refrigerator magnet is typically around 50 G), it is the rapid change, i.e., gradient, between the center of the MRI scanner bore and the 5 G line that creates a safety hazard. Ferromagnetic objects brought within the 5 G line can be attracted to the bore center and accelerate rapidly to become a flying projectile, with potential harm to either patient or staff members in its path. Thus, the prevention of projectile incidents is a top priority in MRI safety and is accomplished through proper screening of patients and staff, and the establishment of MRI zones is described further below.

7.2.2 Thermal Injuries and Other Hidden Dangers of MRI

To generate medical images, MRI scanners employ radio-frequency pulses to deliver energy to excite soft tissues in the body part being imaged. These pulses are time-varying magnetic fields that can induce current in electrically conductive materials within the field of excitation. Thus, patients with implants or devices containing metal, either internal or external to their body, are at risk for developing electric currents with potential for resistive heat loss, leading to focal warmth as well as burns. The specific absorption rate (SAR) refers to the amount of heating a tissue will experience during imaging. The SAR associated with a particular MRI sequence can be predicted and is limited during patient imaging to prevent significant heating of body tissue. Of note, this does not apply to implants where focal heating can be much higher than predicted in whole-body models. To prevent a thermal injury, patients should be rigorously screened for implants/devices, while external wires and leads overlying the patients should be either removed or positioned in safe configurations (e.g., to prevent a loop configuration). Thermal injuries are among the most frequently reported MR safety incidents to the US Food and Drug Administration (FDA) [7] and also need to be reported to the Joint Commission during inspections in the United States.

Internal implants that are ferromagnetic can also be displaced by the MR's strong static magnetic field, with potentially fatal complications in the case of a brain aneurysm clip. In addition, implants with electronic circuits such as pacemakers can malfunction in the MR environment. These potential complications further emphasize the need for rigorous screening of patients for medical implants and devices.

Peripheral nerve stimulation is a distinct risk from thermal injury, which is caused by rapidly changing magnetic field gradients used during imaging [8]. These can be mild and noticeable as a tingling sensation and only rarely are painful to patients in MRI. The rate of gradient flux is closely regulated by the FDA, and

serious effects of nerve stimulation (i.e., cardiac block) have been removed from clinical MR scanning.

7.2.3 Developing an MRI Safety Program

Based on the danger in MRI outlined above, the rationale is clear for the screening of both patients and staff members, to avoid the introduction of potential projectiles as well as medical implants that may lead to injuries or even fatalities. How does an institution create a safe MRI workplace environment in practice? In 2013, the American College of Radiology (ACR) Guidance Document on MR Safe Practices was published, which outlines comprehensive steps for the creation of an MRI safety program [9].

The first step in creating an MRI safety program is to create a leadership structure to oversee its implementation and establish institutional policies and procedures that will guide the conduct of all staff members who work in the MR environment. An MRI safety steering committee should be created that regularly meets and is led by an MR medical director. The steering committee should include membership from various stakeholders, including members from radiologists, MRI technologists, hospital administration, medical physics, nursing, and a number of medical departments who have physicians working at various MRI sites on a routine basis, such as anesthesia. It is through a constant desire to improve MRI safety that the MR medical director and hospital leadership in safety can establish a successful and sustainable MR safety program.

Additional leaders in an MRI safety program may include an MR safety officer (MRSO) and an MR safety expert (MRSE). The MR safety officer frequently is a lead technologist who is well versed in the subtleties of MR safety and can enforce existing policies and procedures. The MRSE is a medical physicist acting as an advisor to support radiologists and technologists when difficult questions of MR safety arise and there are no clear guidelines to answer them. At this time, certification exams for MR medical director, MRSO, and MRSE are offered by an independent organization, the American Board of Magnetic Resonance Safety [10].

Despite the comprehensive nature of the ACR Guidance document, there remain many gray areas where decision about whether or not to proceed with an MRI in a specific patient requires further investigation into risk/benefit that may be beyond the expertise of the MR medical director or MRSO. Even with the advice of an MRSE, it is often ultimately the responsibility of the MR medical director to decide among the many risks and benefits of MRI in challenging medical scenarios.

7.2.4 MRI Zoning: Controlling Access and Screening for Danger

To implement MR safety policies and procedures, the concept of MR zoning needs to be applied to each MR site (Fig. 7.3), with each zone representing an area of increasingly restricted access to patients and staff members. The objectives of

Fig. 7.3 MRI zone concepts
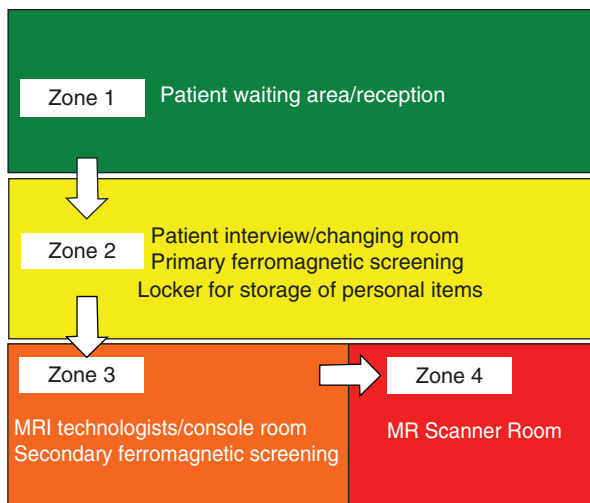
designating MR zones are to ensure the proper screening for ferromagnetic material and implants and to prevent the accidental introduction of unsafe objects into Zone 4, the room in which the MR scanner is situated. A patient typically first registers at a reception desk in an unrestricted area of the hospital or outpatient facility, which is designated as Zone 1. They are then escorted to Zone 2 for screening of medical devices and other pertinent history. A screening form for implants and devices should be filled out by the patient and reviewed by an appropriately trained MR staff member. The practice of changing patients into gown is also helpful, to remove the risk of patients carrying personal items such as cell phones into the MRI suite. Once changed into gowns, they are escorted into Zone 3 for additional screening with ferromagnetic detectors. This additional screening is performed to verify the absence of personal items that may be dangerous or cause artifacts in the MRI scanner (e.g., hair pins and bras) or to detect superficial implants that the patient may have forgotten about (e.g., pacemaker). At our institution, each patient undergoes additional verbal screening for implants in Zone 3, as a layer of redundancy for the occasional forgetful patient. If they pass this stage, they are then allowed to proceed to Zone 4 for the actual MR scan.

Staff members are also required to screen themselves when they work in MRI. They can first perform self-screening in Zone 2 or 3 with ferromagnetic detectors, to prevent the accidental introduction of personal items including pens and mobile phones. Creating a culture where self-screening becomes routine is critical for the hospital to prevent projectile incidents. Staff members who do not routinely access MRI may be screened by an MR technologist at the time of entry. Given the high traffic through an MRI suite, the accidental introduction of small ferromagnetic objects remains a risk. It is important for the institution to encourage the reporting of both actual and near-miss incidents to identify potential weaknesses in the daily screening process. In addition, in the United States, the Joint Commission requires a log of events for foreign objects entering Zone 4.

An uncommon situation that merits further discussion is in the care of the patient in MRI who is rapidly deteriorating. A patient who needs either resuscitation or acute medical care should not be treated by a medical response team in Zone 4. For example, if a hospital has a "code" team that is activated for emergency responses, this team will rush to the aid of a patient at the request of hospital personnel at any site. Since a resuscitation attempt is conducted by a team of physicians and nurses who often carry multiple metallic devices, performing such a resuscitation in Zone 4 poses a large risk. Thus, each MR site should predetermine a safe location in which to place patients outside of Zone 4 (e.g., in Zone 3). Basic life support measures (e.g., chest compressions) can be conducted by personnel while transferring the patient out of Zone 4 to the emergency area.

Given the concept of MR zones and the importance of ferromagnetic screening, any new MRI site should be planned with experts in MR safety participating at the design stage, in order to give feedback on the feasibility of implementing safety zones. For example, combining console rooms for MRI and other imaging modalities such as CT unnecessarily increases the number of staff members and patients who need to be screened. If the MR site is already built, identifying zones retroactively can sometimes be challenging due to the number of entryways and/or the presence of shared spaces with other medical services. In this case, securing access to prevent accidental entry into Zone 4 becomes a priority.

7.2.5   MR Personnel: Training and Responsibilities

Staff members who work in MRI sites should be properly educated on principles of MR safety, and their training should be documented annually if following guidelines from the Joint Commission [11]. Since staff members who work in MRI vary in their responsibilities, they are not expected to all undergo the same level of training. The ACR MR Safety Guidance Document proposes a distinction between Level 1 and Level 2 personnel.

Level 1 personnel have passed minimal educational efforts to ensure their own safety as they work in Zone 3 and Zone 4. This group includes security, IT and facilities personnel who may have access to the MRI site, including Zone 4. Level 2 personnel will also have passed minimal Level 1 educational training but require additional training in MR safety, for example, in the prevention of thermal injury and in ferromagnetic screening. Generally, all radiologists and nurses who work in MRI and all MR technologists should undergo Level 2 training. Additional physicians who routinely care for patients in MRI, such as certain anesthesiologists and neurosurgeons who work in an operating room with MRI, will need Level 2 training as well. Only Level 2 personnel can directly be responsible for patients in Zone 4 and can perform ferromagnetic screening for patients and other staff members. While MR staff will not lie in the MR scanner themselves, they may stand at the edge of the MR scanner bore while positioning patients or accessing an intravenous line and become subject to very high magnetic field and spatial gradients. Thus, they should also fill out a screening form for medical implants and devices to ensure their

own safety. For example, a staff member with a pacemaker may not be allowed to work in MRI for obvious reasons. Most institutions require a screening form to be filled out (or updated) at the time of annual MR safety training for each Level 2 personnel.

Physicians and nurses who escort unstable patients from other services may occasionally need access to MRI. These and other non-MR personnel do not require special training before entry, but they need to be screened for ferromagnetic material as well as implants and devices, similar to patients. For example, a physician who has a pacemaker should not be allowed in Zone 4, but they may not realize the need to voluntarily disclose this medical history. Thus, non-MR personnel are treated to the same rigors of patient screening if they wish to step into the MRI Zones 3 and 4.

7.2.6 Challenges to Patient Screening in Practice

A screening questionnaire is first filled out by patients for the disclosure of implants and to provide pertinent medical history, either before or after their arrival to the MRI suite. Ideally, patients should prefill screening forms before their appointment, which may help the radiology department preemptively identify individuals with a contraindicated device (e.g., pacemaker), requiring an alternative imaging examination. A decision support system at the time of MRI order that reviews a patient's list of medical implants can help reduce the number of MR cancelations or delays.

Examples of MR screening forms are available on various websites [12] as well as in the ACR MR Safety Guidance Document. The goal of MR screening is not only to document medical implants but also to screen for nonmedical implants and ferromagnetic objects, such as metallic fragments or shrapnel injury, the presence of medication patches, or even tattoos that rarely but occasionally carry a risk for thermal injury. A discussion of every nonmedical device and their risk is beyond the scope of this chapter.

Screening questionnaires are also helpful to identify patients who may have renal failure or are on dialysis, with implications on the safe use of MR contrast agents. Numerous articles and documents are available to guide a radiology department in the use of MR contrast agents, for example, the ACR Contrast Manual, which is updated every few years [13]. The questionnaire could also be used to screen for possible pregnancy. Most radiology departments already have existing policies for handling pregnant patients, which may preclude the use of MR contrast agents in this special population.

In the absence of contraindications to MRI, a recurrent challenge in the workflow of any MRI suite is the patient with MR conditional medical devices. Numerous medical devices, including coronary stents, certain aneurysm clips, and even pacemakers, are designated as MRI conditional (Fig. 7.4). In contrast to MR unsafe devices (which should not be brought into Zone 4), and MR safe objects that are nonmetallic, MR conditional devices or objects can be safely brought into an MRI for scanning but only under specified conditions. Conditions may include the specified strength of the MRI

Fig. 7.4 US Food and Drug Administration labeling developed by the ASTM International [17], including MR safe (green square), MR conditional (yellow triangle), and MR unsafe (red circle). Only objects known to be nonmetallic in composition are MR Safe. MR conditional devices account for the majority of implants that are brought into MRI scanners and require an understanding of specific conditions of operation
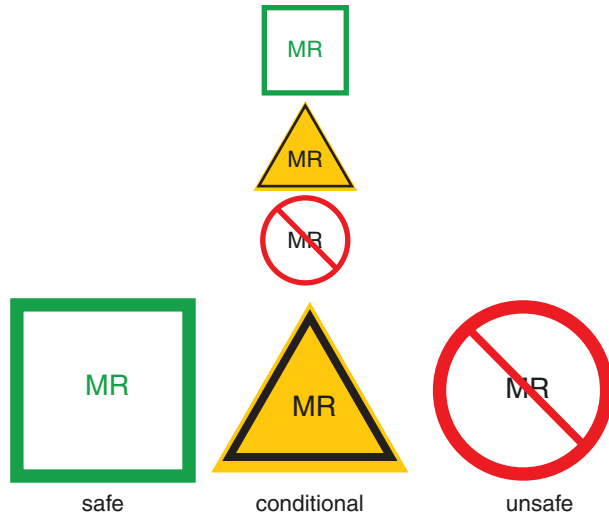
scanner (safe at 1.5 T and/or 3.0 T), maximum gradient strengths, and specific MR operator modes (e.g., normal mode or research mode). This can present daily challenges to the practice of MR safety, because clear documentation is necessary for identifying safe conditions for each patient. Most patients obtain information cards for their devices at the time of surgical implantation, but they may forget to bring their cards at the time of their MRI appointment. Unless unambiguous medical documentation is available, it is not prudent to assume that scanning the patient at 1.5 T instead of 3.0 T is sufficient to prevent a patient injury. In the emergent setting and in the absence of implant documentation, the risk and benefits should be evaluated by a physician who is familiar with principles of MR safety.

Another challenge to the practice of screening is in the setting of unresponsive patients or patients who are unreliable historians, such as pediatric patients. The screening in these cases should be performed by the patient's parent or guardian. In an emergent setting without available parent or guardian, the patient should be examined by a Level 2 personnel for evidence of implant, both by direct inspection and based on review of other imaging tests (e.g., chest x-ray). Final decision to scan the patient should be made by the MR medical director or an attending radiologist with Level 2 training, after reviewing all available information.

The screening of patients for MRI can be a time-consuming and frustrating process. Patients often forget to bring required documentation for their devices, or forget about surgeries conducted years ago, or maybe even lie to avoid questioning that they may perceive is unfairly impeding their access to MRI. They may even receive faulty information from their referring physician, who are rarely knowledgeable about the differences between devices that are MRI conditional and what was formerly called MRI compatible (an outdated term). Identifying and investing in processes that improve the workflow of patients related to screening in the MRI suite can pay enormous dividends. Unfortunately, the screening process is one of the

most resource-intensive steps of an MR safety program and should not be taken lightly. While MR safety incidents are rare, a proper assessment of resources required to adopt MR safe practices is important.

7.2.7 Other Risks in MRI

The ACR Guidance Document elaborates on a number of risks common for all patients who undergo MRI. We have already alluded to the risk of thermal injury from implanted medical devices, medication patches, and certain nonmedical items such as tattoos. Medication patches that contain metallic components can heat up and cause thermal injury during MRI and generally need to be removed. Each patch manufacturer website usually provides documentation to ascertain the absence of metal, the safety of their patch in direct MRI testing, or a contact number for further safety information. It may be prudent for the MR medical director to work with their institution's pharmacy to identify potentially dangerous medication patches or to suggest to place MR safe patches on formulary when there is more than one option. Tattoos are infrequently at risk for heating, but a few have been shown to contain dark inks that can put a patient at risk for injury. Thermal injuries can also occur from patient skin directly contacting the machine's bore or imaging coils themselves, in the absence of appropriate padding. For tattoos and other unexpected risks of thermal injury, proper training is essential to raise awareness among Level 2 MR technologists who are in direct communication with the patients during scanning.

MRI sites should provide ear protection in the form of earplugs and/or protective headphones. Even with such protection, patients may still complain of unacceptable noise levels, and an MR technologist should consider terminating the exam to avoid injury. Finally, patients with claustrophobia may not be able to tolerate an MR exam without adequate premedication.

Since a PET/MRI may be a new purchase at your institution, nonclinical, non-research MRIs may be performed to optimize your imaging protocols. These MRIs consist of those scans used appropriately in human subjects that constitute neither clinical care nor research. For example, an MRI may be performed on a volunteer when a new sequence becomes available or to verify a commercially available coil that is new to your practice; the department may ask volunteers among the staff to lie in the magnet to test run a whole-body MRI protocol before its use on actual patients. Guidelines for documentation and consent for nonclinical non-research MRI in human subjects were recently published and suggest the use of informed consent with the application of standard MR safety procedures, as well as reporting of incidental findings, similar to research MRI [14].

7.2.8 Developing a Culture of MRI Safety

One of the most important lessons is that MR safety requires a true team effort. While policies and procedures are necessary and training programs are mandatory,

it is the implementation of a culture that prioritizes the safety of all patients that ultimately prevents injuries and even deaths. Unfortunately, it takes just one Level 2 personnel to skip an established safety process in the rush of scanning a patient to create a hazardous situation. MR technologists are generally smart and diligent members within radiology departments. However, if they are incentivized to scan more and more patients in shorter amounts of time, they will learn to create shortcuts that may involve reducing screening efforts.

Even the best MR technologist may occasionally make mistakes. While punitive actions may be necessary for egregious behavior, a large number of medical errors are caused by human lapses that are unintentional. In these specific cases, punitive action may actually backfire, causing the MR staff to shy away from reporting near-miss events [15]. An alternative is to seek to understand the root causes of these errors, to identify challenges faced by Level 2 personnel in their daily practice, and ultimately to design better safety protocols that have redundant processes. This will reduce the risk that any one human error escalates to a catastrophic one. Thus, encouraging staff members to report near misses, providing feedback on new safety measures, and rewarding positive behaviors are all measures that encourage each MR team to perform at their best and sustain a culture of safe MRI practices.

Conclusion

There are both important radiation safety and MRI safety considerations for PET/MRI. It is important that MRI technologists learn radiation safety and that nuclear medicine technologists learn MRI safety in order to prevent patient injury and radiation exposure to patients and technologists alike. For radiation safety, technologists need to be educated about exposure and the principles behind ALARA. Dose, shielding, and time are three ways to decrease radiation exposure. For MRI safety, ensuring proper Level 2 MR training of radiology staff unfamiliar with MRI is a priority. Technologists should become well versed in the risk of projectile incidents, thermal injuries, and proper ferromagnetic screening. Developing a governing structure and identifying an MR medical director, MR safety officer, and MR safety experts can also be helpful to improve communication between leadership and frontline staff. In summary, safety is a process-driven but people-intensive investment for radiology departments to consider.

References

1. Lederer CM, Shirley VS. Table of isotopes. 7th ed. New York: Wiley; 1978.
2. Unger LM, Trubey DK. Specific gamma-ray dose constants for nuclides important to dosimetry and radiological assessment. Oak Ridge, TN: Oak Ridge National Laboratory. ORNL/RSIC-45; 1981.
3. NRC: 10 CFR 20.1201 Occupational dose limits for adults. United States Nuclear Regulatory Commission. https://www.nrc.gov/reading-rm/doc-collections/cfr/part020/part020-1201.html. Accessed 1 June 2017.
4. NRC: 10 CFR 20.1208 Dose equivalent to an embryo/fetus. United States Nuclear Regulatory Commission. https://www.nrc.gov/reading-rm/doc-collections/cfr/part020/part020-1208.html. Accessed 1 June 2017.

5. NRC: 10 CFR 20.1301 Dose limits for individual members of the public. United States Nuclear Regulatory Commission. https://www.nrc.gov/reading-rm/doc-collections/cfr/part020/part020-1301.html. Accessed 1 June 2017.
6. NRC: 10 CFR 35.75 Release of individuals containing unsealed byproduct material or implants containing byproduct material. United States Nuclear Regulatory Commission. https://www.nrc.gov/reading-rm/doc-collections/cfr/part035/full-text.html#part035-0075. Accessed 1 June 2017.
7. Hardy PT, Weil KM. A review of thermal MR injuries. Radiol Technol. 2010;81:606–9.
8. Abart J, Eberhardt K, Fischer H, et al. Peripheral nerve stimulation by time-varying magnetic fields. J Comput Assist Tomogr. 1997;21:532–8.
9. Expert Panel on MR Safety, Kanal E, Barkovich AJ, et al. ACR guidance document on MR safe practices: 2013. J Magn Reson Imaging. 2013;37:501–30.
10. American Board of Magnetic Resonance Safety. ABMRS. http://www.ABMRS.org. Accessed 1 June 2017.
11. Accreditation, Health Care, Certification|Joint Commission. The Joint Commission. http://www.jointcommission.org. Accessed 1 June 2017.
12. MRI Safety. mrisafety.com. http://mrisafety.com. Accessed 1 June 2017.
13. ACR Manual of Contrast Media – Version 10.3. American College of Radiology. 2017. p. 1–127. https://www.acr.org/Quality-Safety/Resources/Contrast-Manual.
14. Reeder SB, Kimbrell V, Owman T, Steckner M, Calamante F. Guidelines for documentation and consent for nonclinical, nonresearch MRI in human subjects. J Magn Reson Imaging. 2017;45:36–41.
15. Marx D. How building a "just culture" helps an organization learn from errors. OR Manager. 2003;19(5):1–14.
16. Benatar NA, Cronin BF, ODoherty MJ. Radiation dose rates from patients undergoing PET: implications for technologists and waiting areas. Eur J Nucl Med. 2000;27:583–9.
17. ASTM International – Standards Worldwide. ASTM International. http://www.astm.org. Accessed 1 June 2017.

Imaging of Tumour Heterogeneity: Functional MR Techniques in Oncology

8

Christian Kelly-Morland, Gary Cook, and Vicky Goh

Contents

8.1 Introduction

The concept of tumour heterogeneity refers to the regional differences within a tumour, not only at a genetic level due to DNA mutation but also secondary to epigenetic influences altering genetic expression, and ultimately phenotype, such as disordered DNA methylation or histone variation. Branched evolution, the presence of varying subclonal cell lines within a tumour, contributes to intra-tumoural heterogeneity within a lesion. From a cellular perspective, differences in metabolism,

C. Kelly-Morland • G. Cook • V. Goh (✉)
Division of Imaging Sciences & Biomedical Engineering, King's College London, London, UK
e-mail: gary.cook@kcl.ac.uk; vicky.goh@kcl.ac.uk

apoptosis and angiogenesis also contribute to heterogeneity. Metastatic spread of particular cell lines from the same primary leads to inter-tumoural or inter-metastatic heterogeneity [1]. The differing tumour biology within the primary lesion itself and between metastatic lesions poses a unique set of challenges when it comes to selecting appropriate targeted therapies and assessing therapeutic effect. During therapy tumours will respond differentially and also dynamically, for example, developing resistance to a previously effective drug treatment [2].

Recent advances in technology have allowed for unprecedented investigation of the complex genetic mechanisms underpinning tumour biology with the use of next-generation sequencing techniques such as whole exon and whole genome sequencing. This has expedited the discovery of new genes and mutational patterns associated with cancer, identifying surprisingly complex and previously unchartered interactions at the cellular metabolic, as well as the epigenetic and phenotypic levels [3]. On the phenotypic level, there has been parallel interest in the potential of imaging to assess image heterogeneity [4–7]. Quantifiable morphological or biological heterogeneity can be assessed with different imaging modalities including magnetic resonance imaging (MRI). Imaging can overcome some of the issues with in vivo histopathological assessment including ethical and safety considerations posed by repeated sequential biopsy as well as the potential for sampling error. By complementing standard staging and response to treatment, imaging has the potential to individualise treatment, predict response to a particular therapy in a single patient as well as detect treatment resistance at an earlier time point and guide earlier therapeutic transition. The advent of integrated PET/MRI provides a unique opportunity to extend the capability of PET and MRI for assessing phenotypic heterogeneity. Key features related to functional MRI techniques will be addressed further in this chapter.

8.2 Functional MRI and Heterogeneity

A number of "functional" MRI techniques are available currently in clinical practice that augment standard anatomical imaging that provide insight into tumour physiology. These include techniques that assess water molecule diffusivity, tumour perfusion, tumour oxygenation and tumour metabolism [8]. Quantitative or semi-quantitative parameters can be derived from these techniques pertaining to diffusivity (apparent diffusion coefficient, ADC), vascularity (integrated area under the curve, transfer constant), oxygenation status ($R2^*$ relaxation rate) or metabolic activity (metabolite ratios) that complement standard qualitative reporting of morphological features, for example, spiculate versus well-circumscribed borders in pulmonary or breast lesions as a strong marker of malignant probability [9].

Additionally agnostic features can be extracted from MRI images by radiomic techniques [6]. These post-processing advanced computational methods may infer "phenotype signatures" of tumours for characterisation or prognostication [10] and also inform on therapy effects. Textural analysis of image heterogeneity

is achieved through mathematical modelling and can be applied to multiple modalities [5, 7, 11]. Statistical-based methods of texture analysis are grouped into three tiers (Table 8.1).

8.3 Summary of Texture-Based Methods

First-order statistics refer to histogram analysis on a per-pixel basis and have been used most commonly in medical imaging. The true spatial relationship between adjacent pixels is ignored, and the histogram obtained is a function of the number of pixels in the image of the same signal intensity. For example, the mean (average), mode (most frequently occurring value) and standard deviation of the histogram are calculated as is the kurtosis (representative of the shape of distribution), skewness (the asymmetry of the distribution) and entropy (a reflection of randomness in the distribution) [12]. Second-order statistics evaluate the probability of two pixels of different values coinciding at specific locations relative to each other, most commonly using a grey-level co-occurrence matrix (GLCM) so-called Haralick feature analysis [5, 13, 14]. Higher-order statistics measure three or more pixel intensities relative to each other and include neighbourhood grey-tone difference matrix (NGTDM) and grey-level zone matrices (GLZM) [5]. Model-based methods such as fractal analysis, for example, using a box-counting method, may also be applied, evaluating the pattern irregularity within an image by imposing a series of grids of set scales onto an image to classify how an object occupies the image. The higher

Table 8.1 Texture analysis methods

Statistical method	Number of pixels interrogated	Properties derived
First order (histogram analysis)	1	Mean
		Standard deviation
		Mode
		Kurtosis
		Entropy
		Skewness
		Enhancing fraction
		Grey-level frequency distribution
Second order (texture analysis)	2	Energy
		Entropy
		Uniformity
		Homogeneity
		Parameter map (directionality)
		Grey-level co-occurrence matrix (Haralick features)
Higher order	3	Neighbourhood grey-tone difference matrices
		Grey-level zone matrices; non-uniformity, short-run emphasis, run percentage

the derived fractal dimension, the more heterogeneous the image [8, 15]. These agnostic features complement quantitative functional imaging techniques.

8.4 Surrogate Assessment of Tumour Cellular Density and Proliferation

8.4.1 Diffusion-Weighted Imaging

Diffusion-weighted imaging (DWI) is one of the most commonly performed techniques. DWI is widely available as a standard sequence on clinical MRI scanners. This measures the impedance (restriction) of the movement of water molecules within tissues [16, 17]. The degree of impedance is influenced by the cellular density, volume, membrane permeability and macromolecular structure of the underlying tissue. DWI usually employs echo-planar spin echo sequences which negate motion artefact with oscillating gradient reversal pulses used rather than 180° rephrasing pulses. The repetition time (TR) is relatively long, minimising T1 signal, though the short echo time (TE) can lead to T2-weighted signal persistence on the resultant images, so-called shine-through [18] (Fig. 8.1). DWI can be performed for locoregional assessment or extended to the whole body (Fig. 8.2) which brings certain challenges by virtue of scanner and protocol design, as well as patient factors. The technique is becoming more widely established in particular in the oncology arena due to the improved sensitivity and specificity in the evaluation of skeletal disease in particular. There are promising results in terms of a role in response assessment over that provided by traditional methods such as bone scintigraphy where lytic deposits may provide a false-negative result and the flare phenomenon can cause false positives [19–21].

Modern scanners with moving table capability and dedicated body surface coils can provide excellent anatomical and functional detail at both 1.5 and 3 T magnet strengths in terms of contrast to noise ratio, slice thickness and spatial resolution, a whole-body acquisition including morphological sequences (T1/T2 weighted) and

Fig. 8.1 Axial T2 (left), b900 diffusion-weighted (middle) and apparent diffusion coefficient maps (right) at the level of the prostate gland demonstrate persistence of high signal (T2 shine-through) in the normal peripheral zone (arrows) on all sequences due to the short echo times utilised in the sequence
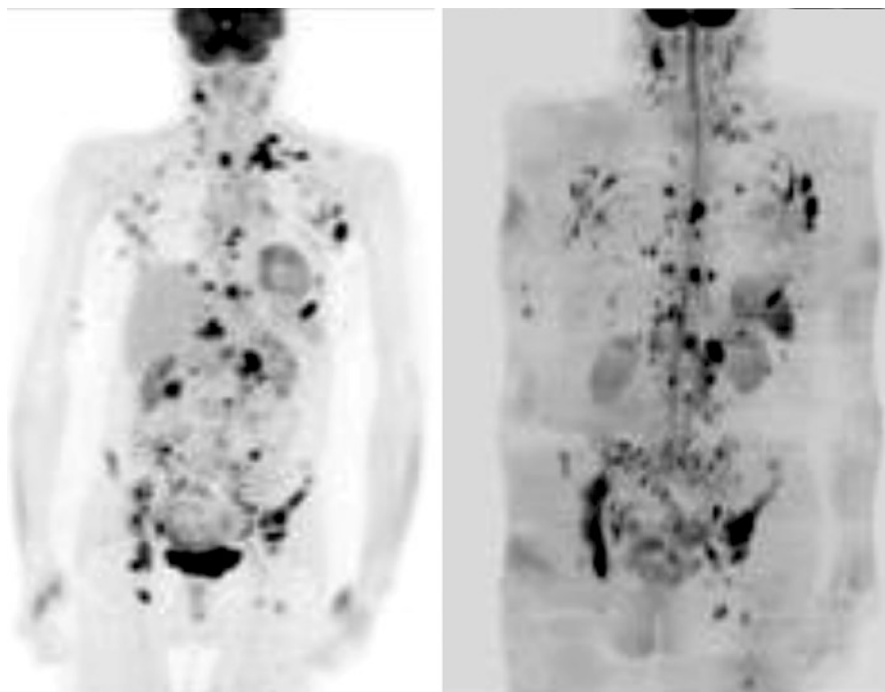
Fig. 8.2 Whole-body coronal maximum intensity projection images; [18]FDG PET (left) and inverted whole-body b900 diffusion-weighted images at 3 T (right) in a patient with stage IV lymphoma. Areas of abnormal increased tracer accumulation are seen at multiple nodal stations above and below the diaphragm and in the vertebrae and pelvis. These correspond to sites of abnormal restricted diffusion

diffusion weighted can be accomplished in less than an hour though this time constraint is an important consideration when it comes to workflow planning and patient comfort.

Combined whole-body PET/MRI lends itself well to improve diagnostic confidence as the differing properties assessed by each modality (Fig. 8.2) (e.g. glucose analogue metabolism in ^{18}F-FDG PET and cellular density in DWI) complement each other particularly in areas where one technique is limited. An example would be in differentiating pathological but non-enlarged nodes by their metabolic activity with PET, as these structures by virtue of their physiological composition demonstrate restricted diffusion in normal circumstances. Compare this to accurately delineating intracerebral pathology using DWI against the background generalised increased physiological PET tracer uptake which alone could mask pathology [21].

Several technical challenges exist when optimising whole-body diffusion-weighted protocols. The rapid switching of gradients employed by echo planar sequences results in the formation of eddy currents which lead to inhomogeneity in the main magnetic field; this is a particular problem at higher field strengths and can lead to distortion or shearing artefact resulting in malalignment when attempting to

co-register morphological sequences with the diffusion-weighted images. Increasing receiver bandwidth and altering the maximum gradient amplitudes applied can solve the problem [22]. Careful attention to shimming, the use of continuous table motion and applying a uniform frequency centre across imaging stations can combat image stack malalignment between stations. The use of non-selective fat suppression techniques (e.g. short-tau inversion recovery, STIR) should increase the uniformity of fat suppression, decreasing the likelihood of ghosting artefacts [19]. Susceptibility artefacts at air/bone/soft tissue interfaces as well as around implanted devices are also exaggerated [23–25].

The apparent diffusion coefficient (ADC, mm^2/s) is measured from the rate of signal loss with increasing b-weighting employed during DWI; however, care must be taken in the interpretation of results in terms of reproducibility and referencing as values may differ depending on manufacturer [26] and scanning parameters, in particular the range of *b* values used for acquisition.

Several published studies have shown the promise of DWI for lesion characterisation as well as disease prognostication and response assessment. ADC values have been shown to correlate with tumour differentiation in rectal cancer and tumour Gleason score in prostate cancer [27–29].

A systematic review and meta-analysis of the literature documenting 279 renal lesions found that DWI had a sensitivity of 85% for the differentiation of benign (including cysts, oncocytoma, angiomyolipoma and focal infection) versus malignant pathology and a specificity of 78%. Though there is less evidence to support ADC alone in discriminating between histological subtypes [30, 31] (e.g. clear cell renal carcinoma versus non-clear cell), there was reasonable accuracy when differentiating high from low Fuhrman grade tumours in a series of 110 lesions with a ROC-AUC summary score of 0.83 in this analysis [30].

Several studies have demonstrated a significant association between higher ADC values of the primary tumour at presentation and subsequent local treatment failure in squamous cell carcinoma in the head and neck [32, 33]. One theory is that the decrease in the diffusion impedance in these tumours may correspond to factors such as intra-tumoral micro-necrosis and non-cohesive or widely dispersed tumour cells within abundant stroma—one study of 19 patients demonstrated significant positive correlation between the percentage area of tumour stroma and the correlative ADC [34], a known histopathological predictor of higher metastatic potential [35]. Investigators have also found a significantly lower ADC in human papilloma virus positive tumours which respond more favourably to chemoradiotherapy [36].

DWI has also been found to be a potential prognostic marker in uterine cervical malignancy, using histogram analysis of whole-tumour ADC values. Downey et al. [37] found that in a sample of 60 patients, median ADC was significantly lower in poorly differentiated tumours (50th percentile, $1113 \pm 177 \times 10^{-6}$ mm^2/s). Similar findings were published by Lin et al. [38] in a study of 38 patients who found that the median ADC was significantly higher in well or moderately differentiated tumours versus poorly differentiated [37, 38]. Several studies have found ADC in squamous cell carcinoma of the cervix to be lower than that of adenocarcinoma [38, 39] though there is overlap.

Inter-tumoral heterogeneity has also been demonstrated by DWI with differing ADC values seen between ovarian primary tumours and associated peritoneal and omental deposits; a study of 20 patients found significantly lower ADC values in the peritoneal and omental deposits when compared to the ovarian primary tumour [40] reflecting the varying composition of primary and metastatic deposits in the same disease entity and the potential role that quantitative imaging techniques play in illustrating this alongside morphological sequences. The same study found that the vascular signal fraction (an indicator of vascularity) was lower in peritoneal deposits than primary tumours; this raises the possibility that differential disease response to treatment between sites may be due to hypoxia or poor delivery of chemotherapeutic agents in highly cellular but less vascular deposits.

Imaging during treatment in ovarian, SCCHN and cervical tumours have shown that ADC typically increases following treatment [33, 41, 42], and in a study of locally advanced cervical cancer, this corresponded inversely to changes in tumour cell density [41], whilst in SCCHN several studies have demonstrated that the risk of disease relapse is inversely proportional to the percentage increase in mean ADC early in treatment [33, 43].

The use of DWI as a surrogate imaging biomarker requires rigorous standardisation in image acquisition and analysis particularly in the multicentre setting where variation in scan protocols between centres may hamper reproducibility and validation [44]. Relative measures such as histogram analysis or percentage change in ADC values during treatment, for example, may prove a more robust means of assessment to overcome the disparity between manufacturers and models when it comes to absolute data measurements.

8.4.2   Magnetic Resonance Spectroscopy

Proton magnetic resonance spectroscopy (^{1}H-MRS) exploits the unique resonant frequencies of protons within differing molecules in tissue to produce a graphical representation of the distribution of metabolites in a region of interest, expressed as a series of peaks on the horizontal axis and by the parts per million and signal amplitude on the vertical axis. The area under each peak corresponds to the concentration of the metabolite [45]. Careful attention must be paid to voxel placement, minimising magnetic field inhomogeneity by shimming and adequate fat and water suppression methods to address spectral contamination and optimise results. Higher magnet strengths allow for better discrimination between metabolite peaks [46].

The most widely accepted marker of malignancy in MRS is elevation of the metabolite choline (spectral peak 3.2 ppm), an indirect index of cell turnover and proliferation. This is often referenced to the concentrations of citrate (spectral peak 2.6 ppm) and creatine (spectral peak 3.04 ppm) as a ratio [47].

Spectroscopy has been used in the setting of cerebral glioma to inform tumour typing and grading as well as to facilitate targeted biopsy especially when combined with ^{18}F-FDG PET to identify representative areas of higher metabolic activity. Metabolites such as *N*-acetylaspartate (NAA), choline, myoinositol, choline, lipids

and lactate have proven of use in the evaluation of benign and malignant neuropathology. In general astrocytomas tend to show elevated choline with reduced NAA and creatine, whilst glioblastoma multiforme classically demonstrates a high lipid (0.9 and 1.3 ppm) and lactate peak [45, 48].

MRS has also been used in the assessment of prostatic malignancy. The normal peripheral zone usually demonstrates high concentrations of citrate; this decreases in the central gland due to the lower proportion of glandular tissue. A reversal of the normal choline to creatine ratio is seen in malignancy (Fig. 8.3) [46].

Elevated choline/creatine ratios are also seen in breast, cervical, prostate, colorectal, lymphoma and head and neck squamous cell cancers [45, 49, 50]. There may be a role for MRS in the evaluation of treatment response in several tumour types. Two studies evaluating the choline/lipid ratios by 1H-MRS in a total of 94 tumours before and after transcatheter arterial chemoembolisation of hepatocellular carcinoma found a significant decrease in the ratio post-treatment [51, 52]. In a study of 22 patients with uterine cervical carcinoma undergoing neoadjuvant chemotherapy prior to hysterectomy, a significant drop in the triglyceride peak post
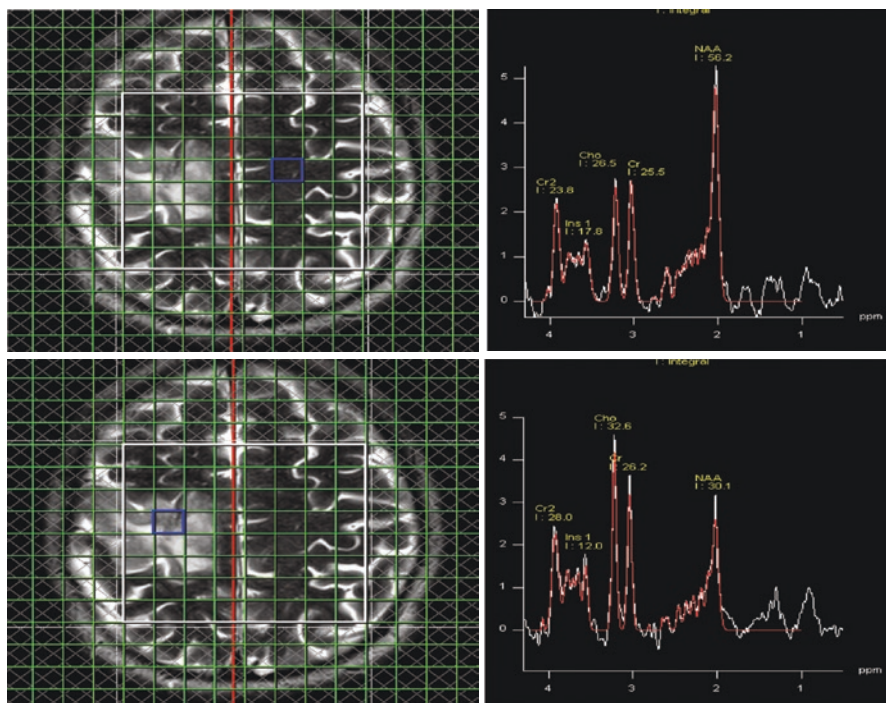
Fig. 8.3 Low-grade right frontotemporal astrocytoma. Top: axial T2-weighted images (left) with single-voxel spectroscopy from an area of normal cerebral parenchyma in the left posterior frontal lobe demonstrate the expected ratio of choline (Cho) to *N*-acetylaspartate (NAA). Bottom: single-voxel MRS in the right cerebral astrocytoma characterised by abnormal high T2 signal and mild cortical expansion in the posterior frontal and parietal cortex demonstrates reversal of the normal NAA-Cho ratio with a choline peak, a marker of cell membrane breakdown and cell proliferation

treatment correlated with a reduction in tumour volume though no advantage was found in terms of survival [53, 54].

In a study of 80 patients with cerebral glioma, MRS, in particular the choline/NAA ratio, was found to be equal in terms of sensitivity (81.8%) but superior to diffusion-weighted imaging in specificity (84 versus 69%), positive (81 versus 69%) and negative predictive values (81 versus 84%) in predicting disease response to treatment [55].

8.5   Surrogate Assessment of Tumour Perfusion, Angiogenesis and Oxygenation

8.5.1   Dynamic Contrast-Enhanced MRI

Tumour microvascular integrity and function can be assessed non-invasively using MRI and dynamic paramagnetic contrast-enhanced 2D or 3D gradient echo T1-weighted sequences, usually with a gadolinium-based contrast agent. Pharmacokinetic modelling, for example, with the Toft's model [56], allows for quantitative evaluation of several parameters including the transfer constant K^{trans}, a measure of volume exchange of contrast material between plasma and the extracellular space and rate constant (k_{ep}). Further parameters which can be extrapolated include blood plasma (v_p) and extravascular extracellular space volume (V_e). Qualitative visual assessment of a time to relative signal intensity curves is now commonly used in clinical practice, in particular when evaluating breast lesions for malignant potential [57, 58]. Typically three patterns of enhancement are demonstrated within lesions: firstly, progressive persistent enhancement in benignity; secondly, a plateau-type curve of initial increase in signal intensity then levelling off; and thirdly, a rapid initial increase in signal intensity followed by a drop-off (washout) over time which has been found to be up to 87% specific for malignant lesions though sensitivity is lower (57% in one series of 266 breast lesions) [59]. When morphology and enhancement patterns are taken into account, overall sensitivity of breast MRI in the detection of invasive malignancy is in the range of 89–100% [60].

Lower post-contrast signal intensity values correspond to reduced contrast enhancement secondary to decreased perfusion and resultant relative hypoxia in the tumour microenvironment. These features are known poor prognostic features for chemo-radiosensitivity/treatment response as well as outcome in malignancy.

In addition to a role in lesion detection, DCE has been demonstrated as a potential biomarker in terms of prediction of overall survival and treatment response in several cancers. A study of 101 patients with cervical cancer evaluated residual tumour volumes and signal intensity of tumour pixels on DCE-MRI and found that tumours in the lower fifth centile for signal intensity values of <2.05 (i.e. 5% of pixels in this tumour are of a signal intensity less than 2.05) found at 2–2.5 weeks into treatment predicted a local control over an 8-year follow-up of 73 versus 100% in those tumours with an SI5% >2.05. Disease-free survival rates in this group were 47 versus 79% [61]. A more recent study used similar cut-off values for signal

intensity in a group of 102 stage IB2-IVa cervical tumours and quantified a functional risk volume (FRV) of tissue within each tumour characterised by reduced enhancement finding it to be a superior predictor of outcome to absolute tumour volume and FRV correlated with local tumour control, disease specific and overall survival [62].

In squamous cell carcinoma head and neck tumours, K^{trans} has been reported to be a putative marker of survival and treatment response. Investigators have shown that a higher lesional K^{trans} pre-treatment with chemoradiotherapy corresponds to improved treatment response and disease-free survival [63]. A study of 13 patients undergoing accelerated radiotherapy found that a diminished maximal tumour enhancement post-treatment correlated with durable local disease control in this group [64]. In a larger cohort of 74 patients, histogram analysis of K^{trans} skewness was found to be the strongest predictor of progression-free and overall survival by Cox regression analysis of outcome in stage IV nodal metastatic disease [65, 66].

A study of DCE-MRI in 17 patients with metastatic renal cell carcinoma showed that the baseline K^{trans} and percentage change during treatment with the tyrosine kinase inhibitor sorafenib were both significantly associated with progression-free survival ($p = 0.02$ and 0.01, respectively) [67]. In a larger study of 48 patients treated with VEGF inhibitors, high pre-treatment k^{trans} and v_p were found to be strongly associated with improved progression-free survival ($p = 0.02$ and 0.01, respectively) [68]. It is postulated that this association may reflect better drug delivery to tumour in this group [69].

In a further study of 28 patients with metastatic renal cell carcinoma undergoing anti-angiogenic targeted therapy, a positive correlation was found between the change in median peak enhancement of metastatic lesions on DCE-MRI and in median progression-free survival. No such correlation was found between median change in the sum of long diameters of tumour lesions per patient and median PFS [70].

As with other functional imaging techniques, the heterogeneity in voxel signal distribution can be captured and textural aspects interrogated. In a study of 58 patients with locally advanced breast cancer in whom DCE-MRI was carried out pre-treatment, 8 out of 16 textural features assessed at presentation using a grey-level co-occurrence matrix were found to be significantly correlated to pathological response (divided into non-response or minimally residual disease) with an area under the curve (AUC) of 0.77 for entropy measures on the 2-min images, with the inference being that those tumours exhibiting higher entropy are more likely to respond to treatment [71]. There is also data supporting a potential role in imaging textural analysis of tumours in predicting oestrogen receptor positivity and lymph node status with one group finding classification accuracies of 84% (AUC 0.83) for receptor positivity and 88% (AUC 0.88) for lymph node involvement.

Yoon et al. [72] also demonstrated that entropy was a significant predictor of 2-year progression-free survival using Cox regression analysis (hazard ratio 10.98, 95%, CI 1.57–64.57) when measured on the 2-min acquisition of the DCE images [72].

In a study of 33 breast tumours, there was a strong association with fractal dimension and tumour hormone receptor status as well as between fractal fit and subsequent response to therapy [73] in DCE-MRI.

In a group of 95 patients with cerebral glioma, 27 low grade and 68 high grade, the application of filtration-histogram analysis to the preoperative contrast-enhanced MRI sequence yielded a sensitivity and specificity of 93 and 81% (AUC 0.91, $p < 0.0001$) in distinguishing between high- and low-grade tumours [74].

8.5.2 Arterial Spin Labelling (ASL)

This technique involves the use of vascular flow sensitisation with the application of an inversion radiofrequency pulse to label intra-arterial water protons for use as an endogenous contrast agent. Images are acquired before and after the inversion pulse, and a subtracted sequence allows for quantification of tissue perfusion in millilitres per 100 g of tissue per minute [75, 76]. Limitations of the technique include a low signal to noise ratio, necessitating a longer scan time and increased susceptibility to motion artefact [77]. The technique is preferable as it obviates the need for the administration of exogenous contrast medium and therefore eliminates the risk of nephrogenic systemic fibrosis.

Researchers have investigated the use of ASL as a biomarker in distinguishing between grades of intracerebral neoplasms, in a group of 26 patients, 19 with high-grade (WHO 3 or 4) and 7 with low-grade (WHO 1 and 2) tumours. They underwent continuous arterial spin-labelled perfusion imaging with calculation of mean and maximum tumour blood flow (TBF), TBF_{max}, and there was a significant difference in the TBF_{max} normalised to global cerebral blood flow between the high- and low-grade tumours ($p = 0.01$) [78]. A further study of 53 patients with glioblastoma who underwent ASL MRI demonstrated high concordance ($\kappa = 0.89$) between three readers for the evaluation of substantial areas of hyper-perfusion within the tumour. There was a significant association with shorter progression-free survival in this group (median progression-free survival of 182 versus 485 days, $p < 0.01$) as well as with the expression of epidermal growth factor receptor variant III ($p < 0.01$), an oncogene mutation expressed in up to 30% of gliomas which has been linked to chemoresistance [79, 80].

A further advantage of ASL MRI is that it is less vulnerable to susceptibility artefact from haemorrhage which confers a benefit over dynamic susceptibility contrast imaging in particular in the evaluation of treatment response post-surgery. It can be difficult to differentiate radiation necrosis from tumour recurrence in glioblastoma patients. In one study of 30 patients having undergone surgery and proton beam radiotherapy, quantitative assessment of normalised ASL was found to have the highest sensitivity (94%) in discriminating between radiation necrosis and recurrent tumour using a cut-off value of 1.3 calculated as a ratio of mean signal intensity within the tumour region of interest over that in contralateral normal brain parenchyma. This was compared to a sensitivity of 76% for dynamic susceptibility contrast-enhanced MRI and 81% for FDG PET examinations [81, 82].

Arterial spin labelling has also been studied in the setting of response assessment. In a small-scale clinical study of 19 patients on anti-angiogenic bortezomib or lenalidomide therapy for multiple myeloma, a significant correlation (correlation

coefficient = 0.535, p = 0.0037) between the decrease observed in mean tumour perfusion from baseline to week 8 of treatment and the clinical and haematological response observed was demonstrated [83].

These preliminary results indicate that ASL may be a useful tool in disease characterisation, prognostication and response assessment with the ability to assess intra-tumoural heterogeneity. To our knowledge there is no published data examining texture analysis in ASL imaging providing a potential avenue for exploration in the future.

8.5.3 Blood Oxygen Level-Dependent (BOLD) Imaging

Imaging of intrinsic tissue susceptibility relative to oxygenation using a gradient echo sequence to exploit the paramagnetic effect of varying concentrations of intravascular deoxyhaemoglobin and the resultant effect on the signal returned is also being explored as a potential biomarker of disease aggressiveness and response. This is of interest as tumour hypoxia is a known poor prognostic factor. Increasing levels of deoxyhaemoglobin leads to an increase in the T2 relaxation time of a tissue due to the local magnetic field inhomogeneity and effects on spin-spin relaxation of protons. The quantifying measure usually applied is $R2^*$ ($1/T2^*$), calculated from a logarithmic plot of $T2^*$ signal intensity against echo time, and is representative of the signal intensity in a particular voxel [84, 85]. Results will be dependent on the concentration of red blood cells present, and by inference, vascular density and blood flow [86].

The majority of the exploration of BOLD imaging as a biomarker has been in the preclinical setting, but several human studies have emerged in recent years.

In a study of 107 renal masses with corresponding histological confirmation of pathology, 91 were malignant and 16 benign. BOLD MRI of these masses and calculation of the $R2^*$ of the whole lesion found good intra-observer agreement for the measurement using two observers (ICC 0.75, 95%CI 0.69–0.79) with sensitivity and specificity of up to 71% and 78%, respectively, in distinguishing benign from malignant lesions. The area under the curve equalled 0.79/0.78 (observer1/observer2) [87].

A small study of seven women undergoing preoperative neoadjuvant treatment for locally advanced breast cancer utilised BOLD imaging with a 6-minute 100% oxygen breathing challenge at baseline, during and after therapy. The study found that in the three participants who achieved a complete response (CR) to treatment, there was a significantly greater BOLD response to the oxygen breathing challenge at baseline (change in mean signal intensity >12% on oxygen in CR group versus <3% in partial response or stable disease groups, $p < 0.001$). The greatest change in signal was seen within the first 2 min of the breathing challenge [88].

In a group of 24 patients with locally recurrent uterine cervical tumours, one study showed that 22 tumours demonstrated elevated $R2^*$ values when compared to benign or fibrotic lesions. This suggested intratumoral hypoxia and decreased tumour perfusion pre-therapy. Subsequently 18 of those 22 cases showed a significant regression in the hypoxic fraction post-treatment, and there was also a positive

correlation between pre-therapy hypoxia and the decrease in the size of the tumour post-treatment ($p = 0.01$). In three cases non-responsive to treatment, there was a greater chronic hypoxic fraction which did not change post-treatment [89].

Relatively few studies examining the clinical utility of $R2*$ imaging have been carried out in human subjects, and the technique requires further larger-scale investigation for validation.

8.6   Assessment of Tissue Biomechanics

8.6.1   Magnetic Resonance Elastography

The non-invasive quantitative MRI assessment of the mechanical properties of tissue is also possible with MR elastography (MRE). This uses the application of external low-frequency mechanical shear waves, typically 50–60 Hz [76], via a driver and specialised software to measure the propagation of force through tissue. This is visually represented with a colour map output corresponding to levels of tissue stiffness termed viscoelasticity with kilopascals as the unit of measurement. The technique has been applied in the assessment of benign hepatic fibrosis, but there is emerging evidence of promising applications in oncology imaging [90]. Malignant tissue tends to be stiffer than normal structures due to a combination of desmoplasia, altered perfusion biomechanics and increased interstitial pressure [91].

In a study of 44 liver lesions, 13 benign and 31 malignant, there was a significant difference ($p = <0.001$) between the mean shear stiffness of malignant tumours (10.1 kPa) versus benign entities (2.7 kPa), fibrotic liver (5.9 kPa) and normal hepatic parenchyma (2.3 kPa) [92].

In a feasibility study, eight patients with histologically confirmed areas of prostate cancer and ten patients with biopsy-confirmed prostatitis were imaged along with ten healthy volunteers. There was a statistically significant difference in the viscoelasticity of prostate cancer versus prostatitis ($p < 0.01$) and between prostate cancer and normal peripheral zone ($p < 0.01$). There was also a positive correlation between elasticity of the malignant lesions and Gleason score, though sample size is obviously small [93].

8.7   Beyond Functional MRI: Texture Analysis of Standard MRI Images

In clinical practice there has been a resurgent interest in the potential of heterogeneity analysis using texture analysis for standard imaging. These techniques have been shown to be reproducible if good quality control is in place for first-order histogram and some locoregional texture parameters [94].

Histogram and fractal analysis have been applied to standard MRI sequences and found to augment lesion detection, characterisation, prognostication and response assessment.

In the textural analysis of the T2-weighted images, 23 prostate tumours prior to prostatectomy showed a significant correlation between entropy and Gleason score as well as median ADC ($p < 0.05$). Higher-grade tumours (Gleason score 4 + 3) were also found to have significantly higher entropy versus Gleason 3 + 4 tumours [95].

In a pilot study of 15 patients with rectal cancer undergoing T2-weighted imaging pre- and mid-treatment, histogram textural analysis found significantly higher kurtosis in the mid-treatment assessment of subsequent complete responders to treatment, whilst change seen in kurtosis between scans was significantly lower in the non-responder or partial responder groups [96].

The available evidence suggests a potentially important role for texture analysis in lesion characterisation and prognostication across a range of modalities and tumour types.

8.8   Making the Most of Functional MRI in PET/MRI

The wide variety of physiological parameters that can be quantified by MRI lend themselves to a personalised approach in medicine. New developments in computational methods and texture analysis add a further dimension [97]. With more widespread use of combined PET/MRI in cancer imaging, there is an opportunity for more comprehensive tumour assessment. A typical whole-body PET/MRI protocol as performed at the authors' institution is illustrated in Table 8.2.

Data integration from multiple sequences still requires refinement in order to optimise the extraction of relevant additional information from PET/MR images. Novel machine learning techniques have shown promise in facilitating radiomic analysis in larger datasets and could be applied to PET/MRI. One such preclinical

Table 8.2 An example of a typical whole-body PET/MRI protocol at our institution (using a Siemens Healthcare Biograph 3T mMR machine) with the addition of locoregional sequences for a particular area, for example, in multi-parametric imaging of the prostate

PET acquision (simultaneous)		
	Whole body MRI 4-5 stations (~45min)	
		Loco-regional assessment (~15min)
-Localiser sequences -MR attenuation correction map	-T2 weighted single shot turbo spin echo sequence (e.g HASTE half-Fourier single shot turbo spin-echo) -T1 2-point Dixon sequence •In and opposed phase images •Fat only •Water only -Diffusion weighted imaging (b50 and b900)	-High resolution T2 sequence -Dynamic contrast enhanced imaging -High resolution diffusion weighted imaging -MR Spectroscopy

study examining the potential of PET/MRI in advanced tumour phenotyping using voxelwise analysis in a breast cancer model was able to distinguish between differing phenotypes within the same tumour, though the sample size was small ($n = 26$ tumours). The co-registration of ADC maps and ^{18}F-FDG maps and application of Gaussian mixture model clustering allowed for distinction between three separate intra-tumoral phenotypes when compared to the histology of the tumour: solid acinar, solid nodular and cystic hyperplastic regions [98].

Whilst PET/MRI allows an unprecedented integrated approach to tumour morphology, function and phenotype, its impact on clinical outcome and healthcare remains unproven. Further larger-scale comparative studies are required to build the evidence base for the modality's role in the extraction of robust and reproducible tumour biomarkers.

References

1. Jamal-Hanjani M, Quezada SA, Larkin J, Swanton C. Translational implications of tumor heterogeneity. Clin Cancer Res. 2015;21:1258–66. https://doi.org/10.1158/1078-0432. CCR-14-1429.
2. Gerlinger M, McGranahan N, Dewhurst SM, et al. Cancer: evolution within a lifetime. Annu Rev Genet. 2014;48:215–38. https://doi.org/10.1146/annurev-genet-120213-092314.
3. Watson I, Takahashi K, Futreal P, Chin L. Emerging patterns of somatic mutations in cancer. Nat Rev Genet. 2013;14:703–18. https://doi.org/10.1038/nrg3539.Emerging.
4. Chicklore S, Goh V, Siddique M, et al. Quantifying tumour heterogeneity in 18F-FDG PET/CT imaging by texture analysis. Eur J Nucl Med Mol Imaging. 2013;40:133–40. https://doi.org/10.1007/s00259-012-2247-0.
5. Davnall F, Yip CSP, Ljungqvist G, et al. Assessment of tumor heterogeneity: an emerging imaging tool for clinical practice? Insights Imaging. 2012;3:573–89. https://doi.org/10.1007/s13244-012-0196-6.
6. Gillies RJ, Beyer T. PET and MRI: is the whole greater than the sum of its parts? Cancer Res. 2016;76:6163–6.
7. Gillies RJ, Kinahan PE, Hricak H. Radiomics: images are more than pictures, they are data. Radiology. 2015;278:151169. https://doi.org/10.1148/radiol.2015151169.
8. O'Connor JPB, Rose CJ, Waterton JC, et al. Imaging intratumor heterogeneity: role in therapy response, resistance, and clinical outcome. Clin Cancer Res. 2015;21:249–57. https://doi.org/10.1158/1078-0432.CCR-14-0990.
9. Oliver A, Freixenet J, Martí J, et al. A review of automatic mass detection and segmentation in mammographic images. Med Image Anal. 2010;14:87–110. https://doi.org/10.1016/j.media.2009.12.005.
10. Lambin P, Rios-Velazquez E, Leijenaar R, et al. Radiomics: extracting more information from medical images using advanced feature analysis. Eur J Cancer. 2012;48:441–6. https://doi.org/10.1016/j.ejca.2011.11.036.
11. Hatt M, Tixier F, Pierce L, et al. Characterization of {PET/CT} images using texture analysis: the past, the present… any future? Eur J Nucl Med Mol Imaging. 2016;44:151–65. https://doi.org/10.1007/s00259-016-3427-0.
12. Just N. Improving tumour heterogeneity MRI assessment with histograms. Br J Cancer. 2014;111:2205–13. https://doi.org/10.1038/bjc.2014.512.
13. Haralick RM, Shanmugam K, Dinstein I. Textural features for image classification. IEEE Trans Syst Man Cybern. 1973;3:610–21. https://doi.org/10.1109/TSMC.1973.4309314.
14. Srinivasan G, Shobha G. Statistical texture analysis. Proc World Acad Sci Eng Technol. 2008;36:1264–9.

15. Hayano K, Yoshida H, Zhu AX, Sahani DV. Fractal analysis of contrast-enhanced CT images to predict survival of patients with hepatocellular carcinoma treated with sunitinib. Dig Dis Sci. 2014;59:1996–2003. https://doi.org/10.1007/s10620-014-3064-z.

16. Le Bihan D, Breton E, Lallemand D, et al. MR imaging of intravoxel incoherent motions: application to diffusion and perfusion in neurologic disorders. Radiology. 1986;161:401–7. https://doi.org/10.1148/radiology.161.2.3763909.

17. Le Bihan D, Turner R, Douek P, Patronas N. Diffusion MR imaging: clinical applications. Am J Roentgenol. 1992;159:591–9. https://doi.org/10.2214/ajr.159.3.1503032.

18. Bonekamp S, Corona-Villalobos CP, Kamel IR. Oncologic applications of diffusion-weighted MRI in the body. J Magn Reson Imaging. 2012;35:257–79. https://doi.org/10.1002/jmri.22786.

19. Koh D-M, Blackledge M, Padhani AR, et al. Whole-body diffusion-weighted mri: tips, tricks, and pitfalls. Am J Roentgenol. 2012;199:252–62. https://doi.org/10.2214/AJR.11.7866.

20. Lecouvet FE, Talbot JN, Messiou C, et al. Monitoring the response of bone metastases to treatment with magnetic resonance imaging and nuclear medicine techniques: a review and position statement by the European Organisation for Research and Treatment of Cancer imaging group. Eur J Cancer. 2014;50:2519–31. https://doi.org/10.1016/j.ejca.2014.07.002.

21. Padhani AR, Koh D-M, Collins DJ. Whole-body diffusion-weighted MR imaging in cancer: current status and research directions. Radiology. 2011;261:700–18. https://doi.org/10.1148/radiol.11110474.

22. Tanenbaum LN. Clinical 3T MR imaging: mastering the challenges. Magn Reson Imaging Clin N Am. 2006;14:1–15. https://doi.org/10.1016/j.mric.2005.12.004.

23. Koh D-M, Blackledge M, Collins DJ, et al. Reproducibility and changes in the apparent diffusion coefficients of solid tumours treated with combretastatin A4 phosphate and bevacizumab in a two-centre phase I clinical trial. Eur Radiol. 2009;19:2728–38. https://doi.org/10.1007/s00330-009-1469-4.

24. Ma J. Dixon techniques for water and fat imaging. J Magn Reson Imaging. 2008;28:543–58. https://doi.org/10.1002/jmri.21492.

25. Merkle EM, Dale BM, Paulson EK. Abdominal MR Imaging at 3T. Magn Reson Imaging Clin. 2006;14(1):17–26. https://doi.org/10.1016/j.mric.2005.12.001.

26. Benz MR, Vargas HA, Sala E. Functional MR imaging techniques in oncology in the era of personalized medicine. Magn Reson Imaging Clin N Am. 2016;24:1–10. https://doi.org/10.1016/j.mric.2015.08.001.

27. Bollineni VR, Kramer G, Liu Y, et al. A literature review of the association between diffusion-weighted MRI derived apparent diffusion coefficient and tumour aggressiveness in pelvic cancer. Cancer Treat Rev. 2015;41:496–502. https://doi.org/10.1016/j.ctrv.2015.03.010.

28. Curvo-Semedo L, Lambregts DMJ, Maas M, et al. Rectal cancer: assessment of complete response to preoperative combined radiation therapy with chemotherapy – conventional mr volumetry versus diffusion-weighted MR imaging. Radiology. 2011;260:734–43. https://doi.org/10.1148/radiol.11102467.

29. deSouza NM, Riches SF, VanAs NJ, et al. Diffusion-weighted magnetic resonance imaging: a potential non-invasive marker of tumour aggressiveness in localized prostate cancer. Clin Radiol. 2008;63:774–82. https://doi.org/10.1016/j.crad.2008.02.001.

30. Kang SK, Zhang A, Pandharipande PV, et al. DWI for renal mass characterization: systematic review and meta-analysis of diagnostic test performance. Am J Roentgenol. 2015;205:317–24. https://doi.org/10.2214/AJR.14.13930.

31. Manenti G, Di Roma M, Mancino S, et al. Malignant renal neoplasms: correlation between ADC values and cellularity in diffusion weighted magnetic resonance imaging at 3 T. Radiol Med. 2008;113:199–213. https://doi.org/10.1007/s11547-008-0246-9.

32. Hatakenaka M, Nakamura K, Yabuuchi H, et al. Pretreatment apparent diffusion coefficient of the primary lesion correlates with local failure in head-and-neck cancer treated with chemoradiotherapy or radiotherapy. Int J Radiat Oncol. 2011;81:339–45. https://doi.org/10.1016/j.ijrobp.2010.05.051.

33. King AD, Thoeny HC. Functional MRI for the prediction of treatment response in head and neck squamous cell carcinoma: potential and limitations. Cancer Imaging. 2016;16:23. https://doi.org/10.1186/s40644-016-0080-6.

34. Driessen JP, Caldas-Magalhaes J, Janssen LM, et al. Diffusion-weighted MR imaging in laryngeal and hypopharyngeal carcinoma: association between apparent diffusion coefficient and histologic findings. Radiology. 2014;272:456–63. https://doi.org/10.1148/radiol.14131173.

35. Thomas GR, Nadiminti H, Regalado J. Molecular predictors of clinical outcome in patients with head and neck squamous cell carcinoma. Int J Exp Pathol. 2005;86:347–63. https://doi.org/10.1111/j.0959-9673.2005.00447.x.

36. Driessen JP, van Bemmel AJM, van Kempen PMW, et al. Correlation of human papillomavirus status with apparent diffusion coefficient of diffusion-weighted MRI in head and neck squamous cell carcinomas. Head Neck. 2016;38:E613–8. https://doi.org/10.1002/hed.24051.

37. Downey K, Riches SF, Morgan VA, et al. Relationship between imaging biomarkers of stage i cervical cancer and poor-prognosis histologic features: quantitative histogram analysis of diffusion-weighted MR images. Am J Roentgenol. 2013;200:314–20. https://doi.org/10.2214/AJR.12.9545.

38. Lin Y, Li H, Chen Z, et al. Correlation of histogram analysis of apparent diffusion coefficient with uterine cervical pathologic finding. Am J Roentgenol. 2015;204:1125–31. https://doi.org/10.2214/AJR.14.13350.

39. Kuang F, Ren J, Zhong Q, et al. The value of apparent diffusion coefficient in the assessment of cervical cancer. Eur Radiol. 2013;23:1050–8. https://doi.org/10.1007/s00330-012-2681-1.

40. Sala E, Priest AN, Kataoka M, et al. Apparent diffusion coefficient and vascular signal fraction measurements with magnetic resonance imaging: feasibility in metastatic ovarian cancer at 3 tesla technical development. Eur Radiol. 2010;20:491–6. https://doi.org/10.1007/s00330-009-1543-y.

41. Fu C, Feng X, Bian D, et al. Simultaneous changes of magnetic resonance diffusion-weighted imaging and pathological microstructure in locally advanced cervical cancer caused by neoadjuvant chemotherapy. J Magn Reson Imaging. 2015;42:427–35. https://doi.org/10.1002/jmri.24779.

42. Kyriazi S, Collins DJ, Messiou C, et al. Metastatic ovarian and primary peritoneal cancer: assessing chemotherapy response with diffusion-weighted MR imaging – value of histogram analysis of apparent diffusion coefficients. Radiology. 2011;261:182–92. https://doi.org/10.1148/radiol.11110577.

43. Johnston K, Levy AR, Lorigan P, et al. Economic impact of healthcare resource utilisation patterns among patients diagnosed with advanced melanoma in the United Kingdom, Italy, and France: results from a retrospective, longitudinal survey (MELODY study). Eur J Cancer. 2012;48:2175–82. https://doi.org/10.1016/j.ejca.2012.03.003.

44. Padhani AR, Liu G, Koh DM, et al. Diffusion-weighted magnetic resonance imaging as a cancer biomarker: consensus and recommendations. Neoplasia. 2009;11:102–25. https://doi.org/10.1593/neo.81328.

45. García-Figueiras R, Baleato-González S, Padhani AR, et al. Proton magnetic resonance spectroscopy in oncology: the fingerprints of cancer? Diagn Interv Radiol. 2016;22:75–89. https://doi.org/10.5152/dir.2015.15009.

46. Martín Noguerol T, Sánchez-González J, Martínez Barbero JP, et al. Clinical imaging of tumor metabolism with 1H magnetic resonance spectroscopy. Magn Reson Imaging Clin N Am. 2016;24:57–86. https://doi.org/10.1016/j.mric.2015.09.002.

47. Hoeks CMA, Barentsz JJO, Hambrock T, et al. Prostate cancer: multiparametric MR imaging for detection, localization, and staging. Radiology. 2011;261:46–66. https://doi.org/10.1148/radiol.11091822.

48. Griffin JL, Bollard M, Nicholson JK, Bhakoo K. Spectral profiles of cultured neuronal and glial cells derived from HRMAS1H NMR spectroscopy. NMR Biomed. 2002;15:375–84. https://doi.org/10.1002/nbm.792.

49. Abdel Razek AAK, Poptani H. MR spectroscopy of head and neck cancer. Eur J Radiol. 2013;82:982–9. https://doi.org/10.1016/j.ejrad.2013.01.025.

50. Kim MM, Parolia A, Dunphy MP, Venneti S. Non-invasive metabolic imaging of brain tumours in the era of precision medicine. Nat Rev Clin Oncol. 2016;13:725–39. https://doi.org/10.1038/nrclinonc.2016.108.

51. Bian D-J, Xiao E-H, Hu D-X, et al. Magnetic resonance spectroscopy on hepatocellular carcinoma after transcatheter arterial chemoembolization. Chin J Cancer. 2010;29:198–201.

52. Kuo Y-T, Li C-W, Chen C-Y, et al. In vivo proton magnetic resonance spectroscopy of large focal hepatic lesions and metabolite change of hepatocellular carcinoma before and after transcatheter arterial chemoembolization using 3.0-T MR scanner. J Magn Reson Imaging. 2004;19:598–604. https://doi.org/10.1002/jmri.20046.

53. deSouza NM, Soutter WP, Rustin G, et al. Use of neoadjuvant chemotherapy prior to radical hysterectomy in cervical cancer: monitoring tumour shrinkage and molecular profile on magnetic resonance and assessment of 3-year outcome. Br J Cancer. 2004. doi:https://doi.org/10.1038/sj.bjc.6601870.

54. Harry VN. Novel imaging techniques as response biomarkers in cervical cancer. Gynecol Oncol. 2010;116:253–61. https://doi.org/10.1016/j.ygyno.2009.11.003.

55. Lotumolo A, Caivano R, Rabasco P, et al. Comparison between magnetic resonance spectroscopy and diffusion weighted imaging in the evaluation of gliomas response after treatment. Eur J Radiol. 2015;84:2597–604. https://doi.org/10.1016/j.ejrad.2015.09.005.

56. Tofts PS, Kermode AG. Measurement of the blood-brain barrier permeability and leakage space using dynamic MR imaging. 1. Fundamental concepts. Magn Reson Med. 1991;17:357–67.

57. Winfield JM, Payne GS, deSouza NM. Functional MRI and CT biomarkers in oncology. Eur J Nucl Med Mol Imaging. 2015;42:562–78. https://doi.org/10.1007/s00259-014-2979-0.

58. Salem A, O'Connor JPB. Assessment of tumor angiogenesis. Magn Reson Imaging Clin N Am. 2015;24:45–56. https://doi.org/10.1016/j.mric.2015.08.010.

59. Kuhl CK, Mielcareck P, Klaschik S, et al. Dynamic breast MR imaging: are signal intensity time course data useful for differential diagnosis of enhancing lesions? Radiology. 1999;211:101–10. https://doi.org/10.1148/radiology.211.1.r99ap38101.

60. Kuhl CK. The current status of breast imaging part I. Choice of technique, image interpretation, diagnostic accuracy, and transfer to clinical practice. Radiology. 2007;244:356–78. https://doi.org/10.1148/radiol.2442051620.

61. Yuh WTC, Mayr NA, Jarjoura D, et al. Predicting control of primary tumor and survival by DCE MRI during early therapy in cervical cancer. Investig Radiol. 2010;44:343–50. https://doi.org/10.1097/RLI.0b013e3181a64ce9.

62. Mayr NA, Huang Z, Wang JZ, et al. Characterizing tumor heterogeneity with functional imaging and quantifying high-risk tumor volume for early prediction of treatment outcome: cervical cancer as a model. Int J Radiat Oncol Biol Phys. 2012;83:972–9. https://doi.org/10.1016/j.ijrobp.2011.08.011.

63. Chawla S, Kim S, Loevner LA, et al. Prediction of disease-free survival in patients with squamous cell carcinomas of the head and neck using dynamic contrast-enhanced MR imaging. AJNR Am J Neuroradiol. 2011;32:778–84. https://doi.org/10.3174/ajnr.A2376.

64. Hoskin PJ, Saunders MI, Goodchild K, et al. Dynamic contrast enhanced magnetic resonance scanning as a predictor of response to accelerated radiotherapy for advanced head and neck cancer. Br J Radiol. 1999;72:1093–8. https://doi.org/10.1259/bjr.72.863.10700827.

65. Jansen JFA, Parra C, Lu Y, Shukla-Dave A. Evaluation of head and neck tumors with functional MR imaging. Magn Reson Imaging Clin N Am. 2016;24:123–33. https://doi.org/10.1016/j.mric.2015.08.011.

66. Shukla-Dave A, Lee NY, Jansen JFA, et al. Dynamic contrast-enhanced magnetic resonance imaging as a predictor of outcome in head-and-neck squamous cell carcinoma patients with nodal metastases. Int J Radiat Oncol. 2012;82:1837–44. https://doi.org/10.1016/j.ijrobp.2011.03.006.

67. Flaherty KT, Rosen MA, Heitjan DF, et al. Pilot study of DCE-MRI to predict progression-free survival with sorafenib therapy in renal cell carcinoma. Cancer Biol Ther. 2008;7:496–501.

68. Hahn OM, Yang C, Medved M, et al. Dynamic contrast-enhanced magnetic resonance imaging pharmacodynamic biomarker study of sorafenib in metastatic renal carcinoma. J Clin Oncol. 2008;26:4572–8. https://doi.org/10.1200/JCO.2007.15.5655.
69. O'Connor JPB, Jayson GC. Do imaging biomarkers relate to outcome in patients treated with VEGF inhibitors? Clin Cancer Res. 2012;18:6588–98.
70. Panebianco V, Iacovelli R, Barchetti F, et al. Dynamic contrast-enhanced magnetic resonance imaging in the early evaluation of anti-angiogenic therapy in metastatic renal cell carcinoma. Anticancer Res. 2013;33:5663–6.
71. Teruel JR, Heldahl MG, Goa PE, et al. Dynamic contrast-enhanced MRI texture analysis for pretreatment prediction of clinical and pathological response to neoadjuvant chemotherapy in patients with locally advanced breast cancer. NMR in Biomed. 2014;27(8):887–96. https://doi.org/10.1002/nbm.3132.
72. Yoon SH, Park CM, Yoon J-H, et al. Tumor heterogeneity in lung cancer: assessment with dynamic contrast-enhanced MR imaging. Radiology. 2016;280:940–8.
73. Di Giovanni P, Ahearn TS, Semple SIK, et al. The biological correlates of macroscopic breast tumour structure measured using fractal analysis in patients undergoing neoadjuvant chemotherapy. Breast Cancer Res Treat. 2012;133:1199–206. https://doi.org/10.1007/s10549-012-2014-8.
74. Skogen K, Schulz A, Dormagen JB, et al. Diagnostic performance of texture analysis on MRI in grading cerebral gliomas. Eur J Radiol. 2016;85:824–9. https://doi.org/10.1016/j.ejrad.2016.01.013.
75. de Leon AD, Costa D, Pedrosa I. Role of multiparametric {MR} imaging in malignancies of the urogenital tract. Magn Reson Imaging Clin N Am. 2016;24:187–204. https://doi.org/10.1016/j.mric.2015.08.009.
76. Luna A, Pahwa S, Bonini C. Multiparametric MR Imaging in abdominal malignancies. Magn Reson Imaging Clin N Am. 2016;24:157–86. https://doi.org/10.1016/j.mric.2015.08.005.
77. Grade M, Hernandez Tamames JA, Pizzini FB, et al. A neuroradiologist's guide to arterial spin labeling MRI in clinical practice. Neuroradiology. 2015;57:1181–202. https://doi.org/10.1007/s00234-015-1571-z.
78. Wolf RL, Wang J, Wang S, et al. Grading of CNS neoplasms using continuous arterial spin labeled perfusion MR imaging at 3 tesla. J Magn Reson Imaging. 2005;22:475–82. https://doi.org/10.1002/jmri.20415.
79. Nagane M, Levitzki A, Gazit A, et al. Drug resistance of human glioblastoma cells conferred by a tumor-specific mutant epidermal growth factor receptor through modulation of Bcl-XL and caspase-3-like proteases. Proc Natl Acad Sci U S A. 1998;95:5724–9.
80. Qiao XJ, Ellingson BM, Kim HJ, et al. Arterial spin-labeling perfusion MRI stratifies progression-free survival and correlates with epidermal growth factor receptor status in glioblastoma. Am J Neuroradiol. 2015;36:672–7. https://doi.org/10.3174/ajnr.A4196.
81. Haller S, Zaharchuk G, Thomas DL, et al. Arterial spin labeling perfusion of the brain: emerging clinical applications. Radiology. 2016;281:337–56. https://doi.org/10.1148/radiol.2016150789.
82. Ozsunar Y, Mullins ME, Kwong K, et al. Glioma recurrence versus radiation necrosis? A pilot comparison of arterial spin-labeled, dynamic susceptibility contrast enhanced MRI, and FDG-PET imaging. Acad Radiol. 2010;17:282–90. https://doi.org/10.1016/j.acra.2009.10.024.
83. Fenchel M, Konaktchieva M, Weisel K, et al. Early response assessment in patients with multiple myeloma during anti-angiogenic therapy using arterial spin labelling: first clinical results. Eur Radiol. 2010;20:2899–906. https://doi.org/10.1007/s00330-010-1870-z.
84. Chopra S, Foltz WD, Milosevic MF, et al. Comparing oxygen-sensitive MRI (BOLD R2*) with oxygen electrode measurements: a pilot study in men with prostate cancer. Int J Radiat Biol. 2009;85:805–13. https://doi.org/10.1080/09553000903043059.
85. Glover GH. Overview of functional magnetic resonance imaging. Neurosurg Clin N Am. 2011;22:133–9. https://doi.org/10.1016/j.nec.2010.11.001.

86. Ammari S, Thiam R, Cuenod CA, et al. Radiological evaluation of response to treatment: application to metastatic renal cancers receiving anti-angiogenic treatment. Diagn Interv Imaging. 2014;95:527–39. https://doi.org/10.1016/j.diii.2013.01.019.

87. Wu G-Y, Suo S-T, Lu Q, et al. The value of blood oxygenation level-dependent (BOLD) MR imaging in differentiation of renal solid mass and grading of renal cell carcinoma (RCC): analysis based on the largest cross-sectional area versus the entire whole tumour. PLoS One. 2015;10:e0123431. https://doi.org/10.1371/journal.pone.0123431.

88. Jiang L, Weatherall PT, Mccoll RW, et al. Blood oxygenation level-dependent (BOLD) contrast magnetic resonance imaging (MRI) for prediction of breast cancer chemotherapy response: a pilot study. J Magn Reson Imaging. 2013;37:1083–92. https://doi.org/10.1002/jmri.23891.

89. Mahajan A, Engineer R, Chopra S, et al. Role of 3T multiparametric-MRI with BOLD hypoxia imaging for diagnosis and post therapy response evaluation of postoperative recurrent cervical cancers. Eur J Radiol Open. 2016;3:22–30. https://doi.org/10.1016/j.ejro.2015.11.003.

90. Mariappan YK, Glaser KJ, Ehman RL. Magnetic resonance elastography: a review. Clin Anat. 2010;23:497–511. https://doi.org/10.1002/ca.21006.

91. Pepin KM, Ehman RL, McGee KP. Magnetic resonance elastography (MRE) in cancer: technique, analysis, and applications. Prog Nucl Magn Reson Spectrosc. 2015;90–91:32–48.

92. Venkatesh SK, Yin M, Glockner JF, et al. MR elastography of liver tumors: preliminary results. Am J Roentgenol. 2008;190:1534–40. https://doi.org/10.2214/AJR.07.3123.

93. Li S, Chen M, Wang W, et al. A feasibility study of MR elastography in the diagnosis of prostate cancer at 3.0T. Acta Radiol. 2011;52:354–8. https://doi.org/10.1258/ar.2010.100276.

94. Gourtsoyianni S, Doumou G, Prezzi D, Taylor B, Stirling JJ, Taylor NJ, Siddique M, Cook GJ, Glynne-Jones R, Goh V. Repeatability of global and locoregional magnetic resonance imaging (MRI) texture features in primary rectal cancer. Radiology. 2017;284:552–61.

95. Nketiah G, Elschot M, Kim E, et al. T2-weighted MRI-derived textural features reflect prostate cancer aggressiveness: preliminary results. Eur Radiol. 2016;27:3050–9. https://doi.org/10.1007/s00330-016-4663-1.

96. De Cecco CN, Ganeshan B, Ciolina M, et al. Texture analysis as imaging biomarker of tumoral response to neoadjuvant chemoradiotherapy in rectal cancer patients studied with 3-T magnetic resonance. Investig Radiol. 2015;50:239–45. https://doi.org/10.1097/RLI.0000000000000116.

97. Cook GJR, Siddique M, Taylor BP, et al. Radiomics in PET: principles and applications. Clin Transl Imaging. 2014;2:269–76. https://doi.org/10.1007/s40336-014-0064-0.

98. Schmitz J, Schwab J, Schwenck J, et al. Tumor and stem cell biology decoding intratumoral heterogeneity of breast cancer by multiparametric in vivo imaging: a translational study. Cancer Res. 2016;76(18):5512–22. https://doi.org/10.1158/0008-5472.CAN-15-0642.

Workflow and Protocol Considerations

9

Ambros Beer and Patrick Veit-Haibach

Contents

9.1 Introduction

PET and MRI are clinically available for roughly 25 years and both modalities are very well established in clinical practice. The clinical introduction of combined PET/CT was the foundation of the success of hybrid imaging. However, the last decades were also marked by great improvements in MRI as an imaging modality of great clinical importance not only for morphological imaging but also functional imaging.

A. Beer (✉)
Klinik für Nuklearmedizin, Universitätsklinikum Ulm, Ulm, Germany
e-mail: Ambros.Beer@uniklinik-ulm.de

P. Veit-Haibach
Joint Depatment Medical Imaging, University Health Network, University of Toronto, Toronto, Canada
e-mail: patrick.veit-haibach@uhn.ca

151

Running a dual-modality hybrid system is significantly different from running stand-alone systems side-by-side. The combination of PET and CT into one-hybrid system certainly brought up several technical challenges; however, those were solved efficiently in a relative short time. In comparison, the integration of PET detectors into an MRI is significantly different. Standard photomultipliers are not compatible with magnetic fields normally used in MRI, and there is mutual interference of the MRI magnetic fields and the PET detectors concerning image quality in many ways. This issue was addressed by developing integrated PET/MRI systems, which "protects" one imaging modality from the other and using a new and technologically different generation of PET detectors (see corresponding chapters in this book). However, a different nontechnical challenge is now to operate PET/MRI in an efficient way to potentially move it from a research tool into a valuable clinical addition in hybrid imaging. This needs dedicated hybrid imaging concepts and workflow considerations.

The current chapter discusses the main issues concerning simultaneous PET/MRI system workflow and some specific imaging applications to help the readers understand the needs and requirements for clinically effective PET/MRI and the differences when compared with PET/CT – and MR – stand-alone imaging.

9.2 Workflow Scenarios: General Strategies

PET/MRI protocols all share some common aspects. First, MRI localizers have to be acquired (corresponding to the scout scan or topogram in PET/CT) to plan the subsequent acquisition and define the axial range for the joint PET/MRI examination. Next, the number and localization of bed positions of the PET acquisition have to be defined using the localizer. PET usually works in the so-called step-and-shoot mode, in which the two main acquisition parameters to be defined are the number of bed positions and the acquisition time for each bed position. In the scanners currently used, the axial range of a single bed position is about 25 cm, with a certain percentage of overlap between adjacent bed positions (depending on the vendor). The acquisition time can either be kept similar to that in PET/CT, typically 2–4 min per bed position, or this time can be increased to make use of the potentially longer time required for the simultaneous MRI sequences. Similar to PET/CT, the PET data can either be acquired in a dynamic way as list-mode data or as a static acquisition. In principle, it is also feasible to acquire PET and MRI data while the patient bed is continuously moving, as recently described for combined PET/MRI [1]. This extremely interesting approach might substantially facilitate the workflow for whole-body PET/MRI but is not yet routinely integrated in currently used PET/MRI systems. The major technical advantage is the reduction in sensitivity "drop" at the edges of the field of view, which should in theory also result in a more flexible acquisition time. However, also an improvement concerning psychological burdens has been described. Claustrophobic patients seem to appreciate the continuous motion as it actually suggests an ongoing procedure instead of "waiting" for the next bed position.

The time needed for the PET acquisition can then be used to acquire the needed MRI data for each bed position. There is only one mandatory MRI sequence, which

is the one used for attenuation correction (AC) as the attenuation data in PET/MRI are derived from the MRI scan [2]. This sequence is usually acquired first for each bed position. There are various techniques used for AC in PET/MRI, but most commonly a two-point or three-point Dixon sequence is used. A separate breath-hold acquisition is necessary for each bed position, which usually takes about 14–19 s per bed position for higher-resolution T1 imaging. This sequence is preceded by scanning preparations that include shimming to optimize the homogeneity of the magnetic field. The MRI data are then segmented to identify air, lung tissue, fatty tissue, and watery tissue as required for AC [3]. The Dixon sequence has been found valuable for anatomic localization of PET-positive lesions, as the sequence is acquired over the whole field of view (i.e., all PET bed positions) and can be nearly isotropic [4]. Other approaches in use for MRI-based AC are using a three-dimensional T1-weighted sequence as in the sequential PET/MRI scanner [5]. However, one major disadvantage of these techniques is that the bone is neglected, which might be of special relevance in areas with a high density of the bone like the skull or the pelvis. To partly compensate for that problem, one vendor is currently using a CT atlas for the attenuation correction of the head. One potential, more general solution to this problem is the use of an ultrashort echo time/zero echo time sequence to identify bone, like used routinely in one system for the skull and brain imaging [6]. Moreover, other atlas-based techniques can be used for identification of the bones [7]. There are also now different region-specific solutions being developed [8], as well as there are intentions to use zero echo time imaging for whole-body attenuation correction.

After acquisition of the data for AC, the MRI component can be used to acquire any further sequences within the current field of view, simultaneously with the corresponding PET acquisition, which runs in parallel. Currently there are no restrictions in the choice of MRI sequences in hybrid PET/MRI scanners. The MRI sequences can also extend beyond the PET acquisition time planned for the current bed position, with the rest of the examination being consequently delayed.

Thus, the length of the MRI protocol mainly defines the total duration of an oncologic PET/MRI examination. Moreover, the choice of the right MRI protocol in PET/MRI is the most complex part of workflow optimization, due to the wide variety of MRI sequences available, due to the different techniques and acronyms of the various vendors, and due to sometimes lack of standardization of MRI protocols for a given indication between centers. We will now give an overview of the basic choices one has to make concerning PET/MRI workflows in oncology including suggestions for specific protocols for the most common oncological indications.

For oncologic PET/MRI in clinical routine, one can envision three main scenarios that have important implications concerning scan time, complexity of the acquired MRI data, and consequently also complexity of image analysis and reading/reporting of the PET/MRI scan:

First stand-alone PET/MRI protocols, which should answer all relevant questions, independent of other potentially available/planned examinations. Either, these can be fully diagnostic, with correspondingly longer scan times and greater complexity

of the MRI protocols. This would be like a fully diagnostic PET/CT with contrast-enhanced and potentially multiphasic CT protocols, or these protocols can be focused on the PET part with only a minimal set of basic MRI sequences but also requiring less scan time. This approach is very similar to a low-dose unenhanced PET/CT, thus sometimes referred to as "low-dose PET/MRI" (which of course literally does not make sense, but which is a good term to keep in mind).

Second "PET/CT-guided" PET/MRI protocols. In centers having access to both PET/CT and PET/MRI, it might in certain cases make sense to first perform a standard PET/CT with diagnostic CT and then focus on only one specific area of interest with PET/MRI, depending on the clinical question. Such a scenario could, e.g., be useful in primary staging of cervical cancer, focusing just on the primary tumor/pelvis with PET/MRI.

Third "CT-guided" PET/MRI protocols. This is interesting in cases where a PET is warranted/indicated but when there is also already extensive CT imaging for staging available and only very specific questions for MRI left. Thus, one can focus on the PET part for the whole-body examination ("low-dose PET/MRI") and add only a few specific MRI sequences on one region of interest, like e.g., brain imaging in primary staging for lung cancer.

Finally outside clinical routine and simple staging/restaging workflow scenarios, one of the most interesting aspects of PET/MRI is of course the ability to acquire a multitude of quantitative data for characterization of tumor biology and physiology simultaneously/near simultaneously from both PET and MRI. Thus in the fourth part of this chapter, we present an outlook on potential region-specific scan protocols to make maximum use of the true power of PET/MRI as a novel and innovative stand-alone "imaging biomarker."

9.2.1 Stand-Alone PET/MRI Protocols

9.2.1.1 PET-Focused PET/MRI ("Low-Dose PET/MRI")

This approach is very similar to the scenario, when only a standard, low-dose, and unenhanced PET/CT is needed. Such a basic protocol has a similar imaging time compared with that of PET/CT, however, with the advantage of less radiation exposure and potential diagnostic benefits in some areas from the MR, even if only a few basic sequences are performed.

It might be useful, for example, for follow-up studies to evaluate therapy response in known lesions like in Hodgkin's lymphoma and in young patients, where minimizing radiation exposure is of special relevance. MRI pulse sequences in such protocols are limited basically to the sequences required for AC and additional higher-resolution axial T1w Dixon and coronal or axial fast T2w sequences (e.g., short-tau inversion recovery or fast-recovery fast spin echo). These sequences can be done truly simultaneously with PET and within a PET acquisition segment of only 2–3 min. In a large study with more than 100 patients evaluating the overall diagnostic accuracy of a limited, non-contrast-enhanced PET/MRI protocol, the overall diagnostic accuracy was comparable to that of PET/CT [9]. Other large

patient studies have shown the same diagnostic accuracy of such limited protocols compared to PET/CT, too [10].

In the future another option might be to extend the length of the two-point Dixon AC sequence to the length of the PET measurement and skipping all other MRI sequences. The advantage would be to have a near isotropic sequence with improved spatial resolution covering the whole scan area, which is ideal for image fusion with the PET data in all three planes. Moreover, the Dixon technique provides multiple contrasts (water only, fat only, in-phase, opposed phase), which is well suited for anatomical localization of PET-positive lesions and might even provide important diagnostic information, e.g., differentiation of thymic rebound from lymphoma, differentiating adrenal metastases from adenomas, or concerning the bone marrow when looking for bone metastases/lymphoma involvement.

Adding more MRI pulse sequences or additionally using MRI contrast media would only extend the examination time and might mostly provide redundant information because the main determinants of therapy response are adequately evaluated with such a limited protocol, namely, reduction of tracer uptake and morphologic changes in lesion size. An example is presented in (Fig. 9.1).

9.2.1.2 Fully Diagnostic PET/MRI Protocol

If patients present without extensive previous imaging data, complete diagnostic coverage of the partial or whole body and specific areas of interest might be required, especially for primary staging.
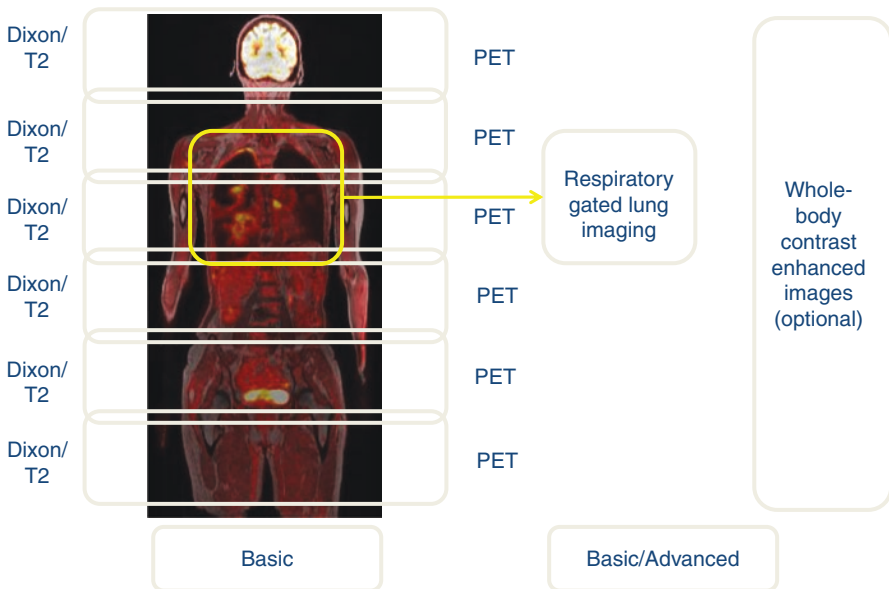

Fig. 9.1 Schematic diagram of a basic (and partly advanced) PET/MR-protocol. The left part represents the described "basic" PET/MR protocol where only T1- sequences and T2-sequences are acquired simultaneously with PET. Additionally, "basic" protocols using a respiratory-gated sequence for the lung and a quick, whole-body postcontrast acquisition have been described too

However, covering the whole body (WB) with adequate diagnostic MRI sequences is time-consuming. Current standard WB MRI may take up to 60 min, which is substantially longer compared to standard PET/CT, which can be done nowadays usually between 10 and 20 min. Thus, if the MRI time considerably exceeds the PET time, a PET/MRI is mostly used as for a quite expensive MRI acquisition because only the minority of imaging/acquisition time would be used with true simultaneity. Imaging protocols in PET/MRI therefore need to be optimized with regard to the specific needs of hybrid imaging to achieve the highest diagnostic accuracy in a reasonable timeframe. This optimization is complex but possible because a hybrid system in many ways is more than just the sum of two parts—it is a genuine novel "single" modality. Thus sensitivity and specificity do not have to be optimized for each component individually but jointly for the hybrid system. In fact, as information coming from both components can be either complementary, confirmatory, or redundant, any protocol for a hybrid PET/MRI needs to try to minimize redundant information. Obviating those MRI pulse sequences which might make sense in a conventional WB MRI protocol, but which only provide redundant information with regard to the now available additional PET information in PET/MRI, is able to comply to this specific imaging needs. Of course, many protocols or individual variations are feasible, but the workflow scenarios we will describe in the next section encompass most adult oncologic examinations currently performed on the majority of PET/MRI systems, trying to gather the maximum amount of information from MRI and PET within a reasonable total examination time, avoiding redundancy 10.

Full diagnostic staging protocols in oncology can cover either the head to the toes (*whole body*) or the base of the skull to the mid-thigh (*partial body*), comparable to PET/CT, along with specific regions of interest depending on the patient's diagnosis.

For certain indications, true whole-body coverage from head to toe or assessment of the central nervous system is mandatory as, for example, in melanoma patients or lung cancer patients. In these cases, protocols with four to six bed positions and between 2–5 min each covering the torso and three to five additional bed positions of 2 min each covering the legs (depending on the size of the patient) have so far been used.

During this time, usually axial and/or coronal T1w and T2w (with or without fat saturation) are acquired simultaneously during the PET acquisition. For melanoma or tumors known to metastasize in unusual patterns, T2w sequences with fat sat (or equivalent) are often used as they better highlight soft tissue lesions such as small lymph nodes or cutaneous lesions from an MR standpoint. Then, full diagnostic MRI is performed only for liver or for central nervous system coverage. For the lungs there are so far rather restricted protocols used since in patients with suspicion for/proven lung cancer, a recent chest CT should be available before staging with PET/MRI. However, several sequences (respiratory gated and consecutive PET-gating, UTE/ZTE) are currently under evaluation [11].

Such "fully diagnostic" MRI protocols are, however, time-consuming and partly require 60–70 min of MR scanning time (depending on the size and compliance of the patient), despite the advantage of having an integrated system. Alternatively, one could acquire in addition to the basic axial and/or coronal T1w and T2w sequence the body stem only with quick axial T1w Dixon sequences after administration of IV contrast, skipping all other lengthier MRI sequences and more relying on the PET information. This could be done, e.g., in most pediatric oncological scenarios and many other indications to shorten the scan time.

For (mostly used) *partial-body* examinations, four to five PET bed positions are usually required to cover the area from the base of the skull to the upper thigh, with an acquisition time of about 2–5 min per bed position. Depending on the used PET/MRI system, this might be slightly longer than in the first described PET-focused (or "low-dose") PET/MRI scenario but gives enough time to obtain additional diagnostic MRI sequences after the mandatory AC sequence. In our experience, the maximum information for most indications in oncology can be obtained in the available limited time by combining a breath-hold axial and/or coronal T1-weighted TSE (or breath-hold higher-resolution Dixon sequence) and a fast axial and/or coronal T2-weighted sequence, either with or without fat saturation. Depending on the patient's compliance and size, this part usually takes about 15–25 min. With this "basic" protocol, unenhanced T1- and T2-weighted sequences are obtained in two planes, allowing both diagnosis of bone metastases and denomination of conditions such as simple cysts or enlarged lymph nodes. Reconstructions of the in-phase image of a Dixon sequence in the sagittal planes are then especially helpful for assessment of bone lesions in the spine [11, 12].

This initial (basic) part of the partial-body examination is followed by imaging of a specific region of interest determined by the clinical question. Here several prominent areas of evaluation have been reported in the literature: head and neck cancer, primary tumors of the upper abdomen (liver, pancreas), liver metastases, and gynecological indications (Fig. 9.2).
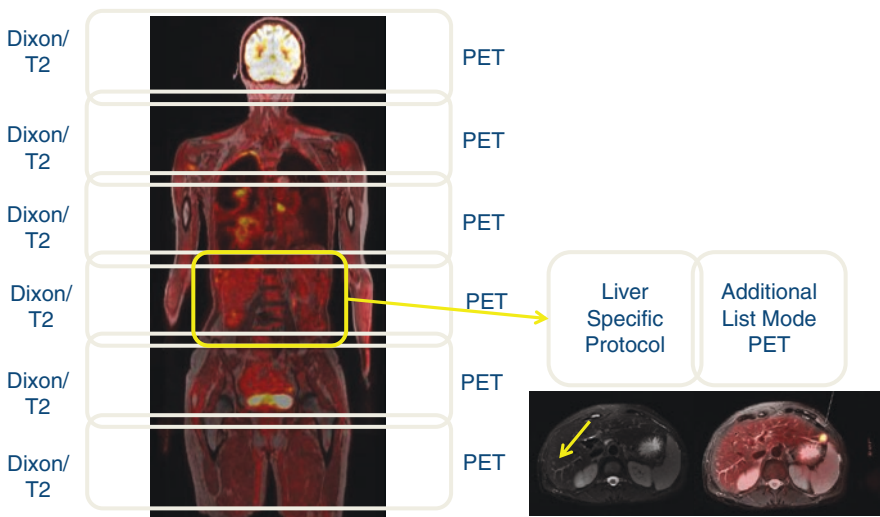
Fig. 9.2 Schematic diagram of a diagnostic PET/MR-protocol, here an example for a fully diagnostic MR-protocol of the liver. First, the "basic" part of the PET/MR is acquired (*left part of the diagram*), afterwards, a fully diagnostic MRprotocol in the area of interest is acquired (*right part of the diagram*). In addition to that, a longer PET-acquisition in this area can be acquired, too. In this case, a small hepatic metastases in the right liver lobe (*yellow arrow*) is additionally diagnosed to the PET-positive liver metastases in the left liver lobe

In those scenarios, often a list-mode of 15–20-min PET with simultaneous acquisition of a dedicated MRI protocol focused on the specific region is performed. For example, patients with head and neck cancer or thyroid cancer would undergo dedicated contrast-enhanced MRI of the neck, providing information relevant for local and lymph node staging or for assessment of tumor recurrence, respectively [14–19].

Finally, a contrast-enhanced axial fat-saturated T1-weighted sequence of the torso can be amended; hence this is not necessary (depending on the examined disease) in all indications since the "basic" protocol (together with the PET component) would be sufficient for detection of most of the anticipated metastases.

However, as a general diagnostic limitation of all the mentioned protocols, the inferiority of conventional MRI, in comparison with CT, for detecting small pulmonary nodules and assessing subtle parenchymal changes should be kept in mind. Rauscher et al. showed better accuracy for small pulmonary nodules with the contrast-enhanced, T1w VIBE sequence when compared with the AC sequence, however, still with substantial limitations concerning the sensitivity for lung lesion smaller than 1 cm [20]. An unenhanced low-dose CT scan of the lungs might be added until systematic studies have addressed in more detail the performance of PET/MRI for evaluation of small lung metastases.

More specific MRI protocols in addition to the sequences described above, such as respiration-triggered or respiration-gated MRI sequences, could also be included. However, these protocols may be time-consuming and probably can be efficiently applied only for specific lung-evaluation indications. In this respect, simultaneously respiratory-gated PET/MRI acquisition can improve the accuracy for small lung lesions, e.g., a respiratory-gated sequence for the chest and upper abdomen (e.g., T2 PROPELLER) or navigator-based imaging for the chest can be added to the WB T2w imaging. In one study, a limited protocol including a respiratory-gated sequence for the chest showed the same diagnostic accuracy as that of PET/CT, even for pulmonary lesions [21]. It has to be mentioned that even this protocol still detects fewer pulmonary lesions compared to CT, however, comprising mostly small lesions of uncertain diagnostic relevance [4]. Other publications however found that, if only the AC is used for anatomical imaging, the in-phase reconstruction is actually the best for pulmonary nodule detection [22].

Another potential limitation of the described protocols is that except for liver-focused scenarios, the liver is imaged only in the venous equilibrium phase, thus making detection of small liver lesions somewhat difficult. However, for some common PET/MRI indications like in prostate cancer or thyroid cancer, liver metastases are rare and, when occurring, are usually within the context of diffuse metastatic disease and not single small lesions. In other common PET/MRI indications like head and neck cancer, liver metastases can occur despite being relatively rare. However, the lack of portal-venous contrast-enhanced MRI information about the liver may be compensated by the available 18F-FDG PET data, which have been demonstrated to be highly sensitive for assessment of metastatic disease, including liver lesions in patients with head and neck cancer [23]. Ultimately, when the liver is the focus of the examination (e.g., detection or characterization of small liver lesions), a liver-specific protocol can be performed within the context of PET/

MRI. For the sake of timing issues, it should be then, however, considered to run the above-described "basic protocol" for whole-body evaluation, especially when liver-specific contrast media is used (see also below).

The use of whole-body DWI in PET/MRI protocols is being discussed controversially. Some publications showed value of DWI in staging or restaging lung, head and neck, gynecologic, and colorectal cancer as well as lymphoma [24–27]. However, WB DWI is time-consuming, and it has been documented that information obtained from DWI is partly redundant to PET imaging, for example, in head and neck cancers, not adding significant diagnostic value [17]. Overall, it is currently unclear in which indications DWI should be used in the context of PET/MRI. There might be rules during follow-up examinations, where radionuclide uptake is decreased and diagnostic evaluation therefore has to be based more on the MRI component. Additionally, with the advent of multiband DWI, which can significantly accelerate acquisition times, adding DWI might be less time-consuming and therefore could be integrated into a PET/MRI protocol for better advantage.

For head and neck cancer staging, additional T1 and T2, diffusion-weighted, and contrast-enhanced T1w images may be acquired in different planes, adding approximately 20–30 min to the basic protocol (ca. 45 min total study time). As an additional option, a dedicated PET acquisition can be done during the additional MRI, resulting in higher image quality. As indicated earlier, this scenario should be used for primary staging, and the situation is different for surveillance or after systemic treatment. Although data from single-modality imaging studies support the importance of DWI for such a patient population, initial data demonstrated that DWI offers mostly redundant clinical information compared with that by PET [17, 28].

For patients with the focus on potential liver metastases, such as from breast cancer, colorectal cancer, or neuroendocrine tumors, dedicated MRI of the liver including dynamic contrast-enhanced sequences and diffusion-weighted imaging should be performed. Especially, diffusion-weighted imaging has evolved over the last few years to be a sensitive tool for detection of liver lesions and is superior to 18F-FDG PET for lesions smaller than 1 cm [29]. Dynamic contrast-enhanced MRI is also a sensitive method and is useful for lesion classification as well [30]. In the context of PET/MRI, it has been shown that the DWI again is not needed, since no advantage was found when T1w sequences, respiratory-gated T2w sequences, dynamic contrast enhancement, and the PET component performed [31].

Concerning the choice of contrast media, there is a large body of literature available showing the superiority of dinatriumgadoxetat (Primovist) in detection and characterization of liver lesions. It remains to be seen if that is still the case for liver metastases in PET/MRI, where the additional PET component adds already substantial information on the characterization of these lesions. Additionally, simultaneous respiratory gating can be used to increase PET image quality, especially for small lesions.

A different scenario applies to liver tumors (hepatocellular carcinoma [HCC] and cholangiocellular carcinoma), where the (18F-FDG)-PET component frequently does not help to identify and characterize the tumor (e.g., well-differentiated HCC), and the MRI would definitively be the leading imaging component. However,

the differentiation of dysplastic liver nodules and early- or well-differentiated HCC is complicated even in MRI with dinatriumgadoxetat. Combined PET/MRI with different tracers (18F-choline and 11C-acetate) might actually be helpful in the evaluation of these "borderline" cases [32–37].

In pelvic oncology protocols, adding a 3D isotropic T2w image sequence of the pelvis is recommended for better anatomical assessment of disease extent, rather than high-resolution multiplanar acquisitions [37]. From such a data set, different imaging planes of the pelvis can be reconstructed, depending on the disease to be imaged (uterus, cervix, and ovaries). Since this certainly takes some time, an additional PET frame with extended acquisition time can be performed for enhanced PET image quality here, too.

In restaging of prostate cancer, again the 15–20-min PET acquisition of the pelvis is accompanied by dedicated MRI sequences of this region. To be more specific, a T2-weighted axial sequence is acquired to provide excellent anatomic detail. Diffusion-weighted imaging and dynamic contrast-enhanced MRI are performed mostly for evaluation of small local recurrences. Recent data imply that dynamic contrast-enhanced MRI is especially valuable for this purpose, as areas of local recurrence usually show early and intense contrast enhancement, whereas in later phases scar tissue might also enhance, thus making detection of small tumors in the prostate bed difficult.

9.2.2 "PET/CT-Guided" PET/MRI

As explained before in "PET/CT-guided" PET/MRI protocols, first a conventional PET/CT scan for staging would be performed, followed by only one bed position in PET/MRI, focusing on one or two body compartments (e.g., chest, liver, or even the whole abdomen) of interest according to the specific clinical question. Such a scenario could make sense, e.g., in primary staging of malignancies of the pelvis in general, like cervical/endometrial cancer, rectal cancer, or prostate cancer, as MRI can provide synergistic information to PET and CT in this area (Fig. 9.3). Moreover, in many cases, MRI would be part of routine staging anyhow, so the time needed for the MRI can be used for the PET/MRI, and there is no additional scan time needed for the PET component.

Also in sarcoma patients, this strategy might make sense, as MRI is part of the standard workup anyway, and for FDG-PET it is known that standardized uptake value measurements can partly differentiate low-grade from high-grade tumors and have a prognostic value in sarcomas [38, 39]. Therefore, the benefits of MRI with its high accuracy in local staging and the benefits of PET, e.g., with the possibility to guide diagnostic biopsies could be combined and, thus, supporting correct staging, grading, and possibly also prediction and follow-up stratification. Another usefulness clinical application is therapeutic response assessment, again especially in soft tissue sarcomas [40]. However, there are many other cancer entities, which would benefit from these imaging capabilities, e.g., neuroendocrine tumors, pancreatic cancer, or primary hepatic cancers. Some possible/future indications will be discussed at the end of this book. If the patients undergo neoadjuvant therapy, like e.g., in rectal cancer or in some cases of sarcomas, then just PET/MRI over the tumor
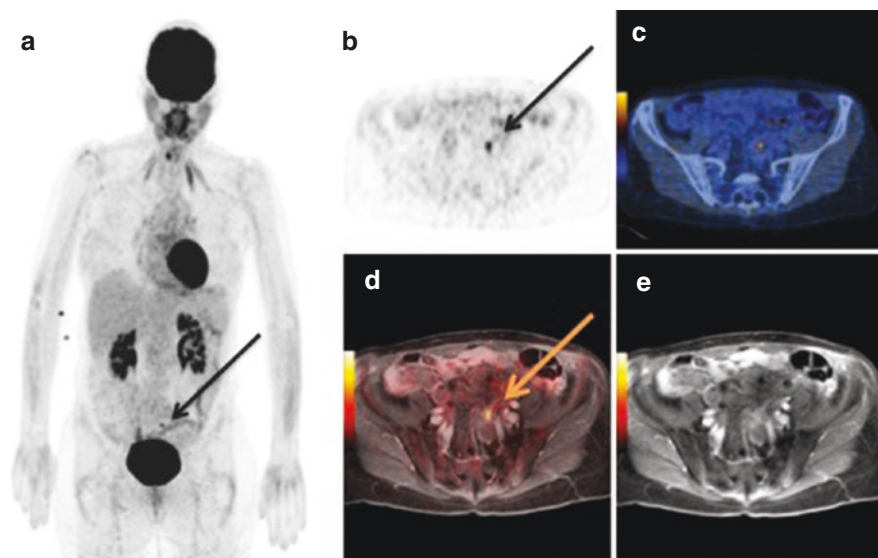
Fig. 9.3 PET/CT of a female patient with suspected gynaecological tumour. Only a very small FDG-avid lesion is seen on the MIP (**a**) and axial PET (**b**). On the PET/CT (**c**), identifying the anatomical localization of this lesion is challenging. The PET/MR and contrast enhanced MR (**d** and **e**) showing the lesion to be in the left ovarian tube

region could be repeated for response evaluation, which would take only about 20 min scan time.

In another scenario, PET/MRI would not specifically be used in a "PET/CT-guided PET/MRI" context but as a general problem-solving tool after single-modality imaging (CT or MR). Examples here could be equivocal lesions of the cervix, uterus, or ovaries and pancreatic lesions of uncertain significance or patients which had an MRI of the prostate or the breast and are rated as PRIRADS/BIRADS III. Here, PET/MRI with rather low doses could be performed to gain more information about the lesion in question [41].

9.2.3 "CT-Guided" PET/MRI

"CT-guided" PET/MRI protocols might be interesting in cases where a PET is indicated, when there is already complete CT imaging for staging available, and only very specific questions for MRI left. Thus, one can focus on the PET part for the whole-body examination ("low-dose PET/MRI") and add only a few specific MRI sequences on the special region of interest, depending on the specific clinical scenario. The advantage of such a protocol is that it is very efficient, as the PET/MRI itself only takes a little longer than a PET/CT, maybe 30 min compared to 20 min, and that the time needed for the MRI is already covered as well, so no second scan slot on a different scanner is necessary. Such a scenario can therefore be beneficial from a logistical and economical point of view.

One potential scenario is in colorectal cancer patients in whom a solitary liver metastasis is found on staging CT. In this patient, a resection of the liver metastasis might be indicated, and to complete staging, MRI of the liver would be requested to rule out further liver lesions and low-dose PET/CT to rule out distant metastases. With PET/MRI, these questions could be answered in a one-stop-shop examination. In this scenario, the focus of MRI would be only the liver, and a partial-body PET examination with four to five bed positions at 2–3 min/bed position could be performed quite quickly (see also "problem-solving" discussion above). During this time, only the Dixon AC sequence would be acquired (perhaps also an axial fast T2-weighted/fat-saturated sequence), as previous staging with CT would already be available (Fig. 9.4). This protocol could be performed within 30 min or even less when standard contrast media is used compared to liver-specific contrast media.

Another scenario might be primary staging of lung cancer. At first glance, it might not appear useful to stage lung cancer with PET/MRI, based on the challenging acquisition and inferior image quality in MRI for the lung parenchyma. However, usually patients get their diagnosis of lung cancer based on a CT of the chest, and, therefore, when they come for overall staging, including staging brain metastases with MRI (which according to the National Comprehensive Cancer Network guidelines should be done at stage1B and higher), the local anatomy around the tumor has already been imaged. However, to complete the staging, N and M stages have to still be defined, and brain metastases have to be ruled out by MRI, which can now be done in a one-stop-shop setting with PET/MRI. In this setting, initial PET/MRI studies have shown promising results. In a small study, Kohan et al. [42] have demonstrated very similar accuracy for lymph node staging in patients with lung cancer by comparing PET/MRI vs PET/CT with just one T1w AC sequence [42]. This actually highlights the importance of the PET component in N staging in lung cancer when compared with the morphologic imaging component (MRI or CT), which is well known from a large body of PET/CT literature. Similar information was also obtained in an article where PET/MRI showed no difference in staging accuracy in patients with lung cancer when compared with that using PET/CT [43]. A short protocol published by Schwenzer et al. [44] showed comparable diagnostic and staging accuracy between contrast-enhanced PET/CT and PET/MRI in patients with lung carcinoma, using just two pulse sequences in addition to the Dixon AC sequence, showing that a basic set of sequences is adequate [44]. In another study,
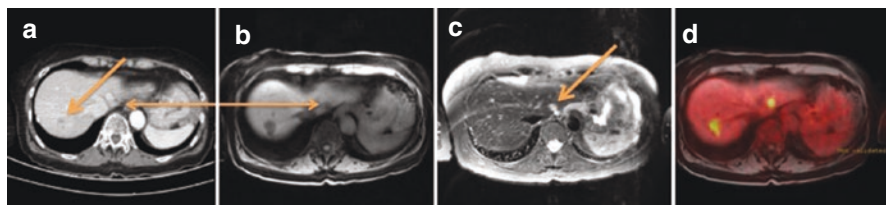
Fig. 9.4 CT of a patient with hepatic metastases of a colorectal cancer. While one metastases in the right liver lobe is obvious (*single yellow arrow*, **a**), there is another metastases close to the hepatic vein confluence (*double yellow arrow*, **a**), which is partly masked and inconclusive on the CT. However, on the MR (**b**: non contrast T1 / **c**: respiratory gated T2) and PET/MR the lesion is detectable and can be characterized as an additional metastases

32 patients with NSCLC were analyzed concerning staging with PET/CT when compared with PET/MRI [21]. Here, the T, the N, and the M staging were not statistically significant different. The interesting concept in this study was the limited PET/MRI protocol using just two WB sequences and one dedicated, respiratory-gated T2w sequence in the chest [9].

Finally a "rule-out brain metastases" protocol is added to the PET/MRI examination. Lung cancer frequently metastasizes to the brain, and PET/CT is not able to exclude brain metastases with adequate sensitivity. In such a protocol using three dedicated brain sequences including contrast enhancement after the acquisition of WB PET/MRI, brain metastases can be excluded with high accuracy. If needed, the same contrast media injection can be used for a quick whole (or partial)-body MRI survey with contrast as well. This way, a complete workup including the brain can be done in a clinically acceptable imaging time of 30–40 min.

9.3 Regionally Focused PET/MRI Protocols to Acquire Multiparametric Quantitative PET and MRI Data: PET/MRI as a Novel Imaging Biomarker

While adequate staging and restaging of oncological patients is one major task for PET/MRI in clinical routine, the true potential of combining MRI and PET in PET/MRI most likely lies not so much in lesion detection and characterization as described above but to make maximum use of the quantitative information on tissue biology one gets in a single examination with optimum image coregistration [45]. By analyzing the data on tracer uptake (metabolism, receptor levels, etc.) and quantitative MRI data, like DW-MRI, DCE-MRI, or MRS on a voxel-by-voxel basis (radiomics), a novel set of biomarkers might evolve. There are big expectations that these novel-combined imaging biomarkers derived from PET/MRI add synergistic information on tumor biology to the classical biomarkers derived from tissue biopsy or liquid biopsy [46, 47]. Compared to the latter, PET/MRI-derived biomarkers have several advantages like being noninvasive, allowing for serial whole-body assessment and depicting intra- and inter-lesional heterogeneity. Also the topic of radiogenomics and linking in-depth imaging analysis with genetic analysis, blood/serum markers, or circulating tumor cells via computational biology is expected to put multimodality imaging analysis to a different level and into a different perspective within diagnostic procedures.

Thus in addition to liquid and tissue biopsy, a "virtual biopsy" using PET/MRI might evolve, which could be helpful for biopsy guidance, prognostic assessment, radiation therapy planning, or response evaluation. Such protocols would most likely focus only on one specific area, like the primary tumor, and would combine a basic set of sequences to depict the morphology, like a fat-saturated contrast-enhanced T1w sequence, depending on the anatomical compartment also T2w sequences, and the needed quantitative MRI sequences to analyze tumor biology, e.g., perfusion with DCE-MRI, restricted water movement with DW-MRI, micro-perfusion with IVIM, and tumor metabolites with MRS. Such protocols might take about 20–30 min but would provide a plethora of information in just a single scan slot.

9.4   After the PET/MRI

9.4.1   Post-Processing, Visualization, and Reporting Structure

There are several considerations concerning combined PET/MRI analysis and consecutive reporting compared to PET/CT or single-modality imaging. In PET/CT, medical institutions often established a combined reading platform where physicians from radiology and nuclear medicine are evaluating cases together. However, economically and considering efficiency, it makes partly more sense to have a dual-trained imaging expert read hybrid imaging. For whole-body MRI, generally radiologists trained for body imaging are probably sufficiently trained. However, depending on national qualification and training requirements, body reporting might be divided in chest imaging and abdominal imaging. While such reporting structure generally makes sense for single-modality imaging in terms of specialization, it is at least discussible in oncology imaging, since cancer represents very often a systemic disease. Thus, ideally a consensus is established who reads hybrid oncology imaging since reading carried out by three (or even more) physicians is not effective. On the other hand, in specialized like neuroradiology or pediatric radiology, it is necessary to consult dedicated specialists for combined reading. There are actually already suggestions and partly also program adoptions to prepare physicians in diagnostic radiology, nuclear medicine, and molecular imaging.

There is no standard strategy for PET/MRI reading, and every institution currently establishes its own reading procedure. Generally, the reading process is similar to that of PET/CT, where the PET is read first for the metabolically active components of the disease, which gives usually a sufficient and rather quick overview over the disease status. After that, the morphological imaging component is read which can reveal additional but non-active disease (e.g., in a post-therapy setting) as well as identify residual diseases which is not picked up by the PET, e.g., based on its higher resolution (small lesions). This represents the more detailed and concerning reading, the more lengthy part especially in whole-body MRI—depending how many sequences have been acquired.

It has however to be pointed out that there are some differences between the PET-component acquired during PET/CT and PET/MRI. Especially the PET/MRI acquisitions with a fully diagnostic MRI part usually will have more than one PET data set as compared with PET/CT. These second PET data sets are acquired, as commented previously, when a patient is scanned in the WB mode (2–3 min per bed position) and also receives a dedicated localized PET/MRI in one bed position (brain, neck, liver, prostate, etc.). Such a second data set can be used for dedicated diagnosis of this body compartment since it usually will have a very high PET image quality. On the other side, a consensus should be established that always the same PET imaging time (either primarily acquired during standard WB or reconstructed from secondary localized PET/MRI) is used or available for follow-up studies for adequate quantification.

In cases with artifacts and nondiagnostic imaging areas, the non-attenuated PET image as well as the u-map has to be available to consider if enough diagnostic information is available for adequate diagnosis. This is indeed even more important

in PET/MRI than for PET/CT since the u-map might have differently translated artifacts than the acquired whole-body Dixon sequence.

Other aspects such as fusing the MRI and PET images on dedicated workstations and generating maximum intensity projections are not significantly different from that of PET/CT. However, a multiple screen option is desirable since then the different MRI sequences and planes can be evaluated at the same time and triangulation of lesions on multiple sequences is much easier (and therefore more time efficient). Also different/additional post-processing resources can be necessary in PET/MRI compared to PET/CT. One reason can be the abovementioned additional PET acquisition, but PET detectors from PET/MRI also have higher sensitivities, and, therefore, more reconstruction steps and computer power are needed. Additionally, MRI sequences like DWI or dynamic contrast-enhanced sequences need certain post-processing to obtain at least the standard values like ADC, k-trans, ve, etc.

Conclusion

PET/MRI systems allow simultaneous acquisition of PET and MRI information, but currently the acquisition protocols are often not optimized for the hybrid nature of that system.

Only few centers so far worked on optimization of protocols and workflow for clinical simultaneous PET/MRI. Protocols have to be optimized to provide complementary or confirmatory information instead of redundant information generated by multiple MRI pulse sequences. Development of new and faster MRI sequences is also needed, especially for lung, since current protocols with gating are very lengthy and often not stable. Multiband imaging for standard MRI sequences is expected to help in this regard, too. PET/MRI in these days is more used as a research tool rather than a clinical "workhorse," and certainly more studies are needed to understand its potential clinical superiority when compared with PET/CT. For this target, defining efficient clinical workflow is essential.

References

1. Braun H, Ziegler S, Paulus DH, Quick HH. Hybrid PET/MRI imaging with continuous table motion. Med Phys. 2012;39:2735–45.
2. Zaidi HI. MR-guided attenuation correction a viable option for dual-modality PET/MR imaging? Radiology. 2007;244:639–42.
3. Martinez-Moeller A, Souvatzoglou M, Delso G. Tissue classification as a potential approach for attenuation correction in whole-body PET/MRI: evaluation with PET/CT data. J Nucl Med. 2009;50:520–6.
4. Eiber M, Martinez-Moeller A, Souvatzoglou M, et al. Value of a Dixon-based MR/PET attenuation correction sequence for the localization and evaluation of PET-positive lesions. Eur J Nucl Med Mol Imaging. 2011;38:1691–701.
5. Schulz V, Torres-Espallardo I, Renisch S, et al. Automatic, three-segment, MRbased attenuation correction for whole-body PET/MR data. Eur J Nucl Med Mol Imaging. 2011;38:138–52.
6. Catana C, van der Kouwe A, Benner T, et al. Toward implementing an MRIbased PET attenuation-correction method for neurologic studies on the MR-PET brain prototype. J Nucl Med. 2010;51:1431–8.

7. Hofmann M, Pichler B, Schöllkopf B, Beyer T. Towards quantitative PET/MRI: a review of MR-based attenuation correction techniques. Eur J Nucl Med Mol Imaging. 2009;36(suppl 1):S93–S104.

8. Ladefoged CN, Benoit D, Law I, Holm S, Kjær A, Højgaard L, Hansen AE, Andersen FL. Region specific optimization of continuous linear attenuation coefficients based on UTE (RESOLUTE): application to PET/MR brain imaging. Phys Med Biol. 2015;60(20):8047–65. https://doi.org/10.1088/0031-9155/60/20/8047.

9. Huellner MW, Appenzeller P, Kuhn FP, Husmann L, Pietsch CM, Burger IA, Porto M, Delso G, von Schulthess GK, Veit-Haibach P. Whole-body nonenhanced PET/MR versus PET/CT in the staging and restaging of cancers: preliminary observations. Radiology. 2014;273(3):859–69. https://doi.org/10.1148/radiol.14140090.

10. Barbosa Fde G, von Schulthess G, Veit-Haibach P. Workflow in simultaneous PET/MRI. Semin Nucl Med. 2015;45(4):332–44. https://doi.org/10.1053/j.semnuclmed.2015.03.007.

11. Barbosa FG, Geismar JH, Delso G, Huellner M, Stolzmann P, Veit-Haibach P. Value of respiratory-triggered, PROPELLER T2-weithed imaging in evaluation of pulmonary nodules – analysis with tri-modality PET/CT-MR. Abstract presented: Swiss Congress of Radiology, Davos, 190516–2105.16.

12. von Schulthess GK, Veit-Haibach P. Workflow considerations in PET/MR imaging. J Nucl Med. 2014;55(Supplement 2):19S–24S.

13. Martinez-Möller A, Eiber M, Nekolla SG, Souvatzoglou M, Drzezga A, Ziegler S, Rummeny EJ, Schwaiger M, Beer AJ. Workflow and scan protocol considerations for integrated whole-body PET/MRI in oncology. J Nucl Med. 2012;53(9):1415–26.

14. Kuhn FP, Hüllner M, Mader CE, Kastrinidis N, Huber GF, von Schulthess GK, Kollias S, Veit-Haibach P. Contrast-enhanced PET/MR imaging versus contrast-enhanced PET/CT in head and neck cancer: how much MR information is needed? J Nucl Med. 2014;55(4):551–8. https://doi.org/10.2967/jnumed.113.125443.

15. Queiroz MA, Huellner MW. PET/MR in cancers of the head and neck. Semin Nucl Med. 2015;45(3):248–65. https://doi.org/10.1053/j.semnuclmed.2014.12.005. Review.

16. Queiroz MA, Hüllner M, Kuhn F, Huber G, Meerwein C, Kollias S, von Schulthess G, Veit-Haibach P. PET/MRI and PET/CT in follow-up of head and neck cancer patients. Eur J Nucl Med Mol Imaging. 2014;41(6):1066–75. https://doi.org/10.1007/s00259-014-2707-9.

17. Queiroz MA, Hüllner M, Kuhn F, Huber G, Meerwein C, Kollias S, von Schulthess G, Veit-Haibach P. Use of diffusion-weighted imaging (DWI) in PET/MRI for head and neck cancer evaluation. Eur J Nucl Med Mol Imaging. 2014;41(12):2212–21. https://doi.org/10.1007/s00259-014-2867-7.

18. Sekine T, Barbosa FG, Delso G, Burger IA, Stolzmann P, Ter Voert EE, Huber GF, Kollias SS, von Schulthess GK, Veit-Haibach P, Huellner MW. Local resectability assessment of head and neck cancer: Positron emission tomography/MRI versus positron emission tomography/CT. Head Neck. 2017;39(8):1550–8. https://doi.org/10.1002/hed.24783.

19. Sekine T, de Galiza Barbosa F, Kuhn FP, Burger IA, Stolzmann P, Huber GF, Kollias SS, von Schulthess GK, Veit-Haibach P, Huellner MW. PET+MR versus PET/CT in the initial staging of head and neck cancer, using a trimodality PET/CT+MR system. Clin Imaging. 2017;42:232–9. https://doi.org/10.1016/j.clinimag.2017.01.003.

20. Rauscher I, Eiber M, Fürst S, Souvatzoglou M, Nekolla SG, Ziegler SI, Rummeny EJ, Schwaiger M, Beer AJ. PET/MR imaging in the detection and characterization of pulmonary lesions: technical and diagnostic evaluation in comparison to PET/CT. J Nucl Med. 2014;55(5):724–9.

21. Huellner MW, Pietsch CM, Husmann L, et al. Staging of non-small cell lung cancer With PET/MR and PET/CT. Radiological society of North America 2014 scientific assembly and annual meeting, Chicago IL, 2014.

22. Stolzmann P, Veit-Haibach P, Chuck N, Rossi C, Frauenfelder T, Alkadhi H, von Schulthess G, Boss A. Detection rate, location, and size of pulmonary nodules in trimodality PET/CT-MR: comparison of low-dose CT and Dixon-based MR imaging. Investig Radiol. 2013;48(5):241–6. https://doi.org/10.1097/RLI.0b013e31826f2de9.

23. Haerle SK, Schmid DT, Ahmad N, Hany TF, Stoeckli SJ. The value of 18F-FDG PET/CT for the detection of distant metastases in high-risk patients with head and neck squamous cell carcinoma. Oral Oncol. 2011;47:653–9.

24. Fowler KJ, McConathy J, Narra VR. Whole-body simultaneous positron emission tomography(PET)-MR: optimization and adaptation of MRI sequences. J Magn Reson Imaging. 2014;39(2):259–68.

25. Takenaka D, Ohno Y, Matsumoto K, et al. Detection of bone metastases in non-small cell lung cancer patients: comparison of whole-body diffusion-weighted imaging (DWI),whole-body MR imaging without and with DWI, whole-bodyFDG-PET/CT,and bone scintigraphy. J Magn Reson Imaging. 2009;30(2):298–308.

26. Abdulqadhr G, Molin D, Astrom G, et al. Whole-body diffusion-weighted imaging compared with FDG-PET/CTin staging of lymphoma patients. Acta Radiol. 2011;52(2):173–80.

27. Kekelidze M, D'Errico L, Pansini M, et al. Colorectal cancer: current imaging methods and future perspectives for the diagnosis, staging and therapeutic response evaluation. World J Gastroenterol. 2013;19(46):8502–14.

28. Buchbender C, Hartung-Knemeyer V, Beiderwellen K, et al. Diffusion-weighted imaging as part of hybrid PET/MRI protocols for whole-body cancer staging: does it benefit lesion detection? Eur J Radiol. 2013;82(5):877–82. https://doi.org/10.1016/j.ejrad.2013.01.019. Epub 2013 Feb 18.

29. Taouli B. Diffusion-weighted MR imaging for liver lesion characterization: a critical look. Radiology. 2012;262:378–80.

30. Eiber M, Fingerle AA, Brügel M, et al. Detection and classification of focal liver lesions in patients with colorectal cancer: retrospective comparison of diffusion-weighted MR imaging and multi-slice CT. Eur J Radiol. 2012;81:683–91.

31. Reiner CS, Stolzmann P, Husmann L, Burger IA, Hüllner MW, Schaefer NG, Schneider PM, von Schulthess GK, Veit-Haibach P. Protocol requirements and diagnostic value of PET/MR imaging for liver metastasis detection. Eur J Nucl Med Mol Imaging. 2014;41(4):649–58. https://doi.org/10.1007/s00259-013-2654-x.

32. Park JW, Kim JH, Kim SK, et al. A prospective evaluation of 18F-FDG and 11C-acetate PET/CT for detection of primary and metastatic hepatocellular carcinoma. J Nucl Med. 2008;49(12):1912–21.

33. Hwang KH, Choi DJ, Lee SY, et al. Evaluation of patients with hepatocellular carcinomas using [(11)C]acetate and [(18)F]FDGPET/CT: a preliminary study. Appl Radiat Isot. 2009;67(7–8):1195–8.

34. Cheung TT, Ho CL, Lo CM, et al. 11 C-acetate and 18F-FDG PET/CT for clinical staging and selection of patients with hepatocellular carcinoma for liver transplantation on the basis of Milancriteria:surgeon's perspective. J Nucl Med. 2013;54(2):192–200.

35. Talbot JN, Gutman F, Fartoux L, et al. PET/CT in patients with hepatocellular carcinoma using [(18)F]fluorocholine: Preliminary comparison with [(18)F]FDG PET/CT. Eur J Nucl Med Mol Imaging. 2006;33(11):1285–9.

36. Talbot JN, Fartoux L, Balogova S, et al. Detection of hepatocellular carcinoma with PET/CT: A prospective comparison of 18F-fluorocholine and 18F-FDG in patients with cirrhosis or chronic liver disease. J Nucl Med. 2010;51(11):1699–706.

37. Bieze M, Klumpen HJ, Verheij J, et al. Diagnostic accuracy of (18)F-methylcholine positron emission tomography/computed tomography for intra- and extrahepatic hepatocellular carcinoma. Hepatology. 2014;59(3):996–1006.

38. Bastiaannet E, Groen H, Jager PL, et al. The value of FDG-PET in the detection, grading and response to therapy of soft tissue and bone sarcomas; a systematic review and meta-analysis. Cancer Treat Rev. 2004;30(1):83–101.

39. Folpe AL, Lyles RH, Sprouse JT, et al. (F-18) fluorodeoxyglucose positron emission tomography as a predictor of pathologic grade and other prognostic variables in bone and soft tissue sarcoma. Clin Cancer Res. 2000;6(4):1279–87.

40. Lee IS, Jin YH, Hong SH, et al. Musculoskeletal applications of PET/MR. Semin Musculoskelet Radiol. 2014;18(2):203–16.

41. Sekine T, Delso G, Zeimpekis K, Barbosa de Galiza F, Ter Voert EGW, Huellner M, Veit-Haibach P. Reduction of 18F-FDG Dose in Clinical PET/MR Imaging by Using Silicon Photomultiplier Detectors. Radiology. 2017:162305. doi: 10.1148/radiol.2017162305. [Epub ahead of print].

42. Kohan AA, Kolthammer JA, Vercher-Conejero JL, et al. N staging of lung cancer patients with PET/MRI using a three-segment model attenuation correction algorithm: Initial experience. Eur Radiol. 2013;23(11):3161–9.

43. Heusch P, Buchbender C, Kohler J, et al. Thoracic staging in lung cancer: prospective comparison of 18F-FDG PET/MR imaging and 18F-FDG PET/CT. J Nucl Med. 2014;55(3):373–8.

44. Schwenzer NF, Schram lC, Muller M, et al. Pulmonary lesion assessment: Comparison of whole-body hybrid MR/PET and PET/CT imaging — Pilot study. Radiology. 2012;264(2):551–8.

45. Weber WA. PET/MR imaging: a critical appraisal. J Nucl Med. 2014;55(Supplement 2):56S–8S.

46. Taouli B, Beer AJ, Chenevert T, Collins D, Lehman C, Matos C, Padhani AR, Rosenkrantz AB, Shukla-Dave A, Sigmund E, Tanenbaum L, Thoeny H, Thomassin-Naggara I, Barbieri S, Corcuera-Solano I, Orton M, Partridge SC, Koh DM. Diffusion-weighted imaging outside the brain: consensus statement from an ISMRM-sponsored workshop. J Magn Reson Imaging. 2016;44(3):521–40.

47. Bailey DL, Pichler BJ, Gückel B, Barthel H, Beer AJ, Botnar R, Gillies R, Goh V, Gotthardt M, Hicks RJ, Lanzenberger R, la Fougere C, Lentschig M, Nekolla SG, Niederdraenk T, Nikolaou K, Nuyts J, Olego D, Riklund KÅ, Signore A, Schäfers M, Sossi V, Suminski M, Veit-Haibach P, Umutlu L, Wissmeyer M, Beyer T. Combined PET/MRI: from Status Quo to Status Go. Summary Report of the Fifth International Workshop on PET/MR Imaging; February 15-19, 2016; Tübingen, Germany. Mol Imaging Biol. 2016;18(5):637–50.

Total-Body PET/MRI in Oncological Applications

10

Ryogo Minamimoto, Valentina Taviani,
Shreyas Vasanawala, and Andrei Iagaru

Contents

10.1 Introduction

One potential advantage of adding PET to MRI is that PET in oncology is the fact that it is routinely a whole-body (skull base to mid-thighs) and sometimes a total-body (vertex to toes) examination. Total-body indications include sarcomas,

R. Minamimoto • A. Iagaru (✉)
Division of Nuclear Medicine and Molecular Imaging, Department of Radiology,
Stanford University, Stanford, CA, USA
e-mail: aiagaru@stanford.edu

V. Taviani
GE Healthcare, Menlo Park, CA, USA

S. Vasanawala
Division of Body MRI, Department of Radiology, Stanford University, Stanford, CA, USA
e-mail: vasanawala@stanford.edu

melanoma, multiple myeloma, cutaneous lymphomas, and evaluation of skeletal metastases [1, 2]. Hybrid positron emission tomography/magnetic resonance imaging (PET/MRI) is one of the multimodality technologies that provides both biological and morphological information of lesions [3, 4]. Compared to PET/CT, advantages of PET/MRI include reduction of radiation exposure, use of MRI to assess organ function, and improvement of diagnostic ability due to better contrast of MRI [5–7].

However, the PET/MRI scan requires longer acquisition time, and the instrumentation has a higher cost than PET/CT. Other limitations are related to counterindications to MRI such as claustrophobia and certain metallic implants that are part of MRI safety standards [8]. Therefore, total-body PET/MRI should be used after giving careful consideration to its strength over PET/CT. In this chapter, we present MRI techniques for total-body imaging and several possible clinical oncological indications for total-body PET/MRI.

10.2　Whole-Body MRI Techniques

Whole-body MRI is an established procedure for several indications. The technique for whole-body PET/MRI is similar to that for whole-body MRI. In general, an exam consists of T2-weighted imaging; T1-weighted imaging, with some institutions including diffusion; and contrast-enhanced imaging. The acquisitions are performed in stations, with most imaging acquired in the coronal plane but DWI and contrast-enhanced imaging performed axially. Of note, when performing PET/MRI, the table position is locked for each PET bed, and, therefore, most of the MRI acquisitions for a given station are obtained during a corresponding PET bed. An exception is the post-contrast imaging, which may be performed after the PET acquisition, both because of the need to rapidly image the whole body and to ensure non-contrast accurate T1-weighted imaging for attenuation correction.

10.2.1　Whole-Body T2-Weighted Imaging

Fast spin echo is the most commonly used pulse sequence for T2-weighted imaging. It consists of a 90° excitation pulse followed by a train of refocusing RF pulses. Several excitations are necessary to fill in k-space as the echo train length is typically a small fraction of the number of prescribed phase encodings. As a result, T2-decaying-induced blurring is usually negligible and excellent image quality and T2 weighting can be achieved. Typically, an inversion preparation pulse is employed (STIR) to obtain fat suppression that is reliable but at a cost of noisy images.

The main limitation of fast spin echo imaging is that acquisitions tend to be lengthy and therefore prone to motion artifacts. Single-shot fast spin echo imaging can be considered as an extreme form of fast spin echo, where the whole k-space

corresponding to a certain slice location is acquired following a single excitation in a fraction of a second. While the speed of the acquisition is such that motion is effectively frozen, T2-induced decay along the long echo train can considerably reduce the effective resolution due to blurring in the phase-encode direction. Parallel imaging and variable refocusing flip angles are routinely used to limit T2-induced blurring, as well as the amount of energy deposition to the subject, thus speeding up the acquisition even further.

Fat-suppressed T2-weighted imaging is often performed alongside conventional unsuppressed imaging. Because of the large anatomical coverage required for whole-body imaging, it is crucial to choose a fat suppression method robust to both B0 and B1 inhomogeneities. Short-tau inversion recovery (STIR) consists of a non-selective adiabatic inversion RF pulse timed so that at the time of the excitation, the longitudinal magnetization from fat is zero. Because STIR relies on T1 differences instead of chemical shifts, it usually results in excellent fat suppression; however, SNR is considerably reduced. Radial spin echo imaging, also known as PROPELLER, BLADE, or VANE, has also been reported for PET/MRI whole-body imaging. In this case, the central portion of k-space is repeatedly acquired in a radial fashion, using progressively rotated and overlapping "blades," which makes this technique both SNR efficient and intrinsically robust to motion, albeit slower than Cartesian fast spin echo.

10.2.2 T1-Weighted Imaging

Conventionally, for whole-body MRI, T1-weighted imaging is performed as a fast spin echo sequence in coronal stations. An alternative that is faster is T1-weighted is fast volumetric gradient-echo acquisitions in axial stations, which can be performed pre-contrast and post-contrast. Two-point water/fat resolved imaging provides high resolution, excellent fat suppression, and additional contrasts that can aid to detect and characterize lesions. While different vendors provide slightly different implementations, the basic principle underlying water/fat separated imaging is pretty simple and relies on the chemical shift between water and fat spins. Because of the different precession frequency, the amount of phase accumulated at a specific echo time is also different. In theory, by choosing two acquire signals at two echo times when water and fat spins are approximately in-phase and out-of-phase, one could separate water and fat by solving a simple linear system of two equations and two unknowns. In practice, phase accrual can also be due to B0 inhomogeneities, so more complicated acquisition schemes and reconstruction algorithms are necessary to reliably separate water and fat. A recently proposed alternative for whole-body T1-weighted imaging, with excellent motion properties, is 3D radial gradient echo imaging. The MRI signals are encoded according to a stack-of-stars pattern, whereby several "stars" are consecutively acquired to cover the desired 3D volume. Because the center of k-space is repeatedly sampled for each "star," motion artifacts can be greatly mitigated by advanced image reconstruction algorithms that exploit data redundancy at the center of k-space.

10.2.3 Diffusion-Weighted Imaging

Single-shot diffusion-weighted echo planar imaging (EPI) is commonly used because of its robustness to motion and high SNR efficiency. However, the long echo-train readout and narrow readout bandwidth in the phase-encoding direction make this technique extremely sensitive to T2*-induced blurring and off resonance, with field inhomogeneities, susceptibility gradients, eddy currents, and chemical shift often resulting in severe geometrical distortion. In particular, distortion is proportional to the local off-resonance field and overall duration of the EPI readout. Whole-body imaging typically requires large FOVs, which means relatively long readouts even for modest image resolutions and often inadequate shimming.

Parallel imaging techniques are routinely used to reduce distortion, although their effectiveness is limited by the performance of the specific array used for signal reception. Higher-order eddy current compensation strategies, either prospective or retrospective, are often used. STIR is the preferred fat suppression method due to its robustness to B0 and B1 inhomogeneities, despite the lower intrinsic SNR. Chemically selective fat suppression methods (fat presaturation, spectral-spatial RF pulses, and gradient reversal), even when used in combination, can result in fat suppression failures that translate in chemical shifts of several pixels across the imaged FOV. Signal averaging during free breathing is routinely used to compensate for the otherwise low SNR due to STIR, and usually no more than two b values are acquired to avoid lengthy acquisitions. Free breathing diffusion-weighted imaging using STIR and signal averaging is often referred to as DWIBS (diffusion-weighted imaging with background suppression) and is one of the most widely used methods for whole-body DWI.

Whole-body diffusion imaging is typically performed axially, with coronal/sagittal reformats generated for the purpose of visualization. A common artifact observed in sagittal reformats is the typical stair-step appearance of the spine, due to center frequency mismatch between different beds. Recently developed prospective and retrospective corrections aimed at minimizing this artifact have greatly improved the appearance of sagittal and coronal reformats of whole-body imaging datasets, facilitating fusion of PET and MRI data.

10.3 Indications

10.3.1 Melanoma

Clinically, physical exam and target biopsy have been the basic strategy for the diagnosis of malignant melanoma. NCCN guidelines recommend imaging in any melanoma stage to assess for specific signs or symptoms suggestive of possible metastasis [9]. Chest/abdomen/pelvis CT with intravenous contrast and/or FDG PET/CT with or without brain MRI with IV contrast are the suggested imaging modalities. The American Joint Committee on Cancer (AJCC) classification defined tumor stage using histopathological diagnosis in terms of ulceration and tumor

thickness [10]. The incidence of locoregional metastases is related to the depth of tumor infiltration. Ultrasound appears to be the most reliable method for detection of locoregional metastases with sensitivity of 60% and specificity of 97%, in contrast to CT with sensitivity of 9% and specificity of 92% and FDG PET/CT with sensitivity of 11% and specificity of 97% [11]. FDG PET/CT has limitation for T staging, detection of locoregional metastases, and early-stage melanoma [12, 13].

The low sensitivity of morphologic and metabolic examination is caused by the limitation for the identification of small lymph node metastases which are routinely present in melanoma patients [14, 15]. Therefore, these imaging studies are recommended to exclude further spread of metastatic lesions [16] rather than for evaluation of locoregional lymph node metastasis.

Horn and colleagues reported that for patients categorized with AJCC stage III based on positive sentinel lymph node biopsy and with negative findings on CT, MRI, and ultrasonography for further spread of disease, FDG PET upstaged them to stage IV in 12% of the cases due to identification of unknown distant metastases [17]. FDG PET sensitivity ranges from 68 to 87%, and specificity ranges from 92–98% for stages III and IV melanoma; however, in contrast, sensitivity ranges from 0 to 67% and specificity 77 to 100% for stages I and II melanoma. Whole-body MRI with a sensitivity, specificity, PPV, NPV, and accuracy of 66%, 77%, 84%, 55%, and 67%, respectively, for the detection of lymph node metastases, has been shown to be equal in accuracy to whole-body CT [18] and inferior to FDG PET/CT [19] but comparable for N-staging if diffusion imaging is combined with conventional MRI sequences [20]. Therefore, FDG PET/CT may aid detection of lesions located in areas not included in routine CT examinations. Whole-body MRI with a combination of conventional MRI sequences and diffusion weighted was at least as accurate as FDG PET/CT for N-staging. Another advantage of whole-body MRI is for the detection of subcutaneous, osseous, hepatic, and brain metastases. Therefore, integrated PET/MRI may be a tool to achieve melanoma staging in a single session.

Although the performance of PET/MRI for staging of melanoma has not been prospectively evaluated, the potential can be estimated from studies comparing the performance of whole-body MRI and PET/CT for melanoma staging [21]. The diagnostic performance of the whole body with DWI (overall sensitivity and specificity of 82%–84% and 87%–97%, respectively) was as good as or better than that of FDG PET/CT (73%–80% and 93%, respectively) [20, 22, 23]. While DWI is useful for detection of extracranial lesions and contrast-enhanced MRI is excellent for evaluation of brain lesions, CT is superior to MRI for detection of lung nodules [19, 22]. However, recent reports indicate new MRI sequences improve the performance of MRI for detection of lung nodules larger than 4 mm [24].

In cases with inguinal lymphadenopathy, recent NCCN guidelines recommend a pelvic dissection if the FDG PET/CT or pelvic CT scan reveals iliac and/or obturator lymph node involvement [9]. The better soft tissue contrast of PET/MRI may provide more precise information needed in this clinical scenario.

The Collaborative Ocular Melanoma Study Group reported that 64% of patients with melanoma were diagnosed with metastatic disease within 6 years of

enrollment. Based on autopsy, the most common metastatic sites were liver, followed by the lung and bone [23]. Compared to FDG PET/CT, the better contrast of MRI appears to be an advantage for detection of subcutaneous, bone, liver, and brain metastases. The sensitivity of FDG PET/CT for detection of osteoblastic lesions is limited [25]. FDG PET/CT has limitations for the detection of small brain metastasis due to high physiological FDG uptake in the brain. MRI is very useful for identification of brain metastases that indicates a poor prognosis of patients with melanoma [26]. Even though FDG PET/CT showed good performance for identification of liver metastases [27], liver MRI is superior to FDG PET/CT especially for small lesions [28]. Therefore, PET/MRI is very likely to play an important role in the evaluation of the liver when identification of hepatic metastases is important for clinical management. FDG PET/CT has also been useful for detection of recurrent metastases. The detection of recurrence with FDG PET/CT is increased with cancer stage [11], and FDG PET/CT influences the surgical planning in 25–75% of patients [29].

Truncation artifacts have been reported with the increasing use of PET/MRI. A truncated attenuation map affects the PET image both through the attenuation correction and through the scatter correction [30, 31]. Simultaneous acquisition of PET and MRI data occasionally results in misregistration due to respiratory motion, which could influence the evaluation of liver lesions [32]. Time-of-flight PET reduces attenuation artifacts and quantification errors in the lungs when compared to non-TOF reconstructions [33].

Lastly, considering the demographics of patients with melanoma (many are diagnosed at young age), the reduction of radiation exposure when using PET/MRI vs PET/CT may be an additional significant advantage.

10.3.2 Sarcomas

Sarcomas are a heterogeneous group of tumors originating from mesenchymal tissues. Bone sarcomas account for 0.2% of all primary cancers in adults and approximately 5% of childhood malignancies. Soft tissue sarcomas are rare tumors, representing approximately 0.7% of adult malignancies. However, in children younger than 15 years of age, they represent 6.5% of all cancers. Multimodality therapy with surgery, neoadjuvant chemotherapy, adjuvant chemotherapy, and radiation therapy is standard protocol for treatment of sarcomas [34]. Preoperative radiation therapy followed by limb-conserving surgery has become the standard of care for truncal and extremity soft tissue sarcomas [35–37].

FDG PET or PET/CT showed promising result for staging and restaging of sarcoma [38], biopsy guidance [39, 40], prediction of tumor grading [41], therapeutic response assessment [42–44], and prognosis [45]. FDG PET detected additional distant metastases that were not identified by standard modalities (e.g., CT, bone scintigraphy) in 14% of patients [46]. Another study showed that FDG PET has similar sensitivity and higher specificity in recurrent Ewing sarcoma and osteosarcoma when compared with standard imaging modalities [47]. A meta-analysis of

the diagnostic performance of FDG PET/CT reported 100% sensitivity and 96% specificity, with 99% overall accuracy for restaging sarcoma patients [48].

The high soft tissue contrast of MRI makes it the standard for evaluating soft tissue and osseous sarcoma lesions. This allows an accurate assessment of local tumor infiltration, as well as the osseous extent of tumor, adjacent joint involvement, and neurovascular envelopment or invasion. Planning for surgical tumor excision is often based on the depth of infiltration found on MRI [49]. However, the accuracy of MRI in discriminating benign from malignant lesions is not optimal [50, 51]. Therefore, other techniques such as DWI and MRI spectroscopy are needed and expected to increase the accuracy [52, 53].

The biological information provided by PET may enhance the diagnostic ability when combined with the diagnostic data obtained from MRI. Although FDG PET does not provide additional information over MRI for T staging in soft tissue sarcomas [54], FDG PET can help identify the tumor-free surgical margin [55]. FDG PET is superior to conventional diagnostic imaging techniques for N-staging, with a sensitivity of 95% vs 25%, respectively [56]. FDG PET can also be used to accurately identify local disease recurrence in sarcoma patients [57]. FDG PET is superior in detecting bone and lymph node metastases in pediatric sarcoma patients compared to conventional imaging [56], leading to more accurate cancer staging [58].

Metastatic lesions occur in up to 60% of patients with sarcoma who have been treated initially with curative intention, and the lung is the most common site of metastasis in most histologic subtypes of sarcoma [59]. Although MRI has limitations for the identification of lung lesions, the PET component of PET/MRI may be able to play a complementary role. FDG PET/MRI and FDG PET/CT perform comparably in the detection and characterization of lung lesions 10 mm or larger. However, the detection rate of PET/MRI was inferior to that of PET/CT in lung lesions smaller than 10 mm [60]. Again, recent reports indicate new MRI sequences improve the performance of MRI for detection of lung nodules larger than 4 mm [24]. Therefore, it is likely that PET/MRI will be a good tool for combined T-, N-, and M-staging in a single imaging session, as suggested by several case reports [61, 62].

DWI sequences combined with ADC maps from MRI and FDG PET have been shown to be useful for treatment response assessment in patients with soft tissue sarcomas [63, 64]. Multiparametric PET/MRI may therefore provide more accurate data in the assessment of treatment response.

There are limitations: one study indicated that FDG-PET for initial staging of soft tissue sarcoma only changed the therapeutic strategy in less than 5% of the cases based on the detection of distant metastases using metabolic imaging [53]. This indicates that prospective study should be promoted to clarify the impact of PET/MRI on management of patients with sarcomas.

As with other indications, PET/MRI can decrease radiation exposure compared to PET/CT, which is especially important in young patients diagnosed with sarcomas. The radiation dose from a typical FDG PET/MRI study is estimated to be equivalent to 20% of that received from a PET/CT scan [65].

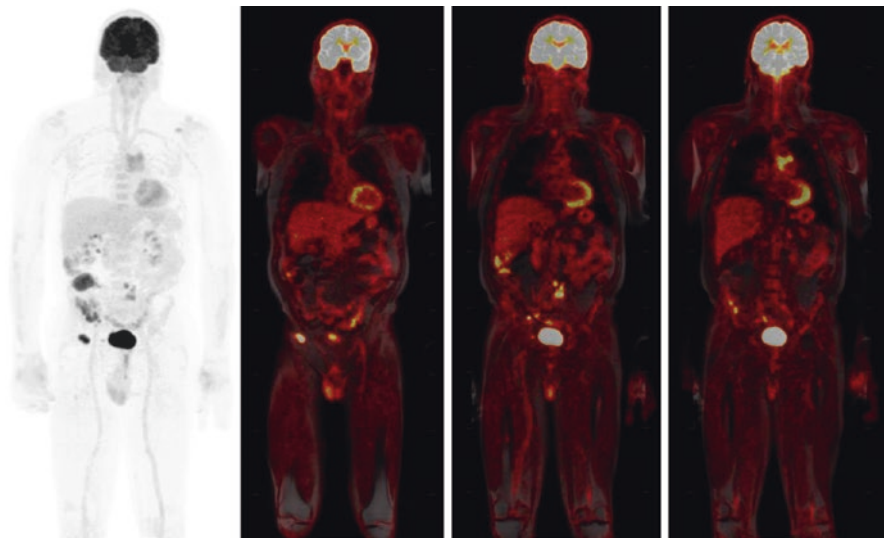An example of whole-body FDG PET/MRI in sarcoma is shown in Fig. 10.1.

Fig. 10.1 Sixty-four-year-old man with angiosarcoma. Maximum intensity projection (MIP) from ¹⁸F FDG PET (left) and fused coronal PET/MRI demonstrate extensive metastatic disease

10.3.3 Multiple Myeloma

Multiple myeloma (MM) is a malignant plasma cell neoplasia characterized by bone marrow infiltration and overproduction of monoclonal immunoglobulins [66]. Patients generally present with excess bone marrow plasma cells, osteolytic bone lesions, renal disease, and immunodeficiency [67]. Standard investigations for MM include complete blood count, serum biochemistry, serum and urine electrophoresis, and whole-body skeletal survey with conventional radiography. The Durie/Salmon staging system introduced in 1975 used the skeletal survey for lytic bone lesions as its only radiological criterion [68]. More recently, the Durie/Salmon PLUS staging system includes imaging techniques such as MRI, CT, and PET/CT [69].

FDG PET/CT is used routinely in patients with MM for the evaluation of both medullary and extramedullary diseases. The advantage of FDG PET is its ability to survey the whole body in a reasonable time frame [69]. FDG PET can detect bone marrow involvement by MM with high sensitivity and specificity. It can also identify the number of active lesions and the area of diffuse bone marrow infiltration. Moreover, it may detect early bone marrow involvement in patients with apparently solitary plasmacytoma [70].

Another use of FDG PET is to be able to distinguish active myeloma from monoclonal gammopathy of undetermined significance (MGUS) or smoldering disease [71]. However, some MM cells do not overexpress the glucose transporter 1; therefore, FDG does not easily distinguish a benign lesion from a low-grade MM lesion.

It has been reported that over a third of intramedullary MM lesions can be missed by FDG PET [72].

MRI can provide information regarding bone marrow involvement, loss of fatty bone marrow components, and replacement by pathologic cells in MM [73]. MRI can detect focal MM lesions before osteolysis can be visualized on a bone survey [74]. Compared with whole-body CT, whole-body MRI showed higher sensitivity for both focal and diffuse patterns of bone marrow involvement and resulted in upstaging of multiple myeloma. Moreover, the detection of lesions, extent of disease, and the rate of bone manifestations are higher with MRI than with CT [75].

One of the limitations of MRI imaging is difficulty in distinguishing between treated bone marrow lesions and viable neoplastic tissue. It may take up to 9–12 months for the response to therapy to be accurately evaluated [76]. Median global ADC from DWI data may serve as a potential response biomarker for differentiation of responders from non-responders [77]. Although ADC data can provide information regarding tumor cellularity and disease activity in MM lesions, the interpretation of these images can be complicated by physiologic factors such as age and bone marrow activation due to physical activity and infection.

PET/MRI appears to be equivalent to PET/CT for detection of MM lesions [78]. Sachpekidis et al. reported that 94% of all focal lesions depicted in the PET part of PET/CT were also seen in the PET part of PET/MRI, reflecting equivalent performance regarding qualitative lesion evaluation. Although without influence in patients' management, PET/MRI missed rib lesions that were seen on PET/CT [79]. Whole-body MRI has limitations in the evaluation of the skull, clavicle, or ribs [74, 80].

Martinez-Möller et al. indicated that the absence of bone in the attenuation map in PET/MRI resulted in an average SUVmax underestimation for osseous lesions of 8.0% [81]. Aznar et al. reported that the application of standard MR-based attenuation correction in PET/MRI imaging causes an underestimation of PET uptake values in soft tissue and bone lesions of approximately 10% in comparison with PET/CT [82]. Marshall et al. described an alternative combined technique for MR-based attenuation correction that included the routinely applied four-component (air, lungs, soft tissue, and fat) segmentation approach and a database of CT scans [83]. This approach resulted in an improvement of the relative error in VOIs adjacent to the bone from a mean of -7.5% to 2% and reduced the magnitude of relative error in bone tissue from −14.6 to 1.3%.

10.3.4 Cutaneous Lymphoma

Cutaneous lymphoma, including cutaneous T-cell lymphoma and cutaneous B-cell lymphoma, is a rare condition accounting for less than 2% of all lymphomas [84]. Numerous subtypes are included in cutaneous lymphoma, and therefore many

clinical presentations exist in the skin and subcutaneous tissues. Some invasive subtypes can have extracutaneous manifestations including lymph node, blood, and visceral organ involvement [85, 86].

10.3.5 Bone Metastases

Bone scintigraphy (BS) with technetium-99 m (^{99m}Tc) methylene diphosphonate (MDP) has been the standard method for detecting osteoblastic bone metastasis [87]. Single photon emission computed tomography (SPECT) alone or in combination with CT (SPECT/CT) can improve the sensitivity and specificity of bone scintigraphy over planar imaging [88]. Other imaging modalities used for the detection of bone metastasis are CT and MRI as morphologic imaging, as well as PET and PET/CT as functional imaging.

FDG PET/CT is sensitive for the detection of osteolytic bone metastases but has limitations for the evaluation of sclerotic bone involvement [89, 90]. Therefore, BS and a FDG PET scan may provide complementary information about bone lesions, given the different mechanisms of radiotracer uptake in the bone [91]. FDG PET/CT and MRI are significantly more accurate for bone metastasis detection than BS and stand-alone CT. FDG PET/CT showed sensitivity of 94% and specificity of 97%, while MRI had sensitivity of 91% and specificity of 95% [92]. However, MRI may perform better than FDG PET/CT because of improved sensitivity for small lesions [93]. DWI MRI showed utility for assessing the therapeutic effect of antiandrogen drugs used for bone metastases from prostate cancer [94]. Therefore, the combination of PET and MRI in a single exam has the potential to enhance the detection of bone metastases compared to PET/CT.

Another radiopharmaceutical used for bone imaging is ^{18}F sodium fluoride (NaF) PET [95–97]. NaF PET/CT is superior to bone scintigraphy for skeletal lesion detection in prostate and breast cancers [96, 98, 99]. Whole-body DWI has higher specificity but lower sensitivity than NaF PET/CT in prostate cancer [100].

The combined administration of NaF and FDG (^{18}F-/^{18}F-FDG) in a single PET/CT scan for cancer detection has been advocated for detecting both extra-skeletal and skeletal lesions [101, 102]. A prospective international multicenter trial showed promising results [103]. In another prospective study, ^{18}F-/^{18}F-FDG PET/CT and whole-body MRI were shown to be superior to BS for evaluation of the extent of skeletal disease. ^{18}F-/^{18}F-FDG PET/CT provided similar diagnostic ability to that of a combination of whole-body MRI and BS in patients with breast and prostate cancer [104]. Quantitative analysis of ^{18}F-/^{18}F-FDG PET/CT has also been reported [105].

^{18}F-/^{18}F-FDG PET/MRI is superior to BS for evaluation of skeletal disease extent. ^{18}F-/^{18}F-FDG PET/MRI detected extra-skeletal disease that may change the management of these patients while allowing a significant reduction in radiation exposure from lower dosages of PET radiopharmaceuticals administered. A combination of ^{18}F-/^{18}F-FDG PET/MRI may provide the most accurate staging of patients with breast and prostate cancers prior to the start of treatment [106]. An example of ^{18}F-/^{18}F-FDG PET/MRI is shown in Fig. 10.2.
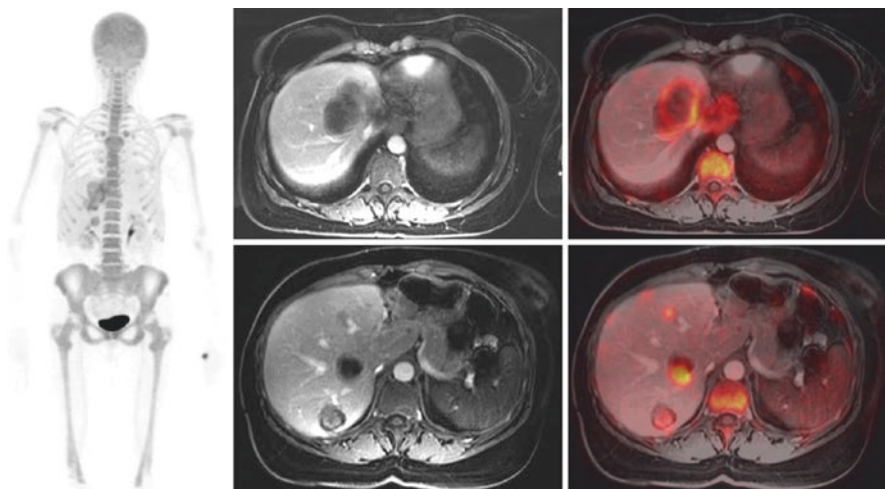
Fig. 10.2 Fifty-year-old woman with stage IV breast cancer. Combined ^{18}F NaF and ^{18}F FDG PET/MRI shows liver metastases on MIP, MRI, and fused PET/MRI

10.4 Summary

Several techniques allow for successful whole-body MRI in oncology. FDG PET is generally used as a whole-body exam in oncology. Therefore, the marriage of FDG PET and MRI in a single total-body study is attractive for accurate evaluation of certain malignancies such as those described in this chapter.

References

1. Fletcher JW, Djulbegovic B, Soares HP, et al. Recommendations on the use of 18F-FDG PET in oncology. J Nucl Med. 2008;49(3):480–508.
2. Boellaard R, Delgado-Bolton R, Oyen WJG, et al. FDG PET/CT: EANM procedure guidelines for tumour imaging: version 2.0. Eur J Nucl Med Mol Imaging. 2015;42(2): 328–54.
3. Iagaru A, Mittra E, Minamimoto R, et al. Simultaneous whole-body time-of-flight 18F-FDG PET/MRI: a pilot study comparing SUVmax with PET/CT and assessment of MR image quality. Clin Nucl Med. 2015;40(1):1–8.
4. Pichler BJ, Kolb A, Nägele T, Schlemmer H-P. PET/MRI: paving the way for the next generation of clinical multimodality imaging applications. J Nucl Med. 2010;51(3):333–6.
5. Buchbender C, Heusner TA, Lauenstein TC, Bockisch A, Antoch G. Oncologic PET/MRI, part 2: bone tumors, soft-tissue tumors, melanoma, and lymphoma. J Nucl Med. 2012;53(8):1244–52.
6. Drzezga A, Souvatzoglou M, Eiber M, et al. First clinical experience with integrated whole-body PET/MR: comparison to PET/CT in patients with oncologic diagnoses. J Nucl Med. 2012;53(6):845–55.
7. Quick HH, von Gall C, Zeilinger M, et al. Integrated whole-body PET/MR hybrid imaging: clinical experience. Investig Radiol. 2013;48(5):280–9.

8. Shellock FG, Spinazzi A. MRI safety update 2008: part 2, screening patients for MRI. Am J Roentgenol. 2008;191(4):1140–9.

9. Coit DG, Thompson JA, Algazi A, et al. Melanoma, version 2.2016, NCCN clinical practice guidelines in oncology. J Natl Compr Cancer Netw. 2016;14(4):450–73.

10. Gershenwald JE, Soong SJ, Balch CM. 2010 TNM staging system for cutaneous melanoma…and beyond. Ann Surg Oncol. 2010;17(6):1475–7.

11. Xing Y, Bronstein Y, Ross MI, et al. Contemporary diagnostic imaging modalities for the staging and surveillance of melanoma patients: a meta-analysis. JNCI J Natl Cancer Inst. 2011;103(2):129–42.

12. Clark PB, Soo V, Kraas J, Shen P, Levine EA. Futility of fluorodeoxyglucose F 18 positron emission tomography in initial evaluation of patients with t2 to t4 melanoma. Arch Surg. 2006;141(3):284–8.

13. Wagner JD, Schauwecker D, Davidson D, et al. Inefficacy of F-18 fluorodeoxy-D-glucose-positron emission tomography scans for initial evaluation in early-stage cutaneous melanoma. Cancer. 2005;104(3):570–9.

14. Wagner JD, Schauwecker D, Davidson D, et al. Prospective study of fluorodeoxyglucose–positron emission tomography imaging of lymph node basins in melanoma patients undergoing sentinel node biopsy. J Clin Oncol. 1999;17(5):1508.

15. Wagner JD, Davidson D, Coleman JJ, et al. Lymph node tumor volumes in patients undergoing sentinel lymph node biopsy for cutaneous melanoma. Ann Surg Oncol. 1999;6(4):398–404.

16. Dummer R, Hauschild A, Lindenblatt N, Pentheroudakis G, Keilholz U. Cutaneous melanoma: ESMO clinical practice guidelines for diagnosis, treatment and follow-up. Ann Oncol. 2015;26(suppl_5):v126–32.

17. Horn J, Lock-Andersen J, Sjøstrand H, Loft A. Routine use of FDG-PET scans in melanoma patients with positive sentinel node biopsy. Eur J Nucl Med Mol Imaging. 2006;33(8):887–92.

18. Müller-Horvat C, Radny P, Eigentler TK, et al. Prospective comparison of the impact on treatment decisions of whole-body magnetic resonance imaging and computed tomography in patients with metastatic malignant melanoma. Eur J Cancer. 2006;42(3):342–50.

19. Pfannenberg C, Aschoff P, Schanz S, et al. Prospective comparison of 18F-fluorodeoxyglucose positron emission tomography/computed tomography and whole-body magnetic resonance imaging in staging of advanced malignant melanoma. Eur J Cancer. 2007;43(3):557–64.

20. Laurent V, Trausch G, Bruot O, Olivier P, Felblinger J, Régent D. Comparative study of two whole-body imaging techniques in the case of melanoma metastases: advantages of multi-contrast MRI examination including a diffusion-weighted sequence in comparison with PET-CT. Eur J Radiol. 2010;75(3):376–83.

21. Schwenzer NF, Pfannenberg AC. PET/CT, MR, and PET/MR in lymphoma and melanoma. Semin Nucl Med. 2015;45(4):322–31.

22. Jouvet JC, Thomas L, Thomson V, et al. Whole-body MRI with diffusion-weighted sequences compared with 18 FDG PET-CT, CT and superficial lymph node ultrasonography in the staging of advanced cutaneous melanoma: a prospective study. J Eur Acad Dermatol Venereol. 2014;28(2):176–85.

23. The Collaborative Ocular Melanoma Study Group. Assessment of metastatic disease status at death in 435 patients with large choroidal melanoma in the collaborative ocular melanoma study (coms): coms report no. 15. Arch Ophthalmol. 2001;119(5):670–6.

24. Burris NS, Johnson KM, Larson PEZ, et al. Detection of small pulmonary nodules with ultrashort echo time sequences in oncology patients by using a PET/MR system. Radiology. 2016;278(1):239–46.

25. Nakai T, Okuyama C, Kubota T, et al. Pitfalls of FDG-PET for the diagnosis of osteoblastic bone metastases in patients with breast cancer. Eur J Nucl Med Mol Imaging. 2005;32(11):1253–8.

26. Strobel K, Dummer R, Steinert HC, et al. Chemotherapy response assessment in stage IV melanoma patients—comparison of 18F-FDG-PET/CT, CT, brain MRI, and tumormarker S-100B. Eur J Nucl Med Mol Imaging. 2008;35(10):1786.

27. Servois V, Mariani P, Malhaire C, et al. Preoperative staging of liver metastases from uveal melanoma by magnetic resonance imaging (MRI) and fluorodeoxyglucose-positron emission tomography (FDG-PET). Eur J Surg Oncol. 2010;36(2):189–94.

28. Francken AB, Fulham MJ, Millward MJ, Thompson JF. Detection of metastatic disease in patients with uveal melanoma using positron emission tomography. Eur J Surg Oncol. 2006;32(7):780–4.

29. Gulec SA, Faries MB, Lee CC, et al. The role of fluorine-18 deoxyglucose positron emission tomography in the management of patients with metastatic melanoma: impact on surgical decision making. Clin Nucl Med. 2003;28(12):961–5.

30. Beyer T, Bockisch A, Kühl H, Martinez M-J. Whole-body 18F-FDG PET/CT in the presence of truncation artifacts. J Nucl Med. 2006;47(1):91–9.

31. Delso G, Martinez-Möller A, Bundschuh RA, Nekolla SG, Ziegler SI. The effect of limited MR field of view in MR/PET attenuation correction. Med Phys. 2010;37(6):2804–12.

32. Mehranian A, Zaidi H. Impact of time-of-flight PET on quantification errors in MR imaging–based attenuation correction. J Nucl Med. 2015;56(4):635–41.

33. Minamimoto R, Levin C, Jamali M, et al. Improvements in PET image quality in time of flight (TOF) simultaneous PET/MRI. Mol Imaging Biol. 2016;18(5):776–81.

34. Partovi S, Chalian M, Fergus N, et al. Magnetic resonance/positron emission tomography (MR/PET) oncologic applications: bone and soft tissue sarcoma. Semin Roentgenol. 2014;49(4):345–52.

35. Pisters PW, Harrison LB, Leung DH, Woodruff JM, Casper ES, Brennan MF. Long-term results of a prospective randomized trial of adjuvant brachytherapy in soft tissue sarcoma. J Clin Oncol. 1996;14(3):859–68.

36. Yang JC, Chang AE, Baker AR, et al. Randomized prospective study of the benefit of adjuvant radiation therapy in the treatment of soft tissue sarcomas of the extremity. J Clin Oncol. 1998;16(1):197–203.

37. Schwarzbach MHM, Dimitrakopoulou-Strauss A, Willeke F, et al. Clinical value of [18-F] fluorodeoxyglucose positron emission tomography imaging in soft tissue sarcomas. Ann Surg. 2000;231(3):380–6.

38. Eary JF, Conrad EU. Imaging in sarcoma. J Nucl Med. 2011;52(12):1903–13.

39. Hicks RJ, Toner GC, Choong PFM. Clinical applications of molecular imaging in sarcoma evaluation. Cancer Imaging. 2005;5(1):66–72.

40. Folpe AL, Lyles RH, Sprouse JT, Conrad EU, Eary JF. (F-18) fluorodeoxyglucose positron emission tomography as a predictor of pathologic grade and other prognostic variables in bone and soft tissue sarcoma. Clin Cancer Res. 2000;6(4):1279–87.

41. Benz MR, Tchekmedyian N, Eilber FC, Federman N, Czernin J, Tap WD. Utilization of positron emission tomography in the management of patients with sarcoma. Curr Opin Oncol. 2009;21(4):345–51.

42. Benz MR, Czernin J, Allen-Auerbach MS, et al. FDG-PET/CT imaging predicts histopathologic treatment responses after the initial cycle of Neoadjuvant chemotherapy in high-grade soft-tissue sarcomas. Clin Cancer Res. 2009;15(8):2856–63.

43. Tateishi U, Kawai A, Chuman H, et al. PET/CT allows stratification of responders to neoadjuvant chemotherapy for high-grade sarcoma: a prospective study. Clin Nucl Med. 2011;36(7):526–32.

44. Iagaru A, Masamed R, Chawla SP, Menendez LR, Fedenko A, Conti PS. F-18 FDG PET and PET/CT evaluation of response to chemotherapy in bone and soft tissue sarcomas. Clin Nucl Med. 2008;33(1):8–13.

45. Schwarzbach MHM, Hinz U, Dimitrakopoulou-Strauss A, et al. Prognostic significance of preoperative [18-F] fluorodeoxyglucose (FDG) positron emission tomography (PET) imaging in patients with resectable soft tissue sarcomas. Ann Surg. 2005;241(2):286–94.

46. Tateishi U, Yamaguchi U, Seki K, Terauchi T, Arai Y, Kim EE. Bone and soft-tissue sarcoma: preoperative staging with fluorine 18 fluorodeoxyglucose PET/CT and conventional imaging. Radiology. 2007;245(3):839–47.

47. Franzius C, Daldrup-Link HE, Wagner-Bohn A, et al. FDG–PET for detection of recurrences from malignant primary bone tumors: comparison with conventional imaging. Ann Oncol. 2002;13(1):157–60.
48. Piperkova E, Mikhaeil M, Mousavi A, et al. Impact of PET and CT in PET/CT studies for staging and evaluating treatment response in bone and soft tissue sarcomas. Clin Nucl Med. 2009;34(3):146–50.
49. Sinha S, Peach AHS. Diagnosis and management of soft tissue sarcoma. BMJ. 2010;341:c7170.
50. Berquist TH, Ehman RL, King BF, Hodgman CG, Ilstrup DM. Value of MR imaging in differentiating benign from malignant soft-tissue masses: study of 95 lesions. Am J Roentgenol. 1990;155(6):1251–5.
51. Kransdorf MJ, Murphey MD. Radiologic evaluation of soft-tissue masses. Am J Roentgenol. 2000;175(3):575–87.
52. Doganay S, Altinok T, Alkan A, Kahraman B, Karakas HM. The role of MRS in the differentiation of benign and malignant soft tissue and bone tumors. Eur J Radiol. 2011;79(2):e33–e7.
53. Schnapauff D, Zeile M, Niederhagen MB, et al. Diffusion-weighted echo-planar magnetic resonance imaging for the assessment of tumor cellularity in patients with soft-tissue sarcomas. J Magn Reson Imaging. 2009;29(6):1355–9.
54. Tateishi U, Hosono A, Makimoto A, et al. Comparative study of FDG PET/CT and conventional imaging in the staging of rhabdomyosarcoma. Ann Nucl Med. 2009;23(2):155–61.
55. Yokouchi M, Terahara M, Nagano S, et al. Clinical implications of determination of safe surgical margins by using a combination of CT and 18FDG-positron emission tomography in soft tissue sarcoma. BMC Musculoskelet Disord. 2011;12(1):166.
56. Völker T, Denecke T, Steffen I, et al. Positron emission tomography for staging of pediatric sarcoma patients: results of a prospective multicenter trial. J Clin Oncol. 2007;25(34):5435–41.
57. Arush MWB, Israel O, Postovsky S, et al. Positron emission tomography/computed tomography with 18fluoro-deoxyglucose in the detection of local recurrence and distant metastases of pediatric sarcoma. Pediatr Blood Cancer. 2007;49(7):901–5.
58. Kneisl JS, Patt JC, Johnson JC, Zuger JH. Is PET useful in detecting occult nonpulmonary metastases in pediatric bone sarcomas? Clin Orthop Relat Res. 2006;450:101–4.
59. Potter DA, Glenn J, Kinsella T, et al. Patterns of recurrence in patients with high-grade soft-tissue sarcomas. J Clin Oncol. 1985;3(3):353–66.
60. Sawicki LM, Grueneisen J, Buchbender C, et al. Comparative performance of 18F-FDG PET/MRI and 18F-FDG PET/CT in detection and characterization of pulmonary lesions in 121 oncologic patients. J Nucl Med. 2016;57(4):582–6.
61. Schuler MK, Richter S, Beuthien-Baumann B, et al. PET/MRI imaging in high-risk sarcoma: first findings and solving clinical problems. Case Rep Oncol Med. 2013;2013:793927.
62. Partovi S, Kohan AA, Zipp L, et al. Hybrid PET/MR imaging in two sarcoma patients – clinical benefits and implications for future trials. Int J Clin Exp Med. 2014;7(3):640–8.
63. Dudeck O, Zeile M, Pink D, et al. Diffusion-weighted magnetic resonance imaging allows monitoring of anticancer treatment effects in patients with soft-tissue sarcomas. J Magn Reson Imaging. 2008;27(5):1109–13.
64. Evilevitch V, Weber WA, Tap WD, et al. Reduction of glucose metabolic activity is more accurate than change in size at predicting histopathologic response to neoadjuvant therapy in high-grade soft-tissue sarcomas. Clin Cancer Res. 2008;14(3):715–20.
65. Hirsch FW, Sattler B, Sorge I, et al. PET/MR in children. Initial clinical experience in paediatric oncology using an integrated PET/MR scanner. Pediatr Radiol. 2013;43(7):860–75.
66. Röllig C, Knop S, Bornhäuser M. Multiple myeloma. Lancet. 2014;385(9983):2197–208.
67. Raab MS, Podar K, Breitkreutz I, Richardson PG, Anderson KC. Multiple myeloma. Lancet. 2009;374(9686):324–39.
68. Durie BGM, Salmon SE. A clinical staging system for multiple myeloma correlation of measured myeloma cell mass with presenting clinical features, response to treatment, and survival. Cancer. 1975;36(3):842–54.
69. Durie BGM. The role of anatomic and functional staging in myeloma: description of Durie/Salmon plus staging system. Eur J Cancer. 2006;42(11):1539–43.

70. Schirrmeister H, Bommer M, Buck A, et al. Initial results in the assessment of multiple myeloma using 18F-FDG PET. Eur J Nucl Med Mol Imaging. 2002;29(3):361–6.

71. Durie BGM, Waxman AD, D'Agnolo A, Williams CM. Whole-body 18F-FDG PET identifies high-risk myeloma. J Nucl Med. 2002;43(11):1457–63.

72. van Lammeren-Venema D, Regelink JC, Riphagen II, Zweegman S, Hoekstra OS, Zijlstra JM. 18F-fluoro-deoxyglucose positron emission tomography in assessment of myeloma-related bone disease: a systematic review. Cancer. 2012;118(8):1971–81.

73. Baur A, Bartl R, Pellengahr C, Baltin V, Reiser M. Neovascularization of bone marrow in patients with diffuse multiple myeloma. Cancer. 2004;101(11):2599–604.

74. Walker R, Barlogie B, Haessler J, et al. Magnetic resonance imaging in multiple myeloma: diagnostic and clinical implications. J Clin Oncol. 2007;25(9):1121–8.

75. Gleeson TG, Moriarty J, Shortt CP, et al. Accuracy of whole-body low-dose multidetector CT (WBLDCT) versus skeletal survey in the detection of myelomatous lesions, and correlation of disease distribution with whole-body MRI (WBMRI). Skelet Radiol. 2009;38(3):225–36.

76. Lütje S, de Rooy JWJ, Croockewit S, Koedam E, Oyen WJG, Raymakers RA. Role of radiography, MRI and FDG-PET/CT in diagnosing, staging and therapeutical evaluation of patients with multiple myeloma. Ann Hematol. 2009;88(12):1161.

77. Giles SL, Messiou C, Collins DJ, et al. Whole-body diffusion-weighted MR imaging for assessment of treatment response in myeloma. Radiology. 2014;271(3):785–94.

78. Vij R, Fowler KJ, Shokeen M. New approaches to molecular imaging of multiple myeloma. J Nucl Med. 2016;57(1):1–4.

79. Sachpekidis C, Hillengass J, Goldschmidt H, et al. Comparison of (18)F-FDG PET/CT and PET/MRI in patients with multiple myeloma. Am J Nucl Med Mol Imaging. 2015;5(5):469–78.

80. Nanni C, Zamagni E, Farsad M, et al. Role of 18F-FDG PET/CT in the assessment of bone involvement in newly diagnosed multiple myeloma: preliminary results. Eur J Nucl Med Mol Imaging. 2006;33(5):525–31.

81. Martinez-Möller A, Souvatzoglou M, Delso G, et al. Tissue classification as a potential approach for attenuation correction in whole-body PET/MRI: evaluation with PET/CT data. J Nucl Med. 2009;50(4):520–6.

82. Aznar MC, Sersar R, Saabye J, et al. Whole-body PET/MRI: the effect of bone attenuation during MR-based attenuation correction in oncology imaging. Eur J Radiol. 2014;83(7):1177–83.

83. Marshall HR, Patrick J, Laidley D, Prato FS, Butler J, Théberge J, Thompson RT, Stodilka RZ. Description and assessment of a registration-based approach to include bones for attenuation correction of whole-body PET/MRI. Med Phys. 2013;40(8):082509.

84. Teras LR, DeSantis CE, Cerhan JR, Morton LM, Jemal A, Flowers CR. 2016 US lymphoid malignancy statistics by World Health Organization subtypes. CA Cancer J Clin. 2016;66(6):443–59.

85. Kempf W, Kazakov DV, Kerl K. Cutaneous lymphomas: an update. Part 1: T-cell and natural killer/T-cell lymphomas and related conditions. Am J Dermatopathol. 2014;36(2):105–23.

86. Jawed SI, Myskowski PL, Horwitz S, Moskowitz A, Querfeld C. Primary cutaneous T-cell lymphoma (mycosis fungoides and Sézary syndrome): part II. Prognosis, management, and future directions. J Am Acad Dermatol. 2014;70(2):223.e1–e17.

87. Jacobson AF, Fogelman I. Bone scanning in clinical oncology: does it have a future? Eur J Nucl Med. 1998;25(9):1219–23.

88. Even-Sapir E. Imaging of malignant bone involvement by morphologic, scintigraphic, and hybrid modalities. J Nucl Med. 2005;46(8):1356–67.

89. Hsu WK, Virk MS, Feeley BT, Stout DB, Chatziioannou AF, Lieberman JR. Characterization of osteolytic, osteoblastic, and mixed lesions in a prostate cancer mouse model using 18F-FDG and 18F-fluoride PET/CT. J Nucl Med. 2008;49(3):414–21.

90. Cook GJ, Houston S, Rubens R, Maisey MN, Fogelman I. Detection of bone metastases in breast cancer by 18FDG PET: differing metabolic activity in osteoblastic and osteolytic lesions. J Clin Oncol. 1998;16(10):3375–9.

91. Chua S, Gnanasegaran G, Cook GJR. Miscellaneous cancers (lung, thyroid, renal cancer, myeloma, and neuroendocrine tumors): role of SPECT and PET in imaging bone metastases. Semin Nucl Med. 2009;39(6):416–30.
92. Yang H-L, Liu T, Wang X-M, Xu Y, Deng S-M. Diagnosis of bone metastases: a meta-analysis comparing 18FDG PET, CT, MRI and bone scintigraphy. Eur Radiol. 2011;21(12):2604–17.
93. Schmidt GP, Schoenberg SO, Schmid R, et al. Screening for bone metastases: whole-body MRI using a 32-channel system versus dual-modality PET-CT. Eur Radiol. 2007;17(4):939–49.
94. Reischauer C, Froehlich JM, Koh D-M, et al. Bone metastases from prostate cancer: assessing treatment response by using diffusion-weighted imaging and functional diffusion maps—initial observations. Radiology. 2010;257(2):523–31.
95. Even-Sapir E, Metser U, Mishani E, Lievshitz G, Lerman H, Leibovitch I. The detection of bone metastases in patients with high-risk prostate cancer: 99mTc-MDP planar bone scintigraphy, single- and multi-field-of-view SPECT, 18F-fluoride PET, and 18F-fluoride PET/CT. J Nucl Med. 2006;47(2):287–97.
96. Even-Sapir E, Mishani E, Flusser G, Metser U. 18F-fluoride positron emission tomography and positron emission tomography/computed tomography. Semin Nucl Med. 2007;37(6):462–9.
97. Blake GM, Park-Holohan S-J, Cook GJR, Fogelman I. Quantitative studies of bone with the use of 18F-fluoride and 99mTc-methylene diphosphonate. Semin Nucl Med. 2001;31(1):28–49.
98. Iagaru A, Mittra E, Dick DW, Gambhir SS. Prospective evaluation of 99mTc MDP scintigraphy, 18F NaF PET/CT, and 18F FDG PET/CT for detection of skeletal metastases. Mol Imaging Biol. 2012;14(2):252–9.
99. Withofs N, Grayet B, Tancredi T, et al. 18F-fluoride PET/CT for assessing bone involvement in prostate and breast cancers. Nucl Med Commun. 2011;32(3):168–76.
100. Mosavi F, Johansson S, Sandberg DT, Turesson I, Sörensen J, Ahlström H. Whole-body diffusion-weighted MRI compared with 18F-NaF PET/CT for detection of bone metastases in patients with high-risk prostate carcinoma. Am J Roentgenol. 2012;199(5):1114–20.
101. Iagaru A, Mittra E, Yaghoubi SS, et al. Novel strategy for a cocktail 18F-fluoride and 18F-FDG PET/CT scan for evaluation of malignancy: results of the pilot-phase study. J Nucl Med. 2009;50(4):501–5.
102. Lin FI, Rao JE, Mittra ES, et al. Prospective comparison of combined 18F-FDG and 18F-NaF PET/CT vs. 18F-FDG PET/CT imaging for detection of malignancy. Eur J Nucl Med Mol Imaging. 2012;39(2):262–70.
103. Iagaru A, Mittra E, Mosci C, et al. Combined 18F-fluoride and 18F-FDG PET/CT scanning for evaluation of malignancy: results of an international multicenter trial. J Nucl Med. 2013;54(2):176–83.
104. Minamimoto R, Loening A, Jamali M, et al. Prospective comparison of 99mTc-MDP scintigraphy, combined 18F-NaF and 18F-FDG PET/CT, and whole-body MRI in patients with breast and prostate cancer. J Nucl Med. 2015;56(12):1862–8.
105. Minamimoto R, Mosci C, Jamali M, et al. Semiquantitative analysis of the biodistribution of the combined 18F-NaF and 18F-FDG administration for PET/CT imaging. J Nucl Med. 2015;56(5):688–94.
106. Sonni I, Minamimoto R, Loening A, et al. Imaging patients with breast and prostate cancers using combined 18F NaF/18F FDG and TOF simultaneous PET/MRI. J Nucl Med. 2016;57(supplement 2):1416.

PET/MRI in Brain Tumors

11

Ida Sonni, Valentina Garibotto, Andrei Iagaru,
Devsmita Das, and Tarik Massoud

Contents

11.1   Introduction

The poor clinical outcome of intracranial malignancies makes them a major medical problem. According to the American Cancer Society, 23,700 new cases of primary brain tumors would be diagnosed in the United States in 2016 [1]. Brain metastases

I. Sonni (✉)
Department of Radiology, Nuclear Medicine and Molecular Imaging, Stanford University, Stanford, CA 94305, USA
e-mail: isonni@stanford.edu, idasonni@gmail.com

V. Garibotto
Division of Nuclear Medicine and Molecular Imaging, Geneva University Hospitals, Geneva, Switzerland

NIMTlab, Faculty of Medicine, Geneva University Hospitals, Geneva, Switzerland

A. Iagaru • D. Das • T. Massoud
Department of Radiology, Division of Neuroimaging and Neurointervention, Stanford University, Stanford, CA 94305, USA
e-mail: aiagaru@stanford.edu

are more common than primary brain tumors as 10–20% of adults with cancer develop metastases to the brain. Even though any malignancy could potentially metastasize to the brain, in the majority of cases, they arise from lung, breast, and skin (melanoma) cancers [2]. Primary brain tumors are a heterogeneous group of neoplasms including different subtypes with a wide range of histopathologic, molecular, and genetic profiles and consequently different clinical presentation and prognosis. The complex pathophysiology and vast heterogeneity of brain tumors make their classification confusing to the most, despite the World Health Organization (WHO) provides us with detailed classification. The fourth edition of the *WHO Classification of Tumors of the Central Nervous System* (CNS) published in 2007 [3] describes numerous tumor entities, variants of entities, and histological patterns. As a means of predicting the biological behavior of the tumor, histological grading is also described. Brain tumors are divided in four grades, primarily based on aggressiveness (Table 11.1). An update of the fourth *WHO Classification of Tumors of the Central Nervous System* was recently released in 2016 [4] and represents a conceptual and practical advance to the 2007 version. In the molecular era that we are living, when a better insight into tumor biology and tumor genetic profiles is warranted, the last updated WHO classification incorporated molecular parameters, in addition to histology, in the definition of many tumor entities [4, 5]. The role played by neuroimaging in this complex scenario is essential. Particularly important is the use of molecular imaging and new advanced magnetic resonance imaging (MRI) techniques that can aid tumor characterization noninvasively, allowing a more targeted therapeutic approach, and consequently improve prognosis of these tumors.

One of the several aspects that make brain tumors unique compared to other systemic tumors is the presence of the blood-brain barrier (BBB) [6]. Brain blood vessels are protected by this selective barrier limiting the exchange of substances between the systemic and cerebral circulations. This aspect is extremely important because the BBB, besides protecting the brain from external insults, may also limit the permeability to contrast media (e.g., gadolinium), to some radiopharmaceuticals for SPECT or PET imaging, as well as some therapeutic agents. The most aggressive brain tumors (high grades), due to their infiltrative growth pattern, are accompanied by disruption of the BBB. But when tumor growth is slow and does not affect BBB integrity (low grades), this may represent a challenge to tumor visualization [6, 7]. Another issue related to the unicity of the BBB is the so-called

Table 11.1 Brain tumor grading

Grading	Proliferative activity	Clinical behavior
Grade I (well differentiated)	Low proliferative potential	Usually curable by surgical resection
Grade II (moderately differentiated)	Low proliferative potential	Recurrence is frequent
	Infiltrative	Tend to progress to higher grades
Grade III (poorly differentiated)	Brisk mitotic activity and nuclear atypia	Tend to recur often
	Infiltrative	
Grade IV (undifferentiated)	Mitotically active	Rapid pre- and postoperative evolution
	Necrosis-prone	Fatal outcome

pseudoprogression [8]. In patients with malignant gliomas treated with radiation therapy, it was found an increase in contrast-enhanced lesions on MRI immediately after treatment that improved without any further treatment. This condition has been defined pseudoprogression, to be distinguished from actual tumor progression, and is due to treatment-induced temporary loss of integrity of the BBB allowing gadolinium enhancement [9].

These important aspects should be considered when imaging brain tumors with contrast-enhanced MRI and PET/CT or PET/MRI.

MRI with and without contrast is the mainstay imaging modality for diagnosis, treatment planning, and posttreatment response assessment of brain tumors [10, 11]. Structural MRI provides excellent anatomical detail, and more advanced recently implemented techniques allow evaluation of metabolic or functional information regarding brain tumors. Molecular imaging with PET can also play an important role in brain tumors, especially in those gray areas where usefulness of MRI is limited.

This chapter will review the main features of different MR techniques and PET radiopharmaceuticals used in brain tumors imaging. The current applications of integrated PET/MRI systems will be described in the final sections, as well as the advantages of the combined approach.

11.2 Neuroimaging of Brain Tumors

11.2.1 Computed Tomography (CT)

In patients with suspected brain tumors, CT remains the first-line imaging modality. This is mainly due to its widespread availability, ease of the procedure, low costs, and relatively low risks, and it is usually well tolerated by patients. CT is very sensitive in identifying mass effect, acute hemorrhage, hydrocephalus, and other structural alterations due to the presence of brain tumors. However, the poor soft tissue contrast of CT represents a major drawback in imaging the brain and limits its ability to detect the subtle changes in brain parenchyma that accompany brain tumors in some cases. Other worth-mentioning disadvantages of CT are the radiation exposure due to the use of ionizing radiations and the high allergenic potential of iodinated contrast agents. For all the reasons described above, CT remains an initial screening technique in patients with suspected brain tumors, but its utility is limited to the exclusion of life-threatening conditions [6, 12].

11.2.2 Magnetic Resonance Imaging (MRI)

Magnetic resonance imaging (MRI) has become a critically important and obligatory diagnostic tool central to the multidisciplinary planning and clinical management of brain tumor patients [13–16]. The inherent high resolution and exquisite soft tissue contrast of MRI allow to gain an understanding of the three-dimensional morphologic and functional features of brain tumors and thus to appreciate the problem these neoplasms pose in patient clinical management. These imaging strategies also allow the fusion of disparate sets of information regarding brain tumors

(e.g., structural, functional, hemodynamic, metabolic, and cellular) into the clinical assessment of patients. Neuroimaging-based MRI tools may therefore be used to diagnose brain tumors and suggest their aggressiveness preoperatively, to plan and guide surgical biopsy or removal intraoperatively, to understand any potential complications arising from treatment, and to assess and monitor therapeutic response and patient prognosis.

Current clinical management of patients with brain tumors depends entirely on the use of up-to-date neuro-MRI techniques. Recent advances in brain tumors imaging offer unique anatomical and pathophysiological information that provide new insights into brain tumor biology and behavior. Here we discuss both structural and advanced MRI methods for the diagnosis of brain tumors, their treatment planning, and for disease monitoring, highlighting the modern clinical application of these techniques in evaluation and treatment of brain tumor patients. A detailed consideration of the underlying MR physics is beyond the scope of this chapter and can be found elsewhere in this book. Instead, we discuss the modern clinical application of neuro-MRI in the daily evaluation and treatment of patients with brain tumors.

11.2.2.1 Structural MRI of Brain Tumors

There are several reasons why structural MRI has a central role in the neuroradiologic assessment of brain tumors [5, 17]. First, because of its relative advantages over CT imaging, it is usually the first study that allows an accurate diagnosis of a brain tumor. Not only can small tumors be missed on CT scanning but this technique may not depict all multifocal lesions. Detailed morphological characteristics as well as the presence of leptomeningeal or intraventricular spread may also be difficult to diagnose on CT scanning. Second, accurate structural characterization, both qualitative and quantitative, of a brain tumor, as reflected in its pathological MRI signal, is crucial for defining the topographical features of the tumor and, in turn, its likely natural history if left untreated. Third, the analysis of these structural MRI features is crucial in helping select the most appropriate treatment. Finally, MRI is used after tumor resection for assessing the extent of tissue removal—the extent of resection, along with histopathology, being two important factors in determining patient prognosis. There are two recent areas of research and development aimed at enhancing the contributions of structural MRI to brain tumor management. One approach uses methods that allow more accurate image segmentation especially of the peripheral zones of tumor infiltration into surrounding cerebral parenchyma to enable better assessment of tumor margins, and the other is the adoption of VASARI (Visually Accessible Rembrandt Images) feature set criteria to provide a more objective standard and use of a numerical score to quantitatively describe the nature and extent of tumor MRI features.

Different chemical compositions and molecular environments in the brain lead to different MRI relaxation times. Both T1 and T2 relaxation times vary for different tissue types and depend on field strengths. T1-weighted images (T1WIs) are best for obtaining contrast between different healthy brain tissues. However, most pathology, including brain tumors, has long T2 and long T1 (high signal on T2WIs and low signal on T1WIs). Structural MRI is generally concerned with visualizing soft

tissue, e.g., brain or tumor parenchyma, or properties derived from the structural integrity of these tissues. Thus, different tumor components have different T1 and T2 values, depending on tissue composition, e.g., tumor, necrosis, edema, hemorrhage, and calcification. In practice, multi-sequence MRI is therefore used to better characterize brain tumors, especially those with aggressive features. The standard protocol most commonly used includes spin-echo T2-weighted images (T2WIs) (Fig. 11.1a), fluid-attenuated inversion recovery images (FLAIR) (Fig. 11.1b), T1-weighted images (T1WIs) (Fig. 11.1c), T1WI after the administration of contrast agent (Fig. 11.1d), and gradient echo images (GRE) (Fig. 11.1e) [18–20]. Most tumors are hypointense on T1WIs and hyperintense on T2WIs in the absence of hemorrhagic changes. In biologically aggressive tumors such as glioblastoma, MRI usually shows a heterogeneous mass with internal cysts, flow voids representing prominent intratumoral vessels, internal T1 hyperintense areas (hemorrhagic foci), neovascularity, necrotic foci, significant peritumoral vasogenic edema, infiltration of surrounding brain, and significant mass effect on adjacent normal brain structures that become effaced or distorted. The structural imaging features of commonly encountered brain tumors are described in Table 11.2. Because of the highly variable appearance of brain tumors, they may mimic other brain diseases on MRI. For example, a glioblastoma cystic mass with rim enhancement may be mistaken for other brain tumors, tumefactive demyelination, radiation necrosis, metastasis, subacute abscess, an infarct, or a resolving hematoma. A low-grade glioma may be mistaken for an infarct, demyelination, cerebritis, or hamartoma. In terms of the imaging appearance of a mass in the spectrum from low-grade glioma to glioblastoma, the following generalizations can be made, although with exceptions: the incidence of calcification decreases toward glioblastoma, whereas the incidence increases toward glioblastoma for enhancement, hemorrhage, necrosis, mass effect, and surrounding vasogenic edema.

The use of gadolinium chelate contrast-enhanced imaging of the brain has become a standard and essential part of the evaluation of most brain pathologies. The accurate delineation of areas with blood-brain barrier (BBB) disruption depends on the contrast sensitivity of the applied MRI technique and the dosage and type of gadolinium-based contrast agent. The latter has been extensively studied for the diagnosis of various diseases including detection of primary or secondary brain tumors where the use of single- or multiple-dose applications of gadolinium contrast agents has been proven.

Fluid-attenuated inversion recovery (FLAIR) imaging is an MRI sequence achieved by applying an inversion pulse with a long recovery time between this pulse and the start of the measurement. It may be used to suppress the high CSF signal on T2WIs so that the pathology adjacent to CSF spaces may be seen more clearly. Also, subtle lesions in the cortex stand out against of the background of attenuated CSF. Vasogenic edema surrounding brain tumors is also better seen and defined on FLAIR images and is therefore used in conjunction with T2WIs. Contrast-enhanced FLAIR MRI may be used by taking advantage of the T1 effect to achieve a particularly high contrast between tumor and background tissue. This allows an exact separation of enhancing and nonenhancing tumor components on

one sequence. Two- and three-dimensional FLAIR techniques are simple to implement. Three-dimensional Cube FLAIR also has the advantage of increased number of image slices that can be reconstructed in three planes.

In the pulse sequence of gradient echo (GRE) MRI, the repetition time (TR) can be reduced because flip angles other than 90° are used. This results in shorter imaging times and less motion artifacts. Therefore, GRE MR images are very sensitive to flow,
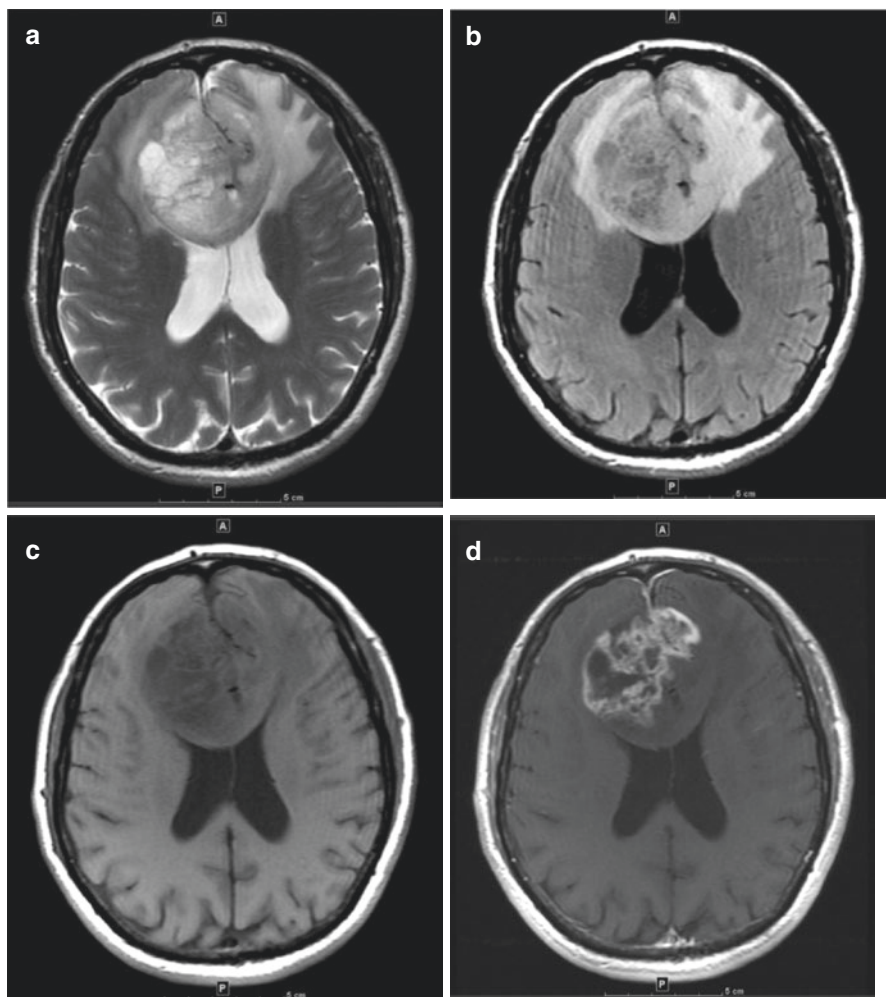
Fig. 11.1 Selected axial MR images of a 78-year-old patient with a large glioblastoma in bilateral anterior frontal lobes and spreading across the anterior corpus callosum (butterfly lesion). (**a**) T2WI shows the multicystic tumor and mass effect on the lateral ventricles. (**b**) Better delineation of the surrounding vasogenic edema on FLAIR T2WI. (**c**) T1WI. (**d**) Irregular heterogeneous thick nodular enhancement on a post-contrast T1WI. (**e**) Patchy increased susceptibility effect (signal dropout) on GRE, suggesting minimal intratumoral hemorrhage. (**f**, **g**) Patchy tumor restricted diffusion on DWI (**f**) and confirmed as dark signal on the ADC map (**g**). (**h**) Increased cerebral blood flow in the anterior aspects of this tumor seen on bolus perfusion imaging
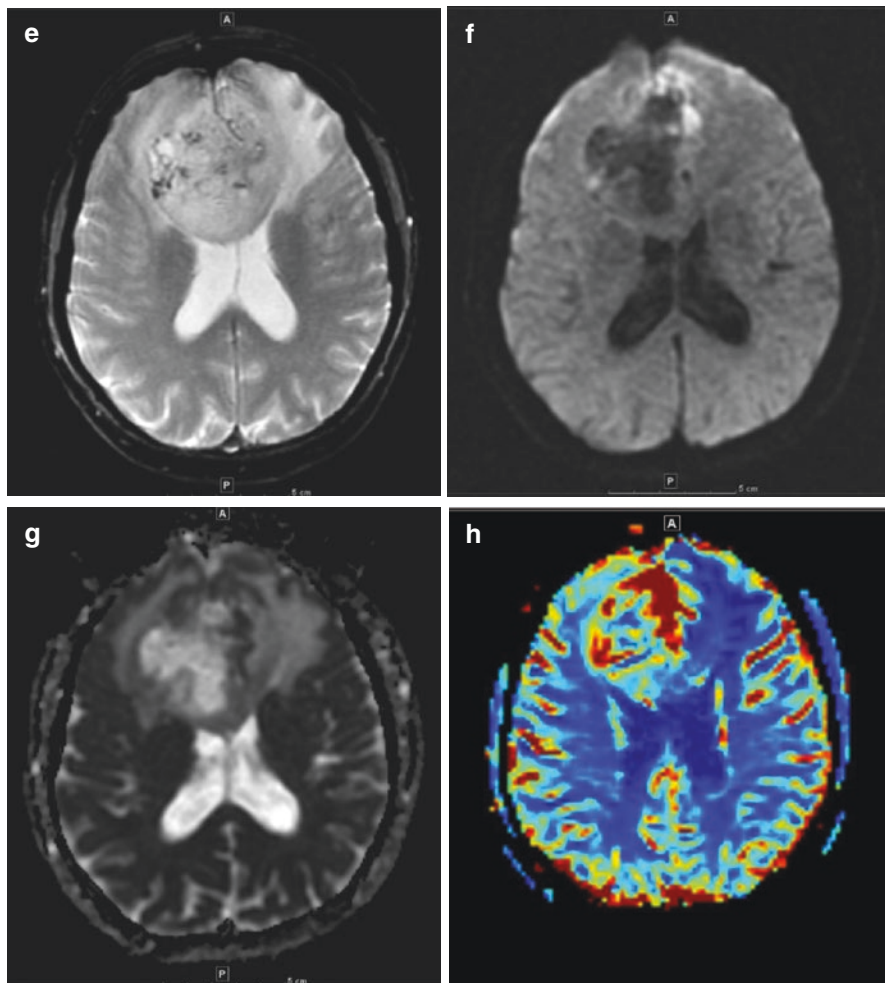
Fig. 11.1 (continued)

can produce images that produce MR angiographic sequences, and also may be used to see regions of signal dropout within a mass that represent calcification or slow flow within tumor vessels. Calcified tumors produce areas of signal void, and GRE pulse sequences are also very sensitive to the presence of hemorrhage, showing signal void owing to increased susceptibility effects. GRE is especially suited to three-dimensional imaging, which is used when high-resolution and thin contiguous slices are required, e.g., in performing time-of-flight MR angiography.

11.2.2.2 Advanced and Functional MRI of Brain Tumors

Over the past three decades, we have witnessed a shift in neuro-oncologic imaging from merely providing structural and anatomical information toward providing additional information about tumor physiology [21, 22]. Newer advanced MRI

Table 11.2 MRI features of selected common glial and other brain tumors

Tumor	T1 features	T2 features	Others
Glioblastoma	Isointense to hypointense	Hyperintense with surrounding edema	Variable enhancement that is peripheral, irregular, nodular. Necrosis. Hemorrhagic products. Variable restricted diffusion. On MRS: choline, lactate, lipids: increased; NAA, myoinositol: decreased
Diffuse astrocytoma (low-grade glioma)	Isointense to hypointense	Mass-like hyperintense. Follows white matter but expands the cortex	No restriction or enhancement. On MRS choline, choline: creatine ratio, and myoinositol and mI/Cr ratio: increase; NAA: decreased. No lactate peak
Pilocytic astrocytoma	Isointense to hypointense	Hyperintense solid component	Usually large cystic component with a brightly enhancing mural nodule. Enhancement. May have calcification
Pleomorphic xanthoastrocytoma	Isointense to hypointense	Isointense to hyperintense	Mural nodule. May have dural tail and remodeling of adjacent skull
Meningioma	Isointense to hypointense	Isointense to hypointense	Extra-axial. Intense enhancement. May show restricted diffusion. CSF vascular cleft sign. Dural tail. Sunburst appearance of vessels. May have vasogenic edema
Metastases	Isointense to hypointense. If hemorrhagic or melanoma, then may be hyperintense	Hyperintense	Uniform, punctate, or ring enhancement. Peritumoral edema may be out of proportion to tumor size
Vestibular Schwannoma	Isointense to hypointense	Heterogeneously hyperintense	Strong contrast enhancement, heterogeneous in large tumors

Table 11.2 (continued)

Tumor	T1 features	T2 features	Others
Ependymoma	Isointense to hypointense	Hyperintense	Foci of blooming from hemorrhage or calcification on GRE. Necrosis, but may be solid. Heterogeneous enhancement. Restricted diffusion
Medulloblastoma	Hypointense	Isointense to hyperintense	Most enhance. Calcification, necrosis, cysts. Surrounding edema. Restricted diffusion Usually vermian, but in adults is more lateral cerebellar
Oligodendroglioma	Hypointense	Hyperintense except for calcification areas	May enhance and show variable increased perfusion

techniques for brain tumors include diffusion and diffusion tensor imaging with tractography, perfusion imaging, MR spectroscopy, and functional imaging using the blood oxygenation level-dependent (BOLD) technique. These MRI techniques allow obtaining a variety of multiparametric information regarding brain tumor pathophysiology and investigating the structural, functional, and metabolic nature of brain tumor microenvironment. The evolution of these techniques has come about from a need for clinical researchers and pharmaceutical companies to have access to early and noninvasive biological information regarding brain tumors that can predict outcome and/or quantify therapeutic efficacy. Therefore, the readouts from these advanced MRI strategies are currently being used clinically, and further investigated as biomarkers for early diagnosis, for predicting outcome in response to specific therapies and monitoring therapeutic efficacy.

Diffusion-Weighted Imaging (DWI)
Diffusion-weighted imaging (DWI) is a unique tissue contrast technique based on a pulse sequence sensitized to the random motion of water molecules, i.e., Brownian motion. Certain pathologies constrain the normal Brownian motion of water molecules in brain tissue (restricted diffusion). Lesions that have restricted diffusion appear hyperintense on DWI and hypointense on the accompanying apparent diffusion coefficient (ADC) maps. Factors such as tissue perfusion, transport of water, or bulk motion can also contribute to the signal loss on ADC; this being the reason why the term ADC is used instead of diffusion coefficient. Thus, it is possible to quantify the diffusion in brain tissues by analyzing the accompanying ADC map. Differences in ADC arise owing to intracellular and extracellular diffusion, cellularity, cell membrane permeability, and overall tissue structure.

In brain tumors, DWI can be helpful in preoperative radiological grading of gliomas [23, 24]. Restricted diffusion in peripheral solid components of a glioma is attributed to hypercellularity and high nuclear to cytoplasmic ratios (Fig. 11.1f, g), corresponding to higher tumor grades, which include anaplastic astrocytoma and glioblastoma, whereas low-grade astrocytomas display increased diffusivity. Other brain tumors that typically show restricted diffusion for similar reasons are lymphoma, medulloblastoma, and meningioma (except that calcified or psammomatous meningiomas have low ADC values). Furthermore, epidermoid cysts almost always display restricted diffusion. DWI can also be used to discriminate tumor tissue from edema or a cystic or necrotic portion of a tumor. The latter may appear hypointense on DWI and show much higher ADC values, whereas the areas of enhancing tissue on T1WIs show high signal intensity on DWI. DWI is also very useful for differentiating a brain abscess from necrotic or cystic tumor. Abscesses have high central restriction on DWI owing to the presence of pus (in the center of a ring enhancing lesion) that restricts water motion within its cavity. An acute arterial infarct will also show bright restricted diffusion on DWI owing to cytotoxic edema.

Diffusion Tensor Imaging and Tractography

Diffusion tensor imaging (DTI) is an imaging technique to study the microarchitecture of brain parenchyma by quantifying physical parameters such as fractional anisotropy (FA) and mean diffusivity [25]. It is centered on the concepts of isotropic and anisotropic diffusion. Since water molecules can diffuse equally in all three directions, this is termed isotropic diffusion. This is found in the cerebral ventricles, but also occurs in gray matter. Instead, free water molecules move anisotropically in white matter, i.e., diffusion of water is not equal in all three directions. In white matter tracts, the myelin sheaths surrounding nerves cause the water molecules to move along the long axis of a fiber bundle and less in other directions. Thus, maximum diffusivity coincides with the orientation of white matter fiber tracts. Consequently, DTI allows identification and characterization of white matter tracts according to the direction and degree of their anisotropic water diffusion.

Information from DTI can be presented in two formats, FA maps and tractography (Fig. 11.2). Quantification of FA can provide an indication of white matter development and degradation. FA maps are images obtained in cross section. These may be formatted in gray scale or may be color coded to depict information on direction of white matter tracts. Conventionally, commissural white matter tracts, e.g., the corpus callosum, are shown in red, association fibers such as the superior longitudinal fasciculus are shown in green, and the superior-inferior running projection fibers are seen in blue. The intensity of color hues is proportional to the extent of FA. It is possible also to generate three-dimensional representations of the major white matter tracts in the brain. The principle direction of diffusion in a voxel is called the eigenvector. Tractography is performed by connecting a given voxel to the appropriate adjacent voxel, in accordance with the orientation of each voxel's principal eigenvector.

One of the most important indications of DTI in clinical practice is to study the relation of a brain tumor to white matter tracts [26]. Within a tumor center white
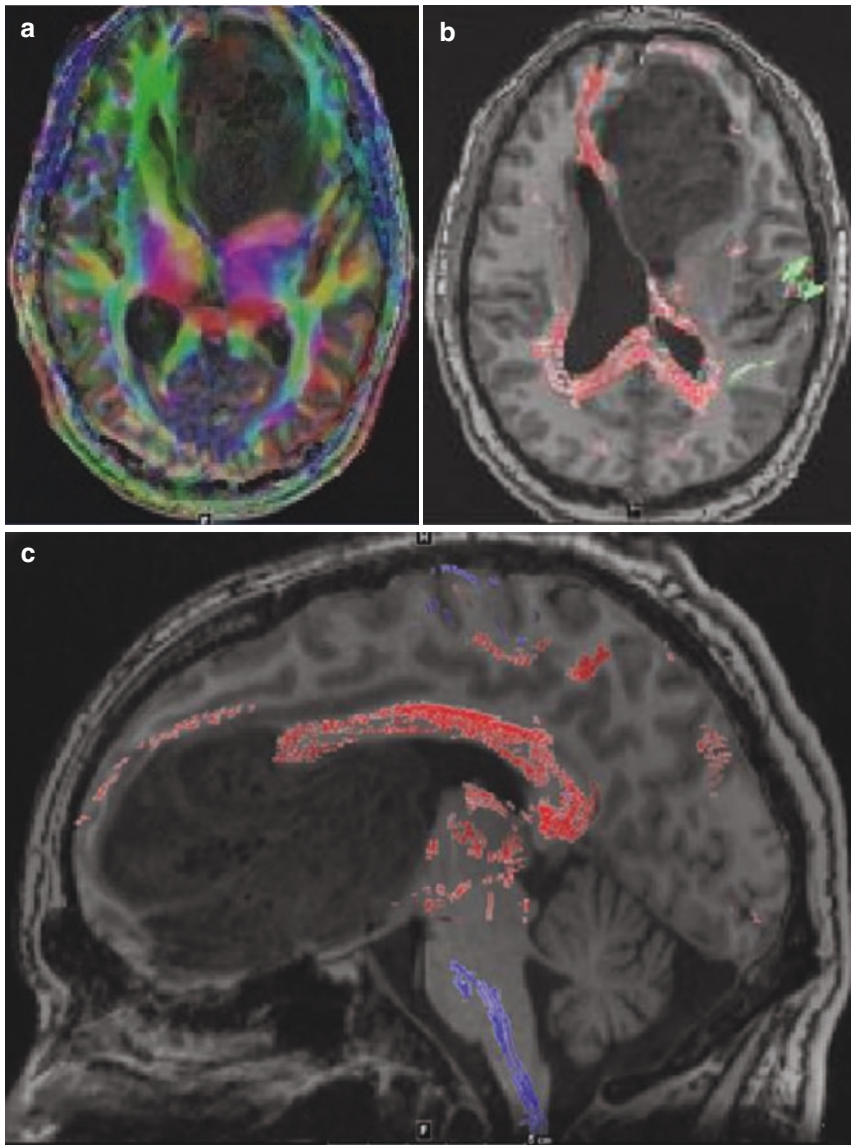
Fig. 11.2 Selected MR images of a 26-year-old patient with a large glioblastoma in the anterior left frontal lobe. (**a**) Axial DTI. (**b**) Axial tractography. (**c**) Sagittal tractography

matter fibers are displaced by cellular infiltration and FA is reduced. A tumor can displace, invade, and destroy surrounding white matter tracts or cause vasogenic edematous changes within them. Therefore, in the periphery and in a narrow rim of white matter rim surrounding a tumor, FA may be preserved or even increased by fiber compression owing to the mass effect of the tumor. When a white matter tract

is destroyed by tumor, there is loss of FA and therefore a reduction in their values, manifested on the gray scale FA maps as a loss of brightness.

There may be FA changes in white matter indicating cellular infiltration beyond the area of tumor enhancement. This can help guide the surgical approach and extent of resection. DTI demonstration of the corticospinal tracts may be used in conjunction with intraoperative fiber stimulation. Preoperative tractography demonstrating tumor involvement of the corticospinal tracts has been correlated to motor deficits, even without involvement of the motor cortex. Normalization depicted on postoperative tractography can predict improvement in function, suggesting a useful prognostic role for intraoperative tractography.

Bolus Perfusion Imaging

Perfusion-weighted imaging provides information about the perfusion status of the cerebral microcirculation [27]. There are two main approaches to measure cerebral perfusion using MRI. The first is application of an exogenous intravascular contrast agent, usually gadolinium-based, to highlight either the susceptibility effects of the contrast agent on the signal echo, namely, first-pass dynamic susceptibility contrast-enhanced (DSC) MR perfusion, or the relaxivity effects of the contrast agent on the signal echo, namely, dynamic contrast-enhanced (DCE) MR perfusion. The second approach is to capitalize on the presence of an endogenous contrast agent by using magnetically labeled arterial blood water as a diffusible flow tracer in arterial spin labeling (ASL) MR perfusion, discussed below. In DSC MR perfusion (or bolus-tracking MRI), the first pass of a bolus of contrast agent through the brain is monitored by a series of T2- or T2*-weighted MR images. The susceptibility effect of the paramagnetic contrast agent results in a signal loss, demonstrated on the signal intensity-time curve. Using the principles of the indicator dilution theory, the signal information can then be converted into a contrast medium concentration-time curve on a pixel-by-pixel basis. From these data, parametric maps of cerebral blood volume (CBV) and flow (CBF) can be derived. Regional CBF and CBV values can be obtained by region-of-interest analysis. DCE is based on the acquisition of serial T1WIs before, during, and after administration of a gadolinium-based contrast agent. The resulting signal intensity-time curve reflects a composite of tissue perfusion, vessel permeability, and extravascular-extracellular space. Using pharmacokinetic modeling of perfusion data, several metrics are commonly derived, of which the most frequently used is k^{trans} and which appears to reproducibly measure permeability in glioma patients.

Perfusion imaging using MRI has become an integral component of the complete radiological assessment of brain tumors [28]. Tumor-associated neoangiogenesis produces very high blood volume in tumor tissue. Thus, the increased capillary density in the tumor causes markedly elevated CBV and CBF (Fig. 11.1h), as compared to normal brain parenchyma. Perfusion imaging is often useful to establish the diagnosis of tumor and to distinguish tumor from tumor mimics, such as abscess or tumefactive demyelination, which show hypoperfusion with low values of CBV and CBF.

Perfusion imaging can noninvasively help evaluate tumor grade. Low-grade astrocytomas are hypoperfused as compared to high-grade lesions. Up to one-third

of the high-grade tumors do not enhance, which may lead to a false radiological impression of low grade. Thus, a perfusion study can demonstrate hyperperfusion associated with higher grade. Moreover, since primary high-grade tumors are infiltrative by nature, their peritumoral edema show elevated CBV values. By contrast, metastases are well marginated and noninfiltrative by nature, and their perilesional edema is purely vasogenic with low CBV values.

CBV maps may also be used to delineate tumor margins. The results of stereotactic biopsy on high-grade tumors such as glioblastomas are frequently negative, and this may be because the tissue sampling has not been obtained from the most aggressive part of the lesion. MR perfusion may therefore help direct the localization of stereotactic biopsies from the most aggressive components of morphologically heterogeneous tumors. Perfusion can also differentiate tumor recurrence from enhancing nonneoplastic tissue such as radiation necrosis (causing an endarteritis) which would also be useful for surgical planning and targeting of biopsies and radiation therapy. Perfusion imaging will likely be increasingly used as a surrogate marker to study response to newer antiangiogenic pharmaceuticals in clinical trials.

Arterial Spin-Labeling Perfusion Imaging

Arterial spin labeling (ASL) is a newer perfusion technique that does not require exogenous contrast, and instead it exploits the spins of endogenous water protons that perfuse the imaging plane. It thus uses electromagnetically labeled arterial blood water as a freely diffusible intrinsic tracer. In clinical applications, this technique has proved reliable and reproducible in the assessment of CBF in various pathologic states, including cerebrovascular and neurodegenerative diseases, and temporal lobe epilepsy [29]. There is also a general positive correlation between ASL signal intensity and density of microvessels in brain tumors. ASL may be useful in differentiating between high- and low-grade gliomas; distinguishing glioblastomas from metastases, CNS lymphomas, and all other glioma grades; and predicting the outcome for metastatic brain tumors after radiosurgery [30]. Hemangioblastomas have significantly higher ASL signal than gliomas, meningiomas, and schwannomas.

Magnetic Resonance Spectroscopy

MRS is a noninvasive technique capable of measuring chemicals within the body. MRS distinguishes various metabolites based on their slightly different chemical shifts or resonance frequencies. Nuclei that can be analyzed using MR are those possessing odd numbers of protons and neutrons, e.g., ^{1}H, ^{31}P, ^{13}C, ^{19}F, and ^{23}Na. Of these, the most commonly used is hydrogen or proton spectroscopy. The metabolic information received is displayed as a graph, with the resonance frequencies plotted on the x-axis to identify each unique metabolite. These frequencies (in parts per million, ppm) are plotted on the y-axis. MRS can analyze single or multiple voxels of the brain. Multivoxel MRS is also called chemical shift imaging (CSI). When using CSI it is possible to construct color maps of metabolites that spatially demonstrate their peaks and ratios. These maps are overlapped with conventional MR images to demonstrate anatomical localization.

Clinically relevant metabolites that feature on a brain spectral graph are branch-chained amino acids, lipid, lactate, alanine, N-acetyl aspartate (NAA), choline, creatine, and myoinositol. MRS can help in establishing the diagnosis of tumor by demonstration of elevated choline, a metabolite that is found in normal brain but is raised in tumors owing to high cell turnover. Indeed, the characteristic spectral graph of a glioma depicts depressed NAA (a neuronal marker), elevated choline and lipid, and/or lactate peaks [21, 31, 32]. It is thus possible to differentiate tumors from other lesions such as abscesses or radiation necrosis. Moreover, when elevated choline is found in peritumoral edema, it may suggest a diagnosis of primary glioma rather than metastasis. Meningiomas, on the other hand, are characterized by elevated alanine. The disadvantages of MRS are that it has poor spatial resolution and it is sometimes nonspecific.

Hyperpolarized ^{13}C MRS

The emergence of hyperpolarized ^{13}C MRS has opened many new possibilities for novel metabolic imaging studies that are translatable to the clinic and can serve to characterize brain tumors and their response to therapy [32, 33]. ^{13}C MRS studies have been challenging owing to the significantly low intrinsic sensitivity of the technique, and when using ^{13}C-labeled compounds, long acquisition times are required, currently limiting the application of this method in patient studies.

Molecules containing NMR-visible nuclei, such as ^{13}C, can be hyperpolarized using dissolution dynamic nuclear polarization. This allows hyperpolarization and dissolution of ^{13}C-labeled compounds that cause an increase in their signal-to-noise ratio by 10,000–50,000-fold as compared with thermal equilibrium. To achieve this, the labeled compound, mixed with a free radical, is placed at low temperature (<2 K) and at high magnetic field (3–5 T). Microwave irradiation then saturates the electron spin resonance, and polarization is transferred from the radical electron to the labeled nucleus. This leads to an increase in polarization from parts per million to 10–50%. However, a limitation of hyperpolarized agents is their lifetime. Relaxation times are typically less than a minute. A meaningful brain study therefore requires rapid dissolution and injection of the hyperpolarized agents, as well as rapid transport across the BBB and a fast metabolic rate. In addition, a rapid data acquisition strategy is required. This has led to a trade-off between spatial resolution and acquisition time. In spite of these challenges, several hyperpolarized ^{13}C agents as well as novel imaging methods have been developed over the past decade to specifically image metabolic pathways that are reprogrammed in brain tumors. This new imaging approach enables study of major metabolic pathways and their reprogramming in cancer in real-time, noninvasively, and with no ionizing radiation involved.

Functional MRI

Functional MRI (fMRI) demonstrates brain function with neuroanatomic localization on a real-time basis. Cortical activity may be studied by fMRI techniques based on detecting focal blood flow and oxygenation changes following neuronal activity,

using BOLD contrast, which requires the detection of very small signal intensity changes, 0–3% at 1.5 T and up to 6% at 3 T, for voxel volumes as small as 3 × 3 × 5 mm. In the BOLD technique, the performance of a predefined cognitive task leads to regionally increased neuronal activity and consequent localized hemodynamic changes that produce a measurable signal. Thus, neural activation is followed by an increase in local blood flow and an increase of oxygenated hemoglobin in the capillaries of the activated brain tissue. The parallel drop in concentration of paramagnetic deoxyhemoglobin leads to a focal signal increase in the affected tissue using T2* sequences (the BOLD effect). This was first used to demonstrate activated brain regions as a result of sensory or motor stimulation.

BOLD imaging in the brain has many useful applications, e.g., localizing neuronal activities, display of areas affected by sensory stimuli or motor activation, and as a noninvasive tool for presurgical mapping of cortical function in patients with intracranial tumors [34, 35]. fMRI imaging is primarily used to preoperatively establish the relationship of a brain tumor to eloquent cortex. The latter may show significant anatomical variability and displacement by the mass effect from a tumor. Although functional MR imaging cannot yet replace intraoperative electrocortical stimulation in patients undergoing neurosurgical tumor resection, it may be useful in guiding surgical planning and mapping, thereby reducing the extent and duration of craniotomy. Thus, fMRI can contribute to more efficient surgical removal of both benign and malignant brain tumors with an increase in patient survival and a decrease in surgical morbidity. In addition, it is necessary to establish hemispheric dominance for language processing preoperatively in brain tumor patients. A preoperative fMR imaging study of language processing provides information on the feasibility of surgical resection and allows adequate assessment of the risk of neurological deficits in the postoperative period. Unfortunately, fMRI is currently unable to distinguish critical areas for brain function, whose resection would lead to permanent disability, from accessory or modulatory brain areas that may be resected without significant postoperative disability.

11.2.2.3 Radiogenomics of Gliomas

Genomic characterization has recently improved the assessment of glioblastoma by describing distinct molecular gene expression profiles, underlying genomic abnormalities, and epigenetic modifications. Radiogenomic mapping (a link between MRI features and underlying molecular data) can potentially address the clinical need for surrogate imaging biomarkers that accurately predict underlying tumor biology and therapy response in glioblastoma [36–39]. For this, gene expression modules are first constructed from information on glioblastomas, e.g., those available in The Cancer Genome Atlas (TCGA), depicting extensive molecular characterization, including gene expression, copy number, and DNA methylation status for each tumor. By correlating quantitative image features with such modules, we can hypothesize on how gene expression patterns may drive the morphologic manifestations captured by quantitative MRI features. The VASARI MRI feature set is a system designed to enable consistent description of gliomas using a

set of defined visual features and controlled vocabulary. These standardized VASARI feature-set criteria are 30 qualitative and quantitative imaging features that describe the size, location, as well as numerous detailed morphological characteristics of a tumor. MRI features of a tumor have been shown to noninvasively reflect to some extent its biology and pathology, tumor microenvironment, and its genomic makeup.

11.2.2.4 Challenges in MRI of Glioblastoma

There are some limitations and challenges to MRI assessment when defining glioblastoma progression and treatment response [17, 40, 41]. First, glioblastomas are frequently irregular in shape and may change anisotropically or differentially in response to therapy, which limits meaningful linear tumor measurements. In addition, visible contrast-enhancing components are not necessarily representative of active tumor volume. The Response Assessment in Neuro-Oncology (RANO) Working Group has suggested criteria for response assessment that include evaluation of nonenhancing areas of tumor. Further, nonenhancing active tumor components and therapy-related changes in enhancement are well-recognized challenges. Radiation necrosis may manifest as edema and a range of nonspecific enhancement patterns, which can be impossible to distinguish from true progression or recurrence of tumor using MRI.

Radiological pseudoprogression, where transient increases in apparent tumor size and enhancement are seen during and shortly after aggressive chemoradiation, is increasingly recognized. Thus, within 12 weeks of chemoradiation, progression should only be considered on imaging if there are areas of new enhancement outside the field of radiation treatment. Pseudoprogression is more common in tumors with favorable methylation status of methylated O6-methyl guanine-DNA methyltransferase (MGMT), and these tumors show better overall treatment response.

Steroid treatment has been shown to decrease BBB permeability and regional CBV (pseudoresponse). Controlling for steroid treatment is therefore important when imaging patient response. Similarly, antiangiogenic agents specifically targeted to vascular endothelial growth factor are used to treat glioblastoma, and may have a complex effect upon vasculature, which in turn modulates contrast enhancement. Accordingly, appearances on MRI following antiangiogenic treatment may mask residual or recurrent disease by showing decreased enhancement without actual tumor regression. Therefore, contrast enhancement alone is not a suitable marker for tumor response in this context.

11.2.3 Positron Emission Tomography (PET)

PET imaging of brain tumors is increasingly used in clinical practice. PET is typically a second-level investigation in patients already evaluated by MRI or in conjunction with it when hybrid technology is available.

The interest of PET imaging is thus to complement MRI for specific questions that are only partially addressed by MRI, namely: (1) contribute to the diagnostic

Table 11.3 Current potential indications of the main PET radiopharmaceuticals used in brain tumors imaging

PET radiopharmaceutical	Diagnosis	Grading	Therapy-induced changes vs. recurrence	Therapy monitoring	Tumor extent delineation
^{18}F-FET, ^{11}C-MET	✓	✓	✓	✓	✓
^{18}F-FDOPA	–	–	✓	✓	✓
^{18}F-FDG	–	–	✓	✓	✓
^{18}F-FMISO	–	✓	–	✓	–
^{18}F-FPPRGD$_2$	–	–	–	✓	–
^{18}F-FLT	✓[a]	✓	✓[a]	✓[a]	✓[a]
[11]C-Acetate	–	✓	–	–	–
[18]F- and ^{11}C-Choline	✓	✓	✓	–	✓
^{68}Ga-DOTA-peptides	✓[b]	✓[b]	✓[b]	✓[b]	✓[b]

[a]In high-grade gliomas
[b]In meningiomas

process of intracranial masses of unknown origin, (2) help grading lesions to establish the appropriate management and target the highest grade component for biopsy planning, (3) define tumor extent for surgical and radiation therapy planning, (4) evaluate treatment response, and (5) differentiate between treatment-induced changes and disease recurrence (Table 11.3).

This section will describe the most important PET radiopharmaceuticals used in brain tumors imaging with a description of their advantages and drawbacks, as well as a brief review of the literature on currently available studies conducted using PET/CT.

11.2.3.1   Radiolabeled Amino Acids (^{11}C-MET) and Amino Acid Analogues (^{18}F-FET, ^{18}F-DOPA)

Brain tumors are characterized by a higher protein metabolism than normal brain tissue and inflammatory lesions; therefore, protein synthesis can represent a good diagnostic marker. L-type amino acid transporter1 (LAT1) is a membrane protein responsible for amino acid (AA) transport through the cell membrane and is typically overexpressed in glial tumors, as well as in case of blood-brain barrier (BBB) rupture, which can modulate and increase AA delivery. AA analogue radiopharmaceuticals have low uptake in normal brain tissue, whereas tumor lesions present as focal uptake on PET imaging.

The first radiopharmaceutical of this extensively used class is ^{11}C-methionine (MET), an essential sulfur AA necessary for cellular proliferation and growth [42]. MET is not only transported within the cells by LAT1 but is also incorporated into proteins, even if its uptake is correlated with methionine transport and not directly with protein synthesis [43]. Its use is mainly limited by the short half-life of ^{11}C, which confines its application to hospitals equipped with an onsite cyclotron. ^{18}F-Fluoro-ethyltyrosin (FET) has been more recently developed and has gained larger use, since fluorinated tracers can be easily delivered in multiple sites [44]. Its

distribution and binding properties are similar to those of MET, with the characteristic of a slower clearance, associated with a higher blood pool signal that might hamper the analysis of regions close to the venous sinuses [45]. Comparative studies have shown similar diagnostic properties and a strong correlation of quantitative measures such as tumor-to-background ratio (TBR) of MET and FET [46].

^{18}F-DOPA is another AA analogue, sharing the same mechanism of uptake by LAT1 as MET and FET. It has been shown that the uptake and distribution of DOPA and MET are overall comparable [47].

A comparative study including DOPA and FET has highlighted some differences, namely, a faster kinetic both in high- and low-grade gliomas and a high contrast to background in extrastriatal regions for DOPA [48]. Indeed, DOPA might have a higher sensitivity in low-grade tumors, as compared with the performances reported for other AA analogues [49]. Its physiologic uptake in the basal ganglia represents the main limitation for use in lesions close to the basal ganglia, even if this can be partly overcome by scanning rapidly after injection (20 min) to limit specific binding to dopamine receptors [47]. In addition, it does not show higher uptake in oligodendroglial lesions, as reported for other AA analogues (see below).

Finally, preliminary data report the use in brain tumors of a synthetic AA analogue, ^{18}F-FACBC, or fluciclovine, a tracer mainly tested in prostate cancer [50, 51].

The use of AA analogues has been examined for all previously mentioned applications. Recently, recommendations for clinical use of PET imaging have been published by the Response Assessment in Neuro-Oncology (RANO) Working Group [52].

Lesion Characterization/Diagnosis

The sensitivity of MET for identification of tumoral lesions is in the range of 80%, with some low-grade lesions having lower uptake, while specificity is higher, around 90% [53, 54].

A meta-analysis has shown that FET PET has a pooled sensitivity of 82% and pooled specificity of 76% to differentiate primary brain tumors from non-tumoral intracranial lesions and suggested a TBRmean of 1.6 and TBRmax of 2.1 as cutoff values [55].

For lesion characterization, almost all high-grade gliomas, brain metastases, and oligodendrogliomas have intense uptake, while false negative (10–30%) might occur in low-grade tumors [53]. Non-tumoral lesions have usually less or no uptake, even if high FET uptake has been reported in hematoma, radiation necrosis, ischemic stroke, and abscesses, given the passive tracer influx in case of rupture of the BBB [56].

Grading and Biopsy Planning

The uptake value on static imaging does not provide reliable grading information with any AA tracer, even if higher-grade tumors usually show higher uptake in case of high-grade tumors [57]. Furthermore, a higher uptake in oligodendroglial, 1p19q codeleted tumors has been reported both for FET and for MET [54, 58, 59]. The significant overlap between grades and the association with histological type does not allow a reliable tumor assessment at an individual level, but justifies the interest of targeting a high uptake region, if any, for biopsy planning, and previous studies

have shown its usefulness [60, 61]. The uptake can also have prognostic value, differentiating benign and grade I lesions from higher-grade lesions for MET [62, 63], for FET [64], and for DOPA [65].

The analysis of the evolution over time of tracer uptake in FET PET dynamic scans provides additional information on tumor grading [66]. Lower-grade lesions or non-tumoral lesions typically show an increasing uptake over time and a late time to peak, more than 15/20 min (pattern I), while higher-grade tumors are typically characterized by an early uptake (less than 15/20 min) followed either by a plateau (pattern II) or a washout (pattern III) [58]. The added value of this analysis has been shown in grading lesions and in characterizing recurrent lesions vs. radiation necrosis [67]. A similar behavior, namely, an early peak in higher-grade lesions, has been reported for DOPA images [68, 69], while it has not been observed for MET [70].

Tumor Delineation and Radiation Therapy Planning

The tumor delineation based on molecular information is able to capture the infiltrative component without BBB rupture and the low-grade component, both for surgical and radiation therapy planning.

The comparative accuracy of AA PET imaging for radiation therapy planning has been compared in a review, showing that both MET and FET have good performances, variable across series but in the range of 90% [71]. A good performance has also been reported in a series of patients evaluated by DOPA [72]. A threshold of 1.6 with contralateral physiological uptake has been suggested for lesion segmentation on the basis of a biopsy-controlled study [73]. Multiple studies concordantly show that the volumes determined on the basis of PET and MRI differ significantly [74]. [75]–[79].

A tumor delineation using the molecular information has shown a positive prognostic impact in a small population study, not confirmed in a subsequent larger study [80, 81]. A randomized controlled trial is ongoing to test the added value of PET in radiation therapy planning [82].

The presence of a residual uptake has negative prognostic value, while the presence of residual contrast enhancement had not [60, 83].

Therapy Response Monitoring

A few studies have shown that AA PET typically shows low uptake in cases of pseudoprogression [46, 84]. AA PET imaging might also identify progressive disease under bevacizumab treatment earlier than MRI, with a favorable impact on costs [85, 86].

The majority of these studies used FET, showing that, after temozolomide, a reduction of TBRmax higher than 20% has a positive prognostic value [87] and that, after bevacizumab, a reduction of more than 45% of the metabolically active volume has a positive prognostic value [88].

The added value in surgical planning has been shown for MET and for DOPA [72, 89, 90].
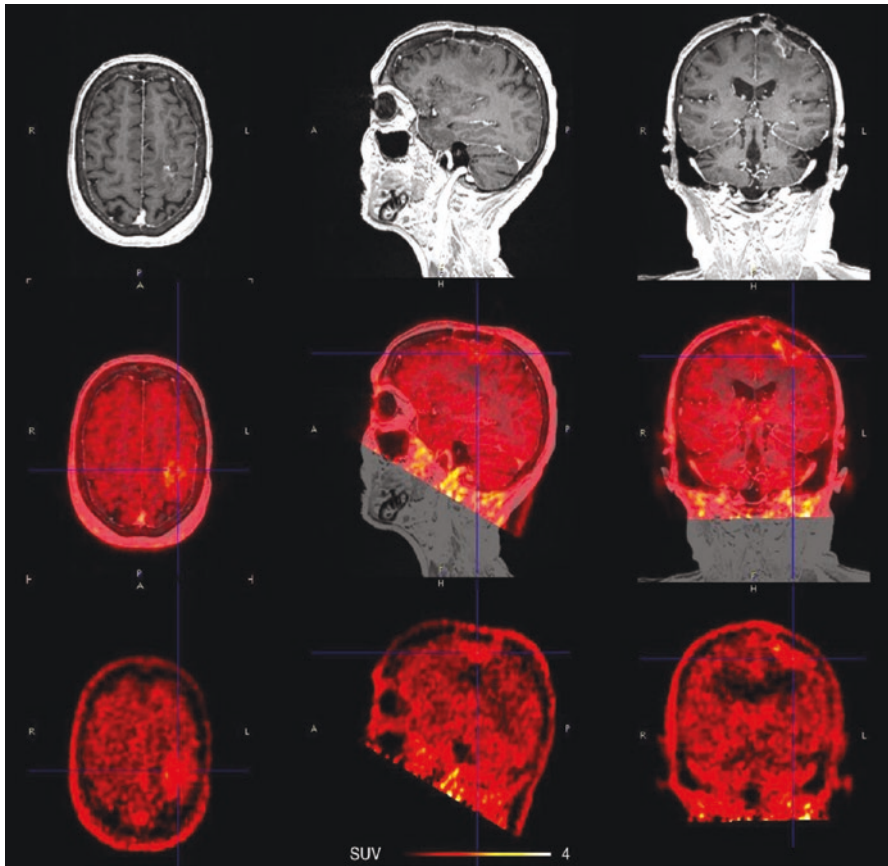
Fig. 11.3 ^{18}F-FET PET/MRI images showing a moderate uptake (SUVmean 1.5) increasing over time (pattern III) in a histologically proven radiation necrosis. From left to right, axial, sagittal, and coronal view. From top to bottom, MRI, fused PET/MRI images, and FET PET images

Differential Diagnosis Recurrence/Treatment-Induced Changes

MET, FET, and DOPA PET have been tested for differentiating high-grade tumor/ metastasis recurrence and treatment-induced changes, reporting high sensitivity and more variable, but overall high specificity, providing additional information as compared to MRI (Fig. 11.3) [66, 67, 91–94].

11.2.3.2 Glucose Metabolism (^{18}F-FDG)

^{18}F-FDG is the most commonly used radiopharmaceutical in oncology, given the strong association between cellular proliferation and glucose metabolism in most tumors. Importantly, ^{18}F-FDG PET uptake is not influenced by BBB rupture, increasing its specificity. However, its use in the brain is limited by the physiologic uptake of the normal brain cortex, which uses glucose as the main metabolic substrate. This limitation can be partly overcome using later imaging times, over 5 h

after administration [95, 96]. A second limitation is the potent effect of corticosteroids, often used to treat edema associated with intracranial masses, on brain tumors' ^{18}F-FDG uptake, through the increase of glycemia and the reduction of cerebral blood volume [97].

The use of ^{18}F-FDG for differential diagnosis of intracranial masses is a well-established indication in differentiating toxoplasmosis and primary lymphoma, reaching a sensitivity and specificity higher than 90%; toxoplasmosis lesions show ^{18}F-FDG uptake lower than the gray matter uptake (SUVmax in the range of 2–6), while lymphomas have uptake higher than the gray matter (SUVmax in the range from 12 to 30) [98].

For grading and prognostic evaluation, ^{18}F-FDG imaging can be useful in glial tumors: low-grade tumors (WHO grades I and II) have an activity in the range of normal white matter, WHO grade III tumor uptake is close to the gray matter activity, and WHO grade IV tumors might have focally higher uptake, with inhomogeneities related to tumor necrosis [99]. A higher tumor-to-normal brain ratio has been consistently associated with shorter survival [100]. For this reason different diagnostic cutoffs with the white matter and cortical activity have been suggested for low- and high-grade glioma, with good sensitivity and specificity [101, 102]. There are relevant exceptions represented by histological types with high glucose metabolism despite a low grade, such as ganglioglioma and pilocytic astrocytomas [103]. Non-glial tumors, namely, lymphomas, also have a high ^{18}F-FDG uptake [104]. ^{18}F-FDG cannot be used for tumor delineation, because of negative findings in low-grade tumors/components and because of the high physiologic metabolism of the brain.

For treatment monitoring, a change in management in 38% of patients was observed in a large series of either primary brain tumors or metastases based on the National Oncologic PET Registry [105].

For differentiating tumor recurrence and treatment-related changes, ^{18}F-FDG PET reaches a good sensitivity of 96% but variable specificity [106] [107]. One study directly compared the performance of MET and ^{18}F-FDG for this indication, showing a higher sensitivity and interrater agreement of MET [63].

11.2.3.3 Tumor Hypoxia (^{18}F-MISO) and Angiogenesis (^{18}F-FPPRGD₂)

Tumor Hypoxia The concept that radiosensitivity of tumor cells is increased in the presence of oxygen has been long known [108]; consequently, it has been thought that tumor hypoxia may have a major importance in the efficacy of radiation therapy, with hypoxic tissues being more radioresistant. Decades of research have brought us to the conclusion that tumor hypoxia changes gene expression patterns in tumor cells, leading to more aggressive survival traits and altering their malignant potential [109, 110]. Tumor hypoxia plays a crucial role in tumor cell survival, tumor development, and resistance to treatment, therefore, it is an attractive target for PET radiopharmaceuticals development [111]. The noninvasive assessment of tumor hypoxia by means of PET could help select patients, prior to radiation therapy treatments that may benefit from the use of radiosensitizing drugs. The

most extensively investigated PET radiopharmaceutical for tumor hypoxia imaging is ^{18}F-fluoromisonidazole (^{18}F-MISO), which showed a good potential in identifying hypoxic brain tumors. It accumulates in tissues binding to intracellular macromolecules when pO_2 is very low ($pO_2 < 10$ mmHg) [109] and in the periphery of the tumor, but not in the necrotic center, because only viable, hypoxic tissue can accumulate the radiopharmaceutical [112]. ^{18}F-MISO has been used in several clinical trials [113, 114], with the first study in humans published in 1992 by Valk et al. [115]. In this proof-of-concept study, three patients affected by malignant gliomas were evaluated, and feasibility of ^{18}F-MISO PET, as well as its ability to detect tumor hypoxia, was demonstrated. 15 years later, in a larger cohort of 22 patients with glioblastoma multiforme, Spence et al. have demonstrated that the hypoxic burden, measured using ^{18}F-MISO PET, impacts time to tumor progression and overall survival in patients previously treated with surgical intervention [116]. Some groups evaluated the possible role of ^{18}F-MISO PET in differentiating tumor grade [117, 118] with promising results, but larger cohorts might be needed to confirm clinical utility. Other groups investigated a possible correlation between tumor hypoxia, measured with ^{18}F-MISO PET, and glucose metabolism, measured with ^{18}F-FDG PET, suggesting discordance between the two modalities [119, 120], but the combination of the two studies was seen to be predictive of progression-free survival and overall survival in glioblastoma patients [121]. Similar results were seen for ^{18}F-MISO PET and MRI in a recently published multicenter study involving 42 patients with glioblastoma and aimed at assessing tumor hypoxia with the two imaging modalities. The lack of strong correlation between PET and MRI parameters shows their complementary role in the assessment of tumor status. Overall, the parameters measured by MRI (tumor blood volume/flow, vascular permeability) and hypoxia measured by ^{18}F-MISO PET are strongly correlated to prognosis in newly diagnosed glioblastoma patients [122].

Angiogenesis There is considerable evidence that hypoxia is strictly connected to angiogenesis, another key player in tumor growth and metastatization [123, 124]. More aggressive and malignant brain tumors have shown an abundant vascular proliferation histologically, and the vascular microenvironment highly influences the pathophysiological characteristics of the tumor [124]. Since angiogenesis has emerged in the last decade as a major target for drug development for malignant brain tumors, it also spurred interest toward the development of PET radiopharmaceuticals that may guide antiangiogenic treatment [125–127]. ^{18}F-FPPRGD$_2$ is a PET radiopharmaceutical targeting integrin $\alpha_v\beta_3$, which is highly expressed in proliferating vascular endothelial cells and plays an important role in angiogenesis [128]. Iagaru et al. used ^{18}F-FPPRGD$_2$ in the evaluation of 17 patients affected by glioblastoma multiforme and suspected recurrence. Patients were imaged before and after treatment with bevacizumab, and PET measured parameters, i.e., SUV_{max} and angiogenesis volume, were shown to be correlated to prognosis.

Despite the high potential utility of hypoxia and angiogenesis PET radiopharmaceuticals, too little is yet available on large cohorts of patients, therefore the use of these families of radiopharmaceuticals is still limited to research settings.

11.2.3.4 Other Radiopharmaceuticals (Radiolabeled Choline, ^{11}C-acetate, ^{18}F-FLT, Somatostatin Receptor)

Phospholipid Synthesis Choline is an essential substrate for biosynthesis of phosphatidylcholine, a major component of all cell membranes. Cancer cells have an increased cellular metabolism compared to normal cells, which entails an increased need of choline, and therefore an increased uptake of radiolabeled choline detected by PET [113]. Choline can be radiolabeled with either ^{11}C or [18]F. ^{11}C-Choline and natural choline are biochemically indistinguishable, whereas ^{18}F-labeled choline, ^{18}F-fluoroethyl-choline (FEC), and ^{18}F-fluoromethyl-choline (FCH) have shown some differences in pharmacokinetics that were not however observed in clinical settings [129, 130]. Radiolabeled choline has been used in a variety of tumors, but the main application remains prostate cancer. In brain tumors radiolabeled choline has been used for the first time in 1997, when Hara et al. described very encouraging results in visualization of brain tumors in 24 patients using ^{11}C-choline. High ^{11}C-choline uptake was seen in brain tumors, as opposed to very low uptake in the surrounding healthy brain parenchyma, allowing easy tumor delineation [131]. Different groups have found that radiolabeled choline is able to differentiate high-grade gliomas (high choline uptake) from low-grade gliomas (low choline uptake) [132, 133], whereas another group found contrasting results [134]. Choline was found able to differentiate benign from malignant lesions [135, 136] and also brain metastases (highest choline uptake) from high-grade gliomas (higher uptake than benign lesions, but lower than brain metastases) and benign lesions (low choline uptake) [137]. In a cohort of 94 patients with suspected brain tumors, Huang et al. found that ^{11}C-choline, despite a superior diagnostic accuracy in comparison to ^{18}F-FDG, had a rate of false positive of 4.55% and false negative of 3.64% [138]. When compared to ^{11}C-methionine, radiolabeled choline had a worse performance than the amino acid analogue in terms of visual evaluation of tumor localization [139] and also in the differential diagnosis between brain tumors and monofocal acute inflammatory demyelination (MAID), a demyelinating disease associated with MRI characteristics (e.g., gadolinium enhancement, edema, and mass effect) mimicking brain malignancies [140]. In the differential diagnosis between tumor recurrence and radionecrosis, radiolabeled choline performed better than MRI and ^{18}F-FDG [141]. In a posttreatment scenario, radiolabeled choline showed good diagnostic accuracy in the detection of recurrence of high-grade glioma [142] and in low-grade gliomas with equivocal findings on other imaging during follow-up [143]. ^{11}C-Choline uptake was also described in patients affected by meningiomas [144]. Despite some studies showing excellent results using radiolabeled choline in brain tumors, the role of the radiopharmaceutical has not been clearly defined yet.

Tumor Proliferation The increase of cell proliferation rate is a key characteristic of cancer; consequently, the identification of an accurate imaging biomarker of cell

proliferation in vivo would be highly desirable. Thymidine, the only nucleoside exclusively incorporated in DNA and not in RNA, has been evaluated for this purpose. It has been initially radiolabeled with [11]C [145], but due to the short half-life of the radioisotope (20 min) and the rapid in vivo degradation of ^{11}C-thymidine, it was considered less suitable for clinical use [146]. The thymidine analogue 3-deoxy-3′-[^{18}F]-fluorothymidine (^{18}F-FLT), developed by Shields et al. in 1998, has more favorable characteristics and is now the most widely used PET radiopharmaceutical for imaging and measuring tumor proliferation. ^{18}F-FLT is taken up and phosphorylated by the enzyme thymidine kinase-1 (TK-1), whose activity is strongly related to cell proliferation, and then trapped in the cell [113, 146]. A recent kinetic analysis study showed that ^{18}F-FLT uptake is more significantly correlated to BBB disruption than to TK-1 phosphorylation activity [147]. The high dependency of ^{18}F-FLT uptake from BBB damage is well known and represents a major disadvantage when evaluating low-grade gliomas, since they are usually not associated with BBB damage. In a comparative evaluation of ^{18}F-FDOPA, ^{18}F-FDG, and ^{18}F-FLT in 15 patients with low-grade gliomas, Tripathi et al. conclude that ^{18}F-FLT PET should not be used in the evaluation of recurrent low-grade gliomas because of its limited utility [148]. Several groups demonstrated that ^{18}F-FLT PET can be useful in grading gliomas and particularly in identifying high-grade gliomas and differentiating them from low grades [149–154]. ^{18}F-FLT has been directly compared to ^{18}F-FDG showing a much better tumor-to-background contrast and better tumor visualization due to the high glucose metabolism and negligible ^{18}F-FLT uptake in normal brain tissue. In a recent meta-analysis, Li et al. showed that ^{18}F-FLT has a better overall diagnostic accuracy in the detection of recurrent gliomas than ^{18}F-FDG [155]. In comparison with the amino acid analogue ^{11}C-MET, ^{18}F-FLT showed a lower sensitivity for tumor detection, but better correlation to cell proliferation index Ki-67, and better tumor grading assessment in gliomas of different grades [154, 156]. In the differential diagnosis between tumor recurrence and radionecrosis, ^{18}F-FLT has been compared to ^{18}F-FDG and ^{11}C-MET in two studies, and both showed no clear superiority of one radiopharmaceutical over the other [157, 158]. The most important application of ^{18}F-FLT seems to be therapy monitoring in high-grade gliomas. Different groups showed that ^{18}F-FLT is a good predictor of progression-free survival and overall survival in patients treated with the antiangiogenic drug bevacizumab [159–163]. ^{18}F-FLT was also used in a large Phase II trial evaluating newly diagnosed glioblastoma patients treated with everolimus, temozolomide, and radiation therapy [164].

Acetate Acetate is a metabolic substrate of β-oxidation and precursor of cholesterol and amino acids. In the cell, it is activated to acetyl-CoA via the enzyme acetyl-CoA synthase, which can follow two different metabolic pathways, depending on the cell type. In myocardial cells, it is mainly oxidized in the mitochondria by the tricarboxylic acid (TCA) cycle, whereas in tumor cells, it is mainly converted into fatty acids which are incorporated into phosphatidylcholine, an important component of cell membranes [165]. Due to its potential role in imaging myocardial cells and tumor proliferating cells, acetate has been radiolabeled with ^{11}C for PET

imaging and initially used for imaging of myocardial oxidative metabolism [166]. In oncology, ^{11}C-acetate is primarily used in prostate cancer imaging, but it has also been evaluated in brain tumors. Different groups showed that ^{11}C-acetate can be useful in grading of brain tumors (gliomas, astrocytomas, and meningiomas), allowing a clear differentiation between high grade and low grade [167–170]. In a comparative study with ^{18}F-FDG and ^{11}C-MET for the evaluation of gliomas, Yamamoto et al. found that ^{11}C-acetate has a better sensitivity than ^{18}F-FDG, but lower than ^{11}C-MET [170].

Somatostatin Receptors Somatostatin receptors (SSTR) are G-protein-coupled membrane glycoproteins that have received, particularly during the last two decades, large interest due to their overexpression in neuroendocrine tumors (NETs). Five subtypes of human SSTR have been identified so far (SSTR-1–SSTR-5) with different expressions and functions. Various PET radiopharmaceuticals targeting SSTRs have been developed, with variable binding affinities to the different SSTR subtypes. The most used are DOTA-TOC, DOTA-TATE, and DOTA-NOC, radiolabeled with ^{68}Ga using the universal chelator DOTA, which forms stable complexes in vivo [171]. Due to the high expression of SSTRs in meningiomas, mostly SSTR-2 [172], several studies have investigated ^{68}Ga-DOTA-peptides in imaging meningiomas. In 2001, Henze et al. described their first experience using ^{68}Ga-DOTA-TOC in a small cohort of patients with meningiomas, finding very promising results and excellent imaging properties of the PET radiopharmaceutical, including very high target-to-background ratio. Several groups described the utility of PET imaging using ^{68}Ga-DOTA-peptides in tumor extent delineation, particularly in the setting of therapy planning [173–179]. ^{68}Ga-DOTA-TATE has been described by Sommerauer et al. as a reliable predictor of tumor growth in WHO I and II meningiomas [180]. In a large study involving 134 patients comparing ^{68}Ga-DOTA-TOC PET to contrast-enhanced MRI in the detection of meningiomas, PET showed a better sensitivity than MRI (190 lesions identified by PET vs. 171 by contrast-enhanced MRI), confirming the importance of the imaging modality also in the diagnostic setting [181]. Another attractive application of PET using ^{68}Ga-DOTA-peptides is the possibility of theranostics, due to the radiolabeling of DOTA-peptides with β^- emitting radio-isotopes for peptide receptor radionuclide therapy (PRRT) [182]. Some groups have evaluated ^{68}Ga-DOTA-peptides in the setting of PRRT for meningiomas, showing that ^{68}Ga-DOTA-peptides PET allows pre-therapeutic assessment of tumor radionuclide uptake in PRRT [183] and can be predictive of outcome [184].

11.3 Integrated PET/MRI in Brain Tumors Imaging

The introduction of integrated PET/CT tomographs in the clinical practice has represented a milestone opening a new era for hybrid imaging. The added value of the simultaneous acquisition of PET and CT goes far beyond the sum of the utilities deriving from the two single modalities performed separately. The thought that the success obtained with PET/CT could be replicated with PET/MRI was obvious.

Table 11.4 PET/MRI studies in brain tumors imaging

Reference	Patient population	Radiopharmaceutical/ MR sequences	Aim	Conclusions
[189]	7 healthy volunteers 4 patients with BT	^{11}C-MET/standard diagnostic MRI, DTI	Feasibility of DTI using simultaneous PET/MRI	DTI is feasible using the combined approach without degradation of image quality
[191]	4 patients with BT	^{18}F-FET /standard diagnostic MRI, DTI, MRS, fMRI	Feasibility of simultaneous PET/MR	Description of acquisition protocols

[190]	15 patients (in total)
	
	5 patients with BT:
	  2 GBM
	  1 low grade
	  1 grade IV
	  1 choroid plexus carcinoma
		^{18}F-FET/standard diagnostic MRI, PWI, DTI	Test performance and clinical applicability of combined approach	Combined approach is feasible in a clinical setting
				
				Satisfactory results

[188]	28 patients with BT
	  16 low grade
	  12 high grade
		^{11}C-MET/standard diagnostic MRI, MRS	Feasibility of simultaneous approach for grading purposes using metabolic mapping	Metabolic mapping of gliomas before histological sampling is feasible using the combined approach

[197]	10 patients with BT:
	  3 low grade
	  1 grade III
	  2 GBM
	  2 atypical neurocytoma
	  3 meningioma
		^{11}C-MET and ^{68}Ga-DOTA-TOC/ standard diagnostic MRI	Comparison with PET/CT
			
			Feasibility and accuracy of combined approach
				Combined approach can be reliably performed in BT imaging. Image quality and quantification are similar to PET/CT

[198]	50 patients in total 29 patients with BT	^{18}F-FDG, ^{11}C-MET, and ^{68}Ga-DOTA-TOC/ standard diagnostic MRI, DTI, ASL, and proton spectroscopy	Comparison with PET/CT Image quality of PET/MRI	Quality of MRI images using the combined PET/MRI approach is uncompromised. Results are in high accordance with PET/CT

Table 11.4 (continued)

Reference	Patient population	Radiopharmaceutical/ MR sequences	Aim	Conclusions
[192]	15 patients with meningioma (33 lesions identified)	^{68}Ga-DOTA-TOC/ standard diagnostic MRI	Comparison with PET/ CT. Feasibility of the combined approach	PET/MRI provides flawless image quality
[193]	26 patients with BT (post-surgery and chemo-RT)	^{18}F-FET/standard diagnostic MRI, DWI, perfusion EPI, MRS	Differentiation of therapy-induced changes from recurrence in glioma patients	FET uptake with Cho/Cr ratio and normalized rCBVmean can distinguish glioma recurrence from radiation necrosis
[194]	20 patients with BT	^{18}F-FDG/standard diagnostic MRI, PWI	Differentiation of therapy-induced changes from recurrence. Tumor grading	PWI has better diagnostic accuracy in differentiating therapy-induced changes from recurrence than PET
[196]	4 pediatric patients: 2 grade I 1 grade III 1 GBM	^{11}C-MET/standard diagnostic MRI	Evaluation of ^{11}C-MET PET/ MRI in preoperative biopsy planning and navigation in pediatric patients	PET/MRI provides high-resolution data for neuronavigation reducing radiation exposure and avoiding additional anesthesia in very young patients
[195]	12 pediatric patients with astrocytic tumors: 8 low grade 4 high grade	^{18}F-Choline/standard diagnostic MRI	Feasibility of the combined approach for diagnosis and response assessment	^{18}F-Choline PET/ MRI is a reliable imaging tool. It permits therapy monitoring
[199]	69 patients with high-grade gliomas	^{11}C-MET/standard diagnostic MRI	Role of ^{11}C-MET PET/MRI in tumor volume evaluation for RT planning	The use of PET/ MRI did not change the target volumes defined on FLAIR MRI
[200]	56 patients with gliomas	^{18}F-FET/standard diagnostic MRI, PWI	Direct comparison of ^{18}F-FET to PWI using PET/MRI	^{18}F-FET PET and PWI yield different information

BT brain tumors, *GBM* glioblastoma multiforme, *DTI* diffusion tensor imaging, *MRS* MR spectroscopy, *fMRI* functional MRI, *ASL* arterial spin labeling, *PWI* perfusion-weighted imaging

One of the settings where a combination of PET and MRI could be more useful is undoubtedly the study of the brain, where a high soft tissue delineation and high resolution are particularly relevant. After the initial attempt to simultaneously acquire PET and MR data in 1997 [185], the first study conducted in humans was a brain study by Schlemmer et al., published one decade later [186]. Fully integrated PET/MRI scanners for humans are available for whole-body imaging since the end of 2010 [187], and their valuable role in research settings is unquestionable. But the real clinical utility of integrated PET/MRI still needs to be proven and sustained by large prospective trials. The focus of this section will be on the current applications of integrated PET/MRI systems, specific advantages of a combined PET/MRI approach in neuro-oncology, and future perspectives.

11.3.1 Current Applications of PET/MRI in Brain Tumors

Only limited literature is currently available and is summarized in Table 11.4. The initial studies conducted using integrated PET/MRI scanners were aiming at assessing feasibility of the combined approach and confirmed that it is feasible and does not degrade image quality of the single modalities [186, 188–191]. Some groups evaluated performances of PET/MRI in comparison to the well-established hybrid PET/CT in the evaluation of brain tumors. Afshar-Oromieh et al. [192] studied 15 patients affected by meningiomas with ^{68}Ga-DOTA-TOC PET/MRI in comparison to PET/CT. Image quality of PET/MRI was described as flawless, but the authors state that the small dimension of their cohort doesn't allow a meaningful comparison, and this would require larger studies. In another study, comparing the performance of PET/CT and PET/MRI in the same population of ten patients affected by different brain tumors, Boss et al. describe similar image quality and quantification. PET/MRI has also been used in the setting of differential diagnosis between therapy-induced changes (radionecrosis and pseudoprogression) and tumor recurrence. Contrast-enhanced MRI cannot distinguish the two conditions, and different PET radiopharmaceuticals have been found superior to MRI for this purpose [52]. Two different groups have evaluated combined PET/MRI in this setting with promising results [193, 194]. Another clinical setting where PET/MRI has been successfully evaluated is that of pediatric patients with brain tumors. In such populations, the reduction of iodizing radiation exposure and number of examinations (with better patient comfort and reduced sedation time in very young patients) deriving from PET/MRI may play a crucial role in the success of the combined approach [195, 196].

11.3.2 Specific Advantages of the Simultaneous PET/MRI Approach in Neuro-oncology

The individual characteristics of PET and MRI in the evaluation of brain tumors have been described in detail above. As for PET/CT, the advantages of the combined PET/MRI approach are greater than the sum of its parts. Before the introduction of

simultaneous PET/MRI scanners, research has been focusing on developing software for co-registration of the two separate examinations, but this approach can be affected by substantial differences in image quality. The simultaneous acquisition of PET and MRI in hybrid scanners allows an optimal temporal and spatial co-registration in one single imaging session. PET/MRI also has the potential to significantly improve diagnostic workflows in neuro-oncology. Considering that a vast part of the population affected by brain tumors require both PET/CT and MRI during their clinical workup, a faster workflow would be considerably more convenient. The lower radiation exposure using MRI instead of CT is another important advantage. These aspects of the combined simultaneous approach are particularly relevant in patients with brain tumors, who generally need repeated scans. PET/MRI is particularly promising in the field of neuro-oncology, but large prospective trials are still needed to demonstrate its practical benefits to the scientific and clinical communities.

References

1. Siegel RL, Miller KD, Jemal A. Cancer statistics, 2016. CA Cancer J Clin. 2016;66(1):7–30.
2. Lin X, DeAngelis LM. Treatment of brain metastases. J Clin Oncol Off J Am Soc Clin Oncol. 2015;33(30):3475–84.
3. Louis DN, Ohgaki H, Wiestler OD, et al. The 2007 WHO classification of tumours of the central nervous system. Acta Neuropathol. 2007;114(2):97–109.
4. Louis DN, Perry A, Reifenberger G, et al. The 2016 World Health Organization classification of tumors of the central nervous system: a summary. Acta Neuropathol. 2016;131(6):803–20.
5. Mabray MC, Barajas RF Jr, Cha S. Modern brain tumor imaging. Brain Tumor Res Treat. 2015;3(1):8–23.
6. Cha S. Neuroimaging in neuro-oncology. Neurotherapeutics. 2009;6(3):465–77.
7. Wen PY, Macdonald DR, Reardon DA, et al. Updated response assessment criteria for high-grade gliomas: response assessment in neuro-oncology working group. J Clin Oncol Off J Am Soc Clin Oncol. 2010;28(11):1963–72.
8. Brandsma D, Stalpers L, Taal W, Sminia P, van den Bent MJ. Clinical features, mechanisms, and management of pseudoprogression in malignant gliomas. Lancet Oncol. 2008;9(5):453–61.
9. Gahramanov S, Muldoon LL, Varallyay CG, et al. Pseudoprogression of glioblastoma after chemo- and radiation therapy: diagnosis by using dynamic susceptibility-weighted contrast-enhanced perfusion MR imaging with ferumoxytol versus gadoteridol and correlation with survival. Radiology. 2013;266(3):842–52.
10. Weller M, van den Bent M, Hopkins K, et al. EANO guideline for the diagnosis and treatment of anaplastic gliomas and glioblastoma. Lancet Oncol. 2014;15(9):e395–403.
11. Fink JR, Muzi M, Peck M, Krohn KA. Multimodality brain tumor imaging: MR imaging, PET, and PET/MR imaging. J Nucl Med. 2015;56(10):1554–61.
12. Cha S. Update on brain tumor imaging. Curr Neurol Neurosci Rep. 2005;5(3):169–77.
13. Bruzzone MG, D'Incerti L, Farina LL, Cuccarini V, Finocchiaro G. CT and MRI of brain tumors. The quarterly journal of nuclear medicine and molecular imaging: official publication of the Italian Association of Nuclear Medicine (AIMN) [and] the International Association of Radiopharmacology (IAR), [and] Section of the Society of…. 2012;56(2):112–37.
14. Chourmouzi D, Papadopoulou E, Marias K, Drevelegas A. Imaging of brain tumors. Surg Oncol Clin N Am. 2014;23(4):629–84.

15. Kim M, Kim HS. Emerging techniques in brain tumor imaging: what radiologists need to know. Korean J Radiol. 2016;17(5):598–619.
16. Mohammadzadeh A, Mohammadzadeh V, Kooraki S, et al. Pretreatment evaluation of Glioma. Neuroimaging Clin N Am. 2016;26(4):567–80.
17. Upadhyay N, Waldman AD. Conventional MRI evaluation of gliomas. Br J Radiol. 2011;84(2):S107–11.
18. Grossman R, Shimony N, Shir D, et al. Dynamics of FLAIR volume changes in glioblastoma and prediction of survival. Ann Surg Oncol. 2016;24(3):794–800.
19. Wintersperger BJ, Runge VM, Biswas J, Reiser MF, Schoenberg SO. Brain tumor enhancement in MR imaging at 3 tesla: comparison of SNR and CNR gain using TSE and GRE techniques. Investig Radiol. 2007;42(8):558–63.
20. Yoo DH, Song SW, Yun TJ, et al. MR imaging evaluation of Intracerebral Hemorrhages and T2 Hyperintense white matter lesions appearing after radiation therapy in adult patients with primary brain tumors. PLoS One. 2015;10(8):e0136795.
21. Brandao LA, Shiroishi MS, Law M. Brain tumors: a multimodality approach with diffusion-weighted imaging, diffusion tensor imaging, magnetic resonance spectroscopy, dynamic susceptibility contrast and dynamic contrast-enhanced magnetic resonance imaging. Magn Reson Imaging Clin N Am. 2013;21(2):199–239.
22. Castellano A, Falini A. Progress in neuro-imaging of brain tumors. Curr Opin Oncol. 2016;28(6):484–93.
23. Baehring JM, Fulbright RK. Diffusion-weighted MRI in neuro-oncology. CNS Oncol. 2012;1(2):155–67.
24. Svolos P, Kousi E, Kapsalaki E, et al. The role of diffusion and perfusion weighted imaging in the differential diagnosis of cerebral tumors: a review and future perspectives. Cancer Imaging. 2014;14:20.
25. Pujol S, Wells W, Pierpaoli C, et al. The DTI challenge: toward standardized evaluation of diffusion tensor imaging tractography for neurosurgery. J Neuroimaging. 2015;25(6):875–82.
26. Ulmer JL, Klein AP, Mueller WM, DeYoe EA, Mark LP. Preoperative diffusion tensor imaging: improving neurosurgical outcomes in brain tumor patients. Neuroimaging Clin N Am. 2014;24(4):599–617.
27. Griffith B, Jain R. Perfusion imaging in neuro-oncology: basic techniques and clinical applications. Magn Reson Imaging Clin N Am. 2016;24(4):765–79.
28. Essig M, Shiroishi MS, Nguyen TB, et al. Perfusion MRI: the five most frequently asked technical questions. AJR Am J Roentgenol. 2013;200(1):24–34.
29. Grade M, Hernandez Tamames JA, Pizzini FB, Achten E, Golay X, Smits M. A neuroradiologist's guide to arterial spin labeling MRI in clinical practice. Neuroradiology. 2015;57(12):1181–202.
30. Noguchi T, Yoshiura T, Hiwatashi A, et al. Perfusion imaging of brain tumors using arterial spin-labeling: correlation with histopathologic vascular density. AJNR Am J Neuroradiol. 2008;29(4):688–93.
31. Kazda T, Bulik M, Pospisil P, et al. Advanced MRI increases the diagnostic accuracy of recurrent glioblastoma: single institution thresholds and validation of MR spectroscopy and diffusion weighted MR imaging. NeuroImage Clin. 2016;11:316–21.
32. Najac C, Ronen SMMR. Molecular imaging of brain cancer metabolism using hyperpolarized 13C magnetic resonance spectroscopy. Top Magn Reson Imaging. 2016;25(5):187–96.
33. Ross BD, Bhattacharya P, Wagner S, Tran T, Sailasuta N. Hyperpolarized MR imaging: neurologic applications of hyperpolarized metabolism. AJNR Am J Neuroradiol. 2010;31(1):24–33.
34. Bailey PD, Zaca D, Basha MM, et al. Presurgical fMRI and DTI for the prediction of perioperative motor and language deficits in primary or metastatic brain lesions. J Neuroimaging. 2015;25(5):776–84.
35. Voss J, Meier TB, Freidel R, et al. The role of secondary motor and language cortices in morbidity and mortality: a retrospective functional MRI study of surgical planning for patients with intracranial tumors. Neurosurg Focus. 2013;34(4):E7.

36. Colen RR, Hassan I, Elshafeey N, Zinn PO. Shedding light on the 2016 World Health Organization classification of tumors of the central nervous system in the era of radiomics and radiogenomics. Magn Reson Imaging Clin N Am. 2016;24(4):741–9.

37. ElBanan MG, Amer AM, Zinn PO, Colen RR. Imaging genomics of glioblastoma: state of the art bridge between genomics and neuroradiology. Neuroimaging Clin N Am. 2015;25(1):141–53.

38. Kotrotsou A, Zinn PO, Colen RR. Radiomics in brain Tumors: an emerging technique for characterization of tumor environment. Magn Reson Imaging Clin N Am. 2016;24(4):719–29.

39. Moton S, Elbanan M, Zinn PO, Colen RR. Imaging genomics of Glioblastoma: biology, biomarkers, and breakthroughs. Top Magn Reson Imaging. 2015;24(3):155–63.

40. Belliveau JG, Bauman G, Macdonald DR. Detecting tumor progression in glioma: current standards and new techniques. Expert Rev Anticancer Ther. 2016;16(11):1177–88.

41. Huang RY, Neagu MR, Reardon DA, Wen PY. Pitfalls in the neuroimaging of glioblastoma in the era of antiangiogenic and immuno/targeted therapy - detecting illusive disease, defining response. Front Neurol. 2015;6:33.

42. Syrota A, Comar D, Cerf M, Plummer D, Maziere M, Kellershohn C. [11C]methionine pancreatic scanning with positron emission computed tomography. J Nucl Med. 1979;20(7):778–81.

43. Ishiwata K, Kubota K, Murakami M, et al. Re-evaluation of amino acid PET studies: can the protein synthesis rates in brain and tumor tissues be measured in vivo? J Nucl Med. 1993;34(11):1936–43.

44. Wester HJ, Herz M, Weber W, et al. Synthesis and radiopharmacology of O-(2-[18F] fluoroethyl)-L-tyrosine for tumor imaging. J Nucl Med. 1999;40(1):205–12.

45. Weckesser M, Langen KJ, Rickert CH, et al. O-(2-[18F]fluorethyl)-L-tyrosine PET in the clinical evaluation of primary brain tumours. Eur J Nucl Med Mol Imaging. 2005;32(4):422–9.

46. Grosu AL, Astner ST, Riedel E, et al. An interindividual comparison of O-(2-[18F] fluoroethyl)-L-tyrosine (FET)- and L-[methyl-11C]methionine (MET)-PET in patients with brain gliomas and metastases. Int J Radiat Oncol Biol Phys. 2011;81(4):1049–58.

47. Becherer A, Karanikas G, Szabo M, et al. Brain tumour imaging with PET: a comparison between [18F]fluorodopa and [11C]methionine. Eur J Nucl Med Mol Imaging. 2003;30(11):1561–7.

48. Kratochwil C, Combs SE, Leotta K, et al. Intra-individual comparison of (1)(8)F-FET and (1)(8)F-DOPA in PET imaging of recurrent brain tumors. Neuro-Oncology. 2014;16(3):434–40.

49. Villani V, Carapella CM, Chiaravalloti A, et al. The role of PET [18F]FDOPA in evaluating low-grade glioma. Anticancer Res. 2015;35(9):5117–22.

50. Kondo A, Ishii H, Aoki S, et al. Phase IIa clinical study of [18F]fluciclovine: efficacy and safety of a new PET tracer for brain tumors. Ann Nucl Med. 2016;30(9):608–18.

51. Sasajima T, Ono T, Shimada N, et al. Trans-1-amino-3-18F-fluorocyclobutanecarboxylic acid (anti-18F-FACBC) is a feasible alternative to 11C-methyl-L-methionine and magnetic resonance imaging for monitoring treatment response in gliomas. Nucl Med Biol. 2013;40(6):808–15.

52. Albert NL, Weller M, Suchorska B, et al. Response assessment in neuro-oncology working group and European Association for Neuro-Oncology recommendations for the clinical use of PET imaging in gliomas. Neuro-Oncology. 2016;18(9):1199–208.

53. Pichler R, Dunzinger A, Wurm G, et al. Is there a place for FET PET in the initial evaluation of brain lesions with unknown significance? Eur J Nucl Med Mol Imaging. 2010;37(8):1521–8.

54. Bette S, Gempt J, Delbridge C, et al. Prognostic value of O-(2-[18F]-Fluoroethyl)-L-tyrosine-positron emission tomography imaging for histopathologic characteristics and progression-free survival in patients with low-grade glioma. World Neurosurg. 2016;89:230–9.

55. Dunet V, Rossier C, Buck A, Stupp R, Prior JO. Performance of 18F-fluoro-ethyl-tyrosine (18F-FET) PET for the differential diagnosis of primary brain tumor: a systematic review and metaanalysis. J Nucl Med. 2012;53(2):207–14.

56. Hutterer M, Nowosielski M, Putzer D, et al. [18F]-fluoro-ethyl-L-tyrosine PET: a valuable diagnostic tool in neuro-oncology, but not all that glitters is glioma. Neuro-Oncology. 2013;15(3):341–51.

57. Rapp M, Heinzel A, et al. Diagnostic performance of 18F-FET PET in newly diagnosed cerebral lesions suggestive of glioma. J Nucl Med. 2013;54(2):229–35

58. Jansen NL, Schwartz C, Graute V, et al. Prediction of oligodendroglial histology and LOH 1p/19q using dynamic [(18)F]FET-PET imaging in intracranial WHO grade II and III gliomas. Neuro-Oncology. 2012;14(12):1473–80.

59. Saito T, Maruyama T, Muragaki Y, et al. 11C-methionine uptake correlates with combined 1p and 19q loss of heterozygosity in oligodendroglial tumors. AJNR Am J Neuroradiol. 2013;34(1):85–91.

60. Pirotte BJ, Levivier M, Goldman S, et al. Positron emission tomography-guided volumetric resection of supratentorial high-grade gliomas: a survival analysis in 66 consecutive patients. Neurosurgery. 2009;64(3):471–81. discussion 81.

61. Popperl G, Kreth FW, Mehrkens JH, et al. FET PET for the evaluation of untreated gliomas: correlation of FET uptake and uptake kinetics with tumour grading. Eur J Nucl Med Mol Imaging. 2007;34(12):1933–42.

62. Kim S, Chung JK, Im SH, et al. 11C-methionine PET as a prognostic marker in patients with glioma: comparison with 18F-FDG PET. Eur J Nucl Med Mol Imaging. 2005;32(1): 52–9.

63. Van Laere K, Ceyssens S, Van Calenbergh F, et al. Direct comparison of 18F-FDG and 11C-methionine PET in suspected recurrence of glioma: sensitivity, inter-observer variability and prognostic value. Eur J Nucl Med Mol Imaging. 2005;32(1):39–51.

64. Floeth FW, Pauleit D, Sabel M, et al. Prognostic value of O-(2-18F-fluoroethyl)-L-tyrosine PET and MRI in low-grade glioma. J Nucl Med. 2007;48(4):519–27.

65. Morana G, Piccardo A, Puntoni M, et al. Diagnostic and prognostic value of 18F-DOPA PET and 1H-MR spectroscopy in pediatric supratentorial infiltrative gliomas: a comparative study. Neuro-Oncology. 2015;17(12):1637–47.

66. Popperl G, Kreth FW, Herms J, et al. Analysis of 18F-FET PET for grading of recurrent gliomas: is evaluation of uptake kinetics superior to standard methods? J Nucl Med. 2006;47(3):393–403.

67. Galldiks N, Stoffels G, Filss CP, et al. Role of O-(2-(18)F-fluoroethyl)-L-tyrosine PET for differentiation of local recurrent brain metastasis from radiation necrosis. J Nucl Med. 2012;53(9):1367–74.

68. Gonzalez-Forero M, Prieto E, Dominguez I, Vigil C, Penuelas I, Arbizu J. Dual time point 18F-FDOPA PET as a tool for characterizing brain tumors. Rev Esp Med Nucl. 2011;30(2):88–93.

69. Schiepers C, Chen W, Cloughesy T, Dahlbom M, Huang SC. 18F-FDOPA kinetics in brain tumors. J Nucl Med. 2007;48(10):1651–61.

70. Moulin-Romsee G, D'Hondt E, de Groot T, et al. Non-invasive grading of brain tumours using dynamic amino acid PET imaging: does it work for 11C-methionine? Eur J Nucl Med Mol Imaging. 2007;34(12):2082–7.

71. Grosu AL, Weber WA. PET for radiation treatment planning of brain tumours. Radiother Oncol. 2010;96(3):325–7.

72. Pafundi DH, Laack NN, Youland RS, et al. Biopsy validation of 18F-DOPA PET and biodistribution in gliomas for neurosurgical planning and radiotherapy target delineation: results of a prospective pilot study. Neuro-Oncology. 2013;15(8):1058–67.

73. Pauleit D, Floeth F, Hamacher K, et al. O-(2-[18F]fluoroethyl)-L-tyrosine PET combined with MRI improves the diagnostic assessment of cerebral gliomas. Brain. 2005;128(Pt 3):678–87.

74. Weber DC, Zilli T, et al. [(18)F]Fluoroethyltyrosine- positron emission tomography-guided radiotherapy for high-grade glioma. Radiat Oncol. 2008;3:44.

75. Nowosielski M, DiFranco MD, et al. An intra-individual comparison of MRI, [18F]-FET and [18F]-FLT PET in patients with high-grade gliomas. PLoS One. 2014;9(4):e95830.

76. Niyazi M, Geisler J, et al. FET-PET for malignant glioma treatment planning. Radiother Oncol. 2011;99(1):44–8.

77. Rosenschold P, Costa J, et al. Impact of [18F]-fluoro-ethyl-tyrosine PET imaging on target definition for radiation therapy of high-grade glioma. Neuro-Oncology. 2015;17(5):757–63.

78. Rieken S, Habermehl D, et al. Analysis of FET-PET imaging for target volume definition in patients with gliomas treated with conformal radiotherapy. Radiother Oncol. 2013;109(3):487–92.

79. Badakhshi H, Graf R, et al. The impact of 18 F-FET PET-CT on target definition in image-guided stereotactic radiotherapy in patients with skull base lesions. Cancer Imaging. 2014;14:25.

80. Piroth MD, Pinkawa M, Holy R, et al. Integrated boost IMRT with FET-PET-adapted local dose escalation in glioblastomas. Results of a prospective phase II study. Strahlenther Onkol. 2012;188(4):334–9.

81. Grosu AL, Weber WA, Riedel E, et al. L-(methyl-11C) methionine positron emission tomography for target delineation in resected high-grade gliomas before radiotherapy. Int J Radiat Oncol Biol Phys. 2005;63(1):64–74.

82. Oehlke O, Mix M, Graf E, et al. Amino-acid PET versus MRI guided re-irradiation in patients with recurrent glioblastoma multiforme (GLIAA) - protocol of a randomized phase II trial (NOA 10/ARO 2013-1). BMC Cancer. 2016;16(1):769.

83. Piroth MD, Holy R, Pinkawa M, et al. Prognostic impact of postoperative, pre-irradiation (18)F-fluoroethyl-l-tyrosine uptake in glioblastoma patients treated with radiochemotherapy. Radiother Oncol. 2011;99(2):218–24.

84. Galldiks N, Dunkl V, Stoffels G, et al. Diagnosis of pseudoprogression in patients with glioblastoma using O-(2-[18F]fluoroethyl)-L-tyrosine PET. Eur J Nucl Med Mol Imaging. 2015;42(5):685–95.

85. Galldiks N, Rapp M, Stoffels G, Dunkl V, Sabel M, Langen KJ. Earlier diagnosis of progressive disease during bevacizumab treatment using O-(2-18F-fluorethyl)-L-tyrosine positron emission tomography in comparison with magnetic resonance imaging. Mol Imaging. 2013;12(5):273–6.

86. Heinzel A, Muller D, Langen KJ, et al. The use of O-(2-18F-fluoroethyl)-L-tyrosine PET for treatment management of bevacizumab and irinotecan in patients with recurrent high-grade glioma: a cost-effectiveness analysis. J Nucl Med. 2013;54(8):1217–22.

87. Galldiks N, Stoffels G, et al. Role of O-(2-(18)F-fluoroethyl)-L-tyrosine PET for differentiation of local recurrent brain metastasis from radiation necrosis. J Nucl Med. 2012;53(9):1367–74.

88. Galldiks N, Stoffels G, et al. Role of O-(2-(18)F-fluoroethyl)-L-tyrosine PET as a diagnostic tool for detection of malignant progression in patients with low-grade glioma. J Nucl Med. 2013;54(12):2046–54.

89. Momose T, Nariai T, Kawabe T, et al. Clinical benefit of 11C methionine PET imaging as a planning modality for radiosurgery of previously irradiated recurrent brain metastases. Clin Nucl Med. 2014;39(11):939–43.

90. Pirotte BJ, Lubansu A, Massager N, et al. Clinical impact of integrating positron emission tomography during surgery in 85 children with brain tumors. J Neurosurg Pediatr. 2010;5(5):486–99.

91. Romagna A, Unterrainer M, Schmid-Tannwald C, et al. Suspected recurrence of brain metastases after focused high dose radiotherapy: can [18F]FET- PET overcome diagnostic uncertainties? Radiat Oncol. 2016;11(1):139.

92. Terakawa Y, Tsuyuguchi N, Iwai Y, et al. Diagnostic accuracy of 11C-methionine PET for differentiation of recurrent brain tumors from radiation necrosis after radiotherapy. J Nucl Med. 2008;49(5):694–9.

93. Herrmann K, Czernin J, Cloughesy T, et al. Comparison of visual and semiquantitative analysis of 18F-FDOPA-PET/CT for recurrence detection in glioblastoma patients. Neuro-Oncology. 2014;16(4):603–9.

94. Minamimoto R, Saginoya T, Kondo C, et al. Differentiation of brain tumor recurrence from post-radiotherapy necrosis with 11C-methionine PET: visual assessment versus quantitative assessment. PLoS One. 2015;10(7):e0132515.

95. Spence AM, Muzi M, Mankoff DA, et al. 18F-FDG PET of gliomas at delayed intervals: improved distinction between tumor and normal gray matter. J Nucl Med. 2004;45(10):1653–9.

96. Prieto E, Marti-Climent JM, Dominguez-Prado I, et al. Voxel-based analysis of dual-time-point 18F-FDG PET images for brain tumor identification and delineation. J Nucl Med. 2011;52(6):865–72.

97. Roelcke U, Blasberg RG, von Ammon K, et al. Dexamethasone treatment and plasma glucose levels: relevance for fluorine-18-fluorodeoxyglucose uptake measurements in gliomas. J Nucl Med. 1998;39(5):879–84.

98. Lewitschnig S, Gedela K, Toby M, et al. (1)8F-FDG PET/CT in HIV-related central nervous system pathology. Eur J Nucl Med Mol Imaging. 2013;40(9):1420–7.

99. Alavi JB, Alavi A, Chawluk J, et al. Positron emission tomography in patients with glioma. A predictor of prognosis. Cancer. 1988;62(6):1074–8.

100. Colavolpe C, Chinot O, Metellus P, et al. FDG-PET predicts survival in recurrent high-grade gliomas treated with bevacizumab and irinotecan. Neuro-Oncology. 2012;14(5):649–57.

101. Padma MV, Said S, Jacobs M, et al. Prediction of pathology and survival by FDG PET in gliomas. J Neuro-Oncol. 2003;64(3):227–37.

102. Delbeke D, Meyerowitz C, Lapidus RL, et al. Optimal cutoff levels of F-18 fluorode-oxyglucose uptake in the differentiation of low-grade from high-grade brain tumors with PET. Radiology. 1995;195(1):47–52.

103. Jacobs AH, Kracht LW, Gossmann A, et al. Imaging in neurooncology. NeuroRx. 2005;2(2):333–47.

104. Kasenda B, Haug V, Schorb E, et al. 18F-FDG PET is an independent outcome predictor in primary central nervous system lymphoma. J Nucl Med. 2013;54(2):184–91.

105. Hillner BE, Siegel BA, et al. Impact of dedicated brain PET on intended patient management in participants of the national oncologic PET Registry. Mol Imaging Biol. 2011;13(1):161–5.

106. Herholz K, Langen KJ, Schiepers C, Mountz JM. Brain tumors. Semin Nucl Med. 2012;42(6):356–70.

107. Caroline I, Rosenthal MA. Imaging modalities in high-grade gliomas: pseudoprogression, recurrence, or necrosis? J Clin Neurosci. 2012;19(5):633–7.

108. Mottram JC. Factors of importance in the radiosensitivity of tumors. Br J Radiol. 1936;9:606–14.

109. Padhani AR, Krohn KA, Lewis JS, Alber M. Imaging oxygenation of human tumours. Eur Radiol. 2007;17(4):861–72.

110. Vaupel P. The role of hypoxia-induced factors in tumor progression. Oncologist. 2004;9(Suppl 5):10–7.

111. Mendichovszky I, Jackson A. Imaging hypoxia in gliomas. Br J Radiol. 2011;84(2):S145–58.

112. Bruehlmeier M, Roelcke U, Schubiger PA, Ametamey SM. Assessment of hypoxia and perfusion in human brain tumors using PET with 18F-fluoromisonidazole and 15O-H2O. J Nucl Med. 2004;45(11):1851–9.

113. Gulyas B, Halldin C. New PET radiopharmaceuticals beyond FDG for brain tumor imaging. The quarterly journal of nuclear medicine and molecular imaging : official publication of the Italian Association of Nuclear Medicine (AIMN) [and] the International Association of Radiopharmacology (IAR), [and] Section of the Society of…. 2012;56(2):173–90.

114. Bell C, Dowson N, Fay M, et al. Hypoxia imaging in gliomas with 18F-fluoromisonidazole PET: toward clinical translation. Semin Nucl Med. 2015;45(2):136–50.

115. Valk PE, Mathis CA, Prados MD, Gilbert JC, Budinger TF. Hypoxia in human gliomas: demonstration by PET with fluorine-18-fluoromisonidazole. J Nucl Med. 1992;33(12):2133–7.

116. Spence AM, Muzi M, Swanson KR, et al. Regional hypoxia in glioblastoma multiforme quantified with [18F]fluoromisonidazole positron emission tomography before radiotherapy: correlation with time to progression and survival. Clin Cancer Res. 2008;14(9):2623–30.

117. Hirata K, Terasaka S, Shiga T, et al. (1)8F-Fluoromisonidazole positron emission tomography may differentiate glioblastoma multiforme from less malignant gliomas. Eur J Nucl Med Mol Imaging. 2012;39(5):760–70.

118. Yamamoto Y, Maeda Y, Kawai N, et al. Hypoxia assessed by 18F-fluoromisonidazole positron emission tomography in newly diagnosed gliomas. Nucl Med Commun. 2012;33(6):621–5.

119. De Clermont H, Huchet A, Lamare F, Riviere A, Fernandez P. Lack of concordance between the F-18 fluoromisonidazole PET and the F-18 FDG PET in human glioblastoma. Clin Nucl Med. 2011;36(12):e194–5.

120. Rajendran JG, Mankoff DA, O'Sullivan F, et al. Hypoxia and glucose metabolism in malignant tumors: evaluation by [18F]fluoromisonidazole and [18F]fluorodeoxyglucose positron emission tomography imaging. Clin Cancer Res. 2004;10(7):2245–52.

121. Toyonaga T, Hirata K, Yamaguchi S, et al. (18)F-fluoromisonidazole positron emission tomography can predict pathological necrosis of brain tumors. Eur J Nucl Med Mol Imaging. 2016;43(8):1469–76.

122. Gerstner ER, Zhang Z, Fink JR, et al. ACRIN 6684: assessment of tumor hypoxia in newly diagnosed Glioblastoma using 18F-FMISO PET and MRI. Clin Cancer Res. 2016;22(20):5079–86.

123. Dewhirst MW, Cao Y, Moeller B. Cycling hypoxia and free radicals regulate angiogenesis and radiotherapy response. Nat Rev Cancer. 2008;8(6):425–37.

124. Thompson G, Mills SJ, Coope DJ, O'Connor JP, Jackson A. Imaging biomarkers of angiogenesis and the microvascular environment in cerebral tumours. Br J Radiol. 2011;84(2):S127–44.

125. Batchelor TT, Reardon DA, de Groot JF, Wick W, Weller M. Antiangiogenic therapy for glioblastoma: current status and future prospects. Clin Cancer Res. 2014;20(22):5612–9.

126. Iagaru A, Chen X, Gambhir SS. Molecular imaging can accelerate anti-angiogenic drug development and testing. Nat Clin Pract Oncol. 2007;4(10):556–7.

127. Iagaru A, Gambhir SS. Imaging tumor angiogenesis: the road to clinical utility. AJR Am J Roentgenol. 2013;201(2):W183–91.

128. Minamimoto R, Jamali M, Barkhodari A, et al. Biodistribution of the (1)(8)F-FPPRGD(2) PET radiopharmaceutical in cancer patients: an atlas of SUV measurements. Eur J Nucl Med Mol Imaging. 2015;42(12):1850–8.

129. Treglia G, Giovannini E, Di Franco D, et al. The role of positron emission tomography using carbon-11 and fluorine-18 choline in tumors other than prostate cancer: a systematic review. Ann Nucl Med. 2012;26(6):451–61.

130. DeGrado TR, Baldwin SW, Wang S, et al. Synthesis and evaluation of (18)F-labeled choline analogs as oncologic PET tracers. J Nucl Med. 2001;42(12):1805–14.

131. Hara T, Kosaka N, Shinoura N, Kondo T. PET imaging of brain tumor with [methyl-11C] choline. J Nucl Med. 1997;38(6):842–7.

132. Hara T, Kondo T, Hara T, Kosaka N. Use of 18F-choline and 11C-choline as contrast agents in positron emission tomography imaging-guided stereotactic biopsy sampling of gliomas. J Neurosurg. 2003;99(3):474–9.

133. Ohtani T, Kurihara H, Ishiuchi S, et al. Brain tumour imaging with carbon-11 choline: comparison with FDG PET and gadolinium-enhanced MR imaging. Eur J Nucl Med. 2001;28(11):1664–70.

134. Utriainen M, Komu M, Vuorinen V, et al. Evaluation of brain tumor metabolism with [11C] choline PET and 1H-MRS. J Neuro-Oncol. 2003;62(3):329–38.

135. Tian M, Zhang H, Higuchi T, Oriuchi N, Endo K. Oncological diagnosis using (11)C-choline-positron emission tomography in comparison with 2-deoxy-2-[(18)F] fluoro-D-glucose-positron emission tomography. Mol Imaging Biol. 2004;6(3):172–9.

136. Tian M, Zhang H, Oriuchi N, Higuchi T, Endo K. Comparison of 11C-choline PET and FDG PET for the differential diagnosis of malignant tumors. Eur J Nucl Med Mol Imaging. 2004;31(8):1064–72.

137. Kwee SA, Ko JP, Jiang CS, Watters MR, Coel MN. Solitary brain lesions enhancing at MR imaging: evaluation with fluorine 18 fluorocholine PET. Radiology. 2007;244(2):557–65.

138. Huang Z, Zuo C, Guan Y, et al. Misdiagnoses of 11C-choline combined with 18F-FDG PET imaging in brain tumours. Nucl Med Commun. 2008;29(4):354–8.

139. Kato T, Shinoda J, Nakayama N, et al. Metabolic assessment of gliomas using 11C-methionine, [18F] fluorodeoxyglucose, and 11C-choline positron-emission tomography. AJNR Am J Neuroradiol. 2008;29(6):1176–82.

140. Takenaka S, Shinoda J, Asano Y, et al. Metabolic assessment of monofocal acute inflammatory demyelination using MR spectroscopy and (11)C-methionine-, (11)C-choline-, and (18)F-fluorodeoxyglucose-PET. Brain Tumor Pathol. 2011;28(3):229–38.

141. Tan H, Chen L, Guan Y, Lin X. Comparison of MRI, F-18 FDG, and 11C-choline PET/CT for their potentials in differentiating brain tumor recurrence from brain tumor necrosis following radiotherapy. Clin Nucl Med. 2011;36(11):978–81.

142. Li FM, Nie Q, Wang RM, et al. 11C-CHO PET in optimization of target volume delineation and treatment regimens in postoperative radiotherapy for brain gliomas. Nucl Med Biol. 2012;39(3):437–42.

143. Gomez-Rio M, Testart Dardel N, Santiago Chinchilla A, et al. (1)(8)F-Fluorocholine PET/CT as a complementary tool in the follow-up of low-grade glioma: diagnostic accuracy and clinical utility. Eur J Nucl Med Mol Imaging. 2015;42(6):886–95.

144. Giovacchini G, Fallanca F, Landoni C, et al. C-11 choline versus F-18 fluorodeoxyglucose for imaging meningiomas: an initial experience. Clin Nucl Med. 2009;34(1):7–10.

145. Vander Borght T, Labar D, Pauwels S, Lambotte L. Production of [2-11C]thymidine for quantification of cellular proliferation with PET. Int J Radiat Appl Instrum Part A. 1991;42(1):103–4.

146. Shields AF, Grierson JR, Dohmen BM, et al. Imaging proliferation in vivo with [F-18]FLT and positron emission tomography. Nat Med. 1998;4(11):1334–6.

147. Shinomiya A, Kawai N, Okada M, et al. Evaluation of 3′-deoxy-3′-[18F]-fluorothymidine (18F-FLT) kinetics correlated with thymidine kinase-1 expression and cell proliferation in newly diagnosed gliomas. Eur J Nucl Med Mol Imaging. 2013;40(2):175–85.

148. Tripathi M, Sharma R, D'Souza M, et al. Comparative evaluation of F-18 FDOPA, F-18 FDG, and F-18 FLT-PET/CT for metabolic imaging of low grade gliomas. Clin Nucl Med. 2009;34(12):878–83.

149. Collet S, Valable S, Constans JM, et al. [(18)F]-fluoro-L-thymidine PET and advanced MRI for preoperative grading of gliomas. NeuroImage Clin. 2015;8:448–54.

150. Yamamoto Y, Ono Y, Aga F, Kawai N, Kudomi N, Nishiyama Y. Correlation of 18F-FLT uptake with tumor grade and Ki-67 immunohistochemistry in patients with newly diagnosed and recurrent gliomas. J Nucl Med. 2012;53(12):1911–5.

151. Choi SJ, Kim JS, Kim JH, et al. [18F]3′-deoxy-3′-fluorothymidine PET for the diagnosis and grading of brain tumors. Eur J Nucl Med Mol Imaging. 2005;32(6):653–9.

152. Ferdova E, Ferda J, Baxa J, et al. Assessment of grading in newly-diagnosed glioma using 18F-fluorothymidine PET/CT. Anticancer Res. 2015;35(2):955–9.

153. Chen W, Cloughesy T, Kamdar N, et al. Imaging proliferation in brain tumors with 18F-FLT PET: comparison with 18F-FDG. J Nucl Med. 2005;46(6):945–52.

154. Jacobs AH, Thomas A, Kracht LW, et al. 18F-fluoro-L-thymidine and 11C-methylmethionine as markers of increased transport and proliferation in brain tumors. J Nucl Med. 2005;46(12):1948–58.

155. Li Z, Yu Y, Zhang H, Xu G, Chen L. A meta-analysis comparing 18F-FLT PET with 18F-FDG PET for assessment of brain tumor recurrence. Nucl Med Commun. 2015;36(7):695–701.

156. Hatakeyama T, Kawai N, Nishiyama Y, et al. 11C-methionine (MET) and 18F-fluorothymidine (FLT) PET in patients with newly diagnosed glioma. Eur J Nucl Med Mol Imaging. 2008;35(11):2009–17.

157. Enslow MS, Zollinger LV, Morton KA, et al. Comparison of 18F-fluorodeoxyglucose and 18F-fluorothymidine PET in differentiating radiation necrosis from recurrent glioma. Clin Nucl Med. 2012;37(9):854–61.

158. Shishido H, Kawai N, Miyake K, Yamamoto Y, Nishiyama Y, Tamiya T. Diagnostic value of 11C-methionine (MET) and 18F-Fluorothymidine (FLT) positron emission tomography in recurrent high-grade Gliomas; differentiation from treatment-induced tissue necrosis. Cancers. 2012;4(1):244–56.

159. Chen W, Delaloye S, Silverman DH, et al. Predicting treatment response of malignant gliomas to bevacizumab and irinotecan by imaging proliferation with [18F] fluorothymidine positron emission tomography: a pilot study. J Clin Oncol Off J Am Soc Clin Oncol. 2007;25(30):4714–21.

160. Harris RJ, Cloughesy TF, Pope WB, et al. 18F-FDOPA and 18F-FLT positron emission tomography parametric response maps predict response in recurrent malignant gliomas treated with bevacizumab. Neuro-Oncology. 2012;14(8):1079–89.

161. Schwarzenberg J, Czernin J, Cloughesy TF, et al. 3′-deoxy-3′-18F-fluorothymidine PET and MRI for early survival predictions in patients with recurrent malignant glioma treated with bevacizumab. J Nucl Med. 2012;53(1):29–36.

162. Wardak M, Schiepers C, Cloughesy TF, Dahlbom M, Phelps ME, Huang SC. (1)(8)F-FLT and (1)(8)F-FDOPA PET kinetics in recurrent brain tumors. Eur J Nucl Med Mol Imaging. 2014;41(6):1199–209.

163. Wardak M, Schiepers C, Dahlbom M, et al. Discriminant analysis of (1)(8)F-fluorothymidine kinetic parameters to predict survival in patients with recurrent high-grade glioma. Clin Cancer Res. 2011;17(20):6553–62.

164. Ma DJ, Galanis E, Anderson SK, et al. A phase II trial of everolimus, temozolomide, and radiotherapy in patients with newly diagnosed glioblastoma: NCCTG N057K. Neuro-Oncology. 2015;17(9):1261–9.

165. Leung K. [11C]acetate. Molecular imaging and contrast agent database (MICAD). Bethesda: National Center for Biotechnology Information (US); 2004.

166. Pike VW, Eakins MN, Allan RM, Selwyn AP. Preparation of [1-11C]acetate--an agent for the study of myocardial metabolism by positron emission tomography. Int J Appl Radiat Isot. 1982;33(7):505–12.

167. Liu RS, Chang CP, Chu LS, et al. PET imaging of brain astrocytoma with 1-11C-acetate. Eur J Nucl Med Mol Imaging. 2006;33(4):420–7.

168. Liu RS, Chang CP, Guo WY, et al. 1-11C-acetate versus 18F-FDG PET in detection of meningioma and monitoring the effect of gamma-knife radiosurgery. J Nucl Med. 2010;51(6):883–91.

169. Tsuchida T, Takeuchi H, Okazawa H, Tsujikawa T, Fujibayashi Y. Grading of brain glioma with 1-11C-acetate PET: comparison with 18F-FDG PET. Nucl Med Biol. 2008;35(2):171–6.

170. Yamamoto Y, Nishiyama Y, Kimura N, et al. 11C-acetate PET in the evaluation of brain glioma: comparison with 11C-methionine and 18F-FDG-PET. Mol Imaging Biol. 2008;10(5):281–7.

171. Al-Nahhas A, Win Z, Szyszko T, et al. Gallium-68 PET: a new frontier in receptor cancer imaging. Anticancer Res. 2007;27(6b):4087–94.

172. Silva CB, Ongaratti BR, Trott G, et al. Expression of somatostatin receptors (SSTR1-SSTR5) in meningiomas and its clinicopathological significance. Int J Clin Exp Pathol. 2015;8(10):13185–92.

173. Combs SE, Welzel T, Habermehl D, et al. Prospective evaluation of early treatment outcome in patients with meningiomas treated with particle therapy based on target volume definition with MRI and 68Ga-DOTATOC-PET. Acta Oncol (Stockh.). 2013;52(3):514–20.

174. Gehler B, Paulsen F, Oksuz MO, et al. [68Ga]-DOTATOC-PET/CT for meningioma IMRT treatment planning. Radiat Oncol. 2009;4:56.

175. Graf R, Nyuyki F, Steffen IG, et al. Contribution of 68Ga-DOTATOC PET/CT to target volume delineation of skull base meningiomas treated with stereotactic radiation therapy. Int J Radiat Oncol Biol Phys. 2013;85(1):68–73.

176. Madani I, Lomax AJ, Albertini F, Trnkova P, Weber DC. Dose-painting intensity-modulated proton therapy for intermediate- and high-risk meningioma. Radiat Oncol. 2015;10:72.

177. Milker-Zabel S, Zabel-du Bois A, Henze M, et al. Improved target volume definition for fractionated stereotactic radiotherapy in patients with intracranial meningiomas by correlation of CT, MRI, and [68Ga]-DOTATOC-PET. Int J Radiat Oncol Biol Phys. 2006;65(1):222–7.

178. Nyuyki F, Plotkin M, Graf R, et al. Potential impact of (68)Ga-DOTATOC PET/CT on stereotactic radiotherapy planning of meningiomas. Eur J Nucl Med Mol Imaging. 2010;37(2):310–8.

179. Thorwarth D, Henke G, Muller AC, et al. Simultaneous 68Ga-DOTATOC-PET/MRI for IMRT treatment planning for meningioma: first experience. Int J Radiat Oncol Biol Phys. 2011;81(1):277–83.

180. Sommerauer M, Burkhardt JK, Frontzek K, et al. 68Gallium-DOTATATE PET in meningioma: a reliable predictor of tumor growth rate? Neuro-Oncology. 2016;18(7):1021–7.

181. Afshar-Oromieh A, Giesel FL, Linhart HG, et al. Detection of cranial meningiomas: comparison of (6)(8)Ga-DOTATOC PET/CT and contrast-enhanced MRI. Eur J Nucl Med Mol Imaging. 2012;39(9):1409–15.

182. Bodei L, Cremonesi M, Kidd M, et al. Peptide receptor radionuclide therapy for advanced neuroendocrine tumors. Thorac Surg Clin. 2014;24(3):333–49.

183. Hanscheid H, Sweeney RA, Flentje M, et al. PET SUV correlates with radionuclide uptake in peptide receptor therapy in meningioma. Eur J Nucl Med Mol Imaging. 2012;39(8):1284–8.

184. Seystahl K, Stoecklein V, Schuller U, et al. Somatostatin receptor-targeted radionuclide therapy for progressive meningioma: benefit linked to 68Ga-DOTATATE/−TOC uptake. Neuro-Oncology. 2016;18(11):1538–47.

185. Shao Y, Cherry SR, Farahani K, et al. Simultaneous PET and MR imaging. Phys Med Biol. 1997;42(10):1965–70.

186. Schlemmer HP, Pichler BJ, Schmand M, et al. Simultaneous MR/PET imaging of the human brain: feasibility study. Radiology. 2008;248(3):1028–35.

187. Delso G, Furst S, Jakoby B, et al. Performance measurements of the Siemens mMR integrated whole-body PET/MR scanner. J Nucl Med. 2011;52(12):1914–22.

188. Bisdas S, Ritz R, Bender B, et al. Metabolic mapping of gliomas using hybrid MR-PET imaging: feasibility of the method and spatial distribution of metabolic changes. Investig Radiol. 2013;48(5):295–301.

189. Boss A, Kolb A, Hofmann M, et al. Diffusion tensor imaging in a human PET/MR hybrid system. Investig Radiol. 2010;45(5):270–4.

190. Garibotto V, Heinzer S, Vulliemoz S, et al. Clinical applications of hybrid PET/MRI in neuroimaging. Clin Nucl Med. 2013;38(1):e13–8.

191. Neuner I, Kaffanke JB, Langen KJ, et al. Multimodal imaging utilising integrated MR-PET for human brain tumour assessment. Eur Radiol. 2012;22(12):2568–80.

192. Afshar-Oromieh A, Wolf MB, Kratochwil C, et al. Comparison of (6)(8)Ga-DOTATOC-PET/CT and PET/MRI hybrid systems in patients with cranial meningioma: initial results. Neuro-Oncology. 2015;17(2):312–9.

193. Jena A, Taneja S, Gambhir A, et al. Glioma recurrence versus radiation necrosis: single-session multiparametric approach using simultaneous O-(2-18F-Fluoroethyl)-L-tyrosine PET/MRI. Clin Nucl Med. 2016;41(5):e228–36.

194. Sacconi B, Raad RA, Lee J, et al. Concurrent functional and metabolic assessment of brain tumors using hybrid PET/MR imaging. J Neuro-Oncol. 2016;127(2):287–93.

195. Fraioli F, Shankar A, Hargrave D, et al. 18F-fluoroethylcholine (18F-Cho) PET/MRI functional parameters in pediatric astrocytic brain tumors. Clin Nucl Med. 2015;40(1):e40–5.

196. Preuss M, Werner P, Barthel H, et al. Integrated PET/MRI for planning navigated biopsies in pediatric brain tumors. Childs Nerv Syst. 2014;30(8):1399–403.

197. Boss A, Bisdas S, Kolb A, et al. Hybrid PET/MRI of intracranial masses: initial experiences and comparison to PET/CT. J Nucl Med. 2010;51(8):1198–205.

198. Schwenzer NF, Stegger L, Bisdas S, et al. Simultaneous PET/MR imaging in a human brain PET/MR system in 50 patients--current state of image quality. Eur J Radiol. 2012;81(11):3472–8.

199. Navarria P, Reggiori G, Pessina F, et al. Investigation on the role of integrated PET/MRI for target volume definition and radiotherapy planning in patients with high grade glioma. Radiother Oncol. 2014;112(3):425–9.

200. Filss CP, Galldiks N, Stoffels G, et al. Comparison of 18F-FET PET and perfusion-weighted MR imaging: a PET/MR imaging hybrid study in patients with brain tumors. J Nuclear Med. 2014;55(4):540–5.

Neuro: Head and Neck Oncology

12

Martin W. Huellner, Spyros S. Kollias, Gerhard F. Huber, and Marcelo A. Queiroz

Contents

M.W. Huellner (✉)
Department of Nuclear Medicine, University Hospital Zurich, Zurich, Switzerland
e-mail: martin.huellner@usz.ch

S.S. Kollias
Department of Neuroradiology, University Hospital Zurich, Zurich, Switzerland

G.F. Huber
Department of Otorhinolaryngology, Head and Neck Surgery, University Hospital Zurich, Zürich, Switzerland

M.A. Queiroz
Department of Nuclear Medicine, University of Sao Paulo, Sao Paulo, Brazil

12.1   Introduction

Soon after the clinical implementation of PET/MR in 2011 and after initial feasibility studies, first comparative studies reported a draw between PET/MR and PET/CT with regard to the staging of head and neck cancer patients [1–8]. In the long run, however, PET/MR is expected to outstrip PET/CT in this field. This chapter aims to highlight current clinical applications and future directions of PET/MR in head and neck oncology.

PET/MR combines the advantages of molecular tumor imaging and high soft tissue contrast in one single examination—in contrast to the traditional approach, which often required both PET/CT and contrast-enhanced MR for a thorough workup of head and neck cancer patients. A more widespread clinical use of PET/MR is currently limited by monetary issues. On the one hand, the price for a PET/MR scanner including its requirements on building infrastructure is at least three-fold the price of a PET/CT scanner. On the other hand, several countries are still lacking reimbursement models for PET/MR.

Centers with access to a PET/MR scanner generally prefer PET/MR over PET/CT in the initial staging of head and neck cancer patients—with the exception of cancers arising in the hypopharynx and larynx, where motion plays a prominent role, mainly swallowing [5]. For the nodal staging, both modalities are generally considered equivalent, although certain functional MR techniques might tip the scales toward PET/MR. The lung is the place where the majority of distant metastases of head and neck cancer patients occurs and was considered a black box for MR imaging for a long time [9]. Recent advances in the development of MR pulse sequences, some of them stimulated by the advent of PET/MR and its intrinsic need for proper lung tissue visualization, help elucidate this black box [10–13].

The scintigraphic imaging of malignant head and neck tumors today is mainly reserved to ^{18}F-fluoro-2-deoxy-*D*-glucose (FDG). Other radiotracers might play a future role in the imaging of FDG-negative salivary gland malignancies, e.g., ^{68}Ga-prostate-specific membrane antigen (PSMA); in neuroendocrine tumors, e.g., ^{68}Ga-1,4,7,10-tetraazacyclododecane-1,4,7,10-tetraacetic acid (Tyr^3)-octreotate (DOTATATE); and in certain non-malignant neoplasms, e.g., ^{18}F-fluorocholine (FCH) in parathyroid adenomas.

Proper photon attenuation correction (AC) is important in the head and neck, owing to oftentimes small-sized lesions of interest, narrow anatomical relationships, and a multitude a neighboring spaces and compartments. This is challenged by an abundance of tissues with different attenuation properties within a small and complex area and by the typical presence of artifacts elicited by dental hardware. Time-of-flight (TOF) PET dataset reconstructions are considered important in the head and neck, both for the detection and correct localization of small lesion but also for decreasing implant-related artifacts and for optimizing the MR-based AC [14–19]. While atlas methods can be used for the head in PET/MR, MR-based AC in the neck mainly relies on the Dixon method, which yields four different tissue properties (air, fat, water, soft tissue), but neglects the bone, which represents another black box for MR. In fact, bone assumes μ

map values similar to air, while the photon attenuation in both structures is entirely different. This issue might be overcome using MR pulse sequences with ultrashort echo time (UTE) or even—by definition—zero echo time (ZTE) [20–22].

12.2 PET/MR Protocols for the Head and Neck

The definition of valid protocols for PET/MR is a key requisite for clinical head and neck cancer assessment. MR pulse sequences should be selected to provide most complementary information or at least confirmatory information with regard to PET data. In integrated PET/MR scanners, the use of TOF PET information helps to identify small lesions, reduces artifacts—particularly those related to metallic implants such as dental hardware—and increases the accuracy of the MR-based AC [14, 15, 17–19]. For whole-body exams, the PET/MR protocol is divided into two separate, yet not independent, parts [23, 24]:

1. A fast basic whole-body oncologic PET/MR acquisition which contains the pulse sequence(s) used for MR-based AC, sufficient anatomic correlation, and basic soft-tissue characterization outside the head and neck area
2. A dedicated head and neck PET/MR acquisition that comprises high-resolution anatomical tumor imaging and enables the definition of specific tumor features, such as cellularity and vascularization

12.2.1 Basic Whole-Body PET/MR Acquisition

For the basic whole-body PET/MR acquisition, the patient should be positioned with arms down. The Z-axis scanning range covers the area from the vertex of the skull to the mid-thighs. A dedicated phased-array head and neck coil is used in conjunction with a body surface coil. PET datasets usually require 4–8 bed positions per patient (depending on the individual body height and on scanner geometry) of 2–5 min each (depending on scanner type and injected activity), using 3D image acquisition and reconstruction. The MR pulse sequences used for the AC are acquired during the PET acquisition. For the trunk, usually a T1-weighted Dixon-type sequence is used, whereas for the head, atlas methods may be used alternatively. Since the extremities are subject to wrapping artifacts in MR, AC of the extremities relies on PET data only. The same Dixon-type MR pulse sequence used for AC may also be used for diagnostic imaging, albeit with higher resolution. Repeating this pulse sequence after the administration of intravenous contrast is not essentially needed in head and neck cancer patients. If done, the acquisition takes place after the accomplishment of the non-contrast-enhanced MR pulse sequences of the head and neck. Using the phase-encoding gradient in anteroposterior direction helps reduce flow artifacts, especially in the posterior pharynx and larynx, although this requires a somewhat longer acquisition time [25].

Another diagnostic whole-body MR pulse sequence acquired is usually a T2-weighted image dataset, preferentially in coronal plane and with fat suppression, e.g., single-shot fast spin echo (SSFSE). One specific MR pulse sequence of the lung should also be part of this first step, especially in patients with a high likelihood of pulmonary metastases (higher T stage, lymph node metastasis in the lower neck, non-epithelial primary carcinoma, more than one primary tumor, etc.) [24, 26]. Most centers use a T2-weighted pulse sequence with motion correction, such as periodically rotated overlapping parallel lines with enhanced reconstruction (PROPELLER; GE Healthcare, Waukesha, WI). This sequence is acquired axially during free breathing and uses respiratory triggering [27, 28]. As an alternative, MR pulse sequences with ultrashort echo time or zero echo time may be considered. A recent study has shown that a free-breathing UTE pulse sequence has a high sensitivity for the detection of small pulmonary nodules (4–8 mm), including those not FDG-avid [29].

The PET acquisition and reconstruction covering the chest may take into account the respiratory motion in order to achieve an optimal standardized uptake value (SUV), particularly in small lung nodules and in lesions located in the base of the lungs. This can be accomplished using bellows-driven gating, MR-driven gating, or PET-driven gating [30]. This first part of the protocol can take from 12 to 25 min, depending on the parameters chosen for PET acquisition and MR pulse sequences.

12.2.2 Regional Head and Neck PET/MR Acquisition

A dedicated head and neck PET/MR protocol should not simply duplicate the clinical head and neck MR protocol routinely performed in the radiology department. A careful selection of MR pulse sequences is needed in order to optimize the diagnostic capability of PET/MR. The field of view and slicing of all regional MR pulse sequences need to be tailored to the head and neck and should not copy the parameters of the whole-body MR pulse sequences. Several studies have addressed the contribution of different MR pulse sequences for the assessment of head and neck tumors with PET/MR.

One typical recommendation is to acquire a T2-weighted sequence in at least two planes, using fat suppression, which gives sufficient information for tumor delineation. This can be supplanted with a T1-weighted sequence without fat suppression in at least one plane, preferably axial. This basic approach is already sufficient in many instances and avoids the injection of MR contrast medium [5]. However, this simple solution is not acceptable for presurgical planning, in stage T4 tumors, in recurrent tumors, and in cases of perineural spread [1, 5]. Here, contrast-enhanced fat-suppressed MR pulse sequences, acquired in at least two planes, are needed [1, 5, 24]. Since such a regional MR acquisition takes comparably long, a separate regional PET acquisition of the head and neck may be part of the protocol—making use of a long local bed time but without increasing the total examination time.

Functional MR sequences are also viable options for tumor characterization. This includes diffusion-weighted imaging (DWI), a surrogate marker of tumor cellularity, and perfusion-weighted imaging, a biomarker of vascularization and neoangiogenesis. Of note, information on tumoral glucose metabolism is already

available from FDG-PET and might obviate the need of such rather time-consuming functional MR pulse sequences. PET data may, e.g., be sufficient for therapy response assessment or the characterization of subcentimeter lymph nodes. Occasionally, FDG-avid pathologic lesions remain occult in areas with high physiologic glucose uptake, such as the lymphoepithelial tissue commonly found in the palatine tonsils and lingual tonsils. Here, functional MR pulse sequences, particularly DWI, assume a more prominent role. Recent studies analyzed the association of glucose metabolism, cellularity, and histological parameters in patients with squamous cell carcinoma and showed that DWI and FDG-PET may work as independent and complementary biomarkers [31–35]. Preliminary data are also available for perfusion-weighted imaging as part of a multiparametric PET/MR protocol for head and neck cancer. Covello and coworkers have proven the feasibility of such a protocol, which enables the simultaneous collection of metabolic and functional data [36]. Such a multiparametric approach may allow for a noninvasive characterization of tumor or recurrent tumor and might facilitate treatment planning.

Acquisition time, patient throughput, and individual patient tolerance are important issues to be considered. An advanced MR head and neck protocol takes about 30–35 min. Patients are instructed to breathe softly and not to swallow during the examination. Such is usually well tolerated. Notably, a multiparametric PET/MR acquisition may take longer, and the surface coils covering the head and neck as well as the torso might be uncomfortable and might preclude long acquisition times.

In summary, a regional PET/MR protocol for head and neck cancer should be tailored according to the specific questions that need to be answered. In most cases, the use of MR contrast medium is required, and functional MR sequences may not be needed. Specific parameters of MR pulse sequences have been suggested previously [24].

12.3 PET/MR Imaging of Carcinoma and Lymphoma in the Head and Neck

12.3.1 T Staging

More than 90% of all head and neck carcinomas are of squamous cell histology. The risk factors for this type of tumor comprise smoking and alcohol in general (exponential risk), and certain viral oncogenes in specific subsets, such as Epstein-Barr virus (EBV) in the nasopharynx and human papillomavirus (HPV) in younger patients, mainly in the oropharynx.

When a patient is referred for the initial imaging staging of a head and neck tumor, typically the tumor has already been identified, and good estimates have been made on its local extension and potential infiltration of adjacent structures [37, 38]. There is ample literature on comparing PET/CT and MRI for the local staging of tumors, which basically shows that MRI identifies the tumor extent more accurately, owing to better soft tissue contrast [37]. On the other hand, MR has also been compared with PET/MR, and most authors found no significant difference in the assessment of primary tumors [5, 39]. Based on these findings, one would expect a higher accuracy of

PET/MR than PET/CT in the T staging of head and neck carcinomas, but this is controversial. Most studies performed with sequential or simultaneous PET/MR scanners could not prove superiority of PET/MR over PET/CT [1, 3, 5, 6, 8]. Vice versa, this means that PET could compensate for the known shortcomings of CT in the head and neck [1]. If MR contrast medium cannot be injected, PET/MR using only T2-weighted neck imaging yields similar accuracy as contrast-enhanced PET/CT [5].

In our opinion, the imaging of head and neck tumors requires a more specific approach. Data derived from studies, where tumors from several sites in the head and neck are literally lumped together, need to be regarded with caution. A site-specific comparison of modalities is desired, but data in the literature is currently sparse. Site-dependent differences in the accuracy of PET/CT and PET/MR are expected to arise from the anatomical component, i.e., CT or MR, respectively, since uptake measurements are comparable and reproducible among both modalities [4, 40].

It is expected that tumors arising in the oral cavity and in the oropharynx should better be imaged with PET/MR than with PET/CT, owing to less artifacts from dental hardware on MR than on CT and higher soft tissue contrast of MR (Fig. 12.1) [5, 41]. The PET data is compromised both by dental artifacts on CT and MR, which deteriorate the AC—although on PET/MR purportedly to a lesser extent than on PET/CT [17, 19, 42, 43]. The puffed cheek approach has not been studied on PET/MR so far and is expected to be more challenging owing to longer regional acquisition time with PET/MR [44]. Tumors hiding within tissue with physiologically high FDG uptake, such as lymphoepithelial tissue, which might be abundant in the oropharynx, can be missed with PET/MR, unless DWI is used [8, 45–48].

In the hypopharynx and larynx, the situation is expected to be different. Artifacts there mainly derive from patient motion, such as swallowing or breathing [5, 49]. The soft tissue contrast of CT in this area is sufficient, owing to comparably sharp density increments between the tissues there, such as intralaryngeal air, laryngeal muscles, paraglottic fat, laryngeal cartilage/ossified cartilage, and paralaryngeal fat and muscles.
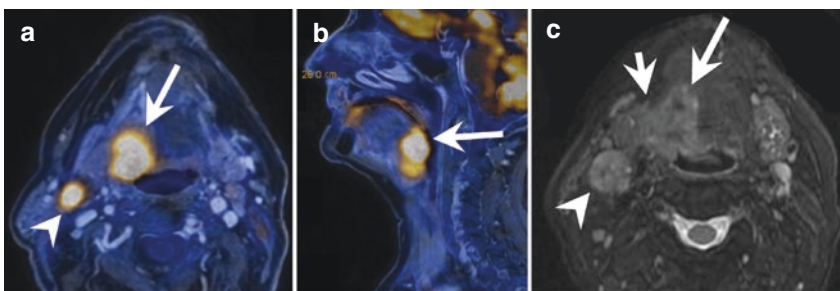

Fig. 12.1 Squamous cell carcinoma arising in the oropharynx. The axial contrast-enhanced, fat-suppressed T1-weighted ^{18}F-FDG-PET/MR image shows an intensively FDG-avid tumor in the base of the tongue on the right side (**a**, *arrow*) and an FDG-avid lymph node metastasis in cervical level IIA (*arrow head*). The tumor extends from the tongue base to the vallecula, as seen on the sagittal T1-weighted ^{18}F-FDG-PET/MR image (**b**, *arrow*). On the fat-suppressed T2-weighted image, the tumor is of inhomogeneous signal intensity with predominant hyperintense areas compared to muscle (**c**, *long arrow*) and infiltrates the intrinsic and extrinsic tongue musculature (**c**, *long arrow*) as well as the parapharyngeal adipose tissue and the right-sided submandibular gland (**c**, *short arrow*). The lymph node metastasis is seen as well (**c**, *arrow head*)

Additionally, CT offers higher spatial resolution. Thus, PET/CT might remain the modality of choice for the imaging of hypopharyngeal and laryngeal tumors, especially for smaller ones—although hybrid imaging is performed uncommonly in T1 tumors, and such small tumors might be missed completely with any imaging modality [5, 50]. There are, however, also studies with small patient cohorts that showed a similar performance of PET/MR and PET/CT in the staging of laryngeal carcinoma [51].

The potential resectability of head and neck tumors depends on several issues [52]. Not all of them are part of the TNM staging system, and if they are part, they not necessarily denote a T4b stage, which is generally considered unresectable. Particularly, the following findings with a head and neck tumor might preclude surgery or lead to a different surgical approach: vascular encasement, invasion of the prevertebral space, perineural spread, orbital invasion, bone infiltration, skull base invasion, dural infiltration, invasion of the laryngeal cartilage, invasion of the brachial plexus, and mediastinal invasion (Fig. 12.2). For all of these items, except bone and cartilage infiltration, PET/MR is expected to yield a higher accuracy than PET/CT, although evidence is currently sparse [1, 5, 53]. Particularly in cases of perineural spread, PET/MR is expected to be more accurate, owing to the higher soft tissue contrast of MR and the availability of differently weighted images [5, 37, 53]. Both contrast-enhanced MR pulse sequences with and without fat suppression may be used for this purpose in general, but preferably non-suppressed sequences should be used in the skull base [38, 54].

PET/MR provides no advantage over PET/CT in specifying FDG-positive incidental findings in the head and neck area [55]. Wang and colleagues showed that FDG-PET/MR can be used for radiation therapy planning in the head and neck, yielding similar gross tumor volumes as contrast-enhanced CT [56].

It is generally agreed upon that local tumor recurrence is best assessed with PET/MR [39, 57–59]. PET/CT is limited in identifying a morphological correlate for focal FDG uptake in the postsurgical head and neck [57, 58]. While PET may guide biopsy in such cases, biopsy might be difficult in lesions that are located in so-called blind spots, e.g., the piriform sinus or the postcricoid area, or if submucosal tumor recurrence is suggested and in-depth biopsy (e.g., using laser) is required. On the other hand, muscle tissue of surgical flaps or orthotopic muscle adjacent to such flaps might present with unusual and remarkable FDG uptake, owing to increased muscle tone as a consequence of the altered anatomy in the postsurgical state [37, 60, 61]. The higher soft tissue contrast of MR allows for a more specific assessment of focal FDG uptake identified on follow-up exams of head and neck cancer patients and for a more reliable discrimination of normal muscle and recurrent tumor [24, 37, 39, 48, 57, 59]. Additionally, DWI may be helpful, particularly in irradiated patients [24, 47, 48, 62].

12.3.2 N Staging

The presence of nodal metastases is a very important and independent prognostic factor, which worsens the prognosis of head and neck cancer patients [37]. One single lymph node metastasis already decreases the overall survival by approximately 50% [37, 63–65]. The prognosis worsens with the number of lymph nodes
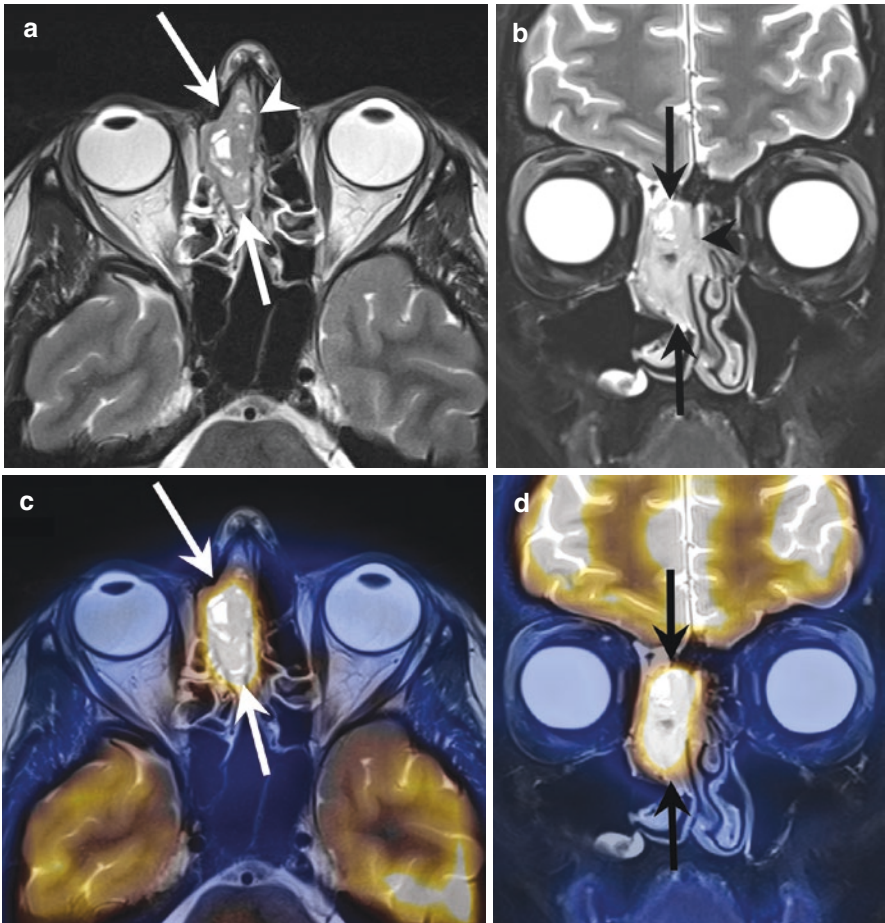
Fig. 12.2 Esthesioneuroblastoma arising in the ethmoid air cells. The axial non-suppressed (**a**) and coronal fat-suppressed (**b**) T2-weighted images show a tumor (*arrows*) in the right-sided ethmoid air cells. The tumor is of intermediate signal intensity and contains cystic spaces. The osseous nasal septum is infiltrated (*arrow head*). No extension into the orbita or infiltration of the dura is seen; the nasal bone is preserved. The axial non-suppressed (**c**) and coronal fat-suppressed (**d**) T2-weighted ^{18}F-FDG-PET/MR images confirm high FDG uptake of the tumor (*arrows*) and absence of pathologic FDG uptake in the orbit

involved, with presence of extracapsular spread, and with pathologic nodes in the lower neck (e.g., level IV) [37, 64–67].

The probably most important tool in the N staging with hybrid imaging is PET, no matter if combined with CT or with MR. Therefore, most studies could not provide evidence that PET/MR surpasses PET/CT in this field [1, 4, 6, 53, 68, 69]. This reflects various previous works on PET/CT, MR, and CT, where a similar accuracy of modalities was found, ranging from approximately 60% to 90% with regard to sensitivity and specificity [9, 37, 50, 70–72]. One possible advantage of PET/MR could lie in the more accurate staging of small nodes, especially those with necrotic

or cystic centers (e.g., with human papillomavirus subtypes 16, 18, or 31), since these might be faintly FDG-avid or even not avid but are more easily identified on fat-suppressed T2-weighted MR images than on CT [37, 73–75]. Another advantage of PET/MR might be the possibility to acquire a regional PET dataset with higher resolution during the regional MR exam, without increasing the total acquisition time. This might help identify small pathologic nodes. The use of DWI does not increase the accuracy of nodal staging with PET/MR [62].

12.3.3 M Staging and Second Primaries

Approximately 10% of all head and neck cancer patients have distant metastases upon initial presentation [37]. Per year, another 5% of patients develop second primary tumors due to field cancerization. The most common site of distant metastases and second primaries in patients with head and neck cancer is the lung [9]. Therefore, PET/MR in head and neck patients should also incorporate adequate lung imaging (see above). Studies have shown that MR lung sequences used in PET/MR, e.g., PROPELLER, detect lung nodules of 3 mm [10, 29]. Moreover, more than 98% of all FDG-negative subcentimeter lung nodules are benign, and 97% of lung nodules missed on PET/MR do not grow [76, 77]. For a more detailed discussion of lung nodules, we refer to Chap. 15 of this book.

Another common site for metastases is the skeleton. Here, some studies with general oncological cohorts reported a higher confidence in PET/MR than PET/CT, although no significant difference was found [2, 78, 79]. Specific studies on bone metastases in head and neck cancer patients today are missing.

Altogether, the majority of the currently published studies report a similar accuracy of PET/CT and PET/MR in the M staging of head and neck cancer patients [1, 2, 4, 36]. An overview on published major PET/MR studies is given in Table 12.1.

12.3.4 Lymphoma

The most common type of primary lymphoma of the head and neck region is non-Hodgkin lymphoma (NHL). Approximately 90% of NHL of the head and neck are of B-cell lineage, while only 10% are of T-cell lineage [80]. Tumors are mainly located in the oral cavity, in the nasal cavity, in the paranasal sinuses, and in major salivary glands (Fig. 12.3). Approximately one third of head and neck lymphomas arise in the bone, one third in soft tissues, and one third in multiple structures [80]. More than half of head and neck lymphomas come without pathologic lymph nodes, while in the rest nodal involvement may skip anatomical levels. Sinonasal lymphoma most often manifests as diffuse large-cell B-cell lymphoma (DLBCL), followed by NK/T-cell lymphoma. Sinonasal lymphoma typically presents as a comparably homogeneous mass that is of intermediate signal intensity on T1-weighted images and of high signal intensity on T2-weighted images. Hodgkin lymphoma often also involves neck lymph nodes, but disease is typically not limited to the neck, but occurs also in the mediastinum and sometimes in the spleen.

Table 12.1 Overview on published major prospective studies in PET/MR of the head and neck, as of May 2017

First author	Year published	PET/MR scanner type	Number of subjects in study	Main findings	Reference number
Schaarschmidt	2017	Simultaneous	81	Incidental tracer uptake in the head and neck cannot be classified more accurately with PET/MR than with PET/CT	[55]
Wang	2017	Simultaneous	11	Gross tumor volume derived by PET/MR and CT is similar in oropharynx carcinoma patients, reverting into similar radiation doses	[56]
Sekine	2017	Sequential	58	PET/MR and PET/CT are reliable in defining head and neck tumor resectability	[53]
Cavaliere	2017	Simultaneous	16	PET/MR is useful for the initial staging of laryngeal cancer	[51]
Sekine	2017	Sequential	27	Whole-body staging with PET/MR yields at least equal diagnostic accuracy as PET/CT in head and neck cancer patients	[1]
Rasmussen	2017	Simultaneous	21	DWI and FDG-PET from PET/MR yield similar radiation therapy volumes. FDG uptake and DWI do not correlate	[32]
Schaarschmidt	2016	Simultaneous	25	PET/MR and PET/CT perform equally well in tumor staging and tumor recurrence assessment	[3]
Surov	2016	Simultaneous	11	ADC and SUV are correlated with different histopathological parameters, enabling their use as complementary biomarkers in head and neck squamous cell carcinoma	[31]

Table 12.1   (continued)

| First author	Year published	PET/MR scanner type	Number of subjects in study	Main findings	Reference number
Covello	2015	Simultaneous	44	PET/MR is feasible for tumor staging and tumor recurrence assessment	[36]
Rasmussen	2015	Simultaneous	30	FDG uptake in PET/CT and PET/MR is identical and highly reproducible	[40]
Varoquaux	2014	Sequential	32	PET/MR and PET/CT are equal in terms of image quality, lesion conspicuity, and lesion localization in head and neck cancer patients	[8]
Platzek	2014	Sequential	38	PET/MR is equal to PET and MR in nodal staging	[69]
Queiroz	2014	Sequential	87	PET/MR is preferred over PET/CT in the workup of head and neck tumor recurrence	[57]
Partovi	2014	Sequential	14	PET/MR and PET/CT are equal in nodal staging and detection of distant metastases in head and neck cancer patients	[4]
Kuhn	2014	Sequential	150	T2-weighted PET/MR is at least equal to contrast-enhanced PET/CT	[5]
				Contrast-enhanced T1-weighted PET/MR is superior to T2-weighted PET/MR with regard to tumor delineation, infiltration of adjacent structures, and perineural spread	
Kubiessa	2014	Simultaneous	17	PET/MR and PET/CT perform identically	[6]
Queiroz	2014	Sequential	188	DWI as part of PET/MR does not provide important additional information for tumor staging	[62]
Platzek	2013	Sequential	20	PET/MR is feasible for head and neck tumor imaging	[7]
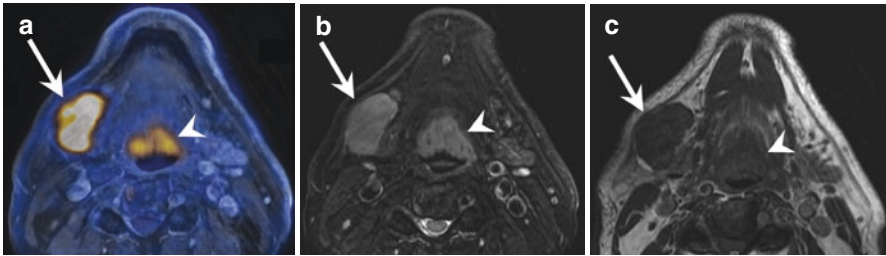
Fig. 12.3 Primary lymphoma of the head and neck, arising from the inferior portion of the submandibular gland. An intensively FDG-avid lesion is seen in the angle of the mandible on the right side on contrast-enhanced, fat-suppressed T1-weighted ^{18}F-FDG-PET/MR image (**a**, *arrow*). The lesion is homogeneously hyperintense on the fat-suppressed T2-weighted image (**b**, *arrow*) and isointense to muscle on the T1-weighted image (**c**, *arrow*). No perilesional stranding is seen in the subcutaneous or parapharyngeal adipose tissue. The lesion displaces the superior portion of the right-sided submandibular gland. Normal lymphoepithelial tissue with moderate FDG uptake is seen as well (*arrow heads* on **a–c**)

Specific PET/MR studies on head and neck lymphoma are currently lacking. PET/MR experience in more general lymphoma cohorts shows that SUVs from PET/CT and PET/MR are strongly correlated [81]. Apparent diffusion coefficient (ADC) values of lymphoma are unrelated to the SUV, which supports the assumption that both parameter sets represent independent biological information [81]. The diagnostic capability of PET/CT and PET/MR is similar and exceeds whole-body MR imaging with DWI [82]. For a more extensive discussion of PET/MR imaging of lymphoma, we refer to Chap. 22 of this book.

In summary, PET/MR has advantages over PET/CT in tumors arising in the oral cavity and in the oropharynx, as well as in recurrent tumors. The one-stop-shop opportunity, the future optimization of MR-based attenuation correction, the incremental use of MR artifact reduction techniques, and the advancement of MR pulse sequences dedicated to lung imaging might emphasize the role of PET/MR in the imaging of head and neck carcinoma and lymphoma.

12.4 PET/MR Imaging of Thyroid Carcinoma and Other Head and Neck Malignancies

The therapy of differentiated thyroid carcinoma requires thyroidectomy along with postoperative radioiodine therapy in most cases. Once there is a suspicion of recurrence, e.g., with rising levels of thyroglobulin, the detection and localization of recurrent tumor is mandatory in order to guide treatment. Recurrence may occur in the thyroid bed, in regional lymph nodes and soft tissues, or uncommonly in distant sites. The search for recurrent tumor is usually performed with hybrid imaging modalities, such as ^{123}I-SPECT/CT or ^{18}F-FDG-PET/CT in case of suspected dedifferentiation. However, abnormal focal radioiodine uptake or ^{18}F-FDG uptake may be present without an obvious pathomorphological correlate in thyroid carcinoma

patients. This can be either because the pathologic lesions are below the spatial resolution of CT or because of certain limitations of the CT protocol. The CT is usually acquired as "low-dose" scan, and ideally without intravenous iodinated contrast, which would render a subsequent radioiodine therapy futile for a couple of weeks.

In this regard, [124]I-PET/MR gained some ground. This modality allows for a better morphological correlation than PET/CT for characterizing neck tissue, especially in lesions smaller than 10 mm, thereby improving the pretherapeutic lesion dosimetry [83]. These results are not completely reflected in more recent work, where [124]I-PET/MR was indeed superior to PET/CT in detecting iodine-positive lesions, although this remains arguable [84, 85]. Yet, [124]I-PET/MR could not distinguish thyroid remnant from metastasis, while the volumetric MR information was considered useful for dosimetry purposes [84, 85].

In another study, ^{18}F-FDG-PET/MR yielded an accuracy similar to contrast-enhanced ^{18}F-FDG-PET/CT in patients with suspicion of dedifferentiated thyroid cancer, except for the detection of lung nodules, where PET/CT was superior [86]. Thus, PET/MR using either [124]I or ^{18}F-FDG is recommended at the moment only in cases of pretherapeutic dosimetry and when the use of iodine-based contrast medium is contraindicated. In all other clinical scenarios, PET/CT should be preferred, which also provides shorter acquisition time, better cost-effectiveness, and a somewhat more accurate AC [87].

On the other hand, parathyroid hyperplasia of single or multiple glands might be well addressed with PET/MR using ^{18}F-fluorocholine (FCH), which might be useful both for diagnosis and pretherapeutic planning (Fig. 12.4) [88]. A prospective pilot study investigated the performance of ^{18}F-FCH-PET/MR imaging in ten patients with biochemical primary hyperparathyroidism and inconclusive results at ultrasound and ^{99m}Tc sestamibi scintigraphy. This small study reported a sensitivity of 90% for PET/MR in this challenging patient cohort, without any false-positive results, allowing for an accurate localization of adenomas and providing detailed anatomic information [89].

Other rare tumors of the head and neck, such as those with neuroendocrine differentiation (paragangliomas) and meningiomas, may also be imaged with PET/MR, especially in conjunction with somatostatin analogue radiotracers, such as ^{68}Ga-1,4,7,10-tetraazacyclododecane-1,4,7,10-tetraacetic acid (Tyr[3])-octreotate (DOTATATE). The combination of specific morphological features of these tumors together with ^{68}Ga-DOTATATE uptake allows for an accurate diagnosis and also opens the opportunity for peptide receptor radionuclide therapy, e.g., with ^{177}Lu-DOTATATE, if surgery is not possible [24, 90].

More recently established clinical imaging using ^{68}Ga-labeled prostate-specific membrane antigen (PSMA) might gain importance in salivary gland malignancies, owing to the comparably high physiologic uptake of ^{68}Ga-PSMA in salivary gland tissue. While the primary tumor within the gland and its extent is delineated by the MR component of PET/MR, pathologic lymph nodes and distant metastases are possibly identified using ^{68}Ga-PSMA-PET [91]. This novel radiotracer might play a role especially in those neoplasms, which generally show only faint ^{18}F-FDG uptake, such as adenoid cystic carcinoma or acinic cell carcinoma [24, 49]. However, comparative studies are currently lacking.
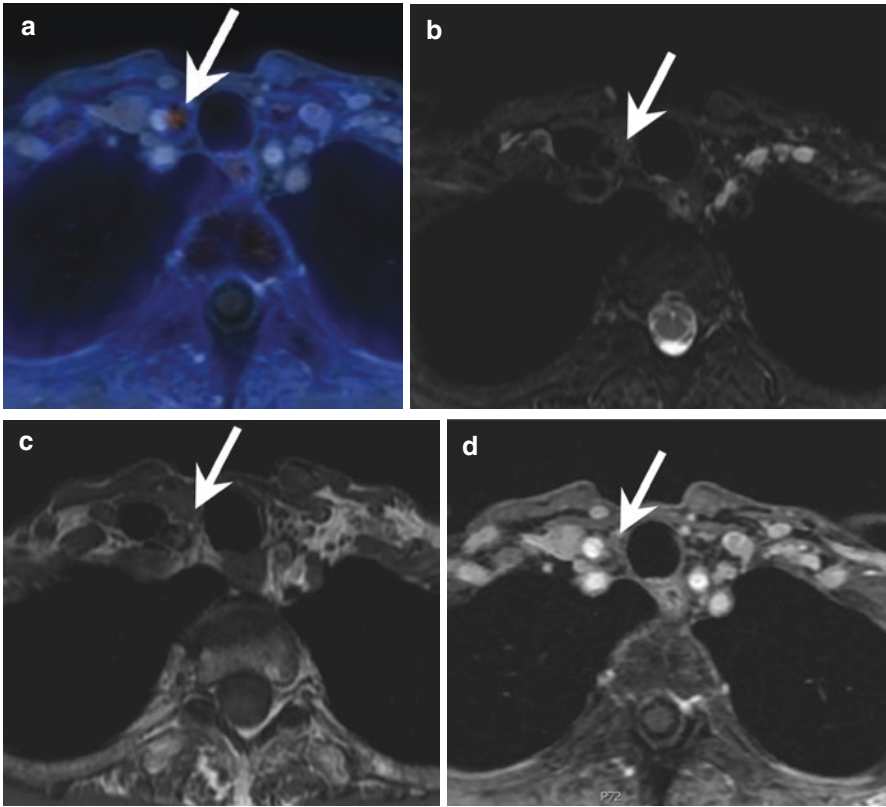
Fig. 12.4 Parathyroid adenoma in a patient with hyperparathyroidism and negative ultrasound and negative dual-isotope subtraction SPECT/CT. A tiny choline-positive nodule is seen below the right thyroid lobe on contrast-enhanced, fat-suppressed T1-weighted ^{18}F-FCH-PET/MR image (**a**, *arrow*). The nodule is isointense to muscle on the fat-suppressed T2-weighted image (**b**, *arrow*), hardly visible as isointense to muscle on the T1-weighted image (**c**, *arrow*), and does not take significant contrast on the contrast-enhanced, fat-suppressed T1-weighted image (**d**, *arrow*)

In summary, the use of PET/MR in head and neck oncology might exceed the traditional assessment of head and neck squamous cell carcinoma with ^{18}F-FDG. The advent of different tracers in the last decade together with the diagnostic capability of MR in lesion detection and characterization may facilitate the dissemination of PET/MR for the imaging of various types of tumors that occur in the head and neck.

12.5   Multiparametric PET/MR

PET/MR in head and neck cancer is mainly performed for one or more of the following reasons: TNM staging, surgery or radiotherapy planning, prognostic information, therapy response assessment, and detection of tumor recurrence. As with

anatomical MR pulse sequences, the use of functional MR pulse sequences should depend on the pertinent clinical information and questions to be answered, in order to optimize the study time and prevent a redundancy of information. The following paragraphs discuss the most commonly used functional MR pulse sequences that might enhance the diagnostic accuracy of PET/MR in head and neck cancer (Fig. 12.5). A summary of the potential benefits of each discussed MR pulse sequence in comparison to the obligatory PET is given in Table 12.2.
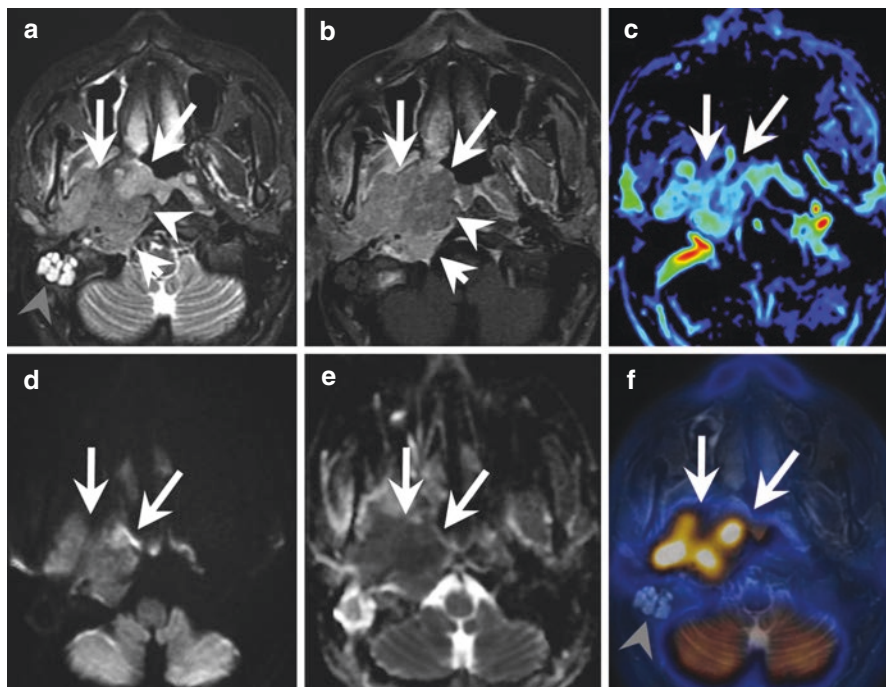
Fig. 12.5 Squamous cell carcinoma of the nasopharynx. Multiparametric PET/MR acquisition including axial T2-weighted image (**a**), contrast-enhanced T1-weighted image with fat suppression (**b**), perfusion-weighted image map of maximum slope of increase (**c**), diffusion-weighted image (**d**) and corresponding ADC map (**e**), as well as co-registered T2-weighted ^{18}F-FDG-PET/MR image (**f**) shows a heterogeneous FDG-avid tumor in the right-sided lateral wall of the nasopharynx (*arrows* on **a–f**). The tumor infiltrates the prevertebral muscles (*arrow head* on **a**, **b**), the right-sided hypoglossal canal (*short arrow* on **a** and **b**), the clivus, the parapharyngeal space including the carotid space, and the masticator space. FDG-negative fluid retention in the right-sided mastoid air cells (*gray arrow* on **a**, **f**) indicates obstruction of the Eustachian tube by the tumor and should not be confused with mastoiditis. Vascularization of the tumor is rather poor (**c**), indicating unfavorable response to treatment. The tumor shows restricted diffusion (**d**, **e**), compatible with high cellularity, and corresponding to poor differentiation, as revealed by subsequent histopathology. Several enlarged and FDG-avid lymph nodes were also seen on the right side (not shown)

Table 12.2 MR pulse sequence benefits in different clinical scenarios in comparison with PET imaging

	Clinical task					
Imaging component	Tumor detection	Surgery planning	Radiotherapy planning	Prognostication	Therapy response assessment	Detection of tumor recurrence
FDG-PET	++	++	++	+	++	++
DWI	+	−	+	++	+	+
DCE	−	−	−	++	+	+
Spectroscopy	−	−	−	+	(+)	(+)
BOLD	−	−	−	+	−	−
SPIO	+	+	−	−	−	−

− means no value; (+) means potential indication; + means limited use; ++ means clinically useful

12.5.1 Diffusion-Weighted Imaging (DWI)

Application of DWI in MR exams for head and neck cancer has been extensively studied and is used for several indications that can be roughly divided into two different scenarios: before and after treatment. The pretreatment scenario provides information on primary tumor location, on nodal status, for therapeutic planning, and for the prediction of treatment response. In the posttreatment scenario, DWI is used for the assessment of therapy response and discrimination of post-therapeutic changes and tumor recurrence.

A recent meta-analysis showed no added value of DWI in detecting the primary tumor but a potential role in nodal staging, allowing the differentiation of benign and metastatic cervical lymph nodes [92]. As to PET/MR, this information is already contained in the 18F-FDG-PET component yet with a higher level of purity [62]. Moving from macroscopic imaging tasks, such as staging, to microscopic imaging tasks, the situation is different. For the assessment of specific features of tumors and lymph nodes, such as their histopathological profile, it was shown that DWI provides information that is complementary to the PET-derived information, similarly as shown before in other parts of the body [31]. Some tumor characteristics, such as high stromal content and low cellularity, are associated with resistance to treatment and increased water diffusivity in head and neck cancers. Thus, in general, high mean ADC values are considered predictors of poor treatment response and outcome [93]. Studies investigating DWI parameters and clinical outcome have shown that high ADC values both in primary tumors and metastatic lymph nodes were able to predict tumor relapse, failure of regional control, and poor disease-free survival [94, 95]. On the other hand, poorly differentiated squamous cell carcinoma usually presents low ADC values and is at higher risk for metastatic disease, being another independent biomarker of poor treatment response [96]. This controversy confirms that prognostication by means of quantitative DWI parameters should be regarded with caution.

For therapeutic planning, DWI has been studied for dose painting in comparison to 18F-FDG-PET. It has been shown that both techniques contain different

information, which might influence the target volumes of radiotherapy [97]. Similarly, Rasmussen and colleagues have recently assessed the overlap of the radiation therapy volume of interest, as measured with DWI and ^{18}F-FDG-PET by multiparametric PET/MR in patients with head and neck cancer [32]. They showed that the target volume for radiotherapy overlapped substantially, although not completely, suggesting that glucose uptake and diffusion coefficient yield complementary information, which may be relevant for radiotherapy treatment planning [32].

DWI after treatment provides valuable information for therapy response assessment. A rising ADC value, which may be more reproducible than a single measurement, was described as an early biomarker of response to treatment and might play a role when gadolinium cannot be used [98–100]. Treatment-related changes in the head and neck region after surgery and radiotherapy limit the discriminability between viable tumor and therapy-induced inflammation. In this regard, DWI might tip the scales by showing significant lower ADC values in tumors compared to posttreatment changes, especially when using high b-values (higher than 1000 s/mm^2) [101, 102].

Some technical issues of DWI need to be addressed. The lack of standardization, such as the choice of b-values and the method to draw the ROI, and the high prevalence of artifacts (susceptibility and movement) might hamper the image acquisition and quality, limiting its reproducibility interindividually and intraindividually [93].

In summary, DWI plays a more complementary than redundant role in the assessment of head and neck cancer using ^{18}F-FDG-PET/MR, with potential clinical benefits in differentiating benign from malignant disease, particularly in the restaging after treatment (recurrence vs. inflammation). It may also play a role for therapy response assessment—provided the protocol is standardized and pertinent thresholds are being established and validated in future studies.

12.5.2 Perfusion-Weighted Imaging

Dynamic contrast-enhanced (DCE) sequences and dynamic susceptibility contrast (DSC) sequences are MR techniques targeting tissue perfusion. They are performed after the intravenous injection of contrast medium. Both techniques depict the vascular properties of a lesion, serving as an imaging biomarker of neoangiogenesis and hypoxia, which can be used to characterize a tissue as malignant and also to predict treatment failure. In head and neck oncology, lesions with high perfusion parameters generally tend to show better response to treatment, probably owing to more appropriate delivery of the therapeutic agents, but are more likely to develop hematogenic metastasis. Some parameters can be extracted from perfusion-weighted MRI, both quantitative parameters such as k^{trans} (derived through pharmacokinetic models) and semiquantitative parameters (analyzed by the time-signal intensity curve). Several parameters were studied in different clinical settings.

Two main applications of perfusion-weighted MRI in head and neck oncology are identified: pretreatment prognostic information and, more commonly, therapy response assessment. In general, high k^{trans} values both in primary tumors and in metastatic lymph nodes are related to favorable treatment response [103–105].

However, the lack of standardization of image acquisition and analysis renders perfusion-weighted MRI challenging, with oftentimes limited reproducible.

On the other hand, head and neck tumors with higher vascularization are candidates to assess treatment response with perfusion-weighted MRI. In these tumors, perfusion parameters might allow an accurate identification of patients with improved response to chemotherapy and radiotherapy and prolonged survival. This is a reflection of the association of high blood flow and increased oxygenation, resulting in better delivery of the antineoplastic agents and increased radiosensitivity [103]. Even more important, change in k^{trans} after therapy is much more consistent than the pretreatment measurement. Recent studies provide preliminary data on the parametric response map as an early predictor of treatment efficacy in head and neck cancer and also highlight the potential of posttreatment DCE-MRI in identifying residual masses [106–108]. Thus, perfusion parameters could help to individualize therapy, avoiding unnecessary treatment and improving patient survival.

In conclusion, similarly to DWI, perfusion-weighted MR imaging has a potential role in the multiparametric analysis of head and neck cancer. Its preferred applications are most likely the prediction of response to treatment by identifying primary tumors with high blood flow and the anticipation of resistance to chemotherapy and radiation therapy.

12.5.3 Other Functional MR Techniques (MR Spectroscopy, IVIM, and BOLD)

A selection of other functional MR pulse sequences may also aid in the assessment of head and neck cancer. Care should be taken on which MR sequence is essential for the PET/MR examination and which could benefit patient management without increasing the scanning time. Otherwise, the translation of PET/MR into clinical routine would be impaired, and PET/MR might only be reserved for special (and rare) occasions.

One of the first functional sequences studied was MR spectroscopy (MRS). Although challenging due to long acquisition time and complex post-processing and analysis, MRS might play a role in tumor prognostication and in monitoring treatment response [109]. High choline-to-creatine ratios in primary head and neck tumors were observed in patients with poor response to therapy [110]. In the post-treatment scenario, the presence of a choline peak in a residual mass may serve as a marker of residual cancer [111]. However, there are only a few and small studies addressing the role of MRS in head and neck cancer. Therefore, one should take into account the imaging time available and the expected findings before considering including MRS into a PET/MR protocol.

The intra-voxel incoherent motion (IVIM) represents an MR technique that allows the simultaneous evaluation of vascularization and diffusion restriction without the use of contrast medium [112]. Thus, the potential applications of DWI and MR perfusion might be covered with a single acquisition. IVIM can be used to

characterize head and neck primary tumors and metastatic lymph nodes [113]. It was also shown useful for monitoring therapy response, where high perfusion parameters were associated with worse clinical outcome, and an increase in IVIM parameters (e.g., diffusion coefficient D) was observed in responders [114, 115]. However, in our experience IVIM still suffers from considerable field inhomogeneities in PET/MR imaging and complex post-processing in general.

Blood-oxygen-level-dependent (BOLD) MR imaging is an indirect biomarker of tumor hypoxia, which might reflect resistance to chemotherapy and radiotherapy of head and neck cancer and consequently poor outcome. The principle of BOLD imaging in oncology is based on tumor oxygenation. It measures the decrease of signal intensity on T2*-weighted images owing to the paramagnetic effect of deoxy-hemoglobin [93]. Although promising, feasible, and potentially reproducible, research effort still is needed to prove its efficacy in a clinical environment.

Another potential utility of MR imaging is the use of superparamagnetic iron oxide (SPIO) as contrast agent. Although only preliminary data is available to date, SPIO MR was shown able to distinguish benign and malignant lymph nodes, which is oftentimes difficult with conventional cross-sectional imaging in lesions smaller than 1 cm [116]. Such might be useful if the information derived from ^{18}F-FDG-PET is equivocal.

In summary, the aforementioned functional MR sequences have yet not translated into clinical routine at most centers. They are time-consuming and their reproducibility is often limited. IVIM has been extensively studied for therapy response assessment and may be considered clinically in the future, provided more stable acquisition and faster post-processing are available. BOLD imaging might be used to predict response to treatment but still lacks consistent literature. MRS is technically challenging and might be considered mainly for research purposes. Thus, the implementation of such MR pulse sequences as part of a clinical PET/MR protocol remains questionable, given the compulsory presence of ^{18}F-FDG-PET. Another counterargument is the availability of different radiotracers that image similar biologic processes, such as ^{18}F-fluoroazomycin arabinoside (FAZA) or ^{18}F-fluoromisonidazole (FMISO) for hypoxia estimation [117–119].

12.6 Summary

The use of PET/MR gains ground on PET/CT for the assessment of head and neck tumor patients. Once certain technical challenges are solved, such as a further improvement of lung imaging and more robust attenuation correction methods, e.g., by using zero echo time MR pulse sequences, a stable and reliable clinical hybrid imaging modality is at hand. This happens parallel to the clinical implementation of new PET radiotracers, the validation of existing clinical PET radiotracers for new indications (e.g., parathyroid imaging with ^{18}F-fluorocholine), and an increase in the availability of functional MR techniques. Altogether, there is prospect of a more sophisticated and complementary characterization of complex biological processes. The combined assessment of different tumor features, such

as glucose metabolism, cellularity, and vascularization, opens up possibilities for a more detailed characterization of the primary tumor and for the prognostication of therapy response and clinical outcome. Therefore, PET/MR represents the optimal non-invasive diagnostic tool for a personalized therapeutic approach in head and neck cancer patients.

References

1. Sekine T, de Galiza Barbosa F, Kuhn FP, Burger IA, Stolzmann P, Huber GF, et al. PET+MR versus PET/CT in the initial staging of head and neck cancer, using a trimodality PET/CT+MR system. Clin Imaging. 2017;42:232–9.
2. Huellner MW, Appenzeller P, Kuhn FP, Husmann L, Pietsch CM, Burger IA, et al. Whole-body nonenhanced PET/MR versus PET/CT in the staging and restaging of cancers: preliminary observations. Radiology. 2014;273(3):859–69.
3. Schaarschmidt BM, Heusch P, Buchbender C, Ruhlmann M, Bergmann C, Ruhlmann V, et al. Locoregional tumour evaluation of squamous cell carcinoma in the head and neck area: a comparison between MRI, PET/CT and integrated PET/MRI. Eur J Nucl Med Mol Imaging. 2016;43(1):92–102.
4. Partovi S, Kohan A, Vercher-Conejero JL, Rubbert C, Margevicius S, Schluchter MD, et al. Qualitative and quantitative performance of (1)(8)F-FDG-PET/MRI versus (1)(8)F-FDG-PET/CT in patients with head and neck cancer. AJNR Am J Neuroradiol. 2014;35(10):1970–5.
5. Kuhn FP, Hullner M, Mader CE, Kastrinidis N, Huber GF, von Schulthess GK, et al. Contrast-enhanced PET/MR imaging versus contrast-enhanced PET/CT in head and neck cancer: how much MR information is needed? Journal of nuclear medicine : official publication. Soc Nucl Med. 2014;55(4):551–8.
6. Kubiessa K, Purz S, Gawlitza M, Kuhn A, Fuchs J, Steinhoff KG, et al. Initial clinical results of simultaneous 18F-FDG PET/MRI in comparison to 18F-FDG PET/CT in patients with head and neck cancer. Eur J Nucl Med Mol Imaging. 2014;41(4):639–48.
7. Platzek I, Beuthien-Baumann B, Schneider M, Gudziol V, Langner J, Schramm G, et al. PET/MRI in head and neck cancer: initial experience. Eur J Nucl Med Mol Imaging. 2013;40(1):6–11.
8. Varoquaux A, Rager O, Poncet A, Delattre BM, Ratib O, Becker CD, et al. Detection and quantification of focal uptake in head and neck tumours: (18)F-FDG PET/MR versus PET/CT. Eur J Nucl Med Mol Imaging. 2014;41(3):462–75.
9. Adams S, Baum RP, Stuckensen T, Bitter K, Hor G. Prospective comparison of 18F-FDG PET with conventional imaging modalities (CT, MRI, US) in lymph node staging of head and neck cancer. Eur J Nucl Med. 1998;25(9):1255–60.
10. Stolzmann P, Veit-Haibach P, Chuck N, Rossi C, Frauenfelder T, Alkadhi H, et al. Detection rate, location, and size of pulmonary nodules in trimodality PET/CT-MR: comparison of low-dose CT and Dixon-based MR imaging. Investig Radiol. 2013;48(5):241–6.
11. Togao O, Tsuji R, Ohno Y, Dimitrov I, Takahashi M. Ultrashort echo time (UTE) MRI of the lung: assessment of tissue density in the lung parenchyma. Magn Reson Med. 2010;64(5):1491–8.
12. Tibiletti M, Paul J, Bianchi A, Wundrak S, Rottbauer W, Stiller D, et al. Multistage three-dimensional UTE lung imaging by image-based self-gating. Magn Reson Med. 2016;75(3):1324–32.
13. Ohno Y, Koyama H, Yoshikawa T, Seki S, Takenaka D, Yui M, et al. Pulmonary high-resolution ultrashort TE MR imaging: comparison with thin-section standard- and low-dose computed tomography for the assessment of pulmonary parenchyma diseases. J Magn Reson Imaging. 2016;43(2):512–32.

14. Ter Voert EE, Veit-Haibach P, Ahn S, Wiesinger F, Khalighi MM, Levin CS, et al. Clinical evaluation of TOF versus non-TOF on PET artifacts in simultaneous PET/MR: a dual centre experience. Eur J Nucl Med Mol Imaging. 2017;44(7):1223–33.

15. de Galiza Barbosa F, Delso G, Zeimpekis KG, Ter Voert E, Hullner M, Stolzmann P, et al. Evaluation and clinical quantification of neoplastic lesions and physiological structures in TOF-PET/MRI and non-TOF/MRI - a pilot study. Q J Nucl Med Mol Imaging. 2015. https://www.ncbi.nlm.nih.gov/pubmed/25964058. Epub ahead of print.

16. Wollenweber SD, Delso G, Deller T, Goldhaber D, Hullner M, Veit-Haibach P. Characterization of the impact to PET quantification and image quality of an anterior array surface coil for PET/MR imaging. MAGMA. 2014;27(2):149–59.

17. Svirydenka H, Delso G, Barbosa FG, Huellner MW, Davison H, Fanti S, et al. The effect of susceptibility artifacts related to metal implants on adjacent lesion assessment in simultaneous TOF PET/MR. J Nucl Med. 2017;58(7):1167–73.

18. Zeimpekis KG, Barbosa F, Hullner M, ter Voert E, Davison H, Veit-Haibach P, et al. Clinical evaluation of PET image quality as a function of acquisition time in a new TOF-PET/MRI compared to TOF-PET/CT--initial results. Mol Imaging Biol. 2015;17(5):735–44.

19. Davison H, ter Voert EE, de Galiza Barbosa F, Veit-Haibach P, Delso G. Incorporation of time-of-flight information reduces metal artifacts in simultaneous positron emission tomography/magnetic resonance imaging: a simulation study. Investig Radiol. 2015;50(7):423–9.

20. Sekine T, Ter Voert EE, Warnock G, Buck A, Huellner M, Veit-Haibach P, et al. Clinical evaluation of zero-Echo-time attenuation correction for brain 18F-FDG PET/MRI: comparison with atlas attenuation correction. J Nucl Med. 2016;57(12):1927–32.

21. Delso G, Wiesinger F, Sacolick LI, Kaushik SS, Shanbhag DD, Hullner M, et al. Clinical evaluation of zero-echo-time MR imaging for the segmentation of the skull. J Nucl Med. 2015;56(3):417–22.

22. Wiesinger F, Sacolick LI, Menini A, Kaushik SS, Ahn S, Veit-Haibach P, et al. Zero TE MR bone imaging in the head. Magn Reson Med. 2016;75(1):107–14.

23. von Schulthess GK, Veit-Haibach P. Workflow considerations in PET/MR imaging. J Nucl Med. 2014;55(Supplement 2):19S–24S.

24. Queiroz MA, Huellner MW. PET/MR in cancers of the head and neck. Semin Nucl Med. 2015;45(3):248–65.

25. Vargas MI, Becker M, Garibotto V, Heinzer S, Loubeyre P, Gariani J, et al. Approaches for the optimization of MR protocols in clinical hybrid PET/MRI studies. MAGMA. 2013;26(1):57–69.

26. Dedivitis RA, Denardin OV, Castro MA, Pfuetzenreiter EG Jr. Risk factors for distant metastasis in head and neck cancer. Rev Col Bras Cir. 2009;36(6):478–81.

27. Pipe JG. Motion correction with PROPELLER MRI: application to head motion and free-breathing cardiac imaging. Magn Reson Med. 1999;42(5):963–9.

28. Huellner MW, de Galiza Barbosa F, Husmann L, Pietsch CM, Mader CE, Burger IA, et al. TNM staging of non-small cell lung cancer: comparison of PET/MR and PET/CT. J Nucl Med. 2016;57(1):21–6.

29. Burris NS, Johnson KM, Larson PE, Hope MD, Nagle SK, Behr SC, et al. Detection of small pulmonary nodules with ultrashort echo time sequences in oncology patients by using a PET/MR system. Radiology. 2016;278(1):239–46.

30. Furst S, Grimm R, Hong I, Souvatzoglou M, Casey ME, Schwaiger M, et al. Motion correction strategies for integrated PET/MR. J Nucl Med. 2015;56(2):261–9.

31. Surov A, Stumpp P, Meyer HJ, Gawlitza M, Hohn AK, Boehm A, et al. Simultaneous (18) F-FDG-PET/MRI: associations between diffusion, glucose metabolism and histopathological parameters in patients with head and neck squamous cell carcinoma. Oral Oncol. 2016;58:14–20.

32. Rasmussen JH, Norgaard M, Hansen AE, Vogelius IR, Aznar MC, Johannesen HH, et al. Feasibility of multiparametric imaging with PET/MR in head and neck squamous cell carcinoma. J Nucl Med. 2017;58(1):69–74.

33. Choi SH, Paeng JC, Sohn CH, Pagsisihan JR, Kim YJ, Kim KG, et al. Correlation of 18F-FDG uptake with apparent diffusion coefficient ratio measured on standard and high b value diffusion MRI in head and neck cancer. J Nucl Med. 2011;52(7):1056–62.

34. Gawlitza M, Purz S, Kubiessa K, Boehm A, Barthel H, Kluge R, et al. In vivo correlation of glucose metabolism, cell density and microcirculatory parameters in patients with head and neck cancer: initial results using simultaneous PET/MRI. PLoS One. 2015;10(8): e0134749.

35. Varoquaux A, Rager O, Lovblad KO, Masterson K, Dulguerov P, Ratib O, et al. Functional imaging of head and neck squamous cell carcinoma with diffusion-weighted MRI and FDG PET/CT: quantitative analysis of ADC and SUV. Eur J Nucl Med Mol Imaging. 2013;40(6):842–52.

36. Covello M, Cavaliere C, Aiello M, Cianelli MS, Mesolella M, Iorio B, et al. Simultaneous PET/MR head-neck cancer imaging: preliminary clinical experience and multiparametric evaluation. Eur J Radiol. 2015;84(7):1269–76.

37. Huellner MW, Kuhn FP, Curtin HD. Head and neck cancer. In: von Schulthess GK, editor. Molecular anatomic imaging - PET/CT, PET/MR and SPECT/CT. 3rd ed. Philadelphia: Wolters Kluwer; 2016. p. 341–61.

38. Curtin HD. Detection of perineural spread: fat suppression versus no fat suppression. AJNR Am J Neuroradiol. 2004;25(1):1–3.

39. Platzek I. (18)F-Fluorodeoxyglucose PET/MR imaging in head and neck cancer. PET Clin. 2016;11(4):375–86.

40. Rasmussen JH, Fischer BM, Aznar MC, Hansen AE, Vogelius IR, Lofgren J, et al. Reproducibility of (18)F-FDG PET uptake measurements in head and neck squamous cell carcinoma on both PET/CT and PET/MR. Br J Radiol. 2015;88(1048):20140655.

41. Gunzinger JM, Delso G, Boss A, Porto M, Davison H, von Schulthess GK, et al. Metal artifact reduction in patients with dental implants using multispectral three-dimensional data acquisition for hybrid PET/MRI. EJNMMI Phys. 2014;1(1):102.

42. Buchbender C, Hartung-Knemeyer V, Forsting M, Antoch G, Heusner TA. Positron emission tomography (PET) attenuation correction artefacts in PET/CT and PET/MRI. Br J Radiol. 2013;86(1025):20120570.

43. Ladefoged CN, Hansen AE, Keller SH, Fischer BM, Rasmussen JH, Law I, et al. Dental artifacts in the head and neck region: implications for Dixon-based attenuation correction in PET/MR. EJNMMI Phys. 2015;2(1):8.

44. Chang CY, Yang BH, Lin KH, Liu RS, Wang SJ, Shih WJ. Feasibility and incremental benefit of puffed-cheek 18F-FDG PET/CT on oral cancer patients. Clin Nucl Med. 2013;38(10):e374–8.

45. Rusthoven KE, Koshy M, Paulino AC. The role of fluorodeoxyglucose positron emission tomography in cervical lymph node metastases from an unknown primary tumor. Cancer. 2004;101(11):2641–9.

46. Sekine T, Barbosa FG, Sah BR, Mader CE, Delso G, Burger IA, et al. PET/MR outperforms PET/CT in suspected occult tumors. Clin Nucl Med. 2017;42(2):e88–95.

47. Varoquaux A, Rager O, Dulguerov P, Burkhardt K, Ailianou A, Becker M. Diffusion-weighted and PET/MR imaging after radiation therapy for malignant head and neck tumors. Radiographics. 2015;35(5):1502–27.

48. Becker M, Zaidi H. Imaging in head and neck squamous cell carcinoma: the potential role of PET/MRI. Br J Radiol. 2014;87(1036):20130677.

49. Huellner MW, Sekine T. Hybrid imaging: local staging of head and neck cancer. In: Hodler J, Kubik-Huch RA, von Schulthess GK, editors. Diseases of the brain, head and neck, spine 2016-2019: diagnostic imaging, vol. 1. Heidelberg: Springer; 2016. p. 261–79.

50. Popperl G, Lang S, Dagdelen O, Jager L, Tiling R, Hahn K, et al. Correlation of FDG-PET and MRI/CT with histopathology in primary diagnosis, lymph node staging and diagnosis of recurrency of head and neck cancer. RoFo. 2002;174(6):714–20.

51. Cavaliere C, Romeo V, Aiello M, Mesolella M, Iorio B, Barbuto L, et al. Multiparametric evaluation by simultaneous PET-MRI examination in patients with histologically proven laryngeal cancer. Eur J Radiol. 2017;88:47–55.

52. Yousem DM, Gad K, Tufano RP. Resectability issues with head and neck cancer. AJNR Am J Neuroradiol. 2006;27(10):2024–36.

53. Sekine T, Barbosa F, Delso G, Burger IA, Stolzmann P, Ter Voert E, et al. Local resectability assessment of head and neck cancer: positron emission tomography/MRI versus positron emission tomography/CT. Head Neck. 2017;39(8):1550–8.

54. Chang PC, Fischbein NJ, McCalmont TH, Kashani-Sabet M, Zettersten EM, Liu AY, et al. Perineural spread of malignant melanoma of the head and neck: clinical and imaging features. AJNR Am J Neuroradiol. 2004;25(1):5–11.

55. Schaarschmidt BM, Gomez B, Buchbender C, Grueneisen J, Nensa F, Sawicki LM, et al. Is integrated 18F-FDG PET/MRI superior to 18F-FDG PET/CT in the differentiation of incidental tracer uptake in the head and neck area? Diagn Interv Radiol. 2017;23(2):127–32.

56. Wang K, Mullins BT, Falchook AD, Lian J, He K, Shen D, et al. Evaluation of PET/MRI for tumor volume delineation for head and neck cancer. Front Oncol. 2017;7:8.

57. Queiroz MA, Hullner M, Kuhn F, Huber G, Meerwein C, Kollias S, et al. PET/MRI and PET/CT in follow-up of head and neck cancer patients. Eur J Nucl Med Mol Imaging. 2014;41(6):1066–75.

58. Meerwein CM, Queiroz M, Kollias S, Hullner M, Veit-Haibach P, Huber GF. Post-treatment surveillance of head and neck cancer: pitfalls in the interpretation of FDG PET-CT/MRI. Swiss Med Wkly. 2015;145:w14116.

59. Nakamoto Y, Tamai K, Saga T, Higashi T, Hara T, Suga T, et al. Clinical value of image fusion from MR and PET in patients with head and neck cancer. Mol Imaging Biol. 2009;11(1):46–53.

60. Matthews R, Shrestha P, Franceschi D, Relan N, Kaloudis E. Head and neck cancers: post-therapy changes in muscles with FDG PET-CT. Clin Nucl Med. 2010;35(7):494–8.

61. Muller J, Hullner M, Strobel K, Huber GF, Burger IA, Haerle SK. The value of (18)F-FDG-PET/CT imaging in oral cavity cancer patients following surgical reconstruction. Laryngoscope. 2015;125(8):1861–8.

62. Queiroz MA, Hullner M, Kuhn F, Huber G, Meerwein C, Kollias S, et al. Use of diffusion-weighted imaging (DWI) in PET/MRI for head and neck cancer evaluation. Eur J Nucl Med Mol Imaging. 2014;41(12):2212–21.

63. O'Brien CJ, Smith JW, Soong SJ, Urist MM, Maddox WA. Neck dissection with and without radiotherapy: prognostic factors, patterns of recurrence, and survival. Am J Surg. 1986;152(4):456–63.

64. Leemans CR, Tiwari R, Nauta JJ, van der Waal I, Snow GB. Regional lymph node involvement and its significance in the development of distant metastases in head and neck carcinoma. Cancer. 1993;71(2):452–6.

65. Leemans CR, Tiwari R, Nauta JJ, van der Waal I, Snow GB. Recurrence at the primary site in head and neck cancer and the significance of neck lymph node metastases as a prognostic factor. Cancer. 1994;73(1):187–90.

66. Snyderman NL, Johnson JT, Schramm VL Jr, Myers EN, Bedetti CD, Thearle P. Extracapsular spread of carcinoma in cervical lymph nodes. Impact upon survival in patients with carcinoma of the supraglottic larynx. Cancer. 1985;56(7):1597–9.

67. Johnson JT, Myers EN, Bedetti CD, Barnes EL, Schramm VL Jr, Thearle PB. Cervical lymph node metastases. Incidence and implications of extracapsular carcinoma. Arch Otolaryngol. 1985;111(8):534–7.

68. Heusch P, Sproll C, Buchbender C, Rieser E, Terjung J, Antke C, et al. Diagnostic accuracy of ultrasound, (1)(8)F-FDG-PET/CT, and fused (1)(8)F-FDG-PET-MR images with DWI for the detection of cervical lymph node metastases of HNSCC. Clin Oral Investig. 2014;18(3):969–78.

69. Platzek I, Beuthien-Baumann B, Schneider M, Gudziol V, Kitzler HH, Maus J, et al. FDG PET/MR for lymph node staging in head and neck cancer. Eur J Radiol. 2014;83(7):1163–8.

70. Bruschini P, Giorgetti A, Bruschini L, Nacci A, Volterrani D, Cosottini M, et al. Positron emission tomography (PET) in the staging of head neck cancer: comparison between PET and CT. Acta Otorhinolaryngol Ital. 2003;23(6):446–53.

71. Stuckensen T, Kovacs AF, Adams S, Baum RP. Staging of the neck in patients with oral cavity squamous cell carcinomas: a prospective comparison of PET, ultrasound, CT and MRI. J Craniomaxillofac Surg. 2000;28(6):319–24.

72. Yoon DY, Hwang HS, Chang SK, Rho YS, Ahn HY, Kim JH, et al. CT, MR, US,18F-FDG PET/CT, and their combined use for the assessment of cervical lymph node metastases in squamous cell carcinoma of the head and neck. Eur Radiol. 2009;19(3):634–42.

73. Corey AS, Hudgins PA. Radiographic imaging of human papillomavirus related carcinomas of the oropharynx. Head Neck Pathol. 2012;6(Suppl 1):S25–40.

74. Kendi AT, Magliocca K, Corey A, Nickleach DC, Galt J, Higgins K, et al. Do 18F-FDG PET/CT parameters in oropharyngeal and oral cavity squamous cell carcinomas indicate HPV status? Clin Nucl Med. 2015;40(3):e196–200.

75. Kim SG, Friedman K, Patel S, Hagiwara M. Potential role of PET/MRI for imaging metastatic lymph nodes in head and neck cancer. AJR Am J Roentgenol. 2016;207(2): 248–56.

76. Raad RA, Friedman KP, Heacock L, Ponzo F, Melsaether A, Chandarana H. Outcome of small lung nodules missed on hybrid PET/MRI in patients with primary malignancy. J Magn Reson Imaging. 2016;43(2):504–11.

77. Chang ST, Nguyen DC, Raptis C, Menias CO, Zhou G, Wang-Gillam A, et al. Natural history of preoperative subcentimeter pulmonary nodules in patients with resectable pancreatic adenocarcinoma: a retrospective cohort study. Ann Surg. 2015;261(5):970–5.

78. Samarin A, Hullner M, Queiroz MA, Stolzmann P, Burger IA, von Schulthess G, et al. 18F-FDG-PET/MR increases diagnostic confidence in detection of bone metastases compared with 18F-FDG-PET/CT. Nucl Med Commun. 2015;36(12):1165–73.

79. Samarin A, Burger C, Wollenweber SD, Crook DW, Burger IA, Schmid DT, et al. PET/MR imaging of bone lesions--implications for PET quantification from imperfect attenuation correction. Eur J Nucl Med Mol Imaging. 2012;39(7):1154–60.

80. Walter C, Ziebart T, Sagheb K, Rahimi-Nedjat RK, Manz A, Hess G. Malignant lymphomas in the head and neck region--a retrospective, single-center study over 41 years. Int J Med Sci. 2015;12(2):141–5.

81. Heacock L, Weissbrot J, Raad R, Campbell N, Friedman KP, Ponzo F, et al. PET/MRI for the evaluation of patients with lymphoma: initial observations. AJR Am J Roentgenol. 2015;204(4):842–8.

82. Herrmann K, Queiroz M, Huellner MW, de Galiza Barbosa F, Buck A, Schaefer N, et al. Diagnostic performance of FDG-PET/MRI and WB-DW-MRI in the evaluation of lymphoma: a prospective comparison to standard FDG-PET/CT. BMC Cancer. 2015; 15:1002.

83. Nagarajah J, Jentzen W, Hartung V, Rosenbaum-Krumme S, Mikat C, Heusner TA, et al. Diagnosis and dosimetry in differentiated thyroid carcinoma using 124I PET: comparison of PET/MRI vs PET/CT of the neck. Eur J Nucl Med Mol Imaging. 2011;38(10):1862–8.

84. Binse I, Rosenbaum-Krumme SJ, Bockisch A. Imaging of differentiated thyroid carcinoma: 124I-PET/MRI may not be superior to 124I-PET/CT. Eur J Nucl Med Mol Imaging. 2016;43(6):1185–6.

85. Vrachimis A, Weckesser M, Schafers M, Stegger L. Imaging of differentiated thyroid carcinoma: (124)I-PET/MRI may not be superior to (124)I-PET/CT. Eur J Nucl Med Mol Imaging. 2016;43(6):1183–4.

86. Vrachimis A, Burg MC, Wenning C, Allkemper T, Weckesser M, Schafers M, et al. [(18)F] FDG PET/CT outperforms [(18)F]FDG PET/MRI in differentiated thyroid cancer. Eur J Nucl Med Mol Imaging. 2016;43(2):212–20.

87. Dercle L, Deandreis D, Terroir M, Leboulleux S, Lumbroso J, Schlumberger M. Evaluation of (124)I PET/CT and (124)I PET/MRI in the management of patients with differentiated thyroid cancer. Eur J Nucl Med Mol Imaging. 2016;43(6):1006–10.

88. Huellner MW, Aberle S, Sah BR, Veit-Haibach P, Bonani M, Schmid C, et al. Visualization of parathyroid hyperplasia using 18F-fluorocholine PET/MR in a patient with secondary hyperparathyroidism. Clin Nucl Med. 2016;41(3):e159–61.

89. Kluijfhout WP, Pasternak JD, Gosnell JE, Shen WT, Duh QY, Vriens MR, et al. 18F Fluorocholine PET/MR imaging in patients with primary hyperparathyroidism and inconclusive conventional imaging: a prospective pilot study. Radiology. 2017;284(2):460–7.

90. van Essen M, Krenning EP, Kooij PP, Bakker WH, Feelders RA, de Herder WW, et al. Effects of therapy with [177Lu-DOTA0, Tyr3]octreotate in patients with paraganglioma, meningioma, small cell lung carcinoma, and melanoma. Journal of nuclear medicine : official publication. Soc Nucl Med. 2006;47(10):1599–606.

91. Lutje S, Sauerwein W, Lauenstein T, Bockisch A, Poeppel TD. In vivo visualization of prostate-specific membrane antigen in adenoid cystic carcinoma of the salivary gland. Clin Nucl Med. 2016;41(6):476–7.

92. Driessen JP, van Kempen PM, van der Heijden GJ, Philippens ME, Pameijer FA, Stegeman I, et al. Diffusion-weighted imaging in head and neck squamous cell carcinomas: a systematic review. Head Neck. 2015;37(3):440–8.

93. King AD, Thoeny HC. Functional MRI for the prediction of treatment response in head and neck squamous cell carcinoma: potential and limitations. Cancer Imaging. 2016;16(1):23.

94. Lambrecht M, Van Calster B, Vandecaveye V, De Keyzer F, Roebben I, Hermans R, et al. Integrating pretreatment diffusion weighted MRI into a multivariable prognostic model for head and neck squamous cell carcinoma. Radiother Oncol. 2014;110(3):429–34.

95. Ng SH, Lin CY, Chan SC, Lin YC, Yen TC, Liao CT, et al. Clinical utility of multimodality imaging with dynamic contrast-enhanced MRI, diffusion-weighted MRI, and 18F-FDG PET/CT for the prediction of neck control in oropharyngeal or hypopharyngeal squamous cell carcinoma treated with chemoradiation. PLoS One. 2014;9(12):e115933.

96. Yun TJ, Kim JH, Kim KH, Sohn CH, Park SW. Head and neck squamous cell carcinoma: differentiation of histologic grade with standard- and high-b-value diffusion-weighted MRI. Head Neck. 2013;35(5):626–31.

97. Houweling AC, Wolf AL, Vogel WV, Hamming-Vrieze O, van Vliet-Vroegindeweij C, van de Kamer JB, et al. FDG-PET and diffusion-weighted MRI in head-and-neck cancer patients: implications for dose painting. Radiother Oncol. 2013;106(2):250–4.

98. King AD, Chow KK, Yu KH, Mo FK, Yeung DK, Yuan J, et al. Head and neck squamous cell carcinoma: diagnostic performance of diffusion-weighted MR imaging for the prediction of treatment response. Radiology. 2013;266(2):531–8.

99. Matoba M, Tuji H, Shimode Y, Toyoda I, Kuginuki Y, Miwa K, et al. Fractional change in apparent diffusion coefficient as an imaging biomarker for predicting treatment response in head and neck cancer treated with chemoradiotherapy. AJNR Am J Neuroradiol. 2014;35(2):379–85.

100. Vandecaveye V, Dirix P, De Keyzer F, de Beeck KO, Vander Poorten V, Roebben I, et al. Predictive value of diffusion-weighted magnetic resonance imaging during chemoradiotherapy for head and neck squamous cell carcinoma. Eur Radiol. 2010;20(7):1703–14.

101. Acampora A, Manzo G, Fenza G, Busto G, Serino A, Manto A. High b-value diffusion MRI to differentiate recurrent tumors from Posttreatment changes in head and neck squamous cell carcinoma: a single center prospective study. Biomed Res Int. 2016;2016:2865169.

102. Hwang I, Choi SH, Kim YJ, Kim KG, Lee AL, Yun TJ, et al. Differentiation of recurrent tumor and posttreatment changes in head and neck squamous cell carcinoma: application of high b-value diffusion-weighted imaging. AJNR Am J Neuroradiol. 2013;34(12):2343–8.

103. Chawla S, Kim S, Dougherty L, Wang S, Loevner LA, Quon H, et al. Pretreatment diffusion-weighted and dynamic contrast-enhanced MRI for prediction of local treatment response in squamous cell carcinomas of the head and neck. AJR Am J Roentgenol. 2013;200(1):35–43.

104. Kim S, Loevner LA, Quon H, Kilger A, Sherman E, Weinstein G, et al. Prediction of response to chemoradiation therapy in squamous cell carcinomas of the head and neck using dynamic contrast-enhanced MR imaging. AJNR Am J Neuroradiol. 2010;31(2):262–8.

105. Shukla-Dave A, Lee NY, Jansen JF, Thaler HT, Stambuk HE, Fury MG, et al. Dynamic contrast-enhanced magnetic resonance imaging as a predictor of outcome in head-and-neck squamous cell carcinoma patients with nodal metastases. Int J Radiat Oncol Biol Phys. 2012;82(5):1837–44.

106. Abdel Razek AA, Gaballa G, Ashamalla G, Alashry MS, Nada N. Dynamic susceptibility contrast perfusion-weighted magnetic resonance imaging and diffusion-weighted magnetic resonance imaging in differentiating recurrent head and neck cancer from postradiation changes. J Comput Assist Tomogr. 2015;39(6):849–54.

107. Baer AH, Hoff BA, Srinivasan A, Galban CJ, Mukherji SK. Feasibility analysis of the parametric response map as an early predictor of treatment efficacy in head and neck cancer. AJNR Am J Neuroradiol. 2015;36(4):757–62.

108. King AD, Chow SK, Yu KH, Mo FK, Yeung DK, Yuan J, et al. DCE-MRI for pre-treatment prediction and post-treatment assessment of treatment response in sites of squamous cell carcinoma in the head and neck. PLoS One. 2015;10(12):e0144770.

109. Abdel Razek AA, Poptani H. MR spectroscopy of head and neck cancer. Eur J Radiol. 2013;82(6):982–9.

110. Bezabeh T, Odlum O, Nason R, Kerr P, Sutherland D, Patel R, et al. Prediction of treatment response in head and neck cancer by magnetic resonance spectroscopy. AJNR Am J Neuroradiol. 2005;26(8):2108–13.

111. King AD, Yeung DK, Yu KH, Mo FK, Hu CW, Bhatia KS, et al. Monitoring of treatment response after chemoradiotherapy for head and neck cancer using in vivo 1H MR spectroscopy. Eur Radiol. 2010;20(1):165–72.

112. Hauser T, Essig M, Jensen A, Laun FB, Munter M, Maier-Hein KH, et al. Prediction of treatment response in head and neck carcinomas using IVIM-DWI: evaluation of lymph node metastasis. Eur J Radiol. 2014;83(5):783–7.

113. Lu Y, Jansen JF, Stambuk HE, Gupta G, Lee N, Gonen M, et al. Comparing primary tumors and metastatic nodes in head and neck cancer using intravoxel incoherent motion imaging: a preliminary experience. J Comput Assist Tomogr. 2013;37(3):346–52.

114. Hauser T, Essig M, Jensen A, Gerigk L, Laun FB, Munter M, et al. Characterization and therapy monitoring of head and neck carcinomas using diffusion-imaging-based intravoxel incoherent motion parameters-preliminary results. Neuroradiology. 2013;55(5):527–36.

115. Paudyal R, Oh JH, Riaz N, Venigalla P, Li J, Hatzoglou V, et al. Intravoxel incoherent motion diffusion-weighted MRI during chemoradiation therapy to characterize and monitor treatment response in human papillomavirus head and neck squamous cell carcinoma. J Magn Reson Imaging. 2017;45(4):1013–23.

116. Mack MG, Balzer JO, Straub R, Eichler K, Vogl TJ. Superparamagnetic iron oxide-enhanced MR imaging of head and neck lymph nodes. Radiology. 2002;222(1):239–44.

117. Mortensen LS, Johansen J, Kallehauge J, Primdahl H, Busk M, Lassen P, et al. FAZA PET/CT hypoxia imaging in patients with squamous cell carcinoma of the head and neck treated with radiotherapy: results from the DAHANCA 24 trial. Radiother Oncol. 2012;105(1):14–20.

118. Servagi-Vernat S, Differding S, Hanin FX, Labar D, Bol A, Lee JA, et al. A prospective clinical study of (1)(8)F-FAZA PET-CT hypoxia imaging in head and neck squamous cell carcinoma before and during radiation therapy. Eur J Nucl Med Mol Imaging. 2014;41(8):1544–52.

119. Hendrickson K, Phillips M, Smith W, Peterson L, Krohn K, Rajendran J. Hypoxia imaging with [F-18] FMISO-PET in head and neck cancer: potential for guiding intensity modulated radiation therapy in overcoming hypoxia-induced treatment resistance. Radiother Oncol. 2011;101(3):369–75.

Lung Nodule Detection Using PET/MRI

13

Paul Flechsig, Esha Baidya Kayal, Amit Mehndiratta, and Frederik L. Giesel

Contents

Technical way of lung nodule examination is strongly dependent on the size of the suspected lesion. In patients without risk factors for malignancy, lung nodules of ≤6 mm are regarded as unspecific [1]. CT examinations are usually performed in pulmonary nodules ≤5 mm surrounded by lung parenchyma, since PET and MRI examinations are more reasonable in lesions of ≥7 mm [2]. CT findings describing benign lesions are calcifications within the lesion, density values ≤10 HU, and the absence of changes in size over 2 years. As stated by the Fleischner Society, the need for further investigations of lung nodules is dependent on nodule diameter and on patients' risk factors [1]. The presence of risk factors might result in additional contrast-enhanced CT examinations, PET examinations, or biopsies. Concerning PET/CT, recent publications stated values

P. Flechsig
Department of Nuclear Medicine, University Hospital Heidelberg, Heidelberg, Germany
e-mail: paul.flechsig@med.uni-heidelberg.de

E.B. Kayal
Centre for Biomedical Engineering, Indian Institute of Technology Delhi, New Delhi, India

A. Mehndiratta
Centre for Biomedical Engineering, Indian Institute of Technology Delhi, New Delhi, India

Department of Biomedical Engineering, All India Institute of Medical Sciences, New Delhi, India

F.L. Giesel (✉)
Department of Nuclear Medicine, University Hospital Heidelberg, Heidelberg, Germany

Clinical Cooperation Unit, Department of Nuclear medicine, DKFZ, Heidelberg, Germany
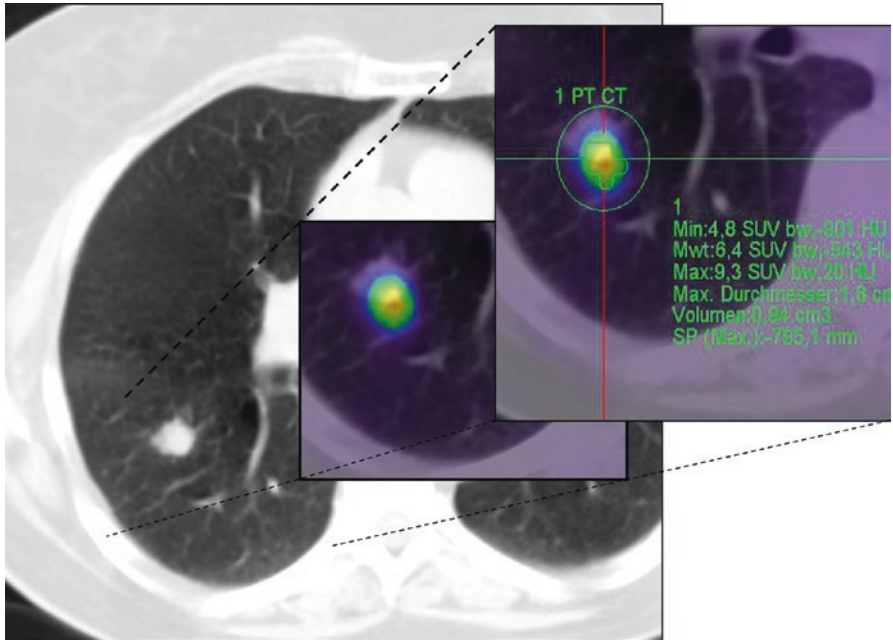e-mail: f.giesel@dkfz-heidelberg.de
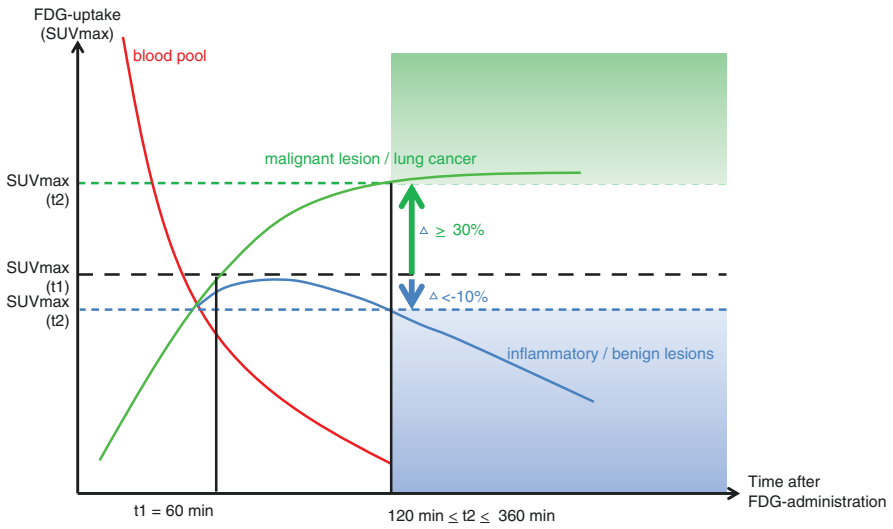
Fig. 13.1 Pulmonary nodule

Fig. 13.2 Two-time-point measurement

for sensitivity and specificity between 90 and 95% for PET imaging in lung nodules ≥7 mm (Fig. 13.1) [3–6]. Superiority of FDG PET/CT over conventional CT for the classification of pulmonary nodules of all sizes was reported in huge meta-analyses with 1474 and 344 patients [7, 8]. According to the above blank space mentioned meta-analyses, the use of FDG PET/CT resulted in fewer unclear imaging findings. Limitations due to motion blur in small lung nodules might be overcome by new generations of PET/CT scanners that offer the possibility of respiratory triggering, which might enable for PET examinations of lung nodules with a diameter ≥3 mm [9]. In cases of FDG-equivocal findings, dual-time-point FDG PET with an additional PET scan 2–3 h after the administration of the radiopharmaceutical are reported to be beneficial (Fig. 13.2) [10]. Due to tumor biology, an increased glucose metabolism over time is found in malignant tissue compared to surrounding normal tissue, measurable during the first 8 h after FDG administration. With respect to the first scan 1 h after administration, an increase in SUVmax of >30% in the delayed scan can be seen as an indicator for malignancy, while a decrease of SUVmax of >10% indicates benignancy, both with a sensitivity of 95–99%. Despite the abovementioned advantages of PET/CT, there is a diagnostic gap in slow-growing lepidic adenocarcinomas and neuroendocrine tumours with missing increase of SUVmax, which might potentially lead to false negative results in FDG PET/CT. Especially in neuroendocrine tumors of high differentiation, which usually present with an increased number of somatostatin receptors on their surface, an additional somatostatin receptor scintigraphy using the somatostatin analogue Tc-99m depreotide or DOTATOC-PET/CT with a higher spatial resolution [11] can help to complete TNM staging. Sensitivity and specificity levels among 85–90% have recently been reported for Tc-99m depreotide scintigraphy, wherefore positive findings were proposed as an independent criterion for malignancy. Due to the fact that depreotide SPECT and DOTATOC-PET/CT are false negative in most cases of undifferentiated tumors, both methods should be used complementarily in order to display the true differentiation of an unclear lung lesion [5, 12, 13].

The use of MRI and PET/MRI examinations is part of ongoing research. As reported recently, nodules ≥3–4 mm can be detected by the MR component with a sensitivity of 80–90% [14]. Especially the use of short inversion time inversion-recovery sequences (STIR), diffusion-weighted sequences (DWI), and liver accelerated volume acquisition (LAVA) images in integrated PET/MRI might possibly improve the discrimination between benign and malignant pulmonary nodules [15, 16]. Recently published data also suggest the use of 3D Dixon-based, dual-echo GRE pulse sequences in whole-body PET/MRI with comparable sensitivities and specificities for the detection of pulmonary nodules as compared to low-dose CT and combination with PET [17]. Use of contrast-enhanced VIBE sequences in integrated PET/MRI significantly improves detection rate of lung nodules, but especially for small nodules detection rate of PET/MRI is still inferior compared to diagnostic CT examinations of the chest within an integrated PET/CT scan [18]. Moreover, a superior role of MRI and PET/MRI over CT and PET/CT has been reported in several studies for the examination of pleural infiltration (Fig. 13.3) and chest wall or bone infiltration in cases of Pancoast tumors (Fig. 13.4) [27].

Regarding therapeutic stratifications in patients suffering from NSCLC, PET/CT and PET/MRI led to comparable therapeutic decisions in a cohort of 77 patients
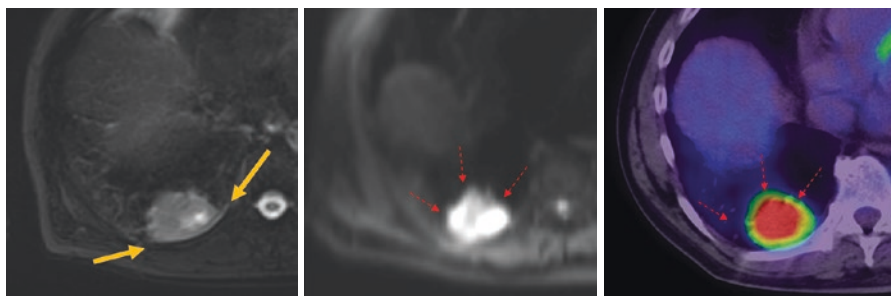
Fig. 13.3 FDG-PET/MRI with tumour infiltration of visceral pleura
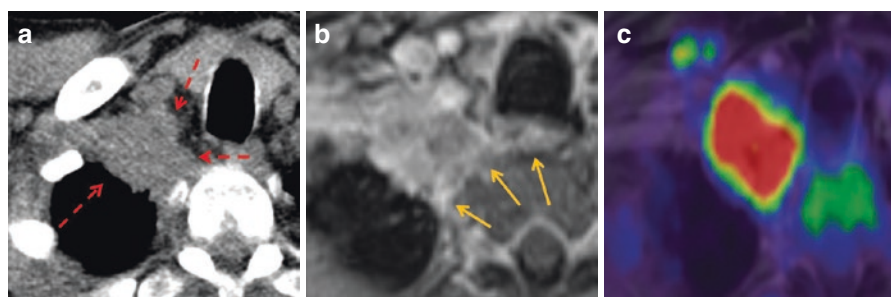

Fig. 13.4 FDG-PET/CT and PET/MRI of patient with pancoast tumour and infiltration of vertebral spine

[19]. A prospective trial with 45 NSCLC patients comparing PET/MRI and PET/CT for preoperative staging showed comparable results in terms of primary tumor assessment and nodal staging, with minor discrepancies in terms of M staging. Therefore, authors concluded that PET/CT and PET/MRI showed comparable results for preoperative NSCLC staging, with a significantly reduced radiation dose in PET/MRI (−31.1%) [20]. In a cohort of 123 patients with different types of confirmed primary cancer, PET/MRI was described as a feasible whole-body imaging modality with advantages for the detection of brain metastases as compared to PET/CT [21]. On the other hand, a prospective trial with 42 patients comparing PET/MRI and PET/CT for staging reasons in NSCLC patients stated that PET/MRI with fast MR protocols did not improve the diagnostic accuracy of the staging of NSCLC [22]. Thus, a potential additive value of PET/MRI compared to PET/CT in lung cancer staging is not yet proven.

In cases of unclear lung lesions, histological tissue sampling is often mandatory for therapy stratification. Usually, lung nodules are diagnosed by means of transbronchial biopsy, thoracoscopy, thoracotomy, or in cases of unclear mediastinal lymph nodes by mediastinoscopy. In cases of peripheral lung nodules, minimally invasive CT-guided transthoracic needle biopsies are often performed, especially in patients with severe comorbidities [23]. As reported by case reports, transthoracic needle biopsies can result in seed metastases along the access channel [24–26], moreover in pneumothorax or bleeding. Nevertheless, seed

metastases were rather uncommon in a retrospective analysis of 250 patients [23]. According to mentioned risks of invasive lung nodule assessments, use of integrated FDG PET/CT is a cost-efficient alternative to invasive lung nodule examinations, especially in cases of benign findings in PET indicated by the absence of increased FDG uptake [27, 28], thus reducing need for invasive lung nodule examinations.

13.1 Texture Analysis and Image Processing in Lung Cancer

Texture analysis (TA) refers to characterizing the spatial variation of pixel intensities in an image and describing the characteristic of image properties by textural features. TA is a quantitative approach for analyzing changes in the biomedical image "texture" that result from changes in pathology that are too subtle to detect visually. Therefore, TA can be applied as a noninvasive tool for diagnosis, prognosis, and characterization of tumors. Before applying TA, the biomedical images are usually preprocessed by filtering for noise removal and image enhancement followed by discretization of voxel values. Approaches for TA can be classified in four major categories—structural methods, model-based methods, statistical methods, and transform-based methods [29]. Structural method of TA characterizes an image by plausible underlying hierarchal structures [30]. Model-based methods are based on the concept of representing image by using sophisticated mathematical model [31, 32]. Statistical methods describe the image using pure numerical analysis of the distribution of pixel intensity values; in this category gray-level co-occurrence matrix (GLCM) proposed by Haralick [33] and gray-level run length matrix (GLRLM) [34] are commonly used statistics. Figure 13.5 showing the commonly used features for textural analysis using GLCM and GLRLM. Transform-based method of TA such as

	Texture features
Gray Level Co-occurrence Matrix(GLCM)	F_1: Contrast
	F_2: Correlation
	F_3: Energy
	F_4: Homogeneity
Gray Level Run Length Matrix (GLRLM)	R_1: Short Run Emphasis (SRE)
	R_2: Long Run Emphasis (LRE)
	R_3: Gray-Level Nonuniformity (GLN)
	R_4: Run Length Nonuniformity (RLN)
	R_4: Run Percentage (RP)
	R_5: Low Gray-Level Run Emphasis (LGRE)
	R_6: High Gray-Level Run Emphasis (HGRE)
	R_7: Short Run Low Gray-Level Emphasis (SRLGE)

Fig. 13.5 Texture features

Fourier [35], Gabor [36], and wavelet [37, 38] transform represents the image in a space whose coordinate system has an interpolation that is closely related to characteristics of texture. Here a brief review on application of TA in diagnosis, prognosis, and characterization of lung lesions and thoracic malignancies has been provided. Most studies investigated TA on CT or FDG PET/CT images because these modalities are more commonly used in lung cancer imaging than MRI [39].

Petkovska et al. [40] analyzed GLCM features on contrast enhancement maps (CEM) of indeterminate lung nodules imaged with contrast-enhanced CT to distinguish benign from malignant lung nodules. Pre- and post-contrast series were subtracted volumetrically and the subtracted voxels in 3D region of interest (ROI) covering lung nodules were quantized into seven color-coded bins to form a CEM. Fourteen textural features were statistically analyzed to give a single aggregate factor as an indicator of malignancy and the receiver operating characteristic (ROC) curve analysis produced good discrimination between malignant and benign lesions with area under curve (AUC) of 0.84. Son et al. [41] analyzed the CT findings of ground-glass nodules (GGNs) diagnosed pathologically as adenocarcinoma in situ (AIS), minimally invasive adenocarcinoma (MIA), and invasive adenocarcinoma for investigating whether quantitative CT parameter evaluation enables for the distinction of invasive adenocarcinoma from preinvasive or minimally invasive adenocarcinoma. Unenhanced CT scans of 178 patients with a total of 191 GGNs were assessed for tumor size in lung setting/mediastinal setting, density, volume, and mass. Histogram analysis of CT attenuation values within tumor ROIs was performed, and tumor heterogeneity was quantified by calculating texture parameters' uniformity and entropy. Two significant factors, the 75th percentile CT attenuation value ($\geq$2470 HU) and entropy ($\geq$7.90), have shown statistical significance independently in predicting invasive adenocarcinoma, and combined ROC analysis produced AUC of 0.78. Chae et al. [42] retrospectively investigated the value of three-dimensional texture features for differentiation of preinvasive lesions from invasive pulmonary adenocarcinomas (IPAs) that manifested as part-solid ground-glass nodules (GGNs). IPAs and preinvasive lesions showed significant differences in histograms and with volumetric parameters such as mass, kurtosis, and entropy ($P < 0.001$).

In a retrospective pilot study Ganeshan et al. [43] measured fine to coarse texture patterns in CT images of non-small-cell lung cancer (NSCLC) and compared the measured parameters—mean grey intensity (MGI), entropy (E), and uniformity (U)—in tumor ROI with tumor FDG uptake (SUV) and stage as determined by the clinical report of the PET/CT imaging. Coarse texture features correlated with tumor SUV, whereas fine texture features correlated with tumor stage. In another study Ganeshan et al. [44] investigated the efficacy of tumor heterogeneity quantified by CT TA in NSCLC to establish an independent marker for patient survival. A total of 54 patients with primary pulmonary lesions were undergone FDG PET/CT for staging and monitored up to minimum follow-up period of 30 months to obtain the survival time. CT images were processed to derive images with, and fine to

coarse texture and uniformity in tumor ROI were evaluated. CT texture feature and PET stage found to be statistically significant in predicting survival of patients independently. Same methodology for texture feature extraction was applied in another study by [45] to differentiate between malignant and benign lymph nodes in the mediastinum in 29 patients suspected for lung cancer. Ravanelli et al. [46] evaluated texture features using Laplacian of Gaussian filtering on contrast-enhanced CT images of advanced NSCLC in 53 patients to predict responsiveness to chemotherapy. Response to chemotherapy was evaluated according to RECIST1.1 [47]. Product of uniformity and mean post-contrast gray level of the lesions correlated well with treatment response for adenocarcinoma group, whereas no association between texture features and chemotherapy response was found in the non-adenocarcinoma group.

Wu et al. [48] implemented an artificial neural network-based model to classify malignant from benign solitary pulmonary nodules (116 malignant and 86 benign) in CT images of 202 patients. Combination of 12 subjective radiological features and 13 quantitative GLCM textural features were used in the discrimination model. Logistic regression framework was applied to select predictive features. Eight radiological and two textural features were obtained after the Lasso-type regularization procedure. While only radiological features achieved AUC of 0.84 in differentiating between malignant and benign lesions, model selected feature combination improved the AUC to 0.91. Dhara et al. [49] extracted GLCM texture features in 3D volumetric data of lung nodules. The optimal texture features were determined, and an ANN framework was applied to classify solitary pulmonary nodules (SPNs) from ground-glass nodule (GGN). They compared the classification using 3D texture features and 2D texture features, and 3D texture features found superior with 97.17% accuracy, while 2D texture features secured 89.1% accuracy.

Ramalho et al. [50] proposed a novel method for lung disease detection based on feature extraction using co-occurrence statistics framework inspired by Haralick feature extraction method. The experimental results achieved 96% accuracy in classifying normal lungs and diseases as chronic obstructive pulmonary disease (COPD) and fibrosis using extreme learning machine neural network (ELMNN). Liu et al. [51] investigated CT-based radiomic features in peripheral lung adenocarcinomas to predict epidermal growth factor receptor (EGFR) mutation status in 298 patients. A total of 219 quantitative 3D features, divided into eight categories, including tumor size, shape, location, air space, pixel intensity histogram, run length and co-occurrence, Laws' texture, and wavelets, were extracted from segmented volumes of each tumor. They found 11 CT-based radiomic features had significant association with EGFR mutations. Dennie et al. [52] in a retrospective study evaluated GLCM texture features in contrast-enhanced (CE) and/or non-contrast-enhanced (NCE) CT images of primary lung cancer and granulomatous nodules in 55 patients. They concluded that TA on NCE CT was more sensitive, specific, and accurate than FDG PET/CT in differentiating primary lung cancers from granulomatous lesions.

There are studies that investigated model-based TA using fractal geometry to estimate geometrical complexity and irregularity of shapes and patterns involved in lung tumor for discriminating lung nodules [53]. Kido et al. [54] measured fractal

dimensions (FD), 2D FD in binary image, and 3D FD in gray-level image of small peripheral pulmonary nodules in 70 patients with different types of bronchogenic carcinomas and 47 patients with benign pulmonary nodules. Fractal dimensions reflect the discriminating characteristics of the lung-nodule interfaces of small peripheral pulmonary nodules. Bronchogenic carcinomas had higher FD values, indicating greater structural complexity. In a similar study by Al-Kadi and Watson [55] aggressiveness of lung tumors was assessed using fractal analysis of contrast-enhanced CT-image time series. They found that the FD of lung-tumor tissue was higher than that of normal lung tissue and that tumor FD was strongly correlated with FDG PET SUVs. They concluded that more aggressive tumors (stages III–IV) had a higher FD compared with nonaggressive tumors (stage I), and the accuracy of classification of advanced-stage and early-stage tumors based on FD analysis was 83.3%. Miwa et al. [56] have shown that FD analysis of FDG uptake in PET image could differentiate malignant and benign pulmonary nodules. They reported that heterogeneity of FDG uptake in the nodules was significantly lower in malignant non-small-cell lung cancer than benign nodules ($P < 0.05$).

Parmar et al. [57] extracted radiomic features based on histogram, GLCM, GLRLM, shape, and wavelet features from pretreatment computed tomography (CT) images and performed disease-specific cluster analysis to identify feature association to patient survival and tumor stage. In another study [58] prediction of adenocarcinoma recurrence was investigated using wavelet-based textural information evaluated from presurgical CT images of 101 patients with surgically resected stage I adenocarcinoma. Derived predictive models from wavelet analysis differentiated recurrence and nonrecurrence groups with AUC = 0.8.

Several studies involving CAD system designing have tried to map clinical information with estimated quantitative image texture features that can help in detection and diagnosis of pulmonary nodules and medical image retrieval [59–62]. McNitt-Gray et al. [63] used nodule size, shape, and GLCM texture features to classify malignant and benign nodules. Wang et al. [64] implemented multilevel binomial logistic prediction model-based CAD method to detect SPNs in 185 patients. Among 14 GLCM features, five texture features, including inertia, entropy, correlation, difference-mean, and sum entropy, were statistically different ($P < 0.05$) between benign and malignant SPNs. Raicu et al. [65] investigated correlation between semantic characteristics (tumor shape and density) and image features of pulmonary nodules in 29 thoracic CT scans and evaluated their prediction capability in diagnosing lung nodules. Among image features 35 textural features were extracted using GLCM and Gabor filtering. High correlations between different semantic terms and promising mappings from image features to certain semantic terms were found. Lam et al. [66] concluded that Gabor texture features produced the best retrieval results regardless of the nodule size, number of retrieved items, or similarity metric than GLCM or Markov texture features in their content-based image retrieval (CBIR) system.

TA of lung cancer images has been applied successfully to FDG PET and CT scans. Studies on lung cancer have shown that TA may have a role in characterizing tumors and predicting treatment response [67]. However, there are lack of standardized methodology and data integration in studies involving TA. TA in medical image analysis needs to be uniform, reproducible, and clinically validated to be successfully deployed.

References

1. MacMahon H, Austin JHM, Gamsu G, Herold CJ, Jett JR, Naidich DP, Patz EF, Swensen SJ. Fleischner society guidelines for management of small pulmonary nodules detected on CT scans: a statement from the Fleischner society. Radiology. 2005;237:395–400.

2. Khan A. ACR appropriateness criteria on solitary pulmonary nodule. J Am Coll Radiol. 2007;4:152–5.

3. Matsuguma H, Nakahara R, Kondo T, Kamiyama Y, Mori K, Yokoi K. Risk of pleural recurrence after needle biopsy in patients with resected early stage lung cancer. Ann Thorac Surg. 2005;80:2026–31.

4. Christensen JA, Nathan MA, Mullan BP, Hartman TE, Swensen SJ, Lowe VJ. Characterization of the solitary pulmonary nodule: 18F-FDG PET versus nodule-enhancement CT. AJR Am J Roentgenol. 2006;187:1361–7.

5. Naalsund A, Maublant J. The solitary pulmonary nodule--is it malignant or benign? Diagnostic performance of Tc-depreotide SPECT. Respiration. 2006;73:634–41.

6. Orlacchio A, Schillaci O, Antonelli L, D'Urso S, Sergiacomi G, Nicolì P, Simonetti G. Solitary pulmonary nodules: morphological and metabolic characterisation by FDG-PET-MDCT. Radiol Med. 2007;112:157–73.

7. Gould MK, Maclean CC, Kuschner WG, Rydzak CE, Owens DK. Accuracy of positron emission tomography for diagnosis of pulmonary nodules and mass lesions: a meta-analysis. JAMA. 2001;285:914–24.

8. Fletcher JW, Kymes SM, Gould M, Alazraki N, Coleman RE, Lowe VJ, Marn C, Segall G, Thet LA, Lee K. VA SNAP cooperative studies group a comparison of the diagnostic accuracy of 18F-FDG PET and CT in the characterization of solitary pulmonary nodules. J Nucl Med. 2008;49:179–85.

9. Werner MK, Parker JA, Kolodny GM, English JR, Palmer MR. Respiratory gating enhances imaging of pulmonary nodules and measurement of tracer uptake in FDG PET/CT. AJR Am J Roentgenol. 2009;193:1640–5.

10. Lan X-L, Zhang Y-X, Wu Z-J, Jia Q, Wei H, Gao Z-R. The value of dual time point (18)F-FDG PET imaging for the differentiation between malignant and benign lesions. Clin Radiol. 2008;63:756–64.

11. Dimitrakopoulou-Strauss A, Georgoulias V, Eisenhut M, Herth F, Koukouraki S, Mäcke HR, Haberkorn U, Strauss LG. Quantitative assessment of SSTR2 expression in patients with non-small cell lung cancer using(68)Ga-DOTATOC PET and comparison with (18)F-FDG PET. Eur J Nucl Med Mol Imaging. 2006;33:823–30.

12. Halley A, Hugentobler A, Icard P, Porret E, Sobrio F, Lerochais J-P, Bouvard G, Zalcman G, Agostini D. Efficiency of 18F-FDG and 99mTc-depreotide SPECT in the diagnosis of malignancy of solitary pulmonary nodules. Eur J Nucl Med Mol Imaging. 2005;32:1026–32.

13. Menda Y, Kahn D. Somatostatin receptor imaging of non-small cell lung cancer with 99mTc depreotide. Semin Nucl Med. 2002;32:92–6.

14. Wielpütz M, Kauczor H-U. MRI of the lung: state of the art. Diagn Interv Radiol. 2012;18:344–53.

15. Kim HS, Lee KS, Ohno Y, van Beek EJR, Biederer J. PET/CT versus MRI for diagnosis, staging, and follow-up of lung cancer. J Magn Reson Imaging. 2015;42:247–60.

16. Huellner MW, Appenzeller P, Kuhn FP, Husmann L, Pietsch CM, Burger IA, Porto M, Delso G, von Schulthess GK, Veit-Haibach P. Whole-body nonenhanced PET/MR versus PET/CT in the staging and restaging of cancers: preliminary observations. Radiology. 2014;273:859–69.

17. Stolzmann P, Veit-Haibach P, Chuck N, Rossi C, Frauenfelder T, Alkadhi H, von Schulthess G, Boss A. Detection rate, location, and size of pulmonary nodules in trimodality PET/CT-MR: comparison of low-dose CT and Dixon-based MR imaging. Investig Radiol. 2013;48:241–6.

18. Rauscher I, Eiber M, Fürst S, Souvatzoglou M, Nekolla SG, Ziegler SI, Rummeny EJ, Schwaiger M, Beer AJ. PET/MR imaging in the detection and characterization of pulmonary lesions: technical and diagnostic evaluation in comparison to PET/CT. J Nucl Med. 2014;55:724–9.

19. Schaarschmidt BM, Grueneisen J, Metzenmacher M, Gomez B, Gauler T, Roesel C, Heusch P, Ruhlmann V, Umutlu L, Antoch G, Buchbender C. Thoracic staging with (18)F-FDG PET/

MR in non-small cell lung cancer - does it change therapeutic decisions in comparison to (18) F-FDG PET/CT? Eur Radiol. 2017;27:681–8.

20. Lee SM, Goo JM, Park CM, Yoon SH, Paeng JC, Cheon GJ, Kim YT, Park YS. Preoperative staging of non-small cell lung cancer: prospective comparison of PET/MR and PET/CT. Eur Radiol. 2016;26:3850–7.

21. Ishii S, Shimao D, Hara T, Miyajima M, Kikuchi K, Takawa M, Kumamoto K, Ito H, Shishido F. Comparison of integrated whole-body PET/MR and PET/CT: is PET/MR alternative to PET/CT in routine clinical oncology? Ann Nucl Med. 2016;30:225–33.

22. Huellner MW, de Galiza Barbosa F, Husmann L, Pietsch CM, Mader CE, Burger IA, Stolzmann P, Delso G, Frauenfelder T, von Schulthess GK, Veit-Haibach P. TNM staging of non-small cell lung cancer: comparison of PET/MR and PET/CT. J Nucl Med. 2016;57:21–6.

23. Flechsig P, Kunz J, Heussel C-P, Bozorgmehr F, Schnabel P, Dienemann H, Kauczor H-U, Sedlaczek O. Invasive lung cancer staging: influence of CT-guided core needle biopsy on onset of pleural carcinomatosis. Clin Imaging. 2015;39:56–61.

24. Inoue M, Honda O, Tomiyama N, Minami M, Sawabata N, Kadota Y, Shintani Y, Ohno Y, Okumura M. Risk of pleural recurrence after computed tomographic-guided percutaneous needle biopsy in stage I lung cancer patients. Ann Thorac Surg. 2011;91:1066–71.

25. Asakura K, Izumi Y, Yamauchi Y, Nakatsuka S, Inoue M, Yashiro H, Abe T, Sato Y, Nomori H. Incidence of pleural recurrence after computed tomography-guided needle biopsy in stage I lung cancer. PLoS One. 2012;7:e42043.

26. Wisnivesky JP, Henschke CI, Yankelevitz DF. Diagnostic percutaneous transthoracic needle biopsy does not affect survival in stage I lung cancer. Am J Respir Crit Care Med. 2006;174:684–8.

27. Flechsig P, Mehndiratta A, Haberkorn U, Kratochwil C, Giesel FL. PET/MRI and PET/CT in lung lesions and thoracic malignancies. Semin Nucl Med. 2015;45:268–81.

28. Kwee TC, Torigian DA, Alavi A. Oncological applications of positron emission tomography for evaluation of the thorax. J Thorac Imaging. 2013;28:11–24.

29. Nailon WH. Texture analysis methods for medical image characterisation. Rijeka: InTech; 2004.

30. Haralick RM. Statistical and structural approaches to texture. Proc. IEEE. 1979;67:786–804.

31. Benoit B. Mandelbrot fractals: form, chance and dimension. New York: W.H. Freeman & Company; 1977.

32. Turcotte DL. Fractals and chaos in geology and geophysics. 2nd ed. New York: Cambridge university press; 1997.

33. Haralick RM, Shanmugam K, Dinstein I. Texture features for image classification. IEEE Trans Syst Man Cybern. 1973;SMC-3:610–21.

34. Galloway MM. Texture analysis using grey-level run lengths. Comput Graphics Image Process. 1975;4:172–9.

35. Rosenfeld A, Weszka J. In: Fu K, editor. Picture recognition in digital pattern recognition. Berlin: Springer-Verlag; 1980.

36. Bovik AC, Clark M, Geisler WS. Multichannel texture analysis using localized spatial filters. IEEE Trans Pattern Anal Mach Intell. 1990;12:55–73.

37. Mallat SG. Multifrequency Channel decomposition of images and wavelet models. IEEE Trans Acoust Speech Signal Process. 1989;37:2091–110.

38. Laine A, Jian F. Texture classification by wavelet packet signatures. IEEE Trans Pattern Anal Mach Intell. 1993;15:1186–91.

39. Sahiner I, Vural GU. Positron emission tomography/computerized tomography in lung cancer. Quant Imaging Med Surg. 2014;4:195–206.

40. Petkovska I, Shah SK, McNitt-Gray MF, Goldin JG, Brown MS, Kim HJ, Brown K, Aberle DR. Pulmonary nodule characterization: a comparison of conventional with quantitative and visual semi-quantitative analyses using contrast enhancement maps original research. Eur J Radiol. 2006;59:244–52.

41. Son JY, Lee HY, Lee KS, Kim J, Han J, Jeong JY, Kwon OJ. Quantitative CT analysis of pulmonary ground-glass opacity nodules for the distinction of invasive adenocarcinoma from pre-invasive or minimally invasive adenocarcinoma. PLoS One. 2014;9:e104066.

42. Adenocarcinomas P, Park CM, Lee SM. Computerized texture analysis of persistent part-solid ground- glass Nodules : differentiation of Preinvasive lesions from invasive pulmonary adeno-carcinomas. Radiology. 2014;273:285–93.

43. Ganeshan B, Abaleke S, Young RCD, Chatwin CR, Miles KA, Imaging C, Centre S, Imaging C, Centre S. Texture analysis of non-small cell lung cancer on unenhanced computed tomography : initial evidence for a relationship with tumour glucose metabolism and stage. Cancer Imaging. 2010;10:137–43.

44. Ganeshan B, Panayiotou E, Burnand K, Dizdarevic S, Miles K. Tumour heterogeneity in non-small cell lung carcinoma assessed by CT texture analysis: a potential marker of survival. Eur Radiol. 2011;22(4):796–802.

45. Andersen MB, Harders SW, Ganeshan B, Thygesen J, Henrik H, Madsen T. CT texture analysis can help differentiate between malignant and benign lymph nodes in the mediastinum in patients suspected for lung cancer. Acta Radiol. 2016;57:669–76.

46. Ravanelli M, Farina D, Morassi M, Roca E. Texture analysis of advanced non-small cell lung cancer (NSCLC) on contrast-enhanced computed tomography: prediction of the response to the first-line chemotherapy. Eur Radiol. 2013;23:3450–5.

47. Eisenhauer EA, Therasse P, Bogaerts J, Schwartz LH, Sargent D, Ford R, Dancey J, Arbuck S, Gwyther S, Mooney M, Rubinstein L, Shankar L, Dodd L. New response evaluation criteria in solid tumours: revised RECIST guideline (version 1. 1). Eur J Cancer. 2008;45:228–47.

48. Wu H, Sun T, Wang J, Li X, Wang W. Combination of radiological and gray level co-occurrence matrix textural features used to distinguish solitary pulmonary nodules by computed tomography. J Digit Imaging. 2013;26:797–802.

49. Dhara AK, Mukhopadhyay S, Khandelwal N. 3D texture analysis of solitary pulmonary nodules using co-occurrence matrix from volumetric lung CT images 3D texture analysis of solitary pulmonary nodules using co-occurrence matrix from volumetric lung CT images. In: Proceedings of SPIE - The International Society for Optical Engineering. 2012.

50. Ramalho GLB, Filho PPR, De FNS, Cortez PC. Lung disease detection using feature extraction and extreme learning machine. Braz J Biomed Eng. 2014;30:207–14.

51. Liu Y, Kim J, Balagurunathan Y, Li Q, Garcia AL, String O, Ye Z, Gillies RJ. Radiomic features are associated with EGFR mutation status in lung adenocarcinomas. Clin Lung Cancer. 2016;17:441–8.

52. Dennie C, Thornhill R, Sethi-virmani V, Souza CA, Bayanati H, Gupta A, Maziak D. Role of quantitative computed tomography texture analysis in the differentiation of primary lung cancer and granulomatous nodules. Quant Imaging Med Surg. 2016;6:6–15.

53. Lennon FE, Cianci GC, Cipriani NA, Hensing TA, Zhang HJ, Chen C, Murgu SD, Vokes EE, Vannier MW, Salgia R. Lung cancer — a fractal viewpoint. Nat Publ Group. 2015;12:664–75.

54. Kido S, Kuriyama K, Higashiyama M, Kasugai T, Kuroda C. Fractal analysis of small peripheral pulmonary nodules in thin-section CT evaluation of the lung-nodule interfaces. J Comput Assist Tomogr. 2002;26:573–8.

55. Al-kadi OS, Watson D. Texture analysis of aggressive and nonaggressive lung tumor CE CT images. IEEE Trans Biomed Eng. 2008;55:1822–30.

56. Miwa K, Inubushi M, Wagatsuma K, Nagao M, Murata T, Koyama M, Koizumi M, Sasaki M. FDG uptake heterogeneity evaluated by fractal analysis improves the differential diagnosis of pulmonary nodules. Eur J Radiol. 2014;83:715–9.

57. Parmar C, Leijenaar RTH, Grossmann P, Rios E, Bussink J, Rietveld D, Rietbergen MM, Haibe- B, Lambin P, Aerts HJWL. Radiomic feature clusters and prognostic signatures specific for lung and head & neck cancer. Sci Rep Nat Publ Group. 2015;5:1–10.

58. Leung AN, Rubin DL. Predicting adenocarcinoma recurrence using computational texture models of nodule components in lung CT. Med Phys. 2015;42:2054–63.

59. Bagci U, Bray M, Caban J, Yao J, Mollura DJ. Computer-assisted detection of infectious lung diseases: a review. Comput Med Imaging Graph. 2012;36:72–84.

60. El-baz A, Beache GM, Gimel G, Suzuki K, Okada K, Elnakib A, Soliman A, Abdollahi B. Computer-aided diagnosis systems for lung cancer: challenges and methodologies. Int J Biomed Imaging. 2013;2013:1–46.

61. Yan P, Suzuki K, Wang F, Shen D. Machine learning in medical imaging. In: Machine vision and applications. Berlin Heidelberg: Springer; 2013. p. 1327–9.
62. Firmino M, Angelo G, Morais H, Dantas MR, Valentim R. Computer - aided detection (CADe) and diagnosis (CADx) system for lung cancer with likelihood of malignancy. Biomed Eng Online. 2016;15:2.
63. McNitt-Gray MF, Wyckoff N, Sayre JW, Goldin JG, Aberle DR. The effects of co-occurrence matrix based texture parameters on the classification of solitary pulmonary nodules imaged on computed tomography. Comput Med Imaging Graph. 1999;23:339–48.
64. Wang H, Guo X, Jia Z, Li H, Liang Z, Li K, He Q. Multilevel binomial logistic prediction model for malignant pulmonary nodules based on texture features of CT image. Eur J Radiol. 2010;74:124–9.
65. Raicu DS, Varutbangkul E, Cisneros JG, Furst JD, Channin DS, Armato SG. Semantics and image content integration for pulmonary nodule interpretation in thoracic computed tomography. In: Proceedings of the SPIE, vol. 6512. SPIE--The International Society for Optical Engineering; 2007.
66. Lam M, Disney T, Pham M, Raicu D, Furst J, Susomboon R. Content-based image retrieval for pulmonary computed tomography nodule images. In: Medical imaging 2007: PACS and imaging informatics, SPIE proceedings, vol. 6516; 2007.
67. Bashir U, Siddique MM, Mclean E, Goh V, Cook GJ. Imaging heterogeneity in lung cancer: techniques, applications, and challenges. AJR. 2016;207(3):534–43.

PET/MRI in Breast Cancer

14

Claire Tabouret-Viaud, Ismini Mainta, Valentina Garibotto,
Diomidis Botsikas, Bénédicte M.A. Delattre,
and Osman Ratib

Contents

C. Tabouret-Viaud (✉)
Division of Nuclear Medicine and Molecular Imaging, Geneva University Hospitals,
Geneva, Switzerland

Service de Médecine Nucléaire du Centre Georges-François Leclerc, Dijon, France
e-mail: ctabouret@cgfl.fr

I. Mainta
Division of Nuclear Medicine and Molecular Imaging, Geneva University Hospitals,
Geneva, Switzerland

V. Garibotto • O. Ratib
Division of Nuclear Medicine and Molecular Imaging, Geneva University Hospitals,
Geneva, Switzerland

Faculty of Medicine, Geneva University, Geneva, Switzerland

D. Botsikas • B.M.A. Delattre
Division of Radiology, Geneva University Hospitals, Geneva, Switzerland

Breast cancer is the most common cancer in women worldwide and represented more than 25% of the newly diagnosed cancer cases in women in 2012 [1]. PET/CT is recommended in the clinical workup of advanced breast cancers and in cases of breast cancer recurrence [2, 3] and may also be proposed in treatment monitoring [4]. PET/MRI is a new imaging technique which is now being used clinically in different countries, and which may replace PET/CT in some selected breast cancer patients, when available [5]. A detailed description of advantages and indications of, respectively, PET and MRI techniques taken separately in breast cancer patients is beyond the scope of the present work and has already been reviewed elsewhere by our group [5]. We will focus upon the technical advantages and disadvantages of combined PET/MRI acquisitions in breast cancer patients from diagnosis to follow-up. In this chapter, we cover the specificities of PET/MRI in terms of quantification and provide a summary of the different protocols performed in breast cancer PET/MRI imaging. We will also discuss the clinical advances for patient management, the potential improvements that may occur in the future, as well as the future role that may be given to this technique.

14.1 Technical Aspects of Hybrid PET/MR in Breast Cancer

14.1.1 Technical Advantages of PET/MRI over PET/CT for Breast Cancer Patients

Compared to PET/CT, ionizing radiation delivered to the patients is lower with PET/MRI: the analysis of Melsaether et al. showed that the dose reduction obtained with breast cancer PET/MRI in comparison to PET/CT could be up to 50%, when including a fully diagnostic CT protocol [6]. It should be noted, however, that the CT-related dose is constantly decreasing, e.g., thanks to the availability of iterative CT reconstruction providing high-quality images with lower exposure. This reduction of radiation dose may have an interest particularly for younger patients with advanced but curable disease who may need to be scanned several times during their clinical workup without increasing the risk of radiation-induced secondary cancer, while they are often already enduring chemotherapies and irradiation from radiotherapy. Moreover, in a near future, selected patients may benefit from different PET acquisitions with several new PET radiopharmaceuticals to better characterize the primary and metastatic lesions, which will help in the treatment planning, and using PET/MRI instead of PET/CT will help reduce the total radiation burden. However, it should be noted that the dose injected to patients can be reduced with the use of PET with time-of-flight detectors, which are increasingly available on new PET/CT and some PET/MRI systems. In this case and given the recent advances on dose reduction for CT, this argument may be discussed. With comparable PET sensitivity, the ionizing dose associated with PET/MRI will always be lower than with a PET/CT.

The major advantage in performing PET/MRI instead of PET/CT in breast cancer patients is the ability to obtain a much better tissue contrast on specific morphological sequences when investigating breast and the most common metastatic sites,

in breast cancer, namely, the bone and liver, even when no contrast agent is injected, in comparison to what can be obtained with unenhanced or even enhanced CT [5]. However, for total body acquisitions that are used for attenuation correction, spatial resolution of MRI is significantly inferior to CT. Dedicated imaging of total body can be added to a PET/MRI protocol but is more time-consuming than a total body CT. Moreover, different MRI sequences such as functional MRI can be performed, which give information that cannot be obtained from CT. The clinical impact of performing PET/MRI instead of PET/CT on lesion detection will largely depend upon the MRI protocols that have been chosen, as we will detail in the next paragraph.

14.1.2   Technical Challenges of PET/MRI Compared to PET/CT in Breast Cancer Imaging

Although some important advances have been made, attenuation correction maps obtained with PET/MRI can still be improved in comparison to what is obtained with PET/CT. The attenuation map obtained from CT is directly dependent on the electronic density of each tissue and structure which is used to estimate the linear attenuation coefficients for 511 KeV photons. In PET/MRI technologies, creating a precise attenuation map is more complex. A 3D T1-weighted whole-body MRI sequence is used to delineate automatically 3- or 4-class tissue types and obtain a 3D attenuation map. In the 3-class tissue-type MR-derived attenuation maps, different attenuation coefficients are given to the lung, to the rest of the "soft" tissues taken together (including the bone, fat, and different organs), and to the air. In the 4-class tissue-type attenuation map, a different attenuation coefficient is given to the fat as well as to the air, to the lung, and to the rest of the "soft" tissues [7, 8]. In both 3-class and 4-class compartment MR-derived attenuation maps, the standard uptake values (SUVs) measured in normal organs were reported to be significantly underestimated in comparison to SUVs obtained on PET/CT acquisitions [9]. In particular, as no specific attenuation coefficient is given in either of these two cases to bones, which attenuate more photons than soft tissues, there is a higher underestimation of SUVs in and near bones, which could potentially be misleading when trying to characterize a lesion adjacent to bone or a bone lesion [9], especially for sclerotic bone metastases for which this underestimation is the highest [10]. Several groups are trying to improve these attenuation correction maps as will be detailed in paragraph 1.3.

Taking into account rigid coils is quite straightforward since they are always positioned at the same place on the MRI table, and a simple attenuation map can be created by digitally adding the table and coils to the estimated attenuation of the individual. However, it is more challenging to account for nonrigid surface coils since their position is unknown for every individual case.

An associated issue is that artifacts in the MR-based attenuation correction (MRAC) map should systematically be checked and ruled out in order to avoid misinterpretation or false SUV measurements [9].

As we previously reported, an overestimation of scatter events coming from a high cardiac metabolism may occur during the scatter correction performed on the dedicated PET acquisition in the specific breast coil, resulting in a low PET activity in a region located on the opposite side of the heart [5]. More precisely, this artifact can occur in the region of the right breast, which can make difficult the characterization of some breast lesions. This can be corrected with better defined scatter correction algorithms or by avoiding scatter correction during PET images reconstruction, as shown on Fig. 14.1 [11].
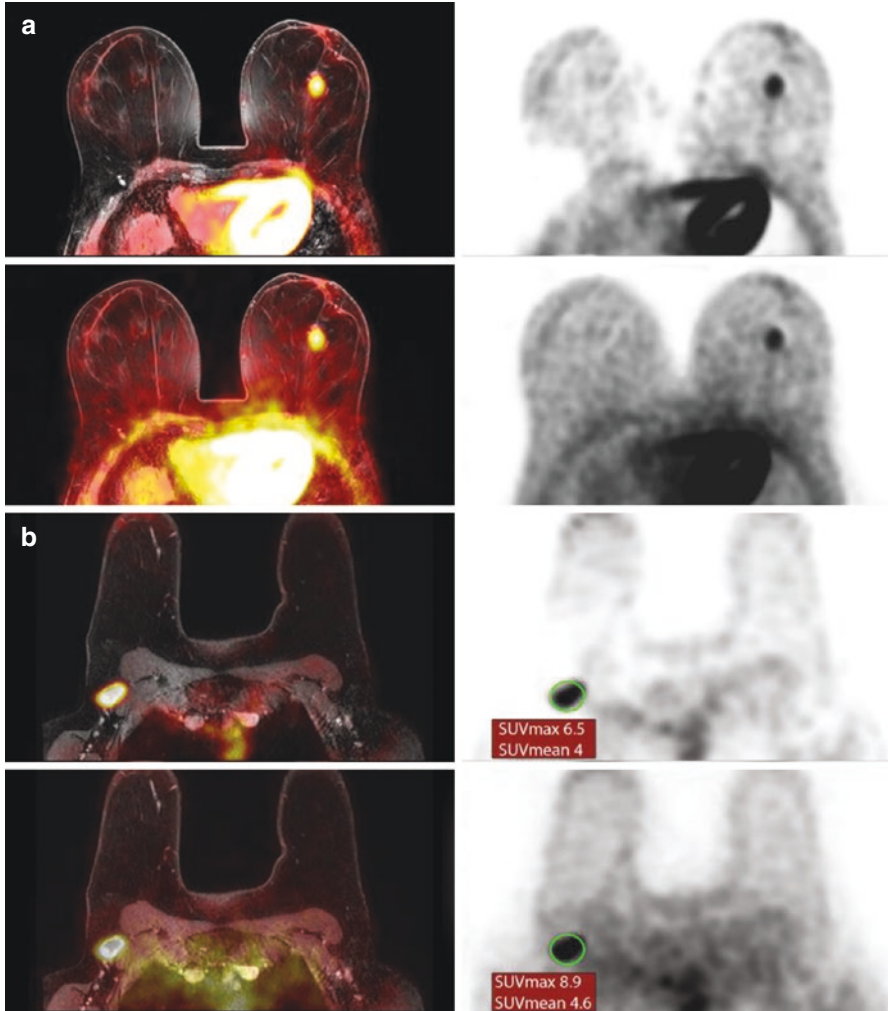
Fig. 14.1 Scatter overestimation artifact. Axial, PET/MRI (**a**), and 18F-FDG PET (**b**) in prone position illustrating the artifact due to overcorrection of scatter contralateral to the high cardiac activity, with impact on detectability of potential lesions and on quantification

Other artifacts have been described on 18F-FDG PET/MRI mammography by Cho et al. however without impact on clinical diagnosis [12].

Finally, depending on the protocol and especially the different MRI sequences that are performed, PET/MRI can be more or less time-consuming. With the current protocol in the Philips sequential unit, the total acquisition time is of 90 min, with a dedicated breast MRI exam and additional whole-body sequences that offer very limited spatial resolution. If one opts for optimal whole-body MR imaging, acquisition time will be very high, and cost-effectiveness issues can arise. One must make sure that the PET/MRI workflow is optimized, by avoiding, for example, MRI sequences that would eventually be redundant with the information given by PET images. Cost-effectiveness studies are also needed to better justify the use of PET/MRI in clinical routine, as it remains an expensive technology.

14.1.3 Quantification in PET/MRI in Comparison to PET/CT

Comparing the quantitative measures in vivo from PET/MRI and PET/CT is arduous for different reasons, including the fact that there is a mandatory time interval between both acquisitions and a varying biodistribution of radiotracers in the different organs during that time. For example, 18F-FDG accumulates through the time and is washed out more slowly in most malignant lesions in comparison to normal tissues. However, some publications dealing with different cancer types and using different radiotracers, but mostly 18F-FDG, showed that the SUVs calculated on PET/MRI devices could be different but well correlated to the values obtained on PET/CT [9, 13–17]. In each of those studies except for the study from Varoquaux et al., PET/MRI was performed after PET/CT, and this delayed PET/MRI acquisition may have changed the quantification results, for malignant lesions in particular, as delayed acquisition is known to improve contrast and lesion detection.

Moreover, a comparison between studies dealing with quantification is made difficult by the fact that different PET/CT scanners and different PET/MRI models are involved, and SUV values depend a lot from the scanning technology and data processing protocols such as the different reconstruction parameters used, which are quite heterogeneous in the literature.

However, some studies compare the SUVs obtained from PET/CT and PET/MRI, such as one from Pace et al. in 36 breast cancer patients, who found equivalent performances in terms of lesion detection and a strong correlation between quantitative measures performed on both devices [18]. Pujara et al. also found a strong organ-specific correlation of PET/CT and PET/MRI quantitative measures of metastases, including bone metastases [19]. The SUVs of those metastases obtained with both devices were not significantly different [19]. However, there was a moderate correlation in most normal structures such as breast, bone, lung, liver, and axillary lymph nodes. Consequently, the ratio of metastasis activity divided by background activity, such as normal liver activity, could be significantly higher from PET/MRI in comparison to those obtained from PET/CT, and if such a ratio should be used to characterize metastatic lesions, the reference thresholds should be calculated

specifically from PET/MRI devices, and not simply extrapolated from studies performed on a PET/CT device.

Finally, it is preferable that whenever possible follow-up images are acquired using the same device in order to be able to compare more reliably lesions' activity and to appreciate better the clinical evolution.

14.1.4 MRI Protocols

The MRI protocols used for PET/MR vary a lot from a center to another, depending on the device available and the physicians' habits, which make it difficult to globally compare PET/MRI's performances to PET/CT's [5]. For example, a specific breast MR coil can be used or not, and specific MRI sequences must be performed to correctly visualize the common metastatic sites in breast cancer patients. Indeed, it has been shown by Appenzeller et al. that the sequence they used for attenuation correction (a Dixon-based T1-weighted 3D gradient echo MR sequence performed with a body coil) was not sufficient to obtain the same diagnostic accuracy as a standard low-dose PET/CT [20]; this is the reason why most PET/MRI protocols include additional whole-body sequences (such as T2 turbo spin echo (TSE) or 3D T1 gradient echo with a higher resolution).

In our institution, and in breast cancer patients, whole-body MRI sequences are performed in supine position for distant staging and include a T2 TSE in coronal plane (spatial resolution $1.5 \times 1.5 \times 8$ mm^3) for a better morphological characterization. A 3D T1-weighted gradient echo sequence using Dixon technique (spatial resolution $0.9 \times 0.9 \times 6$ mm^3) to suppress the fat signal is added and has the advantage to produce four contrasts (T1-weighted in-phase and out-phase images, water, and fat images). A similar sequence with a lower resolution (3D T1 FFE) is performed in order to create an attenuation correction map (spatial resolution $2 \times 2 \times 6$ mm^3). A whole-body PET scan follows. A whole-body diffusion sequence was initially added to the MRI protocol, typically with b-values of 0 and 800 mm^2/s (spatial resolution $1.5 \times 1.5 \times 7$mm^3), but was abandoned as time-consuming and still controversial in the literature due to the redundant information it brings compared to PET [21, 22].

Although the Philips dedicated PET/MRI breast coil has not received FDA approval yet for clinical use, it allows the acquisition of high-quality breast PET and MRI: we perform T2 TSE and diffusion weighted (DW) sequences with 2 b-values in the axial plane in the breast and axillary regions, the patient being placed in prone position. A dynamic contrast-enhanced (DCE) 3D gradient echo T1-weighted sequence is then performed eventually with fat saturation, and some subtracted images can be created from an unenhanced acquisition compared to different enhanced series. In order to obtain good MRI image quality, premenopausal female patients should be investigated between days 5 and 12 of the menstrual cycle [5]. A breast PET acquisition follows in the same position, approximately 120 min after the injection of 18F-FDG. This late acquisition can be useful in better characterizing an inconclusive breast lesion because the

18F-FDG accumulates over time in most breast malignancies, more importantly in invasive versus noninvasive breast lesions [23]. Moreover, analyzing dual time point 18F-FDG-PET with a first acquisition starting 55–60 min after FDG injection and a second acquisition starting 110–120 min after FDG injection has shown a higher sensitivity in detecting cancers in dense breasts or small cancers (less than 1 cm) than analyzing each PET acquisition separately [23]. It is still not feasible to perform the whole-body acquisition in prone position on the breast coil, which would have the advantage of avoiding a position change for the patient: in prone position, the patient's back is too close to the magnet, and most of the time, the image of the back is truncated. Depending on their morphology, some patients can unfortunately not even enter the MRI's bore. The total acquisition time for whole-body and breast PET/MR is approximately 90 min [24]. As illustrated in an atlas published in 2013, high-quality breast PET and MRI sequential acquisitions on this Philips PET/MRI unit can be obtained [25].

The Biograph mMR device allows a simultaneous acquisition of PET and MRI and is equipped with multiple integrated radiofrequency PET-compatible surface coils that can cover the entire body [6, 18]. In the specific case of breast cancer patients, and when no specific breast coil is used for an additional breast PET/MRI, whole-body PET/MRI can be performed within approximately 45 min to cover patient's body from the thighs to the vertex, including 6–7 stations, according to patient's height [19]. Depending on the duration of MRI acquisitions at each station, there is enough time to perform simultaneously a high-quality PET acquisition. A 6 min per station whole-body PET acquisition has been reported [6, 19]. Concerning the MRI protocol, this group acquired a 3D T1-weighted Dixon coronal volumetric interpolated breath-hold (VIBE) sequence for MR attenuation correction to obtain a 4-class tissue-type attenuation map, a 3D T1-weighted radial gradient echo (radial VIBE), and a 2D double-refocused echo-planar diffusion weighted imaging, all three acquisitions being performed in supine position [6, 19]. An MRI contrast agent was injected during the liver station.

However, in the study from Pujara et al. no specific breast PET/MRI was acquired [19]. The use of specific four-channel breast coil by Aklan et al. was however reported with success in 2013 [26]. Later, a 16-channel receiver breast PET/MRI coil prototype was tested by Dregely et al. allowing state-of-the-art MRI acquisitions, but the quality of PET images had yet to be validated in vivo [27]. After further development, Oehmingen et al. published excellent results with the same coil with high MRI and PET quality and accurate quantification [28]. Grueneisen et al. also used a dedicated 16-channel radiofrequency breast coil for 49 patients with high diagnostic performances for local and axillary staging, and distant staging was performed with PET/CT alone and not with PET/MRI [29]. The breast MRI sequences performed in this study were an axial T2 TSE sequence, an axial T2 turbo inversion recovery magnitude (TRIM) sequence, and an axial diffusion weighted (DW) echo-planar imaging (EPI) sequence. A dynamic T1-weighted contrast-enhanced 3D fast low-angle shot sequence (FLASH) was also performed, followed by a 2D FLASH sequence [29].

The SIGNA PET/MR system (GE) benefits from a new generation solid-state digital photomultiplier technology that was recently introduced, this is thus the first PET insert with time-of-flight technology, which is not available on the Siemens mMR Biograph. TOF offers improved spatial resolution and efficiency, and high image quality, although the clinical benefit is not proven yet. However, at the time writing this book chapter, no publication relates specific results of PET/MRI imaging for breast cancer patients with this system.

14.2   Clinical Data Regarding PET/MR Imaging in Breast Cancer

Several studies are now available concerning PET/MRI's performances in breast cancer patients. Some of them globally compare PET/MRI to PET/CT in terms of quantitative measurements on both PET acquisitions, as cited before [18, 19], and others deal with lesion detection more globally. We will now describe their results in different indications in breast cancer patients: staging, evaluation of response to therapy, and detection of recurrence and restaging.

14.2.1 Breast Cancer Staging

Breast cancer staging is crucial before deciding which treatment the patient can benefit from and to estimate prognosis. Contrary to PET/CT, PET/MRI has the advantage of being able to perform an accurate local staging in addition to regional and distant staging: dedicated breast MRI sequences in PET-compatible breast coils can be obtained with the same image quality that can be done on an MRI device. Moreover, the physicians' confidence in their diagnosis when interpreting co-registered PET and MRI images together is increased [30–32].

PET/MRI performances in breast cancer local, regional, and distant staging are discussed in the following sections.

14.2.1.1   Local Assessment of Breast Cancer

Contrary to CT, if specific breast images in a dedicated coil are performed, MRI can be very useful in order to assess breast cancers locally with a high spatial resolution and for treatment planning including surgery [33–35]. Therefore, we recommend the use of a specific breast coil when a local staging is needed. However, MRI's positive predictive value and specificity can be variable and may be improved by adding the functional information given by PET. An example of local staging with PET/MRI is provided in Fig. 14.2. In the study by Moy et al., 36 patients with a total of 90 breast lesions performed separately 18F-FDG PET/CT and breast MRI that were later fused with a semiautomatic program based on landmarks and non-rigid fusion [36]. When adding PET to MRI, the PPV increased from 77 to 98%, and the specificity increased from 53 to 97%, the false-negative rate decreased from 26.7 to 9%, but the sensitivity decreased from 95% for MRI alone to 83% for
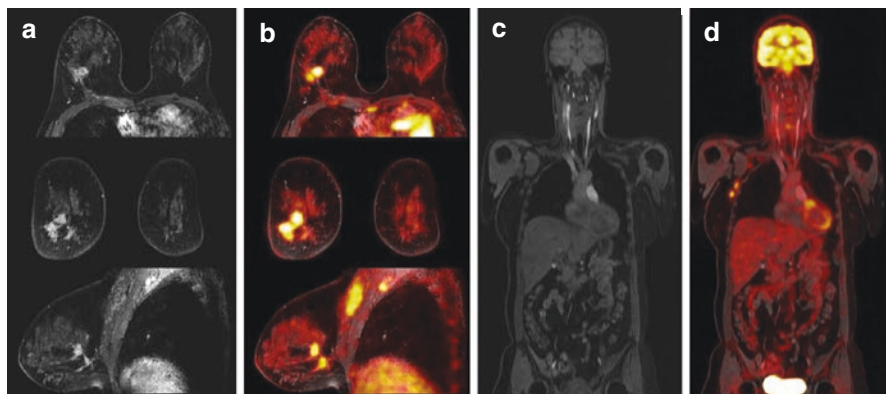
Fig. 14.2 Invasive ductal carcinoma of the right breast extending to the chest wall (pectoralis major) with regional lymphatic metastases (ipsilateral axillary lymph nodes, levels I and II). T1-weighted fat-saturated MRI sequence after gadolinium injection (**a** on axial, coronal, and sagittal plane) and 18F-FDG PET/MRI (**b** on axial, coronal, and sagittal plane) in prone position with the dedicated breast coil. Whole-body, 3D T1-weighted Dixon water sequence (**c**), and 18F-FDG PET/MRI (**d**)

PET/MRI fusion [36]. These promising results with software-based fusion were not corroborated by Grueneisen et al. from Essen with the use of the Biograph mMR system, who compared breast PET/MRI, MRI alone, and PET/CT for lesion detection and local staging in breast cancer patients: they found no advantage of PET/MRI over MRI alone in identifying malignant lesions. However, those two modalities performed better than PET/CT in determining local tumor extent: the T-stage was correctly determined for 82% of the lesions with PET/MRI and for only 68% of the lesions with PET/CT, although the patient's position was not the same on both modalities (PET/MRI was acquired in prone position while PET/CT was acquired supine) [29]. These results may also be influenced by the use of a standard RF breast coil, which was not at that time dedicated to PET/MRI, i.e., the attenuation correction of the hardware components of the coil wasn't taken into account in the attenuation map: this may have altered the image quality, the attenuation correction, and the quantification on PET/MR images. Taneja et al. included 36 breast cancer patients with invasive ductal carcinomas exclusively, known to be classically FDG-avid lesions, who benefited from a whole-body 18F-FDG PET/MRI (Siemens Biograph mMR) and a dedicated breast MRI (without specific prone PET registration) in primary staging conditions, and found no improvement in lesion detection when adding (whole-body) PET to MRI acquisitions [32]. However, physician's confidence in their diagnosis was higher when interpreting PET and MRI together [32]. In our study including 58 patients, MRI alone had a higher sensitivity than PET/MRI or PET alone in characterizing primary tumors [24]. However, it is well known now that the metabolic activity of primary lesions determined on 18F-FDG PET gives important prognostic information. A large study including 578 patients with primary breast cancer found that the SUVmax measured on baseline 18F-FDG PET/CT was a significant and independent

prognostic factor, higher SUVs being correlated with a poorer prognosis especially for triple-negative tumors [37]. Other studies corroborate this finding, and therefore, the 18F-FDG uptake quantification of breast lesions may have a role in the treatment choice [38, 39]. On the opposite, two studies on independent series, the largest including 214 subjects, showed that the ADC value in the tumor that was obtained with the MRI DWI sequence had limited performances in predicting patients' outcome [39, 40].

18F-FDG breast PET could also be of great use to characterize undetermined lesions detected on breast specific MRI sequences. Jalaguier-Coudray et al. retrospectively analyzed 80 patients with biopsy-proven breast cancer who benefited from an 18F-FDG PET/CT and a breast dedicated MRI, observing a high positive predictive value of PET for FDG-avid breast lesions larger than 1 cm [41].

Besides conventional MRI breast sequences, and as detailed in paragraph 1.4, functional MRI sequences can be added like diffusion weighted imaging (DWI), spectroscopy, or dynamic perfusion maps, which can give useful complementary information. Indeed, some publications show how important is the question of better defining the histological, genetic, and molecular heterogeneity within the same tumor [42]. Breast lesions are most of the time characterized with few tumor biopsy samples which are not always representative of the whole lesion and may not give enough information about intratumoral heterogeneity. This could explain some treatment failures and drug resistance. Not only could PET/MRI images help guiding biopsy to the most aggressive part of breast lesions, but also could it help appreciate the whole breast lesions' heterogeneity noninvasively. For example, Schmitz et al. showed that PET/MRI breast images were useful in better characterizing heterogeneous breast tumors in five patients with biopsy-proven invasive breast carcinoma "of no special type": thanks to a voxelwise analysis combining the information of 18F-FDG-PET and of a diffusion weighted MRI sequence, different phenotypes could be correctly identified within the same tumor [43]. These multiparametric 18F-FDG/ADC maps are promising techniques for a better characterization of entire tumors or even their metastases and could eventually be combined to information from other radiotracers (e.g., estrogen and progesterone receptor radioligands) in order to be able to propose a lesion-specific treatment.

An important drawback that the physician has to take into account when interpreting PET/MRI examinations for the purposes of local staging of breast cancer is that the gain of specificity that can be obtained, compared to MRI alone, is always accompanied by a lower sensitivity. From a lesion characterization perspective, the highest sensitivity is to be researched, and the relative lack of specificity can be compensated with a second-look ultrasound with or without percutaneous biopsy.

Overall, PET/MRI with dedicated breast MRI is an excellent tool for local staging of breast cancer as it benefits from the excellent diagnostic performance of MRI. However, combining information of PET/CT and breast MRI acquired separately offers comparable excellent results. The choice of which diagnostic modality should be used is a question of costs, local availability of modalities, and logistics of patient care in different institutions.

14.2.1.2 Regional Staging

Although MRI is not the imaging procedure of choice for lymph node staging in breast cancer patients, several parameters can lead to the suspicion of metastatic lymph nodes such as morphological criteria, dynamic enhancement characteristics, and abnormalities on diffusion sequences [44]. According to a meta-analysis, the sensitivity of MRI for the detection of lymph node metastases in early-stage breast cancer patients was 90%, with a 90% specificity [45].

Concerning 18F-FDG PET, its sensitivity to detect pathological lymph nodes is low (58–60%), because of the small size of some metastases and the finite spatial resolution of the PET detection system, and more generally, because of the partial volume effect [5, 32]. Concerning PET/MRI, we obtained a sensitivity of 79% for lymph node detection [24]. An example of local and regional staging by PET/MRI is shown in Fig. 14.3. However, PET's specificity in this indication is known to be
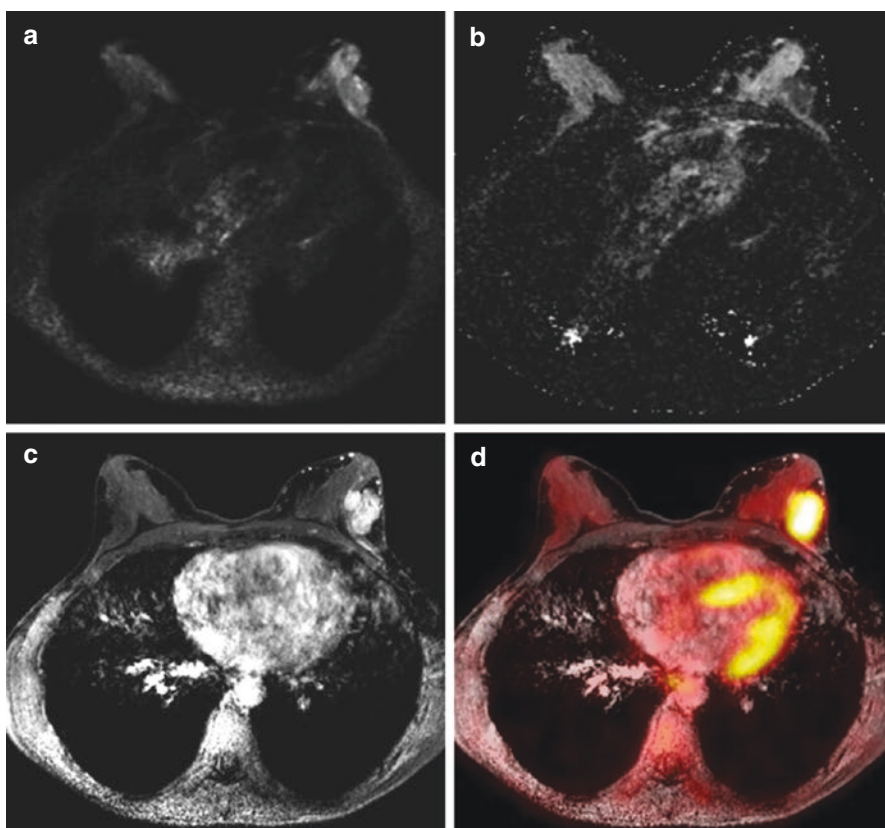
Fig. 14.3 Invasive ductal carcinoma of the left breast. Axial, DWI b1000 (**a**), ADC (**b**), T1-weighted fat-saturated after gadolinium injection (**c**), and 18F-FDG-PET/MR (**d**) in prone position showing a hypermetabolic lesion of the left breast with increased signal intensity on DWI, hypointense on ADC, and gadolinium enhancement

high (higher or equal to 94%) [29, 46, 47] equal or even higher than MRI's (90–92%) [32, 45, 48]. This supports the idea that PET-positive lymph nodes should be considered metastatic and treated consequently. The opposite scenario is not applicable, as for a patient with no positive lymph node detected on PET/MRI, the sentinel node procedure will still be essential for further treatment decision.

Among the previously cited studies, three deserve a more detailed description. First, in the study from Grueneisen et al. PET/CT, PET/MRI and MRI performed similarly for the detection of lymph node invasion in 49 patients [29]. In the study from Melsaether et al. unenhanced 18F-FDG-PET/CT was compared to 18F-FDG-PET/MRI with diffusion weighted and contrast-enhanced MRI sequences in 51 patients with breast cancer and found similar performances as well [6].

Taneja et al. considered 36 cases of histologically proven breast invasive ductal carcinoma and showed the high performances of PET/MRI and MRI, respectively, in detecting axillary lymph nodes metastases, with a 91% specificity for PET and MRI, respectively, and a 93.3% sensitivity for MRI, while the sensitivity for PET alone was much lower (60%) [32]. An advantage of combining both techniques was, once again, an increased diagnostic confidence score in comparison to PET or MRI alone [32].

14.2.1.3 Staging for Distant Metastases

Whole-body imaging to exclude metastases is now widely accepted for locally advanced breast cancers [49]. PET/CT is one of the different possible imaging modalities which can be proposed in this indication, and PET/MRI, showing equivalent performances in comparison to PET/CT in the detection of hypermetabolic lesions, should be considered as well [15], having moreover the advantage of being able to characterize more easily some benign FDG-avid foci [32].

We will discuss hereafter PET/MRI performances in the detection of possible metastases in the four main metastatic sites which together represent more than 83% of all the metastases in breast cancer patients: the bone, lung, liver, and brain.

Bone Metastatic Invasion

Bone is the most common metastatic site in breast cancer patients: approximately 42% of breast cancer metastases are osseous [50]. Therefore, distant staging must include bone imaging.

Even though the SUVs measured in bones with PET/MRI attenuation correction techniques are underestimated in comparison to SUVs obtained from PET/CT, some recent articles showed that combining MRI and PET findings improved the sensitivity of detection of bone metastases in comparison to PET/CT in breast cancer patients [6, 19, 51]. This is probably due to the fact that MRI usually performs better than CT for detection of bone marrow metastasis and that quantitative underestimation has limited impact on lesion detection. According to the largest study evaluating the performances of PET/MR in the detection of osseous metastases, contrast-enhanced PET/MR had a sensitivity of 96.3% for the detection of bone metastases and a specificity of 98.8% [51]. However, whole-body MRI for detection of bone metastasis is time-consuming, and this should be taken into account when deciding the MRI protocol of PET/MRI, especially with the sequential Philips unit. To our experience, and with the sequences

that are currently used in our institution, with a 90 min pure acquisition time, all bone metastases are detected by the means of PET only. This can be clearly reversed if using dedicated surface coils allowing higher-resolution sequences which can be available with more recent PET/MRI systems (Siemens, GE).

Lung Metastases

Representing approximately 22% of breast cancer metastases, lungs are the second most common metastatic sites in breast cancer patients [50]. PET/MRI's performance for lung metastases detection depends on the size of the lesions and the MRI sequences that are used and are still a matter of debate. According to Chandarana et al. PET/MRI had a 95.6% sensitivity to detect FDG-avid nodules and nodules of 5 mm diameter or higher, thanks to a radial T1-weighted gradient echo (radial volumetric interpolated breath-hold examination [VIBE]) MR sequence with simultaneously acquired PET [52]. However, sensitivity dropped to 70.9% when taking all the nodules into account [52]. Stolzmann et al. proposed the use of a three-dimensional (3D) DIXON-based dual-echo gradient echo pulse MRI sequence comparing it in 40 consecutive patients: although MRI showed a lower detection rate of pulmonary nodules in comparison to low-dose CT, they found no significant difference on a patient basis evaluation [53]. In the largest breast PET/MRI study including 51 patients, conducted by Melsaether et al., no significant difference was found on a per-patient analysis, but considering a lesion-based analysis, PET/CT was more sensitive than PET/MRI [6]. The same group however published results on the outcome of lung nodules missed on PET/MRI in patients with different primary malignancies including breast cancer: among 84 nodules missed on MRI and benefitting from a follow-up, only three progressed, ten regressed or even disappeared, and 71 remained stable [54]. In other words, only 3% of missed nodules on PET/MRI were malignant.

Appenzeller et al. found that PET/CT performed significantly better than PET/MRI in the detection of lung metastases from various cancers when using an axial two-point Dixon-based T1-weighted 3D gradient echo MR sequence acquired with the integrated quadrature body coil [20].

The clinical importance of pulmonary nodules smaller than 5 mm that can be found only on CT is a controversial topic and needs to be confirmed by further studies. Such small nodules cannot be biopsied, and the treatment of the patient will not be changed, even if such nodules are shown on preoperative CT.

Liver Metastases

When comparing 18F-FDG PET/CT and PET/MRI for the detection of liver metastasis in cases of gastrointestinal cancer, Reiner et al. showed a significant accuracy improvement when performing dynamic contrast-enhanced and DWI sequences instead of T1-W/T2-W sequences alone or contrast-enhanced PET/CT [55]. The diagnostic confidence was also reported to be higher while performing PET/MRI instead of PET/CT for the detection of liver metastases [55]. This group recommends the acquisition of dynamic contrast-enhanced MRI sequences.

Considering breast cancer patients exclusively, Melsaether et al. found that PET/MRI had a higher sensitivity than PET/CT in the detection of liver metastasis,

thanks to the DWI sequence which depicted 40 metastases in comparison to 28 for PET and 27 for the T1-weighted contrast-enhanced sequence [6]. Those results were obtained, as detailed before, thanks to the injection of a contrast agent during the liver station of the PET/MRI acquisition. However, as contrast enhancement can usually only be done once, the physician will have to choose whether the liver or the breasts will benefit from those enhanced images during this single session.

Brain Metastases

Brain metastases account for approximately 6% of breast cancer metastases. They may be difficult to detect with unenhanced 18F-FDG PET/CT because of the physiological high cerebral FDG uptake, but MRI performs better than does CT, even with non-specific whole-body sequences, when appropriate coils are in place. In the study from Melsaether et al. unfortunately, brain was not included in 27 patients out of 51 PET/CT acquisitions, and among the 24 patients benefiting from brain PET/CT and PET/MRI acquisitions, only one had brain metastases which were not seen on PET/CT but only on PET/MR images [6]. The contrast-enhanced T1-weighted sequence was more efficient in detecting those lesions than the DWI sequence [6].

14.2.2 Evaluation of Response to Therapy

An extensive review of the role of PET imaging in assessing early chemotherapy response in breast cancer was recently conducted by Humbert et al. [4]. It points out how heterogeneous are the publications on that subject: tumor characteristics, type, and sequence of treatments received as well as imaging conditions vary a lot from a study to another. More generally, a better harmonization of PET interpretation criteria would be needed which should take into account the specificity of each tumor subtype and the therapeutic conditions in which this PET is performed. However, 18F-FDG PET does give important information for each of the biological subtypes of breast cancer. This review also highlights the fact that the percentage reduction of SUVmax from pre- to post-chemotherapy is the main parameter nowadays used to assess the response with 18F-FDG PET. In the specific case of luminal HER2-negative subtypes, metabolic tumor volume seems to predict the response more accurately than SUV and, therefore, should be measured in concerned studies [4]. Kinetic metabolic parameters may show better performances for response assessment even though they are more difficult to determine and less used for the moment [4, 56, 57].

Concerning the performances of breast MRI in early prediction of the pathologic response to chemotherapy, a review of 13 articles showed an important data heterogeneity which did not permit statistical meta-analysis [58].

Achieving a pathological complete response (pCR) at the end of chemotherapy has an impact on prognosis [59]. The respective performances of 18F-FDG PET/CT and diffusion weighted MRI sequences in predicting a pCR at the end of a neoadjuvant chemotherapy have been calculated in a recent meta-analysis: 18F-FDG PET/CT has a higher sensitivity, and MRI is more specific, and therefore, both could be combined in order to improve the assessment of pCR after chemotherapy [60].

In this context, PET/MRI is a promising tool for the early assessment of response to therapy that could be used to carry on with more confidence a treatment which works and change a treatment that does not work in order to reduce unnecessary toxicity and to propose an alternative treatment more rapidly.

14.2.3 Detection of a Recurrence and Restaging Breast Cancer Patients

18F-FDG PET/CT is now recognized as a useful technique in assessing breast cancer recurrence [3]. Sawicki et al. recently proved the superiority of PET/MRI over PET/CT, MRI, and CT in whole-body staging of patients with suspected breast cancer recurrence, although only 21 patients were included: 18F-FDG PET/MRI identified correctly 98.5% of the lesions, 18F-FDG PET/CT 94.8%, and MRI 88.1%, whereas CT only identified 57.5% of them [61]. This confirmed earlier results of a meta-analysis showing better performance in the diagnosis of breast cancer recurrence for whole-body MRI and PET taken independently versus CT and ultrasound, and no significant difference between the respective pooled sensitivities of PET and MRI, reaching more than 95% [62]. In a study from Schmidt et al. concerning 33 breast cancer patients, whole-body MRI and 18F-FDG PET/CT showed a similar overall accuracy of 91% each, with sensitivity of 93% and 91%, respectively, and a specificity of 86% and 90%, respectively [63]. A high sensitivity of diffusion weighted whole-body MRI sequence to detect metastases in breast cancer recurrence was also reported, especially for bone, liver, and brain localizations, as well as a higher sensitivity of 18F-FDG PET/CT in comparison to MRI for pathological lymph node detection [63]. Performances of both techniques were reported to be similar in the detection of 15 lung metastases (although no information is given about their dimensions) with the use of a dedicated HASTE (half-Fourier single-shot TSE) sequence which has shown high efficiency in detecting small lung pathologies [63].

However, we have to keep in mind that in case of clinical suspicion of local recurrence, the first-line examination of choice is conventional imaging including digital mammography or tomosynthesis and ultrasound. PET/MR, if available, would have a place in the detection of distant metastases.

14.3   Potential Improvements and Future Role

14.3.1 Optimization of MRI Sequences in PET/MRI Protocols

As previously summarized, PET/MRI protocols have to be defined in order to get complementary information from each imaging modality, to minimize information redundancy, within a reasonably short time frame [64]. MRI sequences have to be optimized and selected specifically for each indication because they are more time-consuming than PET acquisitions [30, 65], and having a simultaneous acquisition of PET and MRI is a clear advantage to limit the total duration of these protocols [65].

Concerning dedicated breast MRI, the use of 3D T1-weighted Dixon sequence was proven to be more robust to fat saturation artifacts and also has the advantage of providing both T1 without and T1 with fat saturation images [66]. Multiparametric MRI with the addition of spectroscopic information to characterize suspicious lesions is also promising since it gives access to specific metabolite measurements such as choline (cellular proliferation), N-acetyl-aspartate, creatine, and lactate [67, 68], which may allow a reduction of unnecessary breast lesion biopsies. However, we need large prospective studies to evaluate its clinical contribution and its cost-effectiveness, and its feasibility is limited by time constraints [69]. MRI has also greatly benefitted from the multi-transmit technology since it was often a problem in breast imaging at 3 T due to RF inhomogeneities in this area. Using multi-transmission also allowed reducing significantly the acquisition time for some sequences since the more homogeneous SAR deposition permitted a shorter TR. In our experience, the acquisition time of T2 TSE sequence could be divided by 2 with improved image homogeneity.

A basic whole-body PET/MRI protocol, in order to obtain at least the diagnostic accuracy of an unenhanced PET/CT, should include whole-body transaxial T1- and T2-weighted acquisitions and dedicated sequences for chest and upper abdomen [65]. Whole-body MRI sequences could also greatly benefit from the systematic use of surface coils. Indeed, it would allow a better signal to noise ratio than with the integrated quadrature body coil and a better resolution for morphological images. This could be performed via parallel imaging acceleration techniques in order to keep the acquisition time reasonable.

14.3.2 New PET Radiopharmaceuticals

The introduction in clinical routine of new PET radiopharmaceuticals, as described in a former work, which will give specific molecular information noninvasively, will probably change clinical workup for many breast cancer patients [5]. More precisely, as metastases in a single patient may have various characteristics, with different genotype profiles and phenotype expressions, the therapeutical strategies would ideally be not only adapted patient by patient, but lesion by lesion, through the use of specific targeted treatments [5]. For example, estrogen and progesterone receptor radioligands can be used in order to decide whether a hormonotherapy should be proposed. 18F-NaF could eventually be injected at the same time as 18F-FDG in order to optimize bone metastasis detection, as proposed by Iagaru et al. [70].

Conclusions

PET/MRI is a valuable diagnostic modality, with performances comparable or higher than PET/CT, for staging, evaluation of response to therapy and restaging breast cancer, except for the evaluation of lung metastases, which is still a debated issue.

Current evidence is based mainly on the use of FDG, but soon the larger use of specific PET tracers in breast cancer patients could improve the accuracy and

sensitivity of metastases' detection and could help establish a "lesion-specific" management. Thus, when available, PET/MRI could replace PET/CT, especially for young patients, in the different phases of breast cancer patients' management. The main open questions are the optimization of PET/MRI protocols, as well as the evaluation of the cost-effectiveness of this new imaging modality.

References

1. Ferlay JSI, Ervik M, Dikshit R, Eser S, Mathers C, Rebelo M, Parkin DM, Forman D, Bray, F. Cancer incidence and mortality worldwide: IARC Cancer Base No. 11 GLOBOCAN 2012 v11; 2012.
2. Cardoso F, Costa A, Norton L, et al. ESO-ESMO 2nd international consensus guidelines for advanced breast cancer (ABC2). Breast. 2014;23(5):489–502.
3. Gradishar WJ, Anderson BO, Blair SL, et al. Breast cancer version 3.2014. J Natl Compr Cancer Netw. 2014;12(4):542–90.
4. Humbert O, Cochet A, Coudert B, et al. Role of positron emission tomography for the monitoring of response to therapy in breast cancer. Oncologist. 2015;20(2):94–104.
5. Tabouret-Viaud C, Botsikas D, Delattre BM, et al. PET/MR in breast cancer. Semin Nucl Med. 2015;45(4):304–21.
6. Melsaether AN, Raad RA, Pujara AC, et al. Comparison of whole-body 18F FDG PET/MR imaging and whole-body 18F FDG PET/CT in terms of lesion detection and radiation dose in patients with breast cancer. Radiology. 2016;281(1):193–202.
7. Schulz V, Torres-Espallardo I, Renisch S, et al. Automatic, three-segment, MR-based attenuation correction for whole-body PET/MR data. Eur J Nucl Med Mol Imaging. 2011;38(1):138–52.
8. Eiber M, Martinez-Moller A, Souvatzoglou M, et al. Value of a Dixon-based MR/PET attenuation correction sequence for the localization and evaluation of PET-positive lesions. Eur J Nucl Med Mol Imaging. 2011;38(9):1691–701.
9. Arabi H, Rager O, Alem A, Varoquaux A, Becker M, Zaidi H. Clinical assessment of MR-guided 3-class and 4-class attenuation correction in PET/MR. Mol Imaging Biol. 2014;17(2):264–76.
10. Samarin A, Burger C, Wollenweber SD, et al. PET/MR imaging of bone lesions--implications for PET quantification from imperfect attenuation correction. Eur J Nucl Med Mol Imaging. 2012;39(7):1154–60.
11. Kalemis A, Delattre BM, Heinzer S. Sequential whole-body PET/MR scanner: concept, clinical use, and optimisation after two years in the clinic. The manufacturer's perspective. MAGMA. 2013;26(1):5–23.
12. Cho I, Kong E, Chun K. Image artifacts from MR-based attenuation correction in dedicated PET/MR breast coil for PET/MR mammography. EJNMMI Phys. 2015;2(Suppl 1):A62.
13. Wiesmuller M, Quick HH, Navalpakkam B, et al. Comparison of lesion detection and quantitation of tracer uptake between PET from a simultaneously acquiring whole-body PET/MR hybrid scanner and PET from PET/CT. Eur J Nucl Med Mol Imaging. 2013;40(1):12–21.
14. Varoquaux A, Rager O, Poncet A, et al. Detection and quantification of focal uptake in head and neck tumours: (18)F-FDG PET/MR versus PET/CT. Eur J Nucl Med Mol Imaging. 2014;41(3):462–75.
15. Drzezga A, Souvatzoglou M, Eiber M, et al. First clinical experience with integrated whole-body PET/MR: comparison to PET/CT in patients with oncologic diagnoses. J Nucl Med. 2012;53(6):845–55.
16. Kershah S, Partovi S, Traughber BJ, et al. Comparison of standardized uptake values in normal structures between PET/CT and PET/MRI in an oncology patient population. Mol Imaging Biol. 2013;15(6):776–85.

17. Heusch P, Buchbender C, Beiderwellen K, et al. Standardized uptake values for [(1)(8)F] FDG in normal organ tissues: comparison of whole-body PET/CT and PET/MRI. Eur J Radiol. 2013;82(5):870–6.
18. Pace L, Nicolai E, Luongo A, et al. Comparison of whole-body PET/CT and PET/MRI in breast cancer patients: lesion detection and quantitation of 18F-deoxyglucose uptake in lesions and in normal organ tissues. Eur J Radiol. 2014;83(2):289–96.
19. Pujara AC, Raad RA, Ponzo F, et al. Standardized uptake values from PET/MRI in metastatic breast cancer: an organ-based comparison with PET/CT. Breast J. 2016;22(3):264–73.
20. Appenzeller P, Mader C, Huellner MW, et al. PET/CT versus body coil PET/MRI: how low can you go? Insights Imaging. 2013;4(4):481–90.
21. Barbosa Fde G, von Schulthess G, Veit-Haibach P. Workflow in simultaneous PET/MRI. Semin Nucl Med. 2015;45(4):332–44.
22. Buchbender C, Hartung-Knemeyer V, Beiderwellen K, et al. Diffusion-weighted imaging as part of hybrid PET/MRI protocols for whole-body cancer staging: does it benefit lesion detection? Eur J Radiol. 2013;82(5):877–82.
23. Zytoon AA, Murakami K, El-Kholy MR, El-Shorbagy E. Dual time point FDG-PET/CT imaging... Potential tool for diagnosis of breast cancer. Clin Radiol. 2008;63(11):1213–27.
24. Botsikas D, Kalovidouri A, Becker M, et al. Clinical utility of 18F-FDG-PET/MR for preoperative breast cancer staging. Eur Radiol. 2016;26(7):2297–307.
25. Osman Ratib MS, Beyer T. Atlas of PET/MR imaging in oncology. Berlin: Springer; 2013.
26. Aklan B, Paulus DH, Wenkel E, et al. Toward simultaneous PET/MR breast imaging: systematic evaluation and integration of a radiofrequency breast coil. Med Phys. 2013;40(2):024301.
27. Dregely I, Lanz T, Metz S, et al. A 16-channel MR coil for simultaneous PET/MR imaging in breast cancer. Eur Radiol. 2015;25(4):1154–61.
28. Oehmigen M, Lindemann ME, Lanz T, Kinner S, Quick HH. Integrated PET/MR breast cancer imaging: attenuation correction and implementation of a 16-channel RF coil. Med Phys. 2016;43(8):4808.
29. Grueneisen J, Nagarajah J, Buchbender C, et al. Positron emission tomography/magnetic resonance imaging for local tumor staging in patients with primary breast cancer: a comparison with positron emission tomography/computed tomography and magnetic resonance imaging. Investig Radiol. 2015;50(8):505–13.
30. Huellner MW, Appenzeller P, Kuhn FP, et al. Whole-body nonenhanced PET/MR versus PET/CT in the staging and restaging of cancers: preliminary observations. Radiology. 2014;273(3):859–69.
31. Kuhn FP, Crook DW, Mader CE, Appenzeller P, von Schulthess GK, Schmid DT. Discrimination and anatomical mapping of PET-positive lesions: comparison of CT attenuation-corrected PET images with coregistered MR and CT images in the abdomen. Eur J Nucl Med Mol Imaging. 2013;40(1):44–51.
32. Taneja S, Jena A, Goel R, Sarin R, Kaul S. Simultaneous whole-body F-FDG PET-MRI in primary staging of breast cancer: a pilot study. Eur J Radiol. 2014;83(12):2231–9.
33. Kuhl C. The current status of breast MR imaging. Part I. Choice of technique, image interpretation, diagnostic accuracy, and transfer to clinical practice. Radiology. 2007;244(2):356–78.
34. Kuhl CK. Current status of breast MR imaging. Part 2. Clinical applications. Radiology. 2007;244(3):672–91.
35. Biglia N, Bounous VE, Martincich L, et al. Role of MRI (magnetic resonance imaging) versus conventional imaging for breast cancer presurgical staging in young women or with dense breast. Eur J Surg Oncol. 2011;37(3):199–204.
36. Moy L, Noz ME, Maguire GQ Jr, et al. Role of fusion of prone FDG-PET and magnetic resonance imaging of the breasts in the evaluation of breast cancer. Breast J. 2010;16(4):369–76.
37. Ohara M, Shigematsu H, Tsutani Y, et al. Role of FDG-PET/CT in evaluating surgical outcomes of operable breast cancer--usefulness for malignant grade of triple-negative breast v. Breast. 2013;22(5):958–63.

38. Uematsu T, Kasami M, Yuen S. Comparison of FDG PET and MRI for evaluating the tumor extent of breast cancer and the impact of FDG PET on the systemic staging and prognosis of patients who are candidates for breast-conserving therapy. Breast Cancer. 2009;16(2):97–104.

39. Kitajima K, Yamano T, Fukushima K, et al. Correlation of the SUVmax of FDG-PET and ADC values of diffusion-weighted MR imaging with pathologic prognostic factors in breast carcinoma. Eur J Radiol. 2016;85(5):943–9.

40. Baba S, Isoda T, Maruoka Y, et al. Diagnostic and prognostic value of pretreatment SUV in 18F-FDG/PET in breast cancer: comparison with apparent diffusion coefficient from diffusion-weighted MR imaging. J Nucl Med. 2014;55(5):736–42.

41. Jalaguier-Coudray A, Delarbre B, Brenot-Rossi I, et al. Contribution of FDG PET/CT for the optimization of the management of additional lesions detected on local staging breast MRI. AJR Am J Roentgenol. 2016;206(4):891–900.

42. Gerlinger M, Rowan AJ, Horswell S, et al. Intratumor heterogeneity and branched evolution revealed by multiregion sequencing. N Engl J Med. 2012;366(10):883–92.

43. Schmitz J, Schwab J, Schwenck J, et al. Decoding Intratumoral heterogeneity of breast cancer by multiparametric in vivo imaging: a translational study. Cancer Res. 2016;76(18):5512–22.

44. He N, Xie C, Wei W, et al. A new, preoperative, MRI-based scoring system for diagnosing malignant axillary lymph nodes in women evaluated for breast cancer. Eur J Radiol. 2012;81(10):2602–12.

45. Harnan SE, Cooper KL, Meng Y, et al. Magnetic resonance for assessment of axillary lymph node status in early breast cancer: a systematic review and meta-analysis. Eur J Surg Oncol. 2011;37(11):928–36.

46. Robertson IJ, Hand F, Kell MR. FDG-PET/CT in the staging of local/regional metastases in breast cancer. Breast. 2011;20(6):491–4.

47. Veronesi U, De Cicco C, Galimberti VE, et al. A comparative study on the value of FDG-PET and sentinel node biopsy to identify occult axillary metastases. Ann Oncol. 2007;18(3):473–8.

48. Heusner TA, Kuemmel S, Hahn S, et al. Diagnostic value of full-dose FDG PET/CT for axillary lymph node staging in breast cancer patients. Eur J Nucl Med Mol Imaging. 2009;36(10):1543–50.

49. Groheux D, Cochet A, Humbert O, Alberini JL, Hindie E, Mankoff D. (1)(8)F-FDG PET/CT for staging and restaging of breast cancer. J Nucl Med. 2016;57(Suppl 1):17S–26S.

50. Schootman M, Jeffe DB, Gillanders WE, Aft R. Racial disparities in the development of breast cancer metastases among older women: a multilevel study. Cancer. 2009;115(4):731–40.

51. Catalano OA, Nicolai E, Rosen BR, et al. Comparison of CE-FDG-PET/CT with CE-FDG-PET/MR in the evaluation of osseous metastases in breast cancer patients. Br J Cancer. 2015;112(9):1452–60.

52. Chandarana H, Heacock L, Rakheja R, et al. Pulmonary nodules in patients with primary malignancy: comparison of hybrid PET/MR and PET/CT imaging. Radiology. 2013;268(3):874–81.

53. Stolzmann P, Veit-Haibach P, Chuck N, et al. Detection rate, location, and size of pulmonary nodules in trimodality PET/CT-MR: comparison of low-dose CT and Dixon-based MR imaging. Investig Radiol. 2013;48(5):241–6.

54. Raad RA, Friedman KP, Heacock L, Ponzo F, Melsaether A, Chandarana H. Outcome of small lung nodules missed on hybrid PET/MRI in patients with primary malignancy. J Magn Reson Imaging. 2016;43(2):504–11.

55. Reiner CS, Stolzmann P, Husmann L, et al. Protocol requirements and diagnostic value of PET/MR imaging for liver metastasis detection. Eur J Nucl Med Mol Imaging. 2014;41(4):649–58.

56. Dunnwald LK, Doot RK, Specht JM, et al. PET tumor metabolism in locally advanced breast cancer patients undergoing neoadjuvant chemotherapy: value of static versus kinetic measures of fluorodeoxyglucose uptake. Clin Cancer Res. 2011;17(8):2400–9.

57. Humbert O, Riedinger JM, Vrigneaud JM, et al. 18F-FDG PET derived tumor blood flow changes after one cycle of neoadjuvant chemotherapy predicts outcome in triple-negative breast cancer. J Nucl Med. 2016;57(11):1707–12.

58. Marinovich ML, Sardanelli F, Ciatto S, et al. Early prediction of pathologic response to neoadjuvant therapy in breast cancer: systematic review of the accuracy of MRI. Breast. 2012;21(5):669–77.
59. von Minckwitz G, Untch M, Blohmer JU, et al. Definition and impact of pathologic complete response on prognosis after neoadjuvant chemotherapy in various intrinsic breast cancer sub-types. J Clin Oncol. 2012;30(15):1796–804.
60. Liu Q, Wang C, Li P, Liu J, Huang G, Song S. The role of (18)F-FDG PET/CT and MRI in assessing pathological complete response to neoadjuvant chemotherapy in patients with breast cancer: a systematic review and meta-analysis. Biomed Res Int. 2016;2016:3746232.
61. Sawicki LM, Grueneisen J, Schaarschmidt BM, et al. Evaluation of (1)(8)F-FDG PET/MRI, (1)(8)F-FDG PET/CT, MRI, and CT in whole-body staging of recurrent breast cancer. Eur J Radiol. 2016;85(2):459–65.
62. Pan L, Han Y, Sun X, Liu J, Gang H. FDG-PET and other imaging modalities for the evaluation of breast cancer recurrence and metastases: a meta-analysis. J Cancer Res Clin Oncol. 2010;136(7):1007–22.
63. Schmidt GP, Baur-Melnyk A, Haug A, et al. Comprehensive imaging of tumor recurrence in breast cancer patients using whole-body MRI at 1.5 and 3 T compared to FDG-PET-CT. Eur J Radiol. 2008;65(1):47–58.
64. von Schulthess GK. Why buy a PET/MR for high end research? J Magn Reson Imaging. 2014;40(2):283–4.
65. von Schulthess GK, Veit-Haibach P. Workflow considerations in PET/MR imaging. J Nucl Med. 2014;55(Supplement 2):19S–24S.
66. Ma J. Dixon techniques for water and fat imaging. J Magn Reson Imaging. 2008;28(3):543–58.
67. Belkic D, Belkic K. Molecular imaging in the framework of personalized cancer medicine. Isr Med Assoc J. 2013;15(11):665–72.
68. Pinker K, Bogner W, Baltzer P, et al. Improved differentiation of benign and malignant breast tumors with multiparametric 18fluorodeoxyglucose positron emission tomography magnetic resonance imaging: a feasibility study. Clin Cancer Res. 2014;20(13):3540–9.
69. Menezes GL, Knuttel FM, Stehouwer BL, Pijnappel RM, van den Bosch MA. Magnetic resonance imaging in breast cancer: a literature review and future perspectives. World J Clin Oncol. 2014;5(2):61–70.
70. Iagaru A, Mittra E, Yaghoubi SS, et al. Novel strategy for a cocktail 18F-fluoride and 18F-FDG PET/CT scan for evaluation of malignancy: results of the pilot-phase study. J Nucl Med. 2009;50(4):501–5.

Hepatobiliary and Pancreatic Cancer PET/MRI

15

Thomas A. Hope

Contents

15.1   Main Pulse Sequences Used for Liver MRI

Liver MRI involves three main imaging sequences: Pre- and post-contrast T1-weighted images, diffusion-weighted imaging, and T2-weighted imaging:

T.A. Hope

Department of Radiology and Biomedical Imaging, University of California, San Francisco, San Francisco, CA, USA

Department of Radiology, San Francisco VA Medical Center, San Francisco, CA, USA
e-mail: thomas.hope@ucsf.edu

15.1.1 T2-Weighted Imaging

T2-weighted imaging in the liver is used to help characterize lesions and biliary anatomy. Signal intensity on T2-weighted imaging can help define benign lesions such as cysts and hemangiomas that have characteristic high T2 signal intensity, while hepatic metastases and primary hepatic tumors have intermediate signal intensities higher than that of background liver.

The three decisions in liver MRI for T2-weighted images are to determine if coronal or axial should be used, whether or not fat saturation should be used, and whether single-shot or fast spin-echo techniques should be used. Typically coronal acquisitions are used to evaluate for biliary anatomy as the common bile duct and pancreatic ducts are typically in plane. Axial acquisitions are used to evaluate for parenchymal lesions as well as lymphadenopathy. Fat saturation is used in order to increase lesion conspicuity in the liver. Single-shot techniques (SSFSE and HASTE) are used to prevent motion artifact and for speed but have intrinsically worse T2 contrast compared to fast spin-echo techniques (FSE and TSE).

15.1.2 Diffusion-Weighted Imaging

Diffusion-weighted imaging (DWI) is an MRI acquisition that is sensitive to the motion of water molecules. Water moves based on Brownian motion and can be restricted by the presence of cell membranes, organelles, and other proteins. The physics of DWI is discussed in Chap. 3. In liver MRI, a low b-value acquisition ($b = 0$ or $b = 50$) is acquired along with a high b-value acquisition ($b = 500$–800). Two b-values are required in order to characterize T2 shine through, which is when there is high signal seen on the high b-value image that is due to intrinsic T2 hyperintensity rather than restricted diffusion. DWI has a high detection rate for metastatic disease within the liver [1, 2], although motion involving the left lobe of the liver and field inhomogeneity along the diaphragm can create significant artifact limiting DWI imaging in the liver. In addition to detection, DWI can be used to characterize treatment response, with an increase in the apparent diffusion coefficient (i.e., less reduced diffusion) associated with cell death and good treatment response [3–5].

15.1.3 Hepatobiliary Phase Imaging

Hepatobiliary phase (HBP) imaging is important in the setting of PET/MRI, and please refer to the chapter on MRI contrast agents for further details on HBP imaging agents. HBP imaging is predominantly used for the detection of metastatic disease to the liver, and gadoxetate has been shown to outperform FDG PET for the detection of hepatic metastases [6], this is particularly important for lesions less than 1 cm. In addition to improved detection sensitivity compared to CT and FDG PET, there are two additional benefits to HBP imaging in PET/MRI:

1. Ability to acquire navigated sequences: In MRI one can use image-based and bellows-based navigators to acquire images during free breathing and reconstruct images from different phases during the respiratory cycle. In PET/MRI this is particularly relevant as PET data are typically reconstructed during end expiration and MRI sequences are acquired during breathholds. This limits the accuracy of fusion for PET and MRI data. When hepatobiliary phase images are acquired using navigated approaches, images during end expiration can be acquired allowing for accurate fusion of PET and MRI images allowing for easier image interpretation [7].

2. Consistent lesion measurement: HBP imaging is not dependent on bolus timing that can dramatically effect lesion measurement during dynamic phases. Therefore when measuring lesion size across time, changes in size are more accurately characterized when comparing HBP images compared to other sequences.

One important false positive on HBP imaging for metastatic disease are hemangiomas. Extracellular contrast agents accurately characterize hemangiomas as they follow blood pool signal intensity, but HBA struggle with hemangiomas as they appear nearly identical to metastatic lesions due to the fast clearance of the contrast agent from the blood pool [8]. Therefore it is important to correlate with T2-weighted images to determine if lesions are metastases or hemangiomas when using HBAs.

15.2   Issues Related to Motion

Simultaneous PET/MRI of the liver results in new issues related to respiratory motion that are not present in PET/CT (Fig. 15.1). In PET/CT, patient's breath shallowly during the entire PET acquisition as the CT acquisition is done sequentially. As the PET data is acquired during the MR acquisition in PET/MRI, there are multiple breathholds that result in respiratory ghosting, which refers to a duplication of the lesions inferior to the actual lesion in the PET images. Additionally there is blurring along the inferior margin of the lesion due to shallow breathing that is seen in both PET/MRI and PET/CT. There are numerous approaches to removing motion artifacts from PET data, which can be found in Chap. 6.

In addition to motion artifacts in the PET data, registration between the MRI and PET images is problematic as most MRI sequences are acquired during an inspiratory breathhold, while PET images are predominantly reconstructed using data from end expiration. One way to address this is by using navigated sequences, where MRI-based motion navigators are used to acquire the MRI data only during end expiration allowing for accurate fusion between PET and MRI data (Fig. 15.1) [9]. Navigators can be used to acquire higher resolution images and are particularly robust during the HBP when the liver parenchyma is hyperintense relative to other tissues [10].
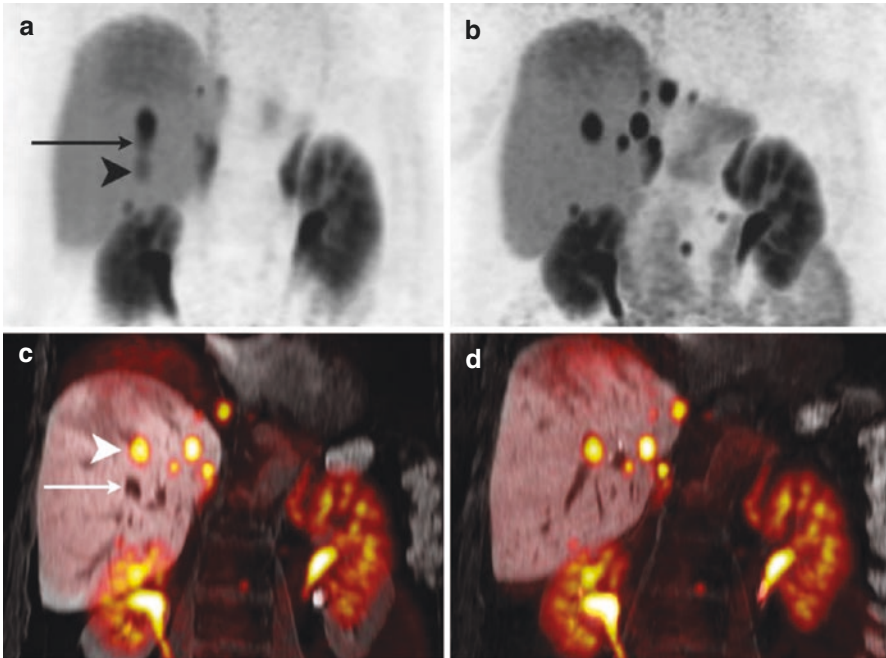
Fig. 15.1 Improved motion compensation with PET/MRI. Seventy-year-old female with small bowel neuroendocrine tumor metastatic to the liver. Fifteen-minute acquisition demonstrates both respiratory blurring (**a**, black arrow) from shallow breathing throughout the acquisition and ghosting (**a**, black arrow hear) from breathholds performed during the simultaneous acquisition. The use of respiratory compensation (bellows based in this case) removes both blurring and ghosting resulting in crisp delineation of the metastatic lesions (**b**). Simultaneous hepatobiliary phase MRI performed with breathholds misregisters to the PET data with the PET lesions (**c**, white arrowhead) being superior to the MRI lesions (**c**, white arrow), while navigated acquisitions allow for accurate fusion between the two acquisitions (**d**)

15.3 Workflow Considerations

There are two main approaches to performing liver PET/MRI. The first is to include the liver acquisition in the whole-body acquisition. This is time efficient but does not allow for significant time to be spent of dedicated liver imaging. Nonetheless it is possible to acquire a few simultaneous liver-specific sequences during a whole-body acquisition.

The second approach is to acquire the whole-body acquisition separate from the dedicated liver acquisition. This is more time intensive but allows for more time to be dedicated to the liver acquisition. A near complete liver MRI can be acquired in about 15–20 min, if DWI and T2-weighted imaging need to be acquired in addition to contrast-enhanced images. Some groups have not acquired PET data during the liver acquisition [11], but we have found the extra PET data to increase detection sensitivity and to allow for better motion correction [7, 9]. One alternative when using

hepatobiliary agents is to acquire the whole-body acquisition in the delay between the portal venous phase acquisition and the HBP acquisition. The split approach allows for more efficient use of time but does not provide DWI and T2-weighted imaging. Therefore this approach is particularly relevant if prior imaging is available to characterize cysts and hemangiomas that may mimic metastases on HBP imaging.

15.4 Clinical Applications of Liver PET/MRI

15.4.1 Metastatic Disease

The most common application of liver imaging in oncology is to evaluate the liver for the presence of metastatic disease (Fig. 15.2). Liver MRI has a higher sensitivity for the presence of metastatic lesions compared to contrast-enhanced CT, particularly with the use of DWI and hepatobiliary phase imaging [6, 12, 13]. Additionally, HBP MRI has been shown to be superior to contrast-enhanced FDG PET/CT for the detection of liver metastases in patients with colorectal cancer [6]. Although PET/MRI has increased detection sensitivity compared to contrast-enhanced CT or FDG PET, it has not yet been demonstrated to be superior to HBP MRI [14, 15].

15.4.2 Neuroendocrine Tumors

The majority of neuroendocrine tumors (NETs) originate in the abdomen, typically in the small bowel or the pancreas. The two most common locations for metastatic disease are mesenteric nodes and the liver. Hepatic metastases are particularly important as liver failure is the most common pathway for morbidity in these patients. Therefore following liver lesions is particularly relevant in these patients.

Somatostatin receptor PET (discussed further in Chap. 17) targets the somatostatin receptor using radiolabeled analogs of somatostatin [16]. ^{68}Ga-DOTA-TATE and ^{68}Ga-DOTA-TOC are the two most commonly used agents, and DOTA-TATE is the
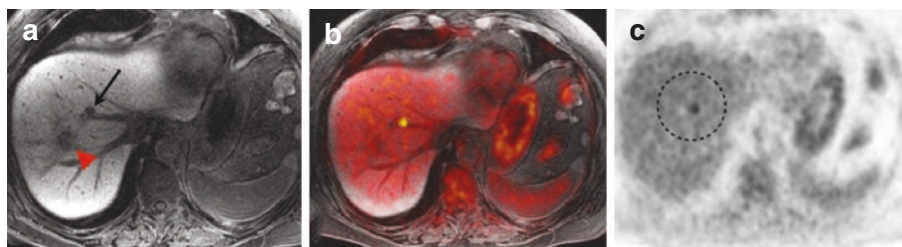

Fig. 15.2 Metastatic liver lesion in a 59-year-old man with metastatic colorectal cancer. FDG PET can help differentiate between posttreatment-related changes and recurrent disease. Hepatobiliary phase hypointensity can be seen in both treatment related changes (**a**, red arrow) and recurrent lesions (**a**, black arrow). Viable metastatic disease can be seen with focal uptake on FDG PET (**c**, dotted circle)

only agent currently approved by the Food and Drug Administration in the United States. The motivation for PET/MRI in NETs is the ability to combine MR liver imaging with somatostatin receptor PET. Additionally, not all NETs express the somatostatin receptor, and therefore DWI and contrast-enhanced sequences are central in lesion characterization [17].

15.4.3 Hepatocellular Carcinoma

Hepatocellular carcinomas (HCCs) are the most common primary tumor of the liver. Although they can arise in normal livers, they most frequently occur in patients with chronic liver diseases such as patients with hepatitis B or hepatitis C virus. The gold standard imaging of HCCs is MRI using extracellular agents, although there also is a role for hepatobiliary phase imaging in these patients as well [18]. MRI is preferred over CT as it is better at characterizing lesions, particularly for detecting the major criteria laid out in the Liver Imaging Reporting and Data System (LI-RADS) [19, 20].

The issue with HCCs is that not all HCCs are hypermetabolic on FDG PET [21]. Poorly differentiated HCCs are more likely to be hypermetabolic on FDG PET, and those lesions with uptake seen on FDG have a poor outcome. Well-differentiated HCCs are better evaluated using radiolabeled choline derivatives [22]. Neither FDG nor choline PET outperforms MRI for the detection and characterization of HCC, and PET is infrequently used to stage or follow patients with HCC. One exception is in patients with chronic kidney disease where contrast agents cannot be administered. In this case, FDG can be used in place of iodinated or gadolinium contrast and helpful to follow tumor response to targeted treatments.

15.4.4 ^{90}Y Radioembolization

There are three roles for PET/MRI in patients being treated with ^{90}Y radioembolization. The first is to help perform target lesion dosimetry. With the increased detector sensitivities used in the PET/MRI compared to PET/CT, the positrons emitted from ^{90}Y can be imaged allowing for direct visualization of administered dose [23, 24], which can allow for prediction of lesion response prior to radiographic evidence of response. Second, PET/MRI can be used to measure treatment response. Multiple studies have also shown that FDG PET can be an earlier response marker than anatomic or DWI, which may allow for earlier adjustments to treatment strategy [25–27].

15.4.5 Cholangiocarcinoma

Cholangiocarcinomas are a tumor of the bile ducts and are broken up by site of origin. Cholangiocarcinomas are almost uniformly hypermetabolic on FDG PET [28]. Cholangiocarcinomas can be broken down into three subtypes: intrahepatic,
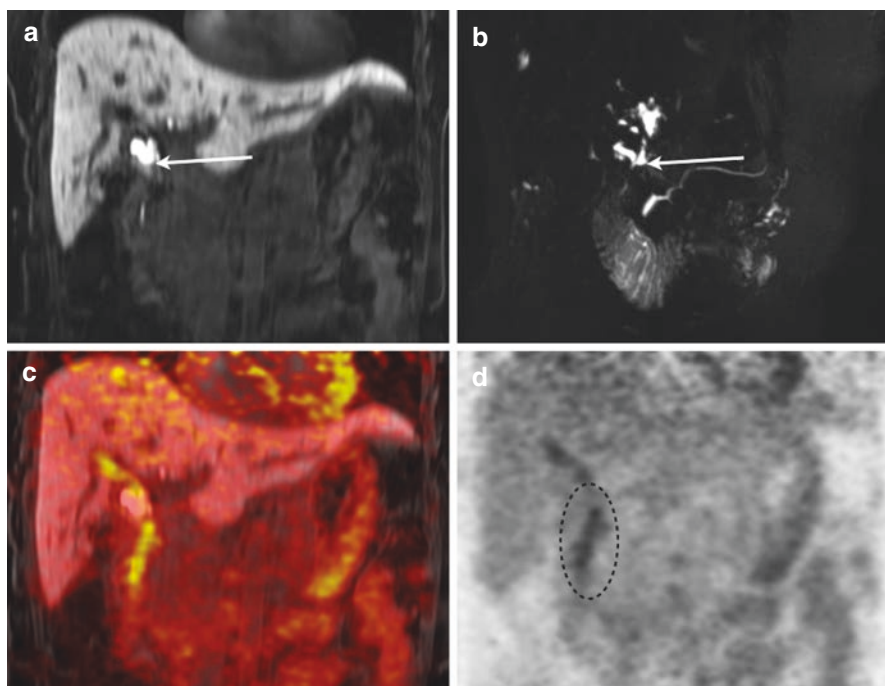
Fig. 15.3 Extrahepatic cholangiocarcinoma. Sixty-year-old man with extra hepatic cholangiocarcinoma extending along the common bile duct (CBD). The CBD is occluded from the confluence to the pancreatic duct with an abrupt cutoff at the biliary confluence (**a**, **b**, white arrow). MRI sequences cannot depict the actual tumor but rather only the narrowing of the CBD. FDG PET (**c**, **d**) shows linear uptake along the length of the stricture delineating the length of tumor involvement.

extrahepatic, and hilar. Hilar and extrahepatic tumors are frequently difficult to directly visualize as they grow along the common bile duct and biliary strictures are frequently the only sign of their presence. FDG PET can be helpful to visualize their extent (Fig. 15.3).

15.4.6 Pancreatic Adenocarcinoma

Initial staging of patients with pancreatic adenocarcinomas is likely to continue to be performed using contrast-enhanced CT, but there is a role for the use of PET/MRI in the evaluation of treatments response. Although one head-to-head study between PET/MRI and PET/CT did demonstrate equivalence in preoperative staging between the two techniques [29]. After treatment, the large fibrotic response within the primary tumor often prevents changes in size to indicate treatment effect, therefore other modalities need to be used such as changes in FDG uptake and ADC values. Although not yet evaluated in the literature, the ability of simultaneous PET/

MRI in this setting remains promising. To overcome the fact that FDG uptake in pancreatic adenocarcinoma is low, the development of novel tracers will increase the role of PET in the imaging of pancreatic adenocarcinoma [30–32].

For the evaluation of intraductal papillary mucinous neoplasm (IPMN), MRI is the optimal imaging modality for evaluating the cystic components of the lesion and evaluating for main duct involvement. FDG PET on the other hand is valuable in determining if there is malignant degeneration within the lesion to adenocarcinoma. Although the use of combined PET/MRI has only briefly been mentioned for this indication, it has potential benefit for patients at high risk for malignant transformation of IPMN [33, 34].

Conclusion

Simultaneous liver PET/MRI will play an important role in the initial staging and evaluating treatment response for liver metastases. HBP imaging is a key component of liver PET/MRI as it allows for high-resolution navigated imaging. Additionally the extra PET data acquired during a dedicated liver PET can be used to implement motion compensation techniques.

References

1. Soyer P, Boudiaf M, Placé V, et al. Preoperative detection of hepatic metastases: comparison of diffusion-weighted, T2-weighted fast spin echo and gadolinium-enhanced MR imaging using surgical and histopathologic findings as standard of reference. Eur J Radiol. 2011;80:245–52.
2. d'Assignies G, Fina P, Bruno O, et al. High sensitivity of diffusion-weighted MR imaging for the detection of liver metastases from neuroendocrine tumors: comparison with T2-weighted and dynamic gadolinium-enhanced MR imaging. Radiology. 2013;268:390–9.
3. Bonekamp S, Jolepalem P, Lazo M, Gulsun MA, Kiraly AP, Kamel IR. Hepatocellular carcinoma: response to TACE assessed with semiautomated volumetric and functional analysis of diffusion-weighted and contrast-enhanced MR imaging data. Radiology. 2011;260:752–61.
4. Gowdra Halappa V, Corona-Villalobos CP, Bonekamp S, et al. Neuroendocrine liver metastasis treated by using intraarterial therapy: volumetric functional imaging biomarkers of early tumor response and survival. Radiology. 2013;266:502–13.
5. Kokabi N, Camacho JC, Xing M, et al. Apparent diffusion coefficient quantification as an early imaging biomarker of response and predictor of survival following yttrium-90 radioembolization for unresectable infiltrative hepatocellular carcinoma with portal vein thrombosis. Abdom Imaging. 2014;39:969–78.
6. Seo HJ, Kim M-J, Lee JD, Chung W-S, Kim Y-E. Gadoxetate disodium-enhanced magnetic resonance imaging versus contrast-enhanced 18F-fluorodeoxyglucose positron emission tomography/computed tomography for the detection of colorectal liver metastases. Investig Radiol. 2011;46:548–55.
7. Hope TA, Pampaloni MH, Nakakura E, et al. Simultaneous (68)Ga-DOTA-TOC PET/MRI with gadoxetate disodium in patients with neuroendocrine tumor. Abdom Imaging. 2015;40:1432–40.
8. Tamada T, Ito K, Yamamoto A, et al. Hepatic hemangiomas: evaluation of enhancement patterns at dynamic MRI with gadoxetate disodium. AJR Am J Roentgenol. 2011;196:824–30.
9. Hope TA, Verdin EF, Bergsland EK, Ohliger MA, Corvera CU, Nakakura EK. Correcting for respiratory motion in liver PET/MRI: preliminary evaluation of the utility of bellows and navigated hepatobiliary phase imaging. EJNMMI Phys. 2015;2:21.

10. Nagle SK, Busse RF, Brau AC, et al. High resolution navigated three-dimensional T_1-weighted hepatobiliary MRI using gadoxetic acid optimized for 1.5 Tesla. J Magn Reson Imaging. 2012;36:890–9.

11. Kang B, Lee JM, Song YS, et al. Added value of integrated whole-body PET/MRI for evaluation of colorectal cancer: comparison with contrast-enhanced MDCT. Am J Roentgenol. 2016;206:W10–20.

12. van Kessel CS, Buckens CFM, van den Bosch MAAJ, van Leeuwen MS, van Hillegersberg R, Verkooijen HM. Preoperative imaging of colorectal liver metastases after neoadjuvant chemotherapy: a meta-analysis. Ann Surg Oncol. 2012;19:2805–13.

13. Jeong HT, Kim M-J, Park M-S, et al. Detection of liver metastases using gadoxetic-enhanced dynamic and 10- and 20-minute delayed phase MR imaging. J Magn Reson Imaging. 2012;35:635–43.

14. Lee DH, Lee JM, Hur BY, et al. Colorectal cancer liver metastases: diagnostic performance and prognostic value of PET/MR imaging. Radiology. 2016;280:782–92.

15. Donati OF, Hany TF, Reiner CS, et al. Value of retrospective fusion of PET and MR images in detection of hepatic metastases: comparison with 18F-FDG PET/CT and Gd-EOB-DTPA-enhanced MRI. J Nucl Med. 2010;51:692–9.

16. Hofman MS, Lau WFE, Hicks RJ. Somatostatin receptor imaging with 68Ga DOTATATE PET/CT: clinical utility, normal patterns, pearls, and pitfalls in interpretation. Radiographics. 2015;35:500–16.

17. Hope TA, Pampaloni MH, Flavell RR, Nakakura EK, Bergsland EK. Somatostatin receptor PET/MRI for the evaluation of neuroendocrine tumors. Clin Transl Imaging. 2017;5:63–9.

18. Hope TA, Fowler KJ, Sirlin CB, et al. Hepatobiliary agents and their role in LI-RADS. Abdom Imaging. 2015;40:613–25.

19. Ehman EC, Behr SC, Umetsu SE, et al. Rate of observation and inter-observer agreement for LI-RADS major features at CT and MRI in 184 pathology proven hepatocellular carcinomas. Abdom Radiol. 2016;41:963–9.

20. Purysko AS, Remer EM, Coppa CP, Leão Filho HM, Thupili CR, Veniero JC. LI-RADS: a case-based review of the new categorization of liver findings in patients with end-stage liver disease. Radiographics. 2012;32:1977–95.

21. Castilla-Lièvre M-A, Franco D, Gervais P, et al. Diagnostic value of combining 11C-choline and 18F-FDG PET/CT in hepatocellular carcinoma. Eur J Nucl Med Mol Imaging. 2015;43:852–9.

22. Talbot J-N, Fartoux L, Balogova S, et al. Detection of hepatocellular carcinoma with PET/CT: a prospective comparison of 18F-fluorocholine and 18F-FDG in patients with cirrhosis or chronic liver disease. J Nucl Med. 2010;51:1699–706.

23. Fowler KJ, Maughan NM, Laforest R, et al. PET/MRI of hepatic 90Y microsphere deposition determines individual tumor response. Cardiovasc Intervent Radiol. 2015;39(6):855–64.

24. Eaton BR, Kim HS, Schreibmann E, et al. Quantitative dosimetry for yttrium-90 radionuclide therapy: tumor dose predicts fluorodeoxyglucose positron emission tomography response in hepatic metastatic melanoma. J Vasc Interv Radiol. 2014;25:288–95.

25. Piduru SM, Schuster DM, Barron BJ, Dhanasekaran R, Lawson DH, Kim HS. Prognostic value of 18f-fluorodeoxyglucose positron emission tomography-computed tomography in predicting survival in patients with unresectable metastatic melanoma to the liver undergoing yttrium-90 radioembolization. J Vasc Interv Radiol. 2012;23:943–8.

26. Fendler WP, Philippe Tiega DB, Ilhan H, et al. Validation of several SUV-based parameters derived from 18F-FDG PET for prediction of survival after SIRT of hepatic metastases from colorectal cancer. J Nucl Med. 2013;54:1202–8.

27. Annunziata S, Treglia G, Caldarella C, Galiandro F. The role of 18F-FDG-PET and PET/CT in patients with colorectal liver metastases undergoing selective internal radiation therapy with yttrium-90: a first evidence-based review. Sci World J. 2014;2014:879469–8.

28. Jiang L, Tan H, Panje CM, Yu H, Xiu Y, Shi H. Role of 18F-FDG PET/CT imaging in intrahepatic Cholangiocarcinoma. Clin Nucl Med. 2016;41:1–7.

29. Joo I, Lee JM, Lee DH, et al. Preoperative assessment of pancreatic cancer with FDG PET/MR imaging versus FDG PET/CT plus contrast-enhanced multidetector CT: a prospective preliminary study. Radiology. 2017;282:149–59.
30. Vag T, Gerngross C, Herhaus P, et al. First experience with chemokine receptor CXCR4-targeted PET imaging of patients with solid cancers. J Nucl Med. 2016;57:741–6.
31. Yin X, Wang M, Wang H, et al. Evaluation of neurotensin receptor 1 as a potential imaging target in pancreatic ductal adenocarcinoma. Amino Acids. 2017;22:1374–11.
32. Viola-Villegas NT, Rice SL, Carlin S, et al. Applying PET to broaden the diagnostic utility of the clinically validated CA19.9 serum biomarker for oncology. J Nucl Med. 2013;54:1876–82.
33. Kauhanen S, Rinta-Kiikka I, Kemppainen J, et al. Accuracy of 18F-FDG PET/CT, multidetector CT, and MR imaging in the diagnosis of pancreatic cysts: a prospective single-center study. J Nucl Med. 2015;56:1163–8.
34. Huo L, Feng F, Liao Q, Jin Z, Li F, Zhao Y. Intraductal papillary mucinous neoplasm of the pancreas with high malignant potential on FDG PET/MRI. Clin Nucl Med. 2016;41:989–90.

PET/MRI in Neuroendocrine Tumours

16

Simon Wan and Jamshed Bomanji

Contents

Neuroendocrine tumours (NETs) constitute a diverse range of neoplastic entities. They have in common a variable degree of neuroendocrine differentiation, histological features of neuroendocrine phenotype and immunohistochemical signatures (e.g. chromogranin A and synaptophysin) [1, 2]. As a group however, they can arise throughout the body, with heterogeneous functional status, tumour aggressiveness, associated clinical features and prognosis.

NETs have an estimated prevalence of 35/100,000 in the United States in 2004 [3]. Collectively, the gastroenteropancreatic neuroendocrine tumour (GEPNET) is the most common subgroup (formerly commonly referred to as carcinoids in the gut

S. Wan (✉) • J. Bomanji
Institute of Nuclear Medicine, University College London, London, UK
e-mail: Simon.Wan@uclh.nhs.uk; jamshed.bomanji@nhs.net

and islet cell tumours in the pancreas), which will form the focus of this chapter. Bronchial carcinoids are the next most common group. No known site is identified in 13% of cases, with patients presenting with presumed metastatic disease. Well-differentiated NET can be associated with neuroendocrine neoplasia syndromes such as multiple endocrine neoplasia type 1 (MEN1) and von Hippel-Lindau syndrome (VHL).

Terminology and nomenclature have evolved as our understanding of NET improved. In general, NETs are divided into well-differentiated and poorly differentiated categories, relating to tumour grades (grade 1–3), which in turn are measured by cellular proliferative rate, defined either by (1) rate of mitotic figures seen under the microscope or (2) percentage of cells labelled with Ki67, an active phase cell cycle marker. This is of particular importance as NET tumour grades are predictor of outcome. Well-differentiated NETs are typically low to intermediate grade (1–2), with generally a more indolent clinical course. Poorly differentiated category, incorporating small-cell carcinoma and large-cell neuroendocrine carcinoma, is typically grade 3 and carries aggressive tumour biology and poor prognosis. Currently widely used European Neuroendocrine Tumour Society (ENETS) grading criteria, endorsed by World Health Organization in 2010, adopts these nomenclatures for GEPNET; whereas for lungs and thymic NET, the terms typical and atypical carcinoids remain in use.

Besides grade and differentiation, NETs may be divided by their anatomical site/embryonic origin as foregut (lung, stomach, duodenum, liver, biliary tree and pancreas), midgut (duodenum, small intestines, appendix, right and proximal transverse colon) and hindgut (distal transverse, left colon and rectum) tumours. They can therefore give rise to a range of site-specific symptoms. In addition, NETs are capable of storing and secreting different peptides and neuroamines, allowing them to be categorised by the substances they produce. The active substances secreted by some of these 'functional' tumours can cause specific clinical syndromes, e.g. insulin secretion by insulinoma and Zollinger-Ellison syndrome caused by gastrinoma, while some are non-functional.

Imaging is pivotal to the diagnosis, staging, treatment selection, prognostication, response evaluation and surveillance of NETs. Comprehensive evaluation often involves a combination of computed tomography (CT), magnetic resonance imaging (MRI), ultrasound (US) to include endoscopic ultrasound (EUS) and radionuclide and hybrid techniques, such as single photon emission tomography (SPECT) or positron emission tomography (PET), with CT.

Hybrid PET/MRI scanners allowing whole-body imaging have become available recently. This has the potential to combine the exquisite sensitivity and molecular relevance of PET imaging, spatial resolution and soft tissue contrast of MRI and the functional imaging capability of both, to synergistic effect. Study of PET/MRI and its impact on NET management is still at its infancy. However, the potential of PET/MRI in this setting can be gained from our experience on existing PET tracers, comparative experience with PET/CT and MRI contrasting their relative merits and the PET/MRI studies to date on this topic.

16.1   PET Radiopharmaceuticals

16.1.1 Somatostatin Receptor PET Tracers

Well-differentiated NET is known to overexpress somatostatin receptor (SSTR) on their cell surface, particularly subtype 2 (of 5 subtypes in humans). This has prompted development of a number of Ga68-labelled positron-emitting peptide ligands to SSTR for studying NET (e.g. Ga68-labelled DOTATOC, DOTANOC and DOTATATE). Ga68 DOTATATE has particular subtype 2 affinity and was recently approved by the FDA in the United States [4, 5].

Compared to traditional indium-111 labelled octreotide scintigraphy (with SPECT/CT), Ga68 SSTR PETCT imaging has been shown to have higher specific and sensitivity, identifying additional lesions and altering management decisions in 70% of In-111 octreotide negative cases [6]. It also carries less radiation dose and does not require delay phase imaging over 2 days. In patients with suspected or metastatic NET, but no known primary lesion despite structural imaging, Ga68 SSRT PET/CT outperformed In-111 octreotide, detecting a primary lesion in 46% compared to 8% of cases [7] (Fig. 16.1). Ga68 SSRT PET has assumed prominent
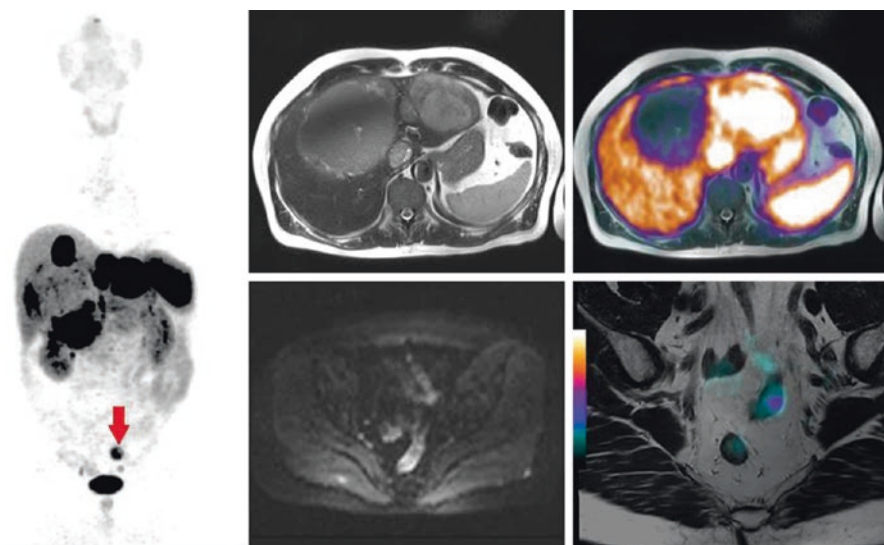

Fig. 16.1   A case of proven NET with unknown primary, showing superiority of SSRT PET in this context. Eventual surgical resection confirmed a small rectal primary. Clockwise from far left: (1) whole-body maximum intensity projection view of Ga68DOTATATE PET showing marked, heterogeneous uptake in multiple liver lesions, with an enlarged avid node in the pelvis (red arrow); (2 and 3) axial T2 HASTE and fused with PET images of the liver showing large volume metastases; (4) small field-of-view coronal oblique T2 turbo-spin-echo sequence of the rectum fused with PET showing a focus of uptake at the upper rectum, with no clear structural correlate despite dedicated MRI; (5) axial DWI ($b = 800$) showing no lesion detection despite DWI

roles in many components of the current ENET consensus guidelines and is often cited as the functional imaging of choice [8–10].

In addition, Ga68 DOTATATE has been shown to be highly accurate in the detection and characterisation of bronchial carcinoid into typical and atypical groups (SUV$_{max}$ >8.2 in typical vs SUV$_{max}$ <2.9 in atypical carcinoid and poorly differentiated pulmonary NET) [11].

Although detailed discussion of targeted radiolabelled peptide therapy is beyond the scope of this chapter, somastatin receptor imaging (with In-111 or Ga68 SSRT PET) is influential in patient selection for radiolabelled peptide therapy, such as with beta-particle emitting Lu177-labelled SSRT agents. The recently published interim report of a multicentre phase 3 randomised controlled trial of Lu177 DOTATATE therapy in patients with metastatic midgut NET has confirmed its efficacy with promising results, showing prolonged progression-free survival compared to controlled group [12]. The study protocol used In-111 octreotide scintigraphy for in vivo confirmation of lesional SSTR hyperexpression. However, it is likely that Ga68 SSRT PET imaging would also have similar predictive value to treatment efficacy.

Currently, Ga68 SSTR PET has restricted availability in centres of excellence, but wider adoption is feasible given that Ga68 are generator produced. Another limitation of Ga68 is its less optimal imaging characteristics compared to F18 [13], leading to greater scatter and partial volume effect. These negatively impact on quantitative accuracy, especially for assessment of standardised uptake values (SUV) of smaller lesions [14]. More recently, Cu64-labelled SSTR PET ligand has been developed with more favourable imaging characteristics and potential to supercede Ga68-labelled PET tracers [15]. Another recent development on SSTR PET imaging is of SSTR antagonists, which have been shown to have higher affinity to SSTR than the agonist ligands which are in common use currently [16]. Larger human studies would be needed to confirm their potential of these Cu64 labelled agents and SSRT antagonists.

16.1.2 Fluorodeoxyglucose (FDG)

FDG is a F18 labelled analogue of native glucose. It is currently the most commonly used PET tracer in general oncology. It is taken up by cells via active glucose transporters and is then believed to be trapped in most cells after phosphorylation by hexokinase. It can be thought of as a marker of glucose consumption, and it is therefore non-specific, with its uptake raised in a variety of neoplastic and inflammatory conditions.

FDG has a limited role in initial diagnosis and staging of well-differentiated NET, being shown to have inferior sensitivity compared to Ga68 SSRT PET and other imaging modalities. However, FDG PET can help with comprehensive assessment of NET by identification of high-grade disease. In comparative studies of Ga68 SSRT and FDG PET, FDG PET uptake intensity is found to be associated with NET tumour grade [17]. FDG PET is shown to be a strong prognosticator for

survival of NET patients [18], leading to management alteration in approximately 1/5 of patients, often to prompt initiation of systemic chemotherapy [19].

16.1.3 Glucagon-Like Peptide-1 (GLP-1) Receptor Radiopharmaceuticals

While insulinoma is mostly benign, the unregulated insulin secretion is medically difficult to manage and can be life threatening. Surgical resection is effective in non-metastatic disease, but localisation of the tumour has proved challenging despite structural imaging techniques and other radionuclide tracers. SSRT PET has been shown to be suboptimal, with sensitivity of about 25%. Arterial calcium-stimulated venous sampling is a useful technique in this setting, but this is invasive.

Insulinoma cells are found to have high expression of GLP-1 receptors. Radiolabelled peptide ligands for these receptors (known as exendin) have been developed for use in the imaging localisation of insulinoma. Tc-99m and In-111 labelled analogues have been reported. More recently, Ga68 labelled exendin have been studied prospectively in human, showing excellent result, unparalleled by Tc-99m SSRT SPECT, CT, MR and EUS [20]. Further confirmation with larger studies would be useful to further validate the technique.

16.1.4 6-ʟ-18F-Fluorodihydroxyphenylalanine (FDOPA)

FDOPA is a F18 labelled amino acid (dihydroxyphenylalanine). FDOPA is an analogue of a metabolic intermediate in catecholamine synthesis pathway, which is active in many NET. It is taken into cells via L large amino acid transporters and mainly decarboxylated by amino acid decarboxylase (AADC) to dopamine, before being processed further downstream [21]. Some authors recommend the use of carbidopa pretreatment before FDOPA PETCT, which theoretically inhibits early decarboxylation, but this remains controversial and this need may be tumour-type dependent.

It has been shown to be superior to In-111 SSRT scintigraphy. Comparative data with other PET tracers is limited but it was shown to be inferior to Ga68 SSRT PET in GEPNET. It may have a role in SSRT PET-negative cases and in other NET entities such as medullary thyroid cancers, paragangliomas and phaeochromocytomas [22].

16.1.5 β-[11 C]-5-Hydroxy-ʟ-Tryptophan (5-HTP)

5-HTP is another amino acid metabolic tracer, which can be used to study the serotonin pathway, thought also to be active in NET. It is taken up into cells and metabolised via mechanisms similar to FDOPA but with the resultant product being serotonin. Tracer synthesis is complex, and the use of this tracer requires an on-site cyclotron,

limiting its availability and use. As such, robust validation study is lacking. Limited studies suggest that it may be inferior to FDOPA in the assessment of NET, and their role may be limited to problem-solving when other tracers are negative [23].

16.2 Comparative PET/CT, MRI and PET/MRI Literature

Over the decades since its introduction, MRI has evolved from being a problem-solving tool in specialist centres to having routine integral roles in many cancer management pathways. In contrast to PET imaging (which is employed ubiquitously as a whole-body imaging technique in the oncology setting), MRI examinations are usually body part specific. Nonetheless, with technological advances, whole-body MRI has recently evolved as a distinct entity. Whole-body MRI staging assessment is now feasible, with efficacy already shown in assessment of malignant bone marrow infiltration (latter most established in cancer type such as myeloma, prostate and breast cancers).

16.2.1 Assessment of Liver Metastases

Accurate evaluation of liver lesions in NET is important because (1) it is the most common site of metastatic disease; (2) hepatic tumour load is associated with higher morbidity and mortality [3] and; (3) a range of treatment options are potentially available for patients with liver metastases, from surgical resection, focal ablation (e.g. radio frequency), locoregional drug application (e.g. trans-arterial chemoembolisation and selective internal radiotherapy) and somatostatin analogues to systemic chemotherapy. Liver resection has been proven to confer survival benefit and can alleviate symptoms by debulking of hormone-producing tumour burden.

It is well established that MRI outperforms CT in the detection and characterisation of liver metastases in NET. A contemporary liver MRI protocol typically includes axial and/or coronal fast sequences such as single-shot partial Fourier spin-echo technique (e.g. HASTE/SS-FSE) or fast imaging with steady state precession (e.g. True FISP), T2-weighted fast/turbo-spin echo (with or without fat suppression), T1-weighted gradient echo (to include in- and out-of-phase images, potentially useful for assessment of intravoxel fat content of any lesion), diffusion-weighted and fat-suppressed T1 sequences with dynamic contrast enhancement (arterial, portovenous and equilibrium phase) using gadolinium contrast agents. Hepatocyte-specific MR contrast agents with delayed phase imaging are also useful.

The 'typical' liver NET metastases on MRI are round or lobulated, with well-defined margins. They demonstrate high signal on diffusion-weighted images with increasing b-values (restricted diffusion) leading to low signal on apparent diffusion coefficient (ADC) parametric maps. They are usually iso- to hyperintensity on T2-weighted images and hypointensity on T1-weighted images. It is common to find multiple small lesions present. Larger lesions have more heterogeneous signal characteristics, often with central necrotic areas and can have high T1 signal components from proteinaceous contents and even fluid levels. With gadolinium

contrast injection, they have avid arterial enhancement, which may be ring shaped or more homogenous, with washout during the portal venous phase. They do not take up 'hepatocyte-specific' MR contrast agents (e.g. Gad-EOB-DTPA) and therefore appear hypointense relative to liver parenchyma on delayed phase imaging if these are used. Differentials on MRI would include other arterialised lesions such as hepatocellular carcinoma, hepatic adenoma, focal nodular hyperplasia and haemangioma.

Studies including comparison of Ga68 SSRT PET/CT with dedicated liver MRI have reported heterogeneous results. Srirajaskanthan et al. showed that standard of care CT ± MRI detected 34 liver metastases compared to only 23 by Ga68 SSTR PET/CT, in a cohort of 47 patients with NET [6]. On the other hand, Frilling et al. showed additional liver metastasis detection by Ga68 SSTR PET/CT, not detected by standard imaging (CT ± MR) [24]. Relationship between metastases detection by the respective imaging modalities and size of the liver metastases has not been specifically reported in these studies. Nonetheless, the latter study included three patients in which explanted liver was available as reference standard. These showed numerous liver lesions <5 mm, which were not disclosed by any of the imaging technique, indicating a limit to the size of liver metastases detectable by these available techniques.

The potential of PET/MRI in the assessment of metastatic liver NET has been shown in earlier studies utilising post-processing image fusion to generate PET/MRI datasets, built from images separately acquired as Ga68 SSTR PET/CT and dedicated liver MRI [25, 26]. In one study involving 22 patients and 181 liver metastases, Ga68 DOTATOC PET/Gad-EOB-DTPA MRI was reported to be most accurate with sensitivity and specificity of liver metastases detection reported at 91.2 and 95.6%, compared to 73.5 and 88.2% for PET/CT and 87.6 and 86.8% for dedicated MRI only. Another study compared PET fused with Gad-EOB-DTPA against PET fused with DWI only. This demonstrated almost complete equivalent detection of 297 liver metastases in 18 patients, with no false negative against reference standard of clinical follow-up multimodality imaging. PET/DWI is however minimally less specific than PET/Gad-EOB-DTPA MRI in this study [26].

To date, only scanty literature exists on the prospective use of dedicated liver MRI sequences on the PET/MRI platform. Hope et al. studied the use of Ga DOTATOC PET/MRI in ten patients, with a crossover whole-body PET/CT vs whole-body PET/MRI design, which includes a dedicated liver section PET/MRI protocol. The study demonstrated that such a single staging protocol is feasible. Liver lesion detection rates were reported to be 99% on the hepatobiliary phase MRI (being superior to all other modalities assessed but particularly for lesion size <1 cm), 83% on DWI and 77% on liver section PET, when these images were read separately [27]. Another study by Sawicki et al. utilised a similar study design and imaging protocol and showed that PET/MRI detected more liver lesions than PET/CT. However, the specific contribution of the individual components of the liver PET/MRI components liver MR was not been separately reported in this study [28]. As per usual liver MR protocols, the liver-directed MRI sequences in this study involve multiple breath holds. The authors did not report misregistration (between these and the PET images) in precluding precise image interpretation. This is consistent with our own experience.

In summary, dedicated MRI is excellent in liver lesion detection in NET, especially with hepatocyte-specific contrast agent. On the other hand, detection of liver lesion with Ga68 SSRT PET is more dependent on size. Limited data suggests there could be a synergistic effect, with enhanced accuracy for assessment of liver disease burden by combining PET and MRI. Furthermore, Ga68 SSRT PET and MRI may have additional strength in exclusion of extrahepatic disease (see below) to guide patient selection for liver-directed therapy (e.g. focal ablation and SIRT).

16.2.2 Assessment of Pancreatic Lesion

Pancreatic NET represents the second most common malignancy of the pancreas. About 1/3 of pancreatic NET are functional tumours, with insulinoma and gastrinoma being the most common. Insulinoma are typically small tumour in the pancreas (40% less than 1 cm in size) with only 10% being malignant [29]. They are usually solitary. Gastrinoma typically resides in the 'gastrinoma triangle' with 60% located within the pancreas and the remainder most commonly located in peripancreatic nodes or in the duodenum, where they are usually small and difficult to detect by noninvasive imaging. Sixty percent show malignant behaviour at presentation. On the other hand, the non-functioning pancreatic NET may present later, often with metastatic disease. Pancreatic NET are associated with a range of genetically related disease such as VHL, MEN1 (Fig. 16.2).
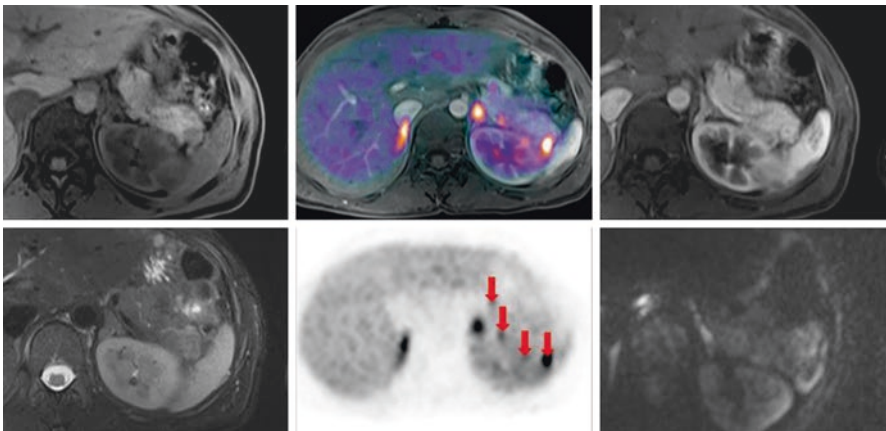

Fig. 16.2 A young patient with multiple endocrine neoplasia type 1 (MEN1) manifesting with multiple small non-functioning pancreatic neuroendocrine tumours. This case demonstrates the clear superiority of SSRT PET in its sensitivity of detecting small NET. There are multiple Ga68 DOTATATE avid lesions in the pancreas (four lesions on this section). Apart from the larger lesion at the tip of the pancreatic tail, the rest are not seen on MRI despite dedicated sequences. Axial sections showing the pancreatic tail. Clockwise from top right: (1) pre-contrast T1 VIBE; (2) Ga68 DOTATATE PET fused with arterial phase T1 VIBE; (3) arterial phase T1 VIBE; (4) DWI (b-value 800); (5) Ga68 DOTATATE PET; (6) T2 TSE with fat suppression

ENET consensus in 2009 reported sensitivity and specificity of diagnosing pancreatic NET by MRI to be 93 and 88%, respectively, compared to 73 and 96% of CT. These have been shown to be superseded by Ga68 SSRT PET/CT on more recent literature, which reported sensitivity and specificity of 86–100% and 79–100%. While CT and MR still remains first line in pancreatic NET assessment, current ENET guideline has recommended concomitant use of SSRT PET in most functioning and non-functioning pancreatic NET, except insulinoma [9].

Nonetheless, MRI has important roles in detection of insulinoma, where sensitivity of SSRT PET is recognised to be limited, and GLP-1 PET imaging is not widely available. MRI can supply information to aid surgical planning (such as vascular relationship) and in diagnosis and assessment of any co-existing liver metastases (see above). In addition, MRI is particularly considered the imaging modality of choice in screening and follow-up of pancreatic NET in patients with genetic syndromes such as MEN1 and VHL. MRI is advantageous in these settings for its lack of ionising radiation, as patients are often subjected to imaging for screening purposes at a relatively young age. They would also likely require regular further follow-up throughout their lifetime.

Typical MR appearances of pancreatic NET is of a rounded lesion showing high T2 and low T1 signal (particularly against the relatively high T1 signal of normal pancreatic parenchyma on a fat-suppressed T1-weighted sequence), restricted diffusion and avid contrast enhancement. This is distinct to the relative hypo-enhancement of the more common pancreatic adenocarcinoma, a main imaging differential. Compared to adenocarcinoma, pancreatic NET is less likely to be associated with ill-defined margins, dilated pancreatic duct or common bile duct or features of chronic pancreatitis [30]. Uncommonly, pancreatic NET may be hypo-enhancing or have a cystic nature.

The two aforementioned 'PET/MRI' studies performed via retrospective fusion of GA68 SSRT PET/CT and upper abdominal MRI showed almost equivalent accuracy between PET/DWI and PET/Gad-EOB-DTPA MRI in six pancreatic lesions with no false negative but one false-positive lesion with PET/Gad-EOB-DTPA MRI [26]. The other study did not specifically report the pancreatic findings separately. The two prospective studies on PET/MRI platform with dedicated upper abdominal MRI sequences have shown feasibility of PETMRI in this context. One study reported PET/MRI and PETCT each detected a pancreatic lesion not detected by the other technique [27]. The other study commented on inclusion of seven pancreatic lesions in the study group, but did not report the performance of PETMRI in pancreatic lesions specifically.

In summary, while PET and MRI have relatively merits in the assessment of pancreatic NET, available data is limited and further research is required to draw robust conclusion on any superiority of PETMRI over and above existing practice.

16.2.3 Small Bowel and Mesenteric Lesion Assessment

Small bowel NET is relatively prevalent, accounting for 20–50% of NET. Patients with locoregional disease should be considered for curative resection, which has been shown to improve outcome. Patients often present with non-specific abdominal

symptoms, which may relate to the primary lesions, desmoplastic reaction of mesenteric nodal disease or endocrine-related symptoms. The fibrotic mesenteric mass, if present, would usually be obvious on standard CT imaging, but the primary lesion within the small bowel is often obscure. Multiple lesions may also co-exist in the small bowel. Precise localisation of these would help surgical planning. Current ENET guideline suggests the use of CT or MR enteroclysis as first-line imaging, followed by SSRT PET imaging [8].

In MR enteroclysis, a nasoenteral tube is inserted for direct infusion of enteric contrast material to achieve optimal small bowel distension to aid lesion detection. Antiperistaltic agents are used to reduce bowel motion artefact. MRI protocol relies to relatively fast sequences such as FISP and gradient-echo technique (e.g. FLASH, VIBE) pre- and post-gadolinium contrast injection. Enterography is an alternative, less invasive but less well-validated technique, where bowel distension is achieved through oral intake of large volume of enteric contrast material. MR enteroclysis has been validated for use in the assessment of small bowel neoplasm in numerous studies. While CT enteroclysis has sensitivity and specificity of 85 and 97% for detection of small bowel tumours, MR enteroclysis is believed to have even superior sensitivity. This may be due to MRI having better soft tissue contrast and lack of ionising radiation, which allows dynamic and multiple acquisitions [31]. One study specifically assessing the use of MR enterography in NET. This reported a sensitivity of 74 and 95% (on a per lesion and per patient basis, respectively) in 27 proven NET lesions in 19 patients [32].

Small bowel NET appears as asymmetrical focal bowel wall thickening or submucosal mass on MRI, with iso-intensity to muscle on T1 and iso-/hyperintensity on T2-weighted images and contrast enhancement. Kinking of the bowel wall can occur. Mesenteric nodal mass and liver metastases may be in the field of view of a dedicated MR small bowel study.

Recently, the feasibility of MR enterography on combined PET/MRI platform has been shown in a study of 19 patients, which included 9 patients with suspected NET using SSRT PET tracer. The study concluded high image quality and excellent coregistration [33]. In one case, the authors identified a NET lesion in the ascending colon. Whether combined PET/dedicated small bowel MR studies could give additional value remains to be validated in larger studies.

16.2.4 Whole-Body Assessment (WB-MRI)

With advances in hardware, software and sequence development, such as use of multiple phase array coils and parallel imaging, high resolution, high soft tissue contrast MRI images of the whole body is achievable in a reasonable scan time and without necessarily exogenous contrast agent. Furthermore, introduction of the technique of diffusion-weighted whole-body imaging with background body signal suppression (DWIBS) in 2004 extended the capability of WB-MRI to give functional information on tissue cellularity, enhancing lesion detection. WB-MRI is also attractive with its lack of radiation and wider availability of MRI scanners compared to the use of PET/CT. A meta-analysis in 2014 have reported that in 13 studies

assessing performance of WB-MRI with DWI and PET/CT in common cancers and metastatic disease, the pooled sensitivity and specificity of PET/CT were 0.90 and 0.98, with MRI comparably at 0.90 and 0.95.

In the context of WB-MRI in NET, Moryoussef et al. reported, in a cohort of 21 NET patients, that WB-DWI had additional value over WB-MRI, detecting additional lesions in 15/21 patients on DWI. However, this is at the expense of specificity with 6/63 evaluable additional lesions on DWI found to be falsely positive by the reference standard.

A three-way comparison of Ga68-DOTATATE PET/CT, Tc99m-HYNIC-Octreotide and WB-DWI involving 19 patients reported overall sensitivity and specificity of Ga68 DOTATATE PET/CT of 96 and 97%, respectively, compared to 72 and 100% with WB-DWI. Ga68 DOTATATE PET/CT was more sensitive for bone lesions but also in the liver, the pancreas and the gastrointestinal tract, and it was the only modality to detect two unknown primary lesions [34].

Another comparative study of PET/CT against WB-MRI (without DWI), including 51 patients, demonstrated overall equivalent accuracy (92 vs 91%), but with PET/CT detecting more nodal and pulmonary disease and WB-MRI detecting more bone and liver lesions. In addition, PET/CT was shown to be more specific, showing 13/593 lesions as falsely positive, compared to 53 false-positive lesions in WB-MRI [35].

Use of WB-MRI is technically and naturally inherent in PET/MRI, as PET is a whole-body technique with MR attenuation correction reliant on whole-body MRI coverage at least with basic sequences. Advanced MR sequences (including DWI) can also be delivered by all commercially available whole-body PET/MRI scanners. In addition, with current PET detector sensitivity, time taken for PET acquisition per bed position usually a few minutes longer than the minimum MR attenuation correction sequences, giving time to accommodate for some of the extra MRI sequences to be acquired for use in additional MRI assessment.

Several studies had been published studying NET patients on combined PET/MRI platform, all with SSRT PET tracers and crossover design (single injection, PET/CT and PET/MRI). An early study utilising only basic WB-MRI sequences (without MR contrast, DWI or dedicated sequences) showed broad quantitative and qualitative equivalence in uptake values and PET visual lesion detection (PET/MRI detected four less liver lesions with subtle uptake, in 157 lesions overall; these four were reported visible on further review) [36]. Visualisation of an anatomical correlate was generally better on the basic MRI component of this study compared to CT component (with oral contrast only) of the respective hybrid studies. Another study compared contrast-enhanced PET/CT against PET/MRI with WB-MRI (WB post contrast and DWI) in eight patients and showed that PET/MRI detected the same number of malignant lesions as on PET/CT [37]. However, PET/MRI did not detect three of four benign/indeterminate, PET negative, lung lesions.

Two further studies on the dedicated PET/MRI platform incorporated more complex protocols to include WB-MRI with contrast, without WB-DWI, but with dedicated upper abdominal PET/MRI section [27, 28], compared against contrast-enhanced PET/CT. In terms of extrahepatic findings, there is broad equivalence between PET/CT and PET/MRI, but when comparing the structural components

alone, there is no clear benefit of WB-MRI with contrast compared to contrast-enhanced CT. There is concern of non-visualisation of small sclerotic bone and lung lesions on the MRI, which may be either below resolution of or non-avid on PET.

In summary, use of whole-body MRI to supplement Ga68 SSRT PET on PET/MRI is feasible. There is heterogeneity of PET/CT and PET/MRI protocols in the small number of PET/MRI studies published. These include using CT and MRI contrast agents or not, and within WB-MRI, whether there is addition of WB-DWI. More studies would be needed to address specific questions, such as how best to optimise the PET/MRI protocols and how these may be integrated into existing pathways for specific circumstances (e.g. can WB PET/MRI with dedicated liver section, supplemented by CT chest, be better than current strategy of CT, with liver MRI and PET/CT as need, as a staging tool and will this change management?).

16.3 Other NET Entities

The role of PET/MRI in the study of non-GEPNETs is more obscured. On the one hand, superiority of PET/MRI in the assessment and follow-up of head and neck paraganglioma may be readily speculated, given the potential benefit of precise co-localisation of the exquisitely sensitive SSRT PET signal in this context, with excellent soft tissue contrast on MRI. The relative reduction of radiation dose compared to PET/CT and ability to have a one-stop approach are also potential advantage for familial cases (e.g. patients with succinate dehydrogenase mutation), where young patients often have multiple lesions and require frequent assessment. On the other hand, while use of PET/CT has confirmed roles in assessment of phaeochromocytoma, medullary thyroid cancer and bronchial carcinoid, especially in the metastatic settings, integration of this with whole-body or regional-specific MRI sequences on the PET/MRI platform would be of much uncertain additional benefit.

Conclusion

The study of the clinical use of PET/MRI in NET patients is only at its early stages. Emerging data would suggest synergistic benefit in the assessment of liver metastases. Among the myriad of other clinical questions and scenarios important to NET patient management, there is a clear need for more work into identifying and establishing other areas where PET/MRI could bring similar synergistic benefit. Further studies would also be needed to rationalise PET/MRI protocols to reduce strain on patient's experience and resources.

References

1. Klimstra DS, Beltran H, Lilenbaum R, Bergsland E. The spectrum of neuroendocrine tumors: histologic classification, unique features and areas of overlap. Am Soc Clin Oncol Educ Book. 2015;35:92–103.

2. Klimstra DS. Pathologic classification of neuroendocrine neoplasms. Hematol Oncol Clin North Am. 2016;30:1–19.
3. Yao JC, Hassan M, Phan A, et al. One hundred years after "carcinoid": epidemiology of and prognostic factors for neuroendocrine tumors in 35,825 cases in the United States. J Clin Oncol. 2008;26:3063–72.
4. Reubi JC, Schar JC, Waser B, et al. Affinity profiles for human somatostatin receptor subtypes SST1-SST5 of somatostatin radiotracers selected for scintigraphic and radiotherapeutic use. Eur J Nucl Med Mol Imaging. 2000;27:273–82.
5. Deppen SA, Liu E, Blume JD, et al. Safety and efficacy of 68Ga-DOTATATE PET/CT for diagnosis, staging, and treatment management of neuroendocrine tumors. J Nucl Med. 2016;57:708–14.
6. Srirajaskanthan R, Kayani I, Quigley AM, Soh J, Caplin ME, Bomanji J. The role of 68Ga-DOTATATE PET in patients with neuroendocrine tumors and negative or equivocal findings on 111In-DTPA-octreotide scintigraphy. J Nucl Med. 2010;51:875–82.
7. Schreiter NF, Bartels AM, Froeling V, et al. Searching for primaries in patients with neuroendocrine tumors (NET) of unknown primary and clinically suspected NET: evaluation of Ga-68 DOTATOC PET/CT and In-111 DTPA octreotide SPECT/CT. Radiol Oncol. 2014;48: 339–47.
8. Niederle B, Pape UF, Costa F, et al. ENETS consensus guidelines update for neuroendocrine neoplasms of the jejunum and ileum. Neuroendocrinology. 2016;103:125–38.
9. Falconi M, Eriksson B, Kaltsas G, et al. ENETS consensus guidelines update for the management of patients with functional pancreatic neuroendocrine tumors and non-functional pancreatic neuroendocrine tumors. Neuroendocrinology. 2016;103:153–71.
10. Pavel M, O'Toole D, Costa F, et al. ENETS consensus guidelines update for the management of distant metastatic disease of intestinal, pancreatic, bronchial neuroendocrine neoplasms (NEN) and NEN of unknown primary site. Neuroendocrinology. 2016;103:172–85.
11. Kayani I, Conry BG, Groves AM, et al. A comparison of 68Ga-DOTATATE and 18F-FDG PET/CT in pulmonary neuroendocrine tumors. J Nucl Med. 2009;50:1927–32.
12. Strosberg J, El-Haddad G, Wolin E, et al. Phase 3 trial of 177Lu-dotatate for midgut neuroendocrine tumors. N Engl J Med. 2017;376:125–35.
13. Sanchez-Crespo A. Comparison of Gallium-68 and Fluorine-18 imaging characteristics in positron emission tomography. Appl Radiat Isot. 2013;76:55–62.
14. Ruf J, Schiefer J, Kropf S, et al. Quantification in (68)Ga-DOTA(0)-Phe(1)-Tyr(3)-octreotide positron emission tomography/computed tomography: can we be impartial about partial volume effects? Neuroendocrinology. 2013;97:369–74.
15. Johnbeck CB, Knigge U, Loft A, et al. Head-to-head comparison of 64Cu-DOTATATE and 68Ga-DOTATOC PET/CT: a prospective study of 59 patients with neuroendocrine tumors. J Nucl Med. 2017;58:451–7.
16. Fani M, Del Pozzo L, Abiraj K, et al. PET of Somatostatin receptor-positive tumors using 64Cu- and 68Ga-Somatostatin antagonists: the chelate makes the difference. J Nucl Med. 2011;52:1110–8.
17. Kayani I, Bomanji JB, Groves A, et al. Functional imaging of neuroendocrine tumors with combined PET/CT using 68Ga-DOTATATE (DOTA-DPhe1,Tyr3-octreotate) and 18F-FDG. Cancer. 2008;112:2447–55.
18. Binderup T, Knigge U, Loft A, Federspiel B, Kjaer A. 18F-fluorodeoxyglucose positron emission tomography predicts survival of patients with neuroendocrine tumors. Clin Cancer Res. 2010;16:978–85.
19. Panagiotidis E, Alshammari A, Michopoulou S, et al. Comparison of the impact of 68Ga-DOTATATE and 18F-FDG PET/CT on clinical management in patients with neuroendocrine tumors. J Nucl Med. 2017;58:91–6.
20. Luo Y, Pan Q, Yao S, et al. Glucagon-like peptide-1 receptor PET/CT with 68Ga-NOTA-exendin-4 for detecting localized insulinoma: a prospective cohort study. J Nucl Med. 2016;57:715–20.

21. Jager PL, Chirakal R, Marriott CJ, Brouwers AH, Koopmans KP, Gulenchyn KY. 6-L-18F-fluorodihydroxyphenylalanine PET in neuroendocrine tumors: basic aspects and emerging clinical applications. J Nucl Med. 2008;49:573–86.

22. Baumann T, Rottenburger C, Nicolas G, Wild D. Gastroenteropancreatic neuroendocrine tumours (GEP-NET) - imaging and staging. Best Pract Res Clin Endocrinol Metab. 2016;30:45–57.

23. Brabander T, Kwekkeboom DJ, Feelders RA, Brouwers AH, Teunissen JJ. Nuclear medicine imaging of neuroendocrine tumors. Front Horm Res. 2015;44:73–87.

24. Frilling A, Sotiropoulos GC, Radtke A, et al. The impact of 68Ga-DOTATOC positron emission tomography/computed tomography on the multimodal management of patients with neuroendocrine tumors. Ann Surg. 2010;252:850–6.

25. Schreiter NF, Nogami M, Steffen I, et al. Evaluation of the potential of PET-MRI fusion for detection of liver metastases in patients with neuroendocrine tumours. Eur Radiol. 2012;22:458–67.

26. Mayerhoefer ME, Ba-Ssalamah A, Weber M, et al. Gadoxetate-enhanced versus diffusion-weighted MRI for fused Ga-68-DOTANOC PET/MRI in patients with neuroendocrine tumours of the upper abdomen. Eur Radiol. 2013;23:1978–85.

27. Hope TA, Pampaloni MH, Nakakura E, et al. Simultaneous (68)Ga-DOTA-TOC PET/MRI with gadoxetate disodium in patients with neuroendocrine tumor. Abdom Imaging. 2015;40:1432–40.

28. Sawicki LM, Deuschl C, Beiderwellen K, et al. Evaluation of 68Ga-DOTATOC PET/MRI for whole-body staging of neuroendocrine tumours in comparison with 68Ga-DOTATOC PET/CT. Eur Radiol. 2017;27(10):4091–9.

29. Tamm EP, Bhosale P, Lee JH, Rohren EM. Sktate-of-the-art imaging of pancreatic neuroendocrine tumors. Surg Oncol Clin N Am. 2016;25:375–400.

30. De Robertis R, D'Onofrio M, Zamboni G, et al. Pancreatic neuroendocrine neoplasms: clinical value of diffusion-weighted imaging. Neuroendocrinology. 2016;103:758–70.

31. Masselli G, Casciani E, Polettini E, Laghi F, Gualdi G. Magnetic resonance imaging of small bowel neoplasms. Cancer Imaging. 2013;13:92–9.

32. Dohan A, El Fattach H, Barat M, et al. Neuroendocrine tumors of the small bowel: evaluation with MR-enterography. Clin Imaging. 2016;40:541–7.

33. Beiderwellen K, Kinner S, Gomez B, et al. Hybrid imaging of the bowel using PET/MR enterography: feasibility and first results. Eur J Radiol. 2016;85:414–21.

34. Etchebehere EC, de Oliveira Santos A, Gumz B, et al. 68Ga-DOTATATE PET/CT, 99mTc-HYNIC-octreotide SPECT/CT, and whole-body MR imaging in detection of neuroendocrine tumors: a prospective trial. J Nucl Med. 2014;55:1598–604.

35. Schraml C, Schwenzer NF, Sperling O, et al. Staging of neuroendocrine tumours: comparison of [(6)(8)Ga]DOTATOC multiphase PET/CT and whole-body MRI. Cancer Imaging. 2013;13:63–72.

36. Gaertner FC, Beer AJ, Souvatzoglou M, et al. Evaluation of feasibility and image quality of 68Ga-DOTATOC positron emission tomography/magnetic resonance in comparison with positron emission tomography/computed tomography in patients with neuroendocrine tumors. Investig Radiol. 2013;48:263–72.

37. Beiderwellen K, Poeppel TD, Hartung-Knemeyer V, et al. Simultaneous 68Ga-DOTATOC PET/MRI in patients with Gastroenteropancreatic neuroendocrine tumors. Investig Radiol. 2013;48:273.

Rectal Cancer

17

Ajit H. Goenka, Cristina Nanni, and Sudhakar K. Venkatesh

Contents

17.1   Introduction

Colorectal cancer is the third most common cancer in men and the second most common cancer in women [1]. Rectum is the site for nearly one third of colonic cancers, and rectal cancers are associated with poor prognosis and higher local recurrence. Total mesorectal excision is the standard surgical treatment for localized cancers, and neo-adjuvant concurrent chemoradiation therapy is performed in selected patients. Low anterior resection, ultralow anterior resection, and abdominoperineal resection are options for tumors involving different parts of the rectum. Sphincter-sparing surgery is preferred as it has the potential to

A.H. Goenka • S.K. Venkatesh (✉)
Department of Radiology, Mayo Clinic, Rochester, MN, USA
e-mail: venkatesh.sudhakar@mayo.edu

C. Nanni
Nuclear Medicine Department, AOU di Bologna, Policlinico S.Orsola-Malpighi,
Bologna, Italy
e-mail: cristina.nanni@aosp.bo.it

improve quality of life. T stage and N stage of the tumor determine outcome, and the involvement of mesorectal fascia (MRF), circumferential resection margin (CRM), and extramural vascular invasion (EMVI) are important prognostic factors. Preoperative accurate staging of rectal carcinoma is, therefore, very important. The modality of choice for initial staging of rectal carcinoma is magnetic resonance imaging (MRI) as it has high soft tissue contrast resolution and can identify important anatomical landmarks such as mesorectal fascia and peritoneal reflections [2, 3]. High-resolution T2 weighted forms the cornerstone for local staging of the rectal cancer. Transverse (axial/oblique axial) images perpendicular to the long axis of the tumor are important to determine the invasion of the tumor through the rectal wall and involvement of the mesorectal fascia [4]. Controversies exist with regard to the need of endorectal coil and the use of rectal gel as these would change the rectum anatomical position and normal state of distension. According to a meta-analysis study, MRI performs well for both T stage and N stage with accuracy of >80% [5].

Recently, MRI has also evolved as the preferred modality for posttreatment assessment of rectal cancers that are locally advanced and treated with neo-adjuvant chemoradiation therapy (CRT) to assess response as well as surgical resectability. However, the accuracy of MRI may be limited following CRT as differentiation of residual tumor from fibrosis is difficult, inflamed rectum (radiation proctitis) can mimic local invasion, and reactive lymphadenopathy may be misdiagnosed as local progression [6, 7]. Positron emission tomography (PET) has been shown to be useful for post-CRT response assessment and also provide prognostic information [8, 9]. It appears, therefore, that a combined evaluation with PET and MRI system may provide more information for local staging and assessment of treatment response.

For metastatic disease at the initial staging and after neo-adjuvant or adjuvant radiation therapy, both CT and MRI have been found useful. Studies have shown similar accuracy for both PET/CT and MRI in the detection of distal organ metastases and better accuracy of PET/CT over MRI for detection of lymph node metastases [10, 11]. However in the recent years, owing to the epidemic of obesity, sensitivity of CT is lower due to increased prevalence of hepatic steatosis in obese patients, which can make it difficult to detect hypodense colorectal metastases [12]. MRI is, therefore, suitable, especially with diffusion-weighted imaging (DWI), which is more sensitive for detection of small metastatic liver lesions [13]. The use of hepatobiliary contrast agents such as Gd-EOB-DTPA is known to improve detection of liver metastases compared to CT [14].

Preoperative imaging of rectal cancer would benefit from accurate definition of surgical planes and evaluation of involvement of lymph nodes and distant metastases. A hybrid PET/MRI system provides capability of high-resolution anatomical imaging, functional imaging with dynamic contrast-enhanced imaging, DWI, evaluation with hepatobiliary-specific agents, and functional information from PET that can be combined for a comprehensive evaluation of rectal cancer. PET/MRI has been recently introduced into clinical practice and reports of its utility are emerging.

17.2 Current Role of PET/CT in Rectal Cancer

Rectal adenocarcinoma, a highly proliferative and aggressive malignancy overexpressing transmembrane GLUT receptors, is easily detectable by FDG PET/CT. However, there is considerable non-negligible false positives from adenomatous or tubulovillous polyps, diverticulitis, inflamed hemorrhoids, inflammatory diseases of the bowel mucosa (such as IBD, post-radiotherapy inflammation, etc.), or non-specific bowel uptake (physiological or consequent to oral antidiabetic drugs such as metformin administration). On the other hand, false-negative results are caused by small rectal adenocarcinomas or by carcinomas obscured by intestinal physiological FDG uptake. FDG PET/CT is limited for the definition of the T parameter in the TNM staging due to inferior anatomic details when compared with MRI. Low-dose and non-enhanced CT, which is used for attenuation correction, is not accurate for detecting primary rectal cancer. Consequently, it is not possible to precisely assess the degree of infiltration of the rectal wall, which is essential to correctly define the T parameter.

On the other hand, the sensitivity of FDG PET for the detection of metastatic lymph nodes has been shown to be similar to that of CT and generally poor (22–29%) [15, 16]. However, its specificity and accuracy were reported to be relatively high (95.5 and 88%, respectively) [17–23]. These results have led to a generally shared opinion that FDG PET/CT has limited role for the N staging and that locoregional lymphadenectomy is more suitable to correctly stage the patient. However, FDG PET/CT is valuable to confirm suspected metastatic lymph nodes detected by other imaging modalities when their size is larger than 5 mm. About 15–25% of patients with primary colorectal cancer have synchronous liver metastases at diagnosis, and 2% have synchronous lung metastases [24]. Furthermore, in rectal cancer, the risk of synchronous secondary lesions is twofold higher as compared to colon cancer [24]. Surgical resection of metastatic lesions at presentation is known to improve prognosis (5-year survival rate of 40% as compared to 0% survival in untreated patients [25]. FDG PET/CT has a sensitivity of 88–91% and specificity of 91–100% for detection of secondary lesions at presentation [15, 26] and has significant impact on management decisions [26, 27].

The utility of FDG PET/CT in assessing resectability following neo-adjuvant chemotherapy and radiation is not clear and due to several factors including different interpretative criteria and technical factors [28–30]. Similarly, FDG PET/CT evaluation of liver metastases treated with locoregional ablation is also limited, especially during early post-intervention period due to inflammatory response around the lesion [28].

The reported accuracy of FDG PET in detecting pelvic recurrences is 95%, as compared with 65% for CT [31]. In particular, Valk et al. [32] demonstrated the sensitivity and specificity of FDG PET to be 93 and 98% when compared with 69 and 96%, respectively, for CT. It is particularly effective in characterizing a presacral lesion following surgery, with a reported sensitivity of 100% and specificity of 96% [33, 34].

Another common indication at some institutions for FDG PET/CT during the follow-up is in the case of rising serum marker level (CEA) that is correlated with the disease relapse. FDG PET/CT was shown to provide positive and negative predictive values of 89 and 100%, respectively [35], but with a variable rate (up to 21%) of false-positive results [36]. The question remains whether all patients with a rising CEA should receive an FDG PET scan. A pitfall of this approach is the false-positive rate of CEA (5–16%). On the other hand, routine FDG PET/CT as a first-line imaging modality, followed by further investigation guided by PET/CT, may also be a valid strategy [37–39].

In conclusion, FDG PET/CT is a valid tool for the evaluation of patients with rectal cancer. It has important clinical impact especially for the M staging at diagnosis and for detection of disease relapse. The limited anatomical resolution of PET/CT, which affects its utility in the context of T and N staging, is expected to improve with PET/MRI.

17.3 PET/MRI Technique and Protocol

The experience with PET/MRI protocols for evaluation of rectal cancer is evolving, and currently there is no validated protocol, which is a reflection of novelty of this hybrid modality. The experimental protocol at our institution involves whole-body metastatic survey followed by high-resolution-focused imaging of the rectum. This protocol is tailored for evaluation of response to neo-adjuvant therapy in locally advanced rectal cancer (LARC). However, we have not yet received IRB approval for our protocol, and therefore, we are yet to perform clinical scans on our patients.

Standard instructions for PET such as fasting for at least 4 h, plenty of oral fluids, and blood sugar levels less than 150 mg/dL are given to patients. Patients receive an injection of 15 ± 10% mCi of F-18 fluorodeoxyglucose (FDG) followed by the standard 60 min uptake time. For the dedicated rectal cancer protocol, patients receive a rectal evacuant (glycerin suppository) 2 h prior to exam. At the time of exam, a small amount of sonographic gel is instilled into the rectum for luminal distension and to increase conspicuity of index lesion on MRI. Adequate patient centering and placement of surface coils are essential to optimize the MRI signal and to reduce potential artifacts related to B0 field inhomogeneity. The time spent with the patient for these steps contributes additional radiation exposure for technologists when compared with PET/CT [40].

The scan begins with an MRI localizer to prescribe scan range, typically from the vertex of the skull through the upper thighs. MR sequences for attenuation correction (MRAC) and PET data are then co-acquired throughout the entire scan range. Whole-body PET/MR data is acquired in 4–5 bed positions with each bed position taking around 2–3 min. The MRAC sequence is a 2-point Dixon 3D fast spoiled gradient-recalled echo (FSPGR) imaging technique (LAVA Flex) that acquires water-only, fat-only, in-phase, and out-of-phase echoes in a single 20 s breath-hold acquisition. This sequence achieves both attenuation correction and anatomic co-localization. It is resistant to the motion artifacts that are often encountered when a T1-weighted (T1W) 3D

GRE sequence is used for MRAC. Although there is time available for an additional axial T2-weighted (T2W) HASTE and/or DWI sequence through each bed position, we do not acquire this routinely. Based on our clinical experience with PET/MR, we believe that this additional sequence is not warranted since the 2-point Dixon-based MRAC suffices for anatomic co-registration. Moreover, as per our institutional policy, diagnostic MR sequences such as T2W HASTE are to be read by specialty-trained MR radiologists. Therefore, acquisition of an additional T2W HASTE sequence through each bed position would mandate involvement of radiologists from at least three different sections for one PET/MR study, which is neither feasible nor warranted.

Our whole-body metastatic survey exam (Fig. 17.1) is followed by dedicated focused PET/MR of the pelvis, which involves list-mode acquisition of PET data co-acquired with dedicated rectal MRI. MR component of protocol is performed according to our clinically utilized rectal cancer staging protocol using pelvic phase-array multichannel coil. In addition, a longer simultaneous single-bed list-mode PET acquisition is obtained to match the MRI station. This is expected to allow accurate evaluation of index lesion due to better matching of the bladder size and position of anatomical structures between PET and MRI [41, 42].

The high-resolution pelvic MRI study includes standard T2W fast spin echo (FSE) sequence in three orthogonal planes through the rectal tumor site and whole-pelvis axial T1W images. Additional oblique axial diffusion-weighted (DWI) echo-planar imaging (EPI) sequences with multiple b-values and apparent diffusion coefficient (ADC) maps are obtained through the tumor site, with imaging planes to match the oblique axial T2W sequence.
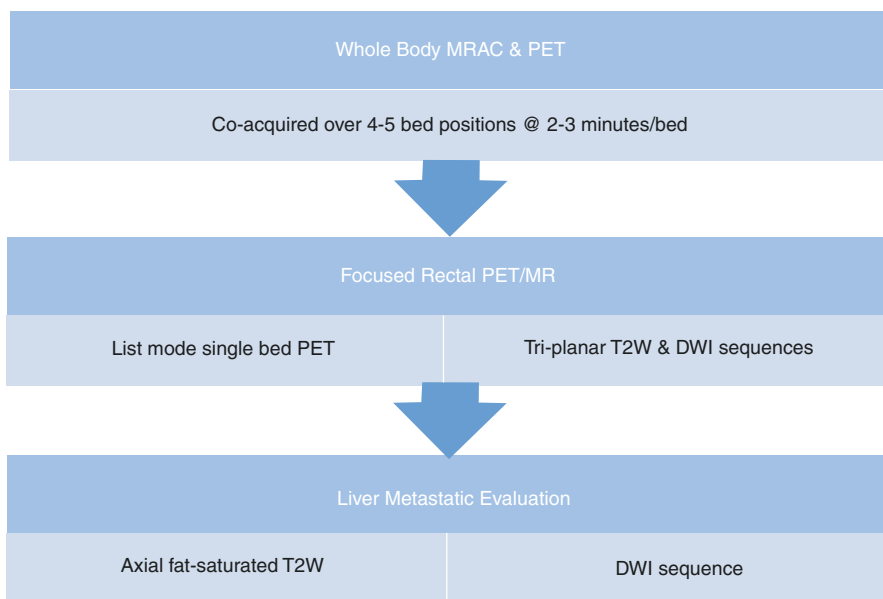

Fig. 17.1 PET/MRI protocol for rectal carcinoma staging

Limited additional MRI sequences of the abdomen (DWI and axial T2 FSE sequence with fat saturation) are also acquired to increase sensitivity for detection of distant metastases. In an effort to keep the protocol duration reasonable for patient comfort and scanner throughput, intravenous gadolinium-enhanced sequences are not part of this protocol. As a corollary, this protocol does not allow the use of perfusion MRI with DCE, which has been shown to have a role in the assessment of response to neo-adjuvant therapy (NAT) in LARC as well as provide information about the status of circumferential resection margin [43–46]. It is anticipated that this PET/MR protocol (whole-body metastatic survey plus focused PET/MR of the pelvis) will require approximately 60 min, which is generally considered to be the maximum scan time limit in view of patient comfort and economic considerations related to scanner throughput [41, 47].

Some investigators have suggested that dual-point PET can predict pathological tumor response better than conventional single-time point pre- and post-chemoradiotherapy (CRT) PET in locally advanced rectal cancer (LARC) [48]. Dual-point PET imaging is feasible with PET/MR. A second stage PET scan (delayed scan) can be performed at 120 min postinjection as a 4–5 min single station list-mode PET acquisition of the pelvis. The disadvantages of dual-time PET include the obvious negative impact on workflow, patient comfort, and economic considerations related to scanner throughput. Therefore, until it can be validated in larger studies, this delayed scan is only part of our research protocol aimed at differentiation of treatment-induced fibrosis and residual viable rectal tumor in the post-neo-adjuvant setting.

When performing PET/MR for evaluation of colonic cancer, another option is to combine the whole-body metastatic survey with focused PET/MR of the abdomen for evaluation of liver metastases. The single-bed list-mode PET acquisition is respiratory bellows-compensated to minimize the effect of respiratory motion and to allow adequate registration with respiratory-triggered or breath-hold liver MRI sequences. The liver MR component can be performed with hepatocyte-specific contrast agent such as gadoxetate (Eovist). It has been shown that navigated hepatobiliary phase imaging using Eovist aligns quite well with respiratory-compensated list-mode liver PET data [49].

The success of an institutional PET/MR practice requires development and validation of individualized scanning protocols that are tailored toward specific clinical indications. For instance, the rectal PET/MR protocol described above is specifically intended for response assessment in patients with LARC. We believe that a one-size-fits-all approach, which is typical for PET/CT, would not be feasible for PET/MR due to challenges inherent to this hybrid imaging modality. Moreover, given the requirement of time-efficient workflow and protocols for the success of a PET/MR practice, a PET/MR protocol should not be designed by simply appending the full set of sequences from a regular MRI protocol. Trade-offs and compromises are required in terms of MRI sequences taking into consideration the incremental benefit of high-quality PET data. In addition, other requirements for building a successful PET/MR practice include buy-in from referring providers and other specialties of radiology, dual-modality trained radiology champions, and trained technologists. At our institution, a certified PET and an MR technologist jointly perform the PET/MR scan. Reporting of PET/MRI studies has not been standardized and dependent on the clinical practice. Two separate reports from nuclear medicine physician and radiologist or a combined single report are options. It's important to have discussion of findings between the two readers to avoid interpretative errors.

17.4   Potential Role of PET/MRI in Rectal Cancer and Initial Results

PET/MR offers several potential advantages over MRI and PET/CT for evaluation of rectal cancer. It can provide actionable insights into disease phenotype and biology beyond that of conventional imaging modalities. When compared with rectal MRI, PET/MR offers the advantage of simultaneous distant metastatic evaluation. Combining potentially complementary metabolic information from PET with multi-parametric MRI has the ability to provide prognostic and treatment response assessment. The superior soft tissue contrast of MRI and the ability to acquire respiratory motion-compensated data with PET/MR are potential benefits over that of PET/CT and contrast-enhanced CT. However, there have been only a few reported studies that have evaluated the utility of PET/MRI in rectal cancer. Most of the reported studies in literature have PET/MRI studies performed immediately after clinical PET/CTs utilizing the same FDG injection and, therefore, are not representative of the manner in which PET/MR will be part of clinical practice. To the best of our knowledge, there has not been any study of integrated stand-alone PET/MR in a homogenous cohort of patients with rectal cancer.

17.5   Staging

Although MRI of the rectum has a significant role in T staging of rectal cancer, its role in N staging is not sufficiently accurate due to reliance on size and morphology of lymph nodes and the known propensity of nodal metastases from rectal cancer to present in normal-sized lymph nodes [13, 50]. Studies have shown that MRI has high sensitivity and PET/CT has high specificity for N staging [51]. Therefore, PET/MR is expected to further improve the staging evaluation of rectal cancer by coupling the incremental metabolic information from PET with high-resolution morphologic evaluation of lymph nodes with MRI. The metabolic information obtained from PET has the potential to influence radiation therapy planning and dose intensification during neo-adjuvant therapy [50].

Paspulati et al. compared the diagnostic accuracy of sequential same-day PET/CT and PET/MR using the same FDG injection in 12 patients with colorectal cancer [52]. PET/MR was performed using the sequential PET/MR system (Ingenuity TF PET/MRI, Philips Healthcare). Of these 12 patients, two patients had advanced rectal cancer. They found high accuracy of high-resolution MRI in determining the T stage of rectal cancer in their two patients. Expectedly, PET data did not contribute to T staging beyond the information provided by MRI. However, the difference in N and M staging performance between PET/CT and PET/MR in these two patients, if any, could not be deciphered from their paper.

PET/MR offers several advantages over PET/CT for detection of small distant metastases through accurate anatomic correlation of small foci of tracer uptake. These advantages arise due to the following technical reasons: (1) soft tissue contrast of MR component of PET/MR is higher than that of CT component of PET/CT; (2) MR and PET data acquisition in PET/MR is truly simultaneous (in hybrid scanners), which ensures high spatial and temporal correlation, as against the sequential CT and PET data acquisition in PET/CT; and (3) the time-of-flight (TOF) capability due to silicon photomultiplier detector (SiPM) of Signa PET/MR (GE Healthcare) provides

higher sensitivity for small metastases. In rectal cancer, these advantages may result in improved detection of small liver metastases or in difficult anatomic locations such as small foci of peritoneal carcinomatosis [53]. Therefore, PET/MR is expected to improve the M staging of rectal cancer. Although not specifically assessed in the context of rectal cancer, PET/MR has shown high accuracy for detection of distant metastases and has contributed to the clinical management more often than PET/CT in a heterogeneous oncologic patient cohort [17, 54]. The use of hepatocyte-specific contrast agent such as Eovist may additionally improve the sensitivity of PET/MR for liver metastases. Therefore, if validated, the whole-body metastatic survey with focused rectal PET/MR protocol has the potential to be a "one-stop-shop" examination for simultaneous local and whole-body staging of rectal cancer.

Kang et al. retrospectively evaluated the added clinical value of integrated whole-body PET/MRI over that of conventional CECT alone in the diagnostic workup of patients with colorectal cancer [55]. Of the 51 patients with colorectal cancer included in their study, 23 patients had rectal adenocarcinoma. Their PET/MRI protocol consisted of a whole-body PET/MRI acquisition and a dedicated MR examination of organs in which lesions were found. They compared the PET/MRI findings with CECT performed within 90 days of the PET/MR. They found inferior performance of PET/MR for detection of pulmonary metastatic nodules (detection rate of 52.9%). However, PET/MRI findings were useful for additional characterization of indeterminate lesions in several anatomic locations, including indeterminate-sized lymph nodes and small hepatic metastases. Hepatic lesions constituted the largest proportion of these additionally characterized lesions. The improved characterization of these lesions with PET/MRI was mainly due to the information provided by MRI. In 21.6% (11/51) patients, treatment strategy was changed after PET/MRI added information to CECT findings. Majority of these findings were again due to liver metastases. However, authors did not report the results separately for the rectal cancer cohort.

In another study, Chandarana et al. reported a 70.3% sensitivity of PET/MRI for all lung nodules seen on prior PET/CT. As expected, the sensitivity was higher for FDG-avid nodules (95.6%) than for non-avid nodules (0.5 cm or larger) (88.6%) [56]. In a heterogeneous oncologic patient population, the same group subsequently reported that the majority of non-FDG-avid lung nodules missed on PET/MRI either disappeared or remained stable on follow-up imaging [57]. Recently introduced free-breathing ultrashort echo time (UTE) sequence has been shown to improve detection of lung nodules on PET/MRI [58]. Detection may also be improved by using a diagnostic 3D contrast-enhanced T1W sequence to the protocol. However, PET/MRI is not yet equivalent to PET/CT for assessment of lung nodules. Therefore, it is prudent to consider CT chest for evaluation of potential lung metastases in patients with rectal or colorectal neoplasms.

17.6 Assessing Response to Neo-adjuvant Therapy (NAT)

The standard of care for LARC consists of long-course neo-adjuvant chemoradiotherapy (NAT) followed by total mesorectal excision (TME). The rationale for this strategy is the observed reduction in the rates of local recurrence and lower

long-term toxicity than postoperative chemotherapy [59]. Around 15–27% of patients will achieve complete pathologic response (pCR) after NAT. Regardless of initial tumor stage, pCR following NAT portends excellent local control and disease-free survival [60–63]. This discovery has led to a paradigm shift in the management of LARC with a number of institutions considering non-operative management for patients that achieve a complete clinicopathologic response after NAT. Outcomes of this non-operative management have been comparable to that of operative management. In view of this consideration, early prediction of pCR has become an important goal of imaging with significant implications for management. MRI assessment of tumor regression may help predict survival. In fact, MRI is considered the technique of choice for restaging rectal cancer after NAT [64]. Likewise, reduction in tumor SUV following NAT correlates with increased likelihood of pCR [65–67]. A comparison of PET alone and MRI alone with combined fused PET/MRI data in post-NAT LARC has noted improvement in diagnostic performance of fused PET/MRI data: sensitivity, specificity, and accuracy of 60 versus 80%, 20 versus 66.7%, and 80 versus 86.7% for MRI data alone versus fused PET-MRI data, respectively [68]. However, neither of the two modalities—MRI or PET—can predict pCR reliably enough to influence clinical decision-making.

Theoretically, PET/MR may provide higher diagnostic performance than current imaging modalities for prediction of pCR subsequent to NAT for LARC. PET/MR performed with DWI combines three complementary pieces of information: gluco-metabolic functional information from PET, morphologic changes in the tumor size from MRI, and cellularity information from DWI. For instance, in a cohort of nine patients with rectal cancer who underwent regional hybrid PET/MR after whole-body PET/CT using the same FDG injection, Jeong et al. [69] found that ADC mean values of the rectal lesion significantly and inversely correlated with the lesions' SUV values. The correlation found between SUVs and ADC values supports the notion that high cellularity due to tumor proliferation results in greater metabolism activity and restricts water diffusion. Such complementary parameters obtained from PET/MR can be combined with clinicopathologic variables and biomarkers such as serum carcinoembryonic antigen (CEA) to generate a statistical model for predication of pathologic response in rectal cancer subsequent to NAT. However, this has not yet been attempted. We are in the process of evaluating PET/MR in this clinical context.

17.7 Limitations of PET/MRI in the Evaluation of Rectal Carcinoma

PET/MRI is promising but has several limitations that need to be addressed when implemented in clinical practice. The limitations include higher cost compared to PET/CT, longer examination times that requires patient cooperation and limits patient throughput, and suboptimal evaluation of lung nodules, which may require additional CT of the chest. Improvement in co-registration and scanning techniques may overcome these limitations in the future (Figs. 17.2, 17.3, and 17.4).
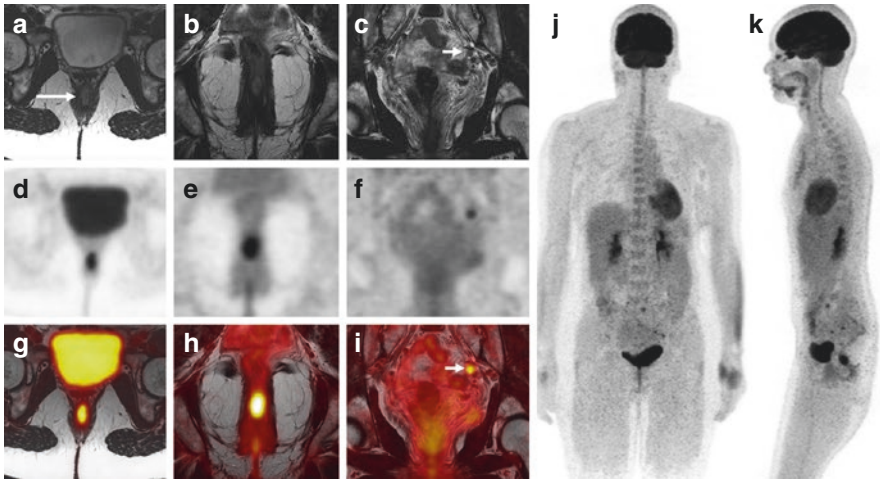
Fig. 17.2 A 53-year-old male with rectal carcinoma confined to the rectal wall (T stage 1/T stage 2). Coronal T2-weighted images (*top row*, **a–c**) and corresponding FDG images (*middle row*, **d–f**) and fused MRI-PET images (*bottom row*, **g–i**) showing intermediate signal intensity oval-shaped mass in the lower rectum with intense FDG uptake and avid left internal iliac lymph node (*short arrow*). Coronal (**j**) and sagittal (**k**) MIP PET images showing the primary rectal tumor (Courtesy Dr. Thomas Hope, MD, UCSF, San Francisco)
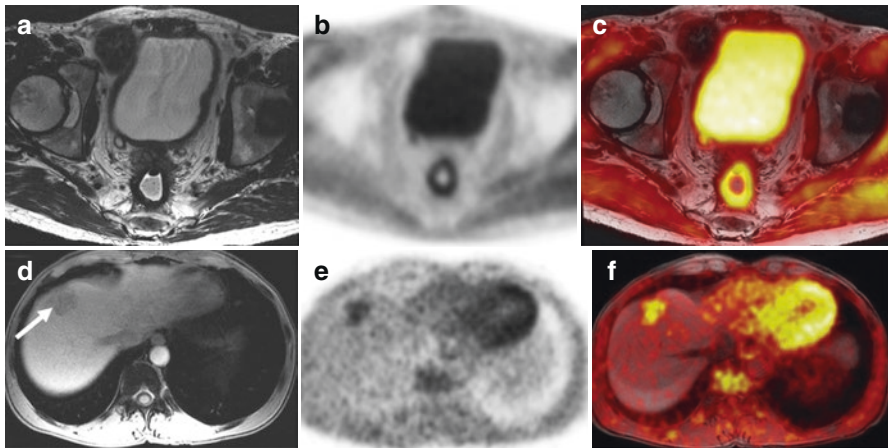
Fig. 17.3 A 46-year-old male with rectal carcinoma treated with neo-adjuvant chemoradiation and PET/MRI performed for staging prior to resection. T2-weighted image (**a**), PET image (**b**), and fused MRI-PET image (**c**) showing primary mass with FDG uptake. Note perirectal stranding due to radiation. Hypointense lesion in the right lobe of the liver on hepatobiliary phase (**d**, *arrow*) which is FDG avid as shown on FDG image (**e**) and fused image (**f**) and consistent with liver metastases. (Courtesy Dr. Thomas Hope, MD, UCSF, San Francisco)
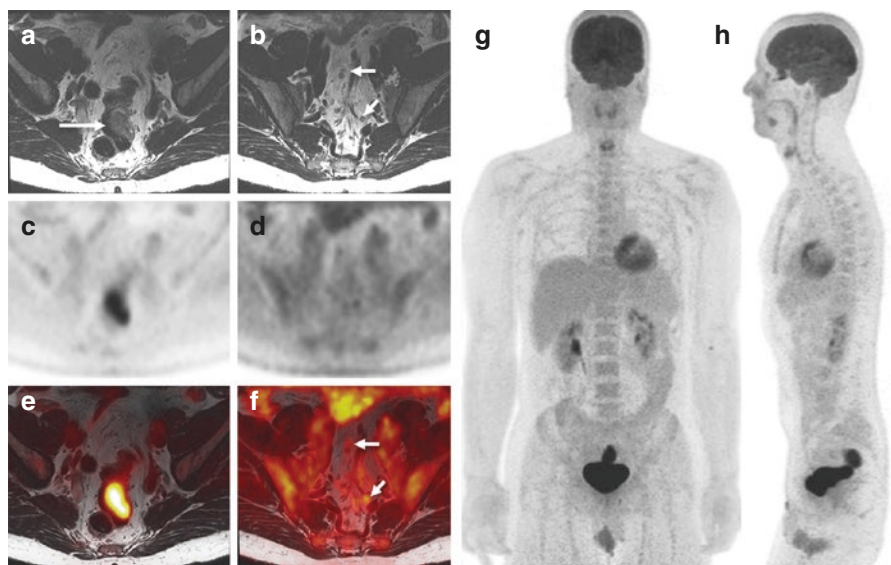
Fig. 17.4 A 45-year-old male with a bulky rectal carcinoma projecting into the lumen (T stage 3a). Axial T2-weighted images (*top row*, **a**, **b**), corresponding PET images (*middle row*, **c**, **d**), and fused MRI-PET images (*bottom row*, **e**, **f**) showing primary mass with FDG uptake and mildly FDG-avid perirectal lymph nodes (*short arrows*). Coronal (**g**) and sagittal (**h**) MIP images showing primary mass behind the bladder (Courtesy Dr. Thomas Hope, MD, UCSF, San Francisco)

References

1. Ferlay J, Soerjomataram I, Dikshit R, Eser S, Mathers C, Rebelo M, Parkin DM, Forman D, Bray F. Cancer incidence and mortality worldwide: sources, methods and major patterns in GLOBOCAN 2012. Int J Cancer. 2015;136(5):E359–86.
2. Kaur H, Choi H, You YN, Rauch GM, Jensen CT, Hou P, Chang GJ, Skibber JM, Ernst RD. MR imaging for preoperative evaluation of primary rectal cancer: practical considerations. Radiographics. 2012;32(2):389–409.
3. Brown G, Daniels IR, Richardson C, Revell P, Peppercorn D, Bourne M. Techniques and trouble-shooting in high spatial resolution thin slice MRI for rectal cancer. Br J Radiol. 2005;78(927):245–51.
4. Taylor FG, Swift RI, Blomqvist L, Brown G. A systematic approach to the interpretation of preoperative staging MRI for rectal cancer. Am J Roentgenol. 2008;191(6):1827–35.
5. Kwok H, Bissett IP, Hill GL. Preoperative staging of rectal cancer. Int J Color Dis. 2000;15(1):9–20.
6. Del Vescovo R, Trodella LE, Sansoni I, Cazzato RL, Battisti S, Giurazza F, Ramella S, Cellini F, Grasso RF, Trodella L, Beomonte Zobel B. MR imaging of rectal cancer before and after chemoradiation therapy. Radiol Med. 2012;117(7):1125–38.
7. Jhaveri KS, Hosseini-Nik H. MRI of rectal cancer: an overview and update on recent advances. Am J Roentgenol. 2015;205(1):W42–55.
8. Calvo FA, Domper M, Matute R, Martínez-Lázaro R, Arranz JA, Desco M, Alvarez E, Carreras JL. 18F-FDG positron emission tomography staging and restaging in rectal cancer treated with preoperative chemoradiation. Int J Radiat Oncol Biol Phys. 2004;58(2):528–35.
9. Antoch G, Bockisch A. Combined PET/MRI: a new dimension in whole-body oncology imaging? Eur J Nucl Med Mol Imaging. 2009;36(Suppl 1):S113–20.

10. Denecke T, Rau B, Hoffmann KT, Hildebrandt B, Ruf J, Gutberlet M, Hünerbein M, Felix R, Wust P, Amthauer H. Comparison of CT, MRI and FDG-PET in response prediction of patients with locally advanced rectal cancer after multimodal preoperative therapy: is there a benefit in using functional imaging? Eur Radiol. 2005;15(8):1658–66.

11. Schmidt GP, Baur-Melnyk A, Haug A, Utzschneider S, Becker CR, Tiling R, Reiser MF, Hermann KA. Whole-body MRI at 1.5 T and 3 T compared with FDG-PET-CT for the detection of tumour recurrence in patients with colorectal cancer. Eur Radiol. 2009;19(6):1366–78.

12. Oliva MR, Saini S. Liver cancer imaging: role of CT, MRI, US and PET. Cancer Imaging. 2004;4(Special Issue A):S42–6.

13. Koh DM, Scurr E, Collins DJ, Pirgon A, Kanber B, Karanjia N, Brown G, Leach MO, Husband JE. Colorectal hepatic metastases: quantitative measurements using single-shot echo-planar diffusion-weighted MR imaging. Eur Radiol. 2006;16(9):1898–905.

14. Vreugdenburg TD, Ma N, Duncan JK, Riitano D, Cameron AL, Maddern GJ. Comparative diagnostic accuracy of hepatocyte-specific gadoxetic acid (Gd-EOB-DTPA) enhanced MR imaging and contrast enhanced CT for the detection of liver metastases: a systematic review and meta-analysis. Int J Color Dis. 2016;31(11):1739–49.

15. Abdel-Nabi H, Doerr RJ, Lamonica DM, Cronin VR, Galantowicz PJ, Carbone GM, Spaulding MB. Staging of primary colorectal carcinomas with fluorine-18 fluorodeoxyglucose whole-body PET: correlation with histopathologic and CT findings. Radiology. 1998;206(3):755–60.

16. Mukai M, Sadahiro S, Yasuda S, Ishida H, Tokunaga N, Tajima T, Makuuchi H. Preoperative evaluation by whole-body 18F-fluorodeoxyglucose positron emission tomography in patients with primary colorectal cancer. Oncol Rep. 2000;7(1):85–7.

17. Facey K, Bradbury I, Laking G, Payne E. Overview of the clinical effectiveness of positron emission tomography imaging in selected cancers. Health Technol Assess. 2007;11(44):iii–v. xi-267

18. Furukawa H, Ikuma H, Seki A, Yokoe K, Yuen S, Aramaki T, Yamagushi S. Positron emission tomography scanning is not superior to whole body multidetector helical computed tomography in the preoperative staging of colorectal cancer. Gut. 2006;55(7):1007–11.

19. Llamas-Elvira JM, Rodríguez-Fernández A, Gutiérrez-Sáinz J, Gomez-Rio M, Bellon-Guardia M, Ramos-Font C, Rebollo-Aguirre AC, Cabello-García D, Ferrón-Orihuela A. Fluorine-18 fluorodeoxyglucose PET in the preoperative staging of colorectal cancer. Eur J Nucl Med Mol Imaging. 2007;34(6):859–67.

20. Kosugi C, Saito N, Murakami K, Ochiai A, Koda K, Ono M, Sugito M, Ito M, Oda K, Seike K, Miyazaki M. Positron emission tomography for preoperative staging in patients with locally advanced or metastatic colorectal adenocarcinoma in lymph node metastasis. Hepato-Gastroenterology. 2008;55(82–83):398–402.

21. Tsunoda Y, Ito M, Fujii H, Kuwano H, Saito N. Preoperative diagnosis of lymph node metastases of colorectal cancer by FDG-PET/CT. Jpn J Clin Oncol. 2008;38(5):347–53.

22. Akiyoshi T, Oya M, Fujimoto Y, Kuroyanagi H, Ueno M, Yamaguchi T, Koyama M, Tanaka H, Matsueda K, Muto T. Comparison of preoperative whole-body positron emission tomography with MDCT in patients with primary colorectal cancer. Color Dis. 2009;11(5):464–9.

23. Ono K, Ochiai R, Yoshida T, Kitagawa M, Omagari J, Kobayashi H, Yamashita Y. Comparison of diffusion-weighted MRI and 2-[fluorine-18]-fluoro-2-deoxy-D-glucose positron emission tomography (FDG-PET) for detecting primary colorectal cancer and regional lymph node metastases. J Magn Reson Imaging. 2009;29(2):336–40.

24. Mitry E, Guiu B, Cosconea S, Jooste V, Faivre J, Bouvier AM. Epidemiology, management and prognosis of colorectal cancer with lung metastases: a 30-year population-based study. Gut. 2010;59(10):1383–8.

25. Geoghegan JG, Scheele J. Treatment of colorectal liver metastases. Br J Surg. 1999;86(2):158–69.

26. Kantorová I, Lipská L, Bêlohlávek O, Visokai V, Trubač M, Schneiderová M. Routine (18) F-FDG PET preoperative staging of colorectal cancer: comparison with conventional staging and its impact on treatment decision making. J Nucl Med. 2003;44(11):1784–8.

27. Lake ES, Wadhwani S, Subar D, Kauser A, Harris C, Chang D, Lapsia S. The influence of FDG PET-CT on the detection of extrahepatic disease in patients being considered for resection of colorectal liver metastasis. Ann R Coll Surg Engl. 2014;96(3):211–5.

28. de Geus-Oei LF, Vriens D, van Laarhoven HW, van der Graaf WT, Oyen WJ. Monitoring and predicting response to therapy with 18F-FDG PET in colorectal cancer: a systematic review. J Nucl Med. 2009;50(Suppl 1):43S–54S.

29. Capirci C, Rubello D, Pasini F, Galeotti F, Bianchini E, Del Favero G, Panzavolta R, Crepaldi G, Rampin L, Facci E, Gava M, Banti E, Marano G. The role of dual-time combined 18-fluorodeoxyglucose positron emission tomography and computed tomography in the staging and restaging workup of locally advanced rectal cancer, treated with preoperative chemoradiation therapy and radical surgery. Int J Radiat Oncol Biol Phys. 2009;74(5):1461–9.

30. Martoni AA, Di Fabio F, Pinto C, Castellucci P, Pini S, Ceccarelli C, Cuicchi D, Iacopino B, Di Tullio P, Giaquinta S, Tardio L, Lombardi R, Fanti S, Cola B. Prospective study on the FDG-PET/CT predictive and prognostic values in patients treated with neoadjuvant chemoradiation therapy and radical surgery for locally advanced rectal cancer. Ann Oncol. 2011;22(3):650–6.

31. Schiepers C, Penninckx F, De Vadder N, Merckx E, Mortelmans L, Bormans G, Marchal G, Filez L, Aerts R. Contribution of PET in the diagnosis of recurrent colorectal cancer: comparison with conventional imaging. Eur J Surg Oncol. 1995;21(5):517–22.

32. Valk PE, Abella-Columna E, Haseman MK, Pounds TR, Tesar RD, Myers RW, Greiss HB, Hofer GA. Whole-body PET imaging with [18F]fluorodeoxyglucose in management of recurrent colorectal cancer. Arch Surg. 1999;134(5):503–11. discussion 511–3

33. Choi H, Yoon HJ, Kim TS, Oh JH, Kim DY, Kim SK. Voxel-based dual-time 18F-FDG parametric imaging for rectal cancer: differentiation of residual tumor from postchemoradiotherapy changes. Nucl Med Commun. 2013;34(12):1166–73.

34. Even-Sapir E, Parag Y, Lerman H, Gutman M, Levine C, Rabau M, Figer A, Metser U. Detection of recurrence in patients with rectal cancer: PET/CT after abdominoperineal or anterior resection. Radiology. 2004;232(3):815–22.

35. Flanagan FL, Dehdashti F, Ogunbiyi OA, Kodner IJ, Siegel BA. Utility of FDG-PET for investigating unexplained plasma CEA elevation in patients with colorectal cancer. Ann Surg. 1998;227(3):319–23.

36. Flamen P, Hoekstra OS, Homans F, Van Cutsem E, Maes A, Stroobants S, Peeters M, Penninckx F, Filez L, Bleichrodt RP, Mortelmans L. Unexplained rising carcinoembryonic antigen (CEA) in the postoperative surveillance of colorectal cancer: the utility of positron emission tomography (PET). Eur J Cancer. 2001;37(7):862–9.

37. Makis W, Kurzencwyg D, Hickeson M. 18F-FDG PET/CT superior to serum CEA in detection of colorectal cancer and its recurrence. Clin Imaging. 2013;37(6):1094–7.

38. Kamel IR, Cohade C, Neyman E, Fishman EK, Wahl RL. Incremental value of CT in PET/CT of patients with colorectal carcinoma. Abdom Imaging. 2004;29(6):663–8.

39. Yap JT, Carney JP, Hall NC, Townsend DW. Image-guided cancer therapy using PET/CT. Cancer J. 2004;10(4):221–33.

40. Goh V, Prezzi D, Mallia A, Bashir U, Stirling J, John J. Positron emission tomography/magnetic resonance imaging of gastrointestinal cancers. Semin Ultrasound CT MR. 2016;37(4):352–7.

41. Lee D, Lee J. Whole-body PET/MRI for colorectal cancer staging: is it the way forward? J Magn Reson Imaging. 2016;45(1):21–35.

42. Yoo H, Lee J, Lee J. Integrated whole body MR/PET: where are we? Korean J Radiol. 2015;16(1):32–49.

43. Gollub MJ, Cao K, Gultekin DH, Kuk D, Gonen M, Sohn M, Schwartz LH, Weiser MR, Temple LK, Nash GM, Guillem JG, Wang M, Garcia-Aguilar J, Goodman K, Paty PB. Prognostic aspects of DCE-MRI in recurrent rectal cancer. Eur Radiol. 2013;23(12):3336–44.

44. Kim S, Lee J, Gupta SN, Han J, Choi B. Dynamic contrast-enhanced MRI to evaluate the therapeutic response to neoadjuvant chemoradiation therapy in locally advanced rectal cancer. J Magn Reson Imaging. 2014;40(3):730–7.

45. Oberholzer K, Menig M, Pohlmann A, Junginger T, Heintz A, Kreft A, Hansen T, Schneider A, Lollert A, Schmidberger H, Christoph D. Rectal cancer: assessment of response to neo-

adjuvant chemoradiation by dynamic contrast-enhanced MRI. J Magn Reson Imaging. 2013;38(1):119–26.

46. Lollert A, Junginger T, Schimanski C, Biesterfeld S, Gockel I, Düber C, Oberholzer K. Rectal cancer: dynamic contrast-enhanced MRI correlates with lymph node status and epidermal growth factor receptor expression. J Magn Reson Imaging. 2014;39(6):1436–42.

47. Sotoudeh H, Sharma A, Fowler KJ, McConathy J, Dehdashti F. Clinical application of PET/MRI in oncology. J Magn Reson Imaging. 2016;44(2):265–76.

48. Yoon H-j, Kim S-k, Kim T-S, Im H-J, Lee E, Kim H, Park J, Chang H, Choi H, Kim D, Oh J. New application of dual point 18F-FDG PET/CT in the evaluation of neoadjuvant chemoradiation response of locally advanced rectal cancer. Clin Nucl Med. 2013;38(1):7.

49. Hope TA, Verdin EF, Bergsland EK, Ohliger MA, Corvera CU, Nakakura EK. Correcting for respiratory motion in liver PET/MRI: preliminary evaluation of the utility of bellows and navigated hepatobiliary phase imaging. EJNMMI Phys. 2015;2(1):1–11.

50. Matthews R, Choi M. Clinical utility of positron emission tomography magnetic resonance imaging (PET-MRI) in gastrointestinal cancers. Diagnostics. 2016;6(3):35.

51. Kim D, Kim J, Ryu Y, Jeon T, Yu J-S, Chung J-J. Nodal staging of rectal cancer: high-resolution pelvic MRI versus 18F-FDGPET/CT. J Comput Assist Tomogr. 2011;35(5):531.

52. Paspulati R, Partovi S, Herrmann KA, Krishnamurthi S, Delaney CP, Nguyen NC. Comparison of hybrid FDG PET/MRI compared with PET/CT in colorectal cancer staging and restaging: a pilot study. Abdom Imaging. 2015;40(6):1415–25.

53. Catalano OA, Masch WR, Catana C, Mahmood U, Sahani DV, Gee MS, Menezes L, Soricelli A, Salvatore M, Gervais D, Rosen BR. An overview of PET/MR, focused on clinical applications. Abdom Radiol. 2017;42(2):631–4.

54. Catalano OA, Rosen BR, Sahani DV, Hahn PF, Guimaraes AR, Vangel MG, Nicolai E, Soricelli A, Salvatore M. Clinical impact of PET/mr imaging in patients with cancer undergoing same-day PET/CT: initial experience in 134 patients—a hypothesis-generating exploratory study. Radiology. 2013;269(3):857–69.

55. Kang B, Lee J, Song Y, Woo S, Hur B, Jeon J, Paeng J. Added value of integrated whole-body PET/MRI for evaluation of colorectal cancer: comparison with contrast-enhanced MDCT. Am J Roentgenol. 2016;206(1):20.

56. Chandarana H, Heacock L, Rakheja R, DeMello LR, Bonavita J, Block TK, Geppert C, Babb JS, Friedman KP. Pulmonary nodules in patients with primary malignancy: comparison of hybrid PET/MR and PET/CT imaging. Radiology. 2013;268(3):874–81.

57. Raad RA, Friedman KP, Heacock L, Ponzo F, Melsaether A, Chandarana H. Outcome of small lung nodules missed on hybrid PET/MRI in patients with primary malignancy. J Magn Reson Imaging. 2016;43(2):504–11.

58. Burris NS, Johnson KM, Larson PE, Hope MD, Nagle SK, Behr SC, Hope TA. Detection of small pulmonary nodules with ultrashort echo time sequences in oncology patients by using a PET/MR system. Radiology. 2016;278(1):239–46.

59. Sauer R, Becker H, Hohenberger W, Rödel C, Wittekind C, Fietkau R, Martus P, Tschmelitsch J, Hager E, Hess CF, Karstens J-H, Liersch T, Schmidberger H, Raab R, German Rectal Cancer Group. Preoperative versus postoperative chemoradiotherapy for rectal cancer. N Engl J Med. 2004;351(17):1731–40.

60. Maas M, Nelemans PJ, Valentini V, Das P, Rödel C, Kuo L-J, Calvo FA, García-Aguilar J, Glynne-Jones R, Haustermans K, Mohiuddin M, Pucciarelli S, Small W, Suárez J, Theodoropoulos G, Biondo S, Beets-Tan RGH, Beets GL. Long-term outcome in patients with a pathological complete response after chemoradiation for rectal cancer: a pooled analysis of individual patient data. Lancet Oncol. 2010;11(9):835–44.

61. Habr-Gama A, Perez R, Nadalin W, Sabbaga J, Jr U, Ribeiro U Jr, e Sousa AH Jr, Campos FG, Kiss DR, Gama-Rodrigues J. Operative versus nonoperative treatment for stage 0 distal rectal cancer following chemoradiation therapy: long-term results. Ann Surg. 2004;240:711–7.

62. Smith RK, Fry RD, Mahmoud NN, Paulson CE. Surveillance after neoadjuvant therapy in advanced rectal cancer with complete clinical response can have comparable outcomes to total mesorectal excision. Int J Color Dis. 2015;30(6):769–74.

63. Garcia-Aguilar J, Shi Q, Thomas CR, Chan E, Cataldo P, Marcet J, Medich D, Pigazzi A, Oommen S, Posner MC. A phase II trial of neoadjuvant chemoradiation and local excision for T2N0 rectal cancer: preliminary results of the ACOSOG Z6041 trial. Ann Surg Oncol. 2011;19(2):384–91.
64. Tudyka V, Blomqvist L, Beets-Tan RGH, Boelens PG, Valentini V, van de Velde CJ, Dieguez A, Brown G. EURECCA consensus conference highlights about colon & rectal cancer multidisciplinary management: the radiology experts review. Eur J Surg Oncol (EJSO). 2014;40(4):469–75.
65. Patel UB, Taylor F, Blomqvist L, George C, Evans H, Tekkis P, Quirke P, Sebag-Montefiore D, Moran B, Heald R, Guthrie A, Bees N, Swift I, Pennert K, Brown G. Magnetic resonance imaging-detected tumor response for locally advanced rectal cancer predicts survival outcomes: MERCURY experience. J Clin Oncol Off J Am Soc Clin Oncol. 2011;29(28):3753–60.
66. Cascini G, Avallone A, Delrio P, Guida C, Tatangelo F, Marone P, Aloj L, Martinis F, Comella P, Parisi V, Lastoria S. 18F-FDG PET is an early predictor of pathologic tumor response to preoperative radiochemotherapy in locally advanced rectal cancer. J Nucl Med Off Publ Soc Nucl Med. 2006;47(8):1241–8.
67. Huh J, Min J, Lee J, Kim H, Kim Y. The predictive role of sequential FDG-PET/CT in response of locally advanced rectal cancer to neoadjuvant chemoradiation. Am J Clin Oncol. 2012;35(4):340–4.
68. Metser U, Jhaveri KS, Murphy G, Halankar J, Hussey D, Dufort P, Kennedy E. Multiparameteric PET-MR assessment of response to neoadjuvant chemoradiotherapy in locally advanced rectal cancer: PET, MR, PET-MR and tumor texture analysis: a pilot study. Adv Mol Imaging. 2015;5(03):49.
69. Jeong J, Cho I, Chun K, Kong E, Kwon S, Kim J. Correlation between apparent diffusion coefficients and standardized uptake values in hybrid 18F-FDG PET/MR: preliminary results in rectal cancer. Nucl Med Mol Imaging. 2016;50(2):150–6.

PET/MRI for Gynecological Malignancies

18

Ephraim Parent, Vanessa Sanders, Farrokh Dehdashti, and Kathryn Fowler

Contents

E. Parent
Division of Nuclear Medicine, Emory University, Atlanta, GA, USA

V. Sanders
Edward Mallinckrodt Institute of Radiology, St. Louis, MO, USA

Alvin J. Siteman Cancer Center, St. Louis, MO, USA

F. Dehdashti • K. Fowler (✉)
Edward Mallinckrodt Institute of Radiology, St. Louis, MO, USA

Alvin J. Siteman Cancer Center, St. Louis, MO, USA

Washington University School of Medicine, St. Louis, MO, USA
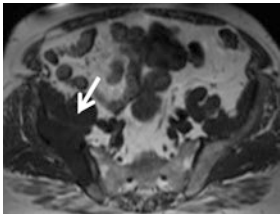e-mail: fowlerk@mir.wustl.edu

18.1   Introduction
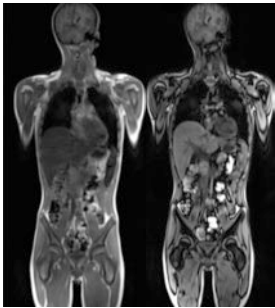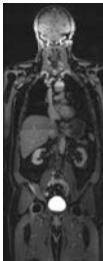
2-[^{18}F]Fluoro-2-deoxy-D-glucose (FDG) PET/MRI has emerged as another diagnostic tool for gynecological cancer in recent years. PET/MRI combines the unique tissue characterization and functional information of MRI with the quantifiable molecular information provided by PET. There are two major ways in which these imaging modalities are combined or fused, namely, hardware based and retrospective software based. Hardware-based image fusion is performed by means of hybrid scanners, which enable the real-time acquisition and fusion of two different imaging modalities within a single device. Retrospective software-based image fusion relies on dedicated software to fuse two separate imaging datasets, most often from CT or MRI and single-photon emission tomography (SPECT) or PET. This technique, called "image registration," is used to align both sets of data so that each voxel corresponds to the same anatomical landmarks in both images [1]. Integrated systems place solid-state PET detectors, which are compatible with external magnetic fields, inside the MRI gantry, with further details available in Chapter 1. The integrated design allows for simultaneous PET and MRI acquisition with advantages such as reduced scanning time, improved co-registration, and simultaneous imaging of dynamic processes visualized on both PET and MRI [2].

In gynecologic cancer patients, FDG PET/MRI protocols are intended to provide treatment planning in a single imaging session. The examination assesses the locoregional extent of pelvic tumor and evaluates the entire body for nodal, peritoneal, and skeletal metastases. During the PET acquisition, whole-body Dixon MR images are acquired for attenuation correction and may be used for anatomic correlation. Additional whole-body MR sequences may be acquired with little time penalty to supplement anatomic correlation and characterization of PET findings. While no uniformly agreed upon protocols exist, most protocols incorporate rapid acquisition T2-weighted fast or turbo spin echo with or without fat suppression and T1-weighted fast or turbo spin echo sequences. For T2-weighted images, some groups use single-shot fast spin echo techniques which are faster than fast or turbo spin echo sequences. The combination of T1- and T2-weighted imaging provides a broad overview of organ anatomy and evaluation of marrow replacement.

In addition to whole-body sequences, dedicated pelvic MR imaging is indicated for most gynecological cancers and typically includes high-resolution T2-weighted images, diffusion imaging, and dynamic contrast-enhanced T1-weighted fat-suppressed images. Tables 18.1 and 18.2 illustrate a sample protocol and details related to some of the sequences. Patient table times on the current scanners last approximately 35–60 min.
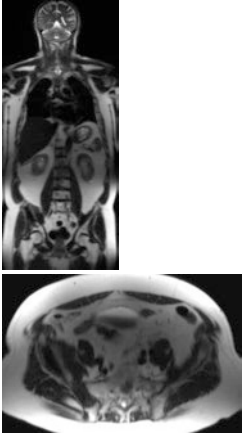
We present in detail below the current status of gynecological oncologic imaging and review the available literature on hybrid PET/MRI. Additionally, we will discuss potential future work with some non-FDG PET tracers that show promise as useful tools for gynecologic imaging.

Table 18.1 Sample protocol and sequence details. MRAC-magnetic resonance attenuation correction

MRI sequence	Acquisition details	Diagnostic details	Example images
Whole-body sequences			
Attenuation correction sequences			
Dixon-based MRAC	Breath hold	T1-weighted gradient recall echo	
	~20 s	Generally lower resolution	
		Produces inphase (left image), opposed phase (right image), and fat-only and water-only (not shown) images from which a map is generated	
Diagnostic T1-weighted sequences: often is performed after contrast to evaluate for enhancement			
T1-weighted SPGR	Breath hold	T1-weighted spoiled gradient echo	
	20–30 s	Can be performed with spectral fat saturation or Dixon-based fat saturation	
T1 weighted turbo spin echo	Breath hold	T1W turbo spin echo often acquired with parallel imaging	
		Anatomic correlation for bone	
		Fluid/water structures are dark	
		Marrow replacing lesions are dark as is shown by the arrow indicated a large right iliac wing mass	

(continued)

Table 18.1 (continued)

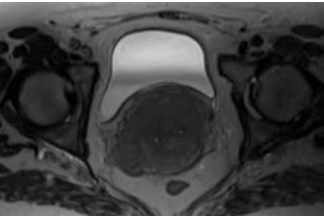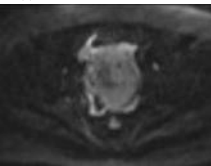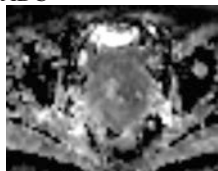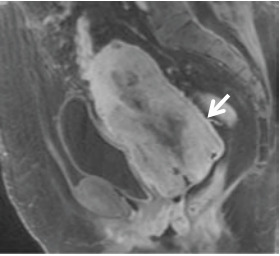| MRI sequence	Acquisition details	Diagnostic details	Example images
Diagnostic T2-weighted sequences: at least one T2-weighted set of images will be acquired			
T2 weighted	Free breathing or multi-breath hold	T2W fast/turbo spin echo often acquired with parallel imaging and partial Fourier techniques to increase speed	
		Anatomic correlation for organs	
Fast/turbo spin echo		Fluid/water structures are bright	
		Relatively motion insensitive	
T2-weighted single-shot fast spin echo	Free breathing	SSFSE or HASTE sequence, motion robust and fast	

18.2 Cervical Cancer

18.2.1 Background

Worldwide, cervical cancer is the second most common gynecologic malignancy. The overall 5-year survival rate of cervical cancer is 67.9%. This number drastically improves if the disease is confined to the primary site (90.9%) and becomes much worse if there are regional lymph nodes (57.1%) or distant metastases (16.1%) [3]. In patients with metastatic cervical cancer, the median survival time is only 8–13 months [4].

The prevalence of lymph node involvement in early stage cervical cancer is estimated to be approximately 15–20%, and approximately 33% of patients with locally advanced cervical cancer have para-aortic lymph node metastases [5]. Extrapelvic disease is uncommon with only 12% of patients having metastases beyond the regional lymph nodes at the time of diagnosis. Hematogenous spread is rare with

Table 18.2 Pelvic sequences for PET/MRI

MRI sequence	Acquisition details	Diagnostic details	Example images
Pelvic station			
T2-weighted high resolution	Long acquisitions	T2W images show anatomic detail for staging, tumor volumes, and characterization of findings	
	Free breathing		
	Multi-average	Key sequence for fusion. Be sure to place oblique axial planes perpendicular to the uterus or cervix as needed	
	May be acquired in multiple planes or as isotropic 3D		
Diffusion-weighted imaging (DWI)	Free breathing	Depicts functional information related to Brownian motion of water molecules	DWI
	B-value range from 50–1000 or even higher	Relatively low resolution	
	Multi-average for improved signal	Bright structures on DWI may be inherently T2 bright or restricting diffusion (ADC signal dark)	ADC
	Consider reduced field of view diffusion if available	ADC tumor volumes correlate well in cervical cancer with FDG isocontours	
Pre- and post-contrast T1-weighted imaging	Breath hold	Often 3D gradient recall echo T1W fat-suppressed sequences	
	Multi-phase acquisition to capture dynamic phases of contrast	Contrast-enhanced imaging can be valuable in staging endometrial cancer and uterine involvement (see image of cervical cancer indicated by arrow) and characterizing findings in the pelvis	
	Oblique sagittal plane through the uterus should be obtained for uterine malignancy		

ADC apparent diffusion coefficient

most common metastasis to the lungs, liver, and bones. Distant organ disease is unlikely in the absence of pelvic lymph node involvement.

18.2.2 MRI of Cervical Cancer

Cross-sectional imaging such as CT and MRI is increasingly used to determine the extent of cervical cancer and may occasionally be used to replace components of traditional FIGO scoring system. In current clinical practice, MRI is the primary tool used for the evaluation of tumor morphology and local extent of cancer. It accurately evaluates tumor prognostic features such as size, endocervical growth, parametrial infiltration, and pelvic sidewall or adjacent organ (bladder, rectum) involvement. Reported MRI accuracy rates for determining tumor stage range from 75 to 96% [6]. The American College of Radiology Imaging Network (ACRIN)/Gynecologic Oncology Group (GOG) performed a multicenter clinical trial which compared the performance of MRI, CT, and FIGO clinical staging of invasive cervical cancer, verified by pathologic analysis of hysterectomy specimens [7]. The ACRIN-6651/COG-183 multicenter trial showed that MRI had higher agreement with pathology than CT or clinical examination for delineating tumor margins and measuring tumor size [8]. N-staging by prospective imaging showed 37 and 31% sensitivity, respectively, for both MRI and CT (not significantly different); however, specificity was significantly higher for MRI (94%) than CT (86%).

MRI is highly accurate in assessing tumor size to within 5 mm of the histological specimen in 70–90% of patients [9] and may be more accurate than colposcopy for endocervical extension of tumor (Fig. 18.1). Apparent diffusion coefficient (ADC) values derived from DWI have been shown to be negatively correlated with cellularity, producing relatively low ADC values for various malignancies [10] and may be able to distinguish tumor from surrounding healthy, inflammatory, or scar tissue [11]. MRI features suggestive of parametrial involvement include cervical contour nodularity, irregular borders between tumor and parametrial tissue, and presence of a soft tissue mass within the parametrium (which may encase the periuterine vascular plexus). Tumor signal is generally brighter on T2 than the cervical stroma; a hypointense T2 stromal cervical rim of >3 mm has been shown to exclude parametrial involvement with a specificity of 96–99% and a NPV of 94–100% [12]. When there is loss of the hypointense cervical rim without parametrial irregularity, accurate delineation of tumor extension into parametrial tissue is decreased.

18.2.3 FDG PET/CT of Cervical Cancer

FDG PET/CT is complementary to MR imaging for staging cervical cancer by providing additional benefit for locating nodal and distant metastases. Both MRI and CT inadequately distinguish between enlarged, inflammatory, and metastatic lymph nodes [6]. A meta-analysis for cervical cancer demonstrated pooled sensitivity and
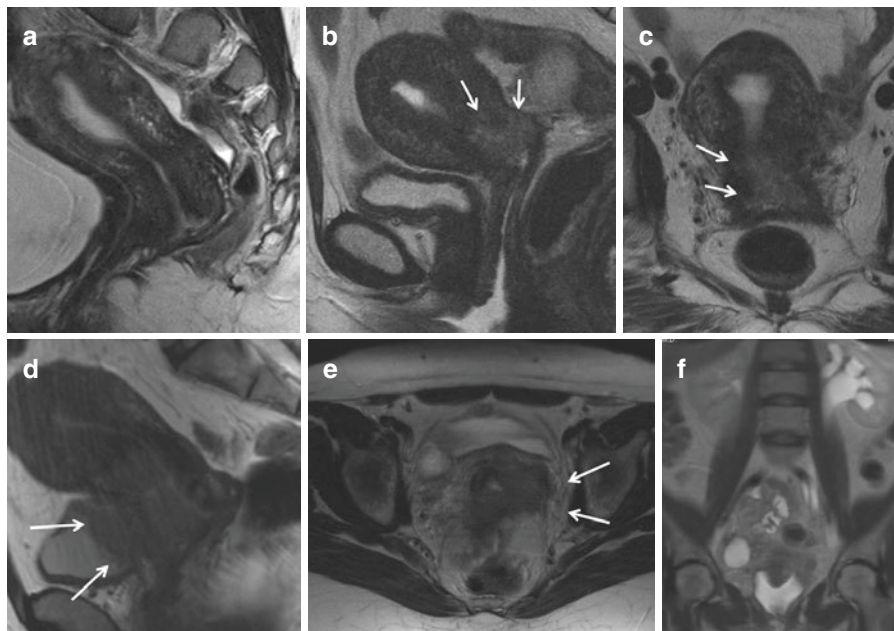
Fig. 18.1 Small field of view T2-weighted image, typically acquired in three planes, is critical for evaluation of primary cervical and endometrial tumors (**a–e**). The normal cervical stroma is dark on T2-weighted images (**a**), which is used to determine if there is invasion into the parametrium. Images (**b**, **c**) show intermediate high T2 signal intensity of tumor replacing portions of the T2 dark cervical stroma. Images (**d**, **e**) demonstrate locally advanced disease with tumor invading the bladder (**d**) and extending the pelvic sidewall (**e**) with resultant left hydronephrosis (**f**)

pooled specificity of FDG PET for para-aortic lymph node metastases was 84 and 95%, respectively, and a sensitivity and specificity of 79 and 99% for pelvic lymph node metastases [13]. PET outperforms MRI or CT with regard to sensitivity and specificity for detection of metastatic lymph nodes [14]. PET/CT demonstrates less robust sensitivity but retains high specificity in lymph nodes smaller than 5 mm. Partial volume effect may cause the usual discriminator of FDG uptake, as assessed by maximum standardized uptake value (SUV_{max}) for differentiating malignant from benign lymph nodes to be unreliable [15]. Despite this limitation, FDG PET remains the most effective tool for detecting metastases including lymph nodes with superior sensitivity and specificity compared to CT or MRI [14].

With regard to the primary tumor, FDG PET can help delineate margins using thresholding; however, greater value is derived from prognostic information related to SUV values. FDG uptake is correlated with tumor cellularity and prognosis. A prospective study of 25 patients demonstrated higher average SUV_{max}, and metabolic tumor volume (MTV) on pretreatment and intratherapy FDG PET/CT studies are correlated with poor response [16]. MTV and total lesion glycolysis (TLG) have likewise been shown to be prognostic of recurrence-free survival and locoregional control [17].

18.2.4 Monitoring Treatment Response

In surgically treated patients with no clinical evidence of tumor, follow-up imaging is not recommended. In patients with high risk of relapse, follow-up MRI is recommended every 6 months for 2 years. In patients with clinical evidence of tumor recurrence, FDG PET/CT is the preferred imaging modality, as it can more accurately evaluate lymph nodes and extrapelvic spread of disease [18]. FDG PET/CT has a sensitivity and specificity of 90–96% and 81–100%, respectively, for recurrent cervical cancer [19]. Tumor recurrence versus posttreatment inflammation is difficult to distinguish in the first 6 months following chemotherapy and radiotherapy with FDG PET/CT, but it is more reliable than CT or MRI for evaluating distant or nodal spread [18]. The combination of PET and MRI may be complementary in this role. Significant decrease in tumor size 2 months after initiation of therapy, increased tumor ADC values 2 weeks after initiation of radiotherapy, and changes in quantitative pharmacokinetic parameters on dynamic contrast-enhanced (DCE) MRI during early and mid-treatment radiotherapy [20] are all associated with good prognosis (Fig. 18.2).

18.2.5 Data on Fusion or Hybrid Imaging

The complementary information provided by MRI for local staging and PET for evaluation of nodal and distant metastases is well founded in the literature for both modalities separately. However, there is relatively little dedicated literature on fusion or hybrid imaging. In a single-center small cohort, retrospectively fused FDG PET/CT and MRI data were compared to PET/CT and non-fused MRI alone in 35 patients. The study found significantly better accuracy regarding the extent of the primary tumor for fused PET/MRI (83.3%) and non-fused MRI (83.3%) versus PET/CT (53.5%); however, there was no statistical difference between fused PET/MRI and PET/CT for the evaluation of nodal metastases [21]. A separate study which also evaluated post-processing fusion of FDG PET/CT with MRI found a significant difference in the sensitivity of the fused PET/MRI (54%) versus PET/CT (44%) but no difference in specificity in the detection of nodal metastases [22].

A few single-center small series have evaluated the use of simultaneous PET/MRI and shown some advantages over standard PET/CT or MRI alone for staging. In a study involving 18 patients with gynecological malignancies, simultaneous FDG PET/MRI was superior to FDG PET/CT for primary tumor delineation; however, there was no significant difference between the two modalities for detection of regional lymph nodes or abdominal metastases [23]. In another study of 19 patients with gynecological malignancies, FDG PET/CT and FDG PET/MRI were found to be equivalent in identification of malignant lesions, but readers reported higher diagnostic confidence in the discrimination of benign and malignant lesions with PET/MRI [24]. In 34 patients with suspected cervical or ovarian cancer, integrated FDG PET/MRI was compared to MRI alone with statistically significant improvement in nodal detection with hybrid PET/MRI (99%) compared to MRI alone (89%) [25]. This result is not surprising given the added value of specificity and sensitivity of FDG PET for nodal disease.
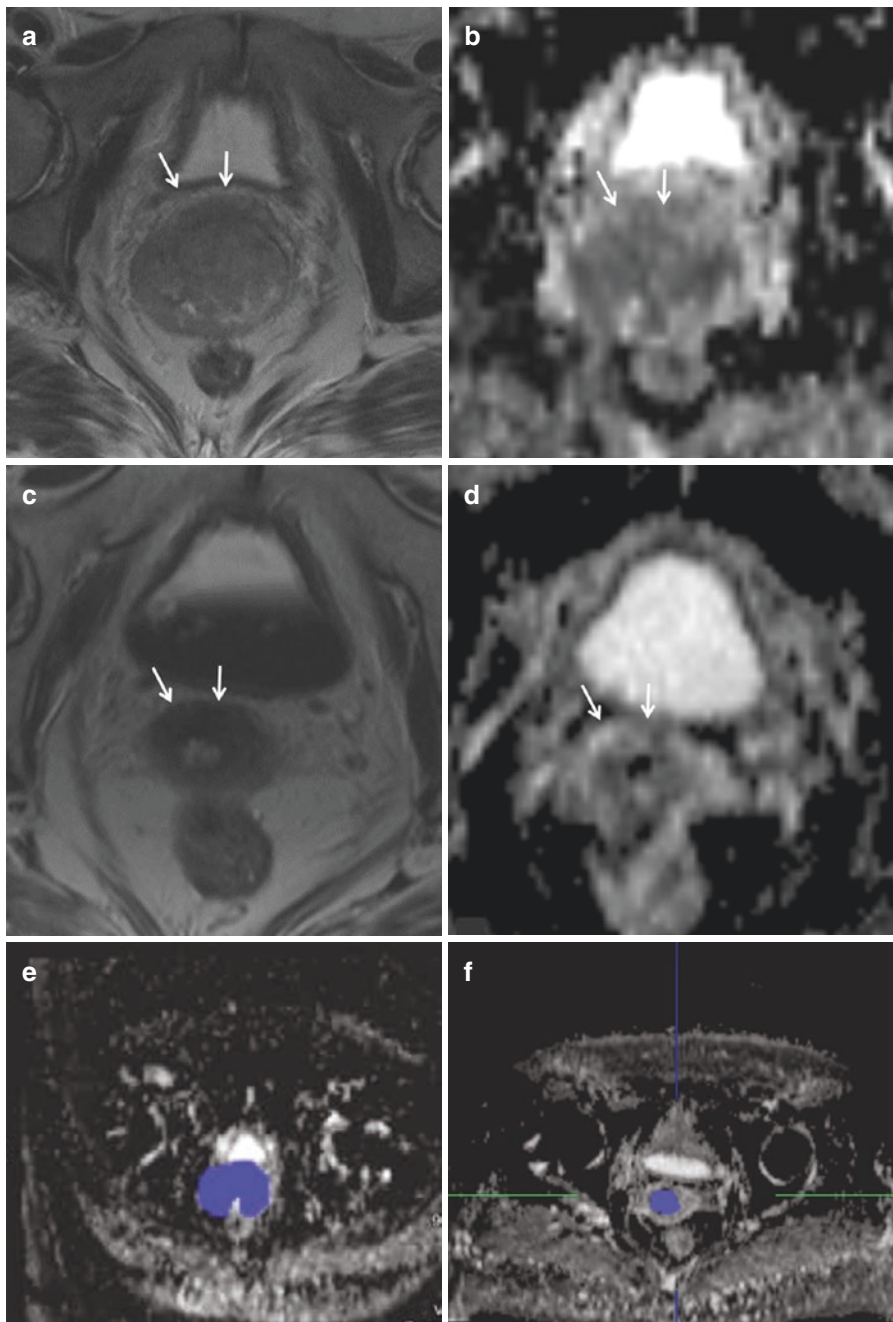
Fig. 18.2 MR features of response to therapy. A 61-year-old woman with stage Ib2 squamous cell carcinoma who underwent definitive chemoradiation therapy. Images (**a** and **b**) show the pretreatment tumor (*arrows*). Images (**c** and **d**) demonstrate the posttreatment findings of decreased T2 signal intensity, reduction in tumor volume, and increased ADC values. Images (**e** and **f**) demonstrate the volumetric change with a contour overlay on the ADC map. The tumor decreased in volume by 96% following therapy (160 mL pre-therapy to 6 mL post-therapy)

In addition to staging information, PET/MRI is able to take advantage of both modalities to provide potential prognostic information. Both SUV and ADC values may be considered surrogates of tumor metabolism and cellular density, respectively. While previous studies have demonstrated at times weak correlations between non-simultaneously acquired $SUV_{max/mean}$ and $ADC_{min/mean}$ values [26–28], simultaneous FDG PET/MRI studies have repeatedly demonstrated a significant and strong inverse correlation between SUV (tumor metabolism) and ADC (high cellularity) in primary tumors and lymph node metastases [29–32].

Figure 18.3 shows a case of cervical cancer on PET/MRI. The hybrid or simultaneous systems have the theoretical advantage of improved registration between the MRI and PET data. This may prove advantageous for radiation planning, especially for centers that utilize an MR-driven linear accelerator. In a study comparing volume concordance between FDG PET, T2W, and diffusion-weighted (DW) imaging of 35 patients with cervical cancer obtained with simultaneous PET/MR imaging, comparable volumes between DW and PET as well as individual regional concordance of metabolic activity and cell density were demonstrated [33].
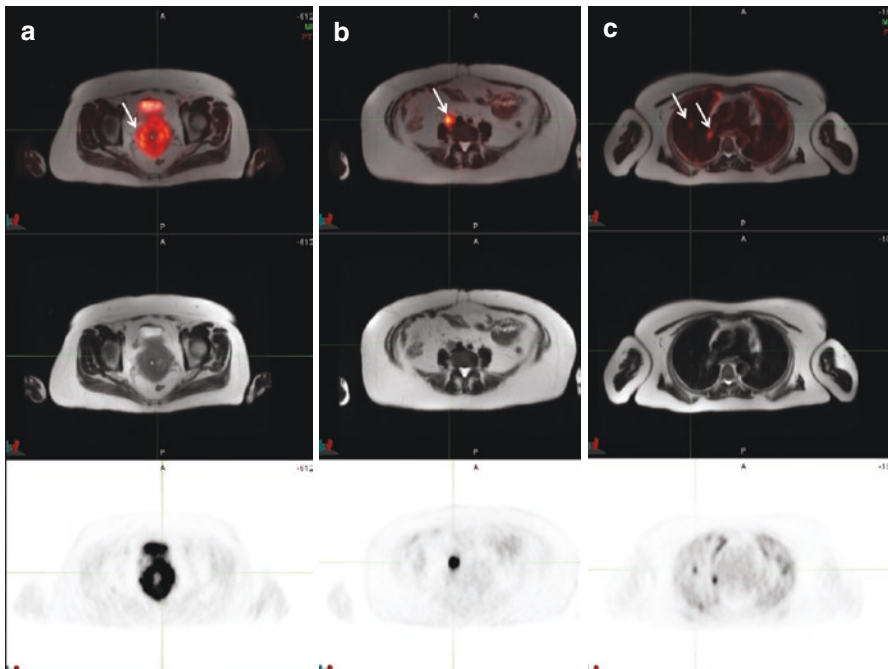

Fig. 18.3 FDG PET/MRI in a patient with metastatic cervical carcinoma. Image panel (**a**) shows the fused T2/PET, T2, and PET images of the primary tumor (arrow). Image panel (**b**) shows metastatic para-aortic lymphadenopathy on fused T2/PET, T2, and PET alone (arrow). Image panel (**c**) shows metastatic pulmonary nodules (arrows) and hilar adenopathy on fused T2/PET, T2, and PET alone

18.3 Endometrial Cancer

18.3.1 Background

Endometrial cancer is the most frequent cancer occurring in the female genital tract in the United States and many other developed countries. Parameters that impact prognosis and survival include the stage of disease at diagnosis, histological grade, depth of myometrial invasion, lymphovascular invasion, and lymph node status [34]. The presence of tumor greater than 50% depth of myometrial invasion is associated with poor survival and a high prevalence of pelvic and para-aortic lymph node metastases.

Endometrial cancer spreads by direct infiltration or via lymphatic, trans-tubal peritoneal seeding, or hematogenous routes. Locally, endometrial cancer initially invades the myometrium and then the endocervix. After trans-serosal spread, direct invasion of the parametrium, bladder, or bowel may occur. Pelvic and para-aortic lymph node status is an important prognostic factor in endometrial cancer because the survival rates of patients with metastases to the nodes are significantly lower than those of patients without nodal metastasis.

18.3.2 Imaging Endometrial Cancer

Cross-sectional imaging is often used to aid in presurgical evaluation and to help direct therapy through assessment of the depth of myometrial invasion, determination of gross cervical invasion, and the identification of suspicious lymph nodes suggestive of metastatic disease [35]. Of traditional imaging modalities, MRI is considered the most accurate imaging modality for the pretreatment local staging of endometrial cancer secondary to its excellent soft tissue delineation and overall staging accuracy. On MRI, endometrial cancer is usually hypo- to isointense on T1-weighted images with intermediate signal intensity lower than the normal endometrium on T2-weighted images (Fig. 18.4). On dynamic post-contrast images, endometrial cancer enhances less than the myometrium with a sensitivity and specificity of 81 and 72%, respectively [36]. The depth of myometrial invasion is typically evaluated with T2-weighted sequences with a sensitivity and specificity of 87 and 58%, respectively [36]. Together dynamic contrast-enhanced images and T2-weighted sequences have an accuracy of 98% for assessing myometrial invasion [37]. DWI also demonstrates high accuracy in assessment of myometrial invasion with a reported sensitivity and specificity of 84.6 and 70.6%, respectively, when compared to sensitivity and specificity of 69.2 and 61.8%, respectively, for dynamic contrast T1 images [38].

Identification of lymph node metastasis on CT and MRI is based on node size with a short-axis diameter greater than 10 mm suggesting metastatic involvement. As with cervical cancer, size criteria alone yield low sensitivity rates for the detection of nodal metastases in endometrial cancer between 27 and 66% with a corresponding specificity rate between 73 and 99% [39].
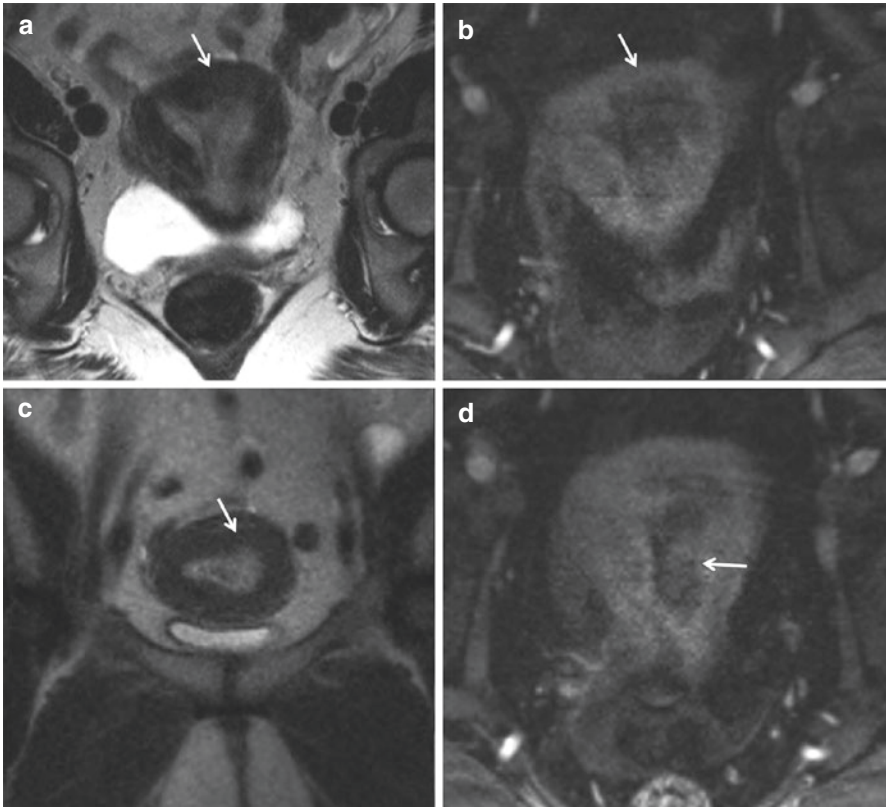
Fig. 18.4 Endometrial Cancer. Coronal T2-weighted image (**a**) and post-contrast images (**b**, **d**) of the uterus show an irregular mass within the left uterus fundus and cornu (arrows). Note that the mass extends into and invades the myometrium and is hypoenhancing to the background tissue. Image (**c**) shows an axial view of the uterus again demonstrating thickening of the endometrial canal with an irregular area of mass in the left aspect (arrow)

FDG PET/CT for endometrial cancer staging is less well studied when compared to cervical or ovarian cancers. Endometrial cancer typically demonstrates increased FDG uptake; however, the added value of FDG PET/CT in initial tumor staging of early stage endometrial cancer is limited due to physiologic uptake in premenopausal women [40]. A recent meta-analysis of FDG uptake, assessed by SUV_{max}, of endometrial cancer demonstrated that tumors with risk factors (grade III, lymphovascular invasion, cervical invasion, myometrial invasion $\geq 50\%$) have a higher average SUV_{max} compared to the tumors with low-risk factors. Thus, a higher preoperative SUV_{max} may be an independent poor prognostic marker of recurrence and increased mortality [41]. Kim et al. demonstrated that the sensitivity, specificity, and accuracy of PET/CT in detecting residual primary lesions in patients with endometrial cancer after endometrial biopsy did not substantially differ from MRI [42].

FDG PET/CT has better sensitivity and specificity than MRI for both pelvic and para-aortic lymph node metastases. As with cervical cancer, evaluation of endometrial cancer lymph node metastasis is limited in lymph nodes with a short-axis diameter <5 mm. DWI has been shown to have higher sensitivity (83 vs. 38%) but lower specificity (51 vs. 96%) than PET/CT, and the accuracy was 57 and 86% for DWI and PET/CT, respectively [43].

18.3.3 Data on Fusion or Hybrid Imaging

Few studies using hybrid or fusion technology have focused specifically on endometrial cancer with the majority of the data coming from small single-center experiences that have combined several gynecological malignancies together for analysis. Kim et al. demonstrated that the sensitivity and specificity of PET/CT and retrospectively fused MRI were 44.1 and 93.9% and 54.2 and 92.7%, respectively [22], in detecting nodal metastases. Additionally, on a per patient basis, the sensitivity, specificity, and accuracy for detecting pelvic nodal metastasis were 100, 96.3, and 96.7% for both fused PET/MRI and PET/contrast-enhanced CT and 66.7, 100, and 96.7% for MRI, respectively [44]. The differences between the three parameters were not statistically significant. Stecco et al. found that retrospective image fusion of PET/MRI-DWI had the same sensitivity (87.5%), specificity (84.2%), and diagnostic accuracy (85.1%) in detecting metastatic lymph nodes in patients with newly diagnosed cervical and endometrial cancer on a per patient basis when compared to PET/CT and MRI-DWI alone but demonstrated better sensitivity (89 vs. 70.2%), specificity (91.6 vs. 90.5%), and diagnostic accuracy (91.2 vs. 87%) on a per node basis [45].

Shih et al. demonstrated using an integrated PET/MRI system that SUV_{max} and ADC_{min} (marker for tumor cellularity) had an inverse relationship and had prognostic implications regarding myometrial invasion, lymphovascular space involvement, and lymph node metastasis; however, there was no correlation to tumor grade [46].

18.4   Ovarian Cancer

18.4.1 Background Information

Ovarian cancer is the leading cause of gynecologic cancer deaths in the Western countries and the fifth leading cause of cancer-related deaths in women [47]. As of 2015, the 5-year survival rate for patients with advanced stage ovarian cancer was a dismal 27% in the United States. High mortality rates are partly attributable to late detection due to a variety of factors including ineffective screening tools, tests, and diagnostic methods. Early diagnosis, in the phase when the tumor is ovary-confined and likely curable, remains a challenge [48].

18.4.2 Imaging of Ovarian Cancer

Pretreatment imaging is used to define tumor extent and identify patients for whom primary surgery is unlikely to be successful [49]. MRI has been the primary modality used to characterize incidental ovarian masses and improve the positive predictive value of the imaging work-up. In a retrospective study of 394 patients with indeterminate adnexal masses, pelvic MRI had a sensitivity of 93.5% and a specificity of 96.6% for detecting malignancy [50]. Whole-body MR diffusion-weighted imaging when compared to FDG PET/CT had a 94% accuracy rate for primary tumor characterization and 91% accuracy for peritoneal staging [51].

FDG PET/CT has a limited role in staging primary ovarian cancer. However, some studies have shown utility in FDG PET/CT for differentiating benign from malignant ovarian masses and directing appropriate management [52]. Small series have shown benefit to PET/CT for detecting extra-ovarian disease and lymphadenopathy. FDG PET/CT may detect positive lesions where CT fails (Fig. 18.5) and may identify recurrent disease prior to CT findings. Preoperative whole-body FDG PET/CT has been shown to lead to the accurate upstaging of ovarian cancer patients
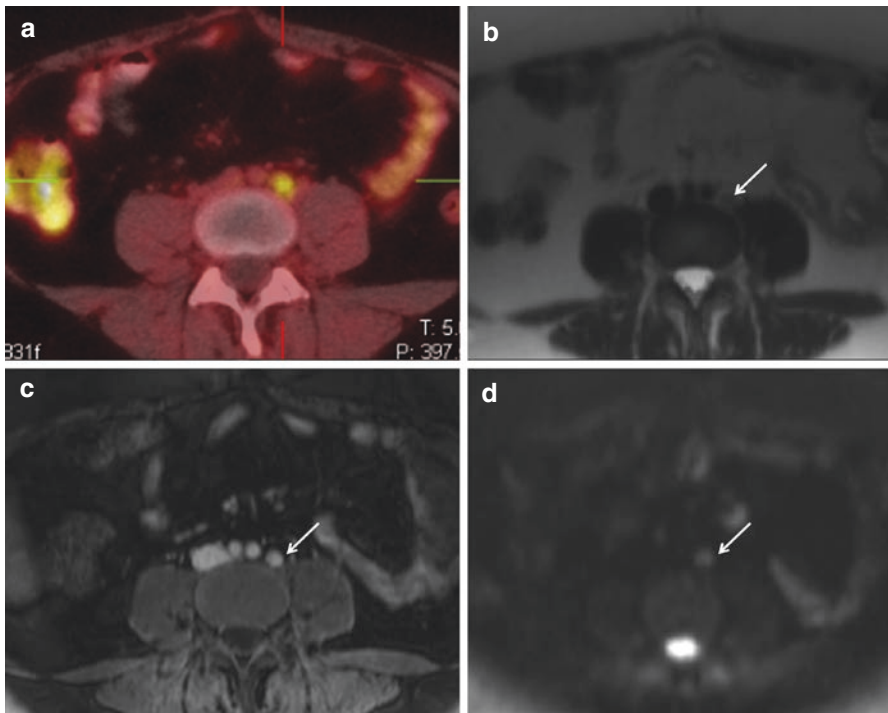

Fig. 18.5 A 31-year-old woman with suspected recurrence of ovarian cancer. PET/CT image (**a**) shows an avid para-aortic node, which was subsequently biopsied and confirmed to be recurrent disease. While this node is visible on MRI (arrows), it is a non-specific finding based on size and appearance on the T2-weighted (**b**), post-contrast (**c**), and diffusion images (**d**)

in regard to nodal involvement [53]. Several studies have demonstrated FDG PET/CT value in predicting overall survival and response to chemotherapy [53, 54].

18.4.3 Data on Fusion or Hybrid Imaging

Even fewer articles reference the value of hybrid PET/MRI for ovarian cancer. In a single study, comparison of FDG PET/CT and FDG PET/MRI in evaluation of metastatic disease in recurrent ovarian cancer (11 patients) and cervical cancer (8 patients) was performed. Both PET/CT and PET/MRI allowed for correct identification of all malignant lesions and equivocal conspicuity; however, diagnostic confidence was significantly higher for PET/MRI in both malignant and benign lesions [24].

18.5 Future Work

Several non-FDG PET tracers have shown promise in evaluating specific biologic features and clinical behavior of gynecologic cancers. While there are relatively few studies that have specifically looked at gynecological malignancies using non-FDG PET tracers, there is early evidence that they may have a future role in gynecological imaging. Hypoxia is a common feature of malignant tumors resulting from a functional disturbance in microcirculation and increased oxygen consumption. Hypoxia causes resistance to chemotherapy and radiotherapy. Copper (Cu)-diacetyl-bis (N4-methylthiosemicarbazone) (Cu-ATSM) is selectively retained in hypoxic tissues due to bioreductive trapping under hypoxic conditions. Several studies in patients with cervical cancer show that ^{60}Cu-ATSM uptake is a predictor of worse survival [55, 56].

^{18}F-Fluoromisonidazle (FMISO) is a derivative of nitroimidazole and is used for imaging oxygen-deprived cells by taking advantage of the accumulation of radicals in hypoxic cells. In a study of 16 patients with advanced cervical cancer, FDG PET/MRI and FMISO PET/MRI were compared and found a strong direct correlation of FDG SUV$_{max}$ and FMISO SUV$_{max}$ and a moderate direct correlation of washout rate with ADC, indicated that highly metabolically active tumors with a high cellular and microvascular density are also prone to develop hypoxic areas [57]. In this case, DWI is complementary as it provides different information from hypoxia PET, as compared to FDG PET where DWI is more duplicative.

Cellular proliferation is a fundamental process in cell biology and is dysregulated in neoplastic cells. To capture evidence of cell division, nucleosides and nucleoside analogues have been developed as PET tracers for measuring proliferation rates. Thymidine analogues are well suited to this purpose. Currently, the most well-established PET tracer in this class is 3′-deoxy-3′-[^{18}F]fluorothymidine (FLT). A pilot study of six patients with cervical cancer, pre-therapy and 1–3 week post-therapy FLT and FDG PET imaging, was performed with a greater decrease in FLT uptake on the post-therapy imaging as compared to FDG suggesting the FLT may be used to assess the effects of chemoradiation therapy with less interference of posttreatment inflammation as seen with FDG [58].

Conclusion

Gynecological malignancies remain a major health concern and imaging plays a critical role in directing management. The majority of the literature to date has focused on cervical cancer and separately on MRI and PET/CT, both showing value in staging and prognostication. In particular, MRI provides high-resolution imaging for staging or characterizing primary tumors, and PET provides increased sensitivity and specificity for detecting nodal and distant metastases. Simultaneous PET/MRI provides all the benefits of both modalities in a single imaging session and with the promise of improved registration, imbedded motion correction, and greater diagnostic confidence due to improved soft tissue contrast for whole-body imaging than PET/CT.

References

1. Yankeelov TE, Peterson TE, Abramson RG, et al. Simultaneous PET-MRI in oncology: a solution looking for a problem? Magn Reson Imaging. 2012;30(9):1342–56.
2. Rosenkrantz AB, Friedman K, Chandarana H, et al. Current status of hybrid PET/MRI in oncologic imaging. AJR Am J Roentgenol. 2016;206(1):162–72.
3. Ferlay J, Steliarova-Foucher E, Lortet-Tieulent J, et al. Cancer incidence and mortality patterns in Europe: estimates for 40 countries in 2012. Eur J Cancer. 2013;49(6):1374–403.
4. van Meir H, Kenter GG, Burggraaf J, et al. The need for improvement of the treatment of advanced and metastatic cervical cancer, the rationale for combined chemo-immunotherapy. Anti Cancer Agents Med Chem. 2014;14(2):190–203.
5. Yildirim Y, Sehirali S, Avci ME, et al. Integrated PET/CT for the evaluation of para-aortic nodal metastasis in locally advanced cervical cancer patients with negative conventional CT findings. Gynecol Oncol. 2008;108(1):154–9.
6. Freeman SJ, Aly AM, Kataoka MY, Addley HC, Reinhold C, Sala E. The revised FIGO staging system for uterine malignancies: implications for MR imaging. Radiographics. 2012;32(6):1805–27.
7. Amendola MA, Hricak H, Mitchell DG, et al. Utilization of diagnostic studies in the pretreatment evaluation of invasive cervical cancer in the United States: results of intergroup protocol ACRIN 6651/GOG 183. J Clin Oncol. 2005;23(30):7454–9.
8. Mitchell DG, Snyder B, Coakley F, et al. Early invasive cervical cancer: tumor delineation by magnetic resonance imaging, computed tomography, and clinical examination, verified by pathologic results, in the ACRIN 6651/GOG 183 intergroup study. J Clin Oncol. 2006;24(36):5687–94.
9. Bourgioti C, Koutoulidis V, Chatoupis K, et al. MRI findings before and after abdominal radical trachelectomy (ART) for cervical cancer: a prospective study and review of the literature. Clin Radiol. 2014;69(7):678–86.
10. Xue H, Ren C, Yang J, et al. Histogram analysis of apparent diffusion coefficient for the assessment of local aggressiveness of cervical cancer. Arch Gynecol Obstet. 2014;290(2):341–8.
11. Liu Y, Liu H, Bai X, et al. Differentiation of metastatic from non-metastatic lymph nodes in patients with uterine cervical cancer using diffusion-weighted imaging. Gynecol Oncol. 2011;122(1):19–24.
12. Sala E, Wakely S, Senior E, Lomas D. MRI of malignant neoplasms of the uterine corpus and cervix. AJR Am J Roentgenol. 2007;188(6):1577–87.
13. Havrilesky LJ, Kulasingam SL, Matchar DB, Myers ER. FDG-PET for management of cervical and ovarian cancer. Gynecol Oncol. 2005;97(1):183–91.

14. Choi HJ, Ju W, Myung SK, Kim Y. Diagnostic performance of computer tomography, magnetic resonance imaging, and positron emission tomography or positron emission tomography/computer tomography for detection of metastatic lymph nodes in patients with cervical cancer: meta-analysis. Cancer Sci. 2010;101(6):1471–9.
15. Sironi S, Buda A, Picchio M, et al. Lymph node metastasis in patients with clinical early-stage cervical cancer: detection with integrated FDG PET/CT. Radiology. 2006;238(1):272–9.
16. Kidd EA, Thomas M, Siegel BA, Dehdashti F, Grigsby PW. Changes in cervical cancer FDG uptake during chemoradiation and association with response. Int J Radiat Oncol Biol Phys. 2013;85(1):116–22.
17. Herrera FG, Breuneval T, Prior JO, Bourhis J, Ozsahin M. [(18)F]FDG-PET/CT metabolic parameters as useful prognostic factors in cervical cancer patients treated with chemoradiotherapy. Radiat Oncol. 2016;11:43.
18. Testa AC, Di Legge A, De Blasis I, et al. Imaging techniques for the evaluation of cervical cancer. Best Pract Res Clin Obstet Gynaecol. 2014;28(5):741–68.
19. Mittra E, El-Maghraby T, Rodriguez CA, et al. Efficacy of 18F-FDG PET/CT in the evaluation of patients with recurrent cervical carcinoma. Eur J Nucl Med Mol Imaging. 2009;36(12):1952–9.
20. Mayr NA, Wang JZ, Zhang D, et al. Longitudinal changes in tumor perfusion pattern during the radiation therapy course and its clinical impact in cervical cancer. Int J Radiat Oncol Biol Phys. 2010;77(2):502–8.
21. Kitajima K, Suenaga Y, Ueno Y, et al. Fusion of PET and MRI for staging of uterine cervical cancer: comparison with contrast-enhanced (18)F-FDG PET/CT and pelvic MRI. Clin Imaging. 2014;38(4):464–9.
22. Kim SK, Choi HJ, Park SY, et al. Additional value of MR/PET fusion compared with PET/CT in the detection of lymph node metastases in cervical cancer patients. Eur J Cancer. 2009;45(12):2103–9.
23. Queiroz MA, Kubik-Huch RA, Hauser N, et al. PET/MRI and PET/CT in advanced gynaecological tumours: initial experience and comparison. Eur Radiol. 2015;25(8):2222–30.
24. Beiderwellen K, Grueneisen J, Ruhlmann V, et al. [(18)F]FDG PET/MRI vs. PET/CT for whole-body staging in patients with recurrent malignancies of the female pelvis: initial results. Eur J Nucl Med Mol Imaging. 2015;42(1):56–65.
25. Grueneisen J, Beiderwellen K, Heusch P, et al. Simultaneous positron emission tomography/magnetic resonance imaging for whole-body staging in patients with recurrent gynecological malignancies of the pelvis: a comparison to whole-body magnetic resonance imaging alone. Investig Radiol. 2014;49(12):808–15.
26. Ho KC, Lin G, Wang JJ, Lai CH, Chang CJ, Yen TC. Correlation of apparent diffusion coefficients measured by 3T diffusion-weighted MRI and SUV from FDG PET/CT in primary cervical cancer. Eur J Nucl Med Mol Imaging. 2009;36(2):200–8.
27. Baba S, Isoda T, Maruoka Y, et al. Diagnostic and prognostic value of pretreatment SUV in 18F-FDG/PET in breast cancer: comparison with apparent diffusion coefficient from diffusion-weighted MR imaging. J Nucl Med. 2014;55(5):736–42.
28. Varoquaux A, Rager O, Lovblad KO, et al. Functional imaging of head and neck squamous cell carcinoma with diffusion-weighted MRI and FDG PET/CT: quantitative analysis of ADC and SUV. Eur J Nucl Med Mol Imaging. 2013;40(6):842–52.
29. Brandmaier P, Purz S, Bremicker K, et al. Simultaneous [18F]FDG-PET/MRI: correlation of apparent diffusion coefficient (ADC) and standardized uptake value (SUV) in primary and recurrent cervical cancer. PLoS One. 2015;10(11):e0141684.
30. Grueneisen J, Beiderwellen K, Heusch P, et al. Correlation of standardized uptake value and apparent diffusion coefficient in integrated whole-body PET/MRI of primary and recurrent cervical cancer. PLoS One. 2014;9(5):e96751.
31. Schmidt H, Brendle C, Schraml C, et al. Correlation of simultaneously acquired diffusion-weighted imaging and 2-deoxy-[18F] fluoro-2-D-glucose positron emission tomography of pulmonary lesions in a dedicated whole-body magnetic resonance/positron emission tomography system. Investig Radiol. 2013;48(5):247–55.

32. Heusch P, Buchbender C, Kohler J, et al. Correlation of the apparent diffusion coefficient (ADC) with the standardized uptake value (SUV) in hybrid 18F-FDG PET/MRI in non-small cell lung cancer (NSCLC) lesions: initial results. Rofo. 2013;185(11):1056–62.

33. Sun H, Xin J, Zhang S, et al. Anatomical and functional volume concordance between FDG PET, and T2 and diffusion-weighted MRI for cervical cancer: a hybrid PET/MR study. Eur J Nucl Med Mol Imaging. 2014;41(5):898–905.

34. Sorosky JI. Endometrial cancer. Obstet Gynecol. 2012;120(2 Pt 1):383–97.

35. Faria SC, Sagebiel T, Balachandran A, Devine C, Lal C, Bhosale PR. Imaging in endometrial carcinoma. Indian J Radiol Imaging. 2015;25(2):137–47.

36. Wu WJ, Yu MS, Su HY, Lin KS, Lu KL, Hwang KS. The accuracy of magnetic resonance imaging for preoperative deep myometrium assessment in endometrial cancer. Taiwan J Obstet Gynecol. 2013;52(2):210–4.

37. Peungjesada S, Bhosale PR, Balachandran A, Iyer RB. Magnetic resonance imaging of endometrial carcinoma. J Comput Assist Tomogr. 2009;33(4):601–8.

38. Rechichi G, Galimberti S, Signorelli M, Perego P, Valsecchi MG, Sironi S. Myometrial invasion in endometrial cancer: diagnostic performance of diffusion-weighted MR imaging at 1.5-T. Eur Radiol. 2010;20(3):754–62.

39. Rockall AG, Meroni R, Sohaib SA, et al. Evaluation of endometrial carcinoma on magnetic resonance imaging. Int J Gynecol Cancer. 2007;17(1):188–96.

40. Brunetti J. PET/CT in gynecologic malignancies. Radiol Clin N Am. 2013;51(5):895–911.

41. Ghooshkhanei H, Treglia G, Sabouri G, Davoodi R, Sadeghi R. Risk stratification and prognosis determination using (18)F-FDG PET imaging in endometrial cancer patients: a systematic review and meta-analysis. Gynecol Oncol. 2014;132(3):669–76.

42. Kim HJ, Cho A, Yun M, Kim YT, Kang WJ. Comparison of FDG PET/CT and MRI in lymph node staging of endometrial cancer. Ann Nucl Med. 2016;30(2):104–13.

43. Kitajima K, Yamasaki E, Kaji Y, Murakami K, Sugimura K. Comparison of DWI and PET/CT in evaluation of lymph node metastasis in uterine cancer. World J Radiol. 2012;4(5):207–14.

44. Kitajima K, Suenaga Y, Ueno Y, et al. Value of fusion of PET and MRI for staging of endometrial cancer: comparison with (1)(8)F-FDG contrast-enhanced PET/CT and dynamic contrast-enhanced pelvic MRI. Eur J Radiol. 2013;82(10):1672–6.

45. Stecco A, Buemi F, Cassara A, et al. Comparison of retrospective PET and MRI-DWI (PET/MRI-DWI) image fusion with PET/CT and MRI-DWI in detection of cervical and endometrial cancer lymph node metastases. Radiol Med. 2016;121(7):537–45.

46. Shih IL, Yen RF, Chen CA, et al. Standardized uptake value and apparent diffusion coefficient of endometrial cancer evaluated with integrated whole-body PET/MR: correlation with pathological prognostic factors. J Magn Reson Imaging. 2015;42(6):1723–32.

47. Siegel RL, Miller KD, Jemal A. Cancer statistics, 2017. CA Cancer J Clin. 2017;67(1):7–30.

48. Sharma SK, Nemieboka B, Sala E, Lewis JS, Zeglis BM. Molecular imaging of ovarian cancer. J Nucl Med. 2016;57(6):827–33.

49. Morgan RJ Jr, Alvarez RD, Armstrong DK, et al. Ovarian cancer, version 3.2012. J Natl Compr Cancer Netw. 2012;10(11):1339–49.

50. Thomassin-Naggara I, Aubert E, Rockall A, et al. Adnexal masses: development and preliminary validation of an MR imaging scoring system. Radiology. 2013;267(2):432–43.

51. Michielsen K, Vergote I, Op de Beeck K, et al. Whole-body MRI with diffusion-weighted sequence for staging of patients with suspected ovarian cancer: a clinical feasibility study in comparison to CT and FDG-PET/CT. Eur Radiol. 2014;24(4):889–901.

52. Kim C, Chung HH, Oh SW, Kang KW, Chung JK, Lee DS. Differential diagnosis of borderline ovarian tumors from stage I malignant ovarian tumors using FDG PET/CT. Nucl Med Mol Imaging. 2013;47(2):81–8.

53. Caobelli F, Alongi P, Evangelista L, et al. Predictive value of (18)F-FDG PET/CT in restaging patients affected by ovarian carcinoma: a multicentre study. Eur J Nucl Med Mol Imaging. 2016;43(3):404–13.

54. Vallius T, Peter A, Auranen A, et al. 18F-FDG-PET/CT can identify histopathological non-responders to platinum-based neoadjuvant chemotherapy in advanced epithelial ovarian cancer. Gynecol Oncol. 2016;140(1):29–35.

55. Dehdashti F, Grigsby PW, Lewis JS, Laforest R, Siegel BA, Welch MJ. Assessing tumor hypoxia in cervical cancer by PET with 60Cu-labeled diacetyl-bis(N4-methylthiosemicarbazone). J Nucl Med. 2008;49(2):201–5.

56. Dehdashti F, Grigsby PW, Mintun MA, Lewis JS, Siegel BA, Welch MJ. Assessing tumor hypoxia in cervical cancer by positron emission tomography with 60Cu-ATSM: relationship to therapeutic response-a preliminary report. Int J Radiat Oncol Biol Phys. 2003;55(5):1233–8.

57. Pinker K, Andrzejewski P, Baltzer P, et al. Multiparametric [18F]fluorodeoxyglucose/ [18F] fluoromisonidazole positron emission tomography/magnetic resonance imaging of locally advanced cervical cancer for the non-invasive detection of tumor heterogeneity: a pilot study. PLoS One. 2016;11(5):e0155333.

58. Cho LP, Kim CK, Viswanathan AN. Pilot study assessing (18)F-fluorothymidine PET/CT in cervical and vaginal cancers before and after external beam radiation. Gynecol Oncol Rep. 2015;14:34–7.

PET/MRI in Prostate Cancer

19

Ida Sonni, Lucia Baratto, Martin T. Freitag, Frederik Giesel, Matthias Eiber, and Andrei Iagaru

Contents

I. Sonni (✉) • L. Baratto • A. Iagaru
Department of Radiology – Division of Nuclear Medicine and Molecular Imaging, Stanford University, Stanford, CA, USA
e-mail: isonni@stanford.edu; idasonni@gmail.com

M.T. Freitag • F. Giesel
Department of Radiology, German Cancer Research Center, Heidelberg, Germany

M. Eiber
Department of Nuclear Medicine, Klinikum Rechts der Isar, Technical University of Munich, Munich, Germany

Department of Molecular and Medical Pharmacology, David Geffen School of Medicine at UCLA, Los Angeles, CA, USA
e-mail: matthias.eiber@tum.de

19.1   Introduction

Despite significant advances in detection and treatment, prostate cancer (PC) remains the most common malignancy and a major cause of cancer death in men worldwide. Data from the American Cancer Society suggests that 180,890 new cases of PC would be diagnosed in the United States in 2016, and PC would have the second highest mortality in men due to cancer, after lung and bronchus tumors, accounting for 26,120 deaths estimated in the same year [1]. Incidence and prevalence of PC vary by geographical location and ethnicity, suggesting a role of environmental factors and lifestyle, in addition to the genetic factors. PC incidence is also affected by prostate-specific antigen (PSA) measurements, with a higher incidence in more developed countries where PSA screening is common practice and allows early detection of latent or asymptomatic cancers [2, 3]. As life expectancy increases, it is anticipated that incidence of the disease will increase as well, making PC a serious endemic health problem.

The most common histology of PC is adenocarcinoma, a malignant glandular neoplasia that is thought to originate from the basal cells of prostate acini. These are stem cells, precursors of the differentiated secretory prostate cells, that can potentially have a malignant transformation during each of the intermediate phases of cell differentiation. This aspect can explain the biological and clinical heterogeneity of prostate cancer [4]. In a successful attempt to predict prognosis for PC patients using a combination of histological grading and clinical staging, in the 1970s Donald F. Gleason introduced the Gleason score, which is now the most commonly used grading system for PC [5]. The Gleason score, ranging from 2 to 10, is a sum of the two prevalent histologic patterns, each numbered from 1 to 5 depending on cell differentiation (1 = well differentiated; 5 = anaplastic), in the prostate tissue specimen [6, 7]. Gleason score, together with clinical tumor stage and serum PSA levels, is one of the parameters used during risk assessment. Patients are stratified into risk groups (very low, low, intermediate, high, and very high risk), and this classification is key in defining initial patient management [8]. During follow-up, serum PSA became an essential biomarker in PC patients, due to its wide availability and cost-effectiveness. After initial therapy, a detectable or rising PSA level is defined as biochemical recurrence of PC (BCR) [9], and up to 40% of the patients will face it within 10 years after initial treatment [10]. Considering that PSA levels can rise months to years before the presence of detectable disease, this can be seen as an

early marker of disease recurrence, but unfortunately it cannot be helpful in localizing disease and differentiating between local, regional, and systemic disease [11]. The accuracy of staging and restaging PC patients is key in choosing the most appropriate management but remains challenging. Morphological, functional, and molecular imaging play a crucial role in this setting, providing noninvasive biomarkers of disease.

This chapter will review the main features of conventional imaging, different PET radiopharmaceuticals, and MR techniques used in prostate cancer imaging. The current applications of integrated PET/MRI systems will be described in the final sections, as well as the advantages of the combined approach.

19.2 Imaging of Prostate Cancer

19.2.1 Ultrasound

Initial detection of PC is based on digital rectal examination, serum PSA levels measurements, and transrectal ultrasound (TRUS) which helps in guiding prostate biopsies [8]. The accuracy of TRUS to identify pathological foci is limited, because on US an important proportion of them results isoechoic to normal prostate parenchyma [12]. TRUS-guided systematic biopsies are therefore "blind" or "random," since they are not directed toward specific abnormalities. Different methods have been introduced in an attempt to increase diagnostic accuracy of TRUS-guided biopsy, such as contrast-enhanced ultrasound (ce-US), which uses microbubble contrast agent injected intravenously, and real-time elastography (RTE), which evaluates the mechanical properties of cancerous tissue by identifying variance in tissue compliance after manual compression and relaxation, and MR-guided TRUS (MR/TRUS), which will be described later. Several studies showed that ce-US and RTE increase the detection rate of PC in comparison to TRUS [13, 14].

19.2.2 Computed Tomography

The role of computed tomography (CT) in the detection and staging of PC is very limited. Despite the increasing temporal resolution of novel CTs and the use of contrast enhancement or new protocols, such as CT perfusion [15], the well-known poor soft-tissue contrast of CT limits its ability to visualize the delicate anatomy of the pelvis including the prostatic fossa. CT could help identify lymph node metastases from PC based on enlargement, but correlation between size and metastatic involvement is poor because nodal metastases are often microscopic. CT can be used in high-risk patients with clinically apparent metastatic disease, and could be useful in identifying and monitoring bone metastases, particularly osteolytic lesions, that may be missed on ^{99m}Tc bone scintigraphy and ^{18}F-NaF PET [16].

19.2.3 Bone Imaging (^{99m}Tc-MDP Bone Scintigraphy and ^{18}F-NaF PET)

The importance of skeletal involvement in the evaluation of PC patients is justified by the fact that PC is the leading cause of bone metastases in men [17]. Considering that the skeletal metastases detection is crucial in defining an optimal therapeutic management, bone scan is indicated in the initial clinical assessment of PC patients in case of PSA levels >20 ng/mL (PSA > 10 ng/mL in T2), Gleason score ≥8, or in T3/T4 [8]. Bone scan is not indicated in patients with low-risk PC, since the likelihood of bone involvement is low [17].

The gold standard imaging technique in bone evaluation is ^{99m}Tc-methylene diphosphonate (^{99m}Tc-MDP) planar scintigraphy, with possibility of tomographic acquisition using single photon emission tomography (SPECT) and hybrid SPECT/CT, that increase diagnostic accuracy [17]. ^{99m}Tc-MDP has several advantageous properties such as high sensitivity in identifying bone metastases, large availability in nuclear medicine facilities worldwide, and the possibility to evaluate the entire skeleton with relatively low costs and a simple, well-tolerated procedure. These aspects made it a successful imaging technique for decades. However, ^{99m}Tc-MDP bone scan has some important downsides, namely, the lack of specificity in differentiating bone metastases from benign bone conditions, the reduced sensitivity in detection of osteolytic metastases, and poor spatial resolution.

Notoriously PET has a better spatial resolution compared to SPECT, and this explains the better performances of ^{18}F-NaF PET/CT compared to ^{99m}Tc-MDP bone scan in the detection of osseous metastases [18, 19]. ^{18}F-NaF is a bone-seeking radiopharmaceutical introduced in 1962 by Blau et al. [20] and initially imaged with γ-cameras [21] despite the 511 keV photons emitted by ^{18}F being suboptimal for conventional nuclear medicine cameras. Due to the recent increase in PET scanners availability, ^{18}F-NaF is now imaged using PET, and this led to the increase of sensitivity and spatial resolution of the technique. ^{18}F-NaF has very similar mechanism of uptake to ^{99m}Tc-MDP, depending on blood flow and osteoblastic activity, but better pharmacokinetic properties [22, 23]. ^{99m}Tc-MDP bone scintigraphy has the important disadvantage of a low specificity because it is not tumor specific and accumulates also in benign bone conditions. Although ^{18}F-NaF PET/CT is better than ^{99m}Tc-MDP bone scan in the detection of osseous metastases, the technique is not yet widely implemented in the clinical practice, possibly because of the lower availability of the radiopharmaceutical, higher costs, and lower availability of PET/CT scanners compared with γ-cameras.

19.3   Multiparametrical MRI (mpMRI) in Prostate Cancer

Multiparametrical magnetic resonance imaging (mpMRI) is accepted as imaging-based method to detect PC of patients with elevated PSA levels, in particular if prior biopsies have been false negative [24]. This technique employs multimodal MRI sequences with complementary diagnostic information for PC detection. To facilitate a standardized and fast reading approach of these parameters, PI-RADS (prostate imaging-reporting

and data system) was proposed in 2012 [25]. According to PI-RADS, the prostate gland is divided into sectors that differentiate between anterior and posterior parts in dependence of the central or the peripheral zone and the third of the prostate itself (base, mid, apex). Such standardization allows for brief diagnostic reports aiming toward improved communication to the clinician. This Likert-scale-based reading scheme provides a final score from 1 to 5 that summarizes the probability to detect PC. The score is obtained after reading each of the sequences employed in mpMRI. PI-RADS 1.0 comprised high-resolution T2-weighted (T2w) spin-echo sequences in at least two dimensions, diffusion-weighted imaging (DWI), dynamic contrast-enhanced (DCE) MRI, and MR spectroscopy (MRS). The sensitivity/specificity of PI-RADS 1.0 was reported with 78/79% for PC detection according to a meta-analysis in 2014 [26]. Three years after the introduction of PI-RADS 1, PI-RADS 2 was proposed adapting to the gained evidence on the value of different MRI sequences and their limitations depending on the location within the prostate [27].

Emerging evidence suggests that mpMRI demonstrates excellent value prior to routine biopsy [24, 28]. For this purpose, mpMRI harmonizes well with transrectal ultrasound (MRI/TRUS) to allow targeted biopsy [29]. It was assumed previously that random core biopsies have a higher probability for histopathological sampling errors so that the cancer lesion itself, or the one with the highest Gleason score, is missed if a non-targeted (random) approach is chosen [24, 28]. For this purpose, fusion images of mpMRI and ultrasound (MR/TRUS) may be acquired to aid the physician for the targeted biopsy. mpMRI was also used in patients under active surveillance to detect clinically significant PC lesions in the baseline examination. The evidence of mpMRI for monitoring active surveillance patients, however, is still scarce [30]. mpMRI does also show promising results to detect recurrent PC after radical prostatectomy in biochemical recurrence of PC [31]. For this purpose, the same mpMRI sequences (T2w/DWI/DCE), as for the standard PI-RADS protocol, may be used. However, PI-RADS reporting is currently only proposed for primary PC and not in the situation of biochemical recurrence.

Because the signal to noise ratio increases proportionately with the field strength, 3 T should be favored over 1.5 T for PC detection [32]. Technically, the use of an endorectal coil for prostate cancer detection is not mandatory despite the usage of them may increase signal to noise ratio. In fact, there is excellent image quality observed with surface coils at 3 T that provide significantly improved patient comfort compared to endorectal coils. The i.v. application of butylscopolamine prior to the scan may be used to reduce bowel motility and subsequent artifacts in MRI despite it is not necessary in every patient [32]. Overall, a typical mpMRI protocol comprises around 30–45 min.

To understand the utilization and also the limitations of mpMRI, one has to dissect this technique into its sequence components that will be briefly summarized in the following chapters. It is important to emphasize that the information derived from mpMRI in its current form results from the signal of water protons in the human body (^{1}H). Higher field strengths than 3 T better allow the excitation of nuclei other than water protons with less concentrations in the human body in the order of several magnitudes such as ^{23}Na. Such new imaging techniques are still in an experimental state.

19.3.1 T2-Weighted Imaging

T2-weighted imaging (T2w) is the sequence that allows the anatomical delineation of the prostate gland and its surrounding anatomy including the seminal vesicles, bladder, ductus deferens, pelvic musculature, vasculature, and closely located regional lymph nodes. For assessment of the prostate gland, T2w is usually conducted as turbo-spin-echo sequence that allow for high in-plane resolutions in order to gain sufficient anatomic detail within reasonable acquisition times. Because DWI and DCE have lower spatial resolution due to methodological reasons, T2w is the sequence that allows best the determination of the sector assessed, that is later noted in the PI-RADS reading protocol. Usually T2w is conducted in at least two dimensions that have to be acquired separately by technologists. Axial orientation is always performed and, secondly, either coronal or sagittal. Using two planes, the prostate volume may be quantified and benign prostate hyperplasia including consecutive lifting of the bladder diagnosed. In PI-RADS 2, T2w is the dominant sequence for the assessment of the central zone meaning that the information derived from it usually overrules the others [27]; see Fig. 19.1. Only if the lesion is unclear (PI-RADS 3), DWI is consulted to potentially upgrade the final PI-RADS score. The criterion for malignancy is the kind of delineation of the T2w hypointense lesion with respect to its borders. Because it is sometimes difficult to correctly describe the delineation of a lesion in the central zone, T2w may have limitations to differentiate between benign nodules due to hyperplasia and cancer tissue [27].

In principle, T2w allows for imaging-based detection of infiltration patterns for clinical T-staging such as extracapsular extension (T3a), infiltration into the seminal vesicles (T3b), or invasion into surrounding structures (T4) if the finding is evident.
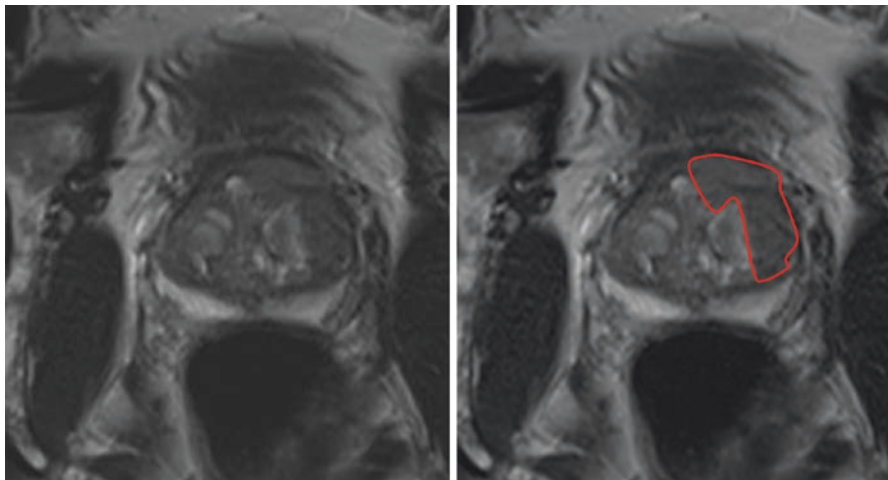

Fig. 19.1 Prostate cancer in the left central zone (Gleason 8, PSA 79 ng/mL) in axial T2w-TSE, delineated by the red line. Scan conducted at 3 T with a surface coil

However, a negative T2w scan does not necessarily exclude (microscopic) capsule extension or seminal vesicles infiltration, and there may be underestimations observed. A meta-analysis on this topic demonstrated overall low sensitivity but high specificity (91–96%) to detect extracapsular extension (sensitivity/specificity 57–91%) or infiltration into seminal vesicles (sensitivity/specificity 58–96%) [33].

19.3.2   Diffusion-Weighted Imaging

DWI is a core sequence used for PC detection and evaluates cellularity by exploiting the diffusive motion of water molecules due to their thermal energy to probe tissue structure. For this purpose, usually a spin-echo sequence is extended by two additional magnetic field gradient pulses to induce diffusion weighting based on the Stejskal and Tanner method [34]. For k-space (the Fourier transform of the MR image) readout, typically an echo-planar imaging (EPI) approach is employed which allows acquiring the entire k-space after only one excitation. Depending on the number of b-values, the resulting acquisition time typically comprises 4–8 min. The resulting diffusion weighting may be modified by changing the b-value, from low b-values (low diffusion weighting) to high b-values (strong diffusion weighting). This value results in simple terms from the configuration of the MRI gradients. If the signal from two experiments using two different b-values is acquired, the apparent diffusion coefficient (ADC) is determinable that provides a very robust parameter for cancer detection. Signal decay, b-value, and ADC are associated as follows:

$$S = S_0 e^{-bADC}$$

where S represents the diffusion-weighted signal, b the b-value in s/mm^2, and ADC the diffusion coefficient. In words, the ADC represents the absolute slope of the signal decay between two b-values on a logarithmic scale. Because there are intrinsic differences in diffusion of water exemplarily in the bladder and in the prostate, simply because cell barriers exist in the prostate, regions with high cellularity such as hyperplasia nodules and cancer may be detected. Because benign nodules of central hyperplasia may also feature a focal hypercellularity, there is some overlap between benign nodules and cancer. To address this limitation, DWI is not the dominant sequence for the central zone in the updated PI-RADS 2 [27]. However, DWI is the dominant sequence for assessment of the peripheral zone where high cellular nodules should not exist. For assessment of the prostate, b-values equal or larger than 1000 s/mm^2 should be strived for as the tumor contrast significantly improves with higher b-values. This improvement is not endless as noise increases with increasing b-values. However, additional models employing kurtosis quantification that take into account a mathematical model for cell barriers may add benefit to detect prostate cancer for b-values larger than 1500 s/mm^2 [35]. Another technique of diffusion-weighted imaging, known as intra-voxel incoherent motion MRI, extracts perfusion information that contributes to the signal in DWI, without the use of contrast agent [36, 37]. This is achieved by acquiring multiple b-values, with

corresponding increase in acquisition time. Both kurtosis and intra-voxel incoherent motion MRI are not part of the routine prostate mpMRI and are currently in the state of exploration.

In clinical routine, the high b-value images and the ADC maps are always consulted. A suspicious lesion should be depicted with hyperintensity in the high b-value image set and with low values in the ADC map (Fig. 19.2). If the DWI assessment of the prostate peripheral zone shows an unclear lesion (PI-RADS 3), DCE MRI is consulted to characterize the vascularization of the lesion in order to determine the final PI-RADS score. In some cases, tissue with long T2 times (e.g., cysts) may "shine through" so that it appears still hyperintense at high b-value images misleadingly indicating a suspicious lesion. Then, the ADC map needs to be consulted. If the corresponding ADC values are high as well, a "T2 shine through" phenomenon may be reliably diagnosed, and the dignity of the lesion classified.

19.3.3 Dynamic Contrast-Enhanced Imaging (DCE)

Neoangiogenesis and hypervascularization are hallmarks of cancer including prostate cancer thus justifying the use of contrast media that may depict these aspects in a dynamic fashion using DCE. It is used to assess the complete prostate by creating a 4D dataset during the intravenous application of gadolinium-based contrast media. The procedure is similar to dynamic PET imaging, and the used fitting models show overlaps. The practical difference to dynamic PET imaging is, assuming a single bed position scan, that the PET camera continuously measures the line of responses, whereas DCE MRI makes use of numerous repeated, complete scans of the prostate, typically in axial orientation. There is always a trade-off between temporal and spatial resolution, and since adequate temporal resolution is needed for PC
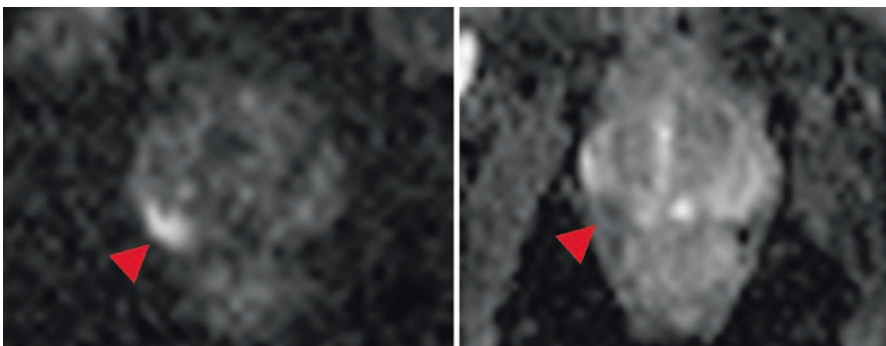

Fig. 19.2 Classical appearance of prostate carcinoma (Gleason 7, PSA 13 ng/mL) in the peripheral zone of the prostate in DWI, depicted hyperintense at $b = 1500$ s/mm^2 (left), and correspondingly, with low ADC values (right). The pathology is indicated by the red triangles. Scan conducted at 3 T with a surface coil

detection, the in-plane resolution does not match that of a T2w turbo-spin-echo sequence. T1-weighted gradient-echo sequence techniques allow for faster image acquisition than turbo-spin-echo sequences and thus, high temporal resolution is combined with acceptable anatomical detail allowing for the characterization of the tissue based on wash-in (enhancement of the contrast agent) and washout (elimination of the contrast agent) phenomena. In its easiest form, DCE is semiquantitatively assessed by measuring the signal in a region of interest (ROI) over time. This is performed analogously to dynamic PET imaging and used to visualize the enhancement pattern where the x-axis describes the time and the y-axis shows the signal (DCE) or activity (PET). There is no mathematical difference between signal-time plots in DCE and activity-time plots in dynamic PET imaging, although the biological information significantly differs. DCE assesses the signal change per tissue depending on the accumulation of gadolinium-based contrast media. In DCE MRI, three different patterns are typically described: (1) continuing enhancement, (2) plateau phase, and (3) washout. All three types may appear in prostate cancer. However, type 2 and 3 are the most typical patterns observed. In particular, the washout (type 3) is indicating a suspicious lesion. Similar to the limitations of T2w and DWI, benign hyperplasia nodules in the central zone may feature washout thus representing a limitation [27]. Further models use voxel-wise plotting of time to peak, area under the curve and more sophisticated approaches such as the quantification of k^{trans}, a parameter used to estimate capillary permeability.

19.3.4 MR Spectroscopy

MRS measures the concentration of metabolites in vivo. The technique is based on the fact that different metabolites feature different resonance frequencies based on the chemical environment of water protons [38]. Its value to provide unique biological information based on the metabolic spectra of prostate tissue has been demonstrated repeatedly with 68/85% sensitivity/specificity [39]. For prostate cancer, typically the metabolism of phospholipids is assessed using ^{1}H-MRS as the prostate physiologically features strong accumulation of citrate, in particular within the glands of the peripheral zone. Increase in choline and decrease of citrate depicted by spectral peaks is characteristic for prostate cancer [40]. The mass-forming effect of cancer tissue impedes the accumulation of citrate which then significantly decreases. Furthermore, the evolution of cancer leads to a change in cell membrane synthesis and subsequently to altered choline concentrations [40] measurable by ^{1}H-MRS. MRS was optional in PI-RADS 1 and is not integrated anymore in PI-RADS 2, potentially due to methodological reasons such as rather longer acquisition times.

A very promising spectroscopic development currently evolving is the "chemical exchange saturation transfer" (CEST). This method still under scientific exploration for prostate cancer exploits the exchange of water protons between molecules and is potentially combinable with dedicated contrast media similar to the tracer principle in PET imaging [41].

19.4   PET Radiopharmaceuticals in Prostate Cancer

19.4.1 ¹⁸F-Fluorodeoxyglucose (¹⁸F-FDG)

The ability of ¹⁸F-FDG PET to detect cancer is based on increased expression of cellular membrane glucose transporter 1 (GLUT1) and enhanced hexokinase II enzyme activity within tumor cells. The increased glycolytic activity in cancer cells (Warburg effect) is a hallmark of cancer and explains the widespread utilization of ¹⁸F-FDG as imaging biomarker in oncology. In PC cell lines, the expression of GLUT1 is higher in poorly differentiated than in well-differentiated hormone-sensitive tumors [42]; therefore, the utility of ¹⁸F-FDG PET seems to depend highly on the phase of disease; it may be relevant in one phase, but limited in another [43, 44].

In primary cancer detection ¹⁸F-FDG PET/CT has a relatively low sensitivity. The two main disadvantages of ¹⁸F-FDG are the close vicinity of the urinary tract [45], which physiologically excretes ¹⁸F-FDG and might negatively impact visualization of the pelvic area, and the overlap of tracer accumulation in the normal prostatic gland, benign prostatic hyperplasia (BPH), and prostate cancer [46]. Nevertheless, an incidental high prostatic ¹⁸F-FDG uptake should not be ignored and requires additional imaging or PSA levels measurements, because of the likelihood of detecting a tumor [47–50]. Limited data is available on the use of ¹⁸F-FDG in the initial staging of PC. In the early analysis of the National Oncologic PET Registry data in the United States including 2042 scans in PC patients, ¹⁸F-FDG PET/CT had an impact on initial clinical management in 32% of patients (95% CI, 30.0–34.1%) [51].

Based on current experience, it appears that ¹⁸F-FDG PET has overall limited utility in the setting of biochemical relapse. Jadvar et al. reported a sensitivity of only 8.1% for detection of occult metastases in 37 men with PSA relapse and negative results on standard imaging [52]. In another study, involving 28 patients with biochemical relapse after definitive primary therapy, the sensitivity and specificity of ¹⁸F-FDG PET/CT were 61.6% and 75%, respectively [53]. In a comparative study of ¹¹C-choline and ¹⁸F-FDG, the sensitivities were 60.6% and 31%, respectively [54], but increased to 80 and 40%, when the serum PSA levels were greater than 1.9 ng/mL, confirming that using both tracers, diagnostic accuracy increases together with PSA level increase.

¹⁸F-FDG PET/CT is useful for detection of aggressive disease, treatment efficacy evaluation in metastatic disease, and prognostication in patients with castration-resistant tumors [44, 55]. Oyama et al. reported a decrease in ¹⁸F-FDG uptake in PC after endocrine therapy, both in primary PC lesions and at metastatic sites, suggesting that the glucose utilization by tumors is suppressed by androgen ablation [56].

In summary, ¹⁸F-FDG has limited utility in the initial evaluation of PC because many primary tumors are well-differentiated and small. Furthermore, uptake patterns can easily overlap with those of BPH or normal prostate. ¹⁸F-FDG has scarce utility in the detection of local recurrence in the treated prostate bed, because of possible overlap with physiological posttreatment changes. The highest utility can

be disease extent evaluation and treatment response evaluation in castration-resistant PC (CRPC).

19.4.2 Radiolabeled Choline

Choline is a substrate for the phosphatidylcholine biosynthesis, the major phospholipid in the cell membrane. The biologic basis for radiolabeled choline uptake in tumors is the malignancy-induced upregulation of choline kinase, which leads to the incorporation and trapping of choline in the form of phosphatidylcholine (lecithin) in the tumor cell membrane via the Kennedy pathway [57]. Due to the short half-life (approximately 20 min) of ^{11}C-choline, a fluorinated version (^{18}F-fluorocholine or FCH) was also developed. The main difference between ^{11}C-choline and ^{18}F-fluorocholine is the earlier urinary appearance of the fluorinated version, which can affect tracer performance for local relapse detection [58].

The value of PET and PET/CT using radiolabeled choline for the diagnosis of primary PC has been evaluated in several studies. The performance of ^{11}C-choline PET/CT in PC staging was retrospectively compared to that of whole-body MRI (WBMRI) [59]. Overall sensitivity and specificity were 97% and 77%, respectively, for ^{11}C-choline PET, and 79 and 94% for WBMRI, demonstrating the complementarity of the two imaging modalities. Another comparative study was conducted with TRUS in 55 patients with clinically localized PC, before radical retropubic prostatectomy, and results showed that both modalities tended to under-stage PC [60]. In 58 patients with suspected PC, Scher et al. reported a sensitivity of 87% and specificity of 62% for the detection of primary PC [61]. Other investigations have found partially controversial results [61–66], suggesting that radiolabeled choline is probably not the ideal radiopharmaceutical in the assessment of tumor within the prostate.

In biochemical failure and restaging, ^{11}C-Choline PET/CT has an important role in the evaluation of lymph nodes metastasis and disease extension, even though its sensitivity is linked to serum PSA levels, with an increase of sensitivity for high PSA values [67]. Reske et al. reported a sensitivity of 73% and specificity of 88% of ^{11}C-choline PET/CT in the detection of local recurrence after radical prostatectomy [68], and another group reported sensitivity and specificity of 64 and 90% in the same setting [69].

Different groups showed that choline uptake in biochemical recurrence of PC is strictly related to PSA values. In this setting Castellucci et al. evaluated 190 patients, and Krause et al. 63 patients, and both groups showed a detection rate increasing proportionally to PSA levels increase, with highest values, respectively, of 67 and 73% in patients with PSA values greater than 5 ng/mL and lowest values, respectively, of 19 and 36%, with PSA < 1 ng/mL [67, 70].

Several studies have also reported good performance of ^{11}C-choline PET/CT in detecting bone metastases [71–73]. Recently it has been suggested that ^{11}C-choline PET/CT imaging could be useful as a diagnostic tool for metastasis-directed therapies as well as for monitoring patients treated with systemic therapies (chemotherapy and androgen deprivation therapy) [74].

[18]F-fluorocholine PET/CT has also been evaluated in PC patients. Beheshti et al. evaluated 132 patients with biopsy-proven intermediate- or high-risk primary PC using ^{18}F-fluorocholine PET/CT, in the preoperative staging. A good specificity (96%) and low sensitivity (45%) were reported for the detection of lymph nodes metastases (a total of 912 lymph nodes were histopathologically examined), and management was changed in 15% of all patients, 20% of high-risk patients [65]. Different groups described that the detection rate of ^{18}F-fluorocholine PET/CT positively correlates with serum PSA levels in the setting of biochemical relapse, similarly to ^{11}C-choline [75, 76].

In summary, the advantages and drawbacks of ^{11}C-choline and ^{18}F-fluorocholine are inverse. ^{11}C-choline provides better visualization of the pelvis due to the low urine excretion, if imaged sufficiently early, but on the other hand, the short half-life of ^{11}C limits the widespread use of the radiopharmaceutical. Conversely, ^{18}F-fluorocholine has a longer half-life, but higher urinary excretion at scanning time, which can cause influence image interpretation. PET/CT using radiolabeled choline is not indicated in the initial evaluation of PC, due to the low specificity for PC, and its main role is the detection of site of relapse in patients presenting with rising PSA levels.

19.4.3 PSMA Compounds

The prostate-specific membrane antigen, also known as glutamate carboxypeptidase II, is an enzyme bound to the cell membrane. It is physiologically expressed in many tissue types and significantly upregulated in PC thus representing a very promising target to visualize the disease including metastases. PSMA-based radiolabeled ligands were already investigated in 2005 at Johns Hopkins University [77] followed by ^{18}F-DCFBC published in 2008 [78] and ^{68}Ga-labeled PSMA inhibitors in 2010 [79]. To this time point, studies were limited on animal PET imaging. First-in-men reports succeeded in Heidelberg, Germany [80, 81] based on the compound Glu-NH-CO-NH-Lys(Ahx)-HBED-CC [82], coupled to ^{68}Ga, also known as ^{68}Ga-PSMA-HBED-CC or ^{68}Ga-PSMA-11. Following this, ^{18}F-DCFPyL was proposed in 2015 and demonstrated in nine patients [83, 84] allowing for a production at a cyclotron. Recently, ^{18}F-PSMA-1007 was introduced as an alternative [85–87] and showed very promising results due to very low accumulation in the urinary tract likely beneficial for imaging PC or local recurrence evolving often with close proximity to the bladder.

Currently, ^{68}Ga-PSMA-11 is the most used diagnostic PSMA ligand in Europe as it is not patent protected and producible using a GMP-compliant (good manufacturing practice guidelines) synthesis at a [68]Ge/^{68}Ga-generator. Because it is not dependent on a cyclotron, the synthesis may be performed even at smaller centers, however, with fewer patients compared to an ^{18}F-coupled ligand. ^{68}Ga-PSMA-11 has been considered as breakthrough in molecular imaging as its sensitivity/specificity values especially for lymph nodes outperform any diagnostic modality hitherto used (Fig. 19.3). An example of ^{68}Ga-PSMA-11 PET/MR is given in Fig. 19.3. A recent meta-analysis reported combined excellent diagnostic performance (sensitivity/specificity of 0.86/0.86 per patient and 0.80/0.97 per lesion) of ^{68}Ga-PSMA-11 to detect pathological findings
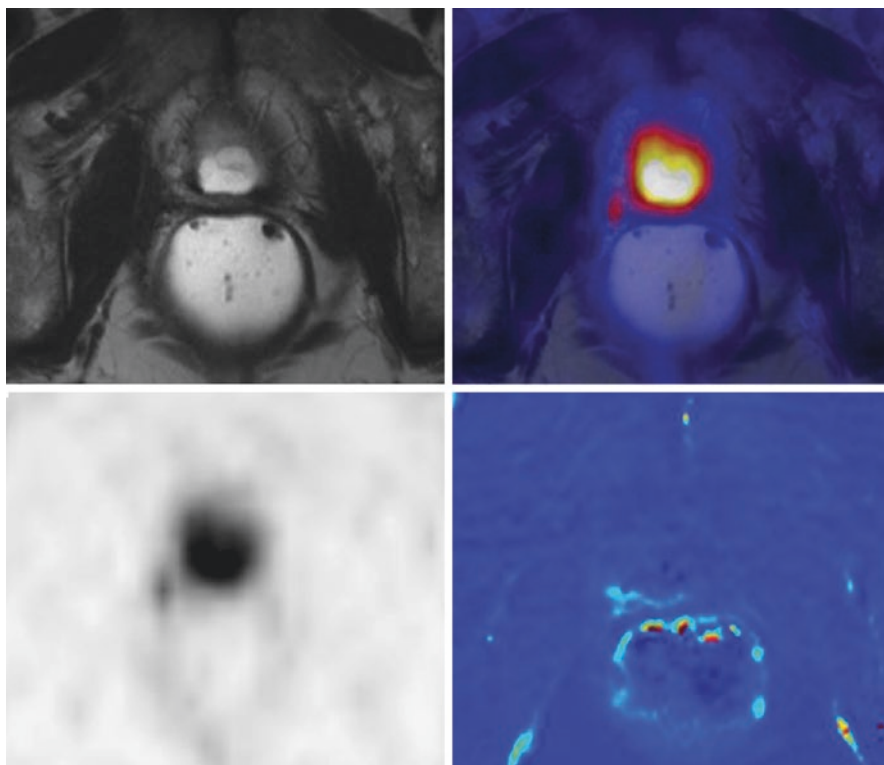
Fig. 19.3 A 66-year-old man with biochemical recurrence (PSA 0.42 ng/mL) after radical prostatectomy. ^{68}Ga-PSMA PET/MR (top right image) shows faint PSMA expression adjacent to the bladder on the right side. iAUC60 derived from DCE shows faint early contrast media influx (bottom right image). The combination of findings from PET (bottom left image) and MR (top left image) increases the evidence for local recurrence by accumulating evidence

in biochemical recurrence of prostate cancer [88]. A modified theranostic variant, PSMA-617 or PSMA-DKFZ-617 [89, 90], allows for diagnostic imaging using the ^{68}Ga-coupled tracer and for therapy using the beta-emitter lutetium-177 [91] or alpha-emitter actinium-225 [92] and has demonstrated very promising results in patients.

19.4.4 Amino Acid Analogues (^{18}F-Fluciclovine or ^{18}F-FACBC)

The rationale for using radiolabeled amino acids in PC imaging resides in the upregulation of amino acid transport and metabolism, due to the higher need for protein synthesis and energy in cancer cells. Many amino acid transporters are highly expressed in different cancers, including PC [93–95]. Both naturally occurring and synthetic amino acids have been radiolabeled for tumor imaging purposes, and the most extensively investigated synthetic amino acid in PC evaluation is anti-1-amino-3-^{18}F-fluorocyclobutane-1-carboxylic acid (^{18}F-fluciclovine or ^{18}F-FACBC). In PC

imaging [18F]-fluciclovine has the advantageous property of absent or mild bladder activity [96]; furthermore it is not metabolized nor incorporated into proteins [97]. A dynamic study showed that [18F]-fluciclovine has an early peak and reaches a plateau between 15 and 20 min; therefore early imaging is recommended [97, 98]. Most of the studies conducted in PC patients using [18F]-fluciclovine are in the setting of recurrent disease. Preliminary studies evaluating [18F]-fluciclovine in PC diagnosis showed that its ability to differentiate cancer from benign prostate hypertrophy (BPH) is limited [98–100]. There is large evidence that [18F]-fluciclovine is useful in the evaluation of patients with suspected recurrent disease due to biochemical failure. In this setting, it showed superiority compared to CT in 53 patients [101], to the radiolabeled anti-PSMA antibody [111In]-capromab pendetide (ProstaScint) in 93 patients, for detection of disease both in the prostatic bed and in extraprostatic localizations [102] and also to [11C]-choline in a large study involving 89 patients [103].

19.4.5 Radiolabeled Bombesin Analogues

Bombesin is a natural 14-amino acid peptide discovered in the 1970s that gave the name to the larger family of the so-called bombesin-like peptides. The mammalian gastrin-releasing peptide (GRP) is another component of the family and is a 27-amino acid peptide sharing with bombesin of a similar structure [104–107]. GRP is physiologically widely distributed in the peripheral nervous system and peripheral tissues and explicates its role binding to GRP receptors (GRPRs). The interaction of GRP-GRPRs is responsible of a mitogenic activity now known to induce cell growth in various tumors [108]. GRP gained wide interest in recent years because of the discovery that several primary tumors, including PC, highly overexpress GRPRs [109, 110]. GRPRs are overexpressed on the cell membranes of prostatic intraepithelial neoplasias (PIN) and in primary PC, as opposed to normal prostate tissue, and, in most cases, benign prostate hyperplasia [111]. Radiolabeling bombesin analogues targeting GRPRs could allow selective imaging of PC, using β^+ emitting isotopes for PET, and open the possibility of new systemic therapeutic strategies, using β^- emitting isotopes for peptide receptor radionuclide therapy (PRRT), in a theranostic approach. In the search for the ideal bombesin analogue for imaging and therapeutic radiolabeling, the initial focus of research was directed toward GRPR agonists, given their ability to be internalized and trapped in the GRPR-expressing cells, which was seen as a desirable characteristic. Later findings showed that internalization of the GRP agonist is the responsible mitogenic effect and led to the diversion of attention toward GRPR antagonists, which don't have this major drawback. Several different GRPR antagonists have been radiolabeled and are in different phases of development [112]. [68Ga]-RM2 (formerly also known as BAY86-7548) is considered at the moment the most promising radiolabeled bombesin analogue translated into the clinical phase (Fig. 19.4). The first study in PC patients using [68Ga]-RM2 PET/CT was conducted in 2013 [113] on 14 patients with PC (11 at initial diagnosis and 3 with biochemical recurrence after surgery). At quantitative analysis, histologically confirmed PC foci showed a higher average SUV (max and mean) compared to benign prostatic hypertrophy and normal prostate tissue. Reported sensitivity, specificity, and accuracy for

the detection of primary PC were 88%, 81%, and 83%, respectively, and sensitivity was 70% for the detection of nodal metastases. In the same study two patients underwent also a ^{11}C-acetate PET/CT, with concordant results, and one had a ^{18}F-choline PET/CT, with discordant results because ^{68}Ga-RM2 failed to identify in bone metastatic lesions positive on ^{18}F-choline. A recently published pilot study [114] compared the biodistribution of ^{68}Ga-RM2 and ^{68}Ga-PSMA-11 in seven patients with biochemically recurrent PC, confirming that the two radiopharmaceuticals have different distribution since they target two different biological processes. Other bombesin analogues used in PC patients are the ^{18}F-labeled BAY-864367 and ^{64}Cu-CB-TE2A-AR06, both showing interesting results [115, 116]. Other GRPr targeting PET radiopharmaceuticals have been recently reported in small cohorts, illustrating the attractiveness of this target for detection of PC. Maina and colleagues evaluated ^{68}Ga SB3 in eight patients with breast cancer and nine patients with prostate cancer. All patients had disseminated disease and had received previous therapies [117]. [68]Ga SB3 did not produce adverse effects and identified cancer lesions in

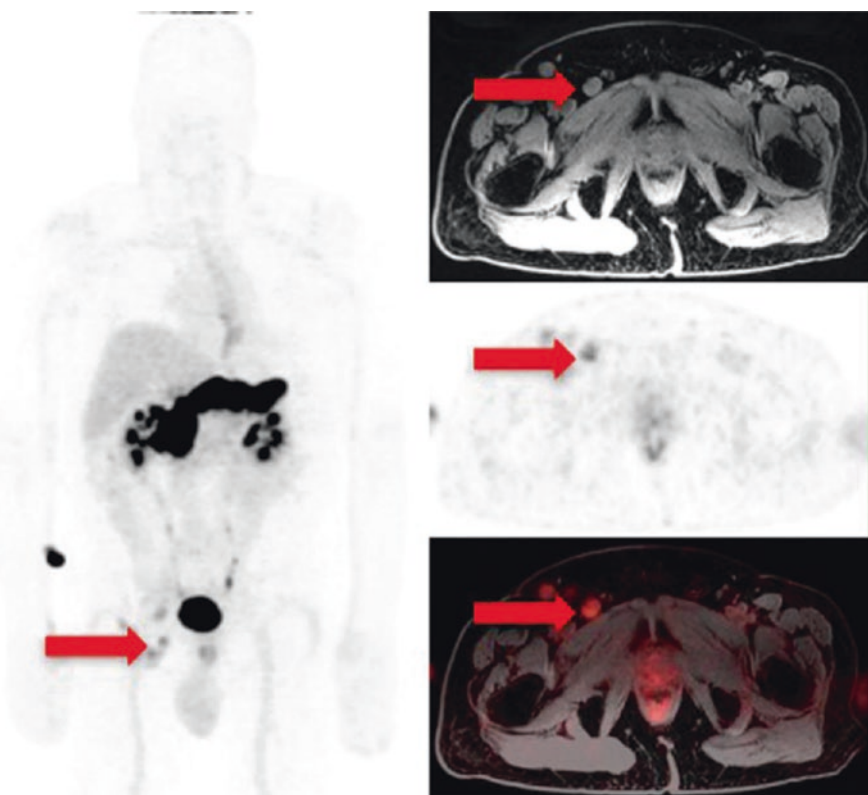**Fig. 19.4** A 72-year-old man with history of prostate cancer (Gleason score 4 + 3) treated with radiation therapy and androgen deprivation, now presenting with biochemical recurrence (PSA rising from 1.36 to 20.3 ng/dL) and noncontributory conventional imaging. ^{68}Ga-RM2 PET/MRI indicates focal uptake in right inguinal lymph nodes (red arrows). Biopsy confirmed metastatic adenocarcinoma of prostate origin

four out of eight (50%) with breast cancer and five out of nine (55%) with PC. An improved version of this radiopharmaceutical, [68]Ga NeoBOMB1, is showing promising results in preliminary studies [118, 119].

Despite promising results using different radiolabeled GRPR antagonists, further larger studies are still needed in order to clearly define the role of these radiopharmaceuticals in PC.

19.4.6 ^{11}C-Acetate

Acetate is a key metabolic substrate of β-oxidation and fatty acid precursor. After being converted to acetyl-CoA, it can participate to either a catabolic or anabolic pathways, depending on the cell type. In myocardial cells, it enters the Krebs cycle and is metabolized in the mitochondria. In cancer cells, the main metabolic destiny of acetyl-CoA is sterol and fatty acid synthesis, via the fatty acid synthase (FAS) enzyme [120]. Since cancer cells have an increased need of fatty acids and cholesterol due to increase need of membrane lipids, the need for acetate is increased accordingly, being the only carbon source in this process. FAS is overexpressed in cancer cells [121], and its expression is correlated to PC aggressiveness and Gleason score [122, 123]. Considering the potential role of acetate as biomarker in different processes, it has been radiolabeled with ^{11}C for PET imaging and initially used to quantify myocardial oxidative metabolism [124]. Acetate has also been radiolabeled with ^{18}F but with very little use [125]. ^{11}C-acetate is mainly eliminated through the respiratory system, and not through the urinary system, which represents a major advantage in PC imaging [58, 126]. As for other radiopharmaceuticals, an important drawback of ^{11}C-acetate is the limited ability to differentiate between BPH and PC. This aspect limits the utility in the phase of PC initial staging and diagnosis. Several groups evaluated ^{11}C-acetate in this setting [127–131]. In one of the earliest studies, Kato et al. [129] studied 36 subjects (21 subjects with normal prostate, 9 with BPH, and 6 patients with PC) using a 20-min dynamic ^{11}C-acetate PET, demonstrating that SUV in the prostate of older patients (≥50 years) and of patients with BPH and PC was not significantly different. This study describes an age-related increase of ^{11}C-acetate uptake in the prostate, which needs to be taken into account in the setting of PC initial evaluation. Jambor et al. [127] evaluated 26 patients with untreated PC using ^{11}C-acetate PET and MR spectroscopy, finding that both methods have limited accuracy (particularly low specificity) and neither of them can provide information regarding cancer aggressiveness. In another study involving 36 patients with untreated PC, the same authors found that the co-registration of ^{11}C-acetate PET and MRI can enhance the detection of localized PC [128]. The evaluation of lymph node metastases with ^{11}C-acetate PET provided overall a limited accuracy. In a large study involving 107 patients with intermediate- or high-risk PC after primary surgery, but before reoperation, ^{11}C-acetate PET showed a modest accuracy in the detection of nodal metastases but showed to independently predict treatment failure-free survival [132].

[11]C-acetate has been used in the setting of biochemical recurrence. In an attempt to define the patient characteristics associated with a higher likelihood of a positive ^{11}C-acetate PET, Dusing et al. retrospectively analyzed 120 patients with suspected PC recurrence. The authors evaluated different parameters and found that the rate of positive scans was correlated to increasing PSA and PSA velocity. Using a PSA level of 1.24 ng/mL and a PSA velocity of 1.32 ng/mL/year, the accuracy of ^{11}C-acetate PET was the highest [133]. Different groups found high detection rates in detection of PC recurrence, both in the prostatic bed and in metastatic disease [134–136]. In a study involving 90 patients with rising PSA levels (>0.2 ng/mL), Spick et al. evaluated the performance of ^{11}C-acetate PET, in comparison to ^{99m}Tc-biphosphonate imaging, in the detection of bone lesions. Results using the two imaging modalities were similar, and therefore ^{11}C-acetate PET is described as a promising tool in the setting of bone metastasis evaluation [137]. Given the similar mechanism of uptake of ^{11}C-acetate PET and radiolabeled choline, some studies also directly compared the two radiopharmaceuticals finding comparable results [138, 139].

19.4.7 Androgen Receptor Targeting Radiopharmaceuticals (FDHT)

PC is an androgen-dependent malignant disease [140], and the androgen receptor (AR) plays a crucial role during all phases of the illness. Standard treatment in hormone-sensitive advanced PC is based on the depletion of testosterone, with either surgical, alone or with anti-androgen, or chemical castration, using gonadotropin-releasing hormone (GnRH) analogues. After initial response to androgen depletion, with PSA decline and tumor regression, there is progression to CRPC, around 1–3 years after initiation of therapy, which is characterized by the transition to the lethal phase of the disease [140, 141]. However, the AR maintains high expression in CRPC and keeps playing a role, independently from the androgen deprivation [142–144]. Imaging AR expression with PET could represent an interesting approach to guide the therapeutic management of patients with PC. The most used PET radiopharmaceutical targeting the AR is 16β-^{18}F-fluoro-5α-dihydrotestosterone (^{18}F-FDHT), an analogue of 5a-dihydrotestosterone (DHT). Different groups assessed the role of ^{18}F-FDHT PET in evaluating AR expression, and overall results showed that the radiopharmaceutical selectively binds to the AR, in both primary tumor and metastatic disease [145–147]. Beattie et al. in 2010 evaluated pharmacokinetic properties of ^{18}F-FDHT in 13 PC patients, showing good correlation of AR expression and tracer uptake. Another study evaluated 38 patients with CRPC aiming to compare the features of bone metastases on CT with glycolytic activity, measured on ^{18}F-FDG PET and AR receptor expression, measured on ^{18}F–FDHT PET. The number of bone lesions on CT, ^{18}F FDG PET, and ^{18}F-FDHT PET, and the intensity of ^{18}F-FDHT uptake were found significantly associated with overall survival [148]. The limited number of published studies using ^{18}F-FDHT may be partly due to the difficult radiolabeling procedure of the radiopharmaceutical. To overcome this issue, a fully automated

system has been recently developed [149]. Despite some encouraging results, very scarce data is available using ^{18}F-FDHT, and its role still needs to be fully explored.

19.5   Integrated PET/MRI in Prostate Cancer Imaging

Imaging plays an essential role in PC patients, helping differentiating between local, regional, and distant disease, which is a prerequisite for effective disease management. Developments in imaging technologies have improved the detection rate of PC, providing quantitative assessment of biochemical and functional process with high-resolution images, which leads to an accurate localization and disease extent definition. After promising initial results obtained by co-registering images of separately acquired scans [59, 128, 150–152], with the introduction of integrated PET/ MRI systems, different groups started evaluating the performance of this state-of-the-art technology in PC. The first study using simultaneously acquired ^{18}F-choline PET/MRI images for evaluating PC was published in 2013 [153] in a comparative study with PET/CT. This first study showed feasibility of the new method and the possibility of a clinical use was opened.

The focus of this section will be on the current application of integrated PET/ MRI systems, specific advantages of a combined PET/MRI approach in prostate cancer, and future prospective (Table 19.1).

19.5.1 Current Applications of PET/MRI in Prostate Cancer

Studies evaluating simultaneous PET/MRI are still limited and are summarized in Table 19.2.

Different groups evaluated PET/MRI in the detection and characterization of PC. Kim et al. evaluated 30 patients with biopsy-proven localized PC using ^{18}F-fluorocholine PET/MRI. The authors compared the ability to detect PC using MRI alone and ^{18}F-fluorocholine PET alone to that of the combined approach and found that the latter performed better, with detection rate of 83.3%, 80.0%, and 93.3%, respectively. The study also evaluated different MRI-assisted PET parameters and found that MRI uptake volume product (UVP_{MRI}), obtained multiplying mean standardized uptake value (SUV_{mean}) and MRI mean tumor volume (MTV_{MRI}), had that highest correlation with serum PSA levels, and was the only parameter significantly associated with the Gleason score [154]. A similar study was conducted in a cohort of 66 patients with biopsy-proven PC by Eiber et al. using ^{68}Ga-PSMA-HBED-CC PET/MRI. PET/MRI outperformed mpMRI and PET alone, with detection rate of 66% and 92%, respectively, for the two modalities alone, and of 98% for the combined approach [155]. Elschot et al. used ^{18}F-fluciclovine PET/MRI in 28 patients diagnosed with high-risk PC, trying to define the optimal protocol for the detection and characterization of PC. They performed a quantitative evaluation of the dynamic uptake of ^{18}F-fluciclovine showing that a late-window PET imaging

Table 19.1 PET radiopharmaceuticals in prostate cancer

	18F-FDG	11C-choline/ 18F-choline	11C-acetate	PSMA	18F-FACBC	68Ga-RM2	18F-FDHT
Mechanism of uptake	Glucose metabolism	Fatty acid metabolism	Fatty acid metabolism	Prostate-specific membrane antigen	Transmembrane amino acid transport	Gastrin-releasing peptide (GRP) receptor	Androgen receptor (AR)
Diagnosis and staging	– Low sensitivity – Low specificity: Overlap in tumor/ BPH/normal tissue	– Good sensitivity – Low specificity: overlap uptake in tumor/BPH/normal tissue – Detection rate correlated to PSA levels	– Good sensitivity – Low specificity: overlap uptake in tumor/BPH/ normal tissue	– High diagnostic and staging accuracy	– Good sensitivity – Low specificity: overlap uptake in tumor/BPH/ normal tissue	– Good sensitivity – Good specificity Limited number of studies	Limited number of studies
Biochemical relapse (BCR)/ restaging/ treatment response assessment	Limited utility in BCR Useful in: – Evaluation of aggressive disease – Disease extent evaluation – Assessment of treatment response in metastatic disease	High sensitivity in BCR (increasing with higher PSA levels) Accurate in detecting bone metastasis Promising performance in treatment planning and response assessment to systemic therapies	– Sensitivity increases with higher values of PSA – Acetate > FDG in restaging of LN and local disease – FDG > acetate distant metastases	– Sensitivity increases with higher values of PSA	Useful in evaluation of BCR Better performance than: – CT – Prostascint – 11C-choline Improvement in the detection rate of recurrent disease	Promising preliminary results in BCR Limited number of studies	Limited number of studies

Table 19.2 PET/MRI studies in prostate cancer imaging

Reference (year)	Patient population	Radiopharmaceutical/ MR sequences	Aim	Conclusions
[153]	15 patients with PC: – 8 biopsy proven PC – 2 repeated prostate biopsies without evidence of PC – 5 suspected PC with rising PSA, but did not have a prostate biopsy	^{18}F-choline/T2w, DWI	Feasibility of simultaneous ^{18}F-choline PET/MRI of prostate cancer	^{18}F-choline PET/MRI is feasible and works in clinical routine
[158]	32 patients with PC: – 9 staging – 23 restaging	^{11}C-choline/Dixon AC, T1w, T2w	^{11}C-choline PET/CT vs. simultaneous whole-body PET/MR in PC	PET/MR is comparable to PET/CT in detecting lesions and allows a better anatomical allocation especially in the bone and pelvis
[162]	55 patients with biopsy proven or suspected recurrent PC	^{18}F-choline/T1w, T2w, DWI	Quantitatively evaluation of bone metastases from PC (SUVs and ADCs values)	Moderate significant inverse correlation between increased choline metabolism and ADC values
[159]	20 patients with biochemical recurrence of pretreated PC	^{68}Ga-PSMA-11/VIBE AC, HASTE, T1w VIBE, T2w, DWI, DCE, TWIST	Feasibility of [68]Ga- PSMA PET/MRI in recurrent PC	PC is detected more easily and more accurately with [68]Ga- PSMA PET/MRI than PET/CT
[157]	35 patients with primary PC	^{18}F-choline/T2w, DWI	Characterize intermediate- and high-risk prostate cancer patients with SUVs and ADCs values	SUV and ADC differ significantly between tumor and healthy tissues, but no correlation was found between the two parameters
[154]	30 patients with localized PC	^{18}F-choline/VIBE, T2w, DWI	Usefulness of MRI-assisted PET parameters for characterization of primary PC	^{18}F-choline PET/MRI has a better diagnostic than each of the modalities alone MRI-assisted metabolic volumetric PET parameters provide accurate characterization of PC

[163]	3 patients with biopsy proven PC	18F-FDG/T2w, DWI, DCE	Feasibility of PET/MRI to guide localization of prostate lesions for dynamic FDG analyses	Dynamic PET/MRI allows localization of small prostate tumors and differentiation between tumor and benign tissues
[155]	53 patients with histologically proven intermediate- or high-risk PC	68Ga- PSMA-11/ mpMRI	Comparison of 68Ga-PSMA PET/ MRI to mpMRI and PET alone in localization of primary PC	68Ga-PSMA PET/MRI improves diagnostic accuracy coin comparison to both mpMRI and PET alone
[156]	28 patients with high-risk PC	18F-fluciclovine/ mpMRI	Characterization of primary prostate cancer by quantitative evaluation of the dynamic uptake of 18F-fluciclovine in cancerous and benign tissue.	Late-window 18F-fluciclovine PET imaging shows promise for distinguishing between prostate tumors and benign tissue and for assessment of tumor aggressiveness.
[114]	7 patients with biochemically recurrent PC who underwent both 68Ga-PSMA-11 PET/CT and 68Ga-RM2 PET/MR	68Ga-PSMA-11 and 68Ga-RM2/T1, DIXON, T2, DWI	To compare: – Biodistribution – Uptake of 68Ga-PSMA-11 outside the expected physiologic biodistribution with that of 68Ga-RM2	68Ga-PSMA-11 and 68Ga-RM2 had distinct biodistributions
[160]	26 patients with PC	68Ga-PSMA-11/T1w, T2w fat saturated, DWI, ceT1w	Evaluate reproducibility of 68Ga-PSMA-11 PET/MRI in depicting lymph node and bone metastasesComparison with PET/CT	68Ga-PSMA-11 PET/MRI accurately depicts lymph node and bone metastases Very low discordance with PET/CT
[161]	119 patients with biochemical recurrence, 18 patients with relapse	68Ga-PSMA-11/ T2w-TSE, DWI, ceT1w	To compare PET/CT and PET/MRI for detection of local recurrence	68Ga-PSMA-11 PET/MRI superior to -PET/CT because mpMRI depicts local relapse cases superimposed by bladder signal

approach may be useful for distinguishing between prostate tumors and benign prostate tissue and also for the assessment of prostate tumor aggressiveness [156].

In a study evaluating 35 patients with intermediate-/high-risk primary PC, Wetter et al. used simultaneous ^{18}F-fluorocholine PET/MRI and compared PET and MRI parameters, SUV (max and mean), and ADC, in the differentiation between PC and healthy prostate tissue. Both SUV and ADC values differed significantly in tumor lesions and healthy tissue, but no significant correlation was found between the two parameters. The authors concluded that their results might be explained by the fact that SUVs and ADC values characterize different parts of tumor biology, and they might be independent biomarkers of primary PC [157].

The performance of PET/MRI was compared to that of PET/CT in different studies. Souvatzoglou et al. evaluated the two hybrid systems using ^{11}C-choline in 32 patients, and found that anatomical allocation of lesions was better with simultaneous PET/MRI than with PET/CT, especially in the bone and pelvis [158]. Afshar-Oromieh et al. did the same comparison using ^{68}Ga-PSMA-11 PET/MRI in the diagnosis of recurrent PC. Twenty patients with biochemical recurrence of PC were evaluated, and the authors found that the detection of disease was easier and more accurate using PET/MRI [159]. Using ^{68}Ga-PSMA-11, Freitag et al. compared PET/MRI to PET/CT in the evaluation of lymph node and bone metastases in a retrospective analysis of 26 patients. All patients had a suspicious PET-positive lymph node or bone finding on the initial PET/CT (PET/CT performed 1 h postinjection and PET/MRI 3 h postinjection). Concordance between the two modalities was very high, 100% in bone lesions and 98.5 in lymph node lesions. SUV values measured with the two different systems were linearly correlated [160]. A recent study compared PET/MRI with PET/CT for the detection of local recurrence of PC using ^{68}Ga-PSMA-11 and demonstrated advantages using PET/MRI [161]. Physiologic accumulation of the tracer in the bladder may superimpose and impede the detection of local relapse in the PET part if it is located very closely to the bladder wall. In such cases being false negative in the PET component, mpMRI may "back up" the PET part and depict the pathology substantiating the complementary value of simultaneous PET/MRI. Hence, the protocols need to be optimized to reduce bladder filling as much as possible to enhance the PET component. Infusion of saline after i.v. application of furosemide is discussed as the standard protocol to reduce the bladder signal and optimize the PET acquisition.

In the setting of biochemical recurrence of disease, Wetter et al. evaluated the potential advantages of PET/MRI for detection of bone metastases. In the study, involving 55 patients with biopsy proven PC and rising PSA levels, the authors used ^{18}F-fluorocholine PET/MRI and quantitatively evaluated bone lesions, using SUV (max and mean) and ADC. The authors found a moderate but significant correlation between increased ^{18}F-fluorocholine metabolism and ADC values of bone lesions [162].

One group performed a pilot study including three patients with biopsy-proven PC to explore the feasibility of simultaneous PET/MRI to guide localization of prostate lesions for dynamic FDG analysis. Simultaneous PET/MRI allowed localization of small prostate tumors for dynamic PET analysis which led to clear differentiation between tumor and benign tissues [163].

Simultaneous PET/MRI has the potential to provide comprehensive information regarding recurrent prostate cancer with respect to local recurrence, lymph node metastases, and bone metastases; however, future prospective studies in larger cohorts are warranted to validate this novel multimodality approach in the imaging assessment of PC.

19.5.2 Specific Advantages of the Simultaneous PET/MRI Approach in Prostate Cancer

In the evaluation of PC, both PET and MRI are individually valuable imaging modalities. mpMRI combines multimodal MRI sequences giving complementary diagnostic information, excellent anatomical visualization of the prostate, and adjacent organs with high-resolution and soft-tissue delineation; it allows detection of areas with high cellularity, using DWI, highlights areas of hypervascularity and neoangiogenesis, using DCE assessing gadolinium enhancement, and shows concentration of metabolites and evaluation of endogenous molecules, using MRS. PET on the other hand offers complementary information to that of MRI, allowing visualization and quantification of tracers' distribution in the whole body, with high sensitivity. Several PET radiopharmaceuticals, exploring different metabolic processes, or receptors' expression increased in PC, have been used. PET is most useful in the setting of biochemical recurrent disease, for the detection of distant localizations of metastatic PC. The integration of the two modalities using simultaneous PET/MRI combines the complementary information deriving from each modality alone and brings some additional benefits in PC patients, which can be summarized as follows: radiation exposure reduction due to the use of MRI instead of CT; workflow optimization, with consequent increased patient comfort in patients with PC who would need to undergo both imaging modalities during the course of their disease (one-stop-shop examination); and increased diagnostic accuracy deriving by the perfect co-registration of the PET and MRI data. Considering the limited number of studies currently available, it is evident that PET/MRI is still in a very early stage, and some work still needs to be done. PET/MRI has clearly the potential of becoming the preferred imaging modality in PC in the next decade, but large prospective studies are warranted to clarify the practical benefits of the combined approach, particularly in management change of PC patients.

19.6 Summary

MRI and PET are two complementary imaging modalities offering essential information in the evaluation of all phases of PC. Integrated PET/MRI has the potential to become the hybrid modality of choice in PC, replacing PET/CT and MRI performed separately. The information deriving from a combined approach can be obtained more easily, more conveniently for the patient, and with radiation exposure reduction. The studies available so far using PET/MRI show that the combined

approach offers better diagnostic accuracy in PC, because the simultaneous acquisition enables an optimal spatial and temporal co-registration. Although PET/MRI is a fairly new technology, results obtained in preliminary studies are encouraging and need to be confirmed by larger prospective trials establishing its role and cost-effectiveness.

References

1. Siegel RL, Miller KD, Jemal A. Cancer statistics, 2016. CA Cancer J Clin. 2016;66(1):7–30.
2. Attard G, Parker C, Eeles RA, et al. Prostate cancer. Lancet. 2016;387(10013):70–82.
3. Zeigler-Johnson CM, Rennert H, Mittal RD, et al. Evaluation of prostate cancer characteristics in four populations worldwide. Can J Urol. 2008;15(3):4056–64.
4. Algaba F, Trias I, Acres Y. Natural history of prostatic carcinoma: the pathologist's perspective. In: Rjad LJ, editor. Prostate cancer. Berlin: Springer; 2007. p. 9–25.
5. Gleason DF, Mellinger GT. Prediction of prognosis for prostatic adenocarcinoma by combined histological grading and clinical staging. J Urol. 1974;111(1):58–64.
6. Gordetsky J, Epstein J. Grading of prostatic adenocarcinoma: current state and prognostic implications. Diagn Pathol. 2016;11:25.
7. Matoso A, Epstein JI. Grading of prostate cancer: past, present, and future. Curr Urol Rep. 2016;17(3):25.
8. Mohler JL, Armstrong AJ, Bahnson RR, et al. Prostate cancer, version 1.2016. J Natl Compr Cancer Netw. 2016;14(1):19–30.
9. D'Amico AV, Whittington R, Malkowicz SB, et al. Pretreatment nomogram for prostate-specific antigen recurrence after radical prostatectomy or external-beam radiation therapy for clinically localized prostate cancer. J Clin Oncol. 1999;17(1):168–72.
10. Isbarn H, Wanner M, Salomon G, et al. Long-term data on the survival of patients with prostate cancer treated with radical prostatectomy in the prostate-specific antigen era. BJU Int. 2010;106(1):37–43.
11. Van Poppel H, Vekemans K, Da Pozzo L, et al. Radical prostatectomy for locally advanced prostate cancer: results of a feasibility study (EORTC 30001). Eur J Cancer. 2006;42(8):1062–7.
12. Ellis WJ, Brawer MK. The significance of isoechoic prostatic carcinoma. J Urol. 1994;152(6 Pt 2):2304–7.
13. Brock M, Eggert T, Palisaar RJ, et al. Multiparametric ultrasound of the prostate: adding contrast enhanced ultrasound to real-time elastography to detect histopathologically confirmed cancer. J Urol. 2013;189(1):93–8.
14. Mitterberger MJ, Aigner F, Horninger W, et al. Comparative efficiency of contrast-enhanced colour Doppler ultrasound targeted versus systematic biopsy for prostate cancer detection. Eur Radiol. 2010;20(12):2791–6.
15. Ives EP, Burke MA, Edmonds PR, Gomella LG, Halpern EJ. Quantitative computed tomography perfusion of prostate cancer: correlation with whole-mount pathology. Clin Prostate Cancer. 2005;4(2):109–12.
16. Hricak H, Choyke PL, Eberhardt SC, Leibel SA, Scardino PT. Imaging prostate cancer: a multidisciplinary perspective. Radiology. 2007;243(1):28–53.
17. Even-Sapir E. Imaging of malignant bone involvement by morphologic, scintigraphic, and hybrid modalities. J Nucl Med. 2005;46(8):1356–67.
18. Even-Sapir E, Metser U, Mishani E, Lievshitz G, Lerman H, Leibovitch I. The detection of bone metastases in patients with high-risk prostate cancer: 99mTc-MDP planar bone scintigraphy, single- and multi-field-of-view SPECT, 18F-fluoride PET, and 18F-fluoride PET/CT. J Nucl Med. 2006;47(2):287–97.
19. Withofs N, Grayet B, Tancredi T, et al. (1)(8)F-fluoride PET/CT for assessing bone involvement in prostate and breast cancers. Nucl Med Commun. 2011;32(3):168–76.

20. Blau M, Nagler W, Bender MA. Fluorine-18: a new isotope for bone scanning. J Nucl Med. 1962;3:332–4.

21. Shirazi PH, Rayudu GV, Fordham EW. Review of solitary 18F bone scan lesions. Radiology. 1974;112(2):369–72.

22. Bombardieri E, Setti L, Kirienko M, Antunovic L, Guglielmo P, Ciocia G. Which metabolic imaging, besides bone scan with 99mTc-phosphonates, for detecting and evaluating bone metastases in prostatic cancer patients? An open discussion. Q J Nucl Med Mol Imaging. 2015;59(4):381–99.

23. Czernin J, Satyamurthy N, Schiepers C. Molecular mechanisms of bone 18F-NaF deposition. J Nucl Med. 2010;51(12):1826–9.

24. (NCCN) NCCN. NCCN guidelines for Prostate Cancer Version 03.2016. 2016 [03.2016]. https://www.nccn.org/professionals/physician_gls/pdf/prostate_blocks.pdf.

25. Barentsz JO, Richenberg J, Clements R, et al. ESUR prostate MR guidelines 2012. Eur Radiol. 2012;22(4):746–57.

26. Hamoen EH, de Rooij M, Witjes JA, Barentsz JO, Rovers MM. Use of the prostate imaging reporting and data system (PI-RADS) for prostate cancer detection with multiparametric magnetic resonance imaging: a diagnostic meta-analysis. Eur Urol. 2015;67(6):1112–21.

27. Weinreb JC, Barentsz JO, Choyke PL, et al. PI-RADS prostate imaging – reporting and data system: 2015, version 2. Eur Urol. 2016;69(1):16–40.

28. Carroll PR, Parsons JK, Andriole G, et al. NCCN guidelines insights: prostate cancer early detection, version 2.2016. J Natl Compr Cancer Netw. 2016;14(5):509–19.

29. Marks L, Young S, Natarajan S. MRI-ultrasound fusion for guidance of targeted prostate biopsy. Curr Opin Urol. 2013;23(1):43–50.

30. Schoots IG, Petrides N, Giganti F, et al. Magnetic resonance imaging in active surveillance of prostate cancer: a systematic review. Eur Urol. 2015;67(4):627–36.

31. Barchetti F, Panebianco V. Multiparametric MRI for recurrent prostate cancer post radical prostatectomy and postradiation therapy. Biomed Res Int. 2014;2014:316272.

32. Barentsz JO, Choyke PL, Cornud F, et al. Reply to Erik Rud and Eduard Baco's letter to the editor re: re: Jeffrey C. Weinreb, Jelle O. Barentsz, Peter L. Choyke, et al. PI-RADS prostate imaging – reporting and data system: 2015, version 2. Eur Urol 2016;69:16–40. Eur Urol. 2016;70(5):e137–8.

33. de Rooij M, Hamoen EH, Witjes JA, Barentsz JO, Rovers MM. Accuracy of magnetic resonance imaging for local staging of prostate cancer: a diagnostic meta-analysis. Eur Urol. 2016;70(2):233–45.

34. Stejskal EO, Tanner JE. Spin diffusion measurements: spin echoes in the presence of a time-dependent field gradient. J Chem Phys. 1965;42(1):288–92.

35. Jensen JH, Helpern JA, Ramani A, Lu H, Kaczynski K. Diffusional kurtosis imaging: the quantification of non-gaussian water diffusion by means of magnetic resonance imaging. Magn Reson Med. 2005;53(6):1432–40.

36. Le Bihan D, Breton E, Lallemand D, Aubin ML, Vignaud J, Laval-Jeantet M. Separation of diffusion and perfusion in intravoxel incoherent motion MR imaging. Radiology. 1988;168(2):497–505.

37. Le Bihan D, Breton E, Lallemand D, Grenier P, Cabanis E, Laval-Jeantet M. MR imaging of intravoxel incoherent motions: application to diffusion and perfusion in neurologic disorders. Radiology. 1986;161(2):401–7.

38. Verma S, Rajesh A, Futterer JJ, et al. Prostate MRI and 3D MR spectroscopy: how we do it. Am J Roentgenol. 2010;194(6):1414–26.

39. Umbehr M, Bachmann LM, Held U, et al. Combined magnetic resonance imaging and magnetic resonance spectroscopy imaging in the diagnosis of prostate cancer: a systematic review and meta-analysis. Eur Urol. 2009;55(3):575–90.

40. Kurhanewicz J, Swanson MG, Nelson SJ, Vigneron DB. Combined magnetic resonance imaging and spectroscopic imaging approach to molecular imaging of prostate cancer. J Magn Reson Imaging. 2002;16(4):451–63.

41. Ward KM, Aletras AH, Balaban RS. A new class of contrast agents for MRI based on proton chemical exchange dependent saturation transfer (CEST). J Magn Reson. 2000;143(1):79–87.

42. Jadvar H, Xiankui L, Shahinian A, et al. Glucose metabolism of human prostate cancer mouse xenografts. Mol Imaging. 2005;4(2):91–7.

43. Jadvar H. Molecular imaging of prostate cancer with 18F-fluorodeoxyglucose PET. Nat Rev Urol. 2009;6(6):317–23.

44. Jadvar H. Imaging evaluation of prostate cancer with 18F-fluorodeoxyglucose PET/CT: utility and limitations. Eur J Nucl Med Mol Imaging. 2013;40(Suppl 1):S5–10.

45. Liu IJ, Zafar MB, Lai YH, Segall GM, Terris MK. Fluorodeoxyglucose positron emission tomography studies in diagnosis and staging of clinically organ-confined prostate cancer. Urology. 2001;57(1):108–11.

46. Salminen E, Hogg A, Binns D, Frydenberg M, Hicks R. Investigations with FDG-PET scanning in prostate cancer show limited value for clinical practice. Acta Oncol. 2002;41(5):425–9.

47. Reesink DJ, van de Putte EE F, Vegt E, et al. Clinical relevance of incidental prostatic lesions on FDG-positron emission tomography/computerized tomography-should patients receive further evaluation? J Urol. 2016;195(4p1):907–12.

48. Brown AM, Lindenberg ML, Sankineni S, et al. Does focal incidental 18F-FDG PET/CT uptake in the prostate have significance? Abdom Imaging. 2015;40(8):3222–9.

49. Kang PM, Seo WI, Lee SS, et al. Incidental abnormal FDG uptake in the prostate on 18-fluoro-2-deoxyglucose positron emission tomography-computed tomography scans. Asian Pac J Cancer Prev. 2014;15(20):8699–703.

50. Kwon T, Jeong IG, You D, Hong JH, Ahn H, Kim CS. Prevalence and clinical significance of incidental (18)F-fluoro-2-deoxyglucose uptake in prostate. Korean J Urol. 2015;56(4):288–94.

51. Hillner BE, Siegel BA, Shields AF, et al. Relationship between cancer type and impact of PET and PET/CT on intended management: findings of the national oncologic PET registry. J Nucl Med. 2008;49(12):1928–35.

52. Jadvar H, Desai B, Ji L, et al. Prospective evaluation of 18F-NaF and 18F-FDG PET/CT in detection of occult metastatic disease in biochemical recurrence of prostate cancer. Clin Nucl Med. 2012;37(7):637–43.

53. Ozturk H, Karapolat I. 18F-fluorodeoxyglucose PET/CT for detection of disease in patients with prostate-specific antigen relapse following radical treatment of a local-stage prostate cancer. Oncol Lett. 2016;11(1):316–22.

54. Richter JA, Rodriguez M, Rioja J, et al. Dual tracer 11C-choline and FDG-PET in the diagnosis of biochemical prostate cancer relapse after radical treatment. Mol Imaging Biol. 2010;12(2):210–7.

55. Jadvar H, Desai B, Ji L, et al. Baseline 18F-FDG PET/CT parameters as imaging biomarkers of overall survival in castrate-resistant metastatic prostate cancer. J Nucl Med. 2013;54(8):1195–201.

56. Oyama N, Akino H, Suzuki Y, et al. FDG PET for evaluating the change of glucose metabolism in prostate cancer after androgen ablation. Nucl Med Commun. 2001;22(9):963–9.

57. Jadvar H. Prostate cancer: PET with 18F-FDG, 18F- or 11C-acetate, and 18F- or 11C-choline. J Nucl Med. 2011;52(1):81–9.

58. Schuster DM, Nanni C, Fanti S. PET tracers beyond FDG in prostate cancer. Semin Nucl Med. 2016;46(6):507–21.

59. Eschmann SM, Pfannenberg AC, Rieger A, et al. Comparison of 11C-choline-PET/CT and whole body-MRI for staging of prostate cancer. Nuklearmedizin Nucl Med. 2007;46(5):161–8. quiz N47-8

60. Rinnab L, Blumstein NM, Mottaghy FM, et al. 11C-choline positron-emission tomography/computed tomography and transrectal ultrasonography for staging localized prostate cancer. BJU Int. 2007;99(6):1421–6.

61. Scher B, Seitz M, Albinger W, et al. Value of 11C-choline PET and PET/CT in patients with suspected prostate cancer. Eur J Nucl Med Mol Imaging. 2007;34(1):45–53.

62. Kotzerke J, Prang J, Neumaier B, et al. Experience with carbon-11 choline positron emission tomography in prostate carcinoma. Eur J Nucl Med. 2000;27(9):1415–9.

63. Watanabe H, Kanematsu M, Kondo H, et al. Preoperative detection of prostate cancer: a comparison with 11C-choline PET, 18F-fluorodeoxyglucose PET and MR imaging. J Magn Reson Imaging. 2010;31(5):1151–6.

64. Kwee SA, Coel MN, Lim J, Ko JP. Prostate cancer localization with 18fluorine fluorocholine positron emission tomography. J Urol. 2005;173(1):252–5.

65. Beheshti M, Imamovic L, Broinger G, et al. 18F choline PET/CT in the preoperative staging of prostate cancer in patients with intermediate or high risk of extracapsular disease: a prospective study of 130 patients. Radiology. 2010;254(3):925–33.

66. Yoshida S, Nakagomi K, Goto S, Futatsubashi M, Torizuka T. 11C-choline positron emission tomography in prostate cancer: primary staging and recurrent site staging. Urol Int. 2005;74(3):214–20.

67. Krause BJ, Souvatzoglou M, Tuncel M, et al. The detection rate of [11C]choline-PET/CT depends on the serum PSA-value in patients with biochemical recurrence of prostate cancer. Eur J Nucl Med Mol Imaging. 2008;35(1):18–23.

68. Reske SN, Blumstein NM, Glatting G. [11C]choline PET/CT imaging in occult local relapse of prostate cancer after radical prostatectomy. Eur J Nucl Med Mol Imaging. 2008;35(1):9–17.

69. Scattoni V, Picchio M, Suardi N, et al. Detection of lymph-node metastases with integrated [11C]choline PET/CT in patients with PSA failure after radical retropubic prostatectomy: results confirmed by open pelvic-retroperitoneal lymphadenectomy. Eur Urol. 2007;52(2):423–9.

70. Castellucci P, Fuccio C, Nanni C, et al. Influence of trigger PSA and PSA kinetics on 11C-choline PET/CT detection rate in patients with biochemical relapse after radical prostatectomy. J Nucl Med. 2009;50(9):1394–400.

71. Fuccio C, Castellucci P, Schiavina R, et al. Role of 11C-choline PET/CT in the restaging of prostate cancer patients showing a single lesion on bone scintigraphy. Ann Nucl Med. 2010;24(6):485–92.

72. Picchio M, Spinapolice EG, Fallanca F, et al. [11C]choline PET/CT detection of bone metastases in patients with PSA progression after primary treatment for prostate cancer: comparison with bone scintigraphy. Eur J Nucl Med Mol Imaging. 2012;39(1):13–26.

73. Ceci F, Castellucci P, Graziani T, et al. 11C-choline PET/CT identifies osteoblastic and osteolytic lesions in patients with metastatic prostate cancer. Clin Nucl Med. 2015;40(5):e265–70.

74. Ceci F, Castellucci P, Mapelli P, Incerti E, Picchio M, Fanti S. Evaluation of prostate cancer with 11C-choline PET/CT for treatment planning, response assessment, and prognosis. J Nucl Med. 2016;57(Suppl 3):49s–54s.

75. Pelosi E, Arena V, Skanjeti A, et al. Role of whole-body 18F-choline PET/CT in disease detection in patients with biochemical relapse after radical treatment for prostate cancer. Radiol Med. 2008;113(6):895–904.

76. Heinisch M, Dirisamer A, Loidl W, et al. Positron emission tomography/computed tomography with F-18-fluorocholine for restaging of prostate cancer patients: meaningful at PSA < 5 ng/ml? Mol Imaging Biol. 2006;8(1):43–8.

77. Foss CA, Mease RC, Fan H, et al. Radiolabeled small-molecule ligands for prostate-specific membrane antigen: in vivo imaging in experimental models of prostate cancer. Clin Cancer Res. 2005;11(11):4022–8.

78. Mease RC, Dusich CL, Foss CA, et al. N-[N-[(S)-1,3-Dicarboxypropyl]carbamoyl]-4-[18F] fluorobenzyl-L-cysteine, [18F]DCFBC: a new imaging probe for prostate cancer. Clin Cancer Res. 2008;14(10):3036–43.

79. Banerjee SR, Pullambhatla M, Byun Y, et al. 68Ga-labeled inhibitors of prostate-specific membrane antigen (PSMA) for imaging prostate cancer. J Med Chem. 2010;53(14):5333–41.

80. Afshar-Oromieh A, Haberkorn U, Eder M, Eisenhut M, Zechmann CM. [68Ga]gallium-labelled PSMA ligand as superior PET tracer for the diagnosis of prostate cancer: comparison with 18F-FECH. Eur J Nucl Med Mol Imaging. 2012;39(6):1085–6.

81. Afshar-Oromieh A, Malcher A, Eder M, et al. PET imaging with a [68Ga]gallium-labelled PSMA ligand for the diagnosis of prostate cancer: biodistribution in humans and first evaluation of tumour lesions. Eur J Nucl Med Mol Imaging. 2013;40(4):486–95.

82. Eder M, Schafer M, Bauder-Wust U, et al. 68Ga-complex lipophilicity and the targeting property of a urea-based PSMA inhibitor for PET imaging. Bioconjug Chem. 2012;23(4):688–97.

83. Szabo Z, Mena E, Rowe SP, et al. Initial evaluation of [(18)F]DCFPyL for prostate-specific membrane antigen (PSMA)-targeted PET imaging of prostate cancer. Mol Imaging Biol. 2015;17(4):565–74.

84. Dietlein M, Kobe C, Kuhnert G, et al. Comparison of [(18)F]DCFPyL and [(68)Ga]Ga-PSMA-HBED-CC for PSMA-PET imaging in patients with relapsed prostate cancer. Mol Imaging Biol. 2015;17(4):575–84.

85. Cardinale J, Schafer M, Benesova M, et al. Preclinical evaluation of [18F]PSMA-1007: a new PSMA-ligand for prostate cancer imaging. J Nucl Med. 2016;58(3):425–31.

86. Giesel FL, Cardinale J, Schafer M, et al. (18)F-labelled PSMA-1007 shows similarity in structure, biodistribution and tumour uptake to the theragnostic compound PSMA-617. Eur J Nucl Med Mol Imaging. 2016;43(10):1929–30.

87. Giesel FL, Hadaschik B, Cardinale J, et al. F-18 labelled PSMA-1007: biodistribution, radiation dosimetry and histopathological validation of tumor lesions in prostate cancer patients. Eur J Nucl Med Mol Imaging. 2016;44(4):678–88.

88. Perera M, Papa N, Christidis D, et al. Sensitivity, specificity, and predictors of positive 68Ga-prostate-specific membrane antigen positron emission tomography in advanced prostate cancer: a systematic review and meta-analysis. Eur Urol. 2016;70(6):926–37.

89. Afshar-Oromieh A, Hetzheim H, Kratochwil C, et al. The theranostic PSMA ligand PSMA-617 in the diagnosis of prostate cancer by PET/CT: biodistribution in humans, radiation dosimetry, and first evaluation of tumor lesions. J Nucl Med. 2015;56(11):1697–705.

90. Benesova M, Schafer M, Bauder-Wust U, et al. Preclinical evaluation of a tailor-made DOTA-conjugated PSMA inhibitor with optimized linker moiety for imaging and endoradiotherapy of prostate cancer. J Nucl Med. 2015;56(6):914–20.

91. Kratochwil C, Giesel FL, Stefanova M, et al. PSMA-targeted radionuclide therapy of metastatic castration-resistant prostate cancer with 177Lu-Labeled PSMA-617. J Nucl Med. 2016;57(8):1170–6.

92. Kratochwil C, Bruchertseifer F, Giesel FL, et al. 225Ac-PSMA-617 for PSMA targeting alpha-radiation therapy of patients with metastatic castration-resistant prostate cancer. J Nucl Med. 2016;57(12):1941–4.

93. Fuchs BC, Bode BP. Amino acid transporters ASCT2 and LAT1 in cancer: partners in crime? Semin Cancer Biol. 2005;15(4):254–66.

94. Jager PL, Vaalburg W, Pruim J, de Vries EG, Langen KJ, Piers DA. Radiolabeled amino acids: basic aspects and clinical applications in oncology. J Nucl Med. 2001;42(3):432–45.

95. Okudaira H, Shikano N, Nishii R, et al. Putative transport mechanism and intracellular fate of trans-1-amino-3-18F-fluorocyclobutanecarboxylic acid in human prostate cancer. J Nucl Med. 2011;52(5):822–9.

96. Schuster DM, Nanni C, Fanti S, et al. Anti-1-amino-3-18F-fluorocyclobutane-1-carboxylic acid: physiologic uptake patterns, incidental findings, and variants that may simulate disease. J Nucl Med. 2014;55(12):1986–92.

97. Schuster DM, Nanni C, Fanti S. Evaluation of prostate cancer with radiolabeled amino acid Analogs. J Nucl Med. 2016;57(Suppl 3):61s–6s.

98. Turkbey B, Mena E, Shih J, et al. Localized prostate cancer detection with 18F FACBC PET/CT: comparison with MR imaging and histopathologic analysis. Radiology. 2014;270(3):849–56.

99. Schuster DM, Taleghani PA, Nieh PT, et al. Characterization of primary prostate carcinoma by anti-1-amino-2-[(18)F] -fluorocyclobutane-1-carboxylic acid (anti-3-[(18)F] FACBC) uptake. Am J Nucl Med Mol Imaging. 2013;3(1):85–96.

100. Suzuki H, Inoue Y, Fujimoto H, et al. Diagnostic performance and safety of NMK36 (trans-1-amino-3-[18F]fluorocyclobutanecarboxylic acid)-PET/CT in primary prostate cancer: multicenter phase IIb clinical trial. Jpn J Clin Oncol. 2016;46(2):152–62.

101. Odewole OA, Tade FI, Nieh PT, et al. Recurrent prostate cancer detection with anti-3-[(18)F] FACBC PET/CT: comparison with CT. Eur J Nucl Med Mol Imaging. 2016;43(10):1773–83.

102. Schuster DM, Nieh PT, Jani AB, et al. Anti-3-[(18)F]FACBC positron emission tomography-computerized tomography and (111)in-capromab pendetide single photon emission computerized tomography-computerized tomography for recurrent prostate carcinoma: results of a prospective clinical trial. J Urol. 2014;191(5):1446–53.

103. Nanni C, Zanoni L, Pultrone C, et al. (18)F-FACBC (anti1-amino-3-(18)F-fluorocyclobutane-1-carboxylic acid) versus (11)C-choline PET/CT in prostate cancer relapse: results of a prospective trial. Eur J Nucl Med Mol Imaging. 2016;43(9):1601–10.

104. Erspamer V. Discovery, isolation, and characterization of bombesin-like peptides. Ann N Y Acad Sci. 1988;547:3–9.
105. Brown M, Marki W, Rivier J. Is gastrin releasing peptide mammalian bombesin? Life Sci. 1980;27(2):125–8.
106. McDonald TJ, Jornvall H, Nilsson G, et al. Characterization of a gastrin releasing peptide from porcine non-antral gastric tissue. Biochem Biophys Res Commun. 1979;90(1):227–33.
107. McDonald TJ, Nilsson G, Vagne M, Ghatei M, Bloom SR, Mutt V. A gastrin releasing peptide from the porcine nonantral gastric tissue. Gut. 1978;19(9):767–74.
108. Levine L, Lucci JA 3rd, Pazdrak B, et al. Bombesin stimulates nuclear factor kappa B activation and expression of proangiogenic factors in prostate cancer cells. Cancer Res. 2003;63(13):3495–502.
109. Sun B, Halmos G, Schally AV, Wang X, Martinez M. Presence of receptors for bombesin/gastrin-releasing peptide and mRNA for three receptor subtypes in human prostate cancers. Prostate. 2000;42(4):295–303.
110. Bologna M, Festuccia C, Muzi P, Biordi L, Ciomei M. Bombesin stimulates growth of human prostatic cancer cells in vitro. Cancer. 1989;63(9):1714–20.
111. Markwalder R, Reubi JC. Gastrin-releasing peptide receptors in the human prostate: relation to neoplastic transformation. Cancer Res. 1999;59(5):1152–9.
112. Mansi R, Minamimoto R, Macke H, Iagaru AH. Bombesin-targeted PET of prostate cancer. J Nucl Med. 2016;57(Suppl 3):67s–72s.
113. Kahkonen E, Jambor I, Kemppainen J, et al. In vivo imaging of prostate cancer using [68Ga]-labeled bombesin analog BAY86-7548. Clin Cancer Res. 2013;19(19):5434–43.
114. Minamimoto R, Hancock S, Schneider B, et al. Pilot comparison of (6)(8)Ga-RM2 PET and (6)(8)Ga-PSMA-11 PET in patients with biochemically recurrent prostate cancer. J Nucl Med. 2016;57(4):557–62.
115. Sah BR, Burger IA, Schibli R, et al. Dosimetry and first clinical evaluation of the new 18F-radiolabeled bombesin analogue BAY 864367 in patients with prostate cancer. J Nucl Med. 2015;56(3):372–8.
116. Wieser G, Mansi R, Grosu AL, et al. Positron emission tomography (PET) imaging of prostate cancer with a gastrin releasing peptide receptor antagonist--from mice to men. Theranostics. 2014;4(4):412–9.
117. Maina T, Bergsma H, Kulkarni HR, et al. Preclinical and first clinical experience with the gastrin-releasing peptide receptor-antagonist [68Ga]SB3 and PET/CT. Eur J Nucl Med Mol Imaging. 2015;43(5):1–10.
118. Dalm SU, Bakker IL, de Blois E, et al. 68Ga/177Lu-NeoBOMB1, a novel radiolabeled GRPR antagonist for theranostic use in oncology. J Nucl Med. 2016;58(2):293–9.
119. Nock BA, Kaloudi A, Lymperis E, et al. Theranostic perspectives in prostate cancer with the GRPR-antagonist NeoBOMB1- preclinical and first clinical results. J Nucl Med. 2016;58(1):75–80.
120. Leung K. [11C]acetate. Molecular imaging and contrast agent database (MICAD). Bethesda: National Center for Biotechnology Information (US); 2004.
121. Swinnen JV, Heemers H, Deboel L, Foufelle F, Heyns W, Verhoeven G. Stimulation of tumor-associated fatty acid synthase expression by growth factor activation of the sterol regulatory element-binding protein pathway. Oncogene. 2000;19(45):5173–81.
122. Epstein JI, Carmichael M, Partin AW. OA-519 (fatty acid synthase) as an independent predictor of pathologic state in adenocarcinoma of the prostate. Urology. 1995;45(1):81–6.
123. Prowatke I, Devens F, Benner A, et al. Expression analysis of imbalanced genes in prostate carcinoma using tissue microarrays. Br J Cancer. 2007;96(1):82–8.
124. Pike VW, Eakins MN, Allan RM, Selwyn AP. Preparation of [1-11C]acetate--an agent for the study of myocardial metabolism by positron emission tomography. Int J Appl Radiat Isot. 1982;33(7):505–12.
125. Ponde DE, Dence CS, Oyama N, et al. 18F-fluoroacetate: a potential acetate analog for prostate tumor imaging--in vivo evaluation of 18F-fluoroacetate versus 11C-acetate. J Nucl Med. 2007;48(3):420–8.

126. Seltzer MA, Jahan SA, Sparks R, et al. Radiation dose estimates in humans for (11)C-acetate whole-body PET. J Nucl Med. 2004;45(7):1233–6.
127. Jambor I, Borra R, Kemppainen J, et al. Functional imaging of localized prostate cancer aggressiveness using 11C-acetate PET/CT and 1H-MR spectroscopy. J Nucl Med. 2010;51(11):1676–83.
128. Jambor I, Borra R, Kemppainen J, et al. Improved detection of localized prostate cancer using co-registered MRI and 11C-acetate PET/CT. Eur J Radiol. 2012;81(11):2966–72.
129. Kato T, Tsukamoto E, Kuge Y, et al. Accumulation of [11C]acetate in normal prostate and benign prostatic hyperplasia: comparison with prostate cancer. Eur J Nucl Med Mol Imaging. 2002;29(11):1492–5.
130. Mena E, Turkbey B, Mani H, et al. 11C-acetate PET/CT in localized prostate cancer: a study with MRI and histopathologic correlation. J Nucl Med. 2012;53(4):538–45.
131. Oyama N, Akino H, Kanamaru H, et al. 11C-acetate PET imaging of prostate cancer. J Nucl Med. 2002;43(2):181–6.
132. Haseebuddin M, Dehdashti F, Siegel BA, et al. 11C-acetate PET/CT before radical prostatectomy: nodal staging and treatment failure prediction. J Nucl Med. 2013;54(5):699–706.
133. Dusing RW, Peng W, Lai SM, et al. Prostate-specific antigen and prostate-specific antigen velocity as threshold indicators in 11C-acetate PET/CTAC scanning for prostate cancer recurrence. Clin Nucl Med. 2014;39(9):777–83.
134. Albrecht S, Buchegger F, Soloviev D, et al. (11)C-acetate PET in the early evaluation of prostate cancer recurrence. Eur J Nucl Med Mol Imaging. 2007;34(2):185–96.
135. Kotzerke J, Volkmer BG, Neumaier B, Gschwend JE, Hautmann RE, Reske SN. Carbon-11 acetate positron emission tomography can detect local recurrence of prostate cancer. Eur J Nucl Med Mol Imaging. 2002;29(10):1380–4.
136. Sandblom G, Sorensen J, Lundin N, Haggman M, Malmstrom PU. Positron emission tomography with C11-acetate for tumor detection and localization in patients with prostate-specific antigen relapse after radical prostatectomy. Urology. 2006;67(5):996–1000.
137. Spick C, Polanec SH, Mitterhauser M, et al. Detection of bone metastases using 11C-acetate PET in patients with prostate cancer with biochemical recurrence. Anticancer Res. 2015;35(12):6787–91.
138. Kotzerke J, Volkmer BG, Glatting G, et al. Intraindividual comparison of [11C]acetate and [11C]choline PET for detection of metastases of prostate cancer. Nuklearmedizin Nucl Med. 2003;42(1):25–30.
139. Vees H, Buchegger F, Albrecht S, et al. 18F-choline and/or 11C-acetate positron emission tomography: detection of residual or progressive subclinical disease at very low prostate-specific antigen values (<1 ng/mL) after radical prostatectomy. BJU Int. 2007;99(6):1415–20.
140. Chen Y, Clegg NJ, Scher HI. Anti-androgens and androgen-depleting therapies in prostate cancer: new agents for an established target. Lancet Oncol. 2009;10(10):981–91.
141. Cookson MS, Roth BJ, Dahm P, et al. Castration-resistant prostate cancer: AUA Guideline. J Urol. 2013;190(2):429–38.
142. Montgomery RB, Mostaghel EA, Vessella R, et al. Maintenance of intratumoral androgens in metastatic prostate cancer: a mechanism for castration-resistant tumor growth. Cancer Res. 2008;68(11):4447–54.
143. Scher HI, Sawyers CL. Biology of progressive, castration-resistant prostate cancer: directed therapies targeting the androgen-receptor signaling axis. J Clin Oncol Off J Am Soc Clin Oncol. 2005;23(32):8253–61.
144. Yuan X, Balk SP. Mechanisms mediating androgen receptor reactivation after castration. Urol Oncol. 2009;27(1):36–41.
145. Larson SM, Morris M, Gunther I, et al. Tumor localization of 16beta-18F-fluoro-5alpha-dihydrotestosterone versus 18F-FDG in patients with progressive, metastatic prostate cancer. Journal of nuclear medicine: official publication. Soc Nucl Med. 2004;45(3):366–73.
146. Dehdashti F, Picus J, Michalski JM, et al. Positron tomographic assessment of androgen receptors in prostatic carcinoma. Eur J Nucl Med Mol Imaging. 2005;32(3):344–50.

147. Beattie BJ, Smith-Jones PM, Jhanwar YS, et al. Pharmacokinetic assessment of the uptake of 16beta-18F-fluoro-5alpha-dihydrotestosterone (FDHT) in prostate tumors as measured by PET. J Nucl Med. 2010;51(2):183–92.
148. Vargas HA, Wassberg C, Fox JJ, et al. Bone metastases in castration-resistant prostate cancer: associations between morphologic CT patterns, glycolytic activity, and androgen receptor expression on PET and overall survival. Radiology. 2014;271(1):220–9.
149. Lazari M, Lyashchenko SK, Burnazi EM, Lewis JS, van Dam RM, Murphy JM. Fully-automated synthesis of 16beta-(18)F-fluoro-5alpha-dihydrotestosterone (FDHT) on the ELIXYS radiosynthesizer. Appl Radiat Isot. 2015;103:9–14.
150. Hartenbach M, Hartenbach S, Bechtloff W, et al. Combined PET/MRI improves diagnostic accuracy in patients with prostate cancer: a prospective diagnostic trial. Clin Cancer Res. 2014;20(12):3244–53.
151. Kitajima K, Murphy RC, Nathan MA, et al. Detection of recurrent prostate cancer after radical prostatectomy: comparison of 11C-choline PET/CT with pelvic multiparametric MR imaging with endorectal coil. J Nucl Med. 2014;55(2):223–32.
152. Piccardo A, Paparo F, Piccazzo R, et al. Value of fused 18F-choline-PET/MRI to evaluate prostate cancer relapse in patients showing biochemical recurrence after EBRT: preliminary results. Biomed Res Int. 2014;2014:103718.
153. Wetter A, Lipponer C, Nensa F, et al. Simultaneous 18F choline positron emission tomography/magnetic resonance imaging of the prostate: initial results. Invest Radiol. 2013;48(5):256–62.
154. Kim YI, Cheon GJ, Paeng JC, et al. Usefulness of MRI-assisted metabolic volumetric parameters provided by simultaneous (18)F-fluorocholine PET/MRI for primary prostate cancer characterization. Eur J Nucl Med Mol Imaging. 2015;42(8):1247–56.
155. Eiber M, Weirich G, Holzapfel K, et al. Simultaneous 68Ga-PSMA HBED-CC PET/MRI improves the localization of primary prostate cancer. Eur Urol. 2016;70(5):829–36.
156. Elschot M, Selnaes KM, Sandsmark E, et al. A PET/MRI study towards finding the optimal [18F]Fluciclovine PET protocol for detection and characterisation of primary prostate cancer. Eur J Nucl Med Mol Imaging. 2016;44(4):695–703.
157. Wetter A, Nensa F, Schenck M, et al. Combined PET imaging and diffusion-weighted imaging of intermediate and high-risk primary prostate carcinomas with simultaneous [18F] choline PET/MRI. PLoS One. 2014;9(7):e101571.
158. Souvatzoglou M, Eiber M, Takei T, et al. Comparison of integrated whole-body [11C]choline PET/MR with PET/CT in patients with prostate cancer. Eur J Nucl Med Mol Imaging. 2013;40(10):1486–99.
159. Afshar-Oromieh A, Haberkorn U, Schlemmer HP, et al. Comparison of PET/CT and PET/MRI hybrid systems using a 68Ga-labelled PSMA ligand for the diagnosis of recurrent prostate cancer: initial experience. Eur J Nucl Med Mol Imaging. 2014;41(5):887–97.
160. Freitag MT, Radtke JP, Hadaschik BA, et al. Comparison of hybrid (68)Ga-PSMA PET/MRI and (68)Ga-PSMA PET/CT in the evaluation of lymph node and bone metastases of prostate cancer. Eur J Nucl Med Mol Imaging. 2016;43(1):70–83.
161. Freitag MRJ, Afshar-Oromieh A, Roethke MC, Hadaschik BA, Gleave M, Bonekamp D, Kopka K, Eder M, Heusser T, Kechelriess M, Wieczorek K, Sachpekidis C, Flechsig P, Giesel F, Hohenfellner M, Haberkorn U, Schlemmer HP, Dimitrakopoulou-Strauss A. Local recurrence of prostate cancer after radical prostatectomy is at risk to be missed in 68Ga-PSMA-11-PET of PET/CT and PET/MRI: comparison with mpMRI integrated in simultaneous PET/MRI. J Nucl Med. 2017;44(5):776–87.
162. Wetter A, Lipponer C, Nensa F, et al. Quantitative evaluation of bone metastases from prostate cancer with simultaneous [18F] choline PET/MRI: combined SUV and ADC analysis. Ann Nucl Med. 2014;28(5):405–10.
163. Rosenkrantz AB, Koesters T, Vahle AK, et al. Quantitative graphical analysis of simultaneous dynamic PET/MRI for assessment of prostate cancer. Clin Nucl Med. 2015;40(4):e236–40.

PET/MRI in Lymphoma

20

Sally F. Barrington and Kent Friedman

Contents

S.F. Barrington (✉)
School of Biomedical Engineering and Imaging Sciences, King's College London and Guy's & St Thomas' PET Centre, King's College London, King's Health Partners, St. Thomas' Hospital, London, UK
e-mail: sally.barrington@kcl.ac.uk

K. Friedman
Division of Nuclear Medicine, Department of Radiology, NYU Langone Medical Center, New York, NY, USA
e-mail: Kent.Friedman@nyumc.org

20.1 Introduction

Imaging has played a critical role in the management of patients with lymphoma for decades. Although not used to screen asymptomatic individuals, imaging has proven useful at virtually all other stages of the disease including for diagnosis in suspected cases, initial staging, treatment response assessment and recurrence detection and surveillance in high-risk individuals [1]. Imaging provides guidance for biopsies [2] and is used to determine the extent of disease based on identification of lymph node enlargement and extranodal disease [3].

PET/CT imaging with 18F-fluorodeoxyglucose (FDG) offered a significant advancement in the ways in which imaging could be used to manage patients with lymphoma. The metabolic signature generated by FDG not only increases sensitivity for lesion detection compared to CT [4] but carries significant prognostic value and has been proven to monitor treatment response and detect recurrent disease with higher performance compared to conventional imaging [1]. For these reasons, FDG PET/CT is a clinical standard for evaluation of patients with most types of lymphoma.

PET/MRI is an exciting new technology that has the potential to improve the value of imaging in patients with lymphoma even more. Advantages include lower radiation exposure (particularly beneficial for children and young adults) and potentially improved image quality with the use of MR-based motion correction [5]. Simultaneous scanners offer improved registration of PET data and anatomical datasets [6], thus facilitating lesion characterisation and potentially helping direct tissue biopsies. Finally, the biological information derived from advanced MR techniques including dynamic contrast-enhanced MRI (DCE-MRI), diffusion-weighted imaging (DWI) [7] and MR spectroscopy (MRS) [8] is an active area of study that holds promise to potentially improve the ability of imaging to detect viable tumour, better assess treatment response and perhaps one day guide selection of specific treatment regimens. PET/MRI scanners offer the two most advanced imaging technologies combined in one scanner which makes it an excellent research tool.

This chapter will provide the reader with an overview of lymphoma biology, management and treatment, review conventional imaging and then provide a detailed discussion of how PET, PET/CT and MR alone have been used in the management of patients with lymphoma. Following this background, the existing literature studying the use of combined PET and MR data (typically acquired on PET/MRI scanners although studies combining separately acquired PET and MR datasets ('PET + MR') will be covered as well) will be comprehensively reviewed. Case examples highlighting the concepts discussed in the emerging PET/MRI literature will be presented. The reader will learn about new PET radiopharmaceuticals that may be relevant to future PET/MRI research, and pitfalls in the PET/MR imaging of patients with lymphoma will be discussed.

20.2   Overview of Lymphoma Biology, Staging and Existing and Emerging Treatments

Lymphomas are the commonest lymphoproliferative disorder worldwide. They are divided into Hodgkin and non-Hodgkin lymphomas.

20.3   Biology

Hodgkin lymphoma (HL) has an annual incidence of 8500 cases in the USA (https://seer.cancer.gov/statfacts/html/hodg.html) and 2100 cases in the UK (http://www.cancerresearchuk.org/health-professional/cancer-statistics/statistics-by-cancer-type/hodgkin-lymphoma). HL is the commonest cancer in the adolescent age group, with a further peak in people aged over 45. It originates from mature B cells with the hallmark of classical HL being the Reed-Sternberg cell, which expresses CD30, but which accounts for less than 1% of nodal masses [9]. Tumour cells are surrounded by many benign inflammatory cells including T cells, macrophages, B cells and eosinophils that produce cytokines which promote tumour growth and help the lymphoma to avoid host mechanisms. The abundance of inflammatory cells has been suggested as a reason why HL is so well imaged with FDG and why FDG changes rapidly in response to treatment [10].

Classical HL (cHL) is divided into nodular sclerosing (around 80% of cHL), mixed cellularity, lymphocyte depleted and lymphocyte rich. Nodular lymphocyte predominant HL (NLPHL) is rare, usually negative for CD30 with lymphocyte predominant cells that are similar to germinal centre B cells [9].

The non-Hodgkin lymphomas have an annual incidence of 72,600 cases in the USA (https://seer.cancer.gov/statfacts/html/nhl.html) and 13,600 cases in the UK. Half of the patients are over 70 years (http://www.cancerresearchuk.org/health-professional/cancer-statistics/statistics-by-cancer-type/non-hodgkin-lymphoma). NHLs can be divided into B- and T-cell malignancies.

The aggressive B-cell NHLs are a heterogeneous group that arise at different stages of B-cell differentiation. They more often involve extranodal sites than HL. The commonest subtype is diffuse large B-cell lymphoma (DLBCL) which nowadays accounts for nearly 50% of NHL in western countries (http://www.cancerresearchuk.org/health-professional/cancer-statistics). The International Prognostic Index (IPI) is used to predict pretreatment prognosis, and more recently the National Comprehensive Cancer Network-IPI has been shown to have better prognostic value [11]. Gene expression profiling has identified genetic alterations which mean DLBCL can be separated by cell of origin into the germinal centre B-cell (GCB) subtype and non-GCB, usually activated B-cell (ABC) subtype, with worse prognosis for the ABC subtype [12]. Subtypes that include translocation of the MYC gene (MYC+) and/or the BCL2 or BCL6 are especially resistant to treatment. Where both MYC and BCL translocations occur, this is referred to as 'double-hit' lymphoma.

The most common type of indolent NHL is follicular lymphoma which accounts for about 20% of NHL (http://www.cancerresearchuk.org/health-professional/cancer-statistics) and is derived from germinal B cells [13]. Taken together HL, DLBCL and FL account for 70% of cases of lymphoma, and most data about PET imaging relates to these subtypes [14].

20.4 Staging

The same staging applies to HL and NHL with a recent modification of the Ann Arbor staging suggested in the Lugano classification (Cheson 2014) as follows:

Stage I—a single lymph node region (I) or a single extralymphatic site (IE)

Stage II—two or more lymph node regions on the same side of diaphragm (II) or stage I or II with contiguous involvement of an extralymphatic site (IIE)

Stage III—nodes on both sides of diaphragm (III) which may include the spleen (sometimes referred to as IIIS)

Stage IV—disseminated extranodal involvement

In Hodgkin lymphoma, the suffix 'A' or 'B' refers to the absence or presence of systemic symptoms, respectively. Where bulky disease is present, the Lugano classification suggests to record the largest tumour diameter.

20.5 Treatment

Early stage good-risk HL is treated with two to four cycles of adriamycin, bleomycin, vinblastine and dacarbazine (ABVD) chemotherapy and radiotherapy, the length of which is determined by clinical factors and prognostic scores such as the German Hodgkin Study Group and European Organisation for Research and Treatment of Cancer criteria (Europe) and the Eastern Cooperative Oncology Group (USA) [15].

Advanced-stage disease or early stage with poor risk is treated with longer courses of ABVD or bleomycin, etoposide, adriamycin, cyclophosphamide, vincristine, procarbazine and prednisolone (BEACOPP) chemotherapy. Radiotherapy is sometimes used to treat patients with initial bulky or residual disease. Progression-free survival (PFS) with ABVD is around 65–75% [16]. PFS with BEACOPP (bleomycin, etoposide, adriamycin, cyclophosphamide, vincristine, procarbazine, prednisolone) is around 85–90% [17] but is associated with more treatment-related side-effects including haematological toxicity, increased risk of infertility and second malignancies. Which chemotherapy to use in advanced-stage disease is debated. Some argue the more effective BEACOPP chemotherapy regimens should be used, whilst others argue that many patients are cured with ABVD which is less toxic than BEACOPP, which should be reserved for a subset of patients [16, 18]. Recent clinical trials have focused on how to assess which patients would benefit most from ABVD and/or BEACOPP, some of which include a PET response-adapted design.

Patients with refractory or relapsed disease are treated with salvage chemotherapy followed by high-dose chemotherapy and autologous stem cell transplant (ASCT), if fit, and this approach cures approximately 50% of patients [19]. Patients unable to have ASCT may be offered consolidation with radiotherapy and/or palliative chemotherapy.

Recently new agents have been developed with good responses in relapsed and refractory HL. Brentuximab vedotin (BV) is an antibody-drug conjugate targeted against CD30 which was reported to have an overall response rate of 75% and a complete response rate of 34% in patients who progressed after ASCT [20]. Overall PFS was short, but 16/34 patients with complete response remained in remission at a median follow-up of 53 months. BV with AVD has recently been evaluated in a clinical trial 'ECHELON' in first-line treatment (https://clinicaltrials.gov/ct2/show/NCT01712490), and results are awaited.

Another promising development in treatment is the immune checkpoint inhibitors. The programmed cell death 1 (PD1) receptor protein and its ligands (PDL1 and PDL2) interfere with T-cell function and enable tumours to evade T-cell attack. Checkpoint inhibitors such as nivolumab and pembrolizumab have demonstrated good responses in patients with Hodgkin lymphoma, most of whom had relapsed after ASCT [21, 22]. Other targeted agents including histone deacetylase (HDAC) inhibitors, e.g. panobinostat; mTOR inhibitors, e.g. everolimus; and phosphatidyl-3-kinase inhibitors, e.g. idelalisib; have shown promising results [23].

DLBCL is most commonly treated with 6–8 cycles of rituximab and cyclophosphamide, doxorubicin, vincristine and prednisone (R-CHOP) with or without consolidation RT which cures about 60–70% of patients [12]. Early stage non-bulky disease may be treated with 3–4 cycles of R-CHOP and involved field radiotherapy (IFRT). The use of rituximab has been associated with significant improvements in outcome for first-line treatment, but patients treated with R-CHOP chemotherapy who relapse have very poor outcomes. The hope is that newer targeted agents will enable therapy aimed at specific molecular subtypes with better patient outcomes.

Recent studies adding the proteasome inhibitor bortezomib in the treatment of non-ABC subtypes to R-CHOP have so far not been shown to improve PFS [24]. Other trials investigating combinations of R-CHOP with the immunomodulatory agents lenalidomide and idelalisib are underway [12].

Second-line treatment options in DLBCL are salvage chemotherapy followed by high-dose chemotherapy and ASCT, but response rates are low. For patients who are not suitable for ASCT, various palliative treatments are available, some of which induce durable remissions [12].

Follicular lymphoma is not curable unless localised and usually follows a relapsing and remitting course over several years. The disease may transform into an aggressive lymphoma. Treatment is aimed at prolonging and maximising the quality of life. Treatment consists of radiotherapy if localised, immunochemotherapy or observation in selected cases until treatment is required. Maintenance treatment is often given for 2 years after immunochemotherapy with the monoclonal antibody, rituximab, which improves disease-free survival but not overall survival [25].

20.6   Overview of Conventional Imaging in Lymphoma

Prior to the advent of FDG PET, PET/CT and advanced MR techniques, x-ray computed tomography (CT) was the standard imaging test for evaluation of patients with lymphoma. To this day, anatomical assessment of disease burden within the lymph nodes, spleen and visceral organs remains critically important and is a key indicator of disease stage and marker of treatment response [26]. Definition of the extent of disease anatomically remains important, given that not all lymphomas are highly FDG-avid, and thus PET imaging with FDG is predominantly used in classical Hodgkin lymphoma and diffuse large B-cell lymphomas. Other histological subtypes including marginal zone lymphoma, small lymphocytic lymphoma and primary cutaneous T-cell lymphomas are less FDG-avid and may be routinely staged by CT alone [14]. The most recent lymphoma staging criteria (Lugano classification) incorporate information from PET but still heavily rely on anatomical disease assessment by CT with short- and long-axis measurements being used to calculate a 'sum of the product diameters' as a means of treatment response, for less FDG-avid histologies [26].

Standard x-rays and ultrasound (US) play a much more limited role in the evaluation of patients with lymphoma. US-guided biopsy techniques may be useful for needle biopsies of enlarged lymph nodes or when lymphoma involvement of the liver is suspected. Typically, fine needle aspiration (FNA) can be used as a screening test, but surgical lymph node excision is required to obtain enough tissue to allow full histological, immunologic and molecular biological characterisations of lymphoma [27]. MR-guided or CT-guided biopsies may be reserved for lesions presenting in challenging anatomical locations [28]. Bone marrow staging is typically done by blind biopsy; however, focal lesions identified on CT can prompt more advanced biopsy techniques for characterisation of focal destructive lesions [29].

20.7   PET in Lymphoma

20.7.1   Adult

PET/CT has become the main imaging modality for assessment of aggressive lymphomas. PET/CT, using 18F-fluorodeoxyglucose (FDG), is recommended for staging and response assessment of FDG-avid lymphomas, replacing CT for these lymphoma subtypes in the most recent international guidelines [14, 26]. Most subtypes of lymphoma are FDG-avid, but exceptions that do not consistently take up FDG include marginal zone lymphomas, small lymphocytic lymphoma and some cutaneous lymphomas [30]. Most published data about PET, however, relate to the most common disease subtypes of Hodgkin lymphoma (HL), diffuse large B-cell lymphoma and follicular lymphoma.

Prognostic indices are used to risk stratify patients at diagnosis, but as most include stage, imaging stage is important. PET/CT using FDG is the most accurate staging technique in HL and non-Hodgkin lymphoma (NHL) with increased

sensitivity over CT alone, particularly for extranodal disease. A number of publications report changes in stage, using PET/CT with upstaging occurring more often than downstaging and management alterations in a proportion of patients [14]. Most often PET/CT is performed as a low-/intermediate-dose examination without contrast for the purposes of localisation and attenuation correction rather than as a full-dose contrast-enhanced scan. In many subtypes this suffices with evidence suggesting using low-dose PET/CT has little, if any, impact on management [31–35]. There are however situations where contrast-enhanced CT offers superior assessment of disease, such as the assessment of bowel involvement in mantle cell lymphomas [36]. Baseline PET/CT also improves the accuracy of subsequent response assessment [37, 38].

PET/CT is sensitive for bone marrow involvement in lymphomas that have predominantly focal involvement of the marrow, including Hodgkin lymphoma [35, 39] and DLBCL [40–42]. In these subtypes, PET/CT is more sensitive than bone marrow biopsy for detecting bone marrow disease. This means that the bone marrow biopsy is no longer considered to be a routine requirement for staging in HL [43]. In DLBCL, reports also suggest that routine bone marrow biopsy does not add value in the majority of patients [44]. PET may however miss small cells in the marrow [45, 46]. When patients have a mix of more indolent disease in the marrow and aggressive large cells in the lymph nodes, this is referred to as 'discordant disease'. For this reason, omitting biopsy in patients with DLBCL is more controversial [47] even though discordant disease does not confer a worse prognosis and there is no evidence that patients with discordant disease have better outcomes if treatment or follow-up is altered [44]. Similarly, PET may not be sufficiently sensitive to detect low-volume disease comprising 10–20% of the marrow, although again this does not affect prognosis [48]. PET/CT is less sensitive in subtypes with diffuse often low-volume marrow disease, and in follicular and other indolent lymphomas, PET is unable to reliably exclude bone marrow involvement [49].

FDG uptake is higher in aggressive than indolent lymphomas, and PET/CT may be used to target sites for biopsy where there is clinical concern regarding suspected transformation [36, 50, 51].

PET/CT is a reliable tool for assessing remission from disease in aggressive lymphomas [14]. Patients with lymphomas often have residual nodal masses at the end of treatment. A 'negative' PET/CT scan excludes the presence of viable tumour cells within masses with a high degree of certainty and has led to the abandonment of the previous response category of complete response unconfirmed which was used to refer to masses on CT thought likely to contain fibrous tissue [52]. The positive predictive value (PPV) is lower than the negative predictive value of course, because FDG is not specific for lymphoma and is taken up in processes with enhanced glycolysis such as infection and inflammation, often treatment related. The PPV is dependent on the subtype and disease prognosis [14]. Residual FDG uptake at the end of treatment may require biopsy in the case of poor prognosis disease when salvage therapy is being contemplated or at the least an interval scan in the case of good prognosis disease where time allows.

Scans performed during treatment are commonly referred to as 'interim' scans. In HL the ability of PET to discriminate chemosensitive from chemoresistant disease after 2–3 courses of ABVD treatment [53, 54] led to testing of response-adapted approaches in international trials. These trials are beginning to report results.

In early stage HL, two European studies examined whether radiotherapy could be omitted in patients with complete metabolic response (CMR) on interim PET [55, 56]. PFS was superior with combined modality treatment compared to ABVD alone by approximately 6% at 3 years; however, patients treated with chemotherapy, but without radiotherapy, still had good prognosis with 3y-PFS of around 90%. Longer follow-up will determine if omitting radiotherapy may improve overall survival for some patient subgroups despite inferior PFS, by ameliorating late effects, e.g. cardiopulmonary disease and second malignancies. Omission of radiotherapy is now considered to be an option for some patients with early stage disease treated with ABVD and CMR on interim PET [57].

In advanced HL, an international study reported that bleomycin could be safely omitted from further treatment in cycles 3–6 after an interim scan showing CMR with ABVD treatment with fewer side-effects [58]. 3y-PFS rates were however 85% even in PET-negative patients, which is lower than reported for BEACOPP chemotherapy [17]. Trials are also in progress investigating response-adapted approaches according to interim PET after BEACOPP chemotherapy for advanced-stage disease (https://clinicaltrials.gov/ct2/show/NCT00515554) and using BEACOPP and ABVD sequentially in intermediate-stage disease (https://clinicaltrials.gov/ct2/show/NCT01356680).

For patients who do not achieve CMR or PET 'negative' status on interim scans, escalation from ABVD to BEACOPP in early and advanced-stage disease appears to be beneficial, improving PFS [58]. A recent Italian study also reported good outcomes for patients with advanced HL escalated to high-dose chemotherapy and transplant on the basis of a 'positive' interim PET scan [59].

At the end of treatment with 6–8 cycles of BEACOPP chemotherapy, a large German Hodgkin Study Group trial reported that consolidation radiotherapy was not required for patients with advanced disease achieving CMR at the end of chemotherapy [17].

In DLBCL, recent reports suggest that CMR on interim PET confers a very good prognosis [60–62]. Failure to achieve CMR at interim is associated with a worse prognosis, but even so most patients have PFS rates of around 50%, and unlike HL, in DLBCL treatment options are more limited. So far, most response-adapted treatments based on an interim PET scan showing inadequate response have failed to improve patient outcomes [63–65].

The place of interim PET scans in HL is generally accepted. In DLBCL the role of interim PET is more controversial [47], but if interim scanning is performed, then PET/CT is more reliable than CT [66].

In follicular lymphoma, PET/CT performed at the end of chemotherapy and rituximab treatment is predictive of relapse [67], but so far, response-adapted treatments have not been tested.

PET/CT is used in the pre-transplant setting to predict prognosis in both HL [68] and DLBCL [69]. Patients who achieve a complete metabolic response on PET have

longer disease-free survival than patients with persistent FDG uptake after high-dose chemotherapy. Patients with a PET-positive scan have been the focus of trials testing alternative regimens or consolidation [70].

The recommended method of assessing response in lymphoma is a five-point scale that compares uptake, if present, with sites of initial disease on a baseline scan using the normal mediastinum and liver as reference regions. The scale is commonly referred to as the 'Deauville criteria' after the place where the first international workshop on PET in lymphoma was held, where the method was adopted and later validated in HL, DLCBL and FL [14, 67, 71]. Scores 1, 2 and 3 on the scale are regarded as showing complete metabolic response with standard treatment, although in some clinical trials, scores 1 and 2 have been used to define CMR to avoid the risk of under-treatment when de-escalating therapy [14].

Deauville criteria score the most intense uptake in a site of initial disease, if present, as:

1. No uptake
2. Uptake ≤ mediastinum
3. Uptake > mediastinum but ≤ liver
4. Uptake moderately higher than liver
5. Uptake markedly higher than liver and/or new lesions

X new areas of uptake unlikely to be related to lymphoma

20.8   Paediatric

PET has high sensitivity and specificity for staging in paediatric patients [72] and for the detection of bone marrow involvement. Similar to adult practice, high negative predictive values are reported in children for interim and end of treatment PET and PET/CT, although the positive predictive value is more variable [73–75]. A low positive predictive value is observed in HL at the end of treatment [73], likely related to the good prognosis of the disease. Radiotherapy is used in intermediate- and advanced-stage HL, and PET/CT is advocated for planning purposes [76]. In the first international study for classical HL in children, patients with early stage disease did not receive radiotherapy after treatment with OEPA, if the early response assessment PET scan was regarded as showing adequate response [77]. In the second international study, this approach has been extended to the intermediate- and advanced-stage groups (https://clinicaltrials.gov/ct2/show/NCT02684708). In this study a less stringent definition of adequate response is being used similar to adults with Deauville scores of 1, 2 and 3 being regarded as CMR. The trial employs a quantitative modification of the Deauville criteria with standardised regions of interest for the residual most intense uptake and the liver [78] referred to as 'qPET'.

Pitfalls that may make interpretation of scans more challenging in children include the occurrence of thymic hyperplasia/rebound with treatment and the more frequent physiological uptake of FDG in brown fat.

20.9   MR in Lymphoma

MR imaging offers the potential of a radiation-free method to obtain high-quality anatomical images in patients with lymphoma. The high tissue contrast associated with this modality makes it an ideal tool for imaging of the brain and spinal regions. Outside of the central nervous system, the performance of anatomical MR has been more limited. Studies of lymphoma focusing on the bone marrow demonstrate high sensitivity [79] but low specificity resulting from false positives related to regenerating marrow or bone marrow inflammation [80]. MR imaging of the lungs has not yet reached the performance of CT [81], and no anatomical MR technique has offered performance that would replace the information obtained from FDG PET. In contrast to limited results in anatomical MR, developments in the arena of functional MR imaging with whole-body diffusion-weighted imaging (DWI) have yielded interesting results.

20.10   Whole-Body Diffusion-Weighted Imaging

Historically, lymphoma has been staged and restaged using CT, and with the advent of FDG PET and PET/CT, molecular imaging has become the standard of care to detect, stage, restage and monitor treatment response in lymphoma. MRI has typically been reserved for evaluation of more unusual scenarios including primary CNS lymphoma or lymphoma with suspected CNS involvement. Visceral organ infiltration may be evaluated by MRI when conventional imaging is equivocal. More recently, technical advances have yielded whole-body techniques that have been compared to CT and PET/CT. The lack of radiation associated with MR has made this an attractive modality for study, particularly for paediatric patients and young adults.

Whole-body diffusion imaging has been studied at numerous centres as a possible replacement for FDG PET/CT. In a recent meta-analysis of six studies, Regacini et al. reported that whole-body MRI with diffusion imaging agreed with findings on FDG PET/CT (with respect to staging) in 91% of all cases. In some cases, MRI detected additional lesions, but the authors could not fully address the potential for these lesions to represent false positives, citing that imaging artefacts in the chest and normal lymph nodes in the inguinal regions can be difficult to assess [82]. With respect to detection of focal bone marrow involvement, preliminary data suggests good agreement between FDG PET/CT and whole-body MRI with diffusion imaging [83].

With respect to treatment response assessment, preliminary data suggests potential utility of diffusion imaging. Lin et al. reported a mean increase of ADC values from 0.658 to 1.501 in residual enlarged lymph nodes after four cycles of chemotherapy and similar changes in areas of organ involvement [84]. Other authors have reported similar increases in ADC in the setting of treatment response, but just how these findings compare to the performance of FDG PET/CT requires further studies before definitive recommendations for or against DWI can be made in the setting of response assessment. One author has demonstrated significant changes in nodal ADC as early as 4.5 days after starting a first cycle of chemotherapy [85]. Response assessment is more challenging in bone due to changes in red marrow and fatty

marrow elements in response to chemotherapy and marrow stimulation, but it has been suggested that an overall increase in ADC is usually associated with a good treatment response [86].

20.11   CNS Lymphoma (Primary and Secondary)

MR imaging has played a more central role in the imaging of known or suspected CNS lymphoma involving the brain parenchyma, meninges, eyes or spinal cord. Most cases of CNS lymphoma present without evidence of disease outside of the CNS, although FDG PET literature has suggested that up to 15% of patients may harbour disease elsewhere [87]. MRI has higher sensitivity than CT and can identify enhancing tumour on the surface of the brain and spinal cord, within the ventricles or in the region of the spinal nerve roots [88, 89]. It is not possible to differentiate between primary and secondary lymphomas of the brain based on MR features alone [90], and therefore body scanning is indicated in patients presenting with CNS lesions.

Primary CNS lymphoma (PCNSL) usually presents as a supratentorial intracranial mass, frequently involving the periventricular white matter and may cross the midline. Smaller deep brain structures can be involved, and a more rare subtype of PCNSL is limited to the dura, usually presenting as a low-grade marginal zone lymphoma [91]. Primary leptomeningeal lymphoma can also occur. Ocular lymphoma may represent direct extension from adjacent structures or in rare cases can originate within the eye [92]. Due to high cellularity, PCNSL typically presents with low to intermediate signal on T2 imaging and relatively low ADC values on diffusion-weighted sequences. Lesions usually enhance on DCE-MRI either homogeneously or peripherally in necrotic lesions [93].

Advanced MR imaging techniques have been employed in the management of PCNSL. Diffusion-weighted imaging research has demonstrated the ADC values are typically lower in PCNSL compared to brain tumours, cellular metastases or toxoplasmosis, but significant overlap remains [94]. ADC has been shown to have prognostic value and can serve as a marker of treatment response [95].

Perfusion imaging based on arterial spin-labelling techniques has demonstrated relatively higher blood flow in gliomas compared to lymphoma and relatively lower values in toxoplasmosis [96, 97]. Vessel permeability measured by DCE-MRI is higher in gliomas than lymphomas [98]. Also, MR spectroscopy has been studied in PCNSL, but overlapping high levels of lipid and macromolecule resonance between PCNSL and toxoplasmosis has limited applications [99]. Susceptibility-weighted imaging is also under study [100]. Unfortunately, none of these techniques are specific enough to obviate tissue biopsy.

20.12   PET/MRI in Lymphoma

Several studies have reported results from hybrid PET/CT and PET/MRI scans performed on the same day in lymphoma patients to assess whether the examinations are equivalent (Table 20.1). It is inevitable with these types of studies that there will

Table 20.1 Studies comparing results from hybrid PET/CT and PET/MRI

Author	Number patients (scans)	Subtype	Timing of scans / Reference standard	PET/MRI	First exam	Mean delay ± sd (m)	Quantification	Radiation dose for PET/MRI
Afaq et al. [102]	66(68)	HL/NHL	Staging/end of treatment, Comparison with PET/CT, Follow-up imaging reviewed for discrepant cases	Simultaneous Anatomical sequences obtained and DWI	PET/CT	136(29)	SUV_{max} similar, Moderate inverse correlation between ADC mean and SUV_{max}	–
Atkinson et al. [107]	10(10) adults	HL/NHL	Staging/restaging, Comparison with PET/CT	Simultaneous Anatomical sequences obtained and DWI	PET/CT	151(43)	SUV_{max} similar, SUV mean higher with PET/CT, No correlation between ADC mean and SUV_{mean} or ADC min and SUV_{max} values	20% lower than low-dose PET/CT, 60% lower than full-dose PET/CT
Giraudo et al. [108]	34(40)	HL/NHL included 15MALT 5 MCL 3 MZL	Staging/restaging, Combined assessment from PET and DWI and histology (where available)	Simultaneous Anatomical sequences obtained and DWI	PET/CT	–	SUV_{max} and SUV_{mean} significantly higher with PET/MRI, No correlation between ADC mean and SUV_{mean} or ADC min and SUV_{max} values	–
Grueneisen et al. [104]	48(52)	HL/NHL	Staging/interim/end of treatment/surveillance, Comparison with PET/CT, biopsy (if available) previous and prior or follow-up imaging ($n = 33$)	Simultaneous Anatomical sequences obtained and DWI	PET/CT	72	SUV_{max} and SUV_{mean} significantly higher with PET/MRI	27% lower than low-dose PET/CT, 77% lower than full-dose PET/CT

Heacock et al. [105]	28(28)	HL/NHL	Treatment of active disease/end of treatment/ surveillance Comparison with PET/CT and bone marrow biopsy (if available)	Simultaneous Anatomical sequences obtained and DWI	PET/CT	57 Range 31–152	Average SUV$_{max}$ higher with PET/CT No correlation between ADC mean and SUV$_{max}$ values	–
Herrmann et al. [103]	61(82) adults	HL/NHL	Staging/restaging/ surveillance Follow-up comprising biopsy imaging and clinical FU	Sequential Tri-modality MR then PET/ CT using same scan table Anatomical sequences obtained and DWI	MR	30	Best cut-off for ADC 1.2 × 10^{-3} mm^2/s	–
Platzek et al. [101]	27	HL/NHL	Staging/response assessment/relapse Follow-up imaging, min FU time 12 months and histology if available	Sequential. MR for AC only	PET/ MRI only no PET/ CT	–	–	–
Ponisio et al. [110]	8(9) children	HL, DLBCL, BL	Response assessment/ suspected recurrence Comparison with PET/CT	Simultaneous Anatomical sequences obtained and DWI	PET/CT	51(10)	SUV$_{max}$ similar SUV$_{mean}$ correlated for normal organs, liver r = 0.86 but only 0.61 for blood pool	39 ± 13% lower than low-dose PET/CT
Sher et al. [111]	25 (40) children	30 HL 10 NHL	Staging/restaging/ surveillance Imaging and clinical follow-up minimum FU 6 m	Sequential. MR for AC only	PET/CT 9 PET/ MRI 31	42(13) 53(22)		45 ± 10% lower than low-dose PET/CT

AC attenuation correction, *ADC* apparent diffusion coefficient, *DWI* diffusion-weighted imaging, *FU* follow-up, *HL* Hodgkin lymphoma, *NHL* non-Hodgkin lymphoma, *SUV$_{max}$* maximum standardised uptake value, *SUV$_{mean}$* mean standardised uptake value

be limitations. All include a mix of lymphoma subtypes and patients scanned at different time points—staging, response assessment and sometimes surveillance. Many patients had no disease at the time of the scan, and very few patients in the studies had extranodal disease, certainly lower than what is usually encountered in lymphoma patient populations. PET/MRI was mostly done following PET/CT to avoid the chance that the patient might not complete the diagnostic or 'standard' examination.

The gold standard, as with all lymphoma studies, for the presence or absence of lymphomatous lesions is imperfect, because it is not ethical to biopsy lesions for these purposes. Some studies simply used PET/CT as the reference standard; others used a combination of biopsy (where available because clinically indicated), clinical and imaging follow-ups. Nonetheless, despite limitations, some important conclusions can be drawn.

20.13 Diagnostic Performance of PET/MRI Compared with PET/CT

The diagnostic performance of PET/MRI appears to be similar to PET/CT with respect to the detection of nodal disease in common lymphoma subtypes (Figs. 20.1, 20.2, and 20.3). Fewer cases with extranodal disease have been assessed, but most report that extranodal lesions were seen using both modalities. One study which
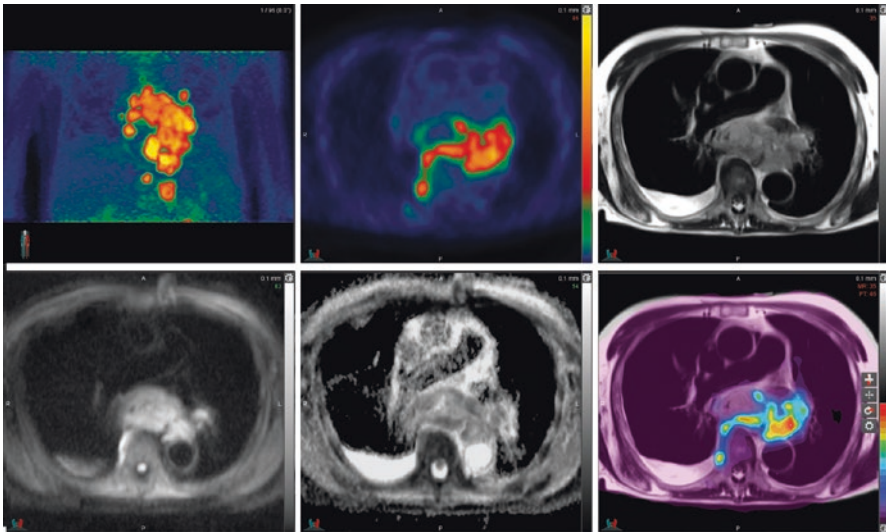

Fig. 20.1 85-year-old male with newly diagnosed diffuse large B-cell lymphoma. FDG PET/MRI demonstrates large mediastinal mass in the posterior mediastinum. Intense FDG uptake (upper middle frame) is seen corresponding to hyperintense foci on diffusion-weighted images (lower left frame) with corresponding relatively low ADC values (lower middle frame; see dark regions anterior to spine and aorta)
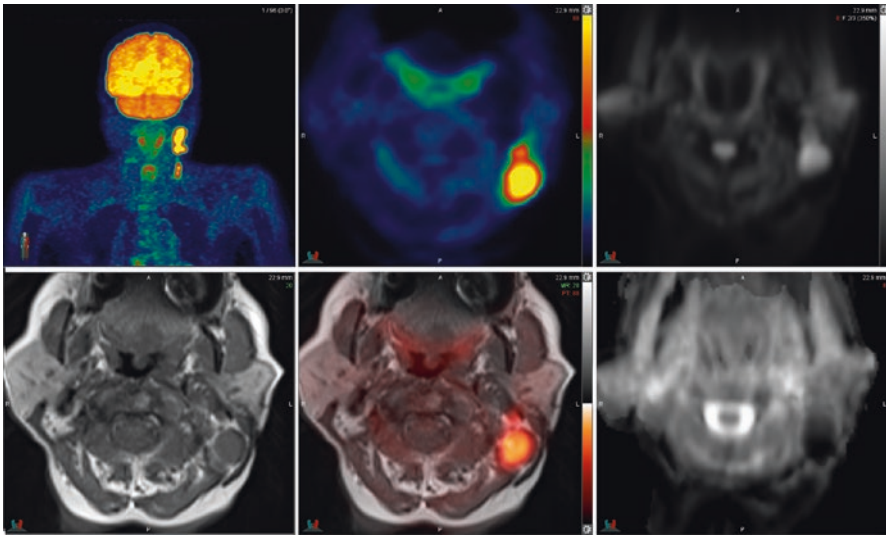
Fig. 20.2 77-year-old female with Hodgkin lymphoma. FDG PET/MRI demonstrates intense uptake in left cervical lymphadenopathy. Lymph node margins are well defined on axial HASTE MR (lower left frame), corresponding DW imaging demonstrates high signal (upper right frame) in left cervical adenopathy with corresponding low signal (dark) on ADC images (lower right frame)
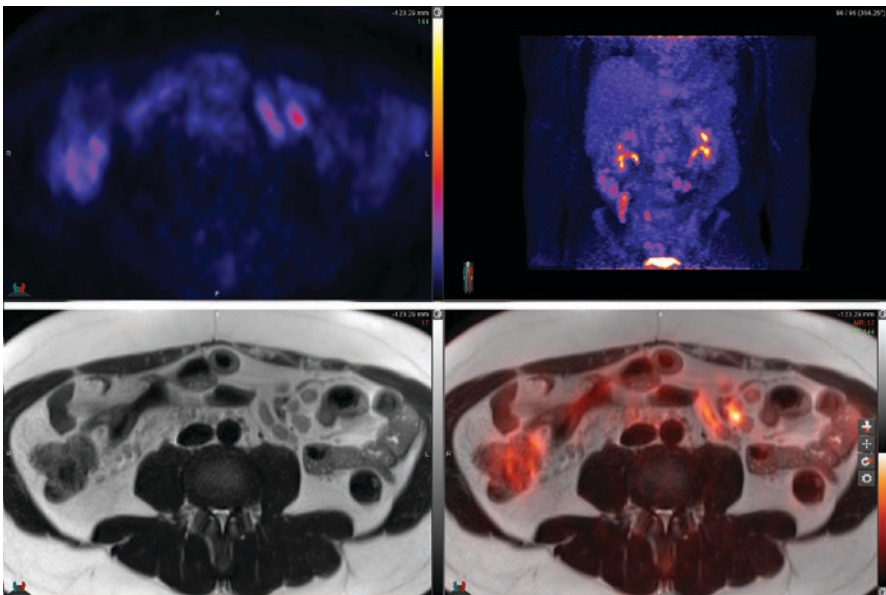

Fig. 20.3 51-year-old male with follicular lymphoma. FDG PET/MRI demonstrates mild FDG uptake within mesenteric adenopathy (upper left frame), well delineated on axial HASTE MR (lower left frame)

evaluated PET/MRI but did not directly compare with PET/CT reported high sensitivity, comparable to PET/CT using MR for AC only [101]. Studies using anatomical sequences reported equal sensitivity for PET/CT and PET/MRI.

Comparative studies also reported equivalent staging using PET/CT and PET/MRI. Staging was identical in all cases performed at baseline in 18 patients with mostly aggressive lymphomas [102]. Herrmann et al. [103] reported that all 188 lesions, which were considered to be 'positive' for lymphoma using their reference standard, were detected on both PET/CT and PET/MRI (29 scans). Eighteen of 188 lesions were extranodal. Lesions assessed included patients with HL [28], DLBCL [26] and intermediate- and low-grade lymphomas [28]. Fourteen out of eighty two of these patient scans were performed for primary staging.

Some studies have reported additional lesions on PET/MRI carried out after PET/CT, possibly related to delayed acquisition with increased uptake occurring in lymphomatous lesions over time [102, 104, 105].

In the study by Afaq et al., nodal lesions in the mesentery and the retroperitoneum in one patient and nodal lesions in the axilla in another patient were seen only on PET/MRI, but PET/MRI scans were carried out on average more than 2 h later than PET/CT [102]. For the first patient, this resulted in an assessment of residual metabolic disease on PET/MRI but complete metabolic response on PET/CT. The second patient had additional lesions such that the 'missed' axillary lesions did not affect disease status which was the same on PET/MRI and PET/CT.

Regarding extranodal disease, Heacock et al. reported discrepancy in bone marrow involvement in the right femoral neck in a patient with follicular lymphoma [105]. Bone marrow involvement was reported by readers on PET/MRI and DWI but not when reading PET/CT. The lesion was more FDG-avid on the PET component of the PET/MRI which was carried out after PET/CT, but there was also a more conspicuous bone lesion seen on the MR sequences including DWI than on the CT component of the PET/CT [105]. Advantages in the assessment of the bone marrow using PET/MRI have not been demonstrated on other studies, but so far these have included only three patients with BMI [102, 103], and more data are needed.

In one patient a probable adrenal lesion was reported as disease on PET/MRI but not PET/CT. The adrenal lesion reduced in size and activity on follow-up imaging and was deemed to be involved by lymphoma. The PET/MRI scans were carried out on average more than 2 h later than PET/CT [102].

In the studies to date, few patients with lung involvement have been reported [102]. This is an area where theoretically PET/CT might have an advantage, but the sizes of lung lesions in lymphoma are often larger than with solid tumours and were all resolved using PET/MRI. A recent study which included patients with solid cancers and lymphoma reported that the vast majority (97%) of small lung nodules that did not take up FDG and were missed on PET/MRI were likely to be benign, as they resolved or remained stable on follow-up [106].

Interobserver agreement between readers for evaluation of the presence or absence of disease was reported as perfect for nodal sites on PET/CT and almost perfect for nodal sites on PET/MRI in an evaluation of 95 nodal sites by 2 observers [102].

Both readers detected the same eight extranodal sites on PET/CT and nine extranodal sites on PET/MRI. Interobserver agreement for assessment of disease status was perfect.

20.14 Diffusion-Weighted Imaging Compared with PET/CT and PET/MRI Diagnostic Sequences

Authors have concluded that DWI either has no additional value or is inferior to PET/CT and PET/MRI.

Afaq et al. reported that no additional sites were found on DWI compared to PET/CT and PET/MRI and that staging was identical, concluding that DWI had no additional value in lymphoma [102]. Other studies reported that DWI was inferior to PET/CT and PET/MRI. Herrmann et al. reported that DWI missed 33% of nodal lesions and 44% of extranodal lesions in their study which included 82 patient scans [103]. Lesions were defined as high signal on high b-value DWI using the optimal cut-off derived from their data and low signal on the corresponding ADC map. No threshold for lesion size was used. This resulted in a large number of false positive lesions on DWI as well as poor sensitivity. The authors commented that the lack of standardised criteria, especially with respect to extranodal involvement, contributed to the high false positive rate. The spleen was a particularly difficult area to assess on DWI. Three cases of splenic involvement were missed using DWI, and three other cases showed restricted diffusion in spleens with normal activity on PET/CT [103] (Fig. 20.4). PET/CT and DWI were concordant for imaging stage in only 18/82 scans. DWI upstaged 60 scans including 45 scans where there was no assessable disease according to Deauville criteria on PET/CT.

Heacock et al. reported 19/51 (37%) of nodal lesions were missed on DWI with 5 false positive lesions [105]. There was disagreement in stage in 10/28 patients
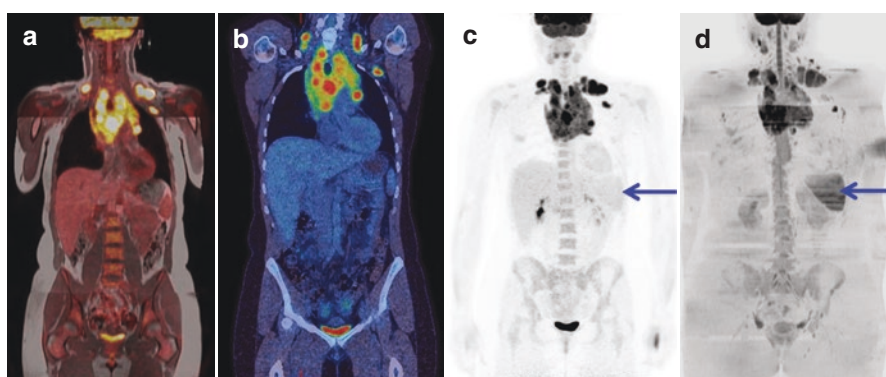

Fig. 20.4 Demonstrates a patient scanned with PET/MRI (**a**) and PET/CT (**b**) after a single administration of FDG on the same day. Note that the spleen has normal activity on FDG PET/MRI (**c**) but restricted diffusion on DWI (**d**) (courtesy of Dr. Andrew Mallia, PET Imaging Centre at St Thomas', King's College London)

compared to PET/CT, one of which was bone marrow involvement correctly assigned by DWI but also on PET/MRI (as above). Atkinson et al. reported 17% of lesions were missed on DWI in a smaller series of 10 patients with increased FDG uptake on PET/CT and PET/MRI [107]. Four out of eleven of the missed lesions on DWI were in the chest which they attributed to signal loss due to respiratory motion artefact.

The difference between the number of positive lymphoma lesions on DWI compared to PET/CT and PET/MRI did not reach statistical significance, when response and surveillance scans were considered in the study by Herrmann et al. [103]. There were however fewer lesions during and after treatment, and DWI still missed ≥50% of positive lymphoma lesions according to the follow-up criteria.

Fewer lesions were also missed in patients with low-grade disease compared to patients with aggressive lymphoma using DWI, but DWI was statistically inferior for the detection of lymphoma even in this group ($p = 0.03$). It seems reasonable to conclude that tumour cellularity is inferior to glucose metabolism in assessing lymphomatous disease.

It has been suggested there may be a role for DWI in subtypes that are not routinely FDG-avid such as MALT lymphoma. Giraudo et al. reported higher sensitivity in non-FDG-avid lymphomas when DWI was added to PET/MRI because of low FDG-avidity in six cases of mucosa-associated lymphoid tissue (MALT) lymphoma, one case of mantle cell lymphoma and one case of marginal zone lymphoma [108]. Size criteria were used for non-FDG-avid lesions on CT and MR and for DWI lesions with restricted diffusion. In these less common subtypes, however, international guidelines already recommend that if not FDG-avid, contrast-enhanced CT and/or MR is a better investigation. DWI may possibly have added value. In another small study by the same group looking at response assessment in 15 patients with MALT lymphoma, the change in SUV on interim PET at 3 cycles of treatment was better at predicting CT response at the end of treatment than change in ADC. Changes in ADC in patients with end of treatment complete response on CT showed much larger standard deviations than changes in SUV which the authors attributed to inhomogeneities in the magnetic field and artefacts [109].

20.15 Quantitation

High correlation has been observed for measurement of the maximum standardised uptake value (SUVmax) on PET/CT and PET/MRI in studies involving 158 patients [102, 104, 105, 107]. Grueneisen et al. however found that SUVmax was significantly higher for PET/MRI with a mean difference in SUVmax between PET/CT and PET/ MRI of −2.5 (95% CI 3.1 to −7.9) which they attributed to the delay in acquisition of PET/MRI with increasing uptake in lymphoma lesions over time [104].

Conversely other studies have reported that SUVmax was higher with PET/CT even when PET/MRI was performed later, suggesting that PET/MRI may underestimate uptake. In the study by Afaq et al. [102], the mean difference in SUVmax was only 0.32 (95% CI −0.12 to 0.75) when PET/MR imaging was performed over 2 h

later than PET/CT (68 patient scans). Heacock et al. [105] reported the mean difference was 1.7 (95% CI −5.8 to 9.2) when PET/MR imaging was performed an average of 1 h after PET/CT.

The mean SUV (SUVmean) was also reported to be significantly higher for PET/CT compared to PET/MRI with SUVmean measured at 20.1 ± 2.1 (PET/CT) and 13.7 ± 1.4 (PET/MRI) [107] where the mean delay between PET/CT and PET/MRI was 151 min. This also suggests that PET/MRI may underestimate intensity of uptake compared to PET/CT. Underestimation or overestimation of SUV measurements with PET/MRI could potentially have implications when measuring response using Deauville criteria.

Afaq et al. reported a moderate inverse correlation between SUVmax and ADC mean in 27 scans where the most FDG-avid lesion corresponded to a measurable lesion on the ADC map [102]. Others have not demonstrated any relationship between SUVmax and SUVmean with ADC values [105, 107].

20.16 Radiation Dose

Radiation dose is reduced in hybrid PET scanning if MR is used instead of CT for anatomical localisation and attenuation correction. The reduction is marked if full-dose 'diagnostic' CT is used but more modest if low-dose CT is used which is usually sufficient for staging and response assessment in aggressive lymphomas [31–33, 35]. Dose reduction with full-dose CT has been reported to be around 60–77% and with low-dose CT around 20–27% [104, 107]. Dose savings may therefore be considerable but may become less with further advances in CT iterative reconstruction.

20.17 Other Factors

Set-up costs are higher for PET/MRI and duration of scans is generally longer than PET/CT. This translates into higher scan costs, and PET/MRI remains a limited resource in most countries [102]. The scan duration depends of course on the sequences chosen for MR imaging. Using a 'fast' protocol that included a coronal 3D volume interpolated breath-hold examination (VIBE) for attenuation correction, DWI, an echo-planar imaging (EPI) sequence, a transverse 2D half Fourier acquisition single-shot turbo spin echo (HASTE) sequence and transverse post-contrast 3D fat-saturated VIBE sequence, Gruniesen reported imaging times of 27.8 ± 3.7 m for PET/MRI versus 17.3 ± 1.9 m for PET/CT using a 4 min per bed acquisition for PET and 4–5 bed positions [104]. Other studies reported imaging times of up to 120 min for anatomical sequences and DWI [108] which is unlikely to be tolerated by elderly or very unwell patients with lymphoma.

Using MR for attenuation correction only, the scan duration for PET/MRI was reported as 23–25 min in another study of which the PET duration was 20–22 min [101]. Using MR just for attenuation correction is however suboptimal as discussed above and results in inferior sensitivity to PET/CT or PET/MRI with anatomical sequences.

20.18 Paediatric PET/MRI Experience

Ponisio et al. performed 9 patient scans in children aged 12–17 years at the time of response assessment. Assessment of response category was the same using PET/CT and PET/MRI, but there were some discordant findings [110]. PET/MRI missed one focus of uptake in a mediastinal mass compared to two foci seen on PET/CT. Conversely PET/CT missed a focus of uptake in the neck compared to two foci on PET/MRI. In one case a renal lesion was not reported on PET/CT because it was obscured by physiological urinary activity but was reported on DWI as it had restricted diffusion. Artefacts were reported on the MR attenuation correction map from dental braces [2], a port catheter [1] and the lungs due to motion artefact [1]; however, there was high correlation in measurements of SUVmax; the average difference was only 1.6% between PET/CT and PET/MRI.

Sher et al. performed 40 patient scans in children with a mean age of 14.6 ± 3.9 years [111]. Sensitivity was similar: 95% with PET/CT and 92% with PET/MRI. Specificity was also similar: 56% with PET/CT and 61% with PET/MRI for individual lesions. Staging was correct in 35 of 40 patients with both modalities, but of these, 29 children had no evidence of lymphoma at the time of scanning. Six lesions were misclassified compared to the reference standard. Two were due to interobserver variation rather than the imaging modality. Three were misclassified on PET/MRI. One reported as mesenteric nodal disease on PET/MRI was reported as physiological uptake in bowel on PET/CT. One dismissed as muscle uptake on PET/MRI was reported as axillary nodal disease on PET/CT. One patient had a left hilar node with lower uptake on PET/MRI (SUVmax 1.6) compared to PET/CT (SUVmax 3.3) which was overlooked on PET/MRI. Dedicated anatomical MR sequences were omitted in this study to reduce scan duration, and this likely accounted for the discrepancies, but scan duration is an issue when imaging children. One lesion was misclassified on PET/CT. A prevascular node was reported correctly on PET/MRI but as physiological right atrial uptake on PET/CT. In one patient a lytic bone lesion that was not FDG-avid was overlooked on both modalities.

This was the only study in those undertaken to date, to perform any PET/MRI scans prior to PET/CT [111]. The authors observed no difference in SUV values when PET/CT was done first but a significant difference when PET/MRI was done first in SUVmax and SUVmean for both benign and malignant lesions identified. This again supports the premise that PET/MRI may underestimate SUV values, as reported in adult studies [102, 105, 107]. In malignant lesions the SUVmax was 6.3 ± 2.8 on PET/MRI and 10.1 ± 4.9 on PET/CT when the PET/MRI was performed first ($p < 0.001$) but 6.2 ± 3.1 on PET/MRI and 5.9 ± 3.2 on PET/CT when the PET/CT was done first ($p < 0.001$) [111]. This suggests that differences may be due to attenuation correction being less reliable in PET/MRI. At these levels, the differences could conceivably have an impact on response assessment, although as with other studies, there was no significant difference in accuracy between the techniques compared to the reference standard. Compared with low-dose PET/CT, there was a 45 ± 10% reduction in effective dose with PET/MRI in the children in this study [111].

20.19 Novel Tracers for PET/MRI in Lymphoma

FDG PET has been a mainstay of lymphoma lesion detection, tumour grading, treatment response monitoring and recurrence detection. This agent is not without flaws, as false positives occur due to inflammation and tumour grading by SUVmax is limited by significant quantitative overlap between low- and high-grade histologies. There is a need to develop better tracers to address these limitations.

18F-Fluorodeoxythymidine (FLT) is a synthetic amino acid tracer that has been developed to indirectly measure cellular proliferation in vivo and is of interest for use in patients with lymphoma. Preliminary studies suggest sensitivity that is very similar to FDG, with some suggestion of potentially improved tumour grading compared to FDG [112]. More recent work has demonstrated potential utility in assessing treatment response and determining prognosis during mid-treatment imaging [113]. A question for PET/MRI researchers is to determine if the performance of FLT can be synergistic with MR parameters in a manner that offers advantages over FDG.

Fludarabine is a drug used in the treatment of low-grade lymphomas, often as a part of combination regimens with other drugs. Given the presence of a fluorine atom on this compound, investigators have substituted the fluorine with 18F-fluorine and thus produced a PET-tracer version of this drug. Preliminary murine studies demonstrated rapid uptake in lymphoma cells that was more intense than FDG and minimal background organ activity [114]. Subsequent mouse studies have demonstrated persistent uptake in viable tumour cells following immunotherapy with rituximab [115] and good specificity with lower uptake in inflammatory lesions compared to FDG [116]. Further studies with PET/MRI to correlate the intratumoural distribution of this new agent and relate it to findings on diffusion or DCE-MR imaging sequences may be of interest to further improve lesion detection and monitoring of treatment responses.

Conclusions

1. PET/MRI is likely equivalent to PET/CT in staging for nodal disease and extranodal disease (but there are limited data regarding extranodal disease to date).
2. PET/MRI may underestimate FDG uptake compared to PET/CT, which could have implications for response assessment, and more data are needed. This may improve as attenuation correction algorithms are optimised.
3. DWI will not replace PET/CT or PET/MRI for evaluation of FDG-avid lymphomas and can probably be omitted in PET/MR imaging for lymphoma.
4. PET/MRI reduces radiation dose, although dose savings may be less as CT dose reduces with iterative reconstruction techniques and needs to be weighed against longer scan duration.

References

1. Wright CL, Maly JJ, Zhang J, et al. Advancing precision nuclear medicine and molecular imaging for lymphoma. PET Clin. 2017;12(1):63–82. S1556-8598 (16)30090-6

2. Povoski SP, Hall NC, Murrey DA Jr, et al. Feasibility of a multimodal (18)F-FDG-directed lymph node surgical excisional biopsy approach for appropriate diagnostic tissue sampling in patients with suspected lymphoma. BMC Cancer. 2015;15:378. https://doi.org/10.1186/s12885-015-1381-z.

3. Sin KM, Ho SK, Wong BY, et al. Beyond the lymph nodes: FDG-PET/CT in primary extranodal lymphoma. Clin Imaging. 2016;42:25–33. S0899-7071 (16)30180-2 [pii]

4. la Fougere C, Hundt W, Brockel N, et al. Value of PET/CT versus PET and CT performed as separate investigations in patients with Hodgkin's disease and non-Hodgkin's lymphoma. Eur J Nucl Med Mol Imaging. 2006;33(12):1417–25. https://doi.org/10.1007/s00259-006-0171-x.

5. Catalano OA, Masch WR, Catana C, et al. An overview of PET/MRI, focused on clinical applications. Abdom Radiol. 2016;42(2):631–44. https://doi.org/10.1007/s00261-016-0894-5.

6. Rakheja R, DeMello L, Chandarana H, et al. Comparison of the accuracy of PET/CT and PET/MRI spatial registration of multiple metastatic lesions. Am J Roentgenol. 2013;201(5):1120–3. https://doi.org/10.2214/AJR.13.11305.

7. Sun B, Song L, Wang X, et al. Lymphoma and inflammation in the orbit: diagnostic performance with diffusion-weighted imaging and dynamic contrast-enhanced MRI. J Magn Reson Imaging. 2016;45(5):1438–45. https://doi.org/10.1002/jmri.25480.

8. de la Pena MD J, Vicente LG, Alonso RC, et al. The multiple faces of nervous system lymphoma. Atypical magnetic resonance imaging features and contribution of the advanced imaging. Curr Probl Diagn Radiol. 2016;46(2):136–45. S0363-0188(16)30007-X [pii]

9. Mathas S, Hartmann S, Kuppers R. Hodgkin lymphoma: pathology and biology. Semin Hematol. 2016;53(3):139–47. https://doi.org/10.1053/j.seminhematol.2016.05.007.

10. Meignan M, Itti E, Gallamini A, et al. FDG PET/CT imaging as a biomarker in lymphoma. Eur J Nucl Med Mol Imaging. 2015;42(4):623–33. https://doi.org/10.1007/s00259-014-2973-6.

11. Zhou Z, Sehn LH, Rademaker AW, et al. An enhanced international prognostic index (NCCN-IPI) for patients with diffuse large B-cell lymphoma treated in the rituximab era. Blood. 2014;123(6):837–42. https://doi.org/10.1182/blood-2013-09-524108.

12. Caimi PF, Hill BT, Hsi ED, et al. Clinical approach to diffuse large B cell lymphoma. Blood Rev. 2016;30(6):477–91. S0268-960X(16)30033-9 [pii]

13. Kahl BS, Yang DT. Follicular lymphoma: evolving therapeutic strategies. Blood. 2016;127(17):2055–63. https://doi.org/10.1182/blood-2015-11-624288.

14. Barrington SF, Mikhaeel NG, Kostakoglu L, et al. Role of imaging in the staging and response assessment of lymphoma: consensus of the international conference on malignant lymphomas imaging working group. J Clin Oncol. 2014;32(27):3048–58. JCO.2013.53.5229 [pii]

15. Engert A, Raemaekers J. Treatment of early-stage Hodgkin lymphoma. Semin Hematol. 2016;53(3):165–70. https://doi.org/10.1053/j.seminhematol.2016.05.004.

16. Vassilakopoulos TP, Johnson PW. Treatment of advanced-stage Hodgkin lymphoma. Semin Hematol. 2016;53(3):171–9. https://doi.org/10.1053/j.seminhematol.2016.05.006.

17. Engert A, Haverkamp H, Kobe C, et al. Reduced-intensity chemotherapy and PET-guided radiotherapy in patients with advanced stage Hodgkin's lymphoma (HD15 trial): a randomised, open-label, phase 3 non-inferiority trial. Lancet. 2012;379(9828):1791–9. https://doi.org/10.1016/S0140-6736(11)61940-5.

18. Engert A. XVII. Treatment of advanced-stage Hodgkin lymphoma. Hematol Oncol. 2015;33(Suppl 1):87–9. https://doi.org/10.1002/hon.2225.

19. Moskowitz CH, Nademanee A, Masszi T, et al. Brentuximab vedotin as consolidation therapy after autologous stem-cell transplantation in patients with Hodgkin's lymphoma at risk of relapse or progression (AETHERA): a randomised, double-blind, placebo-controlled, phase 3 trial. Lancet. 2015;385(9980):1853–62. https://doi.org/10.1016/S0140-6736(15)60165-9.

20. Younes A, Gopal AK, Smith SE, et al. Results of a pivotal phase II study of brentux-imab vedotin for patients with relapsed or refractory Hodgkin's lymphoma. J Clin Oncol. 2012;30(18):2183–9. https://doi.org/10.1200/JCO.2011.38.0410.

21. Ansell SM, Lesokhin AM, Borrello I, et al. PD-1 blockade with nivolumab in relapsed or refractory Hodgkin's lymphoma. N Engl J Med. 2015;372(4):311–9. https://doi.org/10.1056/NEJMoa1411087.

22. Moskowitz CH, Ribrag V, Michot J, et al. PD-1 blockade with the monoclonal antibody pembrolizumab (MK-3475) in patients with classical Hodgkin lymphoma after Brentuximab Vedotin failure: preliminary results from a phase 1b study (KEYNOTE-013). Blood. 2014;124(21):290.

23. Ansell SM. Hodgkin lymphoma: 2016 update on diagnosis, risk-stratification, and manage-ment. Am J Hematol. 2016;91(4):434–42. https://doi.org/10.1002/ajh.24272.

24. Davies AJ, Caddy J, Maishman T, et al. A prospective randomised trial of targeted therapy for diffuse large B-cell lymphoma (DLBCL) based upon real-time gene expression profiling: the Remodl-B study of the UK NCRI and SAKK lymphoma groups. Blood. 2015;126(23):812.

25. Salles G, Seymour JF, Offner F, et al. Rituximab maintenance for 2 years in patients with high tumour burden follicular lymphoma responding to rituximab plus chemotherapy (PRIMA): a phase 3, randomised controlled trial. Lancet. 2011;377(9759):42–51. https://doi.org/10.1016/S0140-6736(10)62175-7.

26. Cheson BD, Fisher RI, Barrington SF, et al. Recommendations for initial evaluation, staging, and response assessment of Hodgkin and non-Hodgkin lymphoma: the Lugano classification. J Clin Oncol. 2014;32(27):3059–68. JCO.2013.54.8800 [pii]

27. Gascoyne RD. Establishing the diagnosis of lymphoma: from initial biopsy to clinical staging. Oncology (Williston Park). 1998;12(10 Suppl 8):11–6.

28. Zangos S, Eichler K, Wetter A, et al. MR-guided biopsies of lesions in the retroperitoneal space: technique and results. Eur Radiol. 2006;16(2):307–12. https://doi.org/10.1007/s00330-005-2870-2.

29. Agid R, Sklair-Levy M, Bloom AI, et al. CT-guided biopsy with cutting-edge needle for the diagnosis of malignant lymphoma: experience of 267 biopsies. Clin Radiol. 2003;58(2):143–7. S0009926002910615 [pii]

30. Weiler-Sagie M, Bushelev O, Epelbaum R, et al. (18)F-FDG avidity in lymphoma read-dressed: a study of 766 patients. J Nucl Med. 2010;51(1):25–30. https://doi.org/10.2967/jnumed.109.067892.

31. Chalaye J, Luciani A, Enache C, et al. Clinical impact of contrast-enhanced computed tomography combined with low-dose (18)F-fluorodeoxyglucose positron emission tomog-raphy/computed tomography on routine lymphoma patient management. Leuk Lymphoma. 2014;55(12):2887–92. https://doi.org/10.3109/10428194.2014.900761.

32. Elstrom RL, Leonard JP, Coleman M, et al. Combined PET and low-dose, noncontrast CT scanning obviates the need for additional diagnostic contrast-enhanced CT scans in patients undergoing staging or restaging for lymphoma. Ann Oncol. 2008;19(10):1770–3. https://doi.org/10.1093/annonc/mdn282.

33. Pinilla I, Gomez-Leon N, Del Campo-Del Val L, et al. Diagnostic value of CT, PET and com-bined PET/CT performed with low-dose unenhanced CT and full-dose enhanced CT in the initial staging of lymphoma. Q J Nucl Med Mol Imaging. 2011;55(5):567–75. R39102188 [pii]

34. Raanani P, Shasha Y, Perry C, et al. Is CT scan still necessary for staging in Hodgkin and non-Hodgkin lymphoma patients in the PET/CT era? Ann Oncol. 2006;17(1):117–22. mdj024 [pii]

35. Barrington SF, Kirkwood AA, Franceschetto A, et al. PET-CT for staging and early response: results from the response-adapted therapy in advanced Hodgkin lymphoma study. Blood. 2016;127(12):1531–8. https://doi.org/10.1182/blood-2015-11-679407.

36. Bodet-Milin C, Touzeau C, Leux C, et al. Prognostic impact of 18F-fluoro-deoxyglucose positron emission tomography in untreated mantle cell lymphoma: a retrospective study from the GOELAMS group. Eur J Nucl Med Mol Imaging. 2010;37(9):1633–42. https://doi.org/10.1007/s00259-010-1469-2.

37. Quarles van Ufford HM, van Tinteren H, Stroobants SG, et al. Added value of baseline 18F-FDG uptake in serial 18F-FDG PET for evaluation of response of solid extracerebral tumors to systemic cytotoxic neoadjuvant treatment: a meta-analysis. J Nucl Med. 2010;51(10):1507–16. https://doi.org/10.2967/jnumed.110.075457.

38. Barrington SF, Mackewn JE, Schleyer P, et al. Establishment of a UK-wide network to facilitate the acquisition of quality assured FDG-PET data for clinical trials in lymphoma. Ann Oncol. 2011;22(3):739–45. https://doi.org/10.1093/annonc/mdq428.

39. El-Galaly TC, d'Amore F, Mylam KJ, et al. Routine bone marrow biopsy has little or no therapeutic consequence for positron emission tomography/computed tomography-staged treatment-naive patients with Hodgkin lymphoma. J Clin Oncol. 2012;30(36):4508–14. https://doi.org/10.1200/JCO.2012.42.4036.

40. Khan AB, Barrington SF, Mikhaeel NG, et al. PET-CT staging of DLBCL accurately identifies and provides new insight into the clinical significance of bone marrow involvement. Blood. 2013;122(1):61–7. https://doi.org/10.1182/blood-2012-12-473389.

41. Berthet L, Cochet A, Kanoun S, et al. In newly diagnosed diffuse large B-cell lymphoma, determination of bone marrow involvement with 18F-FDG PET/CT provides better diagnostic performance and prognostic stratification than does biopsy. J Nucl Med. 2013;54(8):1244–50. https://doi.org/10.2967/jnumed.112.114710.

42. Cerci JJ, Gyorke T, Fanti S, et al. Combined PET and biopsy evidence of marrow involvement improves prognostic prediction in diffuse large B-cell lymphoma. J Nucl Med. 2014;55(10):1591–7. https://doi.org/10.2967/jnumed.113.134486.

43. Cheson BD. Hodgkin lymphoma: protecting the victims of our success. J Clin Oncol. 2012;30(36):4456–7. https://doi.org/10.1200/JCO.2012.45.5402.

44. Alzahrani M, El-Galaly TC, Hutchings M, et al. The value of routine bone marrow biopsy in patients with diffuse large B-cell lymphoma staged with PET/CT: a Danish-Canadian study. Ann Oncol. 2016;27(6):1095–9. https://doi.org/10.1093/annonc/mdw137.

45. Paone G, Itti E, Haioun C, et al. Bone marrow involvement in diffuse large B-cell lymphoma: correlation between FDG-PET uptake and type of cellular infiltrate. Eur J Nucl Med Mol Imaging. 2009;36(5):745–50. https://doi.org/10.1007/s00259-008-1021-9.

46. Pelosi E, Penna D, Douroukas A, et al. Bone marrow disease detection with FDG-PET/CT and bone marrow biopsy during the staging of malignant lymphoma: results from a large multicentre study. Q J Nucl Med Mol Imaging. 2011;55(4):469–75. R39102239 [pii]

47. Moskowitz CH, Schoder H. Current status of the role of PET imaging in diffuse large B-cell lymphoma. Semin Hematol. 2015;52(2):138–42. https://doi.org/10.1053/j.seminhematol.2015.01.004.

48. Campbell J, Seymour JF, Matthews J, et al. The prognostic impact of bone marrow involvement in patients with diffuse large cell lymphoma varies according to the degree of infiltration and presence of discordant marrow involvement. Eur J Haematol. 2006;76(6):473–80. EJH644 [pii]

49. Luminari S, Biasoli I, Arcaini L, et al. The use of FDG-PET in the initial staging of 142 patients with follicular lymphoma: a retrospective study from the FOLL05 randomized trial of the Fondazione Italiana Linfomi. Ann Oncol. 2013;24(8):2108–12. https://doi.org/10.1093/annonc/mdt137.

50. Schoder H, Noy A, Gonen M, et al. Intensity of 18fluorodeoxyglucose uptake in positron emission tomography distinguishes between indolent and aggressive non-Hodgkin's lymphoma. J Clin Oncol. 2005;23(21):4643–51. JCO.2005.12.072 [pii]

51. Watanabe R, Tomita N, Takeuchi K, et al. SUVmax in FDG-PET at the biopsy site correlates with the proliferation potential of tumor cells in non-Hodgkin lymphoma. Leuk Lymphoma. 2010;51(2):279–83. https://doi.org/10.3109/10428190903440953.

52. Cheson BD, Pfistner B, Juweid ME, et al. Revised response criteria for malignant lymphoma. J Clin Oncol. 2007;25(5):579–86. JCO.2006.09.2403 [pii]

53. Hutchings M, Loft A, Hansen M, et al. FDG-PET after two cycles of chemotherapy predicts treatment failure and progression-free survival in Hodgkin lymphoma. Blood. 2006;107(1):52–9. 2005-06-2252 [pii]

54. Gallamini A, Hutchings M, Rigacci L, et al. Early interim 2-[18F]fluoro-2-deoxy-D-glucose positron emission tomography is prognostically superior to international prognostic score in advanced-stage Hodgkin's lymphoma: a report from a joint Italian-Danish study. J Clin Oncol. 2007;25(24):3746–52. JCO.2007.11.6525 [pii]

55. Raemaekers JM, Andre MP, Federico M, et al. Omitting radiotherapy in early positron emission tomography-negative stage I/II Hodgkin lymphoma is associated with an increased risk of early relapse: clinical results of the preplanned interim analysis of the randomized EORTC/LYSA/FIL H10 trial. J Clin Oncol. 2014;32(12):1188–94. https://doi.org/10.1200/JCO.2013.51.9298.

56. Radford J, Illidge T, Counsell N, et al. Results of a trial of PET-directed therapy for early-stage Hodgkin's lymphoma. N Engl J Med. 2015;372(17):1598–607. https://doi.org/10.1056/NEJMoa1408648.

57. Follows GA, Ardeshna KM, Barrington SF, et al. Guidelines for the first line management of classical Hodgkin lymphoma. Br J Haematol. 2014;166(1):34–49. https://doi.org/10.1111/bjh.12878.

58. Johnson P, Federico M, Kirkwood A, et al. Adapted treatment guided by interim PET-CT scan in advanced Hodgkin's lymphoma. N Engl J Med. 2016;374(25):2419–29. https://doi.org/10.1056/NEJMoa1510093.

59. Zinzani PL, Broccoli A, Gioia DM, et al. Interim positron emission tomography response–adapted therapy in advanced-stage Hodgkin lymphoma: final results of the phase II part of the HD0801 study. JCO. 2016;34(12):1376–85. https://doi.org/10.1200/JCO.2015.63.0699.

60. Mamot C, Klingbiel D, Hitz F, et al. Final results of a prospective evaluation of the predictive value of interim positron emission tomography in patients with diffuse large B-cell lymphoma treated with R-CHOP-14 (SAKK 38/07). J Clin Oncol. 2015;33(23):2523–9. https://doi.org/10.1200/JCO.2014.58.9846.

61. Huntington SF, Nasta SD, Schuster SJ, et al. Utility of interim and end-of-treatment [(18)F]-fluorodeoxyglucose positron emission tomography-computed tomography in frontline therapy of patients with diffuse large B-cell lymphoma. Leuk Lymphoma. 2015;56(9):2579–84. https://doi.org/10.3109/10428194.2015.1007506.

62. Carr R, Fanti S, Paez D, et al. Prospective international cohort study demonstrates inability of interim PET to predict treatment failure in diffuse large B-cell lymphoma. J Nucl Med. 2014;55(12):1936–44. https://doi.org/10.2967/jnumed.114.145326.

63. Zijlstra JM, Burggraaff CN, Kersten MJ, et al. FDG-PET as a biomarker for early response in diffuse large B-cell lymphoma as well as in Hodgkin lymphoma? Ready for implementation in clinical practice? Haematologica. 2016;101(11):1279–83. haematol.2016.142752 [pii]

64. Stewart DA, Kloiber R, Owen C, et al. Results of a prospective phase II trial evaluating interim positron emission tomography-guided high dose therapy for poor prognosis diffuse large B-cell lymphoma. Leuk Lymphoma. 2014;55(9):2064–70. https://doi.org/10.3109/10428194.2013.862242.

65. Pardal E, Coronado M, Martin A, et al. Intensification treatment based on early FDG-PET in patients with high-risk diffuse large B-cell lymphoma: a phase II GELTAMO trial. Br J Haematol. 2014;167(3):327–36. https://doi.org/10.1111/bjh.13036.

66. Barrington SF, Mikhaeel NG. PET scans for staging and restaging in diffuse large B-cell and follicular lymphomas. Curr Hematol Malig Rep. 2016;11(3):185–95. https://doi.org/10.1007/s11899-016-0318-1.

67. Trotman J, Luminari S, Boussetta S, et al. Prognostic value of PET-CT after first-line therapy in patients with follicular lymphoma: a pooled analysis of central scan review in three multicentre studies. Lancet Haematol. 2014;1(1):e17–27. https://doi.org/10.1016/S2352-3026(14)70008-0.

68. Moskowitz CH, Matasar MJ, Zelenetz AD, et al. Normalization of pre-ASCT, FDG-PET imaging with second-line, non-cross-resistant, chemotherapy programs improves event-free survival in patients with Hodgkin lymphoma. Blood. 2012;119(7):1665–70. https://doi.org/10.1182/blood-2011-10-388058.

69. Sauter CS, Matasar MJ, Meikle J, et al. Prognostic value of FDG-PET prior to autologous stem cell transplantation for relapsed and refractory diffuse large B-cell lymphoma. Blood. 2015;125(16):2579–81. https://doi.org/10.1182/blood-2014-10-606939.

70. Moskowitz AJ, Schoder H, Yahalom J, et al. PET-adapted sequential salvage therapy with brentuximab vedotin followed by augmented ifosfamide, carboplatin, and etoposide for patients with relapsed and refractory Hodgkin's lymphoma: a non-randomised, open-label, single-centre, phase 2 study. Lancet Oncol. 2015;16(3):284–92. https://doi.org/10.1016/S1470-2045(15)70013-6.

71. Meignan M, Itti E, Bardet S, et al. Development and application of a real-time on-line blinded independent central review of interim PET scans to determine treatment allocation in lymphoma trials. J Clin Oncol. 2009;27(16):2739–41. https://doi.org/10.1200/JCO.2009.22.4089.

72. Uslu L, Doing J, Link M, Rosenberg J, Quon A, Daldrup-Link HE. Value of 18F-FDG PET and PET/CT for evaluation of pediatric malignancies. J Nucl Med. 2015;56(2):274–86.

73. Furth C, Steffen IG, Amthauer H, et al. Early and late therapy response assessment with [18F] fluorodeoxyglucose positron emission tomography in pediatric Hodgkin's lymphoma: analysis of a prospective multicenter trial. J Clin Oncol. 2009;27(26):4385–91. https://doi.org/10.1200/JCO.2008.19.7814.

74. Riad R, Omar W, Kotb M, et al. Role of PET/CT in malignant pediatric lymphoma. Eur J Nucl Med Mol Imaging. 2010;37(2):319–29. https://doi.org/10.1007/s00259-009-1276-9.

75. Bakhshi S, Radhakrishnan V, Sharma P, et al. Pediatric nonlymphoblastic non-Hodgkin lymphoma: baseline, interim, and posttreatment PET/CT versus contrast-enhanced CT for evaluation--a prospective study. Radiology. 2012;262(3):956–68. https://doi.org/10.1148/radiol.11110936.

76. Paulino AC, Margolin J, Dreyer Z, et al. Impact of PET-CT on involved field radiotherapy design for pediatric Hodgkin lymphoma. Pediatr Blood Cancer. 2012;58(6):860–4. https://doi.org/10.1002/pbc.23273.

77. Mauz-Korholz C, Hasenclever D, Dorffel W, et al. Procarbazine-free OEPA-COPDAC chemotherapy in boys and standard OPPA-COPP in girls have comparable effectiveness in pediatric Hodgkin's lymphoma: the GPOH-HD-2002 study. J Clin Oncol. 2010;28(23):3680–6. https://doi.org/10.1200/JCO.2009.26.9381.

78. Hasenclever D, Kurch L, Mauz-Korholz C, et al. qPET – a quantitative extension of the Deauville scale to assess response in interim FDG-PET scans in lymphoma. Eur J Nucl Med Mol Imaging. 2014;41(7):1301–8. https://doi.org/10.1007/s00259-014-2715-9.

79. Kwee TC, Kwee RM, Verdonck LF, et al. Magnetic resonance imaging for the detection of bone marrow involvement in malignant lymphoma. Br J Haematol. 2008;141(1):60–8. https://doi.org/10.1111/j.1365-2141.2008.07020.x.

80. Daldrup-Link HE, Henning T, Link TM. MR imaging of therapy-induced changes of bone marrow. Eur Radiol. 2007;17(3):743–61. https://doi.org/10.1007/s00330-006-0404-1.

81. Cieszanowski A, Lisowska A, Dabrowska M, et al. MR imaging of pulmonary nodules: detection rate and accuracy of size estimation in comparison to computed tomography. PLoS One. 2016;11(6):e0156272. https://doi.org/10.1371/journal.pone.0156272.

82. Regacini R, Puchnick A, Shigueoka DC, et al. Whole-body diffusion-weighted magnetic resonance imaging versus FDG-PET/CT for initial lymphoma staging: systematic review on diagnostic test accuracy studies. Sao Paulo Med J. 2015;133(2):141–50. https://doi.org/10.1590/1516-3180.2014.8312810.

83. Albano D, Patti C, Lagalla R, et al. Whole-body MRI, FDG-PET/CT, and bone marrow biopsy, for the assessment of bone marrow involvement in patients with newly diagnosed lymphoma. J Magn Reson Imaging. 2016;45(4):1082–9. https://doi.org/10.1002/jmri.25439.

84. Lin C, Itti E, Luciani A, et al. Whole-body diffusion-weighted imaging with apparent diffusion coefficient mapping for treatment response assessment in patients with diffuse large B-cell lymphoma: pilot study. Investig Radiol. 2011;46(5):341–9. https://doi.org/10.1097/RLI.0b013e3182087b03.

85. Chen Y, Zhong J, Wu H, et al. The clinical application of whole-body diffusion-weighted imaging in the early assessment of chemotherapeutic effects in lymphoma: the initial experience. Magn Reson Imaging. 2012;30(2):165–70. https://doi.org/10.1016/j.mri.2011.09.019.

86. Toledano-Massiah S, Luciani A, Itti E, et al. Whole-body diffusion-weighted imaging in Hodgkin lymphoma and diffuse large B-cell lymphoma. Radiographics. 2015;35(3):747–64. https://doi.org/10.1148/rg.2015140145.

87. Mohile NA, Deangelis LM, Abrey LE. The utility of body FDG PET in staging primary central nervous system lymphoma. Neuro-Oncology. 2008;10(2):223–8. https://doi.org/10.1215/15228517-2007-061.

88. Haldorsen IS, Espeland A, Larsson EM. Central nervous system lymphoma: characteristic findings on traditional and advanced imaging. AJNR Am J Neuroradiol. 2011;32(6):984–92. https://doi.org/10.3174/ajnr.A2171.

89. DeAngelis LM, Boutros D. Leptomeningeal metastasis. Cancer Investig. 2005;23(2):145–54.

90. Senocak E, Oguz KK, Ozgen B, et al. Parenchymal lymphoma of the brain on initial MR imaging: a comparative study between primary and secondary brain lymphoma. Eur J Radiol. 2011;79(2):288–94. https://doi.org/10.1016/j.ejrad.2010.01.017.

91. Rottnek M, Strauchen J, Moore F, et al. Primary dural mucosa-associated lymphoid tissue-type lymphoma: case report and review of the literature. J Neuro-Oncol. 2004;68(1):19–23.

92. Kuker W, Herrlinger U, Gronewaller E, et al. Ocular manifestation of primary nervous system lymphoma: what can be expected from imaging? J Neurol. 2002;249(12):1713–6. https://doi.org/10.1007/s00415-002-0919-6.

93. Nabavizadeh SA, Vossough A, Hajmomenian M, et al. Neuroimaging in central nervous system lymphoma. Hematol Oncol Clin North Am. 2016;30(4):799–821. https://doi.org/10.1016/j.hoc.2016.03.005.

94. Schroeder PC, Post MJ, Oschatz E, et al. Analysis of the utility of diffusion-weighted MRI and apparent diffusion coefficient values in distinguishing central nervous system toxoplasmosis from lymphoma. Neuroradiology. 2006;48(10):715–20. https://doi.org/10.1007/s00234-006-0123-y.

95. Barajas RF Jr, Rubenstein JL, Chang JS, et al. Diffusion-weighted MR imaging derived apparent diffusion coefficient is predictive of clinical outcome in primary central nervous system lymphoma. AJNR Am J Neuroradiol. 2010;31(1):60–6. https://doi.org/10.3174/ajnr.A1750.

96. Yamashita K, Yoshiura T, Hiwatashi A, et al. Differentiating primary CNS lymphoma from glioblastoma multiforme: assessment using arterial spin labeling, diffusion-weighted imaging, and (1)(8)F-fluorodeoxyglucose positron emission tomography. Neuroradiology. 2013;55(2):135–43. https://doi.org/10.1007/s00234-012-1089-6.

97. Pollock JM, Tan H, Kraft RA, et al. Arterial spin-labeled MR perfusion imaging: clinical applications. Magn Reson Imaging Clin N Am. 2009;17(2):315–38. https://doi.org/10.1016/j.mric.2009.01.008.

98. Kickingereder P, Sahm F, Wiestler B, et al. Evaluation of microvascular permeability with dynamic contrast-enhanced MRI for the differentiation of primary CNS lymphoma and glioblastoma: radiologic-pathologic correlation. AJNR Am J Neuroradiol. 2014;35(8):1503–8. https://doi.org/10.3174/ajnr.A3915.

99. Chinn RJ, Wilkinson ID, Hall-Craggs MA, et al. Toxoplasmosis and primary central nervous system lymphoma in HIV infection: diagnosis with MR spectroscopy. Radiology. 1995;197(3):649–54. https://doi.org/10.1148/radiology.197.3.7480733.

100. Kickingereder P, Wiestler B, Sahm F, et al. Primary central nervous system lymphoma and atypical glioblastoma: multiparametric differentiation by using diffusion-, perfusion-, and susceptibility-weighted MR imaging. Radiology. 2014;272(3):843–50. https://doi.org/10.1148/radiol.14132740.

101. Platzek I, Beuthien-Baumann B, Ordemann R, et al. FDG PET/MRI for the assessment of lymph node involvement in lymphoma: initial results and role of diffusion-weighted MR. Acad Radiol. 2014;21(10):1314–9. https://doi.org/10.1016/j.acra.2014.05.019.

102. Afaq A, Fraioli F, Sidhu H, et al. Comparison of PET/MRI with PET/CT in the evaluation of disease status in lymphoma. Clin Nucl Med. 2017;42(1):e1–7. https://doi.org/10.1097/RLU.0000000000001344.

103. Herrmann K, Queiroz M, Huellner MW, et al. Diagnostic performance of FDG-PET/MRI and WB-DW-MRI in the evaluation of lymphoma: a prospective comparison to standard FDG-PET/CT. BMC Cancer. 2015;15:1002. https://doi.org/10.1186/s12885-015-2009-z.

104. Grueneisen J, Sawicki LM, Schaarschmidt BM, et al. Evaluation of a fast protocol for staging lymphoma patients with integrated PET/MRI. PLoS One. 2016;11(6):e0157880. https://doi.org/10.1371/journal.pone.0157880.

105. Heacock L, Weissbrot J, Raad R, et al. PET/MRI for the evaluation of patients with lymphoma: initial observations. AJR Am J Roentgenol. 2015;204(4):842–8. https://doi.org/10.2214/AJR.14.13181.

106. Raad RA, Friedman KP, Heacock L, et al. Outcome of small lung nodules missed on hybrid PET/MRI in patients with primary malignancy. J Magn Reson Imaging. 2016;43(2):504–11. https://doi.org/10.1002/jmri.25005.

107. Atkinson W, Catana C, Abramson JS, et al. Hybrid FDG-PET/MRI compared to FDG-PET/CT in adult lymphoma patients. Abdom Radiol (NY). 2016;41(7):1338–48. https://doi.org/10.1007/s00261-016-0638-6.

108. Giraudo C, Raderer M, Karanikas G, et al. 18F-fluorodeoxyglucose positron emission tomography/magnetic resonance in lymphoma: comparison with 18F-fluorodeoxyglucose positron emission tomography/computed tomography and with the addition of magnetic resonance diffusion-weighted imaging. Investig Radiol. 2016;51(3):163–9. https://doi.org/10.1097/RLI.0000000000000218.

109. Mayerhoefer ME, Karanikas G, Kletter K, et al. Can interim 18F-FDG PET or diffusion-weighted MRI predict end-of-treatment outcome in FDG-avid MALT lymphoma after rituximab-based therapy?: a preliminary study in 15 patients. Clin Nucl Med. 2016;41(11):837–43. https://doi.org/10.1097/RLU.0000000000001395.

110. Ponisio MR, McConathy J, Laforest R, et al. Evaluation of diagnostic performance of whole-body simultaneous PET/MRI in pediatric lymphoma. Pediatr Radiol. 2016;46(9):1258–68. https://doi.org/10.1007/s00247-016-3601-3.

111. Sher AC, Seghers V, Paldino MJ, et al. Assessment of sequential PET/MRI in comparison with PET/CT of pediatric lymphoma: a prospective study. AJR Am J Roentgenol. 2016;206(3):623–31. https://doi.org/10.2214/AJR.15.15083.

112. Buck AK, Bommer M, Stilgenbauer S, et al. Molecular imaging of proliferation in malignant lymphoma. Cancer Res. 2006;66(22):11055–61. 66/22/11055 [pii]

113. Mena E, Lindenberg ML, Turkbey BI, et al. A pilot study of the value of 18F-fluoro-deoxy-thymidine PET/CT in predicting viable lymphoma in residual 18F-FDG avid masses after completion of therapy. Clin Nucl Med. 2014;39(10):874–81. https://doi.org/10.1097/RLU.0000000000000539.

114. Dhilly M, Guillouet S, Patin D, et al. 2-[18F]fludarabine, a novel positron emission tomography (PET) tracer for imaging lymphoma: a micro-PET study in murine models. Mol Imaging Biol. 2014;16(1):118–26. https://doi.org/10.1007/s11307-013-0659-2.

115. Hovhannisyan N, Guillouet S, Fillesoye F, et al. Evaluation of the specificity of [(18)F]fludarabine PET/CT in a xenograft model of follicular lymphoma: comparison with [(18)F]FDG and impact of rituximab therapy. EJNMMI Res. 2015;5:23. eCollection 2015. https://doi.org/10.1186/s13550-015-0101-7.

116. Hovhannisyan N, Dhilly M, Guillouet S, et al. Comparative analysis between [(18)F]Fludarabine-PET and [(18)F]FDG-PET in a murine model of inflammation. Mol Pharm. 2016;13(6):2136–9. https://doi.org/10.1021/acs.molpharmaceut.6b00050.

PET/MRI for Clinical Pediatric Oncologic Imaging

21

Maria Rosana Ponisio, Pooya Iranpour, Geetika Khanna, and Jonathan McConathy

Contents

21.1   Overview

PET/MRI has significant potential advantages over PET/CT for use in pediatric populations including decreasing radiation dose, reducing exposure to sedation and anesthesia, reducing the need for gadolinium-based MR contrast agents, and increasing convenience to children and their families through combining PET and MRI acquisition into a single imaging session. PET/MRI is a clinical reality and is in routine use at a number of academic centers as well as in a few private practices with some centers performing pediatric imaging. Although promising, PET/MRI

M.R. Ponisio • P. Iranpour • G. Khanna
Department of Radiology, Washington University in St. Louis, St. Louis, MO, USA

J. McConathy (✉)
Division of Molecular Imaging and Therapeutics, Department of Radiology,
University of Alabama at Birmingham, Birmingham, AL, USA
e-mail: jmcconathy@uabmc.edu

for pediatric oncology faces significant challenges including the high cost and relatively limited availability of PET/MRI systems, the lack of standardization across centers, limited evidence demonstrating the superiority of PET/MRI compared to PET/CT and other imaging modalities, and variable institutional utilization of PET and whole-body MR imaging in the diagnostic evaluation of children with cancer.

This chapter provides an overview of current and possible future uses of PET/ MRI for clinical oncologic imaging in children. PET/MRI has great potential for basic and translational research in children and adults, but the focus of this chapter is on the use of PET/MRI in routine patient care. The strengths and limitations of this technology and the available PET tracers for specific applications in pediatric oncology are key topics discussed here.

21.2 PET Tracers Relevant to Pediatric Oncology

PET uses compounds labeled with positron-emitting radionuclides to form three-dimensional tomographic images that reflect functional, metabolic, or biochemical information. The structure and pharmacologic properties of the PET tracer determine the biological information obtained through PET imaging, and a very wide range of targets including biological transporters, metabolic pathways, enzymes, and receptors have been successfully targeted with PET. The high sensitivity and molecular specificity of PET make this modality very valuable in oncologic imaging for both routine clinical and research applications. The physical properties of the positron-emitting radionuclide use in a PET tracer can affect resolution and dosimetry, and for some radionuclide the scanner settings and image reconstruction should be adjusted to obtain optimal image quality. An important limitation of PET is the low resolution compared to anatomic techniques such as CT and MRI. Hybrid imaging with PET/CT and PET/MRI allows collection of anatomic and molecular information in a single study.

The most widely used PET tracer for adult and pediatric oncologic imaging is the glucose analogue, 2-deoxy-2-[^{18}F]fluoro-D-glucose (FDG). Most of the PET/MRI studies discussed in this chapter utilize FDG as the PET tracer. FDG is transported into cells via glucose transporters and then phosphorylated by hexokinase enzymes, trapping FDG inside the cell [1]. Many cancer cells have upregulated glycolytic metabolism of glucose (i.e., conversion of glucose to lactate) even in the presence of adequate levels of oxygen to perform oxidative phosphorylation [2, 3]. This phenomenon is known as aerobic glycolysis (the Warburg effect) and is the basis for the utility of FDG-PET for detecting and assessing response to therapy in a wide range of human cancers. One of the limitations of FDG is the high uptake in inflammatory lesions which can lead to false-positive studies for malignancy. FDG also has high physiologic uptake in the brain and moderate uptake in the liver as well as excretion in the urine; this normal biodistribution can obscure malignant lesions in these locations. The uptake of FDG can be low in certain tumors with low glycolytic activity such as mucinous tumor histologies and low-grade neoplasms, leading to false negatives. Finally, FDG-PET evaluates only one aspect of cancer biology, and other

PET tracers may have better sensitivity and specificity for certain cancers and can provide biological information relevant to prognosis and therapy not available with FDG.

A number of PET tracers other than FDG have been developed and have potential utility for PET/MRI in pediatric oncology. However, there is limited data regarding the diagnostic utility of these tracers in children and very little data comparing PET/MRI to PET/CT with non-FDG-PET tracers. The PET tracer sodium [^{18}F]fluoride (NaF) is used for skeletal scintigraphy and is very sensitive for detecting blastic metastases as well as other processes causing increased turnover of the mineralized bone. Radiolabeled amino acids targeting system L amino acid transport can complement MRI for the evaluation of brain tumors by providing better assessment of non-enhancing regions in glioma and increasing the accuracy of assessment of brain tumors after therapy [4–6]. Peptide-based somatostatin receptor ligands labeled with Ga-68 include DOTATOC, DOTATATE, and DOTANOC which are particularly useful for tumors that express somatostatin receptors on their cell surface such as well-differentiated neuroendocrine tumors and meningiomas [7–10]. These somatostatin receptor imaging agents may have roles in evaluating neuroblastoma and pheochromocytoma in children and can also be used for therapy when they are labeled with therapeutic radionuclides such as Lu-177 or Y-90 [11, 12]. The amino acid 3,4-dihydroxy-6-[^{18}F]fluoro-D-phenylalanine (FDOPA) may also be useful for neuroendocrine tumors and for preoperative planning in children with congenital hyperinsulinemia [13–16].

There is also the potential to convert single photon computed tomography (SPECT) agents into PET agents by replacing I-123 or I-131 which are not suitable for PET with the positron-emitting radionuclide I-124. For example, sodium [^{124}I] iodide could be used for imaging differentiated thyroid cancer [17–19], and *meta*-iodobenzylguanidine (MIBG) labeled with I-124 could be used for PET imaging of neuroblastoma [20, 21]. However, these PET analogues of routinely used SPECT agents are not widely available, and very little data regarding their efficacy in pediatric patients are available.

21.3 Pediatric PET/MRI Protocols and Workflows

The available data from pediatric PET/MRI studies and the larger body of work in adult PET/MRI studies suggest that FDG-PET/MRI is equivalent to FDG-PET/CT in terms of whole-body staging for most cancers [22–27]. Many clinical PET/MRI studies are performed when both whole-body staging with PET and local tumor or organ staging with MRI are needed. In some anatomic regions such as the brain, liver, pelvis, and bone marrow, MRI provides superior soft tissue contrast and sensitivity to CT even in the absence of gadolinium-based MR contrast agents. In children and young adults with potentially curable cancers, PET/MRI decreases exposure to ionizing radiation by replacing CT with MRI as discussed in more detail later in this chapter.

In our practice, PET/MRI in the pediatric population is performed chiefly for the following indications: (1) dose reduction in pediatric patients who need a whole-body

PET alone, such as lymphoma; (2) pediatric patients who need a whole-body PET and a dedicated regional MRI, such as brain tumors, sarcomas, and neuroblastoma; and (3) pediatric patients who need a brain PET and MRI for epilepsy evaluation. Protocols in PET/MRI for adults and children typically are modified from standard dedicated MRI to maintain patient throughput and tolerance. The protocols for clinical PET/MRI are evolving, and this section reflects our experience as well as reports and protocols from other institutions. The aim of the modified MRI protocol should be that the entire scan (whole-body PET, whole-body MRI for attenuation correction/localization, and dedicated regional MRI as needed) can be completed within less than 60 min. If regional dedicated MRI is not needed, we aim to complete the whole-body simultaneous PET/MRI in around 30 min. Using this approach, it is feasible to scan children as young as 8 years old without sedation. Table 21.1 gives an example of a modified MRI protocol performed in the simultaneous PET/MRI setting. The whole-body portion is typically performed first in case the study must be terminated early, maximizing the chance the radiopharmaceutical administration results in a diagnostic study. Although not optimal, the regional MRI can be performed separately if the entire whole-body and regional PET/MRI study cannot be completed.

When performing whole-body PET-MRI, multiple phase array coils should be used as opposed to the body coil to provide adequate signal-to-noise ratio. The patient's arms are placed by their side and included in the field of view for attenuation correction and whole-body imaging. If dedicated imaging of the head is not needed, the head coil can be left off, especially in claustrophobic patients. The scan starts with whole-body simultaneous acquisition of PET data, two-point Dixon sequences, single-shot fast spin echo (SSFSE) imaging, and inversion recovery or diffusion-weighted imaging. We typically acquire these sequences in the axial plane

Table 21.1 Example of a modified liver MRI protocol for detection of hepatic metastases used in pediatric simultaneous PET/MRI

Standard liver MRI protocol	Modified liver MRI protocol
Three-plane localization	Part of whole-body acquisition
Coronal single-shot fast spin echo	Omitted
Axial single-shot fast spin echo	Part of whole-body acquisition
Coronal steady-state free procession (e.g., true FISP. FIESTA)	Omitted
Axial coherent gradient echo	Omitted
Axial in/opposed phase	Part of whole-body acquisition
Axial T2 fast spin echo fat saturated	Axial T2 fast spin echo fat saturated
Axial diffusion weighted (b-values 50, 400, 800 mm/s^2)	Axial diffusion weighted (b-values 50, 400, 800 mm/s^2)
Pre-contrast T1 ultrafast gradient echo (e.g., VIBE, LAVA)	Pre-contrast T1 ultrafast gradient echo (e.g., VIBE, LAVA)
Post-contrast T1 ultrafast gradient-echo dynamic × 3	Post-contrast T1 ultrafast gradient-echo dynamic × 3

Some of the standard liver MRI protocol sequences are included in the whole-body MRI acquisition, while others are omitted in the modified liver MRI protocol to reduce the overall length of the examination without reducing detection of metastases

and reconstruct and compose images in the coronal plane to get whole-body images. Acquiring these images in a contiguous rather than interleaved fashion allows reconstruction without blurring or stair-stepping artifact. The scan time at each station is around 3 min, with a z-axis coverage of 25 cm/station. So, whole-body imaging in a typical teenager is achieved in six stations, resulting in an active scanning time of ~20 min for the basic whole-body PET/MRI scan.

The two-point Dixon sequence automatically generates four image sets: in phase, out of phase, fat only, and water only. These are used to create the MR-based attenuation correction map that is applied to the PET data. Studies in adults indicate that the image sets derived from the Dixon sequence can provide similar anatomic localization as the non-contrast CT portion of FDG-PET/CT studies [24, 28]. The in phase/out of phase images should be evaluated for evidence of liver iron deposition, a common problem in pediatric cancer survivors [29]. The water-only sequence is the equivalent of a pre-contrast T1-weighted fat-saturated image and can provide good anatomic detail. The SSFSE sequence is optional but is useful for providing an overview of anatomy and for localization. These are acquired free breathing, without navigation, when performed simultaneous with acquisition of the PET data. Diffusion-weighted imaging is typically performed with three different b-values, 50, 400–500, and 800–1000 mm/s^2, which are then used to generate the apparent diffusion coefficient (ADC) map. The low b-value images have the most T2 weighting and can function as T2 fat-saturated/inversion recovery sequence, which is useful for both lesion detection and localization. Lesion characterization as benign vs. malignant is best performed on the high b-value images in correlation with the ADC map, keeping in mind that several benign lesions (such as focal nodular hyperplasia in the liver) can show diffusion restriction [30].

After the whole-body acquisition, dedicated anatomic imaging of the primary site for locoregional staging or specific metastatic site in question (such as the liver) is performed without and with intravenous contrast. There is an increasing body of literature in the pediatric setting that has questioned the need for the routine use of intravenous contrast in follow-up of pediatric cancer patients [31]. The avoidance of intravenous contrast can help decrease the duration of the scan, avoid the unknown long-term consequences of intracranial gadolinium deposition, and most importantly replace the use of gadolinium-based contrast agents with organ-/tumor-specific contrast agents—such as ferumoxytol for the evaluation of lymph nodes [32–34]. Our experience has been that intravenous contrast is needed for evaluation of visceral metastasis, especially in organs with relatively high physiologic FDG uptake such as the brain, liver, and spleen. Use of hepatocyte-specific contrast agents with delayed imaging obtained in the hepatocyte phase can demonstrate liver metastasis with high sensitivity as seen in Fig. 21.1.

There are several challenges with hybrid PET/MRI scanning that must be considered. The long duration of scans compared to PET/CT may not be tolerated by some patients and can negatively impact patient throughput. The current clinically available PET/MRI systems have 3 T magnets which can lead to encountering specific absorption rate (SAR) limits especially when scanning smaller children and increased susceptibility artifacts such as from bowel gas/surgical clips compared to

MRI at 1.5 T. In addition, hybrid PET/MRI remains less sensitive than CT for the detection of subcentimeter pulmonary metastasis [35–37], so dedicated chest CT is still needed in pediatric tumors that are known to metastasize to the lungs. The use of ultrashort echo time sequences allows better delineation of pulmonary nodules compared with conventional dual-echo gradient-echo sequences and may in part overcome this limitation of PET/MRI [38].

For patients who need a chest CT evaluation of pulmonary metastasis such as sarcoma patients, a non-contrast chest CT is performed before or after the PET/MRI to avoid dependent atelectasis in the lungs. Intravenous contrast is not given for this CT as mediastinal and hilar nodes can be evaluated by PET/MRI and a non-contrast chest CT can be performed without sedation in the vast majority of children, irrespective of age. The nuclear medicine technologist and MRI technologist work in conjunction to screen and prep the patient, while scanning is performed primarily by the MRI technologist. In our institution, joint reading is performed for all PET/MRI scans by nuclear medicine physicians and radiologists. If a dedicated MRI is performed, two reports are generated; however, in patients who undergo the PET/MRI in lieu of a PET/CT with basic whole-body MRI sequences only, only one report is generated by the nuclear medicine physicians.
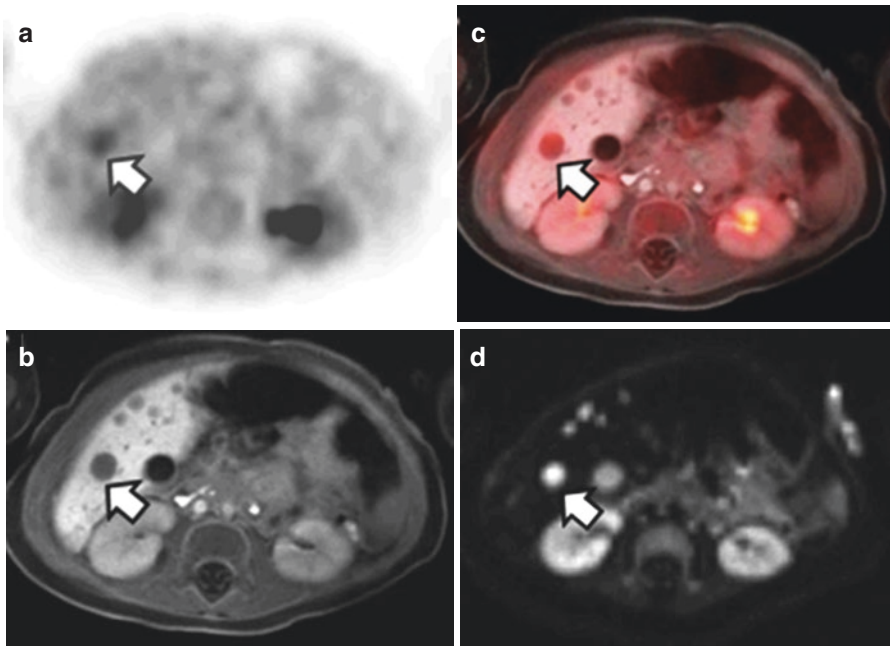

Fig. 21.1 FDG-PET/MRI performed in a 4-month-old girl after recent resection of a right adrenal neuroblastoma. During surgery, liver metastases were discovered that were not well seen on preoperative CT. Whole body FDG PET/MRI shows hepatic lesions which are FGD-avid (**a**), hypoenhancing on the hepatobiliary phase MRI (**b**, **f**) and demonstrates restricted diffusion (**d**). Smaller lesions were not identified on FDG-PET but are well visualized on the hepatobiliary phase and DWI (**d**, **h**). (**a**, **e**) FDG-PET; (**b**, **f**) hepatobiliary phase MRI; (**c**, **g**) fused PET/MRI; (**d**, **h**) Diffusion weighted imaging (DWI); Maximum intensity projection (MIP) is also shown (**i**)
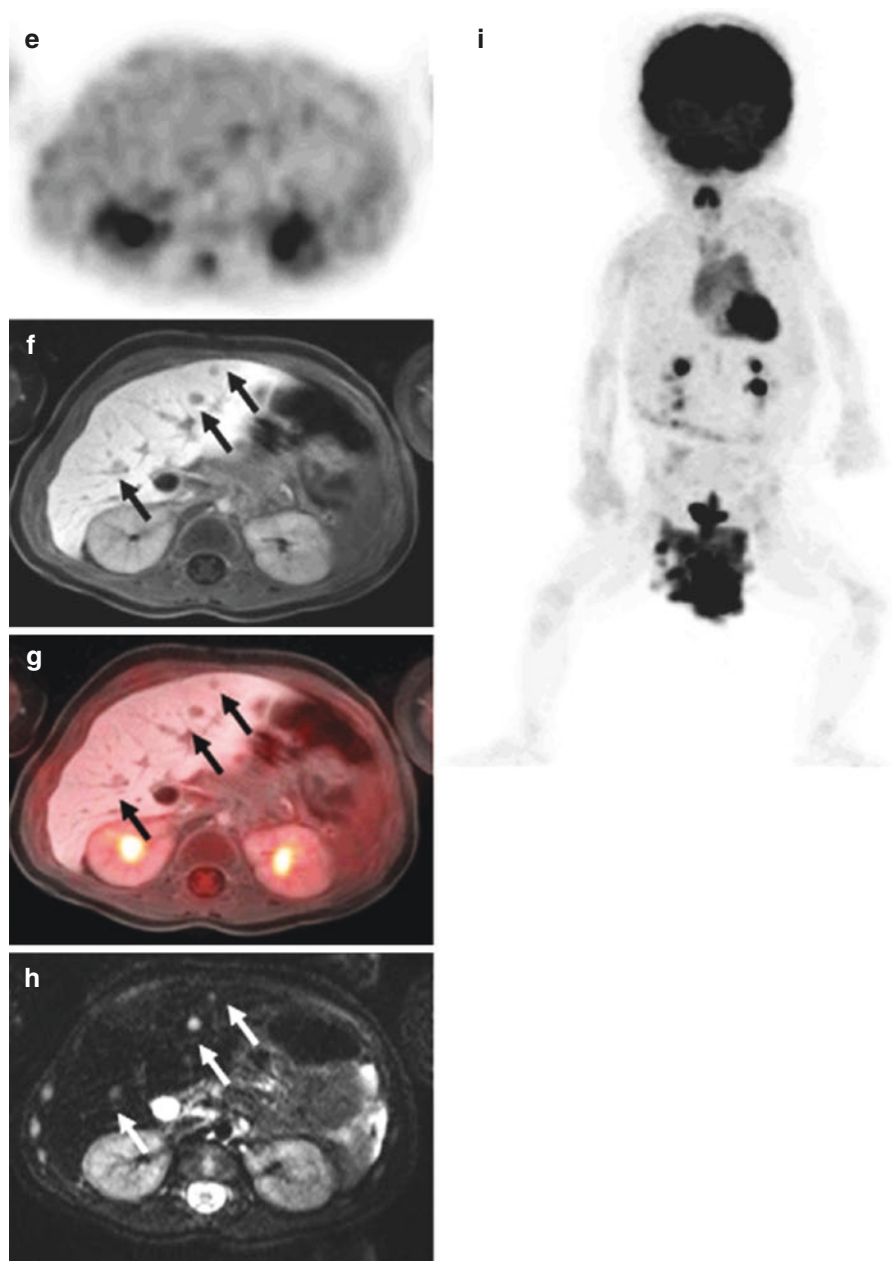
Fig. 21.1 (continued)

21.4   Dose Reduction with PET/MRI

In recent years, there have been major initiatives aimed at reducing ionizing radiation dose from medical imaging. These dose reduction efforts such as the Image Gently campaign for pediatric patients are motivated by the increased utilization of diagnostic imaging combined with the small increased risk of cancer incidence and mortality related to ionizing radiation exposure based on the linear no-threshold model [39]. A general principle that applies to all diagnostic imaging techniques that utilize ionizing radiation is to impart the minimum patient dose needed to answer the clinical question.

PET/MRI has the potential to reduce the radiation dose compared to PET/CT without reducing diagnostic imaging quality by substituting MRI for CT and by reducing the dosage of the PET tracer. However, PET agent still confers a substantial portion of the patient dose, and dose reduction by using PET/MRI instead of PET/CT for [^{18}F]FDG studies ranges from approximately 39 to 73% based on published comparisons [22, 23, 40, 41]. The variability in dose reduction is in large part due to different PET/CT hardware and CT protocols across centers.

Comparisons of the relative radiation exposure from different imaging techniques (e.g., PET compared to CT) are typically expressed as the effective dose (ED) with units of mSv or rem. The ED is a whole-body dose that accounts for both the radiation weighting factor and the tissue weighting factor, which defines the radiosensitivity of each organ that is involved [42, 43]. The ED is equal to what the whole-body equivalent dose of ionizing radiation would be if emitted and/or transmitted uniformly. The ED related to the amount of administered activity from the PET tracer increases with younger ages. For example, the ED related to [^{18}F]FDG is 95 μSv/MBq for a 1-year-old child, 37 μSv/MBq for a 10-year-old child, and 19 μSv/MBq for an adult [44].

The biodistribution, half-life, and emission profile of positron-emitting radionuclide used for labeling affect the dosimetry of a PET tracer. Factors that increase the ED in PET studies include high and persistent tracer accumulation in radiosensitive organs, long physical half-life of the radionuclide, and high fractions of emissions resulting from nuclear decay (e.g., gamma rays) other than positrons. For clinical PET studies, using a different PET radionuclide is generally not an option, so reducing the administered dosage of the PET tracer is the primary method for reducing radiation dose to the patient from the PET component of the study.

Patient dose from CT depends on the tube voltage (kV or kVp), the milliampere-seconds (mA-S), the gantry pitch, and the total beam width [45]. These parameters are often adjusted in PET/CT examinations to impart a lower patient dose than a typical diagnostic CT but still provide substantial structural and morphological information that can aid in the interpretation of the PET findings. The CT dose can be lowered further if only attenuation correction is needed, but only limited structural and morphological information can be obtained from these types of CT studies. The overall estimated increased risk of cancer associated with diagnostic imaging is low compared to the lifetime risk of cancer but is not zero [39, 46]. Because the additional risk for cancer associated with PET/CT is small compared to the overall risk of developing cancer, PET/CT will remain a viable modality for pediatric oncologic imaging even if PET/MRI becomes more widely available.

PET/MRI eliminates the CT portion of the examination while still providing attenuation correction and anatomical localization, and there are additional opportunities for dose reduction [23]. The patient dose related to the PET radiopharmaceutical can be reduced through longer image acquisition times and/or higher sensitivity PET detectors which can reduce the dosage of radiopharmaceutical required [22, 47–49]. Longer PET acquisition times to match that of the MRI examination can also be used to compensate for smaller dosages of the PET tracer. However, prolonged image acquisition must be balanced with patient tolerance as longer imaging times may result in degraded imaging quality due to patient's motion and increased anesthesia time in younger patients.

21.5   Specific Applications of PET/MRI in Pediatric Oncology

21.5.1 Lymphoma

Lymphoma represents 12% of all malignancy in the pediatric population, and of these 40% are Hodgkin lymphomas (HL) [50]. Nodular sclerosis is the most common classical HL subtype occurring prevalently in adolescents. The most common sites involved by HL include mediastinal, cervical, and axillary lymph nodes. Non-Hodgkin lymphoma (NHL) accounts for 60% of childhood lymphomas and has its peak incidence at the age of 7 years. In the pediatric population, NHL is most often an aggressive systemic disease defined by mature B cell immunophenotype. The most common pediatric NHL is Burkitt lymphoma and B cell lymphoblastic lymphoma which represent 40–50% of cases. The classic presentation of lymphoblastic lymphomas, a nodal predominant form of acute lymphoblastic leukemia, is characterized by a large mediastinal mass and infiltration of the spleen, bone marrow, central nervous system, and peripheral lymph nodes. Low-grade NHL such as follicular and mantle cell lymphoma occur in children but are less common than in adults.

The majority of children with lymphoma have a good prognosis, with long-term survival rates >80% following treatment with chemotherapy or in combination with radiotherapy [51–53]. However, survivors of lymphoma are at high risk of second cancers which have been linked to the radiation field. The most common second malignancies include breast cancer in girls, followed by thyroid and gastrointestinal cancer, leukemia, and soft tissue sarcoma [54–56]. Additional side effects include impaired fertility, particularly in boys secondary to cumulative doses of alkylating agents, and treatment-associated cardiovascular disease [57]. Thus, there has been a shift in treatment paradigm, with emphasis on reducing iatrogenic toxicity and late side effects of chemotherapy in this population with increasing life expectancy. This has placed increased emphasis on diagnostic imaging to provide accurate information regarding the staging and response assessment for correct stratification and treatment management.

The role of whole-body MRI (WBMRI) has gained increased relevance for the evaluation of children with lymphoma for initial staging, monitoring treatment, and evaluation of treatment-related side effects, including corticoid-related osteonecrosis, which is an important cause of morbidity [58–60]. WBMRI has the advantages of not using ionizing radiation and providing high soft tissue contrast; however, one

key limitation is the lack of ability to distinguish between benign and malignant lymph nodes, even with the combination of diffusion-weighted imaging and anatomical criteria [61, 62]. A recent study in adult lymphoma patients [63] reported that whole-body diffusion-weighted MRI (WB-DW-MRI), which allowed for calculation of apparent diffusion coefficients (ADC), showed an inferior performance than that of FDG-PET/CT/MRI especially for staging, distinction of nodal and extra-nodal disease, and differentiation of high-grade and low-grade lymphoma.

FDG-PET/CT is a well-established imaging modality for staging and therapy response assessment on pediatric lymphoma patients. The majority of aggressive lymphoma subtypes demonstrate high FDG uptake, with the exception of extra-nodal marginal zone lymphoma and small lymphocytic lymphoma [64]; however, lower-grade lymphomas rarely present in pediatric patients. Accurate initial staging is crucial to define treatment, including intensity of chemotherapy and extension of radiation fields, in order to avoid unnecessary treatment-related side effects. FDG-PET/CT shows markedly greater sensitivity, specificity, and accuracy (95.9%, 99.7%, and 99.6%, respectively) compared with conventional imaging modalities (70.1%, 99.0%, and 98.3%, respectively). Additionally, several studies have reported that FDG-PET/CT imaging changed patient management in 12–50% of the cases [65–67].

In response assessment, FDG-PET has shown high specificity, sensitivity, and negative predictive value (NPV), with various studies concluding that NPV is a better guide of favorable prognosis than positive predictive value (PPV) [68, 69]. The role of NPV in patient management is important, providing a predictor for decreasing therapy intensity to reduce the potential incidence of toxicity in good responders. A significant advantage of PET over conventional imaging is the ability to distinguish residual active tumor from fibrosis/scarring. Responder patients show residual morphological abnormalities, most commonly persistent soft tissue mass with lack of increased FDG activity consistent with treated, nonviable tumor. An example of FDG-PET/MRI and FDG-PET/CT in Hodgkin lymphoma is shown in Fig. 21.2.

PET/MRI has been gaining acceptance in pediatric lymphoma. Table 21.2 summarizes the results of selected recent publications. The limited data on pediatric patients have demonstrated that FDG-PET/MRI is feasible in pediatric patients and provides similar diagnostic performance compared to standard of care FDG-PET/CT [70] with substantial reduction in radiation exposure (range 39–73%) [23, 40, 71], by eliminating the CT component of PET/CT. This is especially important in this population with potentially curable disease, where serial imaging is required during treatment monitoring and/or at completion of therapy. The study by Schafer et al. [23] performed on pediatric cancer patients (lymphoma = 7/14) showed that PET/MRI identified additional findings compared with PET/CT, including malignant bone marrow and renal infiltration and a soft issue metastasis [23].

We recommend that DWI be a standard sequence in whole-body PET/MRI protocols in pediatric oncology, in agreement with prior publications [72, 73]. Restricted diffusion suggests increased cellularity and a change in the nuclear-cytoplasmic ratio and therefore suggests the possibility to identify additional lesions, in particular extra-nodal lymphomatous involvement of the liver, spleen, and kidneys.
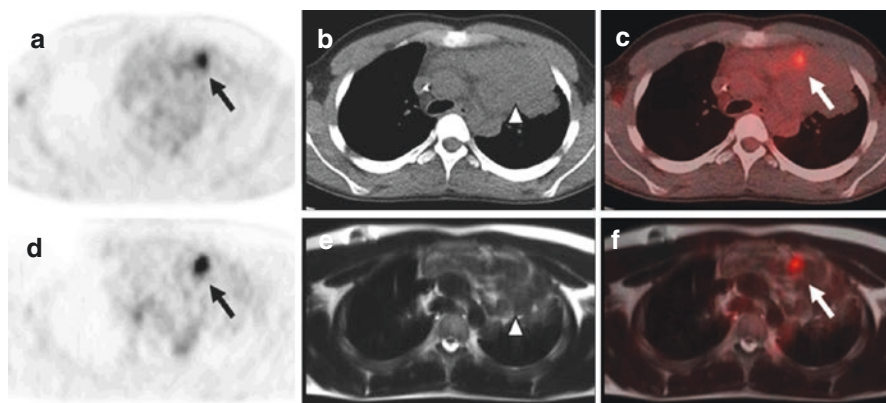
Fig. 21.2 Comparison of simultaneous FDG-PET/MRI with FDG-PET/CT in an 18-year-old male with large B-cell lymphoma for distinguishing fibrosis from viable lymphoma. The PET/MRI was performed immediately following the PET/CT using the same dose of FDG. FDG-PET/CT (**a**–**c**) and simultaneous whole body FDG-PET/MRI (**d**–**f**) demonstrate a large anterior mediastinum soft tissue mass (*arrow heads*) with a focus of increased FDG activity (*arrows*) suspicious for viable tumor. The remaining mass does not demonstrates increased FDG metabolic activity and likely represents scarring/fibrosis (*arrow head*). (**a**) FDG-PET from PET/CT acquisition; (**b**) CT mediastinal window; (**c**) fused FDG-PET/CT; (**d**) FDG-PET from PET/MRI acquisition; (**e**) T2 single shot fast spin echo; (**f**) fused FDG-PET/MRI

Table 21.2 Summary of selected studies evaluating the diagnostic utility of FDG-PET/MRI for pediatric lymphoma

| Study	Number of patients	Average dose reduction	Major findings
Kirchner et al. [75]	12	Not reported	• FDG-PET/MRI was superior to whole-body DWI
			• MR contrast and DWI did not improve diagnostic accuracy of FDG-PET/MRI
Sher et al. [41]	25	45%	• FDG-PET/MRI was similar to PET/CT for
			– Lesion detection and classification
			– Ann Arbor staging
			– FDG uptake strongly correlated with PET/CT
Schafer et al. [23]	18	73%	• FDG-PET/MRI is clinically feasible
			• Equivalent rates of lesion detection to PET/CT
			• CT examination of the thorax might be necessary
Ponisio et al. [40]	8	39%	• FDG-PET/MRI is clinically feasible
			• FDG-PET/MRI was similar to PET/CT for
			– Lesion detection
			– SUV measurements
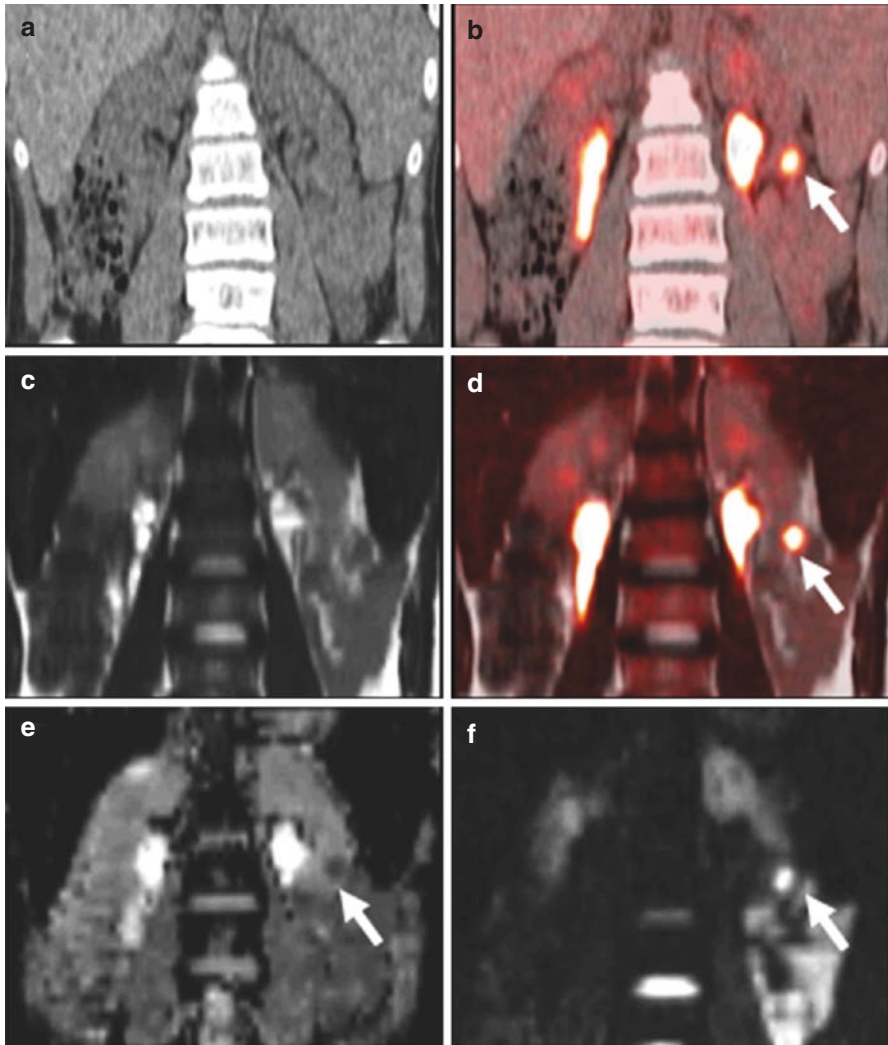
Fig. 21.3 17-year-old male with diffuse large B-cell lymphoma with focal left renal involvement. Restricted diffusion seen on DWI (**f**, *white arrow*) allowed better identification of the renal lesion and differentiation from excreted FDG in the collecting system. The lesion is not well identified on non-contrast CT (**a**) or T2 single shot fast spin echo images (**c**). (**a**): CT from PET/CT; (**b**) fused FDG-PET/CT; (**c**) T2 single shot fast spin echo; (**d**) fused FDG-PET/MRI; (**e**)ADC; (**f**) DWI

As illustrated in Fig. 21.3, the restricted diffusion evaluated on the DWI sequence assisted in the detection and characterization of a FDG-avid renal lesion that was missed on PET/CT due to being obscured by adjacent excreted activity in the renal collecting system [40].

Lymphoma patients undergo multiple contrast examination for staging and treatment monitoring; however, there is an increasing clinical concern over non-macrocyclic gadolinium-based agent deposition in the brain and body after serial examinations [74]; thus, careful review of contrast indication is highly

recommended. A recent publication [75] confirms the feasibility and high diagnostic accuracy of non-contrast FDG-PET/MRI and FDG-PET and that neither the application of contrast agents nor DWI leads to noticeable diagnostic improvement. Furthermore, the study concluded that PET/MRI is significantly superior to WB-MR-DWI for the evaluation of pediatric lymphoma. Agents such as ferumoxytol, an off-label MRI contrast agent, have been proposed as an alternative; however, there is limited pediatric data on its feasibility.

In summary, preliminary data demonstrate that PET/MRI is feasible in pediatric lymphoma patients and comparable to PET/CT for staging and treatment response assessment. Replacement of PET/CT with PET/MRI provides superior soft tissue contrast and functional MR imaging capabilities which can aid in lesion detection especially in solid organs, decreases exposure to ionizing radiation, and potentially limit the use of gadolinium-based contrast agents.

21.6 Brain Tumors

Primary brain tumors are the second most common tumor of childhood after leukemia and represent approximately 25% of childhood neoplasms [76]. Pediatric brain tumors are a diverse group of neoplasms with a wide range of biological aggressiveness and prognosis [77]. Key categories include astrocytomas and other tumors of glial origin, brain stem gliomas, CNS embryonal tumors including medulloblastoma, pineal tumors, CNS germ cell tumors, craniopharyngioma, ependymoma, and choroid plexus tumors. Treatment modalities for brain tumors include surgical resection, radiation therapy, and systemic therapies with cytotoxic, antiangiogenic, and immune-modulating agents. Depending on the tumor type and location, therapy often combines two or more of these modalities. A common treatment regimen is surgical resection followed by radiation therapy often in combination with chemotherapy. Over 70% of children with brain tumors will survive for over 5 years after diagnosis, but long-term disabilities are common due to both the tumor itself and the effects of treatment.

Brain MRI with contrast is the cornerstone of neuroimaging for pediatric neuro-oncology from the time of initial diagnosis through treatment planning and monitoring to long-term follow-up. Contrast-enhanced MRI has excellent sensitivity for detecting tumor with disrupted blood-brain barriers (BBB), while T2, FLAIR, and DWI sequences are valuable for evaluating non-enhancing lesions that do not have a grossly disrupted BBB. Despite its strengths, MRI has substantial limitations for defining tumor boundaries, guiding biopsy for non-enhancing lesions, and distinguishing treatment effects from recurrent tumor.

Combined PET/MRI is well suited to brain tumor imaging as the PET acquisition including dynamic studies for many PET tracers can be performed in the 45–60 min time required for a brain tumor MRI protocol. Data from adult patients suggest the kinetics of O-(2-[^{18}F]fluoroethyl)-L-tyrosine (FET) can distinguish high-grade from low-grade gliomas and can help distinguish radiation necrosis from recurrent tumor [78–82]. While dynamic PET is readily acquired on PET/CT systems, the dynamic acquisition occupies the PET/CT scanner much longer than a static brain or whole-body PET/CT study which can reduce patient throughput. The duration of dynamic PET studies with small-molecule PET tracers such as FDG and radiolabeled amino

acids is well matched to MRI for brain tumors. Unlike some other oncologic applications, CT plays a much smaller role in neuro-oncology compared to MRI and thus provides little beyond attenuation correction during PET/CT examinations.

Although FDG is effective for many solid tumors, it has substantial limitations in neuro-oncology. The high physiologic uptake of FDG in normal gray matter can obscure tumor tissue even when there is FDG uptake by tumor tissue. Additionally, posttreatment inflammation can lead to false-positive studies. Nevertheless, FDG does have some favorable properties for neuro-oncology. As in adults, higher FDG uptake is associated with more aggressive and higher-grade brain tumors in children [83, 84]. The most common pediatric brain tumors with high FDG uptake are glioblastoma and medulloblastoma, although some low-grade pilocytic astrocytomas can have high FDG uptake. There is significant overlap between many high- and low-grade tumors which can make assessment of tumor grade in an individual patient with FDG-PET alone challenging. FDG-PET has also been used to guide brain tumor biopsy based on the area of highest uptake [85, 86]. FDG-PET has been used to distinguish radiation necrosis from recurrent tumor when ambiguous contrast-enhancing lesions are present on MRI after radiation therapy. Recurrent high-grade gliomas typically have higher FDG uptake than radiation necrosis which has been proposed as a method for distinguishing these entities, although utility of FDG-PET for this application remains controversial [87–91]. An example of increased FDG uptake in a recurrent medulloblastoma is shown in Fig. 21.4.

Radiolabeled amino acids targeting system L amino acid transporters including 3,4,-dihydroxy6-[^{18}F]fluoro-L-phenylalanine (FDOPA), L-[^{11}C]methionine (MET), and FET are well-established PET tracers for brain tumor imaging. In 2016, this class of tracers was incorporated into the Response Assessment for Neuro-Oncology (RANO) recommendations for brain tumors [5]. System L transport is activated at the blood-brain barrier (BBB), allowing these tracers to reach the entire tumor volume. Additionally, higher levels of the system L family member, LAT1 (SLC7A5),
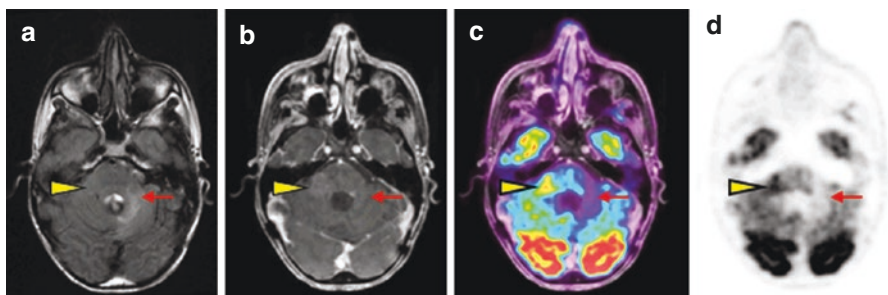

Fig. 21.4 FDG-PET/MRI in a 20-year-old male with suspected recurrence of medulloblastoma. A representative FLAIR image (**a**) demonstrates subtle signal hyperintensity in the region of the right cerebellar peduncle (*yellow arrow head*) and more conspicuous hyperintensity in the left cerebellar hemisphere (*red arrow*). There is contrast enhancement in the right middle cerebellar peduncle but not in the left cerebellar hemisphere (**b**). Fused FDG-PET/MRI (**c**) and PET only (**d**) images demonstrate increased FDG uptake in the right cerebellar peduncle lesion (*yellow arrow head*) but not the left cerebellar hemisphere lesion (*red arrow*), most consistent with recurrence and treatment effect in these locations, respectively. (**a**) FLAIR; (**b**) post-contrast T1; (**c**) fused FDG-PET/MRI; (**d**) FDG-PET

are associated with shorter overall survival in adult gliomas [92–94]. This class of PET tracers has been used extensively in adult neuro-oncology for surgical planning, monitoring response to chemotherapy, and detecting recurrent gliomas after completion of therapy [82, 95–99]. Although there are differences between FDOPA, MET, and FET, they have similar properties in terms of visualizing brain tumors and defining tumor margins [96, 100–102]. Compared to FDG, these tracers have relatively low uptake in the normal brain and less uptake by inflammatory lesions.

Limited studies in pediatric populations suggest that FET and other amino acids targeting system L transport have similar favorable diagnostic properties in pediatric patients as in adults [85, 103–106]. These data suggest that amino acid PET can guide stereotactic biopsy, distinguish high-grade from low-grade tumors, guide surgical resection, monitor response to systemic therapies, and distinguish treatment effects such as radiation necrosis from recurrent tumor. Larger studies are needed to define sensitivity, specificity, and diagnostic accuracy for these applications of amino acid PET in children. Examples of MET-PET/MRI to guide stereotactic biopsy and FDOPA-PET/MRI to monitor response to antiangiogenic therapy are shown in Figs. 21.5 and 21.6, respectively. Currently, very few studies have used amino acid PET combined with simultaneous PET/MRI in children with brain tumors [107, 108]. These studies demonstrate that simultaneous amino acid PET/MRI is feasible in pediatric neuro-oncology patients and that many older children can tolerate the 45 min PET/MRI studies without sedation or anesthesia.

21.7   Sarcoma

Pediatric sarcomas are a heterogeneous group of tumors accounting for approximately 10% of childhood solid tumors, where the various subtypes have distinct biological patterns and incidence (National Cancer Institute. Homepage on the Internet. Available at: http://www.cancer.gov. Accessed February 1, 2016). Sarcomas are divided into two main groups: bone sarcoma (BS) and soft tissue sarcomas (STS). The most common bone sarcomas are osteosarcoma (OS) and Ewing sarcoma (ES); both tumors have a peak incidence during adolescence with the presence of metastases at diagnosis being one of the strongest predictors of survival [109]. The soft tissue sarcomas are further subdivided into rhabdomyosarcomas (RMS), the most common soft tissue malignancy in children and adolescent, and non-rhabdomyosarcomas (N-RMS) which are mainly seen in adolescents. The two most common histologic RMS variants encountered in the pediatric population are embryonal rhabdomyosarcomas (ERMS) which occur in about 65–75% of patients and alveolar rhabdomyosarcoma (ARMS) subtypes.

Treatment of primary musculoskeletal malignancies requires systemic multi-agent therapy, including systemic chemotherapy and local control of tumors. Local-regional control may be achieved with surgery and/or radiation therapy and neoadjuvant chemotherapy. Lesions inadequately treated locally are associated with poor outcome and treatment failure. The 3–5-year event-free survival rates for patients with localized sarcomas are 60–70% [110], for patients with metastatic disease below 20–30%, and for patients with relapsed disease less than 10–20% [111–113].
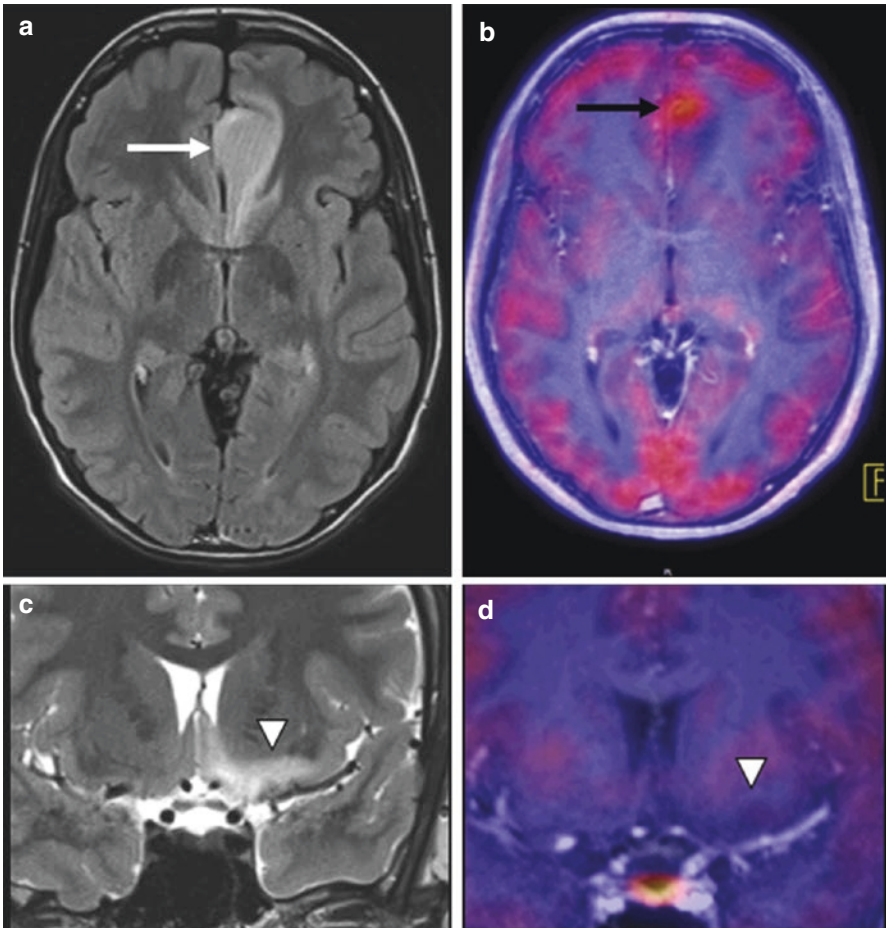
Fig. 21.5 MET-PET/MR imaging in a 15-year-old boy with a non-enhancing multifocal primary brain tumor. The FLAIR MR image (**a**) shows signal hyperintensity in the left frontal lobe adjacent to the falx (*white arrow*). The T2-weighted MR image (**c**) shows signal hyperintensity more inferiorly in the left from lobe (*arrow head*). The fused MET-PET/MR images show focal uptake in the left frontal lesion along the falx (**b**, *black arrow*) but not in the more inferior left frontal lobe (**d**). This focus of increase MET uptake was used to guide stereotactic biopsy and yielded anaplastic astrocytoma. *This figure is courtesy of Drs. Franz Wolfgang Hirsch and Regine Kluge from the University Hospital of Leipzig, Germany*. (**a**) FLAIR; (**b**) fused MET-PET/MRI post-contrast T1; (**c**) T2; (**d**) fused MET-PET/MRI post-contrast T1

The frequency of distant metastasis in pediatric sarcomas varies from 10 to 12% [60]. Regional lymph node disease is a component of the risk-based treatment stratification for rhabdomyosarcoma, and it has been noted that regional lymph node involvement affects the prognosis in patients with alveolar RMS, while outcomes in patients with nodal involvement (N1) are more similar to distant metastatic disease rather than local disease [114].
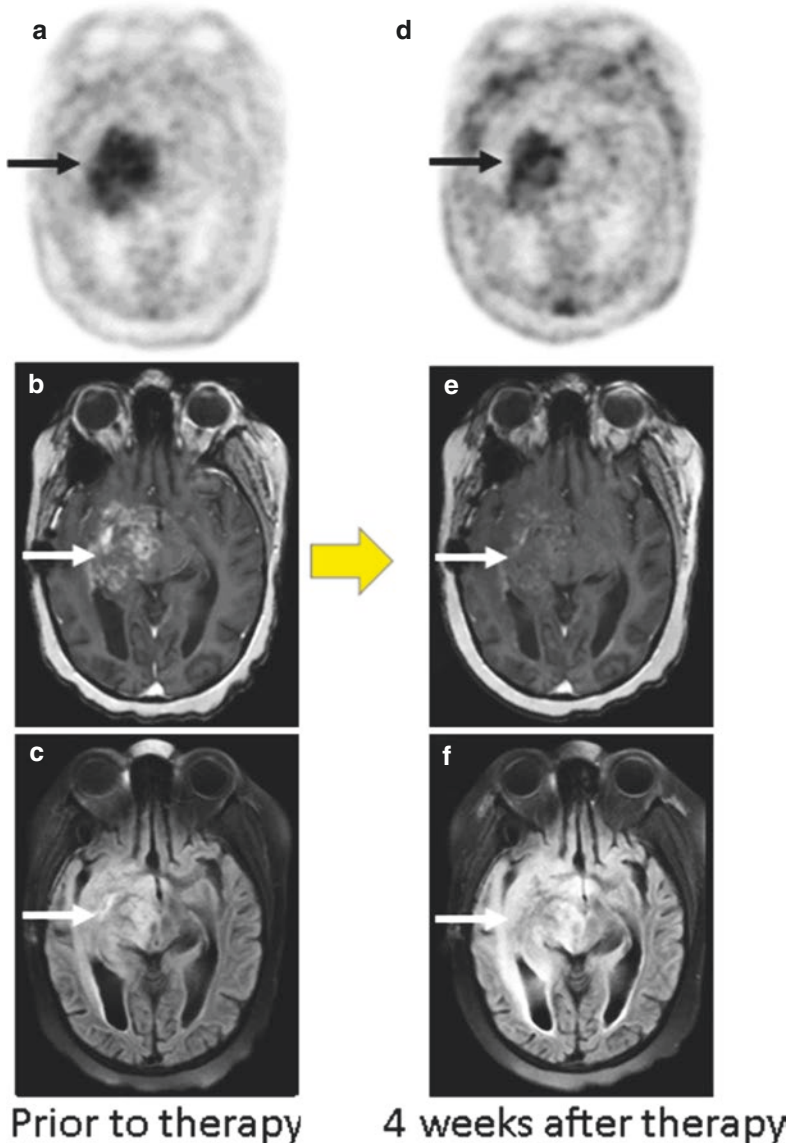
Fig. 21.6 FDOPA-PET/MR imaging in an 8-year-old girl with small cell glioma before and after bevacizumab therapy. The initial FDOPA-PET image (**a**) demonstrates increased uptake throughout the mass (*arrow*) involving the right frontal and temporal lobe as well as the brainstem. This mass shows heterogeneous enhancement on the post-contrast MR image (**b**) and FLAIR signal hyperintensity (**c**). After 4 weeks of bevacizumab, the uptake of FDOPA decreased slightly but there is persistent activity (**d**). The contrast enhancement has nearly completely resolved (**e**), but the FLAIR signal abnormality is unchanged (**f**). The persistent FDOPA uptake suggests poor response to therapy, and the patient subsequently had progressive disease. This case was part of a recent publication examining the potential of FDOPA-PET/MRI to predict response to bevacizumab early in the course of therapy [108]. (**a**) pre-bevacizumab FDOPA-PET; (**b**) pre-bevacizumab post-contrast T1; (**c**) pre-bevacizumab FLAIR; (**d**) post-bevacizumab FDOPA-PET; (**e**) post-bevacizumab post-contrast T1; (**f**) post-bevacizumab FLAIR

Although musculoskeletal sarcomas may have distinguishing imaging features on radiograph or CT, MRI is the preferred modality for assessment of the primary tumor size and extent of organ involvement due to its superior soft tissue contrast [115]. However, the role of MRI is limited in assessment of treatment response and follow-up [116] due to tumor changes during the regression phase, accounting for necrosis, hemorrhage, proliferation of granulation tissue, fibrosis, and organization of a pseudo-capsule [117]. As a result, an increase in tumor volume may be observed in responders, and MRI imaging alone is insufficient to distinguish residual viable tumor from granulation tissue given that both are highly vascular and demonstrate contrast enhancement. In addition, the length of intramedullary signal abnormalities does not vary in response to chemotherapy, which results in uncertainties in the evaluation of posttreatment tumor volume response.

Approximately 20–25% of patients with bone sarcomas present with radiographically detectable distant metastases [118] with the most common site of involvement being the lungs. The primary imaging modality for evaluation of pulmonary involvement is the CT. In patients with RMS, the most common sites for metastases are the lungs, bones, and bone marrow. Given the limitation of MRI for the detection of small lung metastasis, the addition of high-resolution CT of the thorax is generally recommended in the staging of pediatric sarcoma patients. Since RMS can arise throughout the body, metastatic sites may be located outside the field of view; thus, whole-body MRI may be a helpful imaging modality for staging, although there are limited publications with respect to the pediatric population [119, 120].

Currently, whole-body FDG-PET/CT is not considered a standard examination for evaluating disease extent in sarcoma patients [121], despite the promising results from a small number of studies which found FDG-PET/CT better in identifying occult non-pulmonary metastasis compared to conventional imaging [122–125]. The study by Quartuccio et al. [126], which evaluated the diagnostic performance of FDG-PET versus conventional imaging for bone sarcoma in 64 pediatric patients (osteosarcoma 20/64 and Ewing sarcoma 44/64) at initial staging and follow-up, showed that both FDG-PET/CT and MRI were more accurate than CT and skeletal scintigraphy with [^{99m}Tc]MDP in the follow-up. In addition, the authors noted that FDG-PET/CT provided greater diagnostic benefit for ES during clinical management than for OS. In several studies, reduction in the standardized uptake value (SUV) and the absolute post-therapeutic SUV was found to significantly discriminate responders from nonresponders in pediatric osteosarcoma patients [127], but tumor volume reduction measured by MR or CT did not significantly discriminate responders from nonresponders in either subgroup.

The intensity of FDG uptake in the primary and recurrent tumor may provide additional diagnostic and prognostic information with high-grade tumors tending toward higher FDG avidity than low-grade tumors due to higher cellularity, although no established definitive SUV cutoff has been identified. Thus, the identification of areas with high FDG metabolic activity for open biopsies may potentially identify the most aggressive pathology, which may affect treatment planning and prognosis. In addition, several studies have showed significantly prolonged event-free and overall survival for osteosarcomas patients with low FDG uptake at baseline [128] with similar results for RMS.

In a pediatric oncology study using an integrated PET/MR scanner following chemotherapy, Hirsch et al. [71] showed that metabolic changes take place earlier than the morphological response. Similar results were reported on the FDG-PET/MRI study [129] for staging and restaging in pediatric rhabdomyosarcoma ($n = 15/270$), soft tissue sarcoma, and bone sarcoma ($n = 21/270$) which concluded that combined PET/MRI was the methodology of choice for accurate tumor staging. In patients with OS who were imaged with sequential FDG-PET/CT and MRI, early changes in FDG SUV or MTV were noted with corresponding changes on MRI, after one cycle of neoadjuvant chemotherapy.

In pediatric sarcomas, FDG-PET/MRI has potential roles for initial staging as illustrated in Fig. 21.7 and for evaluating tumor response during and after therapy. MRI imaging alone is limited in its ability to accurately distinguish between post-treatment changes from tumor recurrence, due to persistent morphological tissue changes. The combined metabolic imaging capabilities of PET with the superb soft tissue contrast of MRI provide relevant information on regions with complex anatomy such as the neck and pelvis, as shown in Fig. 21.8. In addition, better soft tissue resolution allows for more accurate differentiation from physiologic uptake of)ormal organs, such as ovaries, from uptake associated with malignancy, as illustrated in Fig. 21.9. In this patient, the correct diagnosis was physiologic activity in the ovaries and not bilateral FDG-avid external iliac lymphadenopathy. This diagnosis lead
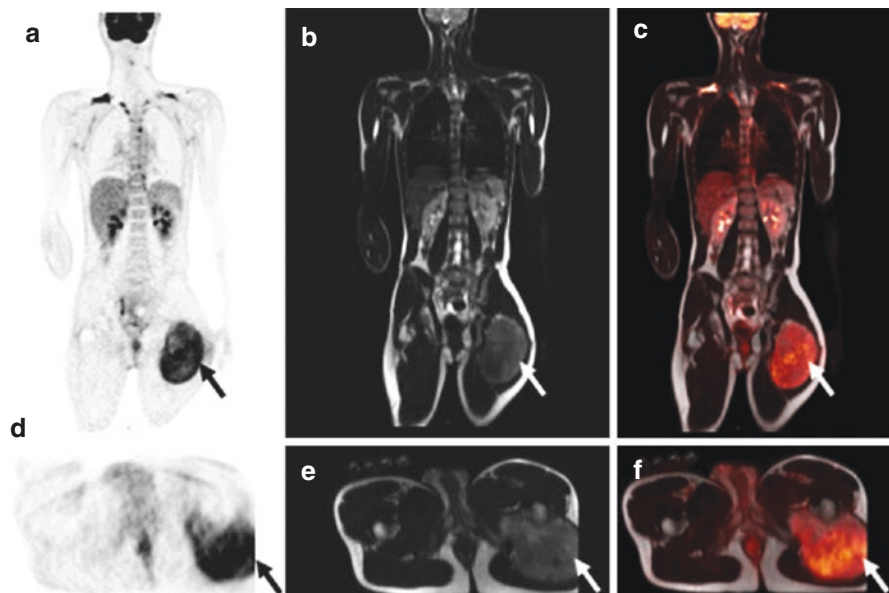

Fig. 21.7 17-year-old boy with spindle cell rhabdomyosarcoma undergoing simultaneous FDG-PET/MRI for initial staging. FDG-avid soft tissue mass is seen extending into the posterior adductor compartments of the left thigh (**a–c**) without locoregional or distant metastasis disease. Dedicated regional PET/MRI (**d–f**) demonstrates avid mass with no bone marrow infiltration. (**a, d**) FDG-PET; (**b, e**) T2 single shot fast spin echo; (**c, f**) fused FDG-PET/MRI
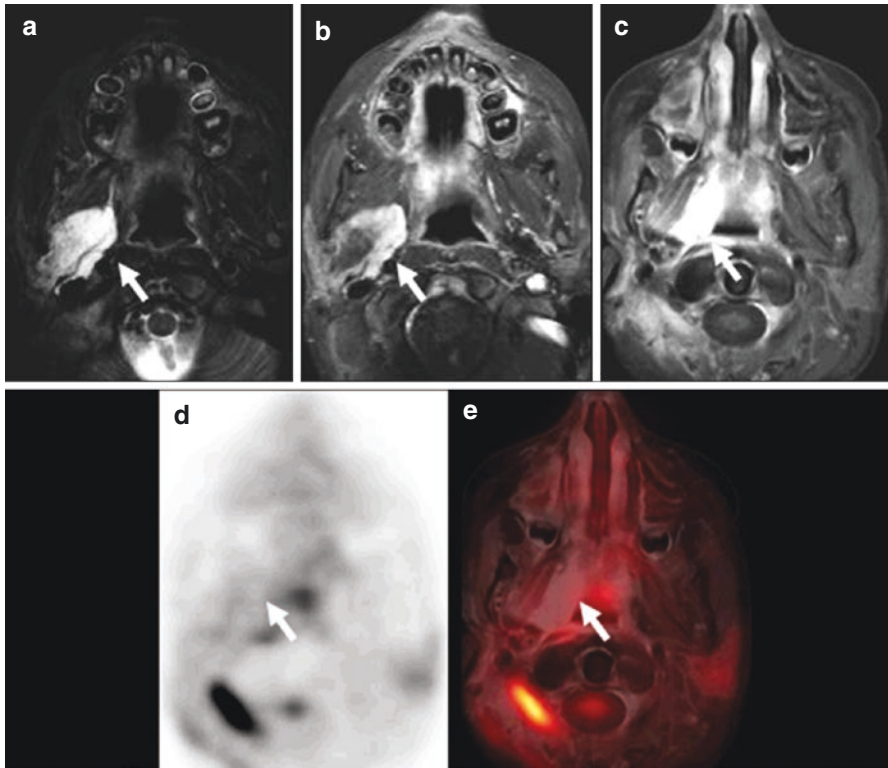
Fig. 21.8 FDG-PET/MRI performed in an 8-year-old girl with right parameningeal rhabdomyo-sarcoma before and after therapy. Neck MRI at initial presentation (**a**, **b**) and simultaneous FDG PET/MRI (**c–e**) after treatment demonstrates T2 hyperintense enhancing right parapharyngeal mass (*white arrows*). PET/MRI showed persistent increased enhancing soft tissue in the right para-pharyngeal resection bed (**c**) after resection and chemoradiation with no FDG uptake on PET (**e**), favored to represent non-viable tumor. Neck MRI (**a**) T2-weighted image; (**b**) T1-weighted image with contrast, PET/MRI; (**c**) T1-weighted images with contrast; (**d**) FDG PET; (**e**) Fused T1-weighted image with FDG PET

to a change in patient management by reducing the radiation field to exclude the pelvis and thus decreasing potential secondary treatment side effects, including pre-mature fusion of the growth plates resulting in asymmetry of muscles and bones in the treated area and infertility. For evaluation of pulmonary metastasis, a non-contrast chest CT performed before or after the PET/MRI should be included in the protocol. The role of PET/MRI for pediatric sarcomas is evolving, and more studies will be needed to document outcomes and impact on clinical patient management.

In summary, pediatric patients being assessed for bone or soft tissues tumors routinely require both PET and MR imaging. These patients are well suited for a simultaneous PET/MRI examination combining MRI for locoregional tumor stag-ing and FDG-PET for nodal and distant metastatic staging. PET/MRI superior soft tissue contrast, anatomic resolution, and functional MR techniques combined with PET metabolic imaging improve the characterization of lesions and allow for early response assessment in patients undergoing therapy.
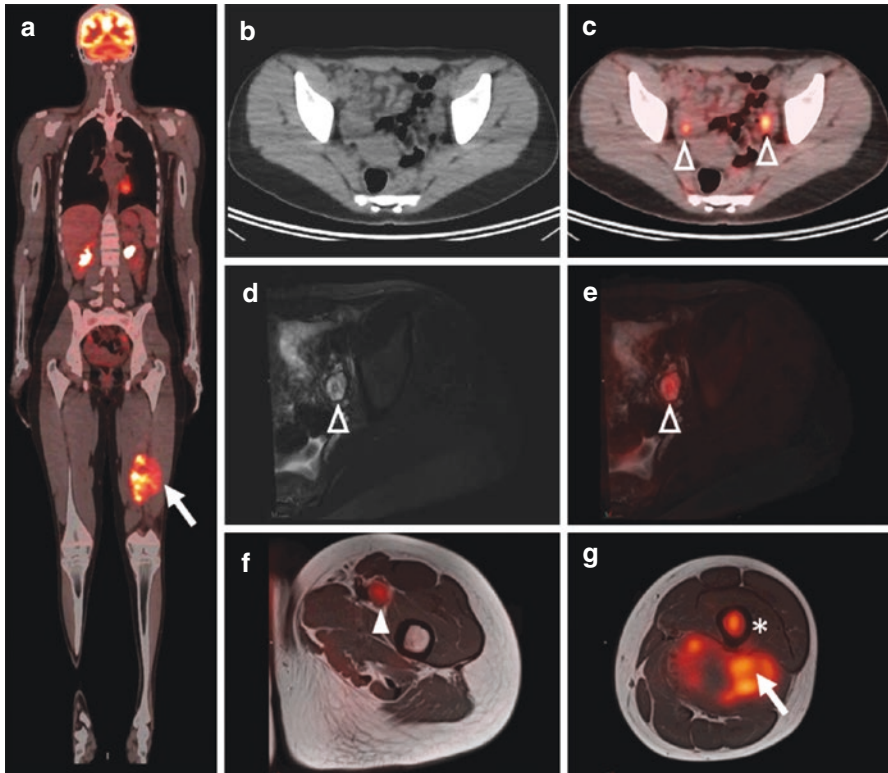
Fig. 21.9 FDG-PET/MRI performed in a 14-year-old girl with extra-osseous Ewing's sarcoma. Whole body FDG-PET/CT demonstrates FDG-avid left posterior thigh mass (**a**, *white arrow*) and bilateral foci of FDG-uptake in the pelvis (**c**, *arrowhead*), which was wrongly diagnosed as bilateral external iliac lymphadenopathy on PET/CT. MRI of the pelvis and left lower extremity demonstrates normal ovary (**d** and **e**, *open arrow head*) which corresponded to the focus of increased uptake on FDG-PET/CT. Fused sequential FDG PET and MRI show a left femoral FDG-avid regional lymph node (**f**, *white arrow head*) and the hypermetabolic extra-osseous mass (**g**, *white arrow*) with bone marrow infiltration (**g**, *asterisk*). (**a**) whole body FDG-PET/CT; (**b**) CT of FDG-PET/CT; (**c**) Fused FDG-PET/CT; (**d**) T2 weighted images; (**e–g**) fused FDG-PET with T2 and T1-weighted images (**f**, **g**)

21.8   Neuroblastoma

Neuroblastoma (NB) is the third most common childhood cancer and represents 6% of the total cases of pediatric malignancies (ages 0–14 years) [76] and is the most frequent extracranial solid tumor affecting children. The median age of diagnosis is 19 months, with 90% of the cases diagnosed in children younger than 5 years. It is rare in adolescents and adults [130]. Neuroblastoma is an embryonic tumor derived from neuroectodermal cells of the neural crest of the sympathetic nervous system. It may develop anywhere in the sympathetic nervous system, and approximately 50% of cases originate in the adrenal medulla, 30% in the paraspinal sympathetic ganglia in the abdomen, 6–7% in the neck, 15% in the chest, and 2–3% in the pelvis, respectively [131]. The variable histological, epidemiological, and biological characteristics of

neuroblastoma tumors can produce changes from spontaneous regression to maturation to more aggressive grade [132, 133]. Metastasis in neuroblastoma patients is noted in 60–70% of the cases at diagnosis [134, 135]. The most frequent metastatic sites are the bone marrow, bone and lymph nodes and to a lesser extent the liver and skin. Central nervous system and pulmonary metastases are less common, affecting more frequently adolescents, and associated with poor outcomes [136].

The treatment and outcome of neuroblastoma are strongly dependent on the patient's age, risk assessment, and disease stage. There are effective therapies for children or under 12 months of age diagnosed with low- to intermediate-risk disease, with excellent survival rates. The survival rates are much less favorable in children over the age of 12 months who present with advanced-stage disease despite the availability of multimodality therapies [133, 137]. Overall, surgical resection is the preferred treatment of localized tumors, where extensive disease requires combined therapy. Thus, accurate staging and risk stratification play an important role in patient management and prognosis.

The current diagnostic imaging examinations to stage neuroblastoma include ultrasonography (US), MRI and/or CT, and [^{123}I]MIBG planar and SPECT scintigraphy that targets the norepinephrine transporter in neuroblastoma cells. Whole-body MRI for neuroblastoma has demonstrated utility in detecting distant metastasis and bone marrow involvement [138, 139]. The major limitation of morphological imaging, including MRI, is the accurate detection of nodal metastases and assessment of tumor viability in the posttreatment setting [140]. FDG-PET and other PET tracers do not currently play a substantial role in the routine evaluation of neuroblastoma patients at most centers. Promising PET tracers for neuroblastoma include [^{124}I]MIBG, ^{68}Ga-labeled somatostatin receptor ligands, and the ^{18}F-labeled amino acid FDOPA [7, 20, 141–143].

[^{123}I]MIBG is a SPECT tracer that has been part of the standard of care for whole-body staging of neuroblastoma patients, with sensitivities over 85% and specificities over 90% [144], particularly for bone and bone marrow diseases. [^{123}I] MIBG plays a critical role in the evaluation of treatment response since MIBG uptake is seen in 90–95% of the patients with neuroblastoma [145]. MIBG imaging is overall considered more specific and superior to FDG-PET, particularly in the delineation of residual disease although [^{123}I]MIBG scintigraphy may produce false-negative results in 10–20% of cases [146, 147]. [^{124}I]MIBG could be used for PET/CT and PET/MRI, but this tracer is not currently widely available.

Currently, the role of FDG-PET is limited, although neuroblastoma demonstrates FDG uptake; its function is providing complementary diagnostic information to assess MIBG-negative tumors with positive clinical symptoms or morphological images [148, 149]. Limitations in staging neuroblastoma with FDG-PET include uptake not related to catecholamine metabolism; low sensitivity to identify bone or bone marrow involvement, which is a common site of disease; and marked changes in FDG uptake in patients receiving chemotherapy or granulocyte colony-stimulating factor (G-CSF) [147, 150].

Several publications have shown in vitro using autoradiography and immunohistochemistry the expression of somatostatin receptor in up to 77–89% in neuroblastoma cells [151, 152]. SSTRs can be targeted with ^{68}Ga-labeled peptides for PET imaging. Recent pediatric study using [^{68}Ga]DOTATE-PET/CT showed

additional sites of disease in up to 38% pediatric patients compared with MIBG [153]. A limited number of studies evaluating the use of PET for somatostatin receptor imaging in pediatric neuroblastoma selected for peptide receptor radionuclide therapy (PRRT) have been published. Preliminary results have shown that a high proportion of neuroblastoma patients (75%, 6/8 patients) have sufficient somatostatin receptor expression on their tumors to be considered for PRRT, especially in children who have failed prior treatment with chemotherapy and [131I] MIBG radionuclide therapy [154].

The radiolabeled amino acid FDOPA is also a promising PET tracer for imaging neuroblastoma. Small studies with FDOPA-PET in this patient population have reported high sensitivity and specificity of 97.6% and 87.5% [155] and sensitivity and accuracy of 95 and 96% [142] which are significantly higher than that of [123I] MIBG scintigraphy. Comparison of FDOPA-PET/CT with CT and MR demonstrated in a prospective study on 21 patients with advanced-stage neuroblastoma (III–IV) that FDOPA-PET/CT had significantly higher sensitivity, specificity, and accuracy compared to MRI and CT with higher lesion detection than CT/MRI in the bone, bone marrow, lymph node, and soft tissue recurrences [141]. An example of FDOPA-PET/MRI in neuroblastoma is shown in Fig. 21.10.
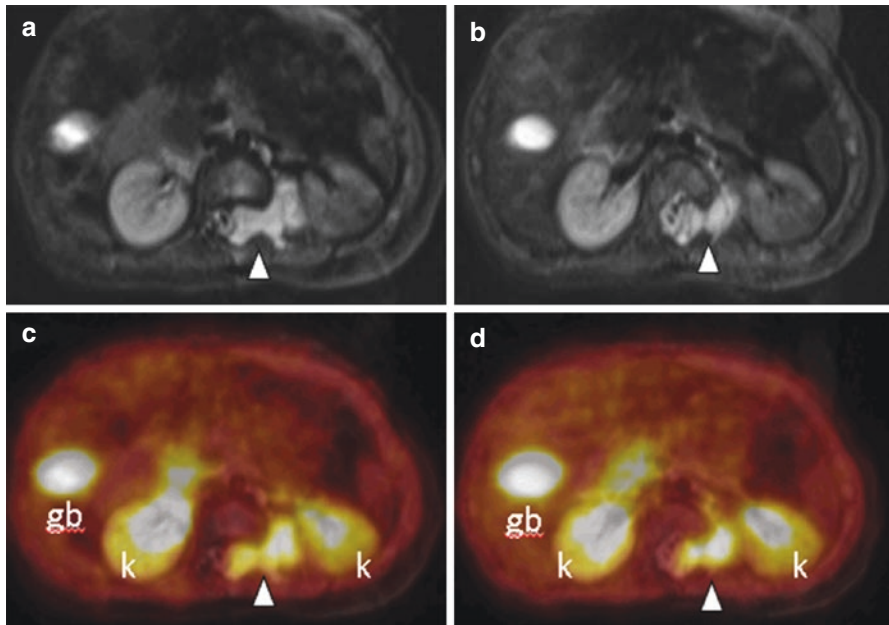

Fig. 21.10 FDOPA-PET/MRI performed in a 2-year old boy undergoing initial staging for a neuroblastoma. The T2 fat saturated MR images (**a**, **b**) show a lobulated T2 hyperintense mass involving the central spinal canal, a spinal neuroforamen and the left paraspinal region (*arrow head*) representing the primary tumor. This lesion demonstrates increased uptake of FDOPA on the fused PET/MRI images (**c**, **d**). No metastases were identified. Note the normal excreted activity in the kidneys (*k*) and gallbladder (*gb*). *This figure is courtesy of Drs. Franz Wolfgang Hirsch and Regine Kluge from the University Hospital of Leipzig, Germany.* (**a**, **b**) T2 fat sat; (**c**, **d**) fused FDOPA-PET/MRI

Pediatric PET/MRI publications of mixed cancer populations, including small sample size of patients with neuroblastoma, demonstrated that FDG-PET/MRI is equivalent to FDG-PET/CT for oncologic imaging in young children for the assessment of tumor spread and monitoring of therapeutic courses [22, 71]. Furthermore, MRI can provide additional diagnostic imaging information on lesions with inconclusive FDG uptake on PET, such as homogeneous bone marrow FDG uptake without visible findings on CT in patients with bone marrow infiltration [23]. In this context, additional MRI functional information can be implemented in standard PET/MRI protocols, such as DWI to identify bone marrow infiltration thus providing a complementary diagnostic tool.

In summary, there are a range of PET/MRI tracers including FDG, ^{68}Ga-labeled somatostatin receptor ligands, FDOPA, and [^{124}I]MIBG that have great potential for imaging neuroblastoma. However, there is limited experience with these tracers in pediatric neuroblastoma with PET/CT, and only a few publications report their use with PET/MRI. The increasing availability of [^{68}Ga]DOTATATE and similar agents coupled with the potential for PRRT targeting somatostatin receptors could help enable the near-term growth of PET/MRI for neuroblastoma.

21.9   Conclusions and Future Directions

PET/MRI is clearly a promising hybrid modality for applications in pediatric oncology through reducing exposure to ionizing radiation and providing a single examination that combines metabolic, anatomic, and functional imaging. As in adults, children that require whole-body PET for staging as well as dedicated organ/regional MRI for tumor staging may benefit from simultaneous PET/MRI. The acquisition of both PET and MRI in the same session reduces the number of sedation/aesthesia and decreases misregistration caused by patient motion or physiologic changes. However, there is a need to produce high-quality evidence to demonstrate that combined PET/MRI examinations are superior to separately acquired PET/CT and MRI studies for specific indications in pediatric oncology.

Several factors are likely to determine the level of utilization of PET/MRI for pediatric oncology. First, a major current limitation for PET/MRI for adults and children is the cost of these systems and the relatively small number of imaging and referring physicians familiar with this technology. More universal availability will require adequate reimbursement, decreased cost differential between PET/MRI and PET/CT systems, and incorporation of PET/MRI into physician and technologist training. Second, the availability and reimbursement of new PET tracers for routine clinical use will be key factors for expanding the growth of both PET/CT and PET/MRI. Strong data showing diagnostic efficacy that leads to patient management and incorporation of PET tracers and PET/MRI in nationally and internationally recognized cancer management guidelines are needed. The studies needed to generate this type of data can be challenging in pediatric oncology due to the relatively small number of pediatric cancer patients combined with the limited number of sites with PET/MRI. Finally, the most common type of pediatric malignancy is leukemia,

which typically does not include PET as part of its routine diagnostic workup. The availability of PET tracers that can detect early response to therapy beyond what is possible by blood tests and marrow biopsies would be a major advance in PET for pediatric leukemia patients. Pediatric PET/MRI is expanding and remains an active area of clinical research with the expectation that progress on many of these fronts will continue.

References

1. Smith TA. The rate-limiting step for tumor [^{18}F]fluoro-2-deoxy-D-glucose (FDG) incorporation. Nucl Med Biol. 2001;28:1–4.
2. Ganapathy V, Thangaraju M, Prasad PD. Nutrient transporters in cancer: relevance to Warburg hypothesis and beyond. Pharmacol Ther. 2009;121:29–40.
3. Potter M, Newport E, Morten KJ. The Warburg effect: 80 years on. Biochem Soc Trans. 2016;44:1499–505.
4. Huang C, McConathy J. Radiolabeled amino acids for oncologic imaging. J Nucl Med. 2013;54:1007–10.
5. Albert NL, Weller M, Suchorska B, et al. Response assessment in neuro-oncology working group and European Association for Neuro-Oncology recommendations for the clinical use of PET imaging in gliomas. Neuro-Oncology. 2016;18:1199.
6. Dunkl V, Cleff C, Stoffels G, et al. The usefulness of dynamic O-(2-^{18}F-fluoroethyl)-L-tyrosine PET in the clinical evaluation of brain tumors in children and adolescents. J Nucl Med. 2015;56:88–92.
7. Kroiss A, Putzer D, Uprimny C, et al. Functional imaging in pheochromocytoma and neuroblastoma with ^{68}Ga-DOTA-Tyr 3-octreotide positron emission tomography and ^{123}I-metaiodobenzylguanidine. Eur J Nucl Med Mol Imaging. 2011;38:865–73.
8. Hope TA, Pampaloni MH, Nakakura E, et al. Simultaneous ^{68}Ga-DOTA-TOC PET/MRI with gadoxetate disodium in patients with neuroendocrine tumor. Abdom Imaging. 2015;40:1432–40.
9. Kunz WG, Jungblut LM, Kazmierczak PM, et al. Improved detection of transosseous meningiomas using ^{68}Ga-DOTATATE PET-CT compared to contrast-enhanced MRI. J Nucl Med. 2017;58(10):1580–87. https://doi.org/10.2967/jnumed.117.191932. Epub 2017 Apr 27
10. Afshar-Oromieh A, Giesel FL, Linhart HG, et al. Detection of cranial meningiomas: comparison of ^{68}Ga-DOTATOC PET/CT and contrast-enhanced MRI. Eur J Nucl Med Mol Imaging. 2012;39:1409–15.
11. Kwekkeboom DJ, Kam BL, van Essen M, et al. Somatostatin-receptor-based imaging and therapy of gastroenteropancreatic neuroendocrine tumors. Endocr Relat Cancer. 2010;17:R53–73.
12. Strosberg J, El-Haddad G, Wolin E, et al. Phase 3 trial of ^{177}Lu-Dotatate for Midgut neuroendocrine tumors. N Engl J Med. 2017;376:125–35.
13. Archier A, Varoquaux A, Garrigue P, et al. Prospective comparison of ^{68}Ga-DOTATATE and ^{18}F-FDOPA PET/CT in patients with various pheochromocytomas and paragangliomas with emphasis on sporadic cases. Eur J Nucl Med Mol Imaging. 2016;43:1248–57.
14. Barthlen W, Blankenstein O, Mau H, et al. Evaluation of [^{18}F]fluoro-L-DOPA positron emission tomography-computed tomography for surgery in focal congenital hyperinsulinism. J Clin Endocrinol Metab. 2008;93:869–75.
15. Liu YL, Lu MY, Chang HH, et al. Diagnostic FDG and FDOPA positron emission tomography scans distinguish the genomic type and treatment outcome of neuroblastoma. Oncotarget. 2016;7:18774–86.
16. Barthlen W, Varol E, Empting S, et al. Surgery in focal congenital hyperinsulinism (CHI) - the "hyperinsulinism Germany international" experience in 30 children. Pediatr Endocrinol Rev. 2016;14:129–37.

17. Dercle L, Deandreis D, Terroir M, Leboulleux S, Lumbroso J, Schlumberger M. Evaluation of [124]I PET/CT and [124]I PET/MRI in the management of patients with differentiated thyroid cancer. Eur J Nucl Med Mol Imaging. 2016;43:1006–10.
18. Vrachimis A, Weckesser M, Schafers M, Stegger L. Imaging of differentiated thyroid carcinoma: [124]I-PET/MRI may not be superior to [124]I-PET/CT. Eur J Nucl Med Mol Imaging. 2016;43:1183–4.
19. Binse I, Poeppel TD, Ruhlmann M, et al. Imaging with [124]I in differentiated thyroid carcinoma: is PET/MRI superior to PET/CT? Eur J Nucl Med Mol Imaging. 2016;43:1011–7.
20. Cistaro A, Quartuccio N, Caobelli F, et al. [124]I-MIBG: a new promising positron-emitting radiopharmaceutical for the evaluation of neuroblastoma. Nucl Med Rev Cent East Eur. 2015;18:102–6.
21. Hartung-Knemeyer V, Rosenbaum-Krumme S, Buchbender C, et al. Malignant pheochromocytoma imaging with [[124]I]mIBG PET/MR. J Clin Endocrinol Metab. 2012;97:3833–4.
22. Gatidis S, Schmidt H, Gucke B, et al. Comprehensive oncologic imaging in infants and preschool children with substantially reduced radiation exposure using combined simultaneous ^{18}F-Fluorodeoxyglucose positron emission tomography/magnetic resonance imaging: a direct comparison to ^{18}F-Fluorodeoxyglucose positron emission tomography/computed tomography. Investig Radiol. 2016;51:7–14.
23. Schafer JF, Gatidis S, Schmidt H, et al. Simultaneous whole-body PET/MR imaging in comparison to PET/CT in pediatric oncology: initial results. Radiology. 2014;273:220–31.
24. Drzezga A, Souvatzoglou M, Eiber M, et al. First clinical experience with integrated whole-body PET/MR: comparison to PET/CT in patients with oncologic diagnoses. J Nucl Med. 2012;53:845.
25. Tian J, Fu L, Yin D, et al. Does the novel integrated PET/MRI offer the same diagnostic performance as PET/CT for oncological indications? PLoS One. 2014;9:e90844.
26. Heusch P, Buchbender C, Beiderwellen K, et al. Standardized uptake values for [^{18}F] FDG in normal organ tissues: comparison of whole-body PET/CT and PET/MRI. Eur J Radiol. 2013;82:870.
27. Spick C, Herrmann K, Czernin J. ^{18}F-FDG PET/CT and PET/MRI perform equally well in cancer: evidence from studies on more than 2,300 patients. J Nucl Med. 2016;57:420–30.
28. Eiber M, Martinez-Moller A, Souvatzoglou M, et al. Value of a Dixon-based MR/PET attenuation correction sequence for the localization and evaluation of PET-positive lesions. Eur J Nucl Med Mol Imaging. 2011;38:1691–701.
29. Rascon J, Rageliene L, Stankeviciene S, et al. An assessment of iron overload in children treated for cancer and nonmalignant hematologic disorders. Eur J Pediatr. 2014;173:1137–46.
30. Taouli B, Koh DM. Diffusion-weighted MR imaging of the liver. Radiology. 2010;254:47–66.
31. Mohd Zaki F, Moineddin R, Grant R, Chavhan GB. Accuracy of pre-contrast imaging in abdominal magnetic resonance imaging of pediatric oncology patients. Pediatr Radiol. 2016;46:1684–93.
32. Murata N, Gonzalez-Cuyar LF, Murata K, et al. Macrocyclic and other non-group 1 gadolinium contrast agents deposit low levels of gadolinium in brain and bone tissue: preliminary results from 9 patients with normal renal function. Investig Radiol. 2016;51:447–53.
33. Murata N, Murata K, Gonzalez-Cuyar LF, Maravilla KR. Gadolinium tissue deposition in brain and bone. Magn Reson Imaging. 2016;34:1359–65.
34. Klenk C, Gawande R, Uslu L, et al. Ionising radiation-free whole-body MRI versus ^{18}F-fluorodeoxyglucose PET/CT scans for children and young adults with cancer: a prospective, non-randomised, single-centre study. Lancet Oncol. 2014;15:275–85.
35. Sawicki LM, Grueneisen J, Buchbender C, et al. Evaluation of the outcome of lung nodules missed on ^{18}F-FDG PET/MRI compared with ^{18}F-FDG PET/CT in patients with known malignancies. J Nucl Med. 2016;57:15–20.
36. Raad RA, Friedman KP, Heacock L, Ponzo F, Melsaether A, Chandarana H. Outcome of small lung nodules missed on hybrid PET/MRI in patients with primary malignancy. J Magn Reson Imaging. 2016;43:504–11.
37. Lee KH, Park CM, Lee SM, et al. Pulmonary nodule detection in patients with a primary malignancy using hybrid PET/MRI: is there value in adding contrast-enhanced MR imaging? PLoS One. 2015;10:e0129660.

38. Burris NS, Johnson KM, Larson PE, et al. Detection of small pulmonary nodules with ultra-short echo time sequences in oncology patients by using a PET/MR system. Radiology. 2016;278:239–46.

39. National Research Council (U.S.) Committee to assess health risks from exposure to low level of ionizing radiation. In: Health risks from exposure to low levels of ionizing radiation: BEIR VII phase, vol. 2. Washington, DC: National Academies Press; 2006.

40. Ponisio MR, McConathy J, Laforest R, Khanna G. Evaluation of diagnostic performance of whole-body simultaneous PET/MRI in pediatric lymphoma. Pediatr Radiol. 2016;46:1258–68.

41. Sher AC, Seghers V, Paldino MJ, et al. Assessment of sequential PET/MRI in comparison with PET/CT of pediatric lymphoma: a prospective study. Am J Roentgenol. 2016;206:623–31.

42. Harrison JD, Streffer C. The ICRP protection quantities, equivalent and effective dose: their basis and application. Radiat Prot Dosim. 2007;127:12–8.

43. Valentin J. The 2007 recommendations of the international commission on radiological protection. ICRP publication 103. Ann ICRP. 2007;37:1–332.

44. ICRP. Radiation dose to patients from radiopharmaceuticals. Addendum 3 to ICRP publication 53. ICRP publication 106. Approved by the Commission in October 2007. Ann ICRP. 2008;38:1–197.

45. Raman SP, Mahesh M, Blasko RV, Fishman EK. CT scan parameters and radiation dose: practical advice for radiologists. J Am Coll Radiol. 2013;10:840–6.

46. Miglioretti DL, Johnson E, Williams A, et al. The use of computed tomography in pediatrics and the associated radiation exposure and estimated cancer risk. JAMA Pediatr. 2013;167:700–7.

47. Seith F, Schmidt H, Kunz J, et al. Simulation of tracer dose reduction in ^{18}F FDG PET/MRI: Effects on oncologic reading, image quality and artifacts. J Nucl Med. 2017;58(10):1699–1705.

48. Gatidis S, Schmidt H, la Fougere C, Nikolaou K, Schwenzer NF, Schafer JF. Defining optimal tracer activities in pediatric oncologic whole-body ^{18}F-FDG-PET/MRI. Eur J Nucl Med Mol Imaging. 2016;43:2283–9.

49. Minamimoto R, Levin C, Jamali M, et al. Improvements in PET image quality in time of flight (TOF) simultaneous PET/MRI. Mol Imaging Biol. 2016;18:776–81.

50. Kaatsch P. Epidemiology of childhood cancer. Cancer Treat Rev. 2010;36:277–85.

51. Friedman DL, Chen L, Wolden S, et al. Dose-intensive response-based chemotherapy and radiation therapy for children and adolescents with newly diagnosed intermediate-risk Hodgkin lymphoma: a report from the Children's oncology group study AHOD0031. J Clin Oncol. 2014;32:3651–8.

52. Mauz-Korholz C, Metzger ML, Kelly KM, et al. Pediatric Hodgkin lymphoma. J Clin Oncol. 2015;33:2975–85.

53. Burkhardt B, Zimmermann M, Oschlies I, et al. The impact of age and gender on biology, clinical features and treatment outcome of non-Hodgkin lymphoma in childhood and adolescence. Br J Haematol. 2005;131:39–49.

54. Bhatia S, Yasui Y, Robison LL, et al. High risk of subsequent neoplasms continues with extended follow-up of childhood Hodgkin's disease: report from the late effects study group. J Clin Oncol. 2003;21:4386–94.

55. Constine LS, Tarbell N, Hudson MM, et al. Subsequent malignancies in children treated for Hodgkin's disease: associations with gender and radiation dose. Int J Radiat Oncol Biol Phys. 2008;72:24–33.

56. Dores GM, Metayer C, Curtis RE, et al. Second malignant neoplasms among long-term survivors of Hodgkin's disease: a population-based evaluation over 25 years. J Clin Oncol. 2002;20:3484–94.

57. Bhakta N, Liu Q, Yeo F, et al. Cumulative burden of cardiovascular morbidity in paediatric, adolescent, and young adult survivors of Hodgkin's lymphoma: an analysis from the St Jude lifetime cohort study. Lancet Oncol. 2016;17:1325–34.

58. Littooij AS, Kwee TC, Enriquez G, et al. Whole-body MRI reveals high incidence of osteonecrosis in children treated for Hodgkin lymphoma. Br J Haematol. 2017;176:637–42.

59. Guimaraes MD, Noschang J, Teixeira SR, et al. Whole-body MRI in pediatric patients with cancer. Cancer Imaging. 2017;17:6.

60. Siegel MJ, Acharyya S, Hoffer FA, et al. Whole-body MR imaging for staging of malignant tumors in pediatric patients: results of the American College of Radiology Imaging Network 6660 trial. Radiology. 2013;266:599–609.

61. Kwee TC, Takahara T, Ochiai R, et al. Complementary roles of whole-body diffusion-weighted MRI and ^{18}F-FDG PET: the state of the art and potential applications. J Nucl Med. 2010;51:1549–58.

62. Kwee TC, Takahara T, Luijten PR, Nievelstein RA. ADC measurements of lymph nodes: inter- and intra-observer reproducibility study and an overview of the literature. Eur J Radiol. 2010;75:215–20.

63. Herrmann K, Queiroz M, Huellner MW, et al. Diagnostic performance of FDG-PET/MRI and WB-DW-MRI in the evaluation of lymphoma: a prospective comparison to standard FDG-PET/CT. BMC Cancer. 2015;15:1002.

64. Weiler-Sagie M, Bushelev O, Epelbaum R, et al. ^{18}F-FDG avidity in lymphoma readdressed: a study of 766 patients. J Nucl Med. 2010;51:25–30.

65. Montravers F, McNamara D, Landman-Parker J, et al. [^{18}F]FDG in childhood lymphoma: clinical utility and impact on management. Eur J Nucl Med Mol Imaging. 2002;29:1155–65.

66. Hermann S, Wormanns D, Pixberg M, et al. Staging in childhood lymphoma: differences between FDG-PET and CT. Nuklearmedizin. 2005;44:1–7.

67. London K, Cross S, Onikul E, Dalla-Pozza L, Howman-Giles R. ^{18}F-FDG PET/CT in paediatric lymphoma: comparison with conventional imaging. Eur J Nucl Med Mol Imaging. 2011;38:274–84.

68. Furth C, Steffen IG, Amthauer H, et al. Early and late therapy response assessment with [^{18}F] fluorodeoxyglucose positron emission tomography in pediatric Hodgkin's lymphoma: analysis of a prospective multicenter trial. J Clin Oncol. 2009;27:4385–91.

69. Furth C, Meseck RM, Steffen IG, et al. SUV-measurements and patient-specific corrections in pediatric Hodgkin-lymphoma: is there a benefit for PPV in early response assessment by FDG-PET? Pediatr Blood Cancer. 2012;59:475–80.

70. Lyons K, Seghers V, Sorensen JI, et al. Comparison of standardized uptake values in normal structures between PET/CT and PET/MRI in a tertiary pediatric hospital: a prospective study. Am J Roentgenol. 2015;205:1094–101.

71. Hirsch FW, Sattler B, Sorge I, et al. PET/MR in children. Initial clinical experience in paediatric oncology using an integrated PET/MR scanner. Pediatr Radiol. 2013;43:860–75.

72. Punwani S, Taylor SA, Saad ZZ, et al. Diffusion-weighted MRI of lymphoma: prognostic utility and implications for PET/MRI? Eur J Nucl Med Mol Imaging. 2013;40:373–85.

73. Afaq A, Fraioli F, Sidhu H, et al. Comparison of PET/MRI with PET/CT in the evaluation of disease status in lymphoma. Clin Nucl Med. 2017;42:e1–7.

74. Radbruch A, Weberling LD, Kieslich PJ, et al. Gadolinium retention in the dentate nucleus and globus pallidus is dependent on the class of contrast agent. Radiology. 2015;275:783–91.

75. Kirchner J, Deuschl C, Schweiger B, et al. Imaging children suffering from lymphoma: an evaluation of different ^{18}F-FDG PET/MRI protocols compared to whole-body DW-MRI. Eur J Nucl Med Mol Imaging. 2017;44:1742.

76. American Cancer Society. Cancer facts & figures 2017. Atlanta: American Cancer Society; 2017.

77. Louis DN, Perry A, Reifenberger G, et al. The 2016 World Health Organization classification of tumors of the central nervous system: a summary. Acta Neuropathol. 2016;131:803–20.

78. Calcagni ML, Galli G, Giordano A, et al. Dynamic O-(2-[^{18}F]fluoroethyl)-L-tyrosine (F-18 FET) PET for glioma grading: assessment of individual probability of malignancy. Clin Nucl Med. 2011;36:841–7.

79. Popperl G, Kreth FW, Mehrkens JH, et al. FET PET for the evaluation of untreated gliomas: correlation of FET uptake and uptake kinetics with tumour grading. Eur J Nucl Med Mol Imaging. 2007;34:1933–42.

80. Pöpperl G, Kreth FW, Herms J, et al. Analysis of ^{18}F-FET PET for grading of recurrent gliomas: is evaluation of uptake kinetics superior to standard methods? J Nucl Med. 2006;47:393–403.

81. Galldiks N, Rapp M, Stoffels G, Dunkl V, Sabel M, Langen KJ. Earlier diagnosis of progressive disease during bevacizumab treatment using O-(2-^{18}F-fluorethyl)-L-tyrosine positron emission tomography in comparison with magnetic resonance imaging. Mol Imaging. 2013;12:273–6.

82. Galldiks N, Stoffels G, Filss CP, et al. Role of O-(2-18F-fluoroethyl)-L-tyrosine PET for differentiation of local recurrent brain metastasis from radiation necrosis. J Nucl Med. 2012;53:1367–74.

83. Zukotynski K, Fahey F, Kocak M, et al. 18F-FDG PET and MR imaging associations across a spectrum of pediatric brain tumors: a report from the pediatric brain tumor consortium. J Nucl Med. 2014;55:1473–80.

84. Patil S, Biassoni L, Borgwardt L. Nuclear medicine in pediatric neurology and neurosurgery: epilepsy and brain tumors. Semin Nucl Med. 2007;37:357–81.

85. Pirotte BJ, Lubansu A, Massager N, et al. Clinical impact of integrating positron emission tomography during surgery in 85 children with brain tumors. J Neurosurg Pediatr. 2010;5(5):486–99.

86. Pirotte BJ, Lubansu A, Massager N, Wikler D, Goldman S, Levivier M. Results of positron emission tomography guidance and reassessment of the utility of and indications for stereotactic biopsy in children with infiltrative brainstem tumors. J Neurosurg. 2007;107:392–9.

87. Torrens M, Malamitsi J, Karaiskos P, et al. Although non-diagnostic between necrosis and recurrence, FDG PET/CT assists management of brain tumours after radiosurgery. In Vivo. 2016;30:513–20.

88. Tan H, Chen L, Guan Y, Lin X. Comparison of MRI, F-18 FDG, and 11C-choline PET/CT for their potentials in differentiating brain tumor recurrence from brain tumor necrosis following radiotherapy. Clin Nucl Med. 2011;36:978–81.

89. Hustinx R, Pourdehnad M, Kaschten B, Alavi A. PET imaging for differentiating recurrent brain tumor from radiation necrosis. Radiol Clin N Am. 2005;43:35–47.

90. Dankbaar JW, Snijders TJ, Robe PA, et al. The use of 18F-FDG PET to differentiate progressive disease from treatment induced necrosis in high grade glioma. J Neuro-Oncol. 2015;125:167–75.

91. Nihashi T, Dahabreh IJ, Terasawa T. Diagnostic accuracy of PET for recurrent glioma diagnosis: a meta-analysis. Am J Neuroradiol. 2013;34:944–50. S1–11

92. Haining Z, Kawai N, Miyake K, et al. Relation of LAT1/4F2hc expression with pathological grade, proliferation and angiogenesis in human gliomas. BMC Clin Pathol. 2012;12:4.

93. Nawashiro H, Otani N, Shinomiya N, et al. L-type amino acid transporter 1 as a potential molecular target in human astrocytic tumors. Int J Cancer. 2006;119:484–92.

94. Nawashiro H, Otani N, Uozumi Y, et al. High expression of L-type amino acid transporter 1 in infiltrating glioma cells. Brain Tumor Pathol. 2005;22:89–91.

95. Suchorska B, Jansen NL, Linn J, et al. Biological tumor volume in 18FET-PET before radiochemotherapy correlates with survival in GBM. Neurology. 2015;84:710–9.

96. Kratochwil C, Combs SE, Leotta K, et al. Intra-individual comparison of 18F-FET and 18F-DOPA in PET imaging of recurrent brain tumors. Neuro-Oncology. 2014;16:434–40.

97. Pauleit D, Stoffels G, Bachofner A, et al. Comparison of 18F-FET and 18F-FDG PET in brain tumors. Nucl Med Biol. 2009;36:779–87.

98. Miyake K, Shinomiya A, Okada M, Hatakeyama T, Kawai N, Tamiya T. Usefulness of FDG, MET and FLT-PET studies for the management of human gliomas. J Biomed Biotechnol. 2012;2012:205818.

99. Galldiks N, Ullrich R, Schroeter M, Fink GR, Kracht LW. Volumetry of [11C]-methionine PET uptake and MRI contrast enhancement in patients with recurrent glioblastoma multiforme. Eur J Nucl Med Mol Imaging. 2009;37:84.

100. Juhasz C, Dwivedi S, Kamson DO, Michelhaugh SK, Mittal S. Comparison of amino acid positron emission tomographic radiotracers for molecular imaging of primary and metastatic brain tumors. Mol Imaging. 2014;13:7290201400015.

101. Grosu AL, Astner ST, Riedel E, et al. An interindividual comparison of O-(2-[18F]fluoroethyl)-L-tyrosine (FET)- and L-[methyl-11C]methionine (MET)-PET in patients with brain gliomas and metastases. Int J Radiat Oncol Biol Phys. 2011;81:1049–58.

102. Becherer A, Karanikas G, Szabo M, et al. Brain tumour imaging with PET: a comparison between [18F]fluorodopa and [11C]methionine. Eur J Nucl Med Mol Imaging. 2003;30:1561–7.

103. Pirotte B, Levivier M, Morelli D, et al. Positron emission tomography for the early postsurgical evaluation of pediatric brain tumors. Childs Nerv Syst. 2005;21:294–300.
104. Pirotte B, Goldman S, Van Bogaert P, et al. Integration of [11C]methionine-positron emission tomographic and magnetic resonance imaging for image-guided surgical resection of infiltrative low-grade brain tumors in children. Neurosurgery. 2005;57:128–39. discussion 128–139
105. Pirotte B, Goldman S, Dewitte O, et al. Integrated positron emission tomography and magnetic resonance imaging-guided resection of brain tumors: a report of 103 consecutive procedures. J Neurosurg. 2006;104:238–53.
106. Misch M, Guggemos A, Driever PH, et al. 18F-FET-PET guided surgical biopsy and resection in children and adolescence with brain tumors. Childs Nerv Syst. 2015;31:261–7.
107. Preuss M, Werner P, Barthel H, et al. Integrated PET/MRI for planning navigated biopsies in pediatric brain tumors. Childs Nerv Syst. 2014;30:1399–403.
108. Gauvain K, Ponisio MR, Barone A, et al. 18F-FDOPA PET/MRI for monitoring early response to bevacizumab in children with recurrent brain tumors: initial experience Neuro-Oncology Pract. 2017. https://doi.org/10.1093/nop/npx008.
109. Bakhshi S, Radhakrishnan V. Prognostic markers in osteosarcoma. Expert Rev Anticancer Ther. 2010;10:271–87.
110. Crist WM, Anderson JR, Meza JL, et al. Intergroup rhabdomyosarcoma study-IV: results for patients with nonmetastatic disease. J Clin Oncol. 2001;19:3091–102.
111. Gorlick R, Janeway K, Lessnick S, Randall RL, Marina N, Committee COGBT. Children's oncology group's 2013 blueprint for research: bone tumors. Pediatr Blood Cancer. 2013;60:1009–15.
112. Bacci G, Ferrari S, Bertoni F, et al. Prognostic factors in nonmetastatic Ewing's sarcoma of bone treated with adjuvant chemotherapy: analysis of 359 patients at the Istituto Ortopedico Rizzoli. J Clin Oncol. 2000;18:4–11.
113. Sung L, Anderson JR, Donaldson SS, et al. Late events occurring five years or more after successful therapy for childhood rhabdomyosarcoma: a report from the soft tissue sarcoma committee of the Children's oncology group. Eur J Cancer. 2004;40:1878–85.
114. Rodeberg DA, Garcia-Henriquez N, Lyden ER, et al. Prognostic significance and tumor biology of regional lymph node disease in patients with rhabdomyosarcoma: a report from the Children's oncology group. J Clin Oncol. 2011;29:1304–11.
115. van Geel AN, Wyrdeman HK, Seynaeve C, et al. Practice guideline 'Diagnostic techniques for soft tissue tumours and treatment of soft tissue sarcomas (revision)'. Ned Tijdschr Geneeskd. 2005;149:924–8.
116. Brisse H, Ollivier L, Edeline V, et al. Imaging of malignant tumours of the long bones in children: monitoring response to neoadjuvant chemotherapy and preoperative assessment. Pediatr Radiol. 2004;34:595–605.
117. Pan G, Raymond AK, Carrasco CH, et al. Osteosarcoma: MR imaging after preoperative chemotherapy. Radiology. 1990;174:517–26.
118. Marina N, Gebhardt M, Teot L, Gorlick R. Biology and therapeutic advances for pediatric osteosarcoma. Oncologist. 2004;9:422–41.
119. Kellenberger CJ, Miller SF, Khan M, Gilday DL, Weitzman S, Babyn PS. Initial experience with FSE STIR whole-body MR imaging for staging lymphoma in children. Eur Radiol. 2004;14:1829–41.
120. Daldrup-Link HE, Franzius C, Link TM, et al. Whole-body MR imaging for detection of bone metastases in children and young adults: comparison with skeletal scintigraphy and FDG PET. Am J Roentgenol. 2001;177:229–36.
121. Weiser DA, Kaste SC, Siegel MJ, Adamson PC. Imaging in childhood cancer: a Society for Pediatric Radiology and Children's oncology group joint task force report. Pediatr Blood Cancer. 2013;60:1253–60.
122. Kneisl JS, Patt JC, Johnson JC, Zuger JH. Is PET useful in detecting occult nonpulmonary metastases in pediatric bone sarcomas? Clin Orthop Relat Res. 2006;450:101–4.
123. Ricard F, Cimarelli S, Deshayes E, Mognetti T, Thiesse P, Giammarile F. Additional benefit of F-18 FDG PET/CT in the staging and follow-up of pediatric rhabdomyosarcoma. Clin Nucl Med. 2011;36:672–7.

124. Buchbender C, Heusner TA, Lauenstein TC, Bockisch A, Antoch G. Oncologic PET/MRI, part 2: bone tumors, soft-tissue tumors, melanoma, and lymphoma. J Nucl Med. 2012;53:1244–52.
125. London K, Stege C, Cross S, et al. ^{18}F-FDG PET/CT compared to conventional imaging modalities in pediatric primary bone tumors. Pediatr Radiol. 2012;42:418–30.
126. Quartuccio N, Fox J, Kuk D, et al. Pediatric bone sarcoma: diagnostic performance of ^{18}F-FDG PET/CT versus conventional imaging for initial staging and follow-up. Am J Roentgenol. 2015;204:153–60.
127. Denecke T, Hundsdorfer P, Misch D, et al. Assessment of histological response of paediatric bone sarcomas using FDG PET in comparison to morphological volume measurement and standardized MRI parameters. Eur J Nucl Med Mol Imaging. 2010;37:1842–53.
128. Franzius C, Bielack S, Flege S, Sciuk J, Jurgens H, Schober O. Prognostic significance of ^{18}F-FDG and ^{99m}Tc-methylene diphosphonate uptake in primary osteosarcoma. J Nucl Med. 2002;43:1012–7.
129. Pfluger T, Melzer HI, Mueller WP, et al. Diagnostic value of combined ^{18}F-FDG PET/MRI for staging and restaging in paediatric oncology. Eur J Nucl Med Mol Imaging. 2012;39:1745–55.
130. Parodi S, Haupt R. The epidemiology of neuroblastoma. New York: Nova Biomedical; 2009.
131. Gutierrez JC, Fischer AC, Sola JE, Perez EA, Koniaris LG. Markedly improving survival of neuroblastoma: a 30-year analysis of 1,646 patients. Pediatr Surg Int. 2007;23:637–46.
132. Matthay KK, Maris JM, Schleiermacher G, et al. Neuroblastoma. Nat Rev Dis Prim. 2016;2:16078.
133. Maris JM, Hogarty MD, Bagatell R, Cohn SL. Neuroblastoma. Lancet. 2007;369:2106–20.
134. Servaes S, Epelman M, Pollock A, Shekdar K. Pediatric malignancies: synopsis of current imaging techniques. Cancer Treat Res. 2008;143:469–91.
135. Sharp SE, Parisi MT, Gelfand MJ, Yanik GA, Shulkin BL. Functional-metabolic imaging of neuroblastoma. Q J Nucl Med Mol Imaging. 2013;57:6–20.
136. Conte M, De Bernardi B, Milanaccio C, et al. Malignant neuroblastic tumors in adolescents. Cancer Lett. 2005;228:271–4.
137. Modak S, Cheung NK. Neuroblastoma: therapeutic strategies for a clinical enigma. Cancer Treat Rev. 2010;36:307–17.
138. Goo HW. Whole-body MRI of neuroblastoma. Eur J Radiol. 2010;75:306–14.
139. Goo HW, Choi SH, Ghim T, Moon HN, Seo JJ. Whole-body MRI of paediatric malignant tumours: comparison with conventional oncological imaging methods. Pediatr Radiol. 2005;35:766–73.
140. Mueller WP, Coppenrath E, Pfluger T. Nuclear medicine and multimodality imaging of pediatric neuroblastoma. Pediatr Radiol. 2013;43:418–27.
141. Lopci E, Piccardo A, Nanni C, et al. ^{18}F-DOPA PET/CT in neuroblastoma: comparison of conventional imaging with CT/MR. Clin Nucl Med. 2012;37:e73–8.
142. Piccardo A, Lopci E, Conte M, et al. Comparison of ^{18}F-dopa PET/CT and ^{123}I-MIBG scintigraphy in stage 3 and 4 neuroblastoma: a pilot study. Eur J Nucl Med Mol Imaging. 2012;39:57–71.
143. Ambrosini V, Morigi JJ, Nanni C, Castellucci P, Fanti S. Current status of PET imaging of neuroendocrine tumours ([^{18}F]FDOPA, [^{68}Ga]tracers, [^{11}C]/[^{18}F]-HTP). Q J Nucl Med Mol Imaging. 2015;59:58–69.
144. Brodeur GM, Pritchard J, Berthold F, et al. Revisions of the international criteria for neuroblastoma diagnosis, staging, and response to treatment. J Clin Oncol. 1993;11:1466–77.
145. Kushner BH. Neuroblastoma: a disease requiring a multitude of imaging studies. J Nucl Med. 2004;45:1172–88.
146. Taggart DR, Han MM, Quach A, et al. Comparison of iodine-123 metaiodobenzylguanidine (MIBG) scan and [^{18}F]fluorodeoxyglucose positron emission tomography to evaluate response after iodine-131 MIBG therapy for relapsed neuroblastoma. J Clin Oncol. 2009;27:5343–9.
147. Sharp SE, Shulkin BL, Gelfand MJ, Salisbury S, Furman WL. ^{123}I-MIBG scintigraphy and ^{18}F-FDG PET in neuroblastoma. J Nucl Med. 2009;50:1237–43.
148. Stauss J, Franzius C, Pfluger T, et al. Guidelines for ^{18}F-FDG PET and PET-CT imaging in paediatric oncology. Eur J Nucl Med Mol Imaging. 2008;35:1581–8.

149. Uslu L, Donig J, Link M, Rosenberg J, Quon A, Daldrup-Link HE. Value of ^{18}F-FDG PET and PET/CT for evaluation of pediatric malignancies. J Nucl Med. 2015;56:274–86.
150. Shulkin BL, Hutchinson RJ, Castle VP, Yanik GA, Shapiro B, Sisson JC. Neuroblastoma: positron emission tomography with 2-[fluorine-18]-fluoro-2-deoxy-D-glucose compared with metaiodobenzylguanidine scintigraphy. Radiology. 1996;199:743–50.
151. Georgantzi K, Tsolakis AV, Stridsberg M, Jakobson A, Christofferson R, Janson ET. Differentiated expression of somatostatin receptor subtypes in experimental models and clinical neuroblastoma. Pediatr Blood Cancer. 2011;56:584–9.
152. Maggi M, Baldi E, Finetti G, et al. Identification, characterization, and biological activity of somatostatin receptors in human neuroblastoma cell lines. Cancer Res. 1994;54:124–33.
153. Kong G, Hofman MS, Murray WK, et al. Initial experience with Gallium-68 DOTA-octreotate PET/CT and peptide receptor radionuclide therapy for pediatric patients with refractory metastatic neuroblastoma. J Pediatr Hematol Oncol. 2016;38:87–96.
154. Gains JE, Bomanji JB, Fersht NL, et al. ^{177}Lu-DOTATATE molecular radiotherapy for childhood neuroblastoma. J Nucl Med. 2011;52:1041–7.
155. Lu MY, Liu YL, Chang HH, et al. Characterization of neuroblastic tumors using ^{18}F-FDOPA PET. J Nucl Med. 2013;54:42–9.

PET/MRI: Future Directions

Since its introduction in 2011, simultaneous PET/MRI already underwent several technological advances, including the addition of time-of-flight enabled PET detectors. The technology and its clinical adoption are now at a stage where continued growth is expected. This growth will most likely be the result of continuous research and development efforts, novel PET radiopharmaceuticals, and MR pulses opening new clinical indications. Based on the developments in new PET detector technology, clinical workflow and protocols are likely to continue to change. Examples here are significantly reduced dosages of PET radiopharmaceuticals to establish PET/MRI additionally as a single-station, problem-solving tool even in "radiation-sensitive" oncological areas as discussed in this book and the integration of MR-multiband techniques to significantly shorten MRI examination times. Hence, PET/MRI may be adopted by larger numbers of non-oncological indications such as evaluation of pain, cardiology, musculoskeletal conditions. This approach will improve the cost-effectiveness of these systems as well.

Additionally, new biological targets can be imaged, addressing a diverse range of processes, such as angiogenesis, apoptosis, fatty acid metabolism, and growth factor receptor expression. Another important step are upcoming radiopharmaceuticals for immunology since this is one of the main pillars of current therapy strategies in oncology.

Although clinical integration of PET/MRI in clinical routine is currently somewhat slower than expected, PET/MR and, certainly similarly important, hybrid imaging in general are likely to gain even more momentum in clinical use with the above-mentioned improvements. Increased accessibility and usability is expected internationally, even in countries with currently limited PET imaging.

As an established technology with advantages in terms of access, cost, speed, and familiarity, PET/CT scanners are unlikely to be replaced by PET/MRI on a one-to-one basis in the near term. Recognizing the advantages of PET/MRI, which include decreased radiation dose, improved motion correction, the convenience of a combined exam and having a multitude of simultaneous MR-techniques for quantification, it is the role of the imaging community to determine where PET/MRI will add the greatest value. Overall, the future of PET/MRI is promising but the precise role that PET/MRI will play remains to be determined. We hope this book will serve as a starting point for everyone involved in the scientific debate regarding the future use of PET/MRI in Oncology.